Dynamics of the McArthur Basin diagenetic/hydrothermal system (Australia) : Timing and nature of fluid flow and constraints on the distribution of mineral resources (U, Cu, Pb-Zn)

Joséphine Gigon

Ecole Doctorale SIReNa (Science et Ingénierie des Ressources Naturelles)

Thèse

Présentée et soutenue publiquement pour l'obtention du titre de
Docteur de l'Université de Lorraine (Nancy)
Mention « Géosciences »

par **Joséphine GIGON**

Dynamique du système diagénétique/hydrothermal du bassin de McArthur (Australie): nature des fluides, datations et contraintes sur la distribution des ressources métalliques (U, Cu, Pb-Zn)

Dynamics of the McArthur Basin diagenetic/hydrothermal system (Australia): Timing and nature of fluid flow and constraints on the distribution of mineral resources (U, Cu, Pb-Zn)

---

15 novembre 2019

Membres du jury:

Rapporteurs:

M Murray W. HITZMAN	Directeur, Irish Centre for Research in Applied Geosciences, Dublin, Irlande
M Ferenc MOLNAR	Professeur, Geological Survey of Finland, Espoo, Finlande

Examinateurs:

Mme Isabelle DUHAMEL-ACHIN	Responsable de l'unité MIN, BRGM, Orléans, France
Mme Sophie DECREE	Chargée de recherche, Geological Survey of Belgium, Brussels, Belgique
Mme Anne-Sylvie ANDRE-MAYER	Professeur, Université de Lorraine, Nancy, France
M Roger G. SKIRROW	Chef de projets de recherche, Geoscience Australia, Canberra, Australie
M Irvine R. ANNESLEY	Professeur, Université de Lorraine, Nancy, France, directeur de thèse
M Antonin RICHARD	Maître de Conférences, Université de Lorraine, Nancy, France, co-directeur de thèse

Membres invités:

M Julien MERCADIER	Chargé de recherche, CNRS, Nancy, France
M Rémy CHEMILLAC	Ingénieur, Direction des Géosciences, Orano Mining, Courbevoie, France

UMR 7359 GeoRessources, Université de Lorraine
Faculté des Sciences et Technologies, Rue Jacques Callot, BP 70239
54506 Vandœuvre-lès-Nancy CEDEX – France

Résumé

Le bassin sédimentaire de McArthur (Northern Territory et Queensland, Australie) est associé à de nombreuses minéralisations diagénétiques/hydrothermales en uranium, cuivre, plomb et zinc dont certains gisements de classe mondiale (ex : Ranger et McArthur River). Certains gisements correspondent à des types de minéralisation bien définis (ex : uranium de type discordance, plomb-zinc de type Sediment-Hosted Massive Sulphide « SHMS »), d'autres ne sont pas reliés à un type précis. Un épisode minéralisateur majeur vers 1650-1600 Ma est reconnu dans les gisements d'uranium au nord (Alligator Rivers Uranium Field – ARUF) et au sud (Westmoreland) du bassin et en plomb-zinc dans le centre (Batten Fault Zone) et a participé au stock métallifère exceptionnel du bassin. De plus, s'il n'est pas établi que les fluides responsables des minéralisations en uranium et plomb-zinc sont de même origine, leurs caractéristiques en termes de température et salinité sont similaires. Cette thèse propose de s'intéresser aux principaux facteurs contrôlant la distribution des ressources métalliques à grande échelle dans ce bassin sédimentaire intracratonique, en étudiant les minéralisations avec une approche essentiellement géochronologique et géochimique et en caractérisant les fluides associés afin de définir leur âge, leur température et certaines de leurs conditions de mise en place.

Une synthèse des données d'inclusions fluides et la détermination de leur composition en gaz rares (Ar, Kr, Xe) et en halogènes (Cl, Br, I) indiquent que des saumures chlorurées sodi-calciques d'origine évaporitique et des fluides peu salés probablement d'origine météorique ont été impliqués dans les minéralisations en uranium de l'ARUF et de la zone de Westmoreland. Cette conclusion est corroborée par l'analyse géochimique et isotopique des tourmalines magnésiennes du gisement de Ranger (ARUF) permettant de relier le métasomatisme à bore et magnésium, caractéristique des altérations proximales de la minéralisation, aux interactions entre les saumures évaporitiques et le socle cristallin. En revanche, l'étude détaillée de la minéralisation uranifère de la zone de Westmoreland (âges U-Pb, teneurs en terres rares, composition des chlorites) montre une dynamique de mise en place différente des processus typiques des gisements de type « discordance » de la zone de ARUF, une importance moindre des interactions entre les fluides minéralisateurs et le socle et une succession d'évènements minéralisateurs possiblement entre 1650 et 350 Ma.

La composition isotopique du plomb des galènes de différentes lentilles minéralisées du gisement McArthur River de type SHMS met en évidence l'implication de deux réservoirs crustaux felsiques en tant que sources de plomb. Ces deux réservoirs ont été mobilisés de manière synchrone et répétée par des fluides hydrothermaux vers 1640 Ma pour former les différentes lentilles. D'autres gisements ou indices enregistrent plusieurs épisodes plus récents (jusqu'à environ 1300 Ma) qui impliquent un mélange entre trois sources de plomb. La signature géochimique des sphalérites et galènes de ces gisements ou indices à plomb-zinc traduit notamment des températures de formation décroissantes pour les épisodes successifs (de 220 °C environ à moins de 100 °C).

En plus de l'épisode majeur vers 1650-1600 Ma, l'histoire métallogénique du bassin montre de nombreuses autres évidences de cristallisation ou de remobilisation du stock de métaux. Certains épisodes de circulation des fluides sont à relier à des grands évènements géodynamiques, comme des inversions du bassin ou des orogenèses situées à des centaines de kilomètres de la zone d'étude. Il semble que les migrations à grande échelle des fluides minéralisateurs (horizontale dans les grands aquifères gréseux, et verticale dans les zones de failles majeures) ont permis la mobilisation des métaux dans différents réservoirs du bassin et du socle et leur précipitation sélective dans des zones favorables.

Abstract

The sedimentary McArthur Basin (Northern Territory and Queensland, Australia) is associated with numerous diagenetic/hydrothermal uranium, copper, lead and zinc concentrations, including some world-class deposits (e.g., Ranger and McArthur River). Some deposits correspond to styles of mineralisation well defined such as unconformity-type for uranium and Sediment-Hosted Massive Sulphide (SHMS) for lead-zinc, but others are not linked to a specific type. A major mineralising event at around 1650-1600 Ma is recorded in the uranium deposits in the North (Alligator Rivers Uranium Field – ARUF) and South (Westmoreland) parts of the basin and in lead-zinc deposits in the centre (Batten Fault Zone), and accounted for the exceptional metalliferous stock of the basin. In addition, even if it has not been established that the fluids responsible for uranium and lead-zinc mineralisation share a common origin, their characteristics in terms of temperature and salinity are similar. This PhD focused on the major factors controlling metals resources distribution at a large scale in this intracratonic sedimentary basin by studying the mineralisation with a geochronological and geochemical approach, and by characterising the associated fluids in order to define its age, temperature and emplacement conditions.

A synthesis of fluid inclusions and the determination of their noble gas (Ar, Kr, Xe) and halogen (Cl, Br, I) composition indicate that Na-Ca-brines of evaporitic origin and low-salinity fluids probably of meteoric origin have been involved in the uranium mineralisation in the ARUF and the Westmoreland area. This is confirmed by geochemical and isotopic analyses of the Mg-rich tourmaline from the Ranger deposit (ARUF) that link the boron and magnesium metasomatism, a fingerprint of the mineralisation proximal alterations, to the interactions between evaporitic brines and crystalline basement. However, the detailed study of the uranium mineralisation in the Westmoreland area (U-Pb ages, REE content, and chlorite composition) shows emplacement dynamics that are different from the typical processes of unconformity-related deposits in the ARUF, a lower importance of the interactions between mineralising fluids and the basement, and a succession of mineralising events possibly between 1650 and 350 Ma.

The lead isotope composition in galena from different mineralised lenses of the SHMS McArthur River deposit highlights the implication of two felsic crustal reservoirs as lead sources. These two reservoirs have been synchronously and repeatedly mobilised by hydrothermal fluids around 1640 Ma to form the different lenses. Other deposits or prospects record several younger events (until around 1300 Ma) that involve a mixing between three lead sources. The geochemical signature of the sphalerite and galena from these lead-zinc deposits or prospects states specific emplacement conditions, in particular decreasing formation temperature in the successive episodes (approximately from 220 °C to less than 100 °C).

In addition to the major event at 1650-1600 Ma, the metallogenic history of the basin shows numerous other evidences for crystallisation or remobilisation of the metalliferous stock. Some of the fluid circulation stages are linked with geodynamic events such as basin inversions or orogeneses located a few hundreds of kilometres from the studied area. It seems that the large scale migrations of mineralising fluids (i.e., overall horizontal in the large sandstone aquifers, and vertical in the major faults zones) allowed the metal mobilisation in different reservoirs from the basin and the basement, and their selective precipitation within favourable zones.

Table of contents - Table des matières

Acknowledgments - Remerciements

Ces trois ans m'ont permis de côtoyer un nombre impressionnant de personnes de différents parcours et spécialités. Beaucoup d'entre vous on fait de cette thèse une belle aventure, et je voudrais ici vous remercier pour ce que vous m'avez apporté lors de ces trois ans.

Tout d'abord un énorme merci à **Antonin** : tu m'as fait confiance dès le début, me soutenant lorsque j'avais des projets un peu fous en dehors du cadre prévu au départ, et me laissant partir seule en Australie rencontrer les partenaires et collecter des échantillons. J'ai ainsi pu réaliser une partie de mon rêve de dater des dolérites, toujours en étant poussée par ton optimisme et ton soutien. Le temps que tu as donné pour cette thèse est colossal, et est clairement une des clés de son succès. Ton calme et ta patience m'ont aussi soutenue dans les moments de rush, et tu as toujours su faire preuve d'une grande humanité ; merci !

Irvine, thanks for the discussions and the bibliography, I will now have more time to go through them!

Julien merci pour ton soutien scientifique et pour toujours m'avoir amenée à me surpasser et à réfléchir sur chacune de mes données. Grâce à toi mes chapitres et papiers sont complets et de qualité.

First I would like to thank the companies that allowed me to get challenging samples and to discuss about them.

- **Aeon Metals** for the samples from Walfrod Creek, and specially Dan Johnson, Ed Jelicich-Kane and Jack Murday, for all the discussions in the field, at the core library in Mount Isa, and then about the results.
- **Teck** for the samples from Myrtle, and specially Nick Hayward for discussions on the global patterns, the sub-basins and the geodynamics around the deposits in the Batten Fault Zone, Mike Taylor for the sampling authorisation and Nik McMillan for the support on the field.
- **Glencore** for the samples from the McArthur River deposit and specially Andrew Morris for the field explanations and sampling, and Kristian Masterman to be co-author of the papers.
- **Laramide** and specially Adrian Buer for the sampling in the prospects from the Westmoreland area.

I also had the chance to work with people from GA:

- **Roger Skirrow**: you welcomed me when I first arrived in Australia and were my guide there. I had the chance to collaborate on many papers, thanks for always being positive and for improving the geological settings of the papers!
- **Dave Huston**: your questions on the lead isotopes have forced me to always go further and find explanations to confirm that the data were not due to analytical artefacts. It was always nice to meet you during various congresses and to have nice scientific discussions!
- **Andrew Cross**: I tried to date the zircons in mafic volcanics but it didn't work as well as I wanted, maybe you will have more chance?
- **Evgeniy Bastrakov**: thanks for the discussions in Canberra, and for been there during my defense!

And to meet in Canberra:

- **Mark Kendrick**: Noble gas and halogens were total strangers for me, before I realised their power! Thanks for your patience when answering all my questions
- **George Gibson**: Our small chat left me with less fear about geodynamics, let's discuss next July
- **Terry Mernagh**: in fact we never had the chance to meet in person, but you were also one of the initiators of this PhD, and always the first to answer my Emails with enthusiasm!

In Darwin, I met people from NTGS that have taken part in the sampling and scientific discussion since before the beginning of my PhD:

- **Dorothy Close:** Thanks for the support during many years and the smiling welcome
- **Andrew Wygralak**: Your advices and motivation throughout this advebture was one of the reason of its success (and your cavern pearl with travel with me to London!)
- And people from the core library, always very helpful with me, I had great time looking at my samples there!

During my two trips to Darwin, I had the chance to meet two people from CSIRO:

- **Marcus Kunzmann**, thanks for all your stratigraphic work, and the discussion about the synsedimentary/diagenetic nature of the McArthur River deposit, that helped me a lot to can then built my models on solid basis.
- **Teagan Blaikie**: I'm impressed by what geophysics can reveal from the depth of "my" basin, thanks for your time explaining this.

I am particularly grateful to Murray W. Hitzman and Ferenc Molnar for agreeing to evaluate this work as reviewers. Thanks also to Isabelle Duhamel-Achin, Sophie Decrée, Anne-Sylvie André-Mayer and Roger G. Skirrow for accepting to be examiners, and Rémy Chemillac to have joined the jury.

Héloïse : c'est avec toi que tout a commencé, toi dont j'ai été le plus proche pendant ces années et probablement celle qui me comprend le mieux vu nos histoires semblables ! Tout a commencé en montant ensemble mes valises jusqu'à mon appart, puis il y a eu des kilomètres de natation

Julien B : tu as été pendant la majorité de ma thèse la clé de voûte de DocGeoRessources, celui qui intègre les nouveaux et qui reste le contact privilégié avec les anciens, merci pour ce rôle.

Julien P : Que de discussions scientifiques ou non, je serai toujours impressionnée par ton intelligence et tes suggestions toujours pertinentes ! Et ce jour est le grand jour du départ, celui que tu attends depuis siiiiiiii longtemps !

Audrey : tu as été la ptite nouvelle de la FST et tu as su apporter une touche de féminité bienvenue dans ce monde de brutes. Ta persévérance est incroyable et je t'admire énormément, tu tiens le bon bout !

Jade : Mais si la vie est belle ;-)

Raph : le calme que tu dégages et ton optimisme m'ont zénifiée pendant ces trois ans, surtout à la fin

Jessica : the second more zen person on the Lab, it was always nice to have a chat with you in the torments of the PhD to get some air.

Dafné (tu fais presque partie du labo ;-))

Alexy : You are so calm, and I'm impressed by the number of hours you spent in front of fluid inclusions, congrats !

Les trois suivants m'ont fait bien stresser rien qu'à suivre leur rédaction, sur ce point vous êtes le modèle que j'ai essayé de ne pas suivre !

Hélène : Je suis bien contente que tu aies trouvé ton petit coin de paradis et que tu aies pris le temps de me rassurer dans les heures difficiles de la rédaction.

François : Super U a du faire venir des camions spéciaux de biscuits au chocolat blanc pour ta rédaction mais ils n'ont pas fait le bonheur des cafards du labo vu ton rythme de descente ! J'envie ton assurance quand tu parles de ton sujet.

Pierre : Merci pour mon initiation à la musique « différente » lors de ma première année de thèse, je me rappellerai ton fluage sous la table et tes pétages de plomb justifiés ; Tu as été mon maître de l'uranium.

Guillaume : Bon la Suze c'est définitivement immonde, mais la raclette je valide !

Yoram et Alizé : quelle passion pour la bonne nourriture (oui oui je mets les sandwichs au fromage du RU dans la catégorie bonne nourriture !) et que de belles soirées partagées avec vous… et merci à ma super infirmière pour le vaccin « même pas mal »

Dimitri : comment ne pas mentionner ce petit moment qui a tellement fait jaser Mr Perret ! Ça valait la peine de marcher dans un quartier glauque en rentrant de la RST juste pour ce moment hahaha

Rémi : de la pure tradition vosgienne, qui m'a presque donné envie de découvrir St-Dié ! bonne chance pour tous tes projets futurs.

Agnès : Noosa est définitivement le plus bel endroit du monde, et quel bonheur d'avoir pu partager avec toi ces moments dans la nature avec dauphins, koala, baleines et tortue !

Et aussi une pensée à tous les autres doctorants, post-doctorants, chercheurs, enseignants-chercheurs et responsables de plateformes avec qui j'ai plus ou moins interagit et qui ont égayé mes journées par leur présence, leur sourire et leur soutien. And a special thought to the other PhD students from who I was not so close, but who made my stay nicer thanks to their presence, smile and support.

Anne-Sylvie: ma vie actuelle te doit beaucoup ! Sans l'Abitibi je doute que j'aurai découvert la belle aventure de la thèse

Etienne : merci pour ces heures de travail au CRPG ! Les isotopes du plomb et le calcul d'erreur ont de moins en moins de secrets pour moi, c'est rassurant !

Spéciale dédicace à **RING**, vous qui m'avez intégrée dans cette belle équipe, vous êtes un exemple d'une équipe dans laquelle on se sent bien et avec qui on a envie de se voir.

Merci aussi aux personnes du **CRPG** avec qui j'ai interagit durant ces 3 ans, le CRPG est devenu mon havre de paix et de calme.

Ma première formation est celle pendant laquelle j'ai tissé les amitiés les plus fortes, avec vous le groupe de Ventron. **Margaux**, quel beau hasard de tomber dans ta chambre suite à un débat sur les sèche-cheveux. J'apprécie ton professionnalisme, ta bonne humeur et ta motivation… et j'ai réussi à écrire quelques lignes en Python grâce à toi, ce programme restera pour moi un superbe exemple de collaboration. **Claire**, quel courage de se lancer dans une aventure plus longue que la nôtre, en étant presque seule au monde…. **Cécile** je regarde tout ce que tu as accompli lors de ta thèse et j'en suis bouche bée ! **Quentin** merci d'être toujours prêt à aider et à remonter le moral. Et **Sylvain** tu vois fallait revenir plus tôt dans le groupe, tu en as manqué des belles soirées, mais il y en a d'autres à venir !

D'autres formations m'ont permis de rencontrer tour à tour des passionnés de vulgarisation, des amoureux de la nature, des gens de tous les pays et de tous les domaines et de pouvoir prendre du recul sur ma thèse.

Alexandre : Entre les congrès et notre passion pour les sphalérites, nous étions faits pour nous rencontrer. Le 15 novembre a été le jour de gloire pour ces beaux minéraux, et j'espère que prochain congrès pour se rencroiser.

Laura et Bertrand : quelle belle amitié… des mois entiers sans se voir, parfois des années, et à chaque fois c'est le même plaisir de vous voir. Vous m'avez vue dans tous les moments clés de ma vie, m'avez soutenu sans me juger et pour ça et tout le reste vous êtes merveilleux !

Francesca et Bastien : souvenir d'une super coloc, qui m'a aidée à me construire mon petit nid douillet à Nancy.

Jean : 4 ans à être mon boss et bien sûr mon ami, 4 ans à partager des 5 à 7 au Trèfle, des virées aux Kékékos ou à Montréal, et surtout des étés de terrain qui m'ont fait grandir et être celle que je suis. Je ne pensais pas vivre autant d'aventures, dans des endroits aussi isolés ! Rouyn restera à jamais une ville dans laquelle je me suis sentie bien et intégrée, en énorme partie grâce à toi.

Mes parents : et oui la géologie m'a amenée au Québec que j'ai eu la chance de découvrir avec vous, puis à Nancy avec de brefs passages en Australie et ailleurs… vous encouragement et votre présence dans les moments de rage, de désespoir et aussi de joie ont été précieux. Depuis tous petits vous nous avez montré les beautés de la nature, et ça a bien sûr guidé mes choix et mon parcours.

Ma mamie : toujours fière… Aurais-tu pensé que la timide Joséphine allait se lancer dans la cartographie dans un pays plein d'ours, gérer des hélicos et des humains, et finalement se lancer dans cette aventure, en me surmontant en allant seule en Australie ? Je sais que tu es fière et ça me rend super heureuse !

Adrien et Laura : soutien sans faille et critiques de premier plan lors de mes débuts en vulgarisation ! Merci pour votre soutien dans les moments de soute et d'avoir toujours cru en moi.

Aurélien : Décembre 2016, un tournant dans ma vie : quitter ma vie au Québec, en redémarrer une à Nancy, et surtout démarrer une superbe histoire avec toi. On savait dès le début que ça voulait dire 3 ans séparés, parfois de milliers de kilomètres ; ne se voir qu'un WE sur 2 ; planifier ; réserver ; et recommencer. Trouver un équilibre entre nous et nos familles, sans oublier les amis. 3 ans pendant lesquels on a visité pas mal de coins : la Bourgogne, Crolles, la Suisse, Orléans, Tours, Lille, l'Alsace, KA, la côte anglaise, et les grandes vacances au ski, à Corfu, Chypre et Madère. 3 ans à se connaitre aussi par correspondance, à rêver de ce moment où on pourrait vivre ensemble. Incroyable de se dire qu'il est arrivé. Merci encore pour ton soutien à toute heure (c'est le cas de le dire !), mon parcours m'aurait paru plus complexe sans toi !

Résumé étendu

La zone d'étude de cette thèse est le bassin sédimentaire paléo-mésoprotérozoïque de McArthur (Northern Territory et Queensland, Australie). Les bassins sédimentaires déposés à cette période, comme les bassins de McArthur et de Mount Isa en Australie et ceux d'Athabasca et de Thelon au Canada, renferment des ressources majeures en uranium (U), plomb-zinc (Pb-Zn) et cuivre (Cu). Ces métaux sont en effet majoritairement associés à des périodes de faible activité dans la croissance crustale terrestre, au contraire de l'or par exemple qui se met en place lors de l'assemblage des supercontinents.

La répartition des ressources dans ces bassins est hétérogène à différentes échelles. Le bassin d'Athabasca renferme majoritairement des gisements d'uranium, et au sein du bassin de McArthur les minéralisations uranifères se situent dans le socle ou à la discontinuité avec le bassin, alors que le plomb et le zinc se trouvent dans la partie centrale du bassin. Le bassin d'Athabasca a été étudié en détail et la minéralisation uranifère est bien contrainte. Mais pour avoir une idée plus globale de la richesse dans un unique bassin, le bassin de McArthur est une cible privilégiée. L'étude des gisements de différents types est une clé pour mieux comprendre les processus liés au dépôt des métaux, et par conséquent pour augmenter les chances de découvrir de nouvelles cibles. Les trajets des fluides, leurs caractéristiques et leur âge sont une autre partie capitale de l'histoire, afin de comprendre si la minéralisation primaire a été remobilisée, et si oui, où sont localisées les ressources actuelles.

En se basant sur les modèles géologiques et les résultats d'inclusions fluides qui montrent des similarités entre plusieurs zones minéralisées, plusieurs questions peuvent être soulevées :

- Quels sont les facteurs qui contrôlent la distribution des métaux dans les bassins ?
- Les gisements d'un même métal sont-ils similaires à l'échelle du bassin (par exemple les gisements d'uranium aux extrémités nord et sud du bassin) ?
- Les métaux peuvent-ils être lessivés d'une source unique pour créer des gisements de classe mondiale ?
- Quels sont les facteurs menant à des gisements de classe mondiale, à des indices minéralisés ou même à des zones stériles ? Est-ce dû à des conditions favorables lors de la précipitation, ou à une meilleure préservation ?
- Les fluides minéralisés partagent-ils des caractéristiques similaires pour un métal (par exemple l'uranium) à l'échelle du bassin ? Et pour des métaux différents ?
- Des bassins sédimentaires « stables » comme celui de McArthur, supposé stable depuis environ 1.5 Ga, peuvent-ils être affectés par plusieurs évènements récents de circulations fluides et de minéralisations ?

- Quelle(s) est (sont) la (les) source(s) des éléments impliquée(s) dans le métasomatisme, qui était un processus clé pour le dépôt des métaux, ainsi qu'un guide pour l'exploration actuelle ?

Certaines réponses à ces questions sont présentées dans les chapitres suivants.

- Le Chapitre 2 se concentre sur le métasomatisme à bore et magnésium observé dans le gisement uranifère de Ranger, situé dans le socle juste sous la discordance avec le bassin de McArthur. Le même type de métasomatisme est aussi présent dans les gisements de type discordance dans le bassin d'Athabasca (Canada). La chlorite et la tourmaline (Mg-foitite) sont riches en magnésium, ce qui confirme l'importance du métasomatisme dans ce gisement. Les valeurs isotopiques du bore dans la tourmaline sont distinctes de celles du bassin d'Athabasca, et s'expliquent par une implication probablement plus grande du socle pour le budget en bore par rapport à des fluides dérivés de l'évaporation de l'eau de mer.
- Le Chapitre 3 s'intéresse à la minéralisation uranifère et présente une comparaison entre les gisements dans les grès de la zone de Westmoreland (partie sud du bassin) et les gisements de l'Alligator Rivers Uranium Field (ARUF, au nord) qui sont de type discordance. La comparaison de différents paramètres des uraninites (spectres des terres rares et contenu en éléments traces), l'âge des épisodes minéralisateurs ainsi que les estimations de températures à partir des chlorites conduit à la conclusion que les gisements de Westmoreland peuvent être distingués des gisements de type discordance. La température relativement haute (>300 °C) et un encaissant d'une autre nature sont vraisemblablement une des explications à ces différences.
- Le Chapitre 4 présente des données de gaz rares et d'halogènes obtenus sur plusieurs générations de quartz dans différentes zones riches en uranium du bassin de McArthur. Ces outils sont utiles pour interpréter plus en détail les caractéristiques des fluides, et ont déjà été utilisés dans le bassin d'Athabasca par exemple. Dans cette étude, ils ont été appliqués à la zone de Westmoreland et à l'ARUF et indiquent la présence d'une saumure issue de l'évaporation de mer ayant faiblement interagi avec la matière organique, mais aussi d'un fluide peu salé. Des hypothèses sur l'intensité de l'interaction avec le socle peuvent aussi être posées.
- Les sources du plomb du gisement de classe mondiale de McArthur sont étudiées dans le Chapitre 5 grâce aux isotopes du plomb dans les galènes qui soulignent la contribution de deux sources de plomb. Plusieurs modèles sont aussi proposés pour expliquer l'origine de ces sources.

- Le Chapitre 6 étend cette étude à des gisements et indices localisés à différentes distances des failles majeures, et même à un gisement situé dans un autre bassin corrélé stratigraphiquement. De stratiforme lors de la diagenèse précoce à tardif sous forme de veines, la diversité des assemblages de sulfures donne une idée de l'étendue des évènements minéralisateurs et confirme l'importance d'obtenir des informations sur la source des métaux et sur l'âge des minéralisations. L'étude des isotopes du plomb dans les galènes de différents gisements et indices révèle la contribution d'au moins trois sources de plomb. Un évènement plus jeune (~1300 Ma) est enregistré dans les minéralisations proches des failles majeures. Les éléments mineurs et traces dans la sphalérite et la galène, en plus d'être économiquement intéressants comme coproduits, donnent des informations précieuses sur les conditions de formation des sulfures. Les estimations de températures décroissent avec le temps, de 220 °C à moins de 100 °C (limite inférieure de calibration).
- Le Chapitre 7 présente une discussion globale sur les résultats de cette thèse.
- L'Appendix 1 propose un essai de datation de la minéralisation en cuivre, car il permettrait de donner des informations sur l'âge des gisements de type brèche et de replacer la minéralisation cuprifère dans le contexte global. Une alternative pour dater les minéralisations cuprifères est de dater la mise en place des Settlement Creek Dolerite, qui serait synchrone de cette minéralisation selon certains auteurs. Les zircons qu'elle renferme ont été analysés pour en déterminer l'âge. Leur taille n'a malheureusement pas permis de donner un âge absolu à cette formation, mais permet d'affirmer que sa mise en place est bien plus jeune que les hypothèses actuelles.
- L'Appendix 2 présente un programme Python qui calcule les âges modèles à partir des ratios des isotopes du plomb selon différentes méthodes. Ce programme est un outil puissant pour calculer en quelques secondes un grand nombre d'âges modèles selon les modèles de Sun et al. (1996) and de Stacey and Kramers (1975). Le paramètre μ, utilisé pour l'interprétation de la nature du réservoir fournissant la source du plomb, est aussi calculé par le programme. De plus, une représentation graphique du diagramme $^{207}Pb/^{204}Pb$ en fonction de $^{206}Pb/^{204}Pb$ est fournie, dans laquelle les données et les isochrones des deux modèles sont reportés.

Au début de chaque chapitre, un préambule en français en résume les conclusions majeures.

L'ensemble des âges de minéralisation du bassin de McArthur (compilés de la littérature et obtenus lors de la thèse) montrent plusieurs épisodes minéralisateurs en uranium et/ou en plomb-zinc. Les plus vieux sont presque équivalents au début du dépôt du bassin (1815 Ma, Ahmad and Munson, 2013), alors que l'évènement le plus récent a eu lieu il y a environ 350 Ma dans la zone de Westmoreland (voir le Chapitre 3). Un contraste important existe en termes de préservation et/ou de remobilisation des métaux entre les gisements ou indices. Dans le gisement de McArthur River, non affecté par des évènements plus jeunes que la minéralisation syngénétique/diagénétique précoce, la préservation est optimale. Des remobilisations tardives sont observées à proximité des failles majeures. Ceci pourrait conduire soit à une perte de métaux si le fluide tardif lessive les métaux, soit à des nouveaux types de minéralisations (veines). Dans les gisements uranifères, plusieurs épisodes de remobilisation ou de remise à zéro entre différents échantillons du même gisement sont mis en évidence. En compilant les datations des minéralisations dans le bassin, le premier épisode minéralisateur a lieu vers 1720–1680 Ma, suivi par celui à 1650–1600 Ma qui affecte les minéralisations en U et en Pb-Zn. Entre 1400 et 350 Ma, chaque épisode minéralisateur est majoritairement observé en un unique endroit au sein du bassin.

A l'échelle du bassin, une zonation des métaux est observée : les gisements d'uranium se trouvent dans le socle, au niveau de la discontinuité avec le bassin ou immédiatement au-dessus. Les gisements de cuivre sont dans des roches plus jeunes dans le bassin, et ceux de plomb-zinc dans un niveau stratigraphique supérieur. Cette zonation est aussi visible en carte, avec les gisements d'uranium en bordure du bassin, le cuivre plus au centre et enfin le plomb-zinc au centre.

D'un point de vue chimique, deux mécanismes peuvent expliquer cette zonation des métaux. Etant donné leurs solubilités respectives, les métaux précipitent selon un ordre spécifique lorsqu'ils sont confrontés à un milieu plus réducteur ou à une diminution de température : uranium – cuivre – zinc. Ces deux scénarios peuvent expliquer la zonation observée dans le cas d'un fluide unique transportant les trois métaux. Augmenter l'état réducteur peut être provoqué par mélange avec un fluide plus réducteur, et par le contact avec des minéraux comme la pyrite ou des formations riches en matière organique comme la Barney Creek Formation, encaissant de la minéralisation dans le gisement de mcArthur River par exemple.

En plus de la zonation en métaux, les gisements d'un même métal peuvent être différents en termes de température et d'âge à l'échelle du bassin. Comme présenté dans le Chapitre 3, les gisements d'uranium au nord et au sud du bassin ont été déposés à partir de fluides aux

caractéristiques spécifiques ou dans des conditions différentes, et les épisodes minéralisateurs avaient des âges variés. Considérant la taille du bassin, cela n'est pas surprenant. Cependant, puisque les fluides partageaient des propriétés communes, une plus grande homogénéité pouvait être attendue. Ce travail a confirmé la nécessité d'étudier des gisements dont les caractéristiques semblent identiques au premier abord.

Différents éléments sont utiles pour l'exploration. Dans le gisement de McArthur River, le halo de Tl autour des zones riches en métaux est visible en analyses de roches totales, dans la pyrite, et cette étude a montré une concentration élevée en Tl dans les métaux de base. Le Tl n'a pas été observé en concentrations importantes dans les autres gisements de métaux de base, mais d'autres marqueurs existent probablement dans ces gisements. Dans le gisement de Ranger, les zones enrichies en B et en Mg sont les témoins du métasomatisme qui a lieu peu avant la minéralisation uranifère. Vu l'épaisseur de la couverture sédimentaire (formations plus jeunes que le bassin de McArthur) au-dessus de certaines zones du bassin, les indicateurs géochimiques sont capitaux pour orienter les futurs travaux d'exploration. Les zones sous couverture sont en effet les cibles pour les découvertes de nouveaux gisements.

Un système minéralisateur se décompose en quatre éléments majeurs : des sources, un moteur d'énergie, un chemin pour les fluides ou une architecture favorable, et un mécanisme de dépôt.

Dans cette étude, l'implication de deux sources de plomb pour les gisements de McArthur River et de Myrtle, et d'une troisième à Walford Creek et Caranbirini a été démontrée, et des modèles pour leur origine proposés. De plus, les fluides responsables du métasomatisme à Ranger montrent une importante contribution du socle en plus de fluides dérivés de l'eau de mer. Pour les fluides minéralisateurs et tardifs à Ranger et dans la zone de Westmoreland, les gaz rares indiquent que les fluides étaient dérivés de l'eau de mer, et il a pu être établi une contribution du socle dans certains échantillons.

Les moteurs de la minéralisation sont des évènements crustaux majeurs (visibles sur le trajet de dérive apparente du pôle), comme l'orogenèse Isan, réactivant les failles. L'énergie est visible dans les températures observées dans la zone de Westmoreland, avec des températures supérieures à 350 °C, lors du métasomatisme à Ranger (101–163 °C) et à McArthur River (150–225 °C, comparé à des épisodes tardifs de plus basse température). En fonction de ces évènements, la température peut être corrélée soit à l'emplacement de roches mafiques ou à une proximité avec le bassin, soit à des fluides de plus haute température réchauffés plus profondément dans le socle ou le bassin.

Les failles ont été les conduits majeurs qui ont connecté les différents réservoirs de fluides, dans le socle et dans le bassin. L'exception est qu'elles pourraient avoir été imperméables au passage des fluides lorsque les argilites n'étaient pas encore consolidées, mais cela représente une fenêtre de temps très réduite. Les roches mafiques et les dykes (comme les Seigal Volcanics) dans la zone de Westmoreland pourraient aussi avoir été des lithologies imperméables, concentrant la minéralisation uranifère. Dans cette étude, il a été démontré que les failles n'étaient pas actives seulement au moment de la minéralisation primaire comme démontré précédemment, mais que les fluides tardifs (~1300 Ma à Caranbirini et Walford Creek par exemple) ont probablement utilisé ces conduits plus tard dans l'histoire du bassin.

Pour former des gisements de classe mondiale, les paramètres mentionnés ci-dessus doivent être combinés à une préservation optimale. Ceci semble être le cas par exemple à McArthur River, où aucun évènement tardif n'est enregistré dans les isotopes du plomb, comparé à Caranbirini localisé à quelques kilomètres seulement.

Cette thèse a exploré certains gisements d'uranium et de plomb-zinc du bassin de McArthur. Les progrès dans les outils d'exploration et dans la l'interprétation des systèmes minéralisés évoluent rapidement, et chaque étape est clé dans la compréhension globale des évènements qui se sont déroulés il y a des centaines de millions d'années. Des débats persistent dans des gisements très étudiés comme McArthur River et Ranger concernant leur structure, les mécanismes de dépôt des métaux et leur âge, et les zones moins étudiées en sont encore davantage aux premières étapes de compréhension. Plusieurs perspectives peuvent être proposées pour aller plus loin dans l'interprétation des systèmes minéralisés.

La première perspective est d'appliquer de nouvelles méthodes ou d'analyser d'autres minéraux d'un gisement ou d'une zone déjà étudiés. Dans la zone de Westmoreland, les inclusions fluides et l'altération pourraient être investiguées en profondeur pour mieux comprendre les caractéristiques des différents épisodes minéralisateurs et la relation entre l'altération et la minéralisation. Pour les gisements de plomb-zinc, l'étude des inclusions fluides dans les sphalérites de taille suffisante permettrait la détermination de la salinité du fluide et une approximation de la température au moment de leur cristallisation. Ceci pourrait par exemple être testé à Myrtle, Caranbirini et Walford Creek. Les isotopes du soufre dans les sulfures, et ceux du carbone et de l'oxygène dans les carbonates et dans les niveaux riches en matière organique des gisements de métaux de base donnent des informations sur les sources du soufre, du carbone et de l'oxygène. Puisque les sources des métaux ont été en partie étudiées ici, ce complément permettrait de déterminer si toutes les sources peuvent être liées ou non. D'autres sulfures comme ceux de cuivre et de cobalt à Walford Creek sont

économiquement capitaux et font partie de l'histoire du gisement, car ils pourraient avoir été transportés par les mêmes fluides que les métaux de base, ou être remobilisés lors des mêmes évènements. Il a été envisagé de dater les minéraux porteurs de cuivre mais la précision des mesures (plusieurs dizaines de millions d'années) n'est pas suffisante pour contraindre l'âge de la minéralisation en cuivre. Les éléments traces dans les sulfures de cuivre et de cobalt pourraient aussi donner une information sur la répartition des éléments traces dans tous les sulfures, en plus de la galène et de la sphalérite.

Une autre perspective serait d'appliquer des méthodes utilisées à de nouvelles cibles. Par exemple, le métasomatisme à B et Mg est un guide pour les gisements uranifères de type discordance, et les isotopes du bore ainsi que la composition des tourmalines et des chlorites peuvent être appliqués à d'autres gisements de ce type pour caractériser la source et l'évènement métasomatique. Les méthodes appliquées aux gisements d'uranium (datation U-Pb, spectres des terres rares sur uraninite, estimation de température à partir des chlorites) pourraient être appliquées aux autres indices dans la zone de Westmoreland, étant donné que les deux études de la zone montrent un total de six épisodes minéralisateurs, chacun ayant des conditions spécifiques. Multiplier les données permettrait de déterminer quels évènements étaient les plus importants, correspondant aux plus hautes teneurs et aux évènements les plus intenses. Les gaz rares et les halogènes sont précieux pour comprendre l'interaction des fluides avec le socle et la matière organique, et peuvent être appliqués dans n'importe quel type de gisement dans lequel le quartz et les carbonates ont des inclusions fluides qui enregistrent l'évènement minéralisateur ou une autre circulation de fluides. Les isotopes du plomb dans la galène ont déjà été acquis pour différents gisements ou unités stratigraphiques du bassin de McArthur. Cette étude met en avant l'importance du nombre d'analyses afin d'être aussi près que possible des pôles, et la nécessité d'échantillonner différentes lentilles ou styles de minéralisations au sein du même gisement pour les comparer en termes d'âge et de source(s). De plus, la méthode SIMS devrait être privilégiée à la méthode TIMS car les variations isotopiques à l'échelle d'un minéral sont diluées par TIMS. Analyser par SIMS des galènes de gisements choisis pour une minéralisation spécifique, un encaissant, un âge supposé, une distance à une faille majeure et l'évidence ou non de remobilisation pourrait donner une idée des processus minéralisateurs à l'échelle du district. Le programme FindAge peut être utilisé pour le jeu de données considérable d'isotopes du plomb afin d'avoir une idée rapide des périodes les plus prolifiques dans le bassin, bien qu'il doive être utilisé avec précaution car les données peuvent correspondre à des termes de mélange.

Les possibilités pour des nouvelles méthodes, des nouvelles cibles ou les deux sont presque illimitées dans une zone comme de bassin de McArthur. En considérant la partie

affleurante du bassin, et l'immense partie sous la couverture de bassins plus jeunes, l'aire de jeu représente des milliers de kilomètres carrés en milieu isolé.

Chapter 1. Introduction

This PhD study focuses on the Paleo-Mesoproterozoic McArthur Basin spreading across the Northern Territory and Queensland of Australia. Sedimentary basins deposited during this period are highly exceptional for hosting major U, Pb-Zn and Cu resources, not only McArthur but also Mount Isa (Australia) and Athabasca and Thelon (Canada). The presence of these metals is often associated with quiescent periods in the Earth's crustal growth history. Gold on the other hand is emplaced mainly during the assemblage of supercontinents (Figure 1-1).

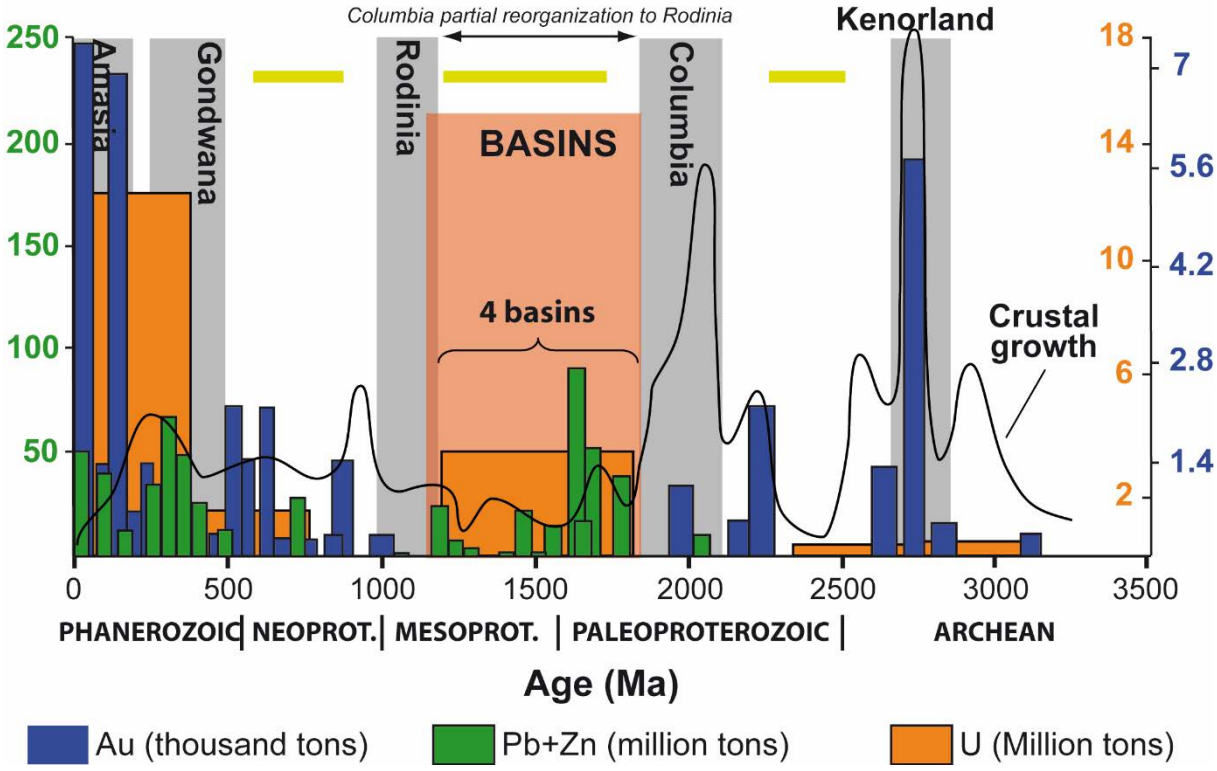

***Figure 1-1**: Compilation of the timing and tonnage of different resources: Au, Pb+Zn and U. The 1.7-1.0 Ga period corresponds to a pause in the tectonic activity following the Columbia supercontinent formation, characterised by the development of sedimentary mega-basins formed by the erosion of the supercontinent. Note that whereas gold is associated with orogens and crustal growth episodes, U and Pb+Zn resources emplace between these crustal growth events. Grey rectangles: supercontinent formation; yellow lines: pause in the global tectonic/magmatic activity. Compilation by J. Mercadier from Cuney (2010), Goldfarb et al. (2010), Huston et al. (2010), and Leach et al. (2010).*

The resources repartition within these basins is heterogeneous at different scales. The Athabasca Basin hosts mainly U deposits, whereas the McArthur Basin contains U, Cu and Pb-Zn resources (Note: recent discoveries are suggesting both basins are polymetallic). In the McArthur Basin, U mineralisation is located near to or within the basement, whereas the Pb-Zn occurrences are in the central part of the basin. The Athabasca Basin has been extensively studied and the conditions of U mineralisation are overall well constrained. However on the larger scale of prospectivity within a single basin, the McArthur Basin is an ideal target. From an exploration perspective, the investigation of deposits from different types is a clue to a better understanding of the processes leading to ore deposition, and therefore identifying vectors for new discoveries. The fluid pathways, their characteristics, and their timing are important

parameters of the metallogenic story, so to better understand if the primary mineralisation has been remobilised, and where the resources are presently located.

1.1. The McArthur Basin

The McArthur Basin is located in the north-eastern Northern Territory and is exposed over an area of about 180 000 km^2 (Ahmad and Munson, 2013). It unconformably overlies the basement complex composed of Archean and Paleoproterozoic metamorphosed and deformed rocks of the Pine Creek Orogen to the west, the Murphy Province to the south and the Arnhem Province to the northeast (Figure 1-2).

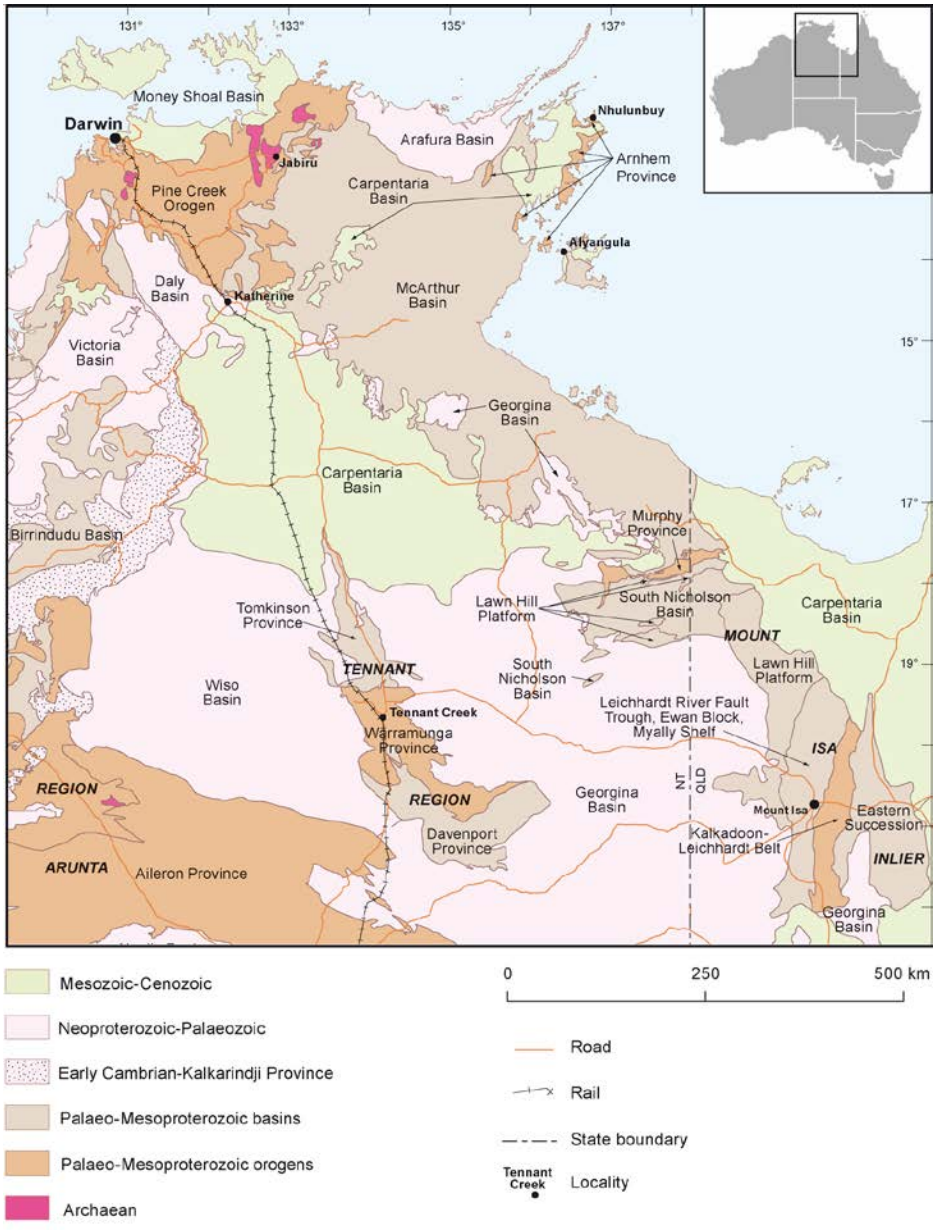

***Figure 1-2**: Geological regions of the Northern Territory and surrounding areas. After Ahmad and Munson (2013)*

The Pine Creek Orogen comprises a succession of clastic, carbonate and carbonaceous sedimentary and volcanic rocks hosting Australia's major unconformity-related uranium deposits (Skirrow et al., 2016). These lithologies unconformably overly Neoarchean granitic and gneissic basement (Ahmad and Munson, 2013).

The McArthur Basin contains a succession of sandstones, volcanic rocks, stromatolitic and evaporitic carbonate rocks and shale (Ahmad and Munson, 2013). The deposition occurred in a variety of environments (lacustrine, fluvial, alluvial, deltaic, and shallow marine). Based on the synthesis of Ahmad and Munson (2013), Jackson et al. (2000, 1999), and Rawlings (1999), the location of the metal resources in the stratigraphy is summed up in the Figure 1-3. The abundance of evaporites in some layers of the basin is a key point for the generation of brines. According to Evans (2006), the volume of evaporites is higher than 23 500 km^3. Their deposition took place mostly between 1640 and 1590 Ma, even if older ones were deposited at circa 1730 Ma in the Redbank Package. In many cases, dolerite dykes located close to mineralised areas are believed to play a role as a source of metals and heat. They may have even acted as impermeable units capping the mineralisation.

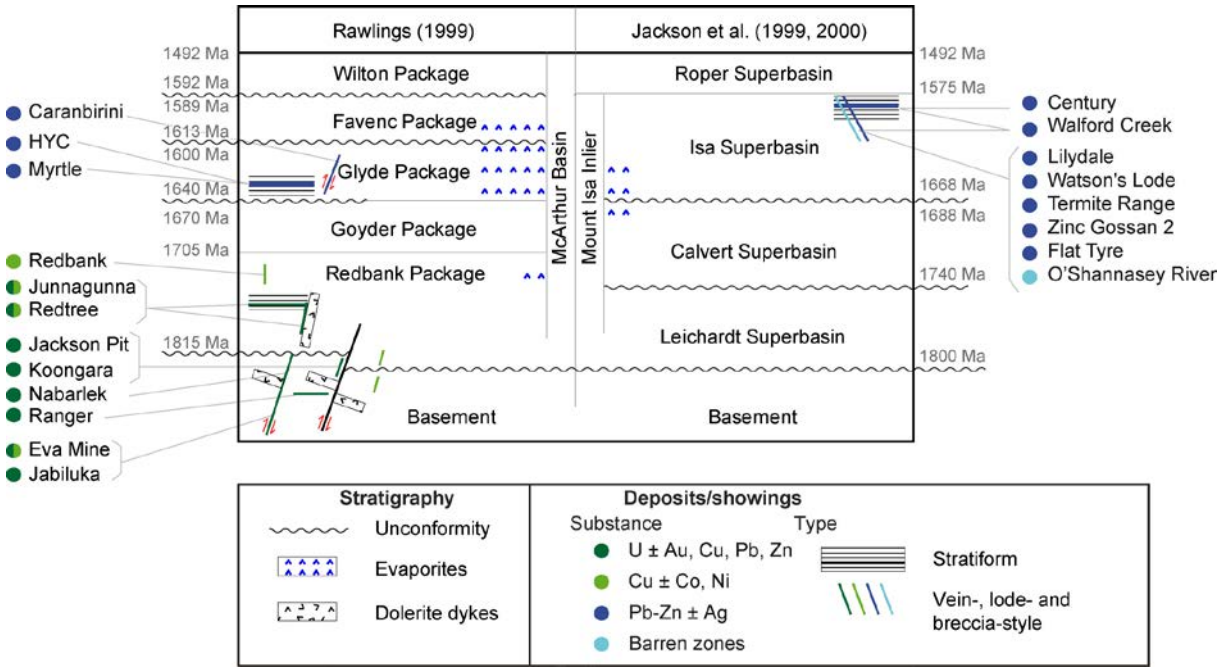

***Figure 1-3**: Subdivisions of McArthur Basin succession by Rawlings (1999) and Jackson et al. (1999, 2000). The emplacement of the studied deposits or barren zones is also reported, with their type and substances replaced in the stratigraphic column.*

The McArthur Basin succession extends southeast to the Isa Superbasin (Queensland) (Figure 1-2). These two basins are separated by the Murphy Inlier (probably a paleogeographical high) and the South Nicholson Basin. The northern and southern parts of the McArthur Basin share many geologic attributes, such as correlative stratigraphic rock types and the abundance of uranium deposits (Rawlings, 1999). The same similarities are also

observed between the center of this basin and that of the Mount Isa Inlier with the Pb-Zn deposits. Some younger basins (Georgina, Carpentaria and Arafura basins) unconformably overlie the Paleo-Mesoproterozoic basins (Ahmad and Munson, 2013).

Two formations are of great importance in this study with respect to uranium mineralization. The first one is the Kombolgie Subgroup (the basal part of the Redbank Package to the North), which comprises a succession of essentially fluvial sandstone and extrusive volcanic units and unconformably overlies the Pine Creek Orogen rocks. The second one is the Westmoreland Conglomerate that corresponds to the basal unit of the McArthur Basin at its southern end and consists in proximal fluvial deposits typical of debris flows, alluvial fans, and braided river systems that are overlain by sandstone (Ahmad and Munson, 2013). The Westmoreland Conglomerate hosts most of the uranium mineralisation in the Westmoreland area (International Atomic Energy Agency, 2018a). The Barney Creek formation in the Glyde Package and its lateral equivalents are the host rocks for most of the Pb-Zn mineralisation.

The investigated areas of this PhD study are essentially unmetamorphosed, except for some areas studied for fluid inclusion compilation in the Mount Isa Inlier belonging to the subgreenschist facies of Blake (1987), refined by the description of Foster and Rubenach (2006). Metamorphism reached amphibolite facies in the Pine Creek Orogen, and granulite facies east of Jabiluka and in the South Horn area (Ahmad and Munson, 2013; Ypma and Fuzikawa, 1980), but the metamorphic events occurred before fluid circulation and mineral deposition, at ca 1880–1850 Ma.

The McArthur Basin and its crystalline basement complex, as well as the South Nicholson Basin and Mount Isa Inlier, are a target to better understanding the processes leading to formation and distribution of the different mineralisation types. Their stratigraphic units host abundant world class deposits (U, Pb, Zn, Cu), comprising a total of 80 Mt Zn, 40 Mt Pb and 300,000 t U (Huston et al., 2006; Leach et al., 2010). They are from the same age and present good spatial, stratigraphic and structural correlations that could correspond to the same big sedimentary complex (Large et al., 2005; Polito et al., 2006a; Southgate et al., 2006).

The McArthur Basin hosts greater than three hundred mineral occurrences (Figure 1-4), but significant mining activity has taken place only at the McArthur River deposit (formerly HYC: 'Here's Your Chance', Pb-Zn), Merlin (diamond), and Redbank (Cu, Ahmad et al., 2013). In addition to these resources of the mcArthur Basin, several uranium deposits are hosted in the Pine Creek Orogen (see chapter 2).

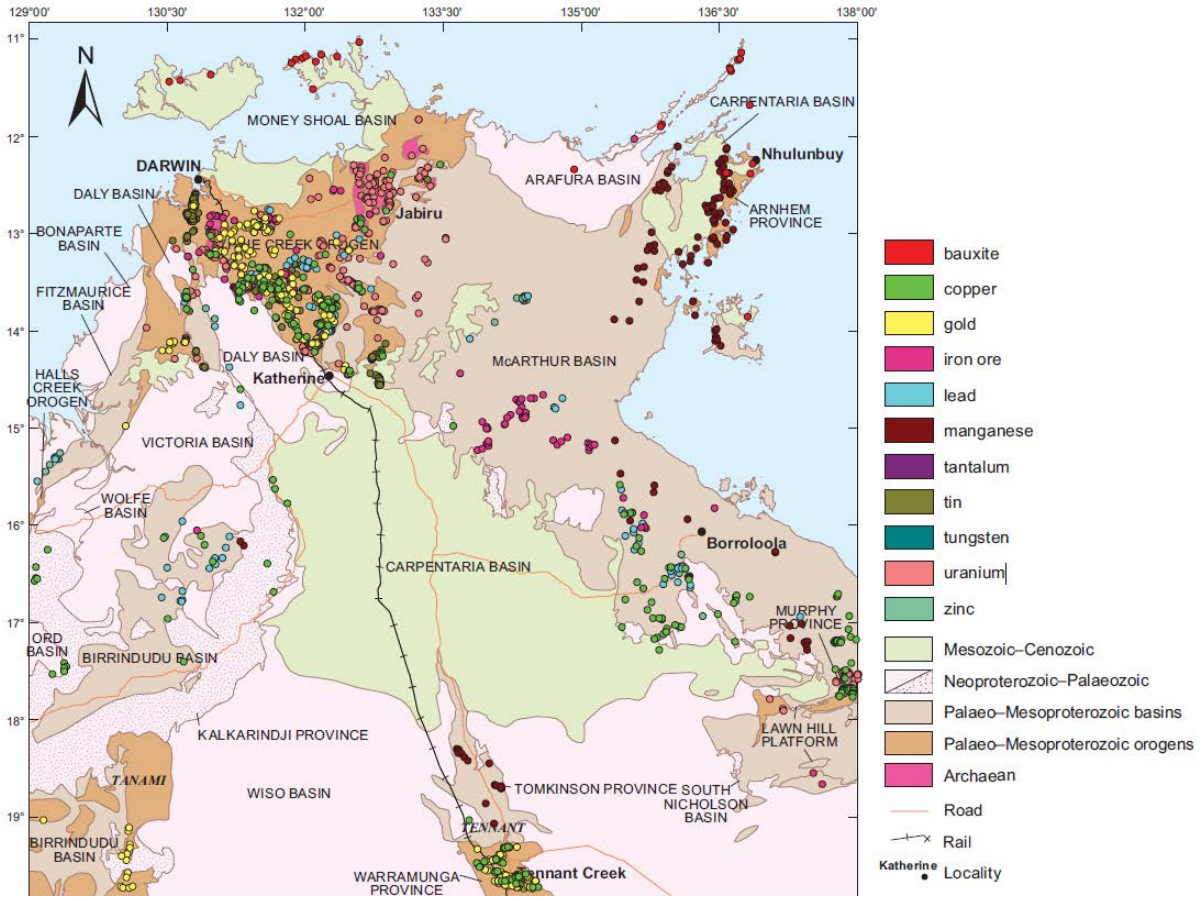

***Figure 1-4**: Location of significant mineral commodities in the Northern Territory. After Ahmad and Munson (2013)*

At a basin scale, a metal zoning of the deposits is observed: uranium deposits are located in the basement, at the unconformity or just above. Copper deposits are located in younger rocks within the basin, and lead-zinc deposits are hosted within an upper stratigraphic level (Figure 1-3). This stratigraphic zoning is also visible on maps, where uranium deposits are located at the edges of the basin, copper further to the basin centre, and finally lead and zinc deposits in the centre. Two mechanisms can lead to this kind of metal zoning. Because of their respective solubilities, the metals precipitate in a specific order when they are affected by changes in the reducing state or in temperature. When the fluid carrying the metals, with a $\log(m\Sigma SO_4/m\Sigma H_2S)$ value close to 0 and a temperature of 350 °C, undergoes a temperature drop (arrow A in Figure 1-5), U solubility decreases until ~320°C, precipitating uranium. Then copper solubility drops from 100 to 1 ppm Cu from ~320 to ~220 °C, followed by the Zn solubility decrease from ~250 to ~170 °C. Another possibility is to begin with an oxidised fluid (arrow B). A similar sequence of solubility decrease is observed, leading to the uranium – copper – lead order of crystallisation when increasing the reduction state of the system.

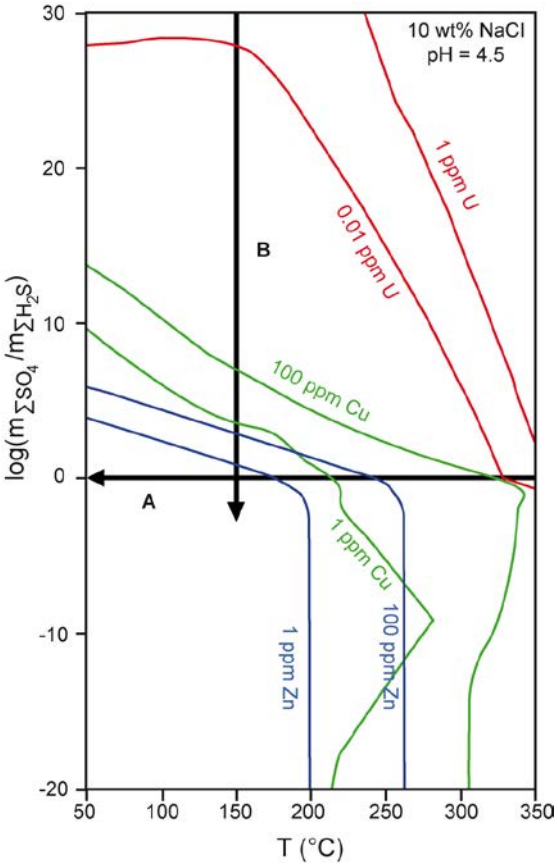

***Figure 1-5**: log (mΣSO₄/mΣH₂S) diagram showing the solubility of Zn, Cu and U. Coloured solid lines indicate solubilities of Cu, Zn and U. The diagram was calculated assuming a fluid salinity of 10 wt% NaCl, a total concentration of sulphur species of $10^{-2.5}$m, and a fluid pH of 4.5. Simplified from Huston et al. (2016).*

The McArthur Basin is of significant interest because of its strategic economic importance, and also for its correlation with other basins worldwide, such as the Mount Isa Inlier in Australia and the Athabasca and Thelon basins in Canada. On the basis of depositional constraints and detrital zircon signatures, the Wernecke Supergroup, broadly contemporaneous with the Thelon and Athabasca sedimentary successions, has also been linked to the Calvert Superbasin (Figure 1-6, Betts and Giles, 2006; Furlanetto et al., 2016 and references herein; Scott et al., 2000). In addition, Furlanetto et al. (2016) have analyzed Nd isotopic signatures of the mudrocks within these basins, which which resulted from the mixing of fine grained detritus during transport and deposition into these basins. Similar signatures from each basin may indicate that the fine sediments were deposited in the same oceanic region from broadly similar sediment inputs.

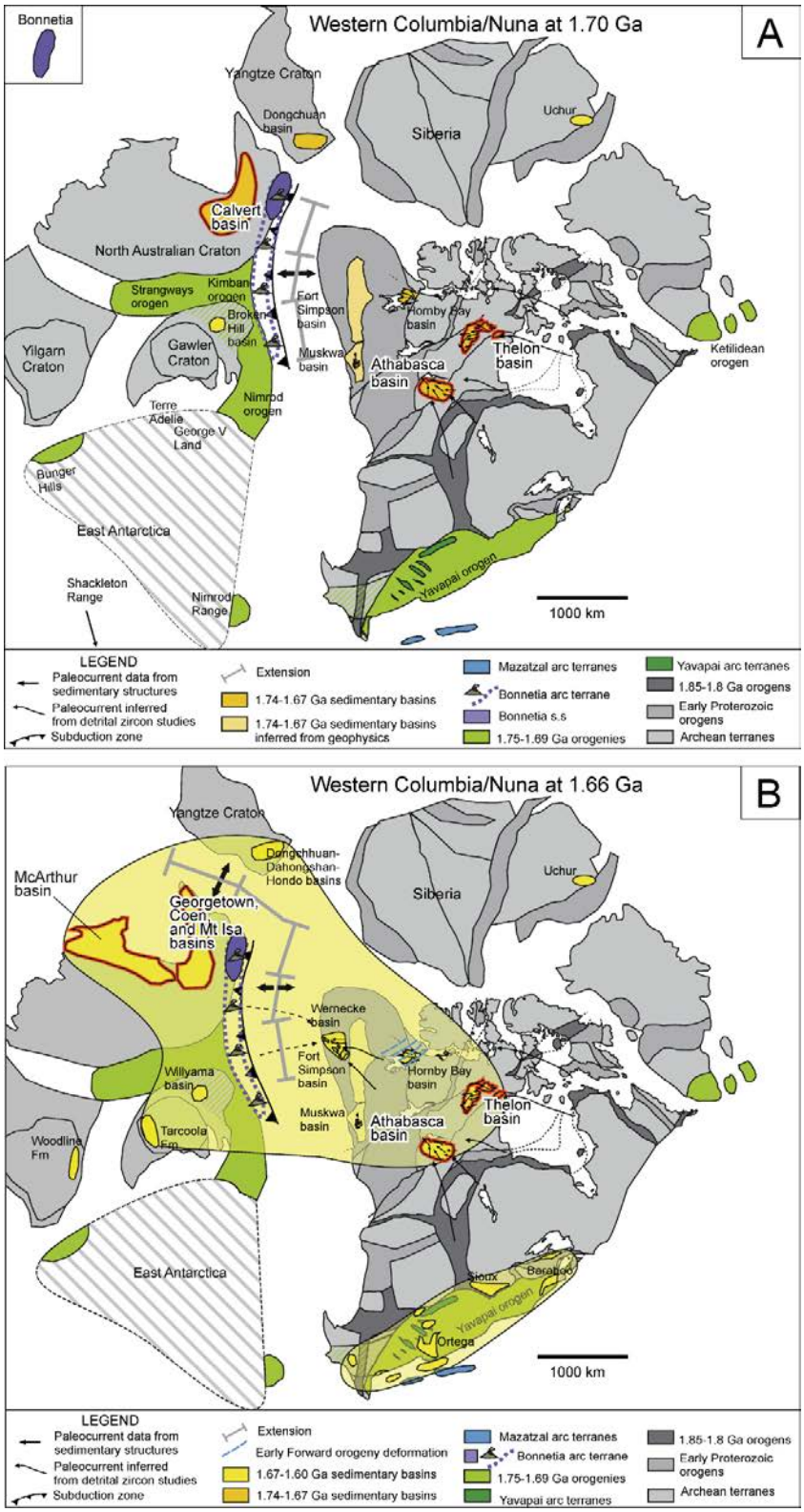

***Figure 1-6**: Possible history of the Columbia from 1.75 Ga to 1.58 Ga. **A**) Western Columbia/Nuna at ca 1.70 Ga. The Mawson continent joined North Australia and West Australia in the Strangways and Kimban orogenies, and all joined Laurentia along the western margin. The future Wernecke basin is facing a narrow basin (width unconstrained) that stretches between northwestern Laurentia, the Curnamona Province and Isa inlier of East Australia, and the Yangtze Craton (north of Northeast Australia). **B**) Breakup of north-western Columbia at ca 1.66 Ga involving separation of Australia and Yangtze from northwestern Laurentia. Also shown are all late Paleoproterozoic sedimentary successions in Laurentia, Australia, and Yangtze (after Furlanetto et al., 2016).*

1.2. Australian uranium resources

Australia possesses the largest share of the world's uranium resources with 29% of the total identified resources (<USD 130/kgU) and 23% of identified resources in the highest cost category (<USD 260/kgU, NEA - IAEA, 2016). Although there are more than 35 deposits with identified resources recoverable at costs <USD 130/kgU, the vast majority of Australia's resources are hosted within the following six individual deposits: Olympic Dam, a world class polymetallic Fe-oxide breccia complex, which is the world's largest uranium deposit (79% of Australia's uranium resources), Carrapateena (South Australia), Ranger and Jabiluka in the Alligator Rivers Uranium Field (ARUF, Northern Territory), and Kintyre and Yeelirrie (Western Australia). At Olympic Dam/, uranium is recovered as a co-product of copper mining, like gold and silver (NEA - IAEA, 2016). In Australia, the majority of the uranium resources are hosted in Proterozoic rocks of the Stuart Region (Figure 1-7, McKay et al., 2010) because of the huge tonnage of Olympic Dam. According to the compilation of McKay et al. (2010), the Pine Creek Orogen is the second largest Australian region for global uranium resources, at 13.3% of global resources.

All uranium deposits studied here are considered to be "basin-related uranium mineral systems". This includes uranium deposits formed during various stages of basin evolution, from sedimentation to diagenesis, and those producedpost-sedimentation fluid-flow (Jaireth et al., 2015). In Australia, 60% of the basin-related uranium mineral systems correspond to unconformity-related deposits (Figure 1-8).

In the McArthur Basin and its underlying basement complex, uranium occurrences can be classified as follows: unconformity-related, vein-type, Westmoreland-Murphy-type, sandstone-hosted, surficial deposits and metasomatite or intrusive-type (Lally and Bajwah, 2006). The first type of this PhD study is the unconformity-related one with the example of the Ranger deposit located in the basement under the northern extremity of the McArthur Basin. Geological architecture of unconformity-related uranium systems in the Pine Creek Orogen can be defined by three important components, which include a major unconformity, reduced Paleoproterozoic metasedimentary rocks below the unconformity, and a relatively thick (4–5 km) package of Paleoproterozoic coarse-grained, dominantly fluvial sedimentary rocks overlying the unconformity (Jaireth et al., 2015). The second type is the Westmoreland-Murphy-type, also classified as "Mafic-dykes/sills in Proterozoic sandstone" by the International Atomic Energy Agency (2018), with the Redtree and Junnagunna deposits hosted in southern part of the McArthur Basin (Figure 1-9). The Westmoreland deposits are sandstone-hosted, and often associated with mafic dykes and sills. A more precise description is presented in Chapter 3 where the results on the Junnagunna and Redtree deposits are detailed.

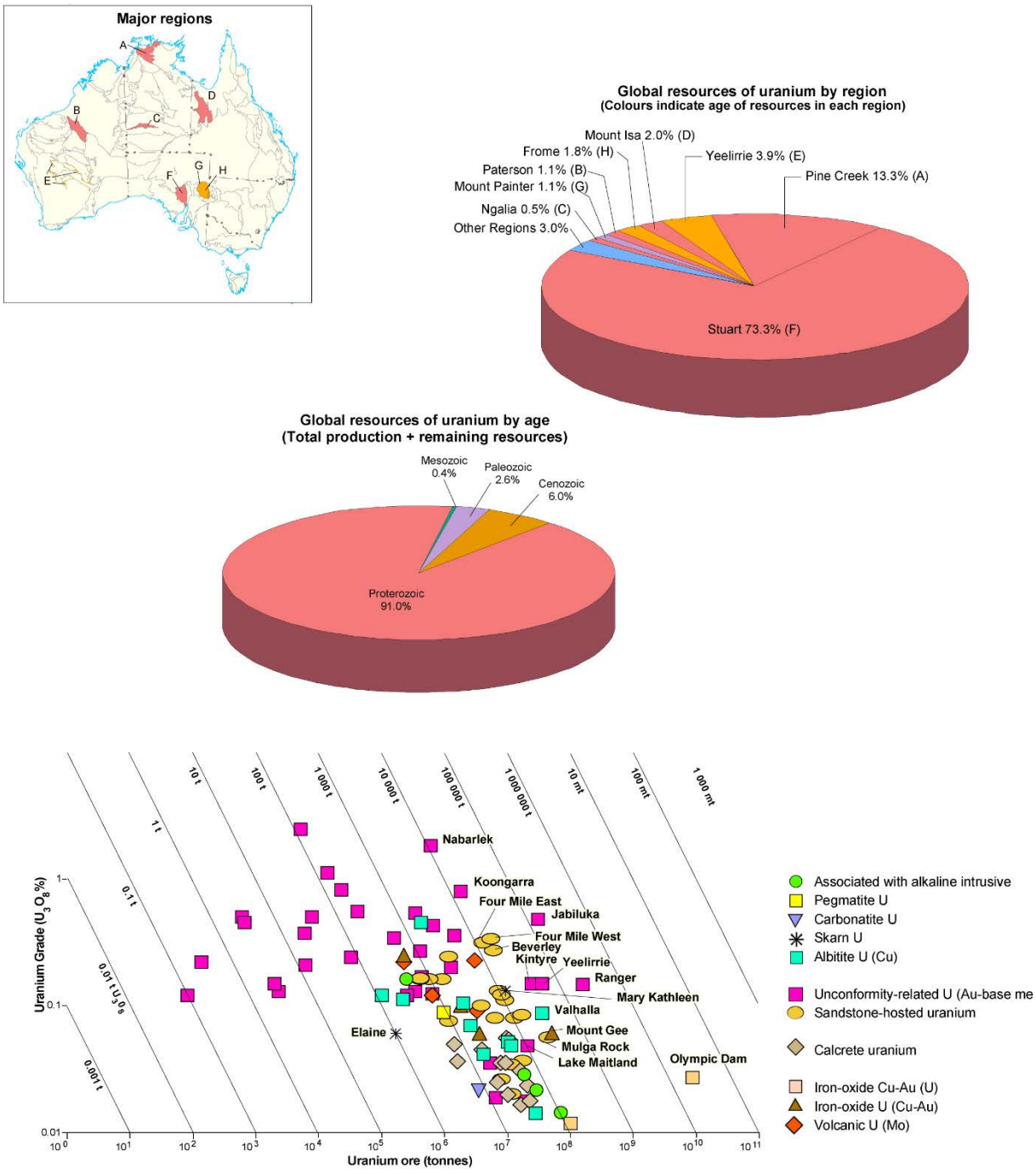

Figure 1-7: *Repartition of the Australian Uranium resources in terms of region and age of the mineralisation, and binary diagram of tonnage vs grade showing the richest deposits, including the Ranger deposit (McKay et al., 2010).*

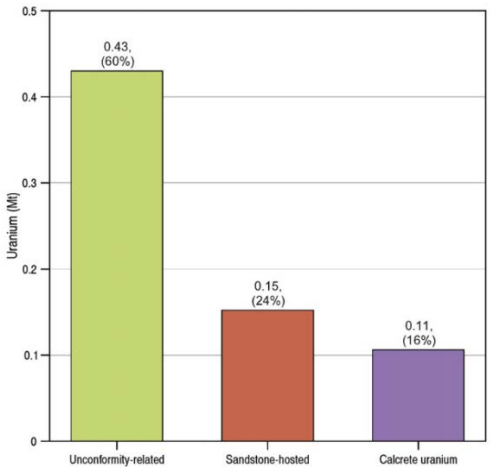

***Figure 1-8**: Uranium resources of basin-related uranium deposits in Australia. After Jaireth et al. (2015).*

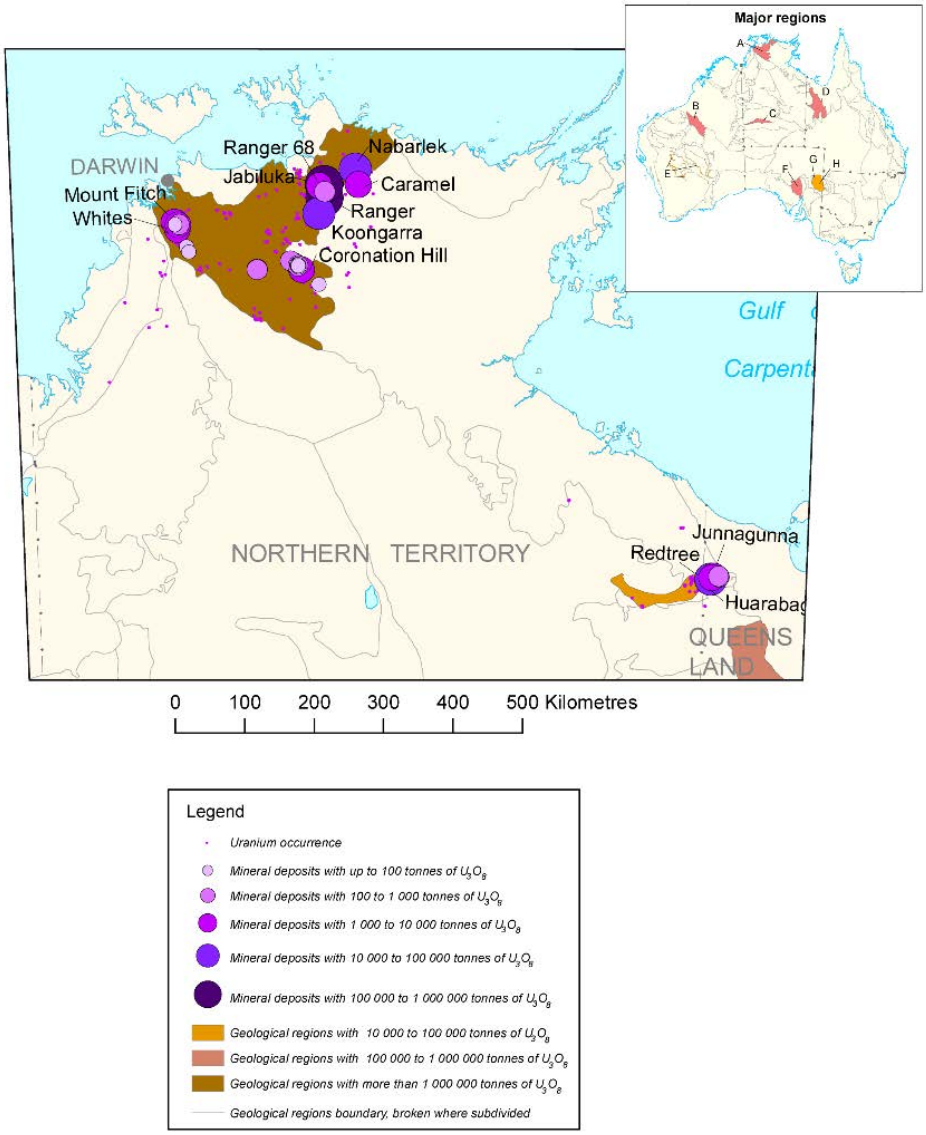

***Figure 1-9**: Location, grade of the uranium deposits or prospects and uranium-rich regions in the McArthur Basin and its basement (McKay et al., 2010).*

Two types of sources for the U-bearing minerals (zircon, monazite and apatite) have been postulated as the source of uranium in unconformity-related uranium deposits (Cuney and Kyser, 2009):

(1) Primary detrital heavy minerals in the sandstones overlying the unconformity:

Mernagh and Wygralak (2011) suggested that uranium and copper in the Westmoreland area were leached from the volcanics or sediments in the McArthur Basin. In the North of the basin, the U concentration in the Kombolgie Sandstone can be up to ~20 ppm (Jaireth et al., 2007)

(2) Uranium-bearing minerals in the metasedimentary rocks below the unconformity: Alternatively, the source minerals could also come from the basement rocks, as hypothesised by Derome et al. (2003). Skirrow et al. (2016) observed that approximately half of the uranium in the sub-unconformity alteration zones was removed and proposed that this alteration zone constitutes part of the uranium source. Ypma and Fuzikawa (1980) postulated that U was dissolved from the basement granite and gneisses, along the unconformity.

The chemical process of U deposition is achieved within structural geochemical traps by mobile and/or in situ reductants. A structural trap focussing the U-bearing fluids is also mentioned, such as the relatively impermeable Redtree dike in the Westmoreland area (Polito et al., 2005a). Uranium precipitation is primarily a result of reduction of U^{6+} to U^{4+}, whereas variations in salinity have only a minor effect on uranium solubility (Mernagh and Wygralak, 2011). Ore deposition was a response either to reduction of the ore-bearing fluid by interaction with graphite and ferrous iron in the wall rocks or by mixing with a methane and higher hydrocarbon-bearing brine (Wilde et al., 1989). All major host rocks of uranium deposits in the Pine Creek Orogen are enriched in carbonaceous material such as graphite, and intraformational redox gradients made of alternating successions of oxidised and carbonaceous-rich reduced sediments. These provided ideal conditions for the formation of sandstone-hosted uranium deposits (Jaireth et al., 2015). In addition, the interaction of the oxidised fluid with reduced lithologies is thought to have resulted in the precipitation of the coeval minerals of uraninite (illite, and hematite, Polito et al., 2004). At Nabarlek, the abundance of hematite and the absence of graphite and methane-bearing fluid inclusions coeval with mineralisation suggests that the Fe^{2+} in the Fe-rich chlorite may have acted as a primary reductant of U^{6+} (Polito et al., 2004). The same process is invoked by Polito et al. (2005a), with the Fe^{2+} in the Fe-rich chlorite adjacent to the Seigal Volcanics as chemical trap that reduced the U^{6+} to precipitate uraninite in the Westmoreland area.

In addition to the host-rock characteristics, some authors lean towards the chemical properties of the fluids for U precipitation. The uraninite deposition model of Derome et al. (2003) is interpreted to be the result of a mixing between a Na-dominated and a Ca-dominated

fluid. However when considering the paragenesis documented by Polito et al. (2005a), this mixing had to occur after uranium precipitation had ended, and thus is not the cause for uraninite precipitation. Derome et al. (2003) point out the role of the major basement faults that are preferred places for a reaction between fluid and graphite from basement lithologies to produce CH_4 that could have been the reducing agent. The mixing of U-bearing brines with the hot and low salinity fluid associated with CH_4 could represent part of the bulk process that caused the uranium deposition (Derome et al., 2003). Basinal fluids are drawn into the basement after faulting and brecciation, thus precipitating uraninite and other alteration minerals and filling the available pore spaces (Polito et al., 2005b). Ypma and Fuzikawa (1980) invoked the mixing between a low salinity CO_2-rich oxidised fluid, transporting uranyl carbonates complexes and a highly saline brine containing CH_4. The low pH of the highly saline brine would have induced the destabilisation of the uranyl-complexes and CH_4 caused the reduction of the uranyl ions to form uraninite.

1.3. Australian lead and zinc resources

Australia contains the largest Pb-Zn resources in the world with 59.5 Mt Pb (41% of the global resource) and 95.4 Mt Zn (28% of the global resource), as well as the second largest economic resource of silver. The exploitation of these resources makes Australia a major producer of lead and zinc, ranking number 2 and number 5, respectively (Britt et al., 2019; Mudd et al., 2016). Depending on which year, Australia continues to maintain or grow significant levels of production (Figure 1-10).

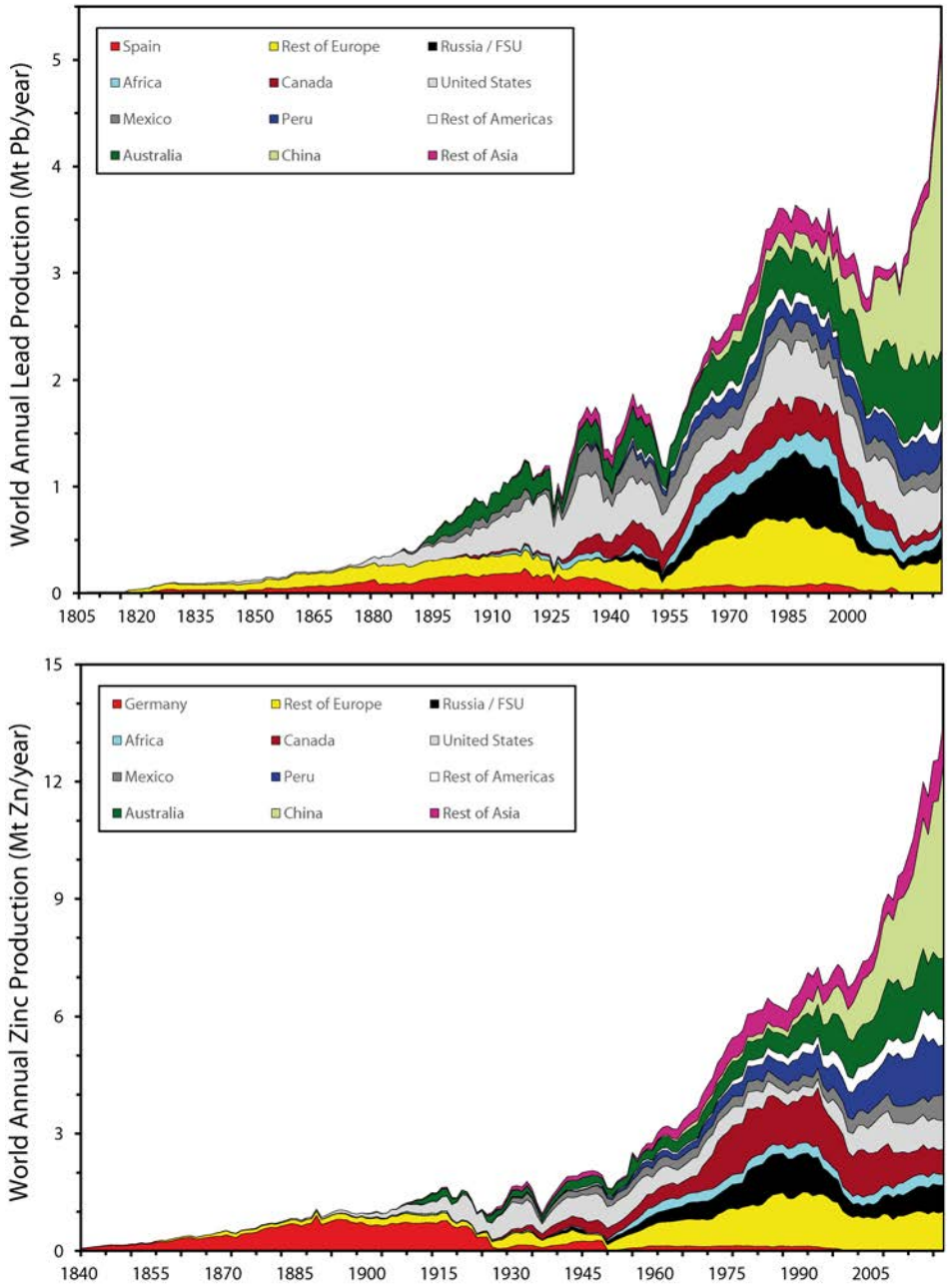

***Figure 1-10**: Historical Pb (top diagram) and Zn (bottom diagram) production by country or region, after Mudd et al. (2016).*

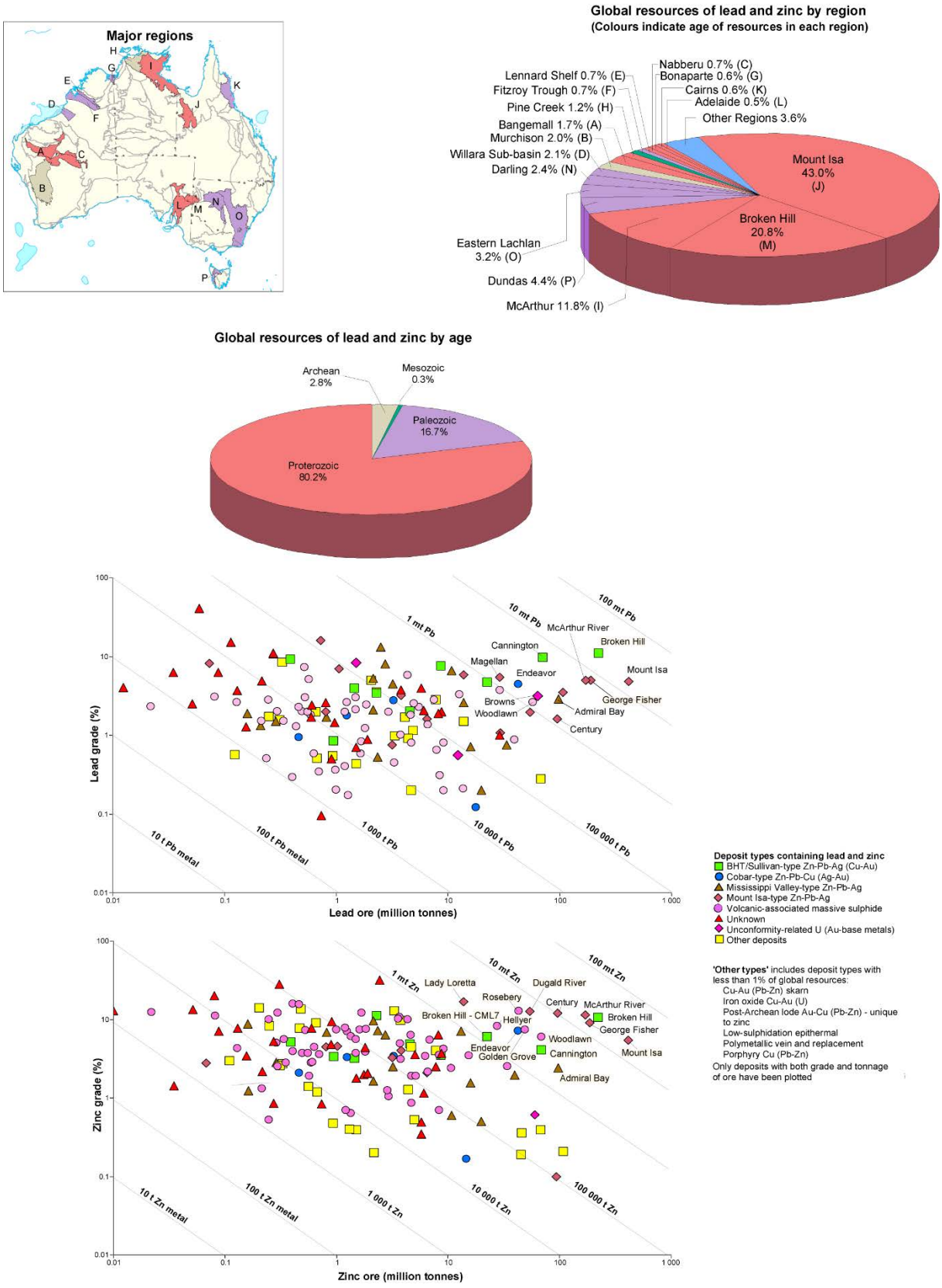

***Figure 1-11**: Repartition of the Australian Pb-Zn resources in terms of region, age of the mineralisation, and binary diagram of tonnage vs grade showing the richest deposits, including the McArthur River (HYC) deposit (Jaireth and Porritt, 2010).*

The McArthur Basin is one of the most significant base metal provinces of Australia (11.8% of the Australian resources) and forms part of the Carpentaria Zinc Belt, extending until Mount Isa to the South, mainly hosted in rocks of Proterozoic age (Figures 1-11 and 1-12). The Carpentaria Zinc Belt hosts several world-class base metals deposits: Mount Isa, Hilton, George Fisher and Century in Queensland and McArthur River (HYC) in the Northern Territory (Ahmad and Munson, 2013). The McArthur River (HYC) deposit is one of the richest deposits in terms of Pb and Zn in Australia (Figure 1-11).

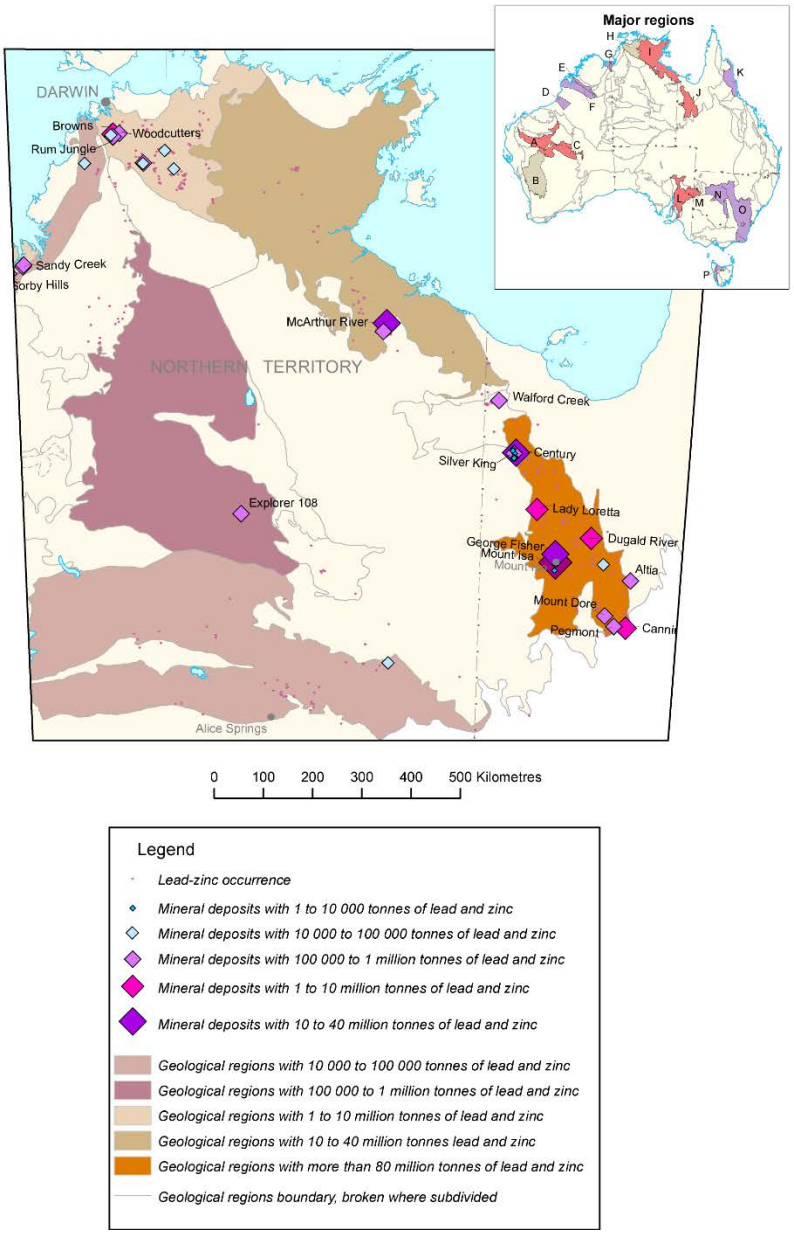

***Figure 1-12**: Location, grade of the Pb-Zn deposits or prospects and Pb-Zn-rich regions in the McArthur Basin, the Mount Isa Inlier and their basement (Jaireth and Porritt, 2010).*

Ahmad and Munson (2013) described the Pb-Zn deposits types in the McArthur Basin as either stratiform and sedimentary hosted in pyritic organic rich shale and siltstone such as McArthur River, or stratabound and discordant. The stratiform or stratabound Zn-Pb-Ag deposits comprise fine-grained pyrite, galena and sphalerite, preferentially concentrated in pyritic bituminous shale. They are considered to have formed either synchronously with sedimentation at the sediment–water interface or by early diagenetic processes. The HYC Pyritic Shale Member of the Barney Creek Formation hosts the only known economic occurrences, the McArthur River deposit. The stratiform deposits are similar to the Mount Isa deposit in Queensland, but whereas the latter is weakly metamorphosed and the sulphides are relatively coarse grained, the currently known deposits in the McArthur Basin are unmetamorphosed. The consequence is the small size of the sulphides, seldom exceed 10 μm at McArthur River. The discordant Pb-Zn-Ag ±Cu deposits occur as open space-filling of coarse-grained pyrite, galena, sphalerite and chalcopyrite in brecciated dolostone, and were generated by low- to moderate temperature hydrothermal fluids (Ahmad and Munson, 2013). A number of these mineralisation is associated with karstification close to silicified regolith. Vein-style deposits are few and are usually chalcopyrite rich (Ahmad and Munson, 2013).

For metal precipitation, the most accepted phenomenon is the sulphate reduction and/or addition of H_2S (via fluid mixing or interaction with diagenetic pyrite) of oxidised metal-bearing fluids. This occurs when a reductive environment is encountered, such as organic-bearing lithologies (Cooke et al., 1998, 2000; Huston et al., 2006; Large et al., 2005). A maximum flooding surface in the HYC Pyritic Shale Member represents the most pyritic and organic-rich interval around the McArthur River deposit. It is an ideal chemical trap for base metals in syngenetic models for mineralisation; however, lithification and compaction would convert this black shale interval into a physical trap in diagenetic models (Kunzmann et al., 2019). The ore-forming process may have involved thermochemical or bacterial sulphate reduction, and thus microorganisms would have played a role in the ore-forming process (Large et al., 2005; Logan et al., 2001).

1.4. Synthesis of mineralising events in the McArthur Basin

Various isotopic methods have been used in the literature to date mineralising or regional events. This include U-Pb or Sm-Nd on uraninites (Maas, 1989; Polito et al., 2005a, 2005b; Skirrow et al., 2016), $^{40}Ar/^{39}Ar$ is used for illite by (Polito et al., 2004, 2005b), $^{207}Pb/^{206}Pb$ on tuffaceous, volcanic input contemporary to sediment deposition (Page and Sweet, 1998), Pb model ages from galena (Carr et al., 2001a) and Rb/Sr on altered ore and white-mica separate (Maas, 1989). All these events were compiled and synthesised at the beginning of the PhD study and are reported in Figure 1-13.

Two main mineralising events have been reported in the McArthur Basin. The oldest one is only observed at the Ranger and Jabiluka uranium deposits and dated between 1720 and 1680 Ma. The second one takes place around 1640 Ma, even if ages vary between 1650 and 1595 Ma. More recent mineralising events have been reported (1400–475 Ma) and are explained by uranium remobilisation.

Based on the basin development and tectonic evolution model proposed by Gibson et al. (2017), the first mineralising event correlates with an extensional event. The second event begins during a collision-related basin inversion event (1650–1640 Ma), occurred during a rifting event and ended during a second inversion event (1615–1575 Ma). It is interesting to note that the age of 1640 Ma relates to the first dated events in the Glyde Package, and to the crossover timing between the Calvert and Isa superbasins.

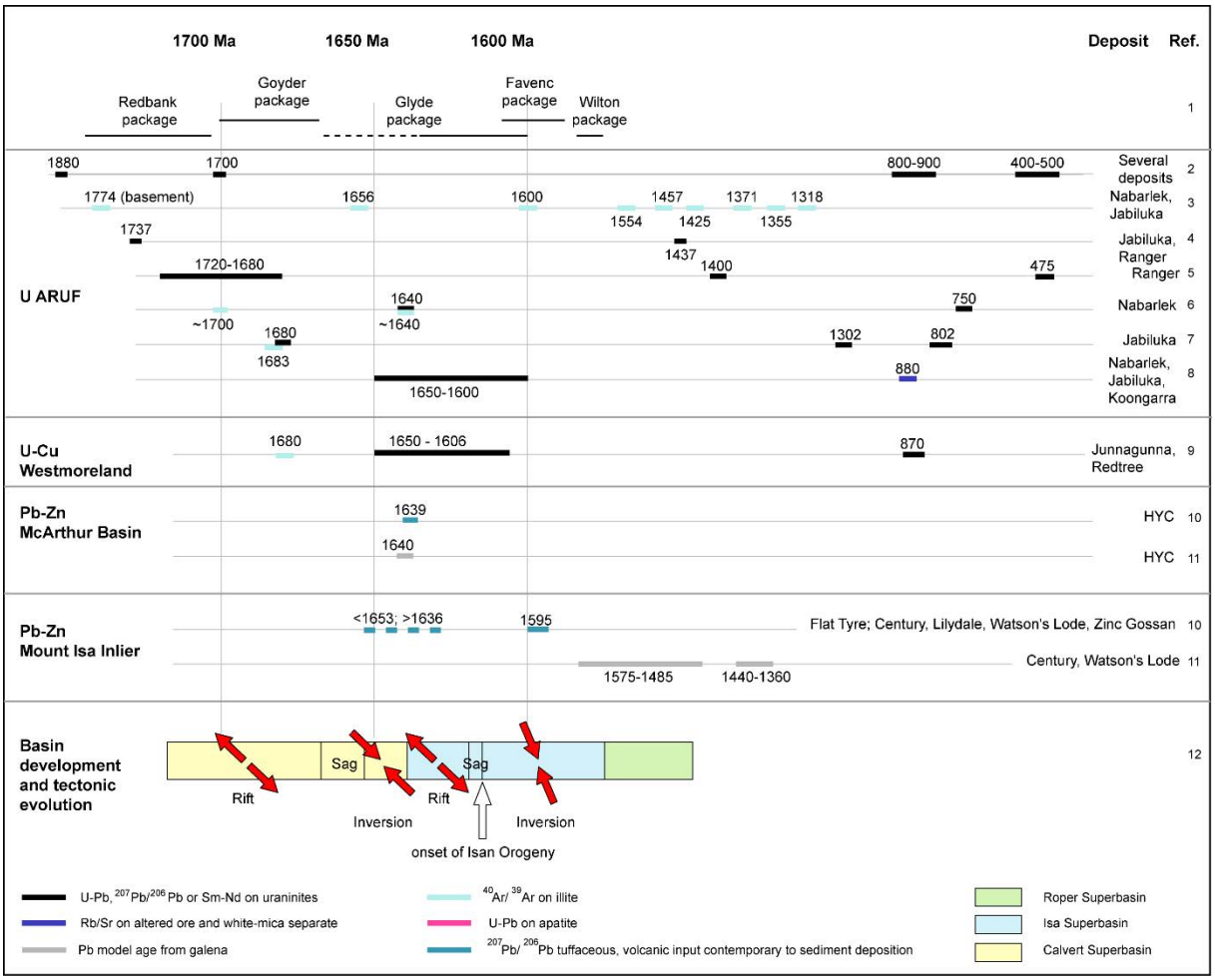

***Figure 1-13**: Synthesis of the geochronological data available in the McArthur Basin and in the unmetamorphosed part of Mount Isa Basin. 1: Ahmad and Munson (2013). 2: Hills and Richards (1976). 3: Clauer et al. (2015). 4: Ludwig et al. (1987). 5: (Skirrow et al., 2016). 6: Polito et al. (2004). 7: Polito et al. (2005a). 8: Maas (1989). 9: Polito et al. (2005a). 10: Page and Sweet (1998); 11: Carr et al. (2001). 12: Gibson et al. (2017).*

1.5. Fluid data synthesis in the McArthur and unmetamorphosed Mont Isa Inlier

Fluid inclusions are key witnesses to better understand the processes leading to fluid flows and their characteristics (salinity, temperature, and composition). A comprehensive review of all available microthermometric data on fluid inclusions in the McArthur and Mount Isa basins is proposed in this section, which covers about twenty publications devoted to fluid inclusions. These basins shows exceptional preservation: the areas on which this study focusses have remained relatively undeformed since ~1.5 Ga and have never been affected by metamorphism. The fluid inclusions of both barren zones and areas associated with deposits or prospects are included in this study (Figure 1-14). A summarised description of the mineralisation can is presented thereafter.

The Alligator Rivers Uranium Field (ARUF) hosts major world-class unconformity-type deposits that occur along the northwest margin of the McArthur Basin. The dominant host lithologies for the ore is a sequence of graphitic schists belonging to the Lower Cahill Formation (Derome et al., 2003; Polito et al., 2005b), within the basement complex, close to the unconformity. The Lower Cahill Formation consists of graphite, muscovite or feldspar quartz-schists, massive chlorite rock and chert frequently interbedded with marble (Needham, 1998). Uranium mineralisation occurs as uraninite veinlets in sheet-like zones, lenses, fine-grained disseminations and breccia zones subparallel to the foliation cemented by chlorite and uraninite (Polito et al., 2005b; Skirrow et al., 2016). At Jabiluka, uranium mineralisation is structurally controlled within semi-brittle shears that are sub-conformable to the basement stratigraphy, and breccias that are developed within the hinge zone of fault-related folds adjacent to the shears (Polito et al., 2005b). The uraninite is massive and homogeneous or colloform with concentric banding and radial shrinkage cracks (Polito et al., 2004).

The Westmoreland uranium field comprises more than 50 uranium prospects of various size and grade (Ahmad and Munson, 2013). Unlike the ARUF, the majority of known mineralisation in the Westmoreland area is primarily sandstone hosted adjacent to volcanic lithologies and belong to belong to “mafic dykes/sills in Proterozoic sandstone” type (International Atomic Energy Agency, 2018b), like the Redtree, Junnagunna, and Huarabagoo deposits. The only exception is the Eva deposit that is the only known significant uranium in the Murphy Inlier (Ahmad and Munson, 2013) and which is therefore a basement-hosted deposit. Some of the deposits show a clear link with three major northeast-trending lineaments: the Redtree deposit flanks the Redtree dike, and the Junnagunna deposit occurs at a fault intersection. The mineralisation can be stratiform and discordant (Polito et al., 2005a).

The McArthur River deposit (McArthur Basin) and Century (Mount Isa Inlier) SHMS deposits show similar morphological, textural, chemical, zoning, and isotopic features that suggest a common origin (Large et al., 2005, Jébrak et al., 2008). The McArthur River deposit shows preserved ore textures and soft sediment-deformed ore clasts of bedded sulphides within the interore sedimentary breccias (Large et al., 2005). In the Mount Isa Inlier, all the studied deposits are hosted in carbonaceous and calcareous shales and siltstones (Polito et al., 2006a, 2006c). The mineralisation at Century is stratiform and hosted in shales. The textural and morphological evidence support a strata-parallel, diagenetic replacement process below the sea floor. Pb model ages show that the main ore stage of mineralisation at Century formed at 1575 Ma (Carr et al., 2003, 1996), about 20 Ma after deposition of the host shale sequence (Polito et al., 2006a). The first mineralisation consists in bedding-parallel sphalerite (in polycrystalline aggregates or very fine grained in replacement of the matrix of the shale and siltstone). A second mineralising event consists in coarse grained sphalerite and galena that

cuts the first generation, and a later generation of sphalerite that occurs in “crackle veins” which postdate all other minerals in the deposit (Broadbent et al., 1998). The other base metal deposits studied in the Mount Isa Inlier are vein- and breccia-style.

At Walford Creek, the mineralisation is located at the intersection between a fault and reduced organic-rich shale units. This prospect is characterised by the superimposition of varying styles of mineralisation: stratiform Zn-Pb, stratabound and discordant Zn-Pb-Cu veins (Rohrlach et al., 1998).

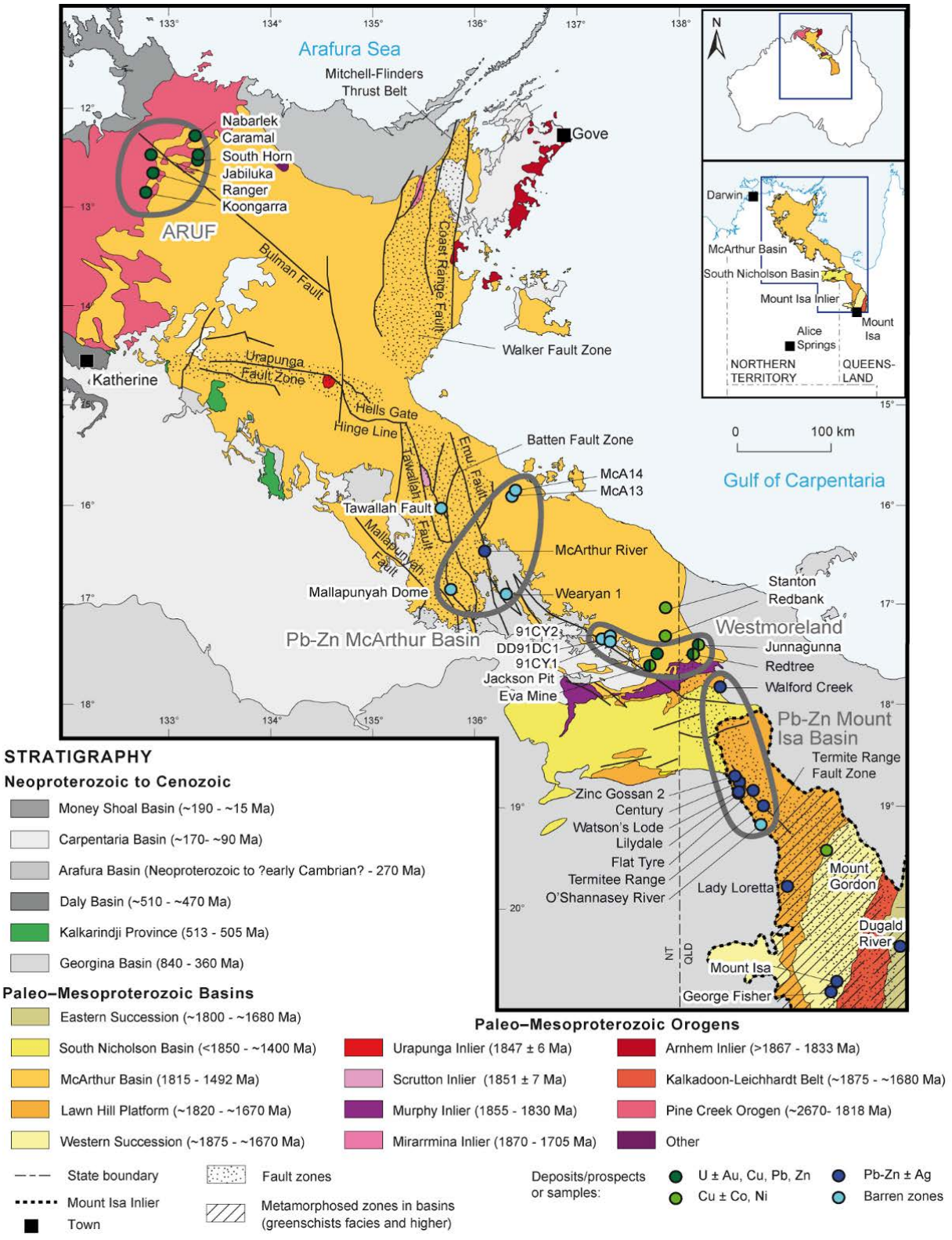

***Figure 1-14**: Simplified geological map of the McArthur Basin and Mount Isa Inlier, Australia. Some small outliers/inliers omitted. Simplified and slightly modified from Ahmad et al. (2013) and Geoscience Australia (GA) Geological Regions National Geoscience Dataset. ARUF: Alligator Rivers Uranium Field.*

The fault zones are well developed in the McArthur Basin and Mount Isa Inlier and are often spatially associated with deposits (Figure 1-14). For example, the faults segment the units and

represent multiple episodes of extensional and compressional deformation around Walford Creek (Rohrlach et al., 1998a). The deposits studied by Polito et al. (2006a) all lie adjacent to the Termite Range fault or are hosted within northeast-southwest–trending splays and faults that tapped the Termite Range fault at some time during the history of the basin. At Jabiluka, the mineralisation is structurally controlled within semi-brittle shears (sub-conformable to the basement stratigraphy) and breccias (Polito et al., 2005b). The Koongarra deposit is hosted in the hanging wall of a silicified reverse fault and the Nabarlek deposit is situated along a fault (Skirrow et al., 2016). Fault activation and/or reactivation could be in some cases the key factor that controls the mineralisation. They acted as fluid conduits focussing metalliferous brines stored in the reservoirs to sedimentary traps on or close to the basin floor (Large et al., 2005), or as preferential mixing zones for the different fluids (Derome et al., 2003), resulting in the formation of the deposits. The Termite Range fault probably focused mineralising fluids into favourable trap rocks and subsidiary structures on the Lawn Hill platform (Polito et al., 2006a). Even if they can be traced for several kilometres, mineralisation is often localised in dilatational zones that preserve multiple episodes of brecciation. In the Westmoreland area, faults have in part reactivated older basement faults. The reactivation of earlier “extensional fault systems” is thought to have occurred at least three times during and after basin development (Scott et al., 2000). Even the stratiform deposits like Century and McArthur deposits are located close to major regional basinal faults. They were active during sedimentation and acted as conduits for transport of metalliferous sedimentary brines from deep in the Mount Isa Inlier and McArthur Basin (Large et al., 2005). The hydraulic brecciation and fault reactivation itself plays an important role, as it is associated with a pressure decrease in active drainage zones where different fluid reservoirs were connected, favouring fluid mixing and the cementation of breccias (Derome et al., 2003, 2007).

1.5.1. Material and methods

All the fluid inclusions taken into consideration within this synthesis are primary or pseudo-secondary types. The amount of this kind of fluid inclusions is sufficient to remove from this study the secondary fluid inclusions and allow better interpretations. Depending on the authors, the fluid inclusion studies present results in salinity and/or melting temperatures (Tm). To convert salinity to melting temperature, the salt composition is needed but not always given. That’s the reason why we chose in this study to plot the salinity and homogenisation temperature in binary diagrams to make the comparison between all the papers possible.

When/where the salinity was documented in the papers, it has been used without any calculation, except a sum when different salts were observed. When the salinity was not given, it has been calculated from ice melting ± hydrohalite melting ± halite melting temperatures of

fluid inclusions. Depending on the nature of the salt present in the fluid, the standards used were the ones from Bodnar (1993) for the H_2O-NaCl system, Bakker (2003) for the H_2O-$CaCl_2$ system and Steele-MacInnis et al. (2011) for the H_2O–NaCl–$CaCl_2$ system. If the salt is not given in the paper, the following systems were used: H_2O-NaCl when the Tm_{ice} is between 0 and -21.2 °C, and H_2O-$CaCl_2$ system when it is lower. The homogenisation temperatures are presented uncorrected for pressure, because of the lack of evidence for burial metamorphism and because the thickness of the overlying sediments is unknown.

One of the aims of this compilation study is to sum up the correlations between the mineralising events, the fluid inclusions contained in the mineral of interest itself (sphalerite) or in the gangue minerals (quartz or dolomite), and the regional events responsible for the mineralization. Based upon the nomenclature proposed by Derome et al. (2003) which acts as a reference ("r"), all the available papers concerning fluid inclusions of this area have been compiled into a unified database. For each paper, quartz, dolomite or sphalerite generations have been renamed to correspond to the nomenclature presented in Figure 1-15. For example, all the Q3r correspond to the first brecciation event associated with quartz growth detailed in one given paper, even if they may not be coeval between the different papers. In the Pb-Zn deposits, Sp3r growth is coeval with Q3r growth.

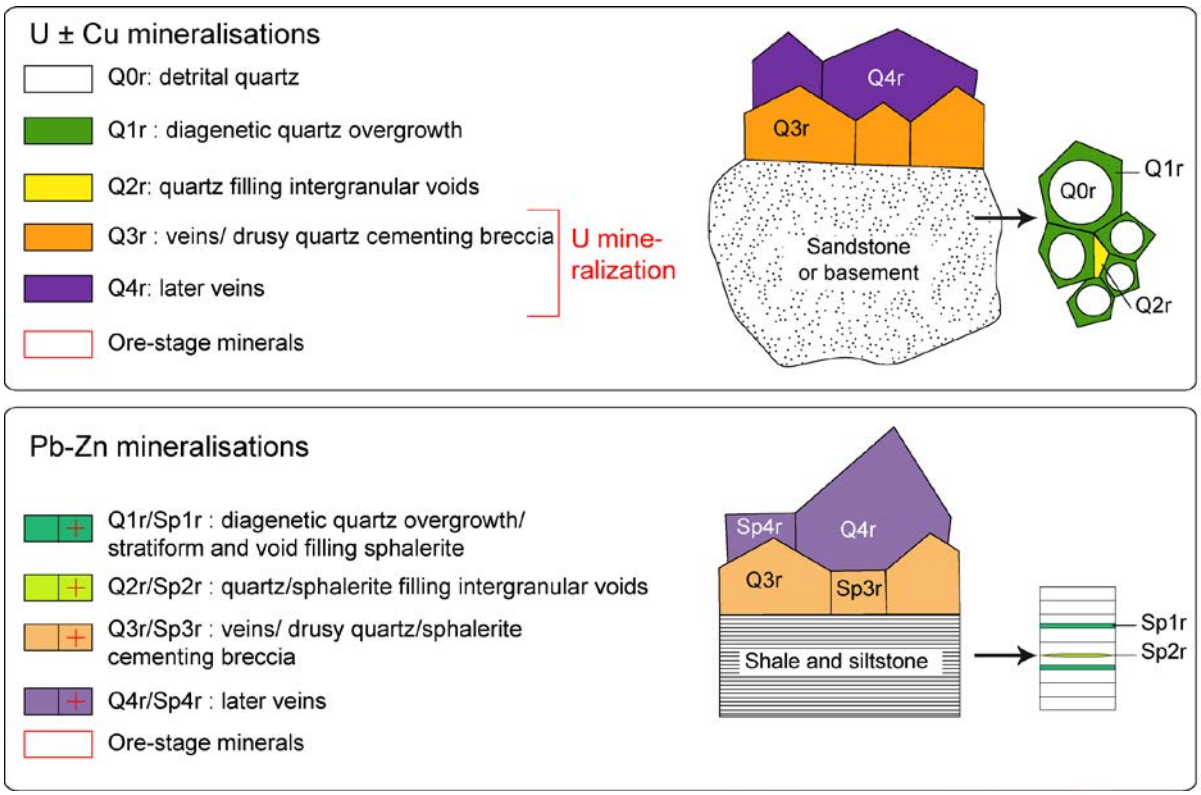

***Figure 1-15**: Quartz, dolomite and sphalerite nomenclature used in this study after Derome et al. (2003).*

1.5.2. Fluids sources

Isotopic studies on oxygen and hydrogen are often used to investigate the origin of fluids. In the McArthur Basin. Some of these isotopic results point to a precise origin, others rather evoke the mixing of fluids. Concerning the nature of sources, evidence for either marine or meteoric origin, or both are reported in literature. In addition, fluids can either originate from the basin or from the basement.

Single marine origin

The first possible origin of fluids in the McArthur Basin is a marine one. Polito et al. (2005a) studied pre- and syn-ore phyllosilicates at Jabiluka. Their stable isotopic values indicate basinal brines that evolved in sandstone aquifers from marine pore fluids with minor contributions from a meteoric source. This is coherent with the measurements of Polito et al. (2005a) on syn-uraninite illite in the Westmoreland area with isotopic values consistent with those from evolved, evaporated marine water. The stable isotope results from Polito et al. (2004) show that the syn-ore illite and uraninite formed from basinal fluids with typically marine values, with minor contributions from a meteoric source. Based on major cation ratios and trace element data from crush–leach analyses, Derome et al. (2007) characterised the source of brines as sedimentary, compatible with evaporated seawater, with Cl/Br ratios typical of deep basinal brines. The Ca-enrichment and Mg-depletion in brines in comparison with seawater or evaporitic brines can be attributed to extensive fluid–rock interactions with the basements rocks. The brines are enriched in Br, and are interpreted as residual brines probably linked to the evaporite layers which are found in the McArthur basin.

Single meteoritic origin

The second possible source for the fluids is a meteoric one. In the ARUF, oxygen isotope data points to water of meteoric origin that was oxygenated and that dissolved U (Ypma and Fuzikawa, 1980). The ore-forming fluid studied by Polito et al. (2004) has characteristics suggesting that a low-temperature meteoric water exchanged hydrogen and oxygen with the interlamellar water and the octahedral hydroxyl groups of the illite. Derome et al. (2003) considered one low salinity fluid that is slightly warmer and presents more frequent and more significant occurrence of CH_4 than the brines. Their interpretation was that this fluid has circulated through deep faults in the basement rocks, where it has been heated and where it has probably reacted with graphite to produce small amounts of CH_4. The low salinity of this fluid suggests a probable meteoric origin. Late fluids trapped in veins show low δD_{fluid} values typical of evolved meteoric water and distinct from the mineralising brines (Polito et al., 2005b).

Abundant data are also available for the post-ore quartz veins. According to Polito et al. (2004), the data indicate formation from a moderately evolved meteoric fluid, with some contribution from an evaporite source. The fluid inclusion studies from Polito et al. (2005a) record isotopic values typical of evolved meteoric water. The interpretation of Cooke et al. (1998) is that the dolomite veins and amygdules in the Settlement Creek Volcanics formed from low-moderate temperature (100 °C), evolved meteoric waters. Increasing temperatures are accompanied by the waters evolving to heavier isotopic compositions and salinities during water-rock interaction (Claypool et al., 1980; Taylor Jr, 1979). Cooke et al. (1998) measured carbon-oxygen isotopes and concluded that meteoric origin is favoured for the diagenetic brines. At Century, microthermometry on fluid inclusions hosted in porous sphalerite shows that the Zn was transported to the deposit by a basinal brine that evolved from meteoric water (Polito et al., 2006a).

Dual source origin

The third hypothesis is a mixed origin of both meteoric and marine fluids. Mixed origin fluids are observed for example during late diagenesis in the Southern McArthur Basin, where the isotopic compositions of illite suggest a dual origin (Polito et al., 2006b). Interestingly, the authors also noted that their values are indistinguishable from those of alteration minerals at the McArthur River deposit or synore illite at the Westmoreland uranium deposit. This suggests that the diagenetic aquifers and the deposits may be linked. In comparison with the fluid that formed Century, later fluids are less saline and have higher δD_{fluid} values, due to mixing between the mineralising fluid and a seawater-derived fluid (Polito et al., 2006a). The forming fluid for the latest quartz veins in the Mount Isa Inlier could have originated from a mixture of evolved meteoric and marine fluids, and the high temperature points to the involvement of deeply sourced metamorphic fluids (Polito et al., 2006a). The data at the lode deposits are attributed to mixing between highly saline, highly evolved meteoric fluids and low-salinity, moderately evolved marine fluids (Polito et al., 2006a).

Basinal or basement fluids

Based on detailed mineral paragenesis, electron microprobe and stable and radiogenic isotope analyses, Polito et al. (2004) proposed that the formation of the Nabarlek deposit involved the incursion of basinal fluids with minor meteoric component. This is consistent with the results of Wilde et al. (1989) from whim the spatial and temporal association of the deposits with sediments of the McArthur basin suggests involvement of sedimentary brines in mineralisation and is also consistent with the presence of hydrocarbons in some of the

analysed inclusions. Wilde et al. (1989) proposed that the calcic brines derived from the oxidised red-bed sediments overlying the deposits (McArthur Basin). Around Century, diagenetic aquifers in the underlying Calvert superbasin appear to have been the most likely sources for the fluids that formed Century and the discordant lode deposits (Polito et al., 2006a). The aquifers can also be located in the overlying sediments. This would be the case in the Pb-Zn Mount Isa where the late veins could have formed from fluids derived from aquifers in overlying sediments of the Roper superbasin (Polito et al., 2006a).

The results obtained by Polito et al. (2004) on fluid inclusions and $\delta^{18}O$ and δD values indicate that the veins formed from basement-derived fluids that may have been heated by a cooling Nabarlek Granite during circulation through faults or shear zones. The Ca–Na brine described by Derome et al. (2003) may result from the evolution of formation waters from evaporitic environment by circulating in the Ca-rich basement lithologies.

1.5.3. Ore-stage fluids and metal transport

In some cases, several fluid with different salinities and homogenisation temperatures mixed at some point in the history of the area. On a salinity vs Th diagram, the effects of this mixing are a triangle-shape pattern, with fluid inclusions that witness fluids ranging from cool (~100 °C) to hot (>300 °C), and having low (<5 wt% eq $_{NaCl}$) to high salinities corresponding to brines (>20 wt% eq $_{NaCl}$). Based on the salinity and temperature, four types of fluids are identified: the brines (Na-rich or Ca-rich), and the low-salinity fluids (cool or hot). In a schematic representation of the mixing pattern (presented in Figure 1-16), three of them correspond to the three points of the triangle. The inside of the triangle (greyed out in the figure) represents the whole range of compositions between the end-members and can be interpreted as fluid mixing that occurred during periods of fluid influx, as no complete homogenisation of the fluids compositions has occurred (Derome et al., 2007).

Ore-stages fluids can carry metals in various amounts depending on their characteristics and record the conditions of metal transport. Cooke et al. (1998) suggests that some fluids could content significant amounts (> 1 ppm) of Zn, Pb, and Cu. The evolved basinal brine that formed the diagenetic minerals in the Westmoreland Conglomerate was the same as that which transported the uranium to the site of uraninite deposition (Polito et al., 2005a). It is important to keep in mind that the high homogenisation temperatures can result from the heating of the fluid by intrusions (such as the dolerite dykes) which would produce a thermal “spike” in the basin (Kyser et al., 2000). In the next paragraphs, a compilation of all the published data on salinity and homogenisation temperature of fluid inclusions in the McArthur Basin are presented. This was realised at the beginning of the PhD to get an up-to-date vision of the available data.

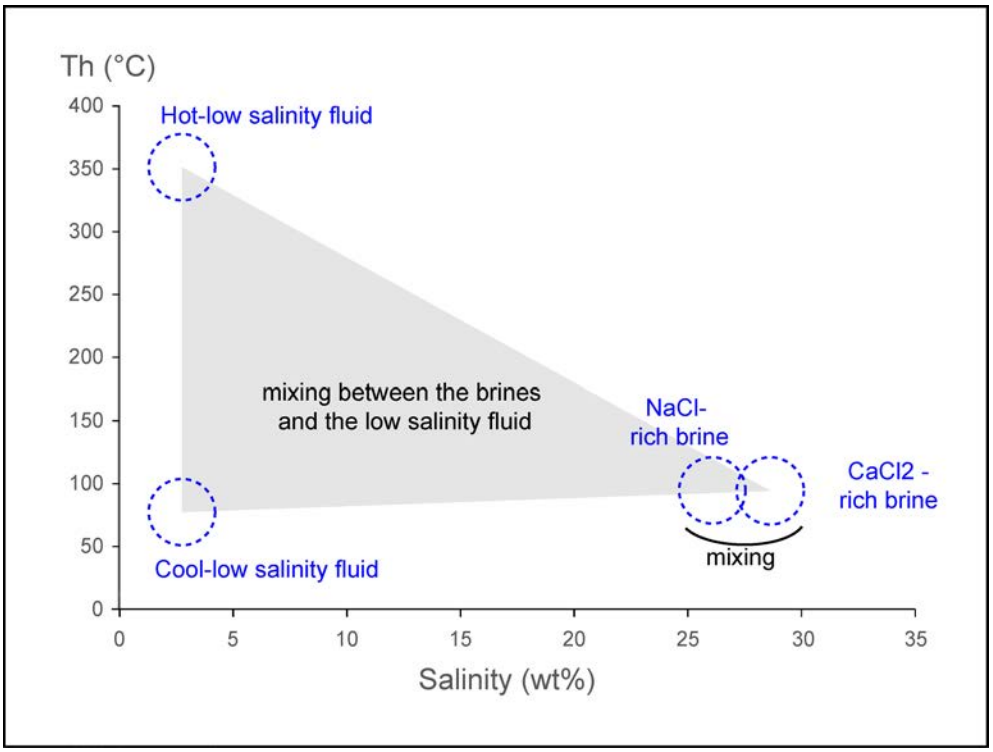

***Figure 1-16**: Synthesis and processes leading to the graphs observed in Figures 1-17 to 1-19. The end-members are from Derome et al. (2007).*

Unconformity-type uranium in the Alligator Rivers Uranium Field

Initial uraninite precipitation occurred in the basement at ca. 1680 Ma in the ARUF (Polito et al., 2005b; Skirrow et al., 2016), coincident with illite ages extracted from diagenetic aquifers, suggesting that fluids were moving out from the sandstone aquifers at this time to form the illite. Mineralisation occurred around 100–200 °C (e. g. Polito et al., 2004; Ypma and Fuzikawa, 1980). The fluids were heterogeneous as they feature the mixing of a very saline brine with a more dilute CO_2-rich fluid (Figure 1-17), both of which occur in the same growth zones of quartz crystals coeval with the mineralisation (Derome et al., 2003). Brines were continuously diluted by a hotter (150–200 °C) low-salinity fluid (Derome et al., 2007). The brines studied were at 100–150 °C with a salinity of 20–35 wt.% Na-Ca-Cl. At Jabiluka, the mineralising brine was saline, but neither saturated, nor Ca-dominated (Polito et al., 2005b), but in other areas halite can be present as daughter phase (Wilde et al., 1989). An inverse correlation between salinity and homogenisation temperature was reported (Derome et al., 2007; Ypma and Fuzikawa, 1980), with the paragenetic later solutions generally more saline and of lower temperature. The nature of the brines is still debated. Polito et al. (2005a) found evidences for fluid inclusions with a tight range of eutectic temperatures consistent with a mixture of $CaCl_2$ and NaCl. This is in contrast with the works of Derome et al. (2003) and Wilde et al. (1989) who both proposed that the syn-ore fluids involved a Ca-dominated component. Concerning the gas phase, the

fluids contained CO_2 and CH_4 and the abundance of CO_2 in fluids is sometimes related to the high-grade U mineralisation (Ypma and Fuzikawa, 1980 and references herein). The Ca-Na oxidised brines represent the most probable vector of dissolved uranium (Derome et al., 2003). Their high oxidation state made them ideal for the simultaneous transport of uranium, gold and platinoids (Wilde et al., 1989).

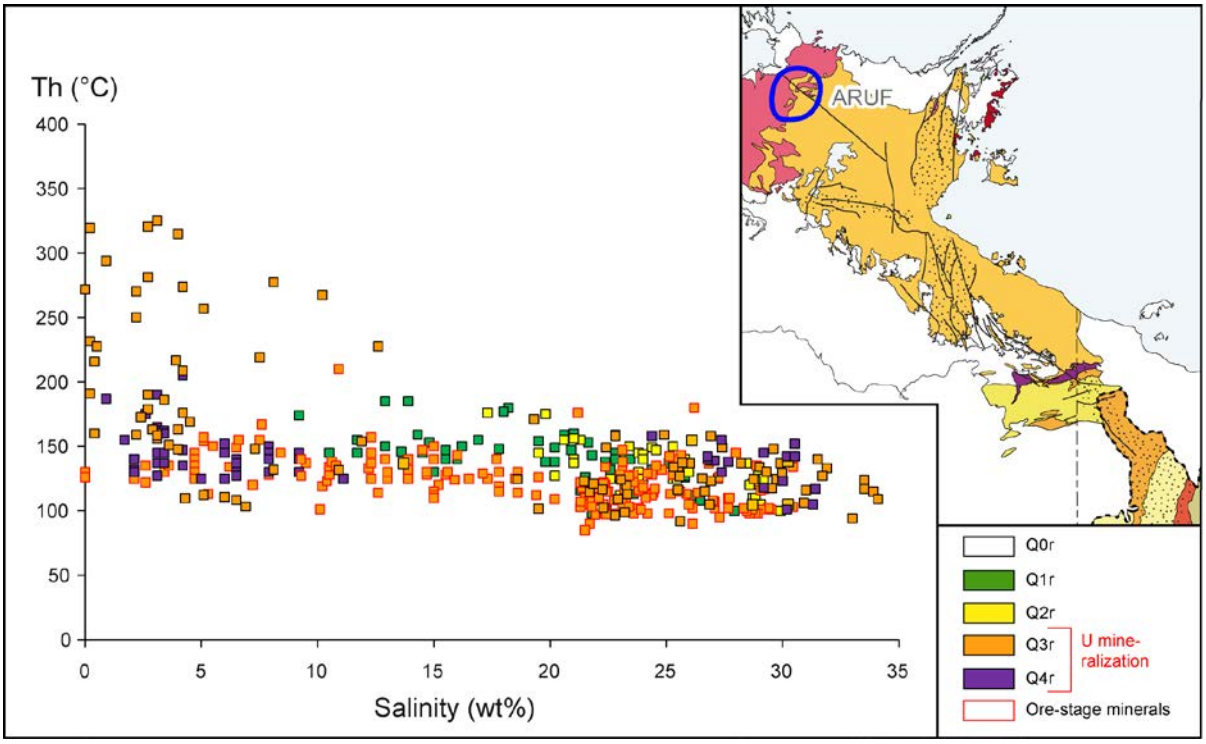

***Figure 1-17**: Homogenisation temperature-salinity plot for samples from the ARUF area. Compiled after Derome et al. (2003, 2007), Durak et al. (1983), Polito et al. (2004, 2005b) and Ypma and Fuzikawa (1980).*

Uranium in the Westmoreland area

For the uranium deposits, Mernagh and Wygralak (2011) noted both a high and a low temperature group (Figure 1-18), with each indicating mainly isothermal mixing between high and low salinity fluids based on the numerical modelling of Dubessy et al. (2003). The fluctuations were interpreted as possible post entrapment modification of inclusions or pressure/ temperature fluctuations at the time of entrapment. For Cu-associated inclusions, the high temperature inclusions indicate isothermal mixing of fluids of high and low salinity where the temperature of the mixed fluid is controlled by the host rock (Dubessy et al., 2003). The low temperature group indicates adiabatic mixing between cooler high salinity fluid and a hotter low salinity fluid. The spread in homogenisation temperatures is indicative of pressure fluctuations for a specific event of fluid circulation corresponding to a single proportion of each fluid end-member (Dubessy et al., 2003).

In the Westmoreland area, U and Cu were simultaneously transported in the oxidised, Na-Ca-Li-bearing saline fluids which have been mixed within the basin (Mernagh and Wygralak, 2011). The metals were transported to the site of deposition by a basinal brine consistent with evolved evaporated seawater, but not with hot, oxidised fluids derived from underlying uraniferous granites or volcanic rocks as previously suggested. U-bearing basinal fluids were migrating through the most porous areas of the Westmoreland Conglomerate where quartz overgrowth development was likely of limited extent or non-existent (Polito et al., 2005a). The NaCl-rich brine became progressively enriched in Ca; either by fluid mixing or by fluid/rock interaction, followed by tectonic movements reactivated basement faults releasing slightly hotter, low salinity fluids into the basin. The mixing of the oxidised brines with the more reduced, low salinity fluid initially led to the precipitation of uranium. Due to the moderate to high salinity of the fluids, most of the copper was not precipitated until the fluids cooled to lower temperatures (i.e., <150 °C, Mernagh and Wygralak, 2011). The hot fluids had homogenisation temperatures of 280–380 °C, which may be explained by a deep-seated origin within the basement rocks, in contrast to to low temperature shallow-seated ones (around 120 °C).

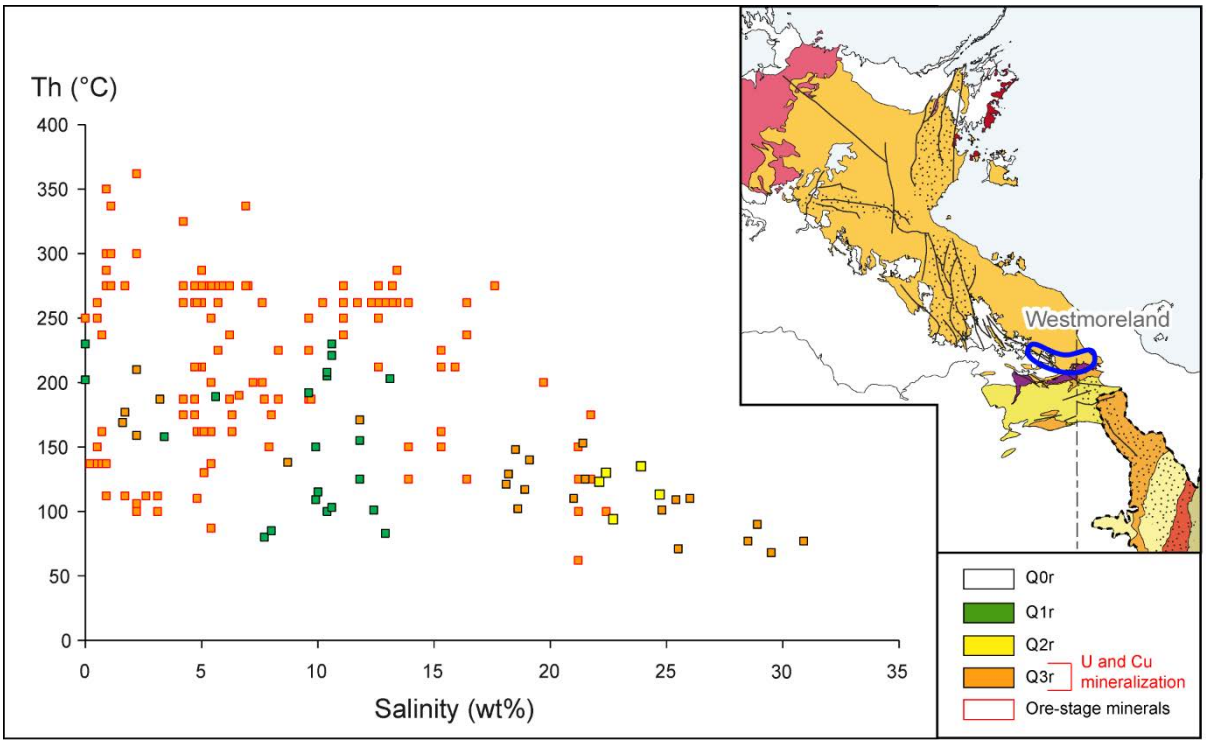

***Figure 1-18**: Homogenisation temperature-salinity plot for samples from the uranium deposits located in the Westmoreland area. Compiled after Mernagh and Wygralak (2011) and Polito et al. (2006b).*

Lead-Zinc

The sphalerite and their gangue minerals (quartz and dolomite) have been studied by Cooke et al. (1998), Polito et al. (2006a, 2006c, 2006b) and Rohrlach et al. (1998). The results

from each paper are presented independently, since they correspond to a separate distinct location, which may or may not be correlated with one another, and are reported as such in Figure 1-19.

In the Mallapunyah Dome in the McArthur Basin, the fluids responsible for metal leaching and K alteration were low temperature (100 °C), hematite-stable, saline (>20wt% eq $_{NaCl}$) brines. These brines possessed high base metal transporting capacity due to their oxidised nature and low H_2S content (Cooke et al., 1998). Hydrocarbons have been identified in the fluid inclusions, whose presence can be explained by brine derivation from the overlying evaporitic carbonates during diagenesis, with meteoric water and seawater descending through the overlying carbonate horizons. Cooke et al. (1998) proposed that the basinal brines migrated downwards along flow boundaries, fracture, joints, vesicles, and sill margins, leaching metal (particularly Pb and Zn). These leached metals t could have been transported long distances laterally away from the site of initial leaching along a suitable aquifer if the brines were sufficiently oxidised and H_2S-deficient.

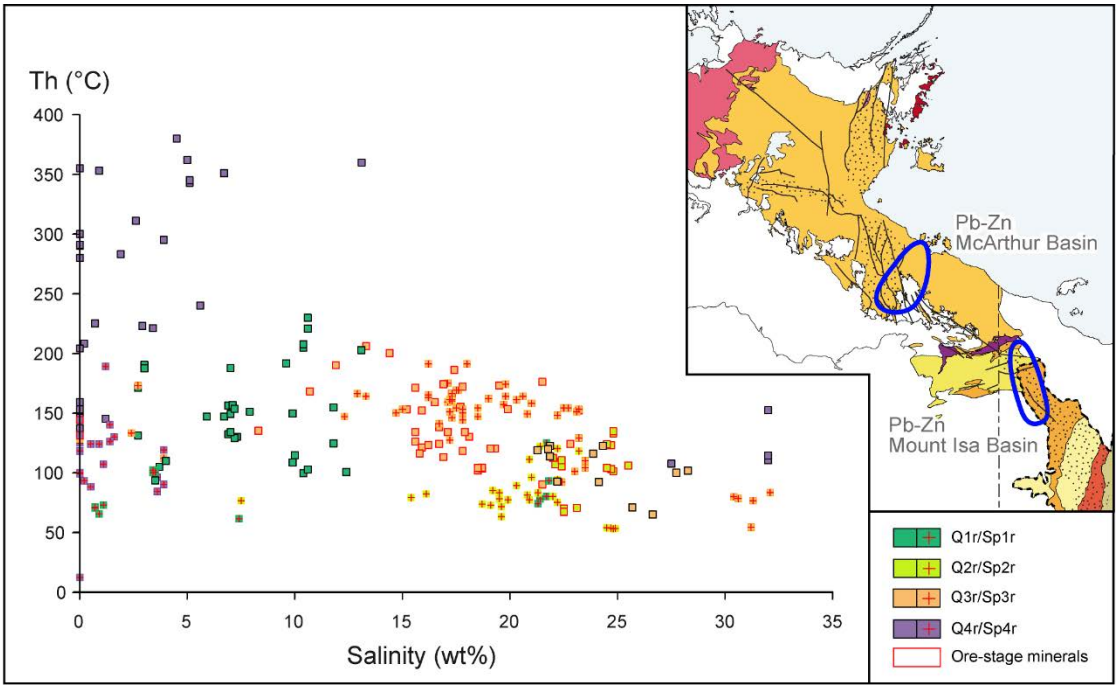

***Figure 1-19**: Homogenisation temperature-salinity plot for samples from the Pb-Zn deposits, in McArthur Basin and in the unmetamorphosed part of Mount Isa Basin. Compiled after Cooke et al. (1998), Polito et al. (2006c, 2006a, 2006b) and Rohrlach et al. (1998).*

Fluid inclusions within dolomite and quartz veins crystallising around the time of mineralisation in the southern part of the McArthur Basin have low eutectic temperatures indicative of Ca^{2+}- and Na^{+}-dominated brines and salinities between 18.5 and 30.9 wt% eq $_{NaCl}$ (Polito et al., 2006b).

At Walford Creek, three successive ore-stages fluids were identified (Rohrlach et al., 1998a). The first has a temperature between 61 and 102 °C with salinity between 0 and 7.5 wt% eq $_{NaCl}$, defining a mixing trend between a high temperature (>180 °C) fluid with > 7 wt% eq $_{NaCl}$, and a low-temperature (<60 °C), low-salinity dilute fluid (< 7 wt% eq $_{NaCl}$). The second stage-fluid corresponds to a mixing between a high temperature (>150 °C) evolved hypersaline brine (20–23 wt% eq $_{NaCl}$) and a cooler (<70 °C) brine of similar salinity. The last mineralising stage fluids had homogenisation temperatures between 54 and 83 °C and were highly saline (30–32 wt% eq $_{NaCl}$).

Primary fluid inclusions in the oldest sphalerite at Century indicate that the ore-stage fluid contained Ca^{2+}, Na^{+}, and possibly Li^{+}. This fluid was homogeneous, highly evolved basin-derived fluid of meteoric origin, close to halite saturation (23.2 wt% eq $_{NaCl}$) and was likely between 120° and 160 °C (Polito et al., 2006a). Between 1575 and 1485 Ma, fluids were intermittently introduced to form the discordant lode deposits and the transgressive and “crackle veins” at Century (Carr et al., 1996; Polito et al., 2006a). At this time, the trend toward lower salinities relative to the earlier mineralising fluids is attributed to mixing between the fluid that formed Century and a seawater-derived fluid with lower salinities down to 10 wt% eq $_{NaCl}$ (Polito et al., 2006a). Late sphalerite and calcite cut sphalerite, quartz, and dolomite in the lode deposits and contain Na^{+}-dominated fluid inclusions with much lower salinities than their older counterparts (Polito et al., 2006a).

In the Mount Isa Inlier, quartz veins were formed by fluids that migrated along faults from the diagenetic aquifers during late diagenesis to form the low-temperature Zn-Pb deposits between 1650 and 1575 Ma and later during the Isan Orogeny to form the high-temperature Cu deposits (Polito et al., 2006c). Quartz veins formed during the later diagenetic history in the Mount Isa basin from a Na^{+} dominated low-salinity fluid, between 2.7 and 10.4 wt% eq $_{NaCl}$ and homogenisation temperatures between 100 and 174ºC. Crosscutting relationships reveal that a subsequent generation of quartz veins host fluid inclusions with a distinctly saline brine, with compositions between 11.9 and 23.2 wt% eq $_{NaCl}$, indistinguishable from fluid inclusion compositions recorded in sphalerite from the Century and Walford Creek Zn deposits in the Lawn Hill platform and the quartz-dolomite-chalcopyrite veins at Mount Isa (Polito et al., 2006c and references herein).

1.5.4. Regional fluids

The pre- or post-ore fluids can be categorised in many types. A selection is presented in this sub-section to illustrate their high variability. In all the studied areas, multiple episodes of fluid flows extending over several hundreds of Ma are recorded. In the Burketown mineral field, fluid flows spanned a period lasting ≥400 Ma from 1575 Ma, the age of the Century deposit

(Carr et al., 1996), to ca. 1150 Ma (Polito et al., 2006a). Fluids were moving out from the sandstone aquifers at the time of uraninite mineralisation in the ARUF, but younger ages from diagenetic aquifers in the greater Kombolgie Subgroup suggest that fluid flow out of these units continued until ca. 1580 Ma (Kyser et al., 2000).

Modifications in fluid composition take place over time. An example of modification is the change of major cations composition in the brines (Ca or Na), identified at the Jabiluka deposit, where Polito et al. (2005a) highlighted that the $CaCl_2$-dominated fluids are later than uranium mineralisation. Another example of modification is the variation in homogenisation temperature and/ or salinity observed by Durak et al. (1983) with homogenisation temperature decrease and salinity increase from the grain boundary to overgrowth. In the Burketown mineral field, a different late fluid generation precipitates, i.e., from low-salinity-low-temperature fluids (140 ± 30ºC with salinities between 0 and 6 wt% eq $_{NaCl}$) to hot (ca. 300 ± 80 °C), low-salinity fluids (Polito et al., 2006a).

1.5.5. Compilation results of fluid inclusions through time

In a given place, fluid inclusions from all generations have generally similar patterns in the salinity vs homogenisation temperature diagram, indicating the presence of brines, low-salinity fluids, and variable homogenisation temperatures. However, the fluid trapping events show a spread between 1820 and 750 Ma (Figure 1-20), which appears to be a continuum of events when considering all of the data at a basin scale, for example. Some parts of the basin record specific fluid circulation timing, while other seems to be affected by multiple fluid events.

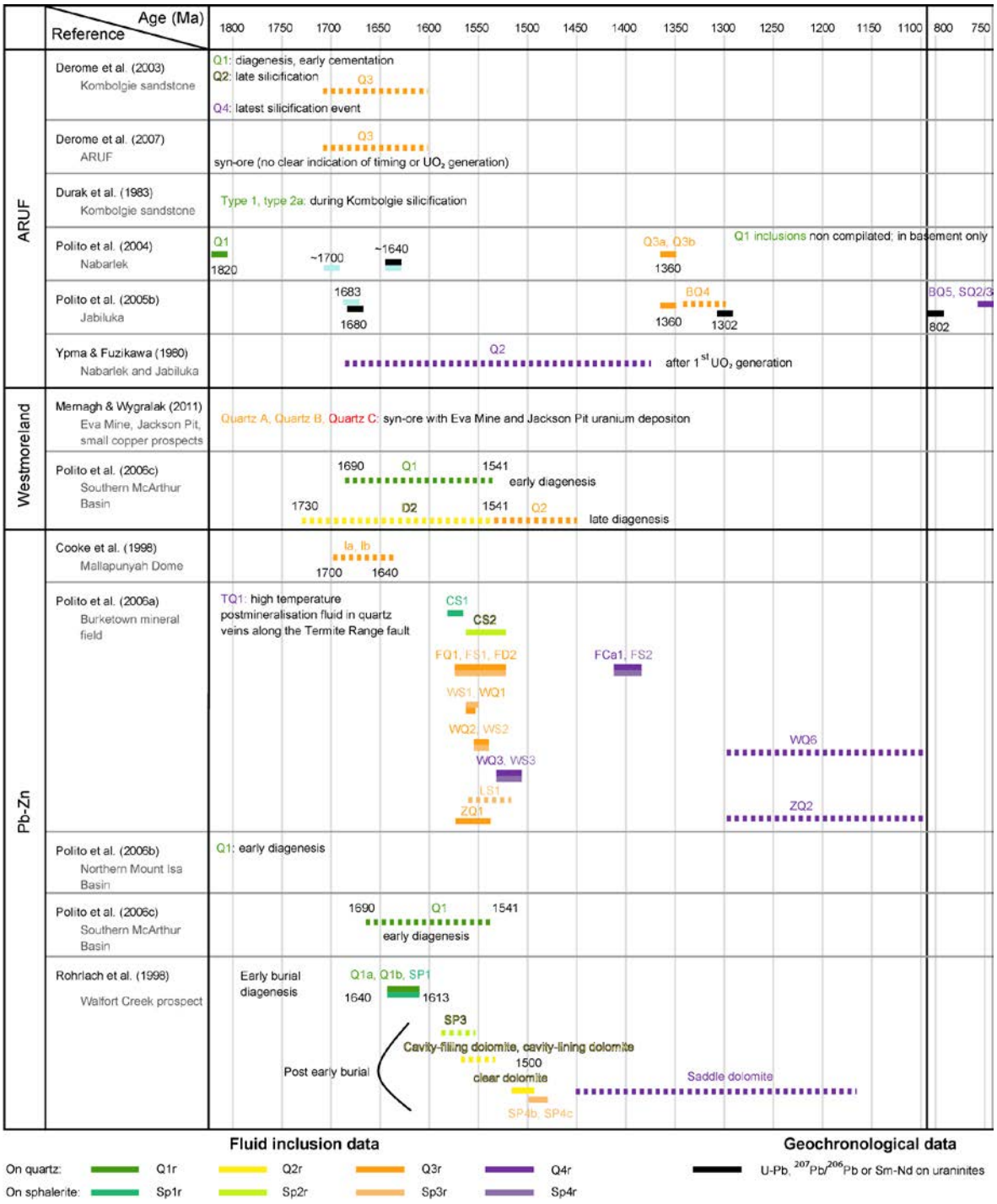

***Figure 1-20**: Timing of the compiled fluid inclusions during this PhD (Cooke et al., 1998; Derome et al., 2003, 2007; Durak et al., 1983; Mernagh and Wygralak, 2011; Polito et al., 2004, 2005b, 2006b, 2006a, 2006c; Rohrlach et al., 1998; Ypma and Fuzikawa, 1980). The geochronological data have been replaced when they are presented in a paper that also deals with fluid inclusions.*

The fluids characteristics have evolved through time in the different areas. When/where the trapping timing was given in the literature, it has been reported on Figure 1-21 for each of the studied areas. Some events are recorded in three places at the same time, but fluid characteristics (salinity and homogenisation temperature) still vary between the areas. It has

to be kept in mind that this compilation of events represents full and partial snapshots of all the fluid events that have happened.

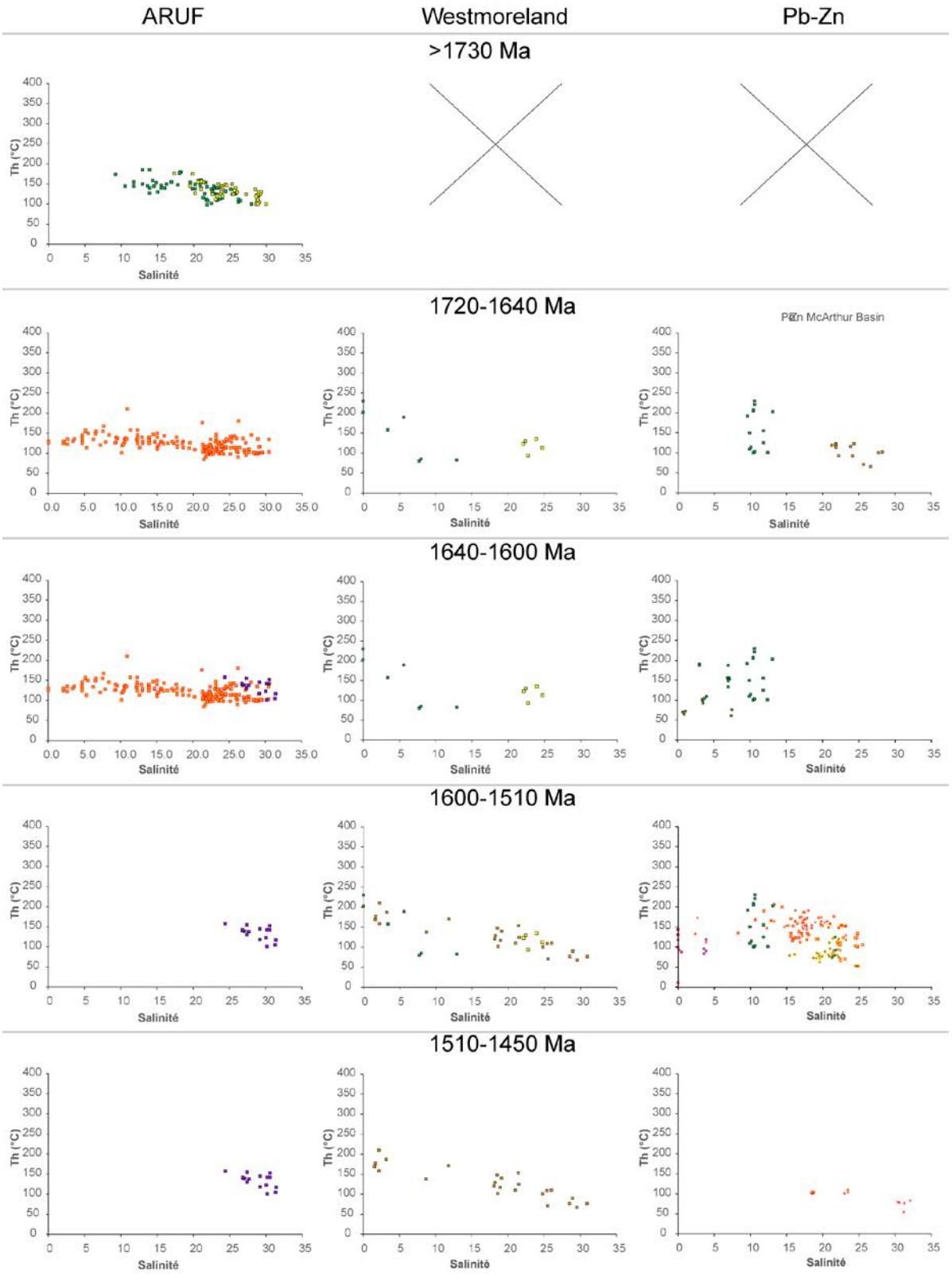

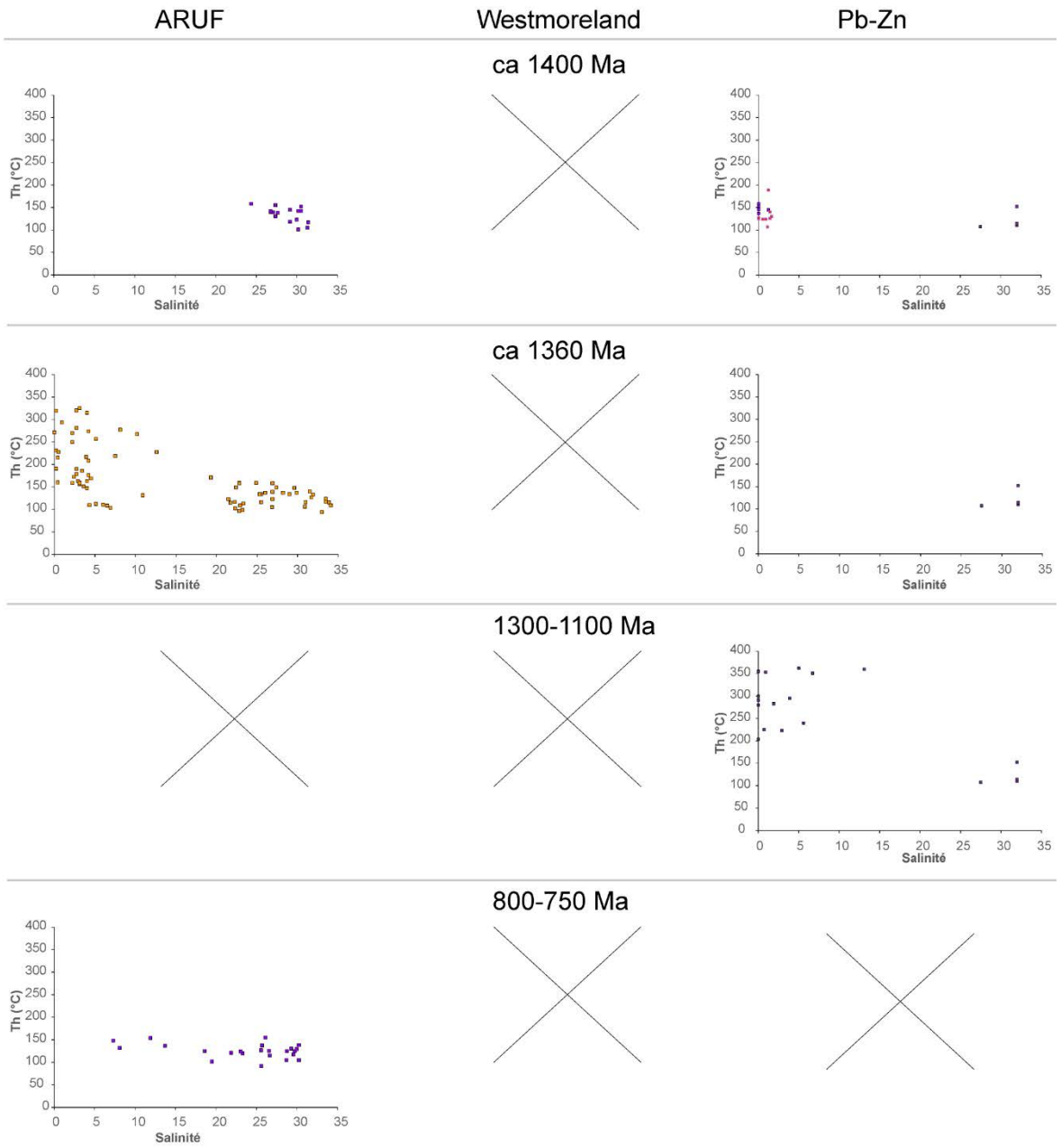

***Figure 1-21**: Evolution of the fluid inclusions characteristics through time in the different mineralising areas (Cooke et al., 1998; Derome et al., 2003, 2007; Durak et al., 1983; Mernagh and Wygralak, 2011; Polito et al., 2004, 2005b, 2006b, 2006a, 2006c; Rohrlach et al., 1998; Ypma and Fuzikawa, 1980).*

1.5.6. Conclusions

The comparison of fluid salinity, temperature, and composition at a basin scale highlights the similarities between the fluid characteristics of different deposits types, such as the unconformity-type uranium and SHMS base metals deposits. In addition, fluids characteristics give a better understanding of the deposit genesis, especially in metamorphosed zones where the primary features of the mineralisation are not present anymore (Polito et al., 2006a). In this sense, mineral prospecting/exploration can benefit from fluid studies because these provide/add to a better understanding of the metallogenic model, including the effects of late-

stage fluid events on remobilizing metals along sequence boundaries and regional faults (Polito et al., 2006a).

In the northern and central part of the McArthur basin, the ore-stage fluids are more saline (until 32 wt% eq $_{NaCl}$) and tend to the Ca-end-member, whereas in the Westmoreland the salinity does not exceed 22 wt% eq $_{NaCl}$, which correspond to the Na-end-member. The large range of salinity and Th are explained by dilution of brines by low-salinity fluids. It is also interesting to note that all deposits are linked to faulting and brecciation events (though most of Pb-Zn mineralisation is stratiform).

Collectively, the compiled data attest for large-scale lateral and vertical migrations of basinal fluids at the time of ore-deposit formation. However, it remains to be determined if one or several basinal brine reservoirs have been involved and what was the origin and importance of low-salinity fluids. Similar brines and low-salinity fluids have also been described along regional sandstones and faults, altered volcanics, and other Cu and Pb-Zn deposits within the basin.

1.6. Key framing questions

The timing of the mineralisation in some of the uranium deposits coincide with the formation of world class SHMS Pb-Zn deposits in the McArthur and Mt Isa basins. In addition, the fluids characteristics show similarities, suggesting that the diagenetic aquifers and the deposits may be linked. Similarities between the northern and southern parts of the McArthur Basin (U deposits) and between the centre of this basin and the Mount Isa Inlier (Pb-Zn deposits) raise many questions regarding possible links in time and/or in space between the fluids involved in the origin of these deposits.

Based on the geological pattern and fluid inclusions results, several important questions can be raised:

- What are the factors controlling the metal distribution in the basins?
- Do deposits of the same metal present similarities at basin scale (e.g. U deposits in the northern and southern part of the basin)?
- Can metals be leached from a single source to create world-class deposits?
- What are the factors leading to world-class deposits or to smaller prospects or even barren zones? Is the presence and wealth of deposit more linked to favourable conditions at the time of deposition, or rather to better preservation?
- Do mineralising fluids for the same metal (e.g. U) share common features at basin scale? Do they have common features across different metals?

- Can a “stable” sedimentary basin, such as the McArthur Basin supposed to be stable since ~1.5 Ga, be affected by several fluid circulation and mineralising events until the past hundreds of millions years?
- What is/are the source(s) of elements implied in metasomatism, which was a key in the process of metal deposition as well as a nowadays guideline for exploration?

The chapters and appendixes presented in this thesis seek to contribute to answering these questions.

- Chapter 2 deals with the boron and magnesium metasomatism, observed in the Ranger deposit, located in the basement just below the unconformity with the McArthur Basin. The same type of metasomatism is also present in unconformity-related deposits in the Athabasca Basin (Canada). The Mg-rich chlorite and tourmaline (Mg-foitite) confirm the importance of the metasomatism in this deposit. The isotopic values in the tourmaline are distinct from the ones in the Athabasca Basin, and imply a probable greater implication of the basement than the seawater-derived fluids in terms of boron budget.
- Chapter 3 is focussed on uranium mineralisation. In contains a study of sandstone-hosted deposits in the Westmoreland area (southern part of the basin), together with a comparison with the Alligator Rivers Uranium Field (ARUF, to the North) typical of the unconformity-related deposits. Based on the comparison of the chemical parameters of uraninite (REE-patterns, trace elements content) and on temperatures estimates from the chlorite, this chapter provides evidence suggesting that the deposits in the Westmoreland area can be distinguished from the unconformity-related deposits. The relatively high temperature (>300 °C) and the distinct host rocks can be part of the explanation.
- Chapter 4 presents noble gas and halogens data from different uranium-rich zones in the McArthur Basin. To go further in the interpretation of the fluids characteristics, noble gas and halogens are a useful tool. This method has already been applied to the study of uranium deposits in the Athabasca Basin. A similar approach is applied in this chapter, with a focus on deposits from the AURF and from the Westmoreland area and indicate a seawater origin for the analysed samples. In both cases it indicates a mixing between a low-salinity fluid and a brine, and a low input of organic matter. The different samples record various noble gas ratios that may either be explained by fractionation due to a difference residence time in the rocks or reflect a mixing between fluids.
- Chapter 5 deals with lead sources which are investigated by means of lead isotopes on galena from the stratiform world-class McArthur River deposit, and highlights the

contribution of two lead sources. Several models can be proposed based on the identified end-members that imply lead leached or remobilised from felsic reservoirs, and that involve lead from the basement, or from the basin that derivate from the basement.

- Chapter 6 extends this study to deposits located at different distance from major faults, and even from a deposit located in another correlated basin. From stratiform/early diagenetic to late veins, the diversity of sulphides assemblages gives insights on the range of mineralising events and confirms the importance to get information on metal sources and timing. This is performed by the study of lead isotopes in galena from several deposits and prospects, and reveals the input of a total of three lead sources. A younger event (~1300 Ma) is highlighted in deposits close to the major faults. Minor and trace elements in sphalerite and galena, in addition to being economically capital to be extracted as by-products, give precious insights on the conditions of sulphides formation. The temperature estimates decrease with time from 220 °C to less than 100 °C (minimum calibration).
- Chapter 7 presents a general discussion on the results obtained during this PhD.
- Appendix 1 presents an attempt to date the Cu mineralisation that could give insights on the timing of breccia-type deposits and replace Cu mineralisation in the global context. To constraint its age, it has been tried to date zircons from the Settlement Creek Dolerite, a mafic intrusive unit that is a candidate for heat and copper source. The data provides an estimated age for the dolerite that is younger that what previous estimates based on stratigraphic relations, and raise the question of a later timing for the Cu-rich breccias.
- Appendix 2 presents a Python program which was used to automate the calculation of model ages from lead isotopes ratios with different methods. This program provides the means of calculating a large number of model ages with the Sun et al. (1996) and Stacey and Kramers (1975) models within seconds instead of the painstaking manual approach used to-date. The μ parameter, used for the interpretation of the nature of the reservoir providing the lead source, is also calculated by the program. A graphic representation of the $^{206}Pb/^{204}Pb$ vs $^{207}Pb/^{204}Pb$ diagram is also automatically generated by the program, in which the analyses and the isochrons for the two methods are plotted.

Chapter 2. Insights into B-Mg-metasomatism at the Ranger U deposit (NT, Australia) and comparison with Canadian unconformity-related U deposits

Published in *Minerals* **2019**, 9, 432; doi:10.3390/min9070432

Joséphine Gigon [1,*], Roger G. Skirrow [2], Matthieu Harlaux [3], Antonin Richard [1], Julien Mercadier [1], Irvine R. Annesley [1] and Johan Villeneuve [4]

[1] Université de Lorraine, CNRS, GeoRessources lab, F-54500 Vandœuvre-lès-Nancy, France

[2] Geoscience Australia, Cnr Jerrabomberra Avenue and Hindmarsh Drive Symonston ACT, GPO Box 378, Canberra ACT 2601, Australia

[3] Department of Earth Sciences, University of Geneva, Rue des Maraîchers 13, CH-1205 Geneva, Switzerland

[4] CRPG, UMR 7358 CNRS-UL, 15 rue Notre Dame des Pauvres, F-54501 Vandœuvre-lès-Nancy, France

Preamble

It has been demonstrated in the previous chapters the economic importance of the unconformity-type deposits for the global uranium resources, as well as the significance of fluid circulations at basin-scale. This chapter focuses on the metasomatism affecting the Ranger deposit, chosen as representative of unconformity-related deposits in the basement just below the McArthur Basin. It presents a multidisciplinary study published in the international scientific journal *Minerals*. The B-Mg-metasomatism has been highly described in the Athabasca Basin (Canada) and is observed at Ranger shortly before the first stage of uranium deposition. The Mg-rich minerals (chlorite and tourmaline) crystallised during this event record the characteristics of the fluid at their origin. Chlorite composition gives an approximation of the temperature which was similar to the one observed in the Athabasca. Boron isotopic composition in tourmaline indicate the importance of the basement as boron source, compared to a minimal input from seawater derived boron. The metamosatism is less present at Ranger than in the Athabasca Basin, but remains a key factor in the exploration process for uranium. Constrain its origin can open new opportunities to find future uranium prospects.

Préambule

Les chapitres précédents ont montré à la fois l'importance économique des gisements d'uranium de type discordance et l'influence des circulations fluides à l'échelle du bassin. Ce chapitre porte sur l'étude du métasomatisme affectant le gisement de Ranger, caractéristique des gisements de type discordance dans le socle juste sous le bassin de McArthur. Il présente une étude multidisciplinaire publiée dans le journal scientifique international *Minerals.* Le métasomatisme à bore et magnésium déjà caractérisé dans le bassin d'Athabasca (Canada) est observé aussi à Ranger, peu de temps avant la mise en place du stock primaire d'uranium. Les minéraux contenant du magnésium qui ont cristallisé lors de cet épisode enregistrent les caractéristiques du fluide dont ils sont issus. La composition des chlorites donne une approximation de leur température de cristallisation, similaire à celle observée dans l'Athabasca. La composition isotopique du bore des tourmalines indique l'importance du socle comme source de bore, comparée à la contribution moindre de bore issu de l'évaporation de l'eau de mer. Bien que moins marquée que dans l'Athabasca, la présence de métasomatisme est un facteur clé de l'exploration de l'uranium et contraindre son origine peut permettre des avancées dans les futures découvertes d'indices minéralisés.

Le gisement de Ranger (Northern Territory, Australie) est l'un des plus grands gisements d'uranium au monde. La minéralisation se trouve dans les roches du socle et est classifiée de

type discordance. Des analyses in situ de chlorites et de tourmalines ont été réalisées pour déterminer les sources du bore et du magnésium ainsi que les fluides associés au métasomatisme à bore et magnésium qui a affecté la zone juste avant et pendant le principal épisode minéralisateur. La composition chimique des tourmalines montre que le site X est vacant et que les tourmalines présentent un faible ratio $Fe_{tot}/(Fe_{tot} + Mg)$ typique de la Mg-foitite. Les chlorites reliées temporellement à l'uranium ont une teneur en fer relativement faible (0.28–0.83 *apfu*) et élevée en Mg (3.08–3.84 *apfu*), avec des ratios Si/Al = 1.08−1.22 et $Mg/(Mg + Fe_{tot})$ = 0.80−0.93 indiquant une composition entre les domaines du clinochlore et de la Mg-amesite. La composition des chlorites indique une température de cristallisation de 101 à 163 °C. La composition isotopique du bore des tourmalines montre des valeurs de $\delta^{11}B$ variant entre ~1 à 9‰. Un modèle est proposé, impliquant deux sources de bore qui contribuent à une signature isotopique mixte : (i) de l'eau de mer évaporée, typiquement enrichie en Mg et B ($\delta^{11}B$ ~40‰), et (ii) du bore du socle ($\delta^{11}B$ ~−30 to +10‰), qui semble être la source majoritaire. Dans l'ensemble, les données indiquent des compositions chimiques des tourmalines similaires et des différences notables en termes de composition isotopiques des tourmalines et de composition des chlorites entre le gisement de Ranger et certains gisements canadien de type discordance. Cependant, l'approche exploratoire basée sur l'identification de zones riches en bore et en magnésium peut être utilisée dans le cadre de l'exploration pour l'uranium en Northern Territory.

Abstract

The Ranger deposit (Northern Territory, Australia) is one of the largest uranium deposits in the world. Uranium mineralisation occurs in crystalline basement rocks and is thought to belong to the unconformity-related category. In order to address the sources of magnesium and boron, and the temperature of the fluids related to boron and magnesium metasomatism that occurred shortly before and during the main uranium stage, in situ analyses of chlorite and tourmaline were carried out. The chemical composition of tourmaline shows an elevated X-site vacancy and a low $Fe_{tot}/(Fe_{tot} + Mg)$ ratio typical of Mg-foitite. Uranium-related chlorite has relatively low Fe content (0.28–0.83 *apfu*) and high Mg content (3.08–3.84 *apfu*), with Si/Al = 1.08−1.22 and $Mg/(Mg + Fe_{tot})$ = 0.80−0.93 indicating a composition lying between the clinochlore and Mg-amesite fields. Chlorite composition indicates crystallisation temperature of 101–163 °C. The boron isotopic composition of tourmaline shows a range of $\delta^{11}B$ values of ~1–9‰. A model is proposed involving two boron sources that contribute to a mixed isotopic signature: (i) evaporated seawater, which is typically enriched in magnesium and boron ($\delta^{11}B$ ~40‰), and (ii) boron from the crystalline basement ($\delta^{11}B$ ~-30 to +10‰), which appears to be the dominant

source. Collectively, the data indicate similar tourmaline chemistry but significant differences of tourmaline boron isotopic composition and chlorite chemistry between the Ranger deposit and some of the Canadian unconformity-related uranium deposits. However, lithogeochemical exploration approaches based on identification of boron- and magnesium-enriched zones may be usefully applied to uranium exploration in the Northern Territory.

Keywords: tourmaline; chlorite; boron isotopes; metasomatism; unconformity-related uranium deposits; Ranger

2.1. Introduction

Unconformity-related uranium (U) deposits occur mainly in or close to the unmetamorphosed Proterozoic Athabasca and Thelon basins (Saskatchewan and Nunavut, Canada) and the McArthur Basin (Northern Territory, Australia). They are located in the vicinity of the intersection between the basin/basement unconformity and multiply-reactivated basement-rooted faults and are currently accounting for ~25% of the world U production (Cuney and Kyser, 2015; International Atomic Energy Agency, 2018b; Jefferson et al., 2007). Multiple mineralisation/remobilisation episodes have been identified in the three areas spanning over one billion years from ~1780 Ma for the primary diagenetic-hydrothermal mineralisation in Australian deposits (Skirrow et al., 2016) to more recent (<300 Ma) low-temperature remobilisation by meteoric fluids in Canadian deposits (e.g., Mercadier et al., 2011a). Based on fluid inclusion and stable isotope studies, the mineralising fluids are widely accepted to be 100–200 °C basinal brines, which underwent significant modification by interaction with basement lithologies. Halogen geochemistry of fluid inclusions indicates that the basinal brines were produced by evaporation of seawater (Derome et al., 2007; Leisen et al., 2012; Richard et al., 2011, 2013b, 2014). In addition to basinal brines, a low-salinity fluid of possible meteoric origin was also involved at the time of U deposition in the Australian deposits (Derome et al., 2003, 2007).

One typical feature of unconformity-related U deposits is the strong Mg-chlorite alteration and associated magnesium enrichment (i.e., Mg-metasomatism) in the vicinity of the ore zones (Earle and Sopuck, 1989; Fisher et al., 2013; Kister et al., 2006, 2005; Nutt, 1989; Skirrow et al., 2016). In the Athabasca Basin, another proximal indicator for U mineralisation is Mg-rich tourmaline alteration and the associated boron enrichment (i.e., B-metasomatism, Earle and Sopuck, 1989; Kister et al., 2006). However, to our knowledge, there is no description of tourmaline alteration in U deposits from the Thelon area. Moreover, tourmaline alteration

appears to be far less important in Australian deposits when compared to the Athabasca Basin (Nutt, 1989; Polito et al., 2005b; Skirrow et al., 2016).

Based on lithogeochemical, trace elements and stable isotope investigations, several models have been proposed for the sources of Mg and B enrichment in the ore zones, involving evaporated-seawater, evaporites, detrital tourmaline and basement rocks (Adlakha et al., 2017; Adlakha and Hattori, 2016; Kister et al., 2006; Mercadier et al., 2012; Skirrow et al., 2016). Thanks to large isotopic fractionation between different reservoirs, B isotopes in tourmaline are well suited for deciphering the source(s) of boron (e.g., seawater, evaporites, magmatic rocks rocks, etc.) in the mineralising fluids and their relative proportions (Adlakha et al., 2017; Marschall and Jiang, 2011; Mercadier et al., 2012). Using the world class Ranger deposit, we present a detailed investigation of the conditions for B-Mg-metasomatism in Australian unconformity-related U deposits (Skirrow et al., 2016). In situ analysis of tourmaline and chlorite was used to elucidate the source(s) of B and Mg as well as the temperature of the fluids related to B-Mg-metasomatism that occurred shortly before and during the main U stage. The chemical composition of chlorite and tourmaline was determined by Electron Probe Microanalyses (EPMA) and the B isotopic composition of tourmaline was determined by Secondary Ion Mass Spectrometry (SIMS). The results are discussed in the frame of a systematic comparison with previous data obtained on Canadian and Australian unconformity-related U deposits highlighting the similarities and the differences between these mineral systems, as well as the consequences for U exploration.

2.2. Geological setting of the Ranger uranium deposit

The Ranger deposit is one of the world's largest uranium deposits with resources estimated at 155.17 Mt of ore grading 0.09% U_3O_8 with past production of 49,194 t U_3O_8 from the Ranger 1 No 3 ore body (ERA, 2011) and 60,961 t of U_3O_8 from the Ranger 1 No 1 ore body (Lally and Bajwah, 2006). The Ranger 1 deposit is one of several large unconformity-related uranium deposits in the Alligator Rivers Uranium Field (ARUF, Figure 2-1), including the Jabiluka, Nabarlek and Koongarra deposits (International Atomic Energy Agency, 2018a). Most of the known major uranium deposits in the ARUF are hosted by pre-McArthur Basin metasedimentary basement rocks (Figure 2-1). The oldest basement in the ARUF is composed of ~2670–2510 Ma granite and gneiss, including the Nanambu Complex to the west of the Ranger and Jabiluka deposits (Hollis et al., 2011, 2009; Hollis and Wygralak, 2012; Worden et al., 2008). The Neoarchean rocks are unconformably overlain by, or in faulted contact with, ~2020 Ma to ~1870–1860 Ma continental to marine basinal and volcanic rocks of the Woodcutters Supergroup and then by the Cahill Formation and Nourlangie Schist. The Cahill

Formation comprises siliciclastic to pelitic schists (including uncommon, thin carbonaceous units), carbonate and calc-silicate rocks and amphibolites, and is the host sequence for the Ranger, Jabiluka and several other uranium deposits in the ARUF. The Nimbuwah orogenic event at ~1865–1855 Ma resulted in metamorphism to medium grade in the ARUF, and was accompanied by deformation and granitoid intrusions of the Nimbuwah Suite (Hollis et al., 2011; Hollis and Wygralak, 2012; Worden et al., 2008). A tourmaline-bearing pegmatite at the Ranger deposit records zircon U-Pb ages of 1867.0 ± 3.5 Ma and 1862.8 ± 3.4 Ma and a monazite U-Pb age of 1847 ± 1 Ma (Annesley et al., 2002). The zircon ages are interpreted to represent igneous crystallization during the Nimbuwah event, whereas the monazite age may record a later igneous or hydrothermal event that is also represented by mafic dykelets and veins at Ranger (Skirrow et al., 2016). In the Pine Creek Orogen to the southwest of the ARUF, volcanism and renewed basin formation at ~1829–1825 Ma (Edith River Group, El Sherana Group) was accompanied and outlasted by intrusive magmatism of the Cullen Suite and Jim Jim Suite between ~1835 and ~1818 Ma (Worden et al., 2008).

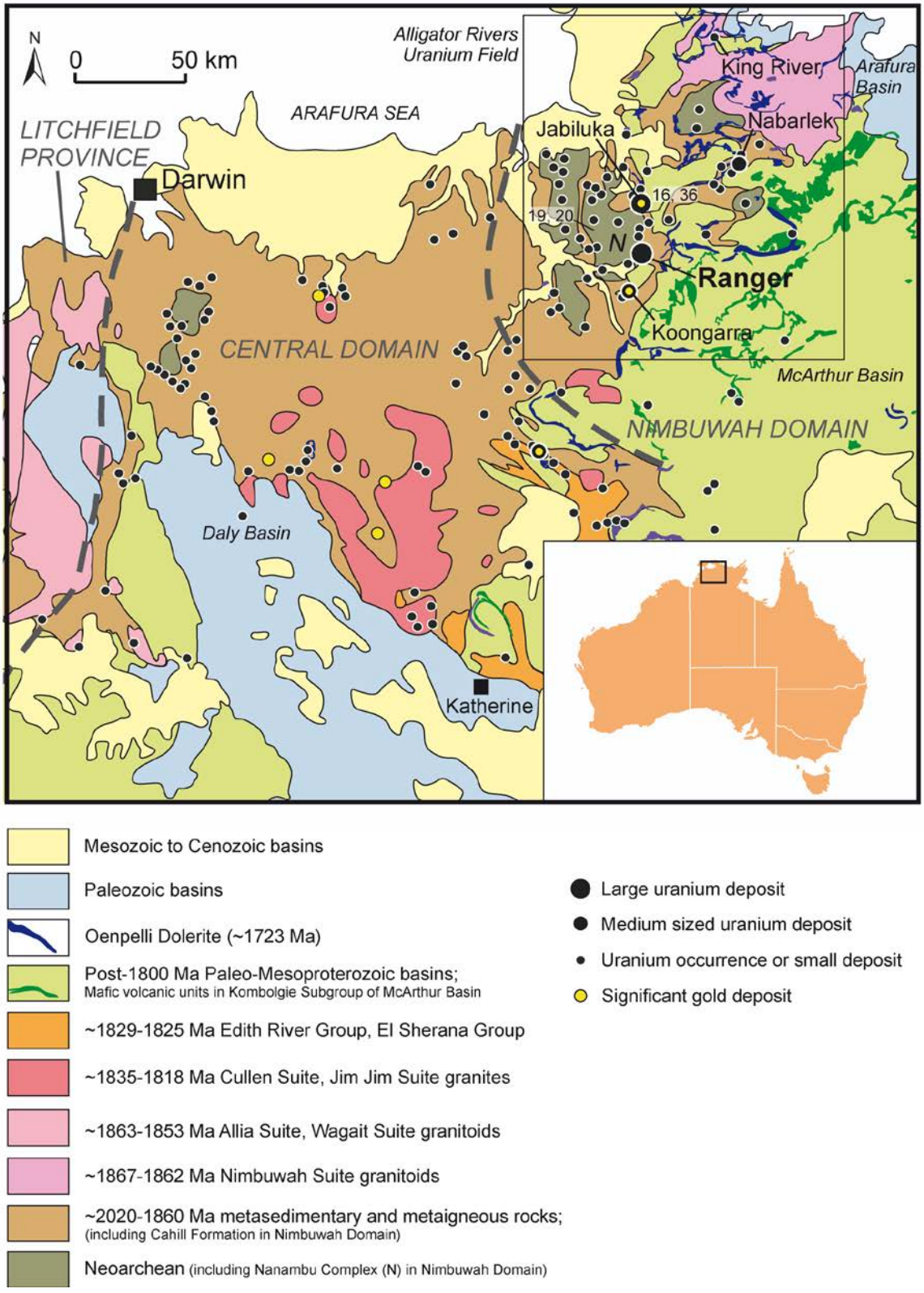

***Figure 2-1**: Location and geology of the Pine Creek Orogen comprising the Nimuwah, Central and Litchfield Domains, and the location of the Ranger deposit and other uranium and gold deposits and occurrences within the Alligator Rivers Uranium Field (labelled box). After Skirrow et al. (2016).*

At the Ranger 1 deposit, the Cahill Formation comprises variably altered pelitic to psammitic and locally carbonaceous schists of the Upper Mine Sequence (UMS) and Hangingwall Schist (HWS), which overlie the carbonate-rich Lower Mine Sequence (LMS, Figure 2-2). The spatial distributions of rock types and whole-rock geochemical patterns at the No 3 orebody were described Fisher et al. (2013), Pevely et al. (2017) and Potma et al. (2012). Most uranium mineralisation occurs within the UMS in zones enriched in Mg, Cu, Au and Ni, and depleted in Na, Ba, K and Ca. Mineralisation extends to more than 500 m depth in the eastern Ranger 1 No 3 Deeps Zone where it tends to be more Cu-rich and terminates against a major north-trending fault (Fisher et al., 2013; Potma et al., 2012). In the Deeps Zone relatively high-grade uranium mineralisation (e.g., 7 m at 1.3% U_3O_8, Energy Resources of Australia Ltd, 2014) occurs mainly within brecciated UMS rocks and in zones of complex faulting. Further details of alteration, geochemistry, zoning, mineralisation, and structure at the Ranger Number 1 orebody including the Deeps Zone are given by Fisher et al. (2013), Pevely et al. (2017) and Skirrow et al. (2016). Pre-ore silicification and/or quartz veining/infilling is present at most if not all of the major uranium deposits in the ARUF as replacements of carbonate rocks (Ranger, Jabiluka), near the Oenpelli Dolerite (Nabarlek) or as silicified fault zones (Koongarra). The fluids that originated the alteration halo and U mineralisation were highly-saline (>20 wt% equivalent NaCl) NaCl-rich and $CaCl_2$-rich basinal brines, that mixed at the deposit with a low-salinity fluid, according to fluid inclusion studies (Derome et al., 2007; Polito et al., 2005b, 2004). The NaCl-rich and $CaCl_2$-rich brines are considered to share a common origin, i.e., evaporation of seawater at the surface of the McArthur Basin, but then underwent different physico-chemical modifications due to different percolation pathways and fluid/rock interactions in the basin/basement environments (Derome et al., 2007). The temperatures of formation for unconformity-related U deposits of the Pine Creek Orogen range between 100 and 300 °C, based on the illite and chlorite geothermometers and fluid inclusion studies (Derome et al., 2003; Kyser et al., 2000; Polito et al., 2004, 2005b).

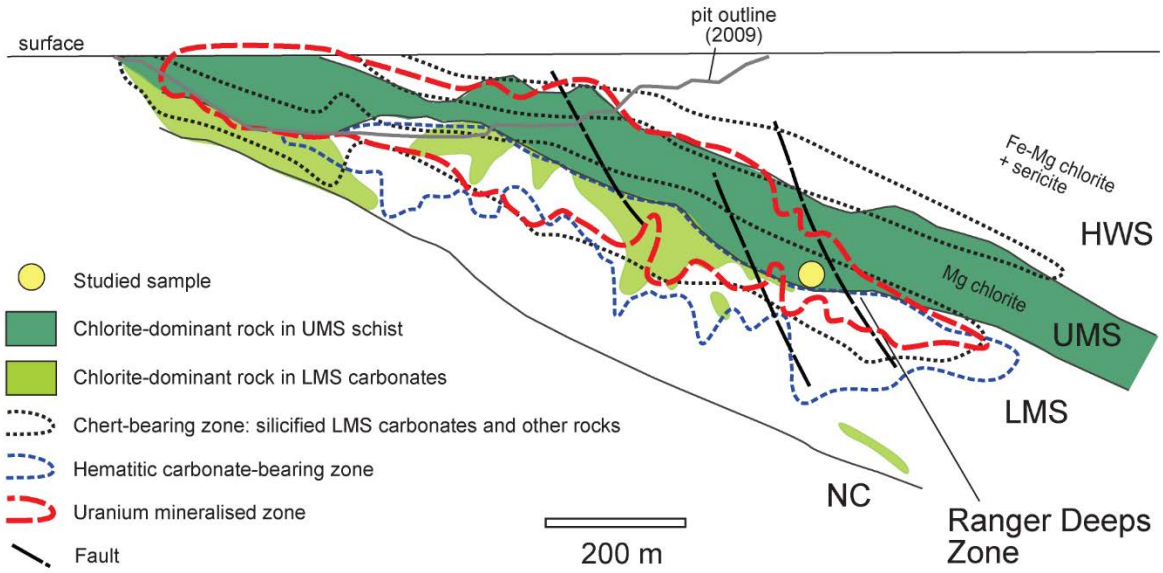

***Figure 2-2**: Generalised east–west cross sections of lithology, alteration and location of the sample investigated, at the Ranger 1 No 3 orebody (Australia). Modified from Skirrow et al. (2016). UMS: Upper Mine Sequence; LMS: Lower Mine Sequence; HWS: Hangingwall Schist.*

2.3. Paragenetic sequence and tourmaline occurrence

A detailed paragenetic sequence for the Ranger 1 deposit is presented in Skirrow et al. (2016) and a simplified version, adapted to the focus of the present study (i.e., Mg-tourmaline and Mg-chlorite), is shown in Figure 2-3. The following descriptions are also taken from Skirrow et al. (2016). The first tourmaline generation in the area is of magmatic origin occurring in tourmaline-bearing pegmatite (not shown in Figure 2-2; see Skirrow et al. (2016) for description). The pegmatite is massive, yet also sericitised and chloritised. Formation of magmatic tourmaline is constrained by zircon U-Pb ages at 1867.0 ± 3.5 Ma and 1862.8 ± 3.4 Ma (Skirrow et al., 2016). Tourmaline-bearing pegmatites cross-cut the main tectonic fabric and are composed of quartz, K-feldspar, muscovite, tourmaline, apatite and zircon.

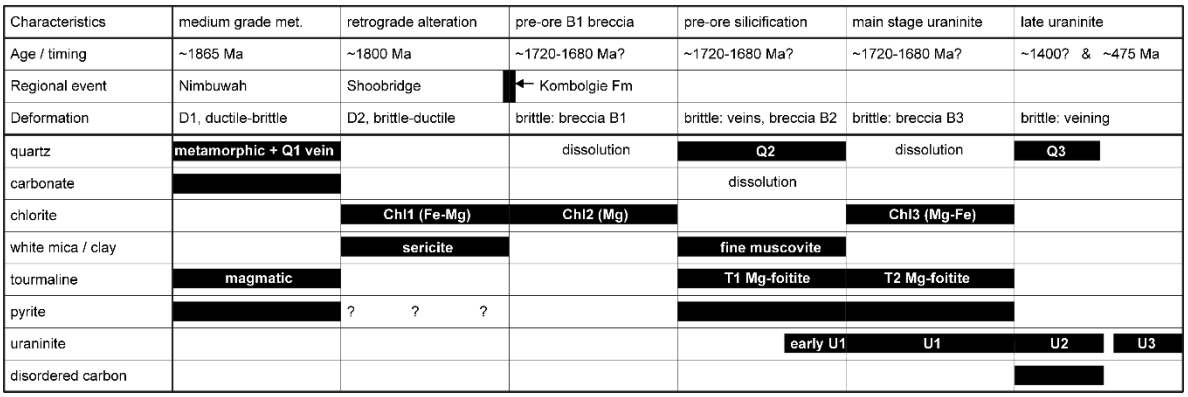

***Figure 2-3**: Simplified paragenetic sequence of the Ranger U deposit (Australia) with a focus on the successive generations of tourmaline, chlorite, quartz and uraninite (after Skirrow et al., 2016). Here, chemical and boron isotopic analyses were carried out on tourmaline T1 and chemical analyses were carried out on chlorite Chl2.*

Two generations of hydrothermal tourmaline are documented, both associated with deformational events (veining and/or brecciation, Figure 2-4A) postdating the formation of the McArthur Basin. Early hydrothermal tourmaline T1 is coeval with quartz Q2, fine-grained muscovite, pyrite, the earliest uraninite early-U1 (dated at 1688 ± 46 Ma, Skirrow et al., 2016, Figure 2-4B), and the dissolution of carbonate (Figure 2-3). This hydrothermal mineral assemblage corresponds to the pre-ore silicification event (Figure 2-3) which is interpreted to have occurred between ~1720 Ma and ~1680 Ma. Tourmaline T1 is acicular, forming fine-grained needles up to 5 µm in width and 100 µm in length, often radiating, intergrown with chlorite Chl2 and quartz Q2 (Figure 2-5). Tourmaline T2 is coeval with chlorite Chl3, pyrite and uraninite U1. In this study, only tourmaline T1 and chlorite Chl2 were investigated for their chemical and isotopic composition. Tourmaline T2 and chlorite Chl3 are too intimately intergrown and of such small grain size that the tourmaline T2 could not be analysed without contamination, even by in situ methods.

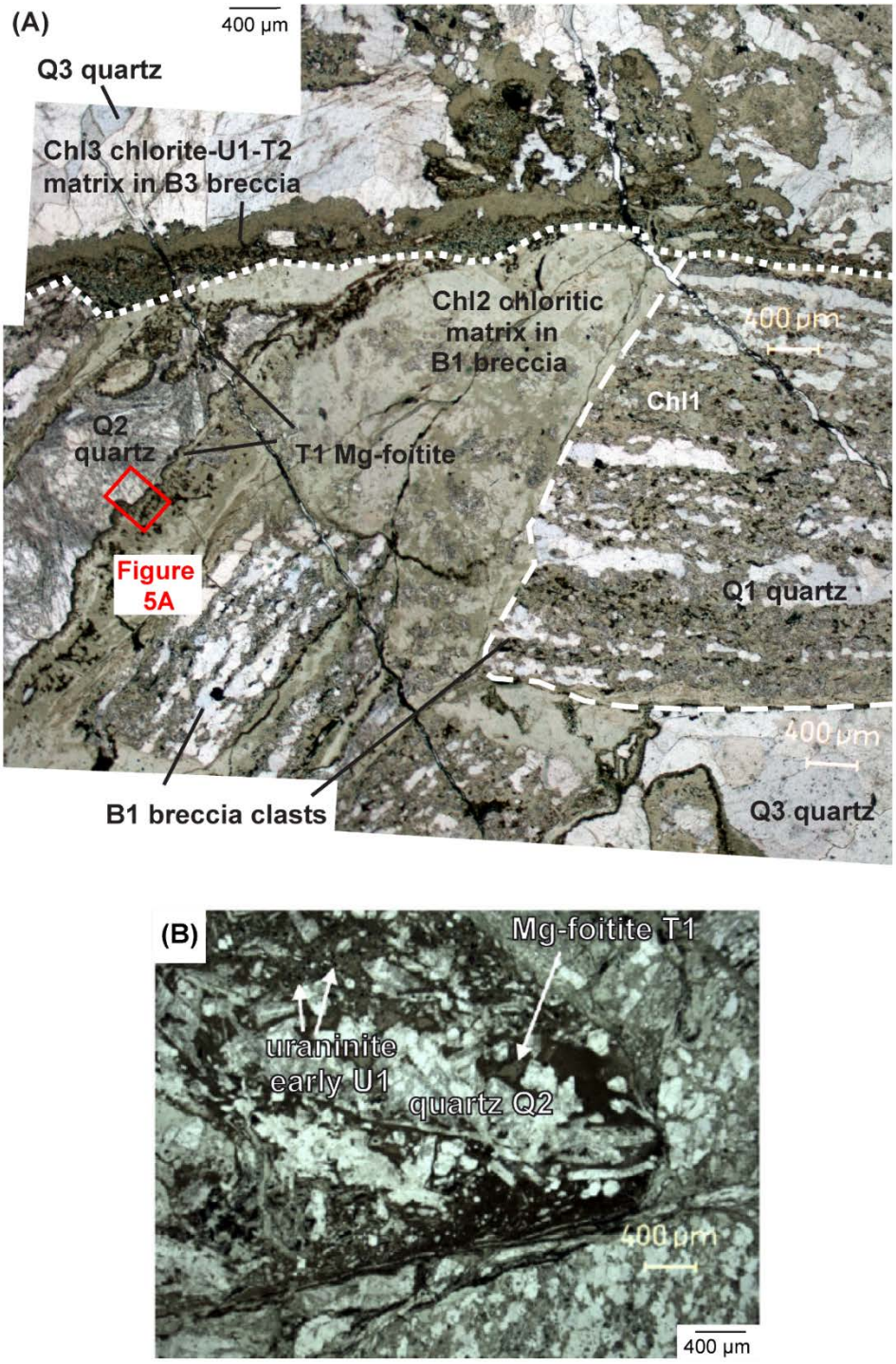

***Figure 2-4**: Chlorite-tourmaline-quartz generations and assemblages at the Ranger U deposit (Australia), from Skirrow et al. (2016). (**A**) Thin section studied for boron isotopes and major elements showing pre-ore B1 breccia, pre-ore silicification and main U1 ore stage. B1 breccia is composed of lithic clasts of banded quartz Q1 and chlorite Chl1 within a matrix of chlorite Chl2 and chlorite Chl3 that corrodes quartz. Some voids in B1 breccia are lined by tourmaline T1 and filled by quartz Q2 corresponding to the pre-ore silicification stage and B2 breccia. Both the B1 breccia and Q2-T1 assemblages were cut by ore-stage B3 breccia, with infill by chlorite Chl3, tourmaline T2, and uraninite U1. Voids in the B3 breccia matrix were filled by quartz Q3. Sample from drillhole S3PD759 402.9 m, transmitted light, from Skirrow et al. (2016). (**B**) Clast in B3 breccia containing intergrowths of euhedral quartz Q2, brownish fine-grained tourmaline T1, and fine-grained disseminated uraninite U1. Sample from drillhole S3PD759 395.3 m, transmitted light, from Skirrow et al. (2016).*

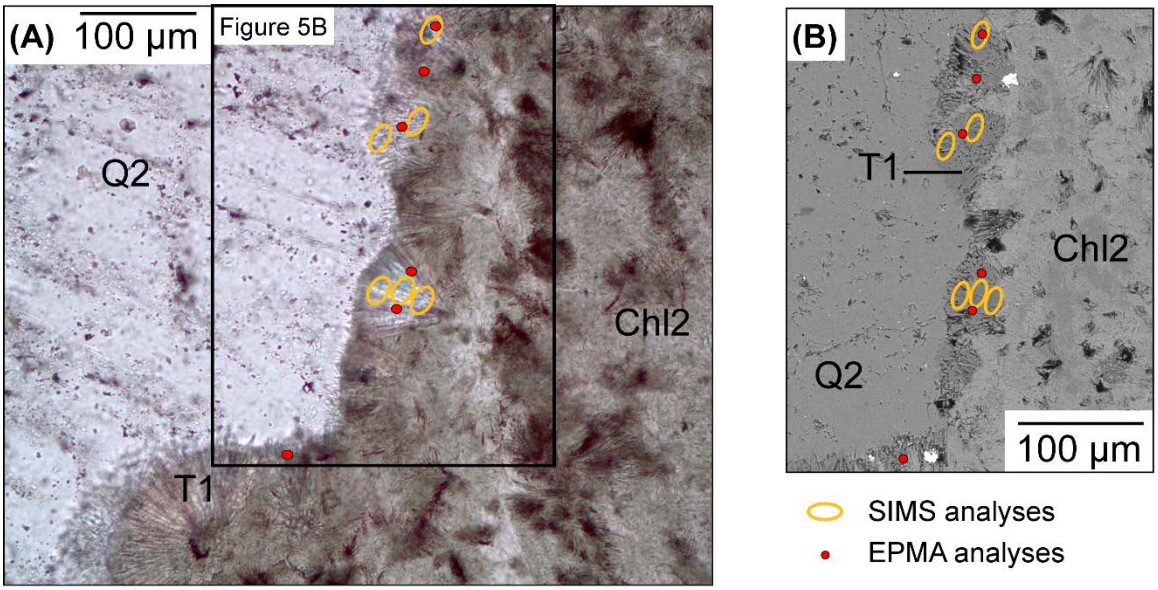

***Figure 2-5**: Zoom on the pre-ore silicification minerals from the Ranger U deposit (Australia): chlorite Chl2, on which very fine-grained rosettes of tourmaline T1 grow, then cemented by quartz Q2 with locations of the EPMA (red dots) and SIMS (orange ellipses) in situ analyses on tourmaline T1; (**A**) transmitted light. (**B**) BSE image. Sample from drillhole S3PD759 402.9 m.*

2.4. Materials and methods

Analytical work was completed on a single, representative polished thin section (DDH: S3PD759, 402.9 m) collected from the chlorite-dominant Upper Mine Sequence schists and within the uranium mineralised zone, in close proximity to the main fault zone (Figure 2-2). The distribution of the major elements and B isotope analyses in tourmaline T1 and major elements on chlorite Chl1 and Chl2 is illustrated in Figure 2-6. For scanning electron microscopy and electron probe microanalyses the entire thin section was carbon coated, and for secondary ion mass spectrometry half of the thin section was cut and gold coated.

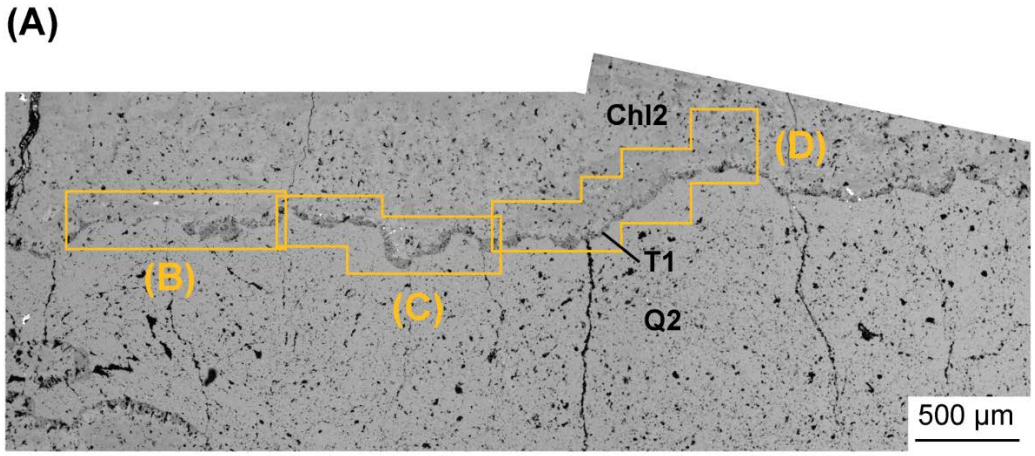
(A)
Chl2
(D)
T1
(B)
(C)
Q2
500 µm

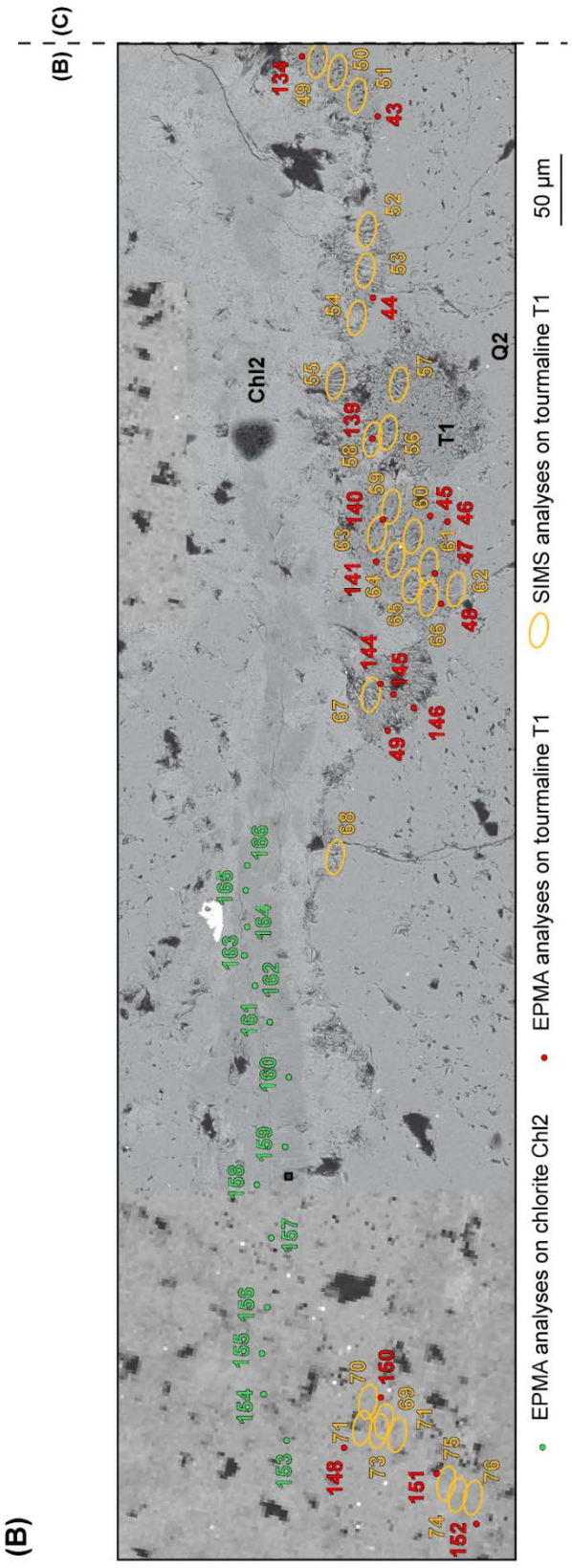
(B)
(B)
(C)
Chl2
T1
Q2
EPMA analyses on chlorite Chl2
EPMA analyses on tourmaline T1
SIMS analyses on tourmaline T1
50 µm

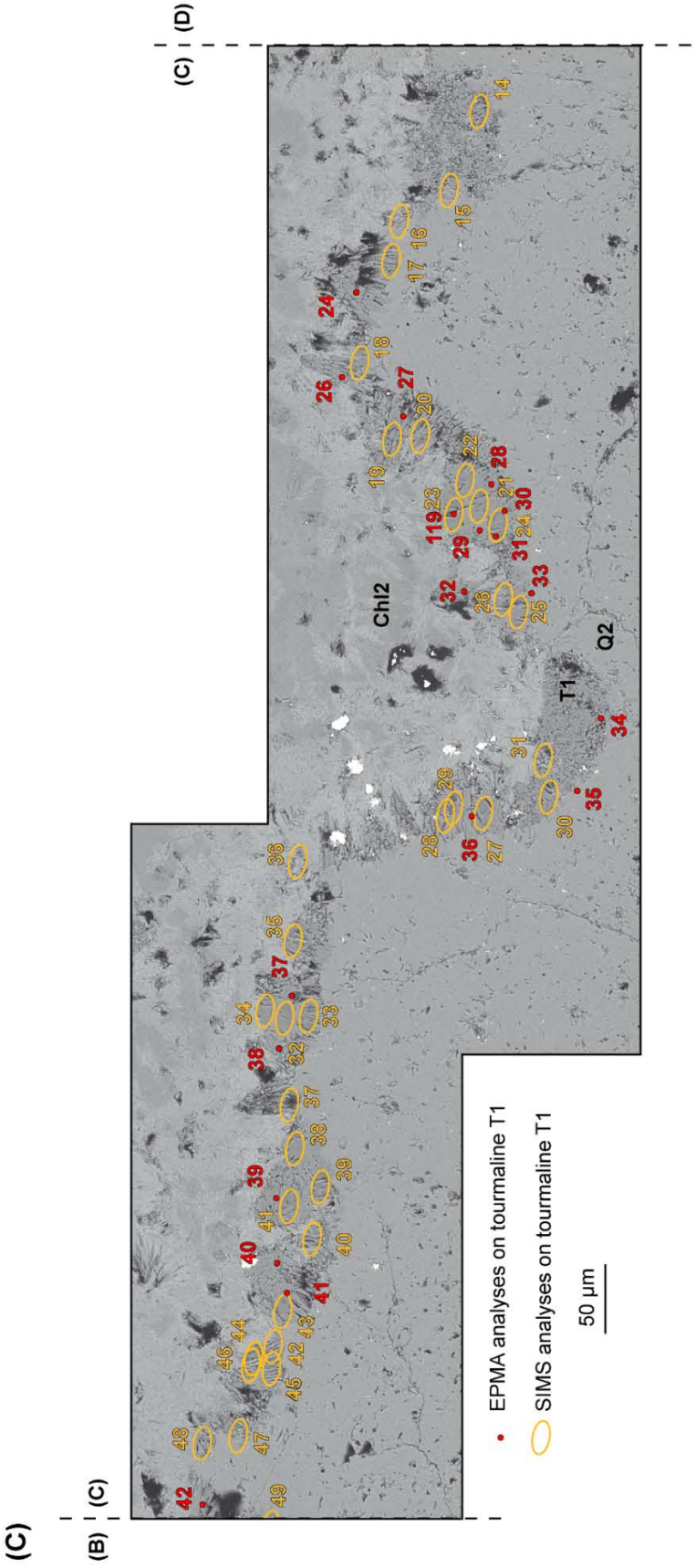
(C)
(B)
(C)
(C)
(D)
Chl2
T1
Q2
EPMA analyses on tourmaline T1
SIMS analyses on tourmaline T1
50 µm

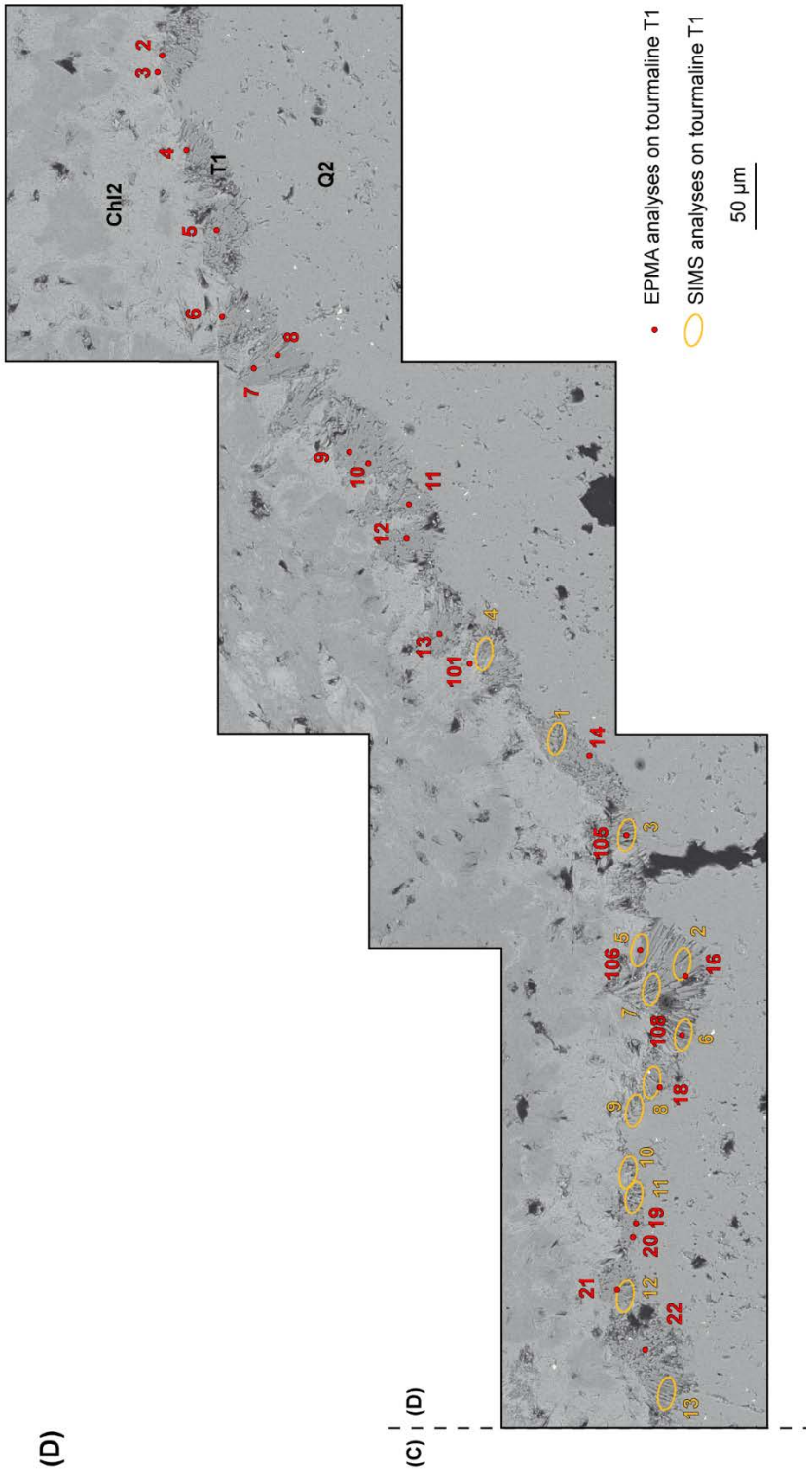

***Figure 2-6**: Locations of the EPMA (red dots for the tourmaline T1 and green dots for the chlorite Chl2) and SIMS (orange ellipse) in situ analyses. (**A**) BSE map of sample from drillhole S3PD759 402.9 m. The paragenetic assemblage of the pre-ore silicification minerals from the Ranger U deposit (Australia) consists of chlorite Chl2, followed by tourmaline T1 and then by quartz Q2. The insets indicate the location of BSE maps (**B**–**D**).*

2.4.1. Scanning Electron Microscopy

Tourmaline and chlorite crystals were characterised using a scanning electron microscope (SEM) Hitachi S-4800 equipped with a SDD-type EDS spectrometer at GeoRessources laboratory (Nancy, France). Backscattered electron (BSE) images were acquired on the polished thin section with an acceleration voltage of 15 kV in order to reveal mineral textures prior to the in situ chemical and isotopic analyses.

2.4.2. Electron Probe Microanalyses

Electron probe microanalyses (EPMA) were carried out at the GeoRessources laboratory (Nancy, France) prior to the in situ isotopic analyses. Tourmaline and chlorite crystals were analysed using a CAMECA SX100 electron probe micro analyser operating with an emission current of 12 nA, an acceleration voltage of 15 kV and a beam diameter of 1 µm. The following elements, monochromators, standards, and limits of detection were used: Na (TAP, albite, 540 ppm), Si (TAP, albite, 450 ppm), Mg (TAP, olivine, 375 ppm), Al (TAP, Al_2O_3, 350 ppm), K (LPET, orthose, 210 ppm), Ca (PET, andradite, 490 ppm), Ti (LPET, $MnTiO_3$, 290 ppm), Mn (LIF, $MnTiO_3$, 120 ppm) and Fe (LIF, Fe_2O_3, 1650 ppm).

Structural formulae of tourmaline were calculated with the WinTcac software (version 1.03, Yavuz et al., 2014), normalising to 15 cations in T-, Z- and Y-sites, and assuming stoichiometric three atoms for B and four atoms for OH + F, based on the general formula $XY_3Z_6(T_6O_{18})(BO_3)_3V_3W$, where X = Na^+, Ca^{2+}, K^+, or vacancy site; Y = Fe^{2+}, Mg^{2+}, Mn^{2+}, Al^{3+}, Li^+, Fe^{3+}, or Cr^{3+}; Z = Al^{3+}, Fe^{3+}, Ti^{4+}, Mg^{2+}, or Cr^{3+}; T = Si^{4+}, Al^{3+}, or B^{3+}; V = OH^-, O^{2-} and W = OH^-, F^- or O^{2-}. The tourmaline nomenclature follows the classification proposed by Henry et al. (2011) according to the different solid solution series. Chemical compositions of tourmaline and chlorite are reported in weight per cent oxides (wt%) and the structural formulae are expressed in atoms per formula unit (*apfu*). The temperature of chlorite formation was calculated using the graphical geothermometer of Bourdelle and Cathelineau (2015).

2.4.3. Secondary Ion Mass Spectrometry

Boron isotopic compositions of tourmaline were measured by secondary ion mass spectrometry (SIMS) at the CRPG-CNRS laboratory (Vandœuvre-lès-Nancy, France). Isotopic measurements were made using a Cameca IMS 1280-HR instrument by following the analytical procedure described by Chaussidon and Albarède (1992). Analyses were performed on the same polished thin section previously analysed by SEM and EPMA, using a 20 nA beam of primary ions O^- accelerated at 13 kV with an ellipsoid ablation spot (20 micron long axis). For each point, a pre-sputtering of 60 s was set in order to clean the surface of contamination.

The secondary ions $^{10}B^+$ and $^{11}B^+$ were accelerated at 10 kV and were measured in monocollection with the axial Faraday cup, during 8 s and 4 s per cycle respectively, over 30 cycles for each measurement. A mass resolution power M/ΔM = 2000 was sufficient to separate isobaric interferences on the $^{10}B^+$ and $^{11}B^+$ masses. Instrumental mass fractionation was determined and corrected using three tourmaline reference materials with different chemical compositions: (1) Spivack standard which is a dravite (Spivack, 1986), (2) dravite Harvard #108796, and (3) schorl Harvard #112566 (Dyar et al., 2001; Leeman and Tonarini, 2001). The matrix effect was corrected using the dravite Harvard #108796 standard because tourmaline T1 has a composition that is closer to dravite than schorl and its external reproducibility was better than for the Spivack dravite (see below). Each standard was measured several times during the analytical SIMS session following a standard-sample-standard bracketing procedure. The measured isotopic ratios $^{11}B/^{10}B$ were normalised to the NIST SRM 951, whose $^{11}B/^{10}B$ ratio is 4.04362 (Catanzaro, 1970) and expressed in $\delta^{11}B$ notation in ‰: $\delta^{11}B = [(^{11}B/^{10}B)_{sample}/(^{11}B/^{10}B)_{SRM\ 951}] \times 10^3$

Internal errors based on the counting statistics range from 0.25 and 1.77‰ (2σ). The external reproducibility (2σ) on standards is 0.13‰ over 28 analyses for the dravite Harvard #108796 and 0.19‰ over 24 analyses for the schorl Harvard #112566. The external reproducibility used is that of the relevant reference material (dravite Harvard #108796). The total uncertainty on individual analysis is the quadratic sum of the internal error and the external reproducibility, and ranges between 0.35 and 1.78‰.

2.5. Results

2.5.1. Tourmaline chemistry

The 60 EPMA analyses of hydrothermal tourmaline T1 show relatively homogeneous major element compositions (Table 2-1) with high Mg (1.9–2.6 *apfu*) and Al (6.3–6.8 *apfu*) contents, and low Fe (0–0.7 *apfu*), Na (0.1–0.2 *apfu*) and Ca (0–0.07 *apfu*) contents, with X-site vacancies of 0.74–0.86 (Figure 2-7A and Tables 2-2 and 2-3). The Ca-Na + K-X-site vacancy ternary diagram showing the X-site occupancy indicates that the tourmaline T1 is alkali-deficient and belongs to the X-vacant group (Figure 2-7A). The binary diagram showing the $Fe_{tot}/(Fe_{tot} + Mg)$ versus X-site vacancy/(X-site vacancy + Na + K) ratios highlight the relatively high Mg content of tourmaline T1, corresponding to a Mg-foitite composition (Figure 2-7B,C). Assuming a stoichiometric content of boron, the average structural formula of tourmaline T1 is

$$\square_{0.811}K_{0.012}Na_{0.145}Ca_{0.032}(Mg_{2.272}Fe^{2+}_{0.046}Al_{0.617})Al_6(Si_{6.055}Al_{0.007})(BO_3)_3(OH)_{3.162}.$$

Analysis #	SiO_2	TiO_2	Al_2O_3	FeO	MgO	CaO	Na_2O	K_2O	F	H_2O	B_2O_3	Total
2	37.93	0	35.25	0.35	10.03	0.16	0.53	0	0.1	2.97	10.98	98.27
3	38.17	0	35.18	0.33	9.55	0.15	0.47	0	0.13	2.92	10.91	97.76
4	38.31	0.02	36.1	0.17	9.88	0.16	0.44	0	0.02	3.02	11.09	99.21
5	37.02	0	34.75	0.26	9.59	0.17	0.36	0	0.08	2.87	10.72	95.78
6	38.11	0	35.74	0.14	9.78	0.13	0.43	0.04	0.14	2.93	11	98.41
7	37.95	0.04	35.96	0.15	9.29	0.18	0.5	0.06	0.12	2.96	10.93	98.09
8	38.38	0.03	35.58	0.18	9.87	0.12	0.47	0.25	0.04	3.04	11.03	98.97
9	37.75	0	36	0.24	9.47	0.17	0.42	0	0.05	2.96	10.95	98
10	38.14	0	36.01	0.22	9.47	0.16	0.42	0.01	0.12	2.94	11	98.44
11	38.59	0	35.88	0.23	9.73	0.11	0.43	0.31	0.06	3.04	11.07	99.43
12	38.68	0.02	35.75	0.17	8.22	0.17	0.44	0	0.13	2.89	10.8	97.22
13	37.97	0	36.28	0.18	9.1	0.22	0.44	0.01	0.06	2.97	10.94	98.15
14	38.61	0	34.71	0.24	9.53	0.17	0.49	0.04	0.08	2.96	10.88	97.69
16	37.89	0	35.88	0.18	8.79	0.25	0.44	0.06	0.06	2.95	10.83	97.3
18	37.63	0	35.06	0.12	9.92	0.15	0.39	0.09	0.09	2.93	10.88	97.24
19	37.25	0	34.87	0.17	9.83	0.16	0.48	0.08	0.1	2.93	10.79	96.64
20	37.65	0	35.49	0.15	9.6	0.14	0.45	0.16	0.11	2.95	10.88	97.53
21	38.74	0	36	0.31	9.52	0.14	0.45	0.04	0.06	3	11.08	99.33
22	37.09	0.04	35.83	0.23	9.07	0.2	0.37	0.07	0.08	2.91	10.78	96.64
24	37.75	0.02	36	0.24	9.66	0.17	0.48	0.09	0.07	3	10.99	98.46
26	38.18	0	35.58	0.24	9.59	0.16	0.38	0.04	0.12	2.92	10.97	98.16
27	38.81	0	35.94	0.29	9.42	0.15	0.39	0.22	0.07	3.01	11.06	99.34
28	36.7	0.01	34.7	0.11	9.88	0.14	0.49	0	0.05	2.92	10.71	95.7
29	37.37	0.03	35.33	0.23	9.63	0.23	0.48	0	0.09	2.95	10.84	97.15
30	36.07	0	33.94	0.25	10.17	0.12	0.5	0.09	0	2.94	10.6	94.68
31	38.35	0	35.88	0.2	9.76	0.2	0.45	0.06	0.07	3	11.05	99
32	37.57	0	35.99	0.27	9.23	0.29	0.45	0.05	0.13	2.94	10.89	97.77
33	38.31	0.01	35.63	0.22	9.62	0.09	0.42	0.1	0.04	2.98	10.99	98.4
34	37.1	0	35.04	0.08	9.78	0.14	0.45	0.03	0.02	2.95	10.78	96.37
35	37.6	0.01	34.94	0.07	9.93	0.09	0.46	0.12	0.1	2.93	10.85	97.08
36	36.05	0.02	33.63	0.17	10.28	0.12	0.55	0.06	0.13	2.88	10.56	94.41
37	37.85	0	35.46	0.17	9.64	0.15	0.49	0.02	0.1	2.95	10.91	97.73
38	38.3	0	34.81	0.51	9.84	0.18	0.55	0.06	0.03	3.02	10.94	98.23
39	37.18	0.01	35.09	0.31	9.58	0.23	0.43	0.03	0.13	2.9	10.79	96.64
40	37.74	0.08	35.47	0.3	9.73	0.21	0.39	0.04	0.11	2.94	10.94	97.92
41	37.71	0	34.95	0.27	9.29	0.21	0.45	0.01	0.06	2.93	10.77	96.62
42	38.06	0	35.72	0.35	9.79	0.17	0.47	0.27	0.07	3.03	11.02	98.94
43	37.85	0.04	34.64	0.38	9.87	0.15	0.61	0.04	0.02	3.01	10.86	97.47
44	35.53	0.06	32.51	0.32	9.53	0.12	0.58	0.04	0.12	2.79	10.24	91.8
45	37.54	0.05	34.94	0.05	9.89	0.14	0.48	0.04	0.02	2.97	10.84	96.97
46	38.16	0.04	34.24	0.21	9.75	0.12	0.65	0.18	0.06	3.01	10.81	97.21
47	38.52	0.01	35.89	0.1	9.43	0.15	0.44	0	0.06	2.97	11.01	98.57
48	36.61	0.07	34.43	0.14	10.9	0.15	0.54	0	0.1	2.97	10.85	96.73
49	37.4	0	34.48	0.35	9.63	0.21	0.5	0.08	0.1	2.93	10.74	96.37

Analysis #	SiO_2	TiO_2	Al_2O_3	FeO	MgO	CaO	Na_2O	K_2O	F	H_2O	B_2O_3	Total
101	36.56	0.01	32.88	4.97	8.83	0.33	0.42	0.12	0	3.01	10.74	97.97
105	37.89	0	35.21	0.16	9.41	0.2	0.39	0.01	0	2.95	10.84	97.06
106	39.35	0.02	36.63	0.22	9.66	0.22	0.49	0.02	0	3.09	11.25	101
108	38.57	0	35.01	0.23	9.39	0.28	0.47	0.05	0	3.01	10.89	97.9
119	35.64	0.02	33.63	0.28	8.56	0.22	0.4	0.03	0	2.81	10.24	91.96
134	40	0	36.71	0.16	10.01	0.14	0.55	0.01	0	3.13	11.39	102.1
139	37.9	0.02	33.24	0.45	8.92	0.16	0.67	0.09	0	2.96	10.52	94.93
140	37.75	0.01	33.71	0.18	8.67	0.29	0.38	0.09	0	2.89	10.49	94.46
141	36.29	0.02	33.27	1.73	9.78	0.25	0.45	0.04	0	2.94	10.61	95.38
144	39.66	0	35.53	0.47	8.86	0.27	0.49	0.07	0	3.05	11.03	99.46
145	38.57	0	34.24	0.39	9.22	0.39	0.46	0.03	0	2.99	10.78	97.07
146	38.07	0	34.58	0.26	9.61	0.22	0.47	0.02	0	2.98	10.82	97.04
148	39.31	0.02	35.8	0.43	8.17	0.32	0.52	0.07	0	3.04	10.9	98.57
150	37.01	0.02	34.69	0.2	9.27	0.2	0.41	0.04	0	2.91	10.65	95.4
151	36.56	0	33.36	0.28	8.66	0.17	0.38	0.02	0	2.81	10.32	92.59
152	39.16	0.01	35.95	0.41	9.82	0.18	0.52	0.06	0	3.09	11.18	100.4

***Table 2-1**: Chemical composition (wt%) of tourmaline T1 (EPMA) and calculated H_2O and B_2O_3 compositions with the WinTcac software (Yavuz et al., 2014).*

Analysis #	Si(T)	B(T)	Al(T)	Total (T)	Al(Z)	Total (Z)	Al(Y)	Ti(Y)	Fe^{2+}(Y)	Mn^{2+}(Y)	Mg(Y)	Total (Y)
2	6.01	0	0	6.01	6	6	0.58	0	0.05	0	2.37	2.99
3	6.08	0	0	6.08	6	6	0.61	0	0.04	0	2.27	2.92
4	6	0	0	6	6	6	0.67	0	0.02	0	2.31	3
5	6	0	0	6	6	6	0.64	0	0.04	0	2.32	3
6	6.02	0	0	6.02	6	6	0.66	0	0.02	0	2.3	2.98
7	6.03	0	0	6.03	6	6	0.74	0.01	0.02	0	2.2	2.97
8	6.05	0	0	6.05	6	6	0.61	0	0.02	0	2.32	2.95
9	5.99	0.01	0	6	6	6	0.73	0	0.03	0	2.24	3.01
10	6.03	0	0	6.03	6	6	0.71	0	0.03	0	2.23	2.97
11	6.06	0	0	6.06	6	6	0.64	0	0.03	0	2.28	2.94
12	6.22	0	0	6.22	6	6	0.78	0	0.02	0	1.97	2.78
13	6.03	0	0	6.03	6	6	0.79	0	0.02	0	2.16	2.97
14	6.17	0	0	6.17	6	6	0.53	0	0.03	0	2.27	2.84
16	6.08	0	0	6.08	6	6	0.79	0	0.02	0	2.1	2.92
18	6.01	0	0	6.01	6	6	0.6	0	0.02	0	2.36	2.99
19	6	0.01	0	6.01	6	6	0.62	0	0.02	0	2.36	3
20	6.01	0	0	6.01	6	6	0.68	0	0.02	0	2.29	2.99
21	6.08	0	0	6.08	6	6	0.66	0	0.04	0	2.23	2.92
22	5.98	0	0.02	6	6	6	0.79	0.01	0.03	0	2.18	3
24	5.97	0.01	0.02	6	6	6	0.69	0	0.03	0	2.28	3.01
26	6.05	0	0	6.05	6	6	0.65	0	0.03	0	2.27	2.95

Analysis #	Si(T)	B(T)	Al(T)	Total (T)	Al(Z)	Total (Z)	Al(Y)	Ti(Y)	Fe^{2+}(Y)	Mn^{2+}(Y)	Mg(Y)	Total (Y)
27	6.1	0	0	6.1	6	6	0.66	0	0.04	0	2.21	2.9
28	5.96	0.01	0.03	6	6	6	0.61	0	0.02	0	2.39	3.01
29	5.99	0.01	0.01	6	6	6	0.67	0	0.03	0	2.3	3.01
30	5.92	0.02	0.06	6	6	6	0.5	0	0.03	0	2.49	3.02
31	6.03	0	0	6.03	6	6	0.65	0	0.03	0	2.29	2.97
32	6	0	0	6	6	6	0.77	0	0.04	0	2.2	3
33	6.06	0	0	6.06	6	6	0.64	0	0.03	0	2.27	2.94
34	5.98	0.01	0.01	6	6	6	0.65	0	0.01	0	2.35	3.01
35	6.02	0	0	6.02	6	6	0.6	0	0.01	0	2.37	2.98
36	5.93	0.02	0.05	6	6	6	0.47	0	0.02	0	2.52	3.02
37	6.03	0	0	6.03	6	6	0.66	0	0.02	0	2.29	2.97
38	6.08	0	0	6.08	6	6	0.52	0	0.07	0	2.33	2.92
39	5.99	0.01	0	6	6	6	0.66	0	0.04	0	2.3	3.01
40	6	0.01	0	6.01	6	6	0.64	0.01	0.04	0	2.31	3
41	6.08	0	0	6.08	6	6	0.65	0	0.04	0	2.23	2.92
42	6.01	0	0	6.01	6	6	0.64	0	0.05	0	2.3	2.99
43	6.06	0	0	6.06	6	6	0.53	0.01	0.05	0	2.35	2.94
44	6.03	0	0	6.03	6	6	0.5	0.01	0.05	0	2.41	2.97
45	6.02	0	0	6.02	6	6	0.6	0.01	0.01	0	2.36	2.98
46	6.14	0	0	6.14	6	6	0.49	0.01	0.03	0	2.34	2.86
47	6.08	0	0	6.08	6	6	0.68	0	0.01	0	2.22	2.92
48	5.87	0.03	0.11	6	6	6	0.39	0.01	0.02	0	2.6	3.03
49	6.05	0	0	6.05	6	6	0.58	0	0.05	0	2.32	2.95
101	5.91	0.03	0.05	6	6	6	0.22	0	0.67	0.01	2.13	3.03
105	6.08	0	0	6.08	6	6	0.65	0	0.02	0	2.25	2.93
106	6.08	0	0	6.08	6	6	0.67	0	0.03	0	2.22	2.92
108	6.15	0	0	6.15	6	6	0.58	0	0.03	0	2.23	2.85
119	6.05	0	0	6.05	6	6	0.73	0	0.04	0.02	2.17	2.95
134	6.1	0	0	6.1	6	6	0.6	0	0.02	0	2.28	2.9
139	6.26	0	0	6.26	6	6	0.47	0	0.06	0	2.2	2.74
140	6.25	0	0	6.25	6	6	0.58	0	0.03	0	2.14	2.75
141	5.95	0.02	0.03	6	6	6	0.39	0	0.24	0	2.39	3.02
144	6.25	0	0	6.25	6	6	0.6	0	0.06	0	2.08	2.75
145	6.22	0	0	6.22	6	6	0.51	0	0.05	0	2.22	2.78
146	6.12	0	0	6.12	6	6	0.55	0	0.04	0	2.3	2.88
148	6.27	0	0	6.27	6	6	0.73	0	0.06	0	1.94	2.73
150	6.04	0	0	6.04	6	6	0.67	0	0.03	0	2.26	2.96
151	6.16	0	0	6.16	6	6	0.62	0	0.04	0	2.18	2.84
152	6.09	0	0	6.09	6	6	0.59	0	0.05	0	2.28	2.91

***Table 2-2**: Structural formula of tourmaline T1 (T, Z and Y sites) calculated with the WinTcac software (Yavuz et al., 2014).*

Analysis #	Ca(X)	Na(X)	K(X)	vacancy(X)	Total (X)	OH(V)	OH(W)	F(W)	O(W)	Total (V+W)
2	0.03	0.16	0	0.81	1	3	0.14	0.05	0.81	4
3	0.03	0.15	0	0.83	1	3	0.11	0.07	0.83	4
4	0.03	0.13	0	0.84	1	3	0.15	0.01	0.84	4
5	0.03	0.11	0	0.86	1	3	0.1	0.04	0.86	4
6	0.02	0.13	0.01	0.84	1	3	0.09	0.07	0.84	4
7	0.03	0.15	0.01	0.8	1	3	0.14	0.06	0.8	4
8	0.02	0.14	0.05	0.79	1	3	0.19	0.02	0.79	4
9	0.03	0.13	0	0.84	1	3	0.14	0.03	0.84	4
10	0.03	0.13	0	0.84	1	3	0.1	0.06	0.84	4
11	0.02	0.13	0.06	0.79	1	3	0.18	0.03	0.79	4
12	0.03	0.14	0	0.83	1	3	0.1	0.07	0.83	4
13	0.04	0.14	0	0.83	1	3	0.15	0.03	0.83	4
14	0.03	0.15	0.01	0.81	1	3	0.15	0.04	0.81	4
16	0.04	0.14	0.01	0.81	1	3	0.16	0.03	0.81	4
18	0.03	0.12	0.02	0.84	1	3	0.12	0.05	0.84	4
19	0.03	0.15	0.02	0.81	1	3	0.15	0.05	0.8	4
20	0.02	0.14	0.03	0.8	1	3	0.14	0.06	0.8	4
21	0.02	0.14	0.01	0.83	1	3	0.14	0.03	0.83	4
22	0.04	0.12	0.01	0.84	1	3	0.13	0.04	0.83	4
24	0.03	0.15	0.02	0.81	1	3	0.17	0.04	0.8	4
26	0.03	0.12	0.01	0.85	1	3	0.09	0.06	0.85	4
27	0.03	0.12	0.04	0.81	1	3	0.15	0.04	0.81	4
28	0.02	0.15	0	0.82	1	3	0.17	0.03	0.81	4
29	0.04	0.15	0	0.81	1	3	0.15	0.05	0.81	4
30	0.02	0.16	0.02	0.8	1	3	0.22	0	0.78	4
31	0.03	0.14	0.01	0.82	1	3	0.15	0.04	0.82	4
32	0.05	0.14	0.01	0.8	1	3	0.13	0.07	0.8	4
33	0.02	0.13	0.02	0.84	1	3	0.14	0.02	0.84	4
34	0.02	0.14	0.01	0.83	1	3	0.17	0.01	0.82	4
35	0.02	0.14	0.03	0.82	1	3	0.13	0.05	0.82	4
36	0.02	0.18	0.01	0.79	1	3	0.16	0.07	0.77	4
37	0.03	0.15	0	0.82	1	3	0.13	0.05	0.82	4
38	0.03	0.17	0.01	0.79	1	3	0.2	0.02	0.79	4
39	0.04	0.13	0.01	0.82	1	3	0.12	0.07	0.81	4
40	0.04	0.12	0.01	0.84	1	3	0.12	0.06	0.83	4
41	0.04	0.14	0	0.82	1	3	0.15	0.03	0.82	4
42	0.03	0.14	0.05	0.77	1	3	0.19	0.04	0.77	4
43	0.03	0.19	0.01	0.78	1	3	0.21	0.01	0.78	4
44	0.02	0.19	0.01	0.78	1	3	0.16	0.06	0.78	4
45	0.02	0.15	0.01	0.82	1	3	0.17	0.01	0.82	4
46	0.02	0.2	0.04	0.74	1	3	0.23	0.03	0.74	4
47	0.03	0.14	0	0.84	1	3	0.13	0.03	0.84	4
48	0.03	0.17	0	0.81	1	3	0.17	0.05	0.78	4
49	0.04	0.16	0.02	0.79	1	3	0.16	0.05	0.79	4

Analysis #	Ca(X)	Na(X)	K(X)	vacancy(X)	Total (X)	OH(V)	OH(W)	F(W)	O(W)	Total (V+W)
101	0.06	0.13	0.03	0.79	1	3	0.25	0	0.75	4
105	0.03	0.12	0	0.84	1	3	0.16	0	0.84	4
106	0.04	0.15	0	0.81	1	3	0.19	0	0.81	4
108	0.05	0.15	0.01	0.8	1	3	0.2	0	0.8	4
119	0.04	0.13	0.01	0.82	1	3	0.18	0	0.82	4
134	0.02	0.16	0	0.81	1	3	0.19	0	0.81	4
139	0.03	0.22	0.02	0.74	1	3	0.26	0	0.74	4
140	0.05	0.12	0.02	0.81	1	3	0.19	0	0.81	4
141	0.04	0.14	0.01	0.81	1	3	0.22	0	0.78	4
144	0.05	0.15	0.01	0.79	1	3	0.21	0	0.79	4
145	0.07	0.14	0.01	0.78	1	3	0.22	0	0.78	4
146	0.04	0.15	0	0.81	1	3	0.19	0	0.81	4
148	0.06	0.16	0.01	0.77	1	3	0.23	0	0.77	4
150	0.04	0.13	0.01	0.83	1	3	0.17	0	0.83	4
151	0.03	0.12	0	0.84	1	3	0.16	0	0.84	4
152	0.03	0.16	0.01	0.8	1	3	0.2	0	0.8	4

***Table 2-3**: Structural formula of tourmaline T1 (X, V and W sites) calculated with the WinTcac software (Yavuz et al., 2014).*

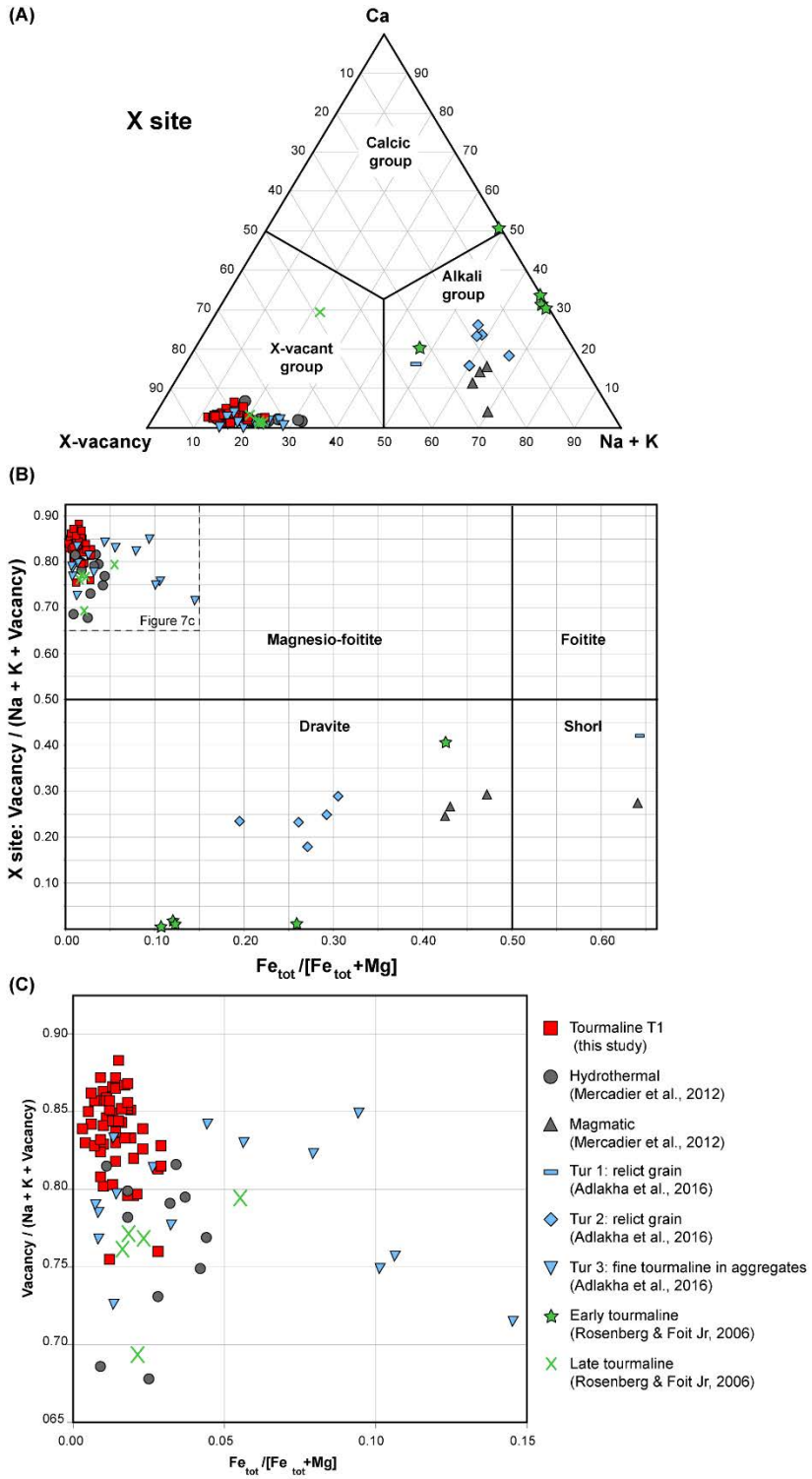

***Figure 2-7**: Classification of tourmaline T1 at the Ranger U deposit (Australia) and for different generations of tourmaline in other unconformity-related U deposits from the Athabasca Basin (Canada, Adlakha and Hattori, 2016; Mercadier et al., 2012; Rosenberg and Foit Jr, 2006a). (**A**) Ca-Na + K-X-site vacancy ternary diagram showing the X-site occupancy; (**B**) binary diagram showing the Fetot/(Fetot + Mg) versus X-site vacancy/(X-site vacancy + Na + K) ratios; (**C**) zoom on the Mg-foitite domain on the Fetot/(Fetot + Mg) versus X-site vacancy/(X-site vacancy + Na + K) diagram. For Canadian deposits, "Hydrothermal" (Mercadier et al., 2012), "Tur 3" (Adlakha and Hattori, 2016) and "Late tourmaline" (Rosenberg and Foit Jr, 2006) correspond to Mg-foitite. Note that each point for "Hydrothermal", Magmatic" (Mercadier et al., 2012), "Tur1", "Tur2", "Tur3" (Adlakha and Hattori, 2016),"early" and "late*

tourmaline" (Rosenberg and Foit Jr, 2006) compositions correspond to the mean values for each sample or generation.

2.5.2. Chlorite chemistry and thermometry

A total of 14 EPMA analyses were obtained on hydrothermal chlorite Chl2 and 16 EPMA analyses on retrometamorphic chlorite Chl1 for comparison. Analyses were carried out on >5 µm size chlorite grains. The chlorite Chl1 is a Fe-Mg chlorite with high Fe contents (2.93–3.40 *apfu*) and relatively low Mg contents (1.10–1.49 *apfu*), with Si/Al = 1.04–1.16, and Mg/(Mg + Fe_{tot}) = 0.25–0.33 (Tables 2-4 and 2-5). The chlorite Chl2 corresponds to Mg-chlorite with compositions that lie between the clinochlore and Mg-amesite fields (Figure 2-8A). It has relatively low Fe contents (0.28–0.83 *apfu*) and high Mg contents (3.08–3.84 *apfu*), with Si/Al = 1.08–1.22, and Mg/(Mg + Fe_{tot}) = 0.80–0.93 consistent with other Mg-chlorite Chl2 (Mg/(Mg + Fe_{tot}) = 0.89–0.92) observed elsewhere in the deposit (Skirrow et al., 2016). All Fe is assumed to be ferrous in the calculations of the structural formulae.

Analysis #	Na_2O	MgO	Al_2O_3	SiO_2	K_2O	CaO	MnO	FeO	TiO_2	Total	Calculated T (°C)
Chl1 2	0.06	6.94	21.66	27.54	0.81	0.09	0.13	33.1	0.03	90.36	162
Chl1 3	0.08	7.26	20.71	27.18	0.6	0.13	0.19	32.83	0.04	89.03	169
Chl1 4	0	7.97	20.77	26.84	0.44	0.11	0.04	32.55	0.04	88.76	182
Chl1 6	0.04	7.23	20.82	26.4	0.36	0.07	0.02	35.16	0.04	90.12	216
Chl1 8	0	7.92	19.53	25.95	0.19	0.09	0.14	34.35	0.03	88.19	240
Chl1 13	0.03	9.11	19.03	25.95	0.06	0.12	0.07	33.44	0.02	87.83	279
Chl1 20	0.02	6.71	19.39	25.76	0.02	0.04	0.04	36.79	0.05	88.8	248
Chl1 21	0	7.59	19.29	25.11	0.04	0.03	0.07	35.28	0.04	87.45	298
Chl1 22	0.05	8.27	19.15	25.51	0.04	0.07	0.07	33.37	0.1	86.64	246
Chl1 33	0	6.93	20.86	25.68	0.05	0.02	0.05	35.29	0.01	88.87	224
Chl1 38	0.04	6.95	20.36	25.08	0.05	0.08	0.16	36.79	0.01	89.51	332
Chl1 39	0.02	7.12	20.17	25.26	0.5	0.11	0.09	33.18	0.03	86.47	221
Chl1 44	0.05	6.88	21.3	26.94	0.6	0.13	0.23	32.79	0.03	88.96	167
Chl1 45	0	8.31	20.01	25.84	0.07	0.02	0.01	33.82	0.14	88.21	235
Chl1 46	0.01	7.89	20.22	25.78	0.35	0.03	0.07	33.46	0.08	87.89	227
Chl1 52	0.03	7.31	19.7	24.8	0.11	0.11	0.07	35.3	0.09	87.53	312
Chl2 153	0.02	21.76	25.3	32.56	0.01	0.11	0.05	6.16	0.02	86	101
Chl2 154	0	23.4	25.33	32.31	0.03	0.08	0	4.54	0.02	85.71	109
Chl2 155	0.02	26.82	23.4	31.83	0.03	0.01	0	3.58	0	85.68	136
Chl2 156	0.04	25.31	21.04	30.25	0.02	0.13	0	6.99	0	83.78	163
Chl2 157	0.03	22.99	21.62	30.25	0	0.05	0.03	10.03	0	85.01	153
Chl2 158	0	23.96	24.48	31.26	0.07	0.05	0.08	5.7	0.04	85.64	129
Chl2 159	0.03	23.77	24.66	31.81	0.06	0.05	0.13	4.8	0	85.29	117
Chl2 160	0.02	25.14	24.39	31.65	0.02	0.03	0.01	3.88	0	85.15	125
Chl2 161	0	23.82	24.68	31.42	0.04	0.06	0	4.52	0	84.53	119
Chl2 162	0.02	24.97	23.95	31.47	0.05	0.05	0	3.85	0	84.36	124
Chl2 163	0	24.02	23.69	31.45	0.03	0.05	0	4.79	0.01	84.06	119
Chl2164	0.03	26.4	22.02	30.72	0.04	0.07	0	4.45	0	83.73	151
Chl2 165	0	25.71	23.87	31.4	0.06	0.06	0	3.97	0	85.06	133
Chl2 166	0	22.65	24.18	30.87	0.04	0.05	0.05	5.87	0	83.73	119

***Table 2-4**: Chemical composition (wt%) and calculated temperature (Bourdelle and Cathelineau, 2015) of chlorite Chl1 and Chl2 (EPMA).*

The geothermometer of Bourdelle and Cathelineau (2015) assumes that quartz and water activities are equal to 1 and is valid for a temperature range of 50 to 350 °C, which makes it applicable to our data based on temperatures estimated from the previously mentioned fluid inclusion studies (Derome et al., 2003; Kyser et al., 2000; Polito et al., 2004, 2005b). This thermometer requires chlorite-quartz equilibrium, and produces estimates of the crystallisation temperatures of retrometamorphic chlorite Ch1 between 162 and 332 °C (average ± standard deviation values are 235 ± 50) and diagenetic-hydrothermal chlorite Chl2 between 101 and 163 °C (average ± standard deviation values are 128 ± 28) when plotted in the Si-R^{2+} diagram of Wiewióra and Weiss (1990, Figure 2-8B).

Analysis #	Na (*apfu*)	Mg (*apfu*)	Al tot (*apfu*)	Al IV (*apfu*)	Al VI (*apfu*)	Si (*apfu*)	K (*apfu*)	Ca (*apfu*)	Mn (*apfu*)	Fe (*apfu*)	Ti (*apfu*)
Chl1 2	0.01	1.1	2.7	1.08	1.62	2.92	0.11	0.01	0.01	2.93	0
Chl1 3	0.02	1.16	2.63	1.07	1.55	2.93	0.08	0.02	0.02	2.96	0
Chl1 4	0	1.28	2.64	1.11	1.53	2.89	0.06	0.01	0	2.93	0
Chl1 6	0.01	1.16	2.64	1.16	1.48	2.84	0.05	0.01	0	3.16	0
Chl1 8	0	1.3	2.53	1.15	1.38	2.85	0.03	0.01	0.01	3.16	0
Chl1 13	0.01	1.49	2.46	1.15	1.32	2.85	0.01	0.01	0.01	3.07	0
Chl1 20	0	1.11	2.52	1.15	1.37	2.85	0	0	0	3.4	0
Chl1 21	0	1.26	2.54	1.2	1.34	2.8	0.01	0	0.01	3.3	0
Chl1 22	0.01	1.37	2.52	1.15	1.36	2.85	0.01	0.01	0.01	3.11	0.01
Chl1 33	0	1.13	2.69	1.19	1.49	2.81	0.01	0	0	3.22	0
Chl1 38	0.01	1.14	2.63	1.25	1.39	2.75	0.01	0.01	0.01	3.38	0
Chl1 39	0	1.19	2.66	1.17	1.49	2.83	0.07	0.01	0.01	3.11	0
Chl1 44	0.01	1.1	2.7	1.1	1.6	2.9	0.08	0.01	0.02	2.95	0
Chl1 45	0	1.35	2.58	1.17	1.41	2.83	0.01	0	0	3.09	0.01
Chl1 46	0	1.29	2.62	1.17	1.45	2.83	0.05	0	0.01	3.07	0.01
Chl1 52	0.01	1.22	2.59	1.23	1.37	2.77	0.02	0.01	0.01	3.3	0.01
Chl2 153	0	3.08	2.83	0.91	1.91	3.09	0	0.01	0	0.49	0
Chl2 154	0	3.3	2.82	0.95	1.87	3.05	0	0.01	0	0.36	0
Chl2 155	0	3.78	2.61	0.99	1.62	3.01	0	0	0	0.28	0
Chl2 156	0.01	3.73	2.45	1.01	1.45	2.99	0	0.01	0	0.58	0
Chl2 157	0.01	3.39	2.52	1.01	1.51	2.99	0	0.01	0	0.83	0
Chl2 158	0	3.41	2.76	1.01	1.74	2.99	0.01	0.01	0.01	0.46	0
Chl2 159	0.01	3.38	2.77	0.97	1.8	3.03	0.01	0.01	0.01	0.38	0
Chl2 160	0	3.56	2.73	0.99	1.74	3.01	0	0	0	0.31	0
Chl2 161	0	3.41	2.79	0.98	1.81	3.02	0	0.01	0	0.36	0
Chl2 162	0	3.57	2.71	0.98	1.73	3.02	0.01	0.01	0	0.31	0
Chl2 163	0	3.46	2.7	0.96	1.74	3.04	0	0.01	0	0.39	0
Chl2164	0.01	3.84	2.53	1	1.53	3	0	0.01	0	0.36	0
Chl2 165	0	3.66	2.68	1	1.68	3	0.01	0.01	0	0.32	0
Chl2 166	0	3.3	2.78	0.98	1.8	3.02	0	0.01	0	0.48	0

Table 2-5: *Structural formula and occupancy sites for chlorite Chl1 and Chl2 calculated on a basis of 14 oxygens.*

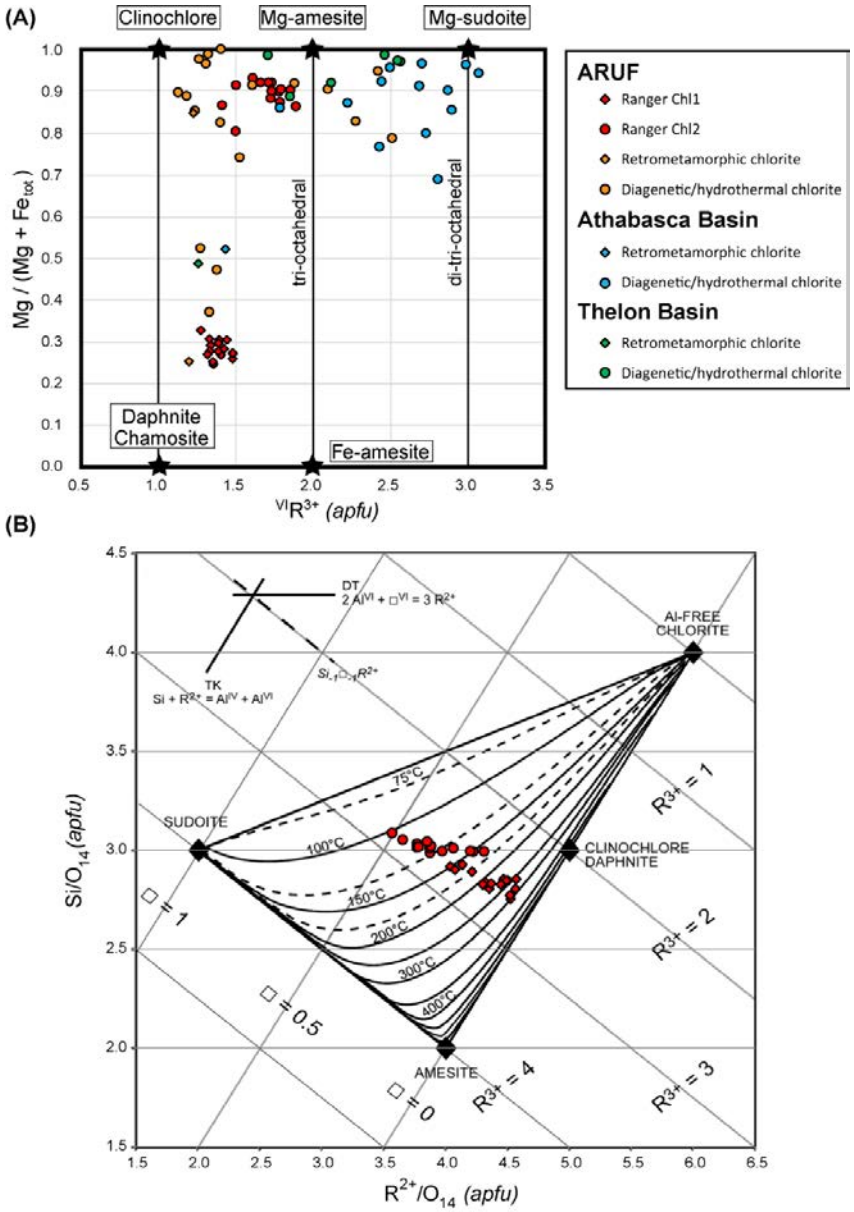

***Figure 2-8**: (**A**) Classification diagram of Plissart et al. (2009) for tri- and di-trioctahedral chlorite. Compositions of chlorite Chl1 and Chl2 from Ranger deposit (this study) are plotted together with chlorite from other deposits from the ARUF (Beaufort et al., 2005; Polito et al., 2004, 2005b), the Athabasca Basin (Billault et al., 2002; Kotzer and Kyser, 1995; Martz, 2017) and the Thelon Basin (Grare et al., n.d.) for comparison. For data from the ARUF (except for Ranger, this study) and the Canadian basins, the plotted data corresponds to the mean compositions for each sample or generation. (**B**) Distribution of temperatures for chlorite Chl1 and Chl2 from Ranger deposit (this study) determined by chlorite thermometry plotted in a T-R^{2+}-Si diagram (Wiewióra and Weiss, 1990), with R^2 = Mm + Mn + Fe (apfu).*

2.5.3. Boron isotopes in tourmaline

Due to the large spot size compared to the tourmaline T1 needles width, SIMS analyses are occurring across many different needles leading to a homogenisation of the $\delta^{11}B$ values. The tourmaline T1 displays a range of positive $\delta^{11}B$ values (0.6–9.4‰, *n* = 76, Table 2-6 and Figure 2-9). The distribution of $\delta^{11}B$ values shows a unique mode at ~4.3‰ (average = 3.7 ±

1.8‰ (1σ) and median = 3.4‰). There is no relationship between $\delta^{11}B$ value and analytical spot location along the investigated tourmaline T1 fringe, or within a single T1 rosette. Therefore, even though some homogenisation of the data may have occurred due to the large spot size compared to the tourmaline needles size, there is no obvious systematic variation of $\delta^{11}B$ value along the c-axis. Moreover, there is no visible relationship between $\delta^{11}B$ value and the chemical composition of tourmaline as measured by EPMA since both parameters are relatively constant.

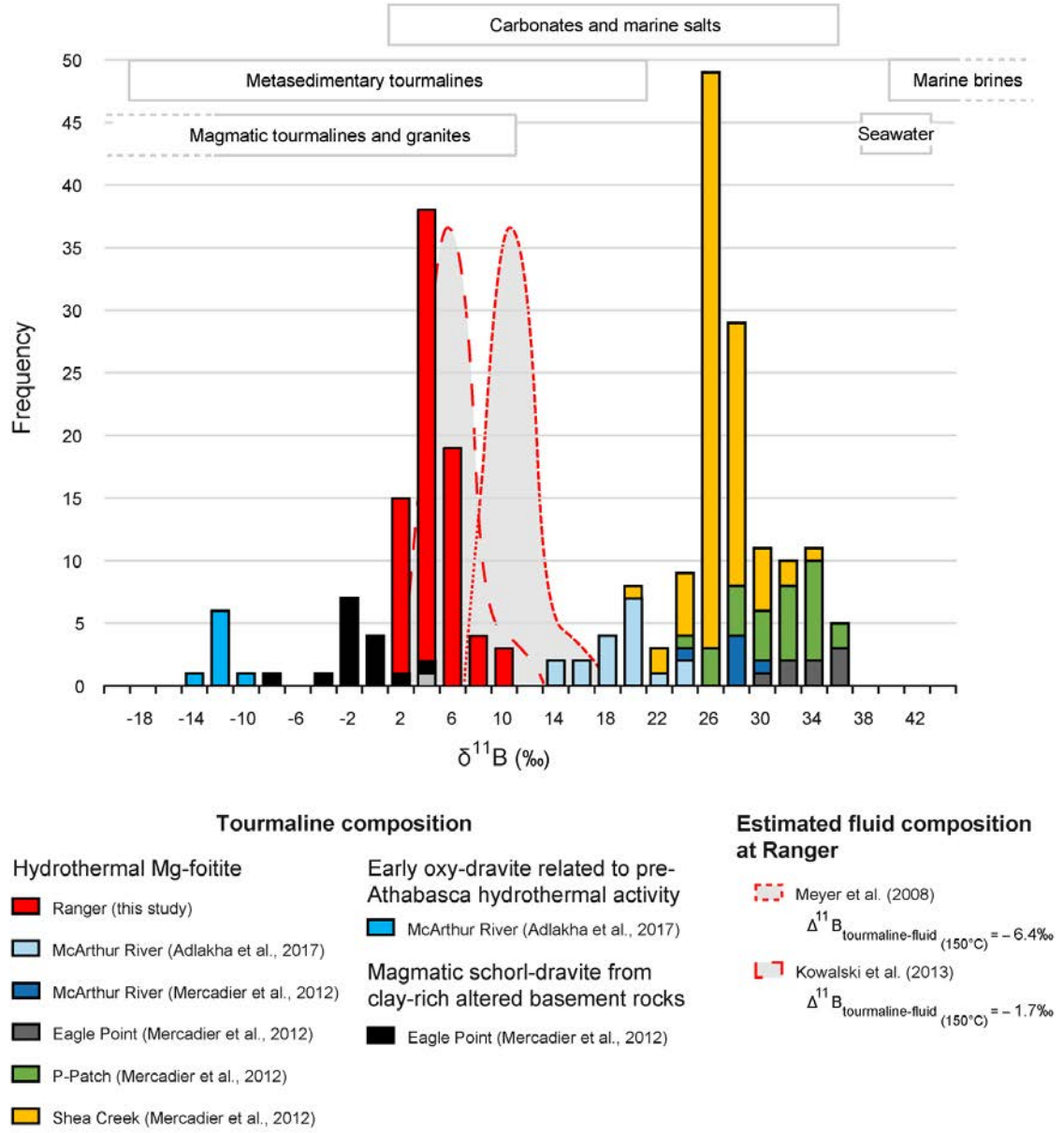

***Figure 2-9**: Histogram of boron isotopic compositions for tourmaline T1 at Ranger U deposit (this study) and for some of the unconformity-related U deposits from the Athabasca Basin (Canada): Adlakha et al. (2017) and Mercadier et al. (2012). The boron isotopic composition for different B reservoirs are shown (Barth, 1993; Palmer and Swihart, 1996; Vengosh et al., 1992 and references therein). The range of the boron isotopic composition of the calculated fluid in equilibrium with tourmaline*

T1 at Ranger is indicated by a grey zone limited by a red dotted line according to two independent methods: Meyer et al. (2008) and Kowalski et al. (2013).

Analysis #	$\delta^{11}B$	2σ	Analysis #	$\delta^{11}B$	2σ	Analysis #	$\delta^{11}B$	2σ
1	1.78	0.62	27	1.8	0.41	52	4.84	0.76
2	1.15	0.37	28	2.72	0.54	53	4.34	0.91
3	1.22	1.01	29	4.41	0.5	54	4.26	0.89
4	0.58	0.7	30	2.66	0.52	55	4.81	1.07
5	2.15	1.22	31	2.92	0.49	56	2.69	0.52
6	1.7	0.53	32	2.91	0.4	57	3.45	0.37
7	1.39	0.49	33	3.66	0.38	58	6.22	0.72
8	3.19	0.58	34	3.36	0.42	59	3.37	0.41
9	2.55	1.07	35	3.17	0.46	60	3.31	0.51
10	5.4	0.85	36	1.66	1.29	61	4.67	0.52
11	3.94	0.72	37	8.09	1.78	62	6.7	1.18
12	1.73	0.49	38	4.65	0.45	63	5.77	0.91
13	3.2	0.57	39	5.45	0.51	64	7.55	0.28
14	3.61	0.39	40	5.63	0.71	65	9.38	0.6
15	3.9	0.6	41	4.73	0.4	66	8.75	0.53
16	3.62	0.97	42	4.95	0.86	67	2.67	0.4
17	4.34	0.54	43	4.88	0.51	68	0.8	0.9
18	2.02	0.51	44	4.79	0.49	69	2.5	0.52
19	1.77	0.47	45	7.42	0.61	70	3.74	0.52
20	0.82	0.66	46	4.23	0.53	71	4.66	0.48
21	2.07	0.47	47	2.84	0.85	72	3.35	0.44
22	3.47	0.59	48	3.99	0.75	73	4.34	0.52
23	3.43	0.52	49	3.59	0.43	74	1.45	0.76
24	3.31	0.55	50	3.88	0.47	75	1.93	0.52
25	3.18	0.55	51	3.97	0.35	76	3.22	0.66
26	3.13	0.52						

***Table 2-6**: B isotope compositions for tourmaline T1.*

2.6. Discussion and conclusions

2.6.1. Comparison between unconformity-related deposits of the Alligator Rivers Uranium Field (Australia) and the Athabasca and Thelon basins (Canada)

The retrometamorphic chlorite Chl1 from Ranger has a composition close to retrometamorphic chlorite from the Athabasca and Thelon basins characterised by a relatively low Mg/(Mg + Fe_{tot}) ratio (Figure 2-8). This means that similar retrometamorphic conditions were encountered in the three localities. In the ARUF, the diagenetic-hydrothermal chlorite (including chlorite Chl2 from Ranger) related to the uranium ore-forming systems has a composition intermediate between clinochlore and Mg-amesite, with $^{VI}R^{3+}$ values between ~1.3 and 1.8 *apfu* and Mg/(Mg + Fe_{tot}) ratio between ~0.8 and 0.95. Some paragenetically equivalent chlorites from uranium deposits of the Athabasca and Thelon basins show

composition similar to chlorite from the ARUF while others tend towards a sudoitic composition with higher $^{VI}R^{3+}$ values up to ~3.0 *apfu* (Figure 2-8A). According to Kister et al. (2005) the occurrence of sudoite instead of clinochlore might reflect higher K^+/H^+ and lower Mg^{2+}/H^+ activity ratios in the fluids of the Athabasca and Thelon basins compared to the ARUF. However, it remains unclear why those parameters would be specifically different in the ARUF compared to Thelon and Athabasca basins. Another possibility to explain this compositional difference is that more intense fluid–rock alteration occurred in the ARUF, leading to an increase in the Mg-content of the chlorites, from sudoite (~14 wt% MgO) to clinochlore (~25 wt% MgO, Beaufort et al., 2005). Nonetheless, while the presence of sudoite is considered a proximal indicator for uranium mineralisation in the Athabasca and Thelon basins (Grare et al., n.d.; Kister et al., 2005), it should not be targeted as such during uranium exploration in the ARUF.

The texture and chemical composition of tourmaline T1 at the Ranger U deposit is consistent with that of the U-related tourmaline found in unconformity-related U deposits from the Athabasca Basin (Canada, Adlakha et al., 2017; Adlakha and Hattori, 2016; Mercadier et al., 2012, Figure 2-7). Collectively, U-related tourmaline has typically an alkali-deficient composition with high X-site vacancy contents ranging between 0.66 and 0.85 *apfu* (except one sample) and low $Fe_{tot}/(Fe_{tot} + Mg)$ ratio ranging between 0.01 and 0.15, typical of Mg-foitite composition. The $\delta^{11}B$ values of tourmaline T1 from Ranger (0.6–9.4‰, this study) are significantly lower than those from four different unconformity-related U deposits the Athabasca Basin (ca. 14 to 35‰; Figure 2-9, Adlakha et al., 2017; Mercadier et al., 2012). The intrasample variation (9‰ at Ranger) is consistent with the largest ones measured in the Athabasca Basin (Adlakha et al., 2017; Mercadier et al., 2012). For the McArthur River deposit, it is noteworthy that the $\delta^{11}B$ values of Mercadier et al. (2012) are shifted by ~+8‰ from those of Adlakha et al. (2017). A possible explanation for this shift between the two studies on the Athabasca Basin is that Mercadier et al. (2012) did not use matrix-match standards (but elbaite standard) while dravite standards were used by Adlakha et al. (2017) and in this study. It is now well documented that matrix-dependent mass fractionation during SIMS analysis of boron isotopes in tourmaline could be significant (Chaussidon and Albarède, 1992; MacGregor et al., 2013; Molnár et al., 2016). Whether the data of Mercadier et al. (2012) should be corrected significantly and, if so, determining the magnitude of the correction is beyond the scope of this study. However, under the assumption that the data of Mercadier et al. (2012) should be shifted by ~-8‰ (in order to align the results obtained by Mercadier et al. (2012) and Adlakha et al. (2017) at the McArthur River U deposit), the overall $\delta^{11}B$ values of U-related tourmaline from unconformity-related U deposits from the Athabasca basin would be ~12–28‰; still significantly higher than for the Ranger deposit (0.6–9.4‰). Therefore the chemical

composition of tourmaline points towards similar physical-chemical conditions for the precipitation of tourmaline in both the Ranger deposit and Canadian deposits of the Athabasca Basin. However, B isotope composition of tourmaline indicates that the sources of B or the relative contribution of different B sources were significantly distinct between the Ranger deposit and some Canadian deposits of the Athabasca Basin.

2.6.2. Insights into boron and magnesium metasomatism

The Mg-driven geochemical signature of the hydrothermal alteration related to U mineralisation in the unconformity-related U deposits in the ARUF is marked for example by the formation of Mg-chlorite Chl2 co-genetic with Mg-tourmaline T1 and early uraninite U1 (Beaufort et al., 2005a; Fisher et al., 2013). Tourmaline has been reported at the Jabiluka deposit within alteration halos around mineralisation (Binns et al., 1980; Nutt, 1989; Polito et al., 2011, 2005b) and in the Kombolgie Sandstones of the McArthur Basin (Durak et al., 1983) and seems to be always linked in time and space with chlorite which is the main indicator of the Mg-metasomatism. The relatively constant chemical and isotopic composition of tourmaline T1 from Ranger indicates rather steady conditions (temperature, pH, eH and fluid composition) during tourmaline precipitation. Analysis of tourmaline T1 and chlorite Chl2 allows determining some of the characteristics of the U-ore-forming fluid that is also related to B-Mg-metasomatism.

As tourmaline T1 formed after chlorite Chl2 and before quartz Q2, the crystallisation temperature of these two minerals can help bracketing the temperature of formation of the tourmaline T1. Here, the calculated range of temperature for chlorite Chl2 is 101–163 °C (128 ± 18 °C). These estimates should be considered with caution because Chl2 precipitated during the pre-ore B1 breccia episode during which quartz dissolution is also noted (Figure 2-3), while the geothermometer of Bourdelle and Cathelineau (2015) assumes that quartz activity is equal to 1. However, the study of primary fluid inclusions hosted in quartz Q2 at Ranger indicates a trapping temperature of 150 ± 20 °C (Derome et al., 2003) compatible with the temperature determined for chlorite Chl2 which suggests that there is no significant temperature variation during the precipitation of Chl2, T1 and Q2. The $\delta^{11}B$ values for the fluid in equilibrium with tourmaline are calculated with two different methods. Using the tourmaline-water B isotopic fractionation factor of Kowalski et al. (2013) at 150 °C ($\Delta^{11}B_{tourmaline\text{-}fluid(150\ °C)}$ = -1.7‰) leads $\delta^{11}B$ values for the fluid in equilibrium with tourmaline ranging between 2 and 11‰. Using the tourmaline-water B isotopic factor of Meyer et al. (2008) extrapolated down to 150 °C ($\Delta^{11}B_{tourmaline\text{-}fluid(150\ °C)}$ = -6.4‰) leads to $\delta^{11}B$ values estimates for the fluid between 7 and 16‰. The $\delta^{11}B$ values for the fluid in equilibrium with tourmaline T1 overlap the $\delta^{11}B$ range of fluids equilibrated with carbonates and evaporites and metasedimentary tourmaline and are distinct

from heavier isotopic composition typical of seawater and marine brines ($\delta^{11}B$ = 40 to 70‰, Figure 2-9). $\delta^{11}B$ values for tourmaline T1 are compatible with the highest values for magmatic tourmaline from various localities worldwide including the Athabasca crystalline basement ($\delta^{11}B$ < 10‰, Figure 2-9).

Adlakha et al. (2017) proposed for the Athabasca Basin a model involving groundwater dissolving carbonate or evaporitic rocks and further ^{11}B enrichment of the fluid through precipitation of illite due to the preferential ^{10}B incorporation into illite (Williams et al., 2001), as a mechanism to achieve heavy boron ($\delta^{11}B$ = 17 to 28‰) and relatively light hydrogen (δD = −15 to −65‰) isotopic compositions for the fluid in equilibrium with tourmaline. Such model is however not supported by the halogen compositions (Cl, Br) of fluid inclusions in Athabasca and ARUF deposits. The latter indicate that the unconformity-related U deposits from the Athabasca Basin and the ARUF were formed by highly-saline basinal brines derived from highly-evaporated seawater (up to epsomite saturation, Derome et al., 2007; Richard et al., 2014, 2011). The dissolution of evaporites in the Athabasca Basin is probably very limited as indicated by halogens ratios (Richard et al., 2014). In addition, low δD values were also measured in fluid inclusions representative of the U-forming brines in the Athabasca Basin and are consistent with seawater evaporation (Richard et al., 2013a). Brines derived from evaporation of seawater are typically enriched in B and Mg during evaporation ([Mg] > 2 mol kg^{-1}, [B] > 10^{-2} mol kg^{-1}, Fontes and Matray, 1993).

Therefore, the following alternative model can be proposed. NaCl-rich and/or $CaCl_2$-rich brines, initially enriched in B and Mg during seawater evaporation and showing a highly positive $\delta^{11}B$ value (source 1, $\delta^{11}B$ > 40‰) leached a light boron reservoir (source 2, neutral to negative $\delta^{11}B$ value) in order to reach intermediate $\delta^{11}B$ value before precipitating chlorite Chl2 and tourmaline T1. Detrital tourmaline in the basin, magmatic tourmaline from pegmatite and metamorphic tourmaline from graphitic pelitic gneiss in the basement are potential candidates for boron source 2. However, they are not altered in the pegmatite even if the pegmatites are known to be partly chloritised and sericitised as a result of interaction with the ore-forming fluids (Skirrow et al., 2016). Other possible candidates for boron source 2 in crystalline basement rocks; feldspar, and biotite/muscovite that are known to contain up to 10 ppm and 200 ppm B, respectively (London et al., 1996), are more reactive than magmatic or detrital tourmaline and are strongly altered in the alteration halo of unconformity-related U deposits. The isotopic signature of magmatic or metamorphic feldspar and biotite/muscovite is poorly documented but it can be proposed that it is comparable with the values obtained in magmatic or metamorphic tourmaline because of the limited isotopic fractionation at high temperature (Kowalski et al., 2013; Meyer et al., 2008). Considering a possible seawater signature ($\delta^{11}B$ ~40‰) for source 1 and $\delta^{11}B$ values for the source 2 ranging from −30 to 10‰, and a mean

$\delta^{11}B$ value of ~8‰ for the fluid in equilibrium with T1 tourmaline, mass balance calculation indicates that source 1 may have contributed between ~0 and 55% and source 2 between ~45 and 100% to the fluid's total boron budget. This would indicate a significantly higher involvement of source 2 (i.e., basement rocks) in ARUF compared to the Athabasca Basin, where source 1 (seawater) is dominant.

One major difference between U deposits from ARUF and the Athabasca Basin is the involvement of a low-salinity fluid in addition to brines as observed in fluid inclusions (Derome et al., 2003, 2007). However, the absence of low-salinity fluid in the Athabasca Basin indicates that it is not a necessary ingredient for tourmaline precipitation and U deposition and probably did not contribute to the B isotope signature of T1 tourmaline. Considering the similarities of host rocks, fluid composition and temperature between the ARUF and the Athabasca Basin, the present results raise the question of the influence of fluid/rock ratio and the duration of fluid/rock interaction on the respective involvement of various B sources, and therefore on the abundance and isotopic composition of hydrothermal tourmaline in unconformity-related U deposits. However, despite its relatively low abundance, hydrothermal tourmaline (alone or in combination with other hydrothermal minerals) should be worth considering as a valuable proximal indicator for uranium mineralisation.

Acknowledgments

Energy Resources Australia and in particular Greg Rogers are thanked for support in sampling at the Ranger mine site. Olivier Rouer and Michel Cathelineau (GeoRessources Lab) are greatly acknowledged for support in EPMA analyses and interpretation of chlorite compositions, respectively. Ion Probe Team Nancy are greatly acknowledged for support in SIMS analyses. The comments of two anonymous reviewers greatly helped improving the manuscript.

Chapter 3. Uranium mobility and deposition over 1.3 Ga in the Westmoreland area (McArthur Basin, Australia)

Submitted to *Mineralium Deposita*

Gigon, J. [1], **Mercadier, J.** [1], **Annesley, I.R.** [1], **Richard, A.** [1], **Wygralak, A.S.** [2], **Skirrow, R.G.** [3], **Mernagh, T.P** [4], **I.P.T.N.** [5]

[1] Université de Lorraine, CNRS, GeoRessources Lab, F-54500 Vandœuvre-lès-Nancy, France

[2] Northern Territory Geological Survey, PO Box 2901, Darwin, NT 0801, Australia

[3] Geoscience Australia, GPO Box 378, Canberra, ACT 2601, Australia

[4] Australian National University, 142 Mills Rd., Acton, ACT 2601, Australia

[5] Ion Probe Team Nancy, CRPG, UMR 7358, CNRS, Université de Lorraine, Vandœuvre-lès-Nancy F-54501, France

Preamble

The previous chapter focussed on the world-class basement-hosted Ranger uranium deposit (unconformity-type) located in the Alligator Rivers Uranium Field (ARUF). The Westmoreland area, located at the other basin end, hosts smaller basin-hosted uranium deposits that are of interest because the primary mineralisation is known to have approximately the same age than in the ARUF. The comparison between deposits in both sides of the basin in terms of mineralogy, alteration, uraninite composition and temperatures gives insights on the differences between two mineralised areas in the same sedimentary basin. It also raises the question of the link between major regional events such as oogenesis and mineralising episodes. The chapter corresponds to a paper in preparation for *Mineralium Deposita.*

Préambule

Le chapitre précédent s'est intéressé au gisement uranifère de classe mondiale Ranger dans l'Alligator Rivers Uranium Field (ARUF), qui est situé dans le socle et qui représente un exemple typique des gisements de type discordance. La zone de Westmoreland, située à l'autre extrémité du bassin, renferme de plus petits gisements d'uranium situés dans le bassin, dont l'âge de la minéralisation primaire est similaire à celle des gisements de l'ARUF. La comparaison entre la minéralisation de part et d'autre du bassin (minéralogie, altération, composition des uraninites et température) donne des informations sur les différences entre deux zones minéralisées partageant le même bassin sédimentaire. Cette étude soulève aussi la question du lien entre les évènements régionaux majeurs comme les orogenèses et les épisodes minéralisateurs. Ce chapitre correspond à un article en préparation pour *Mineralium Deposita.*

Les études précédentes sur la zone de Westmoreland ont montré que la minéralisation uranifère s'est formée dans des conditions similaires à celles connues pour les gisements de type discordance de l'Alligator Rivers Uranium Field (ARUF), située au nord du même bassin sédimentaire. Ici, une étude minéralogique, géochimique et géochronologique, combinée aux études précédentes portant sur différents intervalles minéralisés des gisements de Junnagunna et Redtree, permet l'identification d'au moins six générations d'oxydes d'uranium. Ils se sont formés entre ~1680 et ~350 Ma, ce qui souligne la mobilité prolongée de l'uranium pendant 1.3 Ga. Chaque génération d'oxydes d'uranium est marquée par une composition chimique spécifique, qui indique des conditions physico-chimiques variables lors de leur formation.

Bien que l'épisode minéralisateur à 1680 Ma se soit formé à partir de fluides aux propriétés similaires et en même temps que les gisements de type discordance de l'ARUF, les conditions physico-chimiques de formation de la minéralisation uranifère sont différentes entre les deux zones. La composition des chlorites indique un évènement à haute température (>350 °C) à ~1680 Ma dans la zones de Westmoreland. Les générations successives d'uraninites ont une composition chimique (teneurs en éléments mineurs et traces, incluant les Eléments des Terres Rares) différente de celles de l'ARUF. Le métasomatisme typique des gisements de type discordance, à bore et magnésium, marqué par la présence de chlorites et de tourmalines riches en magnésium, ainsi que les minéraux alumino-phosphate-sulfatés sont absents de la zone de Westmoreland. Sur la base des échantillons étudiés, il est donc peu probable que des gisements majeurs se soient formés dans la zone de Westmoreland. Globalement, les données indiquent un type de minéralisation et des processus atypiques pour les gisements dans le bassin de la zone de Westmoreland.

Abstract

The Westmoreland area is located south of the McArthur Basin (Australia) and hosts several uranium (U) deposits and prospects. Previous studies from this area proposed that U mineralisation formed in conditions similar to those known for the unconformity-related U deposits of the Alligator Rivers Uranium Field (ARUF), located north of the same sedimentary basin. Here, a detailed mineralogical, geochemical and geochronological study, in addition to previous studies on different mineralised intervals from the Redtree, Junnagunna and Huarabagoo deposits, allows identification of at least six generations of U oxides. These formed between ca. 1680 and 350 Ma, highlighting protracted mobility of U over 1.3 Ga. Each generation of U oxide is marked by a specific chemical composition, indicating variable physico-chemical conditions for their formation throughout this period.

Although the 1680 Ma mineralising event formed at the same time and with similar mineralising fluids as the unconformity-related U deposits from the ARUF, the physico-chemical conditions however differed between the two zones at that time. The typical Mg- and B-metasomatism of the unconformity-related U deposits in the ARUF are lacking in the Westmoreland area, that is not marked by Mg-rich chlorite (between the clinochlore and Mg-amesite fields), Mg-foitite (tourmaline), and alumino-phosphate-sulphate minerals. Typical bell-shape chondrite-normalized REE patterns of U oxides of the unconformity-related U deposits are also lacking. Moreover, chlorite thermometry indicates significantly higher temperature conditions (>300°C) than in ARUF for the early U stages. On the basis of the studied samples, it is thus unlikely that significant unconformity-related U deposits have formed

in the Westmoreland area. Collectively, the data point towards fairly atypical ore-forming processes for basin-related U deposits in the Westmoreland area.

Keywords

Uranium, Australia, Westmoreland, U-Pb isotopic ages, uraninite REE-patterns, chlorite temperatures

3.1. Introduction

The Westmoreland area (Northern Territory and Queensland, Australia) hosts several uranium deposits and prospects located in the Paleo- to Mesoproterozoic McArthur Basin and related crystalline basement (Ahmad et al., 2013a; International Atomic Energy Agency, 2018a; Polito et al., 2005b). The five discovered deposits (Redtree, Junnagunna, Huarabogoo, Outcamp and Sue), currently classified as Westmoreland-Murphy-type (WM-type) uranium deposits, have an indicated mineral resource totalling ~ 16 000 t U contained within 18.7 million tonnes at an average grade of 0.089% U_3O_8, and an inferred mineral resource totalling ~ 7 000 t U contained within 9.0 million tonnes at an average grade of 0.083% U_3O_8 (Laramide Resources Ltd, 2019). These deposits and related occurrences are part of a set of deposits known in this large intracratonic basin, with several mineralised areas concentrating various types of metals (U, Pb, Zn, and Cu, Ahmad et al. 2013).

The geological processes and physico-chemical conditions for the origin of the different types of uranium deposits found in the McArthur Basin have been studied for decades, but the research efforts have not been equivalent for the different types of deposits and locations. For uranium, the Alligator Rivers Uranium Field (ARUF) to the North hosts the Jabiluka, Ranger, Nabarlek and Koongarra U deposits among others belonging to the unconformity-related deposits. While the processes related to the uranium deposits in the ARUF have been studied extensively (e.g. Wilde and Wall 1987; McKay and Miezitis 2001; Polito et al. 2004; Lally and Bajwah 2006; Skirrow et al. 2016), the uranium deposits from the Westmoreland area have attracted much less attention (Hills and Richards 1976; Fuchs and Schindlmayer 1981; Ahmad and Wygralak 1989 and references herein; Rheinberger et al. 1998; Polito et al. 2005a; Mernagh and Wygralak 2011). One of the main objectives of the previous research investigations (mainly Polito et al., 2005a and Mernagh and Wygralak 2011) was defining if these U deposits and related occurrences could be analogues to the unconformity-related U deposits known at the border of the Northern part of the McArthur Basin, but also in the Athabasca Basin (Canada; Jefferson et al. 2007; Cuney and Kyser 2015). Unambiguously establishing such relationships between the studied mineralisation and the known

unconformity-related U deposits is indeed important because unconformity-related U deposits have the highest grades and tonnages among all the known U deposits worldwide.

The results from these studies indicate that the mineralogy, paragenesis and geochemistry of the Redtree, Junnagunna and Huarabagoo deposits show some similarities with the uranium deposits of the ARUF (Polito et al., 2005b), thus suggesting that the timing and geological processes for the origin of both uranium provinces were rather identical. The fluid inclusions in the Eva Mine and Jackson Pit uranium deposits, yielded NaCl-rich and $CaCl_2$-rich brines and a low-salinity fluid that mixed in varying degrees (Mernagh and Wygralak, 2011), as documented for the unconformity-related U deposits from the ARUF (Ypma and Fuzikawa 1980; Durak et al. 1983; Derome et al. 2003, 2007; Polito et al. 2004, 2005b). These combined results seem to indicate that the first-order parameters and the timing for the formation of both uranium provinces in the McArthur Basin are identical. The main goal of the present work is thus to refine this comparison and establish further correlations.

New geochemical criteria applicable to uranium oxides, based on Rare Earth Elements content, have been recently published which allow the classification of the different types of uranium deposits (Alexandre et al., 2016; Frimmel et al., 2014; Mercadier et al., 2011b). Such criteria have been applied to the uranium deposits from the ARUF, confirming their affinity with the U deposits from the Athabasca Basin (Canada) and thus their classification as unconformity-related U deposits (Mercadier et al., 2011b). Application of such geochemical markers are lacking for the U deposits of the Westmoreland area. In this work, we complement the existing data on ore mineralogy, geochemistry and age dating for different mineralised intercepts of three Westmoreland-Murphy-type (WM-type) uranium deposits: Redtree, Junnagunna and Huarabagoo. The final objective of this approach focused on the mineralised intercepts is to provide new constraints on the geological model proposed for the formation of the U deposits and occurrences of the Westmoreland area. In this respect, a specific focus was put on the characterisation of potential multiple fluid events, which have affected the area and favoured U mobility through time and space. The new results will be compared with previously published data and models for the same area, for the unconformity-related deposits of the ARUF, and for U deposits in other Proterozoic basins.

3.2. Geological settings

The Westmoreland area is adjacent to the Queensland-NT border on the south-eastern margin of the southern McArthur Basin (Figure 3- 1). The oldest rocks in the Westmoreland region are Paleoproterozoic metasedimentary, volcanic and felsic rocks from the Murphy Province which is the basement to the McArthur Basin. The Murphy Metamorphics (1855–

1830 Ma) are essentially a succession of greenschist-facies metamorphosed shales and greywackes (Ahmad et al., 2013a). Uranium–lead data on detrital zircon suggest a maximum depositional age of 1853 ±4 Ma (Hollis et al., 2009). The Nicholson Granite Complex (Figure 3-2) can be divided into two broad suites based on chemical and mineralogical composition, one hornblende- and/or biotite bearing granite, quartz monzonite and granodiorite and one biotite- and/or muscovite bearing monzonite, granite and alkali granite. Two samples of the Nicholson Granite Complex have yielded SHRIMP U-Pb zircon ages of 1856 ±3 and 1845 ± 3 Ma (Page et al., 2000). The Cliffdale Volcanics are a succession of more than 4km of rhyolite, dacitic lavas, ignimbrites and intrusions that unconformably overlie the Murphy Metamorphics (Ahmad et al., 2013a). SHRIMP U-Pb dating of zircons has yielded an age of 1851 ± 3 Ma (Page et al., 2000).

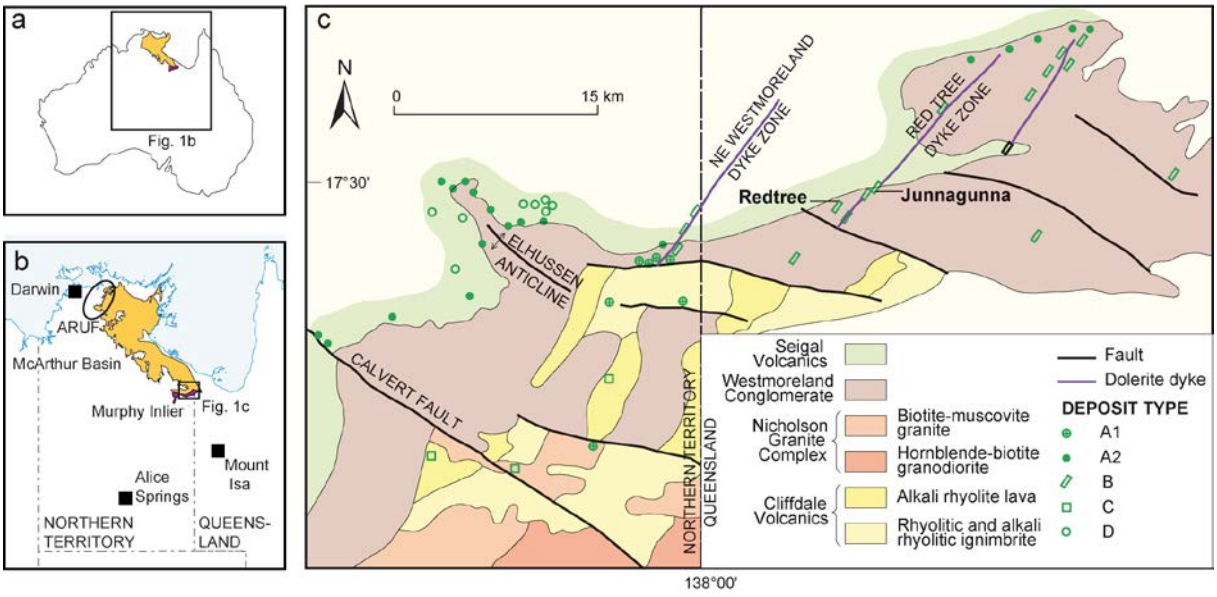

Figure 3-1: *Schematic geological map of the study area, Northern Territory and Queensland, Australia. (**a**) Location of the McArthur Basin and Murphy Inlier in Australia; (**b**) Zoom on the previous map. The Alligator Rivers Uranium Field (ARUF) is also indicated; (**c**) Simplified geological map around the studied deposits. Type A deposits lie at the contact between the Westmoreland Conglomerate and the Cliffdale or Seigal Volcanics (in sub-type A1 occurrences, the contact between the Cliffdale Volcanics and Westmoreland Conglomerate is a reverse fault. In sub-type A2 deposits, the contact between the Westmoreland Conglomerate and Seigal Volcanics is conformable). In type B deposits, mineralisation occurs as sub-horizontal and sub-vertical lenses in the Westmoreland Conglomerate. Type C deposits are hosted by intensely altered Cliffdale Volcanics; Type D occurrences are related to fractures in the lower part of the Seigal Volcanics. After Ahmad et al. (2013).*

The Paleo–Mesoproterozoic McArthur Basin is an up to 10 km thick sequence of mostly unmetamorphosed sedimentary and volcanic rocks that were deposited between 1815 and 1492 Ma that unconformably overlies the Murphy Province (Ahmad et al., 2013a). The basal unit of the McArthur Basin, the Westmoreland Conglomerate (Figure 3-2), is composed mainly of fluvial sandstones and conglomerates and is up to 1,800 m thick. It has been subdivided into five stratigraphic units, each unit representing a major fining-upward cycle of

sedimentation (Ahmad and Wygralak, 1989). Each unit comprises proximal fluvial deposits typical of debris flows, alluvial fans, and braided river systems that are overlain by medium- to coarse-grained, well-sorted sandstones. Breaks in sedimentation are indicated by angular unconformities or disconformities, with each new cycle of pebble or boulder conglomerate commonly defining the beginning of a new unit. Cobbles and coarse sand grains within the basal conglomerate are dominated by reworked quartz veins, chert, and clasts of felsic to mafic volcanic rocks that were likely derived from the Murphy tectonic ridge or similar basement rocks that once existed to the North (Laramide Resources Ltd, 2016). This detrital material and lithic clasts is considered to be a likely source for the uranium (Laramide Resources Ltd, 2016). Most of the uranium mineralisation is hosted within the upper unit (Ptw4), which is a 80–90 m thick porous, coarse-grained sandstone, conglomeratic in part (International Atomic Energy Agency, 2018a). U-Pb dating of detrital zircon from the Westmoreland Conglomerate has returned maximum depositional ages of 1865 ± 7 Ma for the lower section and 1843 ± 4 Ma for the upper section (Ahmad and Wygralak, 1990). The Westmoreland Conglomerate is conformably overlain by the mafic Seigal Volcanics (basaltic lavas), followed by dolomite, sandstone, mafic and felsic volcanic rocks of the upper part of the Tawallah Group. Its deposition age is estimated at 1780 Ma by stratigraphic correlation.

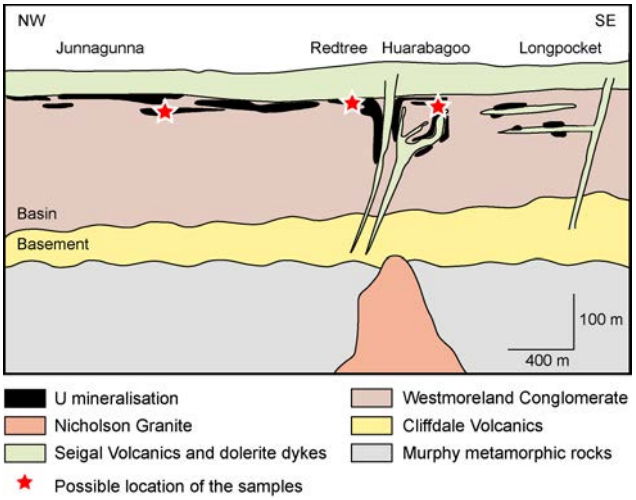

Figure 3-2: *Cross-sections showing the position of the Junnagunna, Redtree, Huarabagoo and Longpocket deposits in the stratigraphic sequence of the McArthur Basin, Australia (compilation after Fuchs and Schindlmayer 1981; Schindlmayr and Beerbaum 1986; International Atomic Energy Agency 2018a, b) and the approximate locations of the samples.*

Dolerite dykes and minor sills, which may have been feeders of the lava flows, intrude along NE trending fault and fracture zones that intersect the Westmoreland Conglomerate (International Atomic Energy Agency, 2018b). Uranium mineralisation is associated with three major northeast-trending lineaments (NE Westmoreland, Redtree and El Nashfa dyke zones), the Redtree dyke zone extending over a strike of 20 km (Ahmad et al., 2013a).

The Westmoreland region was first prospected in the 1890s for Pb-Zn, then for Cu, and finally uraninite has been mined in the Peters Creek Volcanics which overlie the Westmoreland Conglomerate, 20 to 30 km west of Redtree (Laramide Resources Ltd, 2016). The Redtree, Junnagunna and Huarabagoo uranium deposits are hosted largely within the shallow dipping Westmoreland Conglomerate near the unconformity with the Murphy Inlier and lie along the Redtree dyke zone (Figure 3-1). The uranium-rich zones can be oriented parallel to the volcanics or sills, discordant at the contact with mafic dykes, within fractures cross-cutting altered mafic volcanics within fractures or along shear zones in altered felsic volcanics. The studied deposit belong to “mafic dykes/sills in Proterozoic sandstone” (International Atomic Energy Agency, 2018b) or “Westmoreland-Murphy type” (Lally and Bajwah, 2006) categories.

The bulk of the Westmoreland resource base (~50%) is located in the Redtree deposit. It flanks the Redtree dyke zone immediately north of the northwest-trending Namalangi fault and is characterised by a mix of horizontal and vertical lenses of continuous mineralisation in distinctly coarse pebble conglomerates with grades ranging from 0.15% to >2% U_3O_8. Mineralisation is generally shallow, within 10m of surface and is associated with chlorite/hematite alteration. The Redtree dyke (20m-30m wide) broadly extends for 7 km from Redtree to Junnagunna and has used the same structures as the uranium mineralisation, but does not appear to be related, although spatially associated (Laramide Resources Ltd, 2019). The mineralisation thickens and steepens near the dyke, where it is 30–40 m thick (International Atomic Energy Agency, 2018a). The indicated resource is 12.86 Mt of ore at an average grade of 0.09% U_3O_8 and an inferred resource of 4.47 Mt at an average grade of 0.07% U_30_8 (Laramide Resources Ltd, 2016).

The Junnagunna uranium deposit occurs at a fault intersection west of the Redtree dyke zone and south of the northwest trending Cliffdale fault. Mineralisation is generally flat lying on both sides of the Redtree dyke and ranges from 0.5m to 20m in thickness beneath the Seigal-Westmoreland contact. The deposit is covered by alluvium/colluvium clays, sand and weathered Seigal Volcanics (Laramide Resources Ltd, 2019). The indicated resource is 4.36 Mt ore with an average grade of 0.08% U_30_8 and an inferred resource of 2.15 Mt with an average grade of 0.8% U_30_8 (Laramide Resources Ltd, 2016).

The Huarabagoo deposit is about 3 km NE of Redtree along the Redtree dyke zone and straddles the contact of the Seigal Volcanics with the Westmoreland Conglomerate. Mineralisation occurs in 20m thick lenses, which extend to 100- 200 m length and to a depth of 80m (Laramide Resources Ltd, 2019). It outcrops at the southern end and is concealed to the north under 2 to 3 m of sandy alluvium and 5 to 8 m of weathered basalt of the Seigal Volcanics (Laramide Resources Ltd, 2016). The deposit comprises a 3 km zone of vertical

mineralisation associated with a complex dyke geometry with vertical and horizontal branches between the two principal dykes. The strongest mineralisation was found to be associated with chlorite/hematite altered coarse pebbly sandstones similar to Redtree. Most of the mineralization is hosted within the Westmoreland Conglomerate adjacent to the dykes, and the remainder is hosted in the dykes (International Atomic Energy Agency, 2018b). The indicated resource is 1.46 Mt ore at an average grade of 0.08% U_30_8 and an inferred resource of 2.41 Mt at an average grade of 0.11% U308 (Laramide Resources Ltd, 2016).

3.3. Sampling and methodology

A multi-method approach was conducted on different mineral types (uranium oxides, chlorite and apatite), from the Junnagunna, Redtree and Huarabagoo deposits, selected on the basis of a detailed paragenetic study. A specific focus was the selection of samples within the mineralised zones of both deposits, all located within the Westmoreland Conglomerate (Figure 3-2). This selection was based on the paragenesis for the U deposits of the Westmoreland area that was established by Polito et al. (2005a).

Five drill holes were sampled : JDD08-003, WDD07-2, WDD9-128, WDD10-151 and WDD08-106, based on their high U grade: 0.16% U_3O_8 in WDD10-151 between 22 and 31m , 0.21% U_3O_8 in JDD08-003 from 71 to 76m, 0.25% U_3O_8 in WDD07-02 from 48 to 59m and 0.2% from 70 to 75m and 0.31% in WDD08-106 from 8 to 16m (Laramide Resources Ltd, 2016; Vigar and Jones, 2009). The following samples were studied: JDD08-003 at 74.4m, WDD07-2 at 51.7, 55.9 and 73.5m, WDD9-128 at 53.3 and 92.3m, WDD10-151 at 29.4m and WDD08-106 at 10.6m. Selected thin sections were studied by optical and scanning electron microscope (SEM) to propose detailed paragenetic sequences, and the chemical composition for the major elements of chlorite and uranium oxide was determined by Electron Probe Micro Analyses (EPMA). The isotopic U-Pb and Pb/Pb ages of uranium oxide and apatite were measured by Secondary Ion Mass Spectrometry (SIMS) and the concentrations of minor and trace elements in uranium oxides was quantified by Laser Ablation-Inductively Coupled Plasma-Mass Spectrometer (LA-ICP-MS). The locations of the analyses are presented in Supplementary Figures 3-1 to 3-8.

3.3.1. Petrography

Optical microscopy was carried out on thin sections using a numerical microscope VHX-200F with a high resolution objective VH-Z500W to cover the whole sections and a Zeiss Axio Scope A1 microscope for detailed petrography (GeoRessources Lab - Vandœuvre-lès-Nancy, France). SEM images and spectra were obtained using BackScattered Electron detector (BSE)

Tescan Vega3LM with a conventional tungsten source at SCMEM (GeoRessources Lab - Vandœuvre-lès-Nancy, France). The analytical conditions were an acceleration voltage of 15 kV and beam current of around 0.1–1 nA.

3.3.2. Major elements composition of uraninite and chlorite

The quantitative measurements of major elements in uraninite and related chlorite were performed using a CAMECA SX-100 Electron Probe MicroAnalyser (EPMA) at SCMEM with a spot size of 1µm². For uraninite, the calibration was based on natural and synthetic oxides and/or alloys (V for V, andradite for Ca, hematite for Fe, albite for Si, apatite for P, zircon for Zr, UO_2 for U, $MnTiO_3$ for Mn and Ti, Al_2O_3 for Al, ThO_2 for Th, PbS for Pb and YPO_4 for Y). The analytical conditions were 20 nA current, accelerating voltage of 20 kV and counting time of 10 s. Under these conditions, the analysed elements and their limits of detection were the following: Si (534 ppm), P (632 ppm), Ca (763 ppm), U (3879 ppm), Ti (417 ppm), V (1240 ppm), Mn (1545 ppm), Fe (1519 ppm), Zr (3046 ppm), Y (1660 ppm), Pb (1940 ppm), Th (4315 ppm) and Al (517 ppm). For chlorite, the calibration was also based on natural and synthetic oxides and/or alloys (V for V, andradite for Ca, orthose for K, hematite for Fe, albite for Si and Na, olivine for Mg, $MnTiO_3$ for Mn and Ti, Al_2O_3 for Al, and Cr_2O_3 for Cr). The analytical conditions were 12 nA current, accelerating voltage of 15 kV and counting time of 10 s. With these conditions, the analysed elements and their limits of detection were the following: Na (661 ppm), Si (485 ppm), Mg (483 ppm), Al (468 ppm), K (367 ppm), Ca (671 ppm), Ti (373 ppm), Mn (1597 ppm), Fe (2048 ppm), V (1805 ppm) and Cr (900 ppm).

3.3.3. U-Pb isotopic ages of uranium oxides and apatite

The U-Pb and Pb/Pb analyses were carried out at the Centre de Recherches Pétrographiques et Géochimiques (CRPG, Nancy, France) with the Cameca IMS 1280 HR2 and the Hyperion RF O^- source for apatite and with the Cameca IMS 1270 E7 and the duoplasmatron O^- source for uranium oxide. The secondary positive ions were measured with a mass resolution (M/ΔM) of 6000 to separate peaks of interest from isobaric interferences, by ion counting in mono-collection mode on the axial electron multiplier.

For apatite, the primary O^- beam was set at an intensity of 30nA and the spot size was 10 µm. Each measurement consists in a pre-sputtering of 120s, secondary beam and mass centring and 16 cycles of measurement of masses: 178.5, $^{40}Ca^{44}Ca$ $^{31}P^{16}0_4$, ^{204}Pb, ^{206}Pb, ^{207}Pb, ^{208}Pb, ^{238}U, $^{232}Th^{16}O$ and $^{238}U^{16}O$ with counting times of 4 seconds per peak for $^{232}Th^{16}O$ and $^{238}U^{16}O$, 6 seconds per peak for ^{238}U, 8 second per peak for ^{208}Pb and 18 seconds per peak for ^{204}Pb, ^{206}Pb and ^{207}Pb. An energy window of 30 eV was used with no energy offset. $^{40}Ca^{44}Ca$

$^{31}P^{16}0_4$was used as a reference mass to calculate the U and Pb contents. The Madagascar apatite (Chew et al., 2011) was used as standard to determine the relative ionization yield of U and Pb, with the Pb/U ratio expressed as a function of UO/U ratio. The external error on the $^{206}Pb/^{238}U$ ratios, measured on the Madagascar standard (dated at 473.46 Ma) for each session, is propagated on the final error of each sample measurements. With the measurement of the ^{204}Pb isotope it is possible to calculate $^{206}Pb/^{238}U$ corrected ages using the measured $^{204}Pb/^{206}Pb$ ratios and the continental common lead compositions from Stacey and Kramers (1975) at the age of crystallisation. This allows us to calculate probability density plots and weighted average plots using $^{206}Pb/^{238}U$ corrected ages, and compare them to the common lead uncorrected Tera-Wasserburg intercept ages (Tera and Wasserburg, 1972). All data were treated using ISOPLOT software (Ludwig, 2007).

For uranium oxides, the primary O^- beam was set at an intensity of ~5 nA and focussed to a spot of ~15 µm in diameter, in Gaussian mode with a raster of 10µm. The energy window was opened at 30 eV, and centred on the low energy side, 5 eV before maximum value. An offset of -50eV was applied during analyses in order to avoid matrix effects due to mixes between uraninite and silicate in natural samples. Ions were measured by peak jumping in monocollection mode using the axial Faraday cup (FC) for ^{238}U and ^{238}UO and the axial electron multiplier (EM) for ^{204}Pb, ^{206}Pb, ^{207}Pb, ^{208}Pb and ^{232}ThO. Each analysis consisted of 8 successive cycles. Each cycle began with measurement of the mass 203.5 and 203.6 for backgrounds of the FC and the EM. The counting time was 4 s for 203.5, 203.6, ^{208}Pb and ^{238}UO; 3 s for ^{248}ThO; 6 s for ^{206}Pb and ^{238}U, 10 s ^{204}Pb and 20 s for ^{207}Pb (waiting time of 1 s). The standard used was a uraninite from Zambia (Holliger, 1988), which has a given concordant age at 540 ± 4 Ma (Cathelineau et al., 1990). Ages and error correlations were calculated using ISOPLOT (Ludwig, 2007). Uncertainties in the ages are reported at the 2σ level. Common Pb corrections were based on the measured ^{204}Pb content using the Pb isotope composition calculated from Stacey and Kramers (1975) at the supposed age of the uranium oxide crystallisation.

3.3.4. Minor and trace element concentrations in uranium oxides

Minor and trace elements in uranium oxides, including Rare Earth Elements (REEs), were measured with a Laser Ablation-Inductively Coupled Plasma-Mass Spectrometer (LA-ICP-MS) at the GeoRessources laboratory (Nancy, France). UO_2 minerals were ablated using a 193 nm Geolas Q Plus system with an aperture-imaged Complex 103 ArF excimer laser (Microlas, Göttingen, Germany) equipped with beam homogenisation optics. The laser spot sizes were 16 and 24 µm and the fluence was ~5 J/cm^2 with a repetition rate of 5 Hz. Ablated particulate

material was analysed by an Agilent 7500c Quadrupole ICP-MS. The transport gas was a mixture of He and Ar, at typical flow rates of 0.5 and 0.8 $l.min^{-1}$ respectively. All data were acquired in raw counts using time resolved mode. Data reduction was done using Iolite software (Paton et al., 2011). Absolute concentrations and limits of detection were obtained from the equation developed by Longerich et al. (1996). The calibration material (external standard) was a SRM NIST 610 glass standard and SRM NIST 612 glass was analysed to control the precision and accuracy of the measurements (concentrations from Jochum et al. 2011). The methodology used is modified from Lach et al. (2013). The matrix effects when quantifying the REEs in a uraninite using SRM NIST 612 are limited (< 15%; Lach et al. 2013) and are considered to be in the same range for the other measured minor and trace elements in the present study, as previously proposed by Frimmel et al. (2014) and Alexandre et al. (2016). A series of 37 elements were analysed for each experiment: ^{11}B, ^{47}Ti, ^{51}V, ^{53}Cr, ^{55}Mn, ^{59}Co, ^{60}Ni, ^{63}Cu, ^{66}Zn, ^{69}Ga, ^{75}As, ^{88}Sr, ^{89}Y, ^{90}Zr, ^{93}Nb, ^{95}Mo, ^{121}Sb, ^{137}Ba, the 14 Rare Earth Elements, ^{181}Ta, ^{182}W, ^{209}Bi, ^{232}Th and ^{238}U. ^{238} U was the internal standard measured by EPMA and the used concentration was adjusted depending of the analysed sample: 77.05 wt% U for WDD07-2 55.9mA, 76.77 for WDD07-2 55.9mB, 75.58 for WDD10-151 29.4m, 75.16 for WDD08-106 10.6m, 74.93 for WDD07-2 73.5mB and 72.10 for JDD08-003 74.4mB. The analytical precision is calculated for all analysed elements using standard deviation of recorded intensity and is better than ± 20%. The Limit of detection (LOD) varies for each element and each analysis as a function of signal intensity and was calculated for each ablation from signal intensities using the 3σ criterion (Longerich et al., 1996). The LODs are given when the calculated values for a given element are below these values. Values used to calculated ΣLREE/ΣHLREE are chondrite-normalised with chondrite values from Anders and Grevesse (1989) and the following elements were used for calculation: ΣREE=La+Ce+Pr+Nd+Sm+Eu+Tb+Dy+Ho+Er+Tm+Lu ;

$(\Sigma LREE)_N = La_N + Ce_N + Pr_N + Nd_N + Sm_N$;

$(\Sigma HREE)_N = Er_N + Tm_N + Lu_N$.

3.4. Results

3.4.1. Paragenesis

The paragenesis presented hereafter is based only on the observations from the samples for this study, and no data from the literature is included in this “Results” section. A combined paragenesis from this study and the data from Polito et al. (2005a) is presented in Figure 3-3 and discussed in the “Discussion” section. In the mineralised intercepts, the early diagenesis

is represented by hematite crystallisation and quartz overgrowth over detrital quartz (Q0) grains (Figure 3-4a). This was followed by an episode of dissolution of detrital quartz (Q^-) and cementation (Q1) in relation to peak diagenesis (Figure 3-4b). Chlorite in rosette-shape (C1, Figure 3-4c), rutile (R1 not observed previously in the literature, Figure 3-4d), clays minerals (dickite D1 and illite I1) and apatite (Ap; mostly 10–20 µm in width, not observed previously in the literature, Figure 3-5a) form during this stage. Chlorite C1 is altered into clay minerals (I1; Figure 3-4e). A second generation of quartz (Q2, Figure 3-4f) occurs at the end of this stage. A second generation of uranium oxide U2 crystallises in contact with apatite (Ap) in voids produced by quartz dissolution (Figure 3-5a). The U2 postdates apatite as small fractures within apatite grains are filled with U2 and because U2 surrounds the apatite grains. Veins containing quartz Q3, uraninite U4, pyrite Py3 and chalcopyrite (ccp) crosscut the sandstone (Figure 3-5e) and they are thought to be coeval with uraninite U4 emplacing in voids (Figure 3-5c) based on dating results. A fifth (U5) and sixth (U6) generations of uranium oxide occur

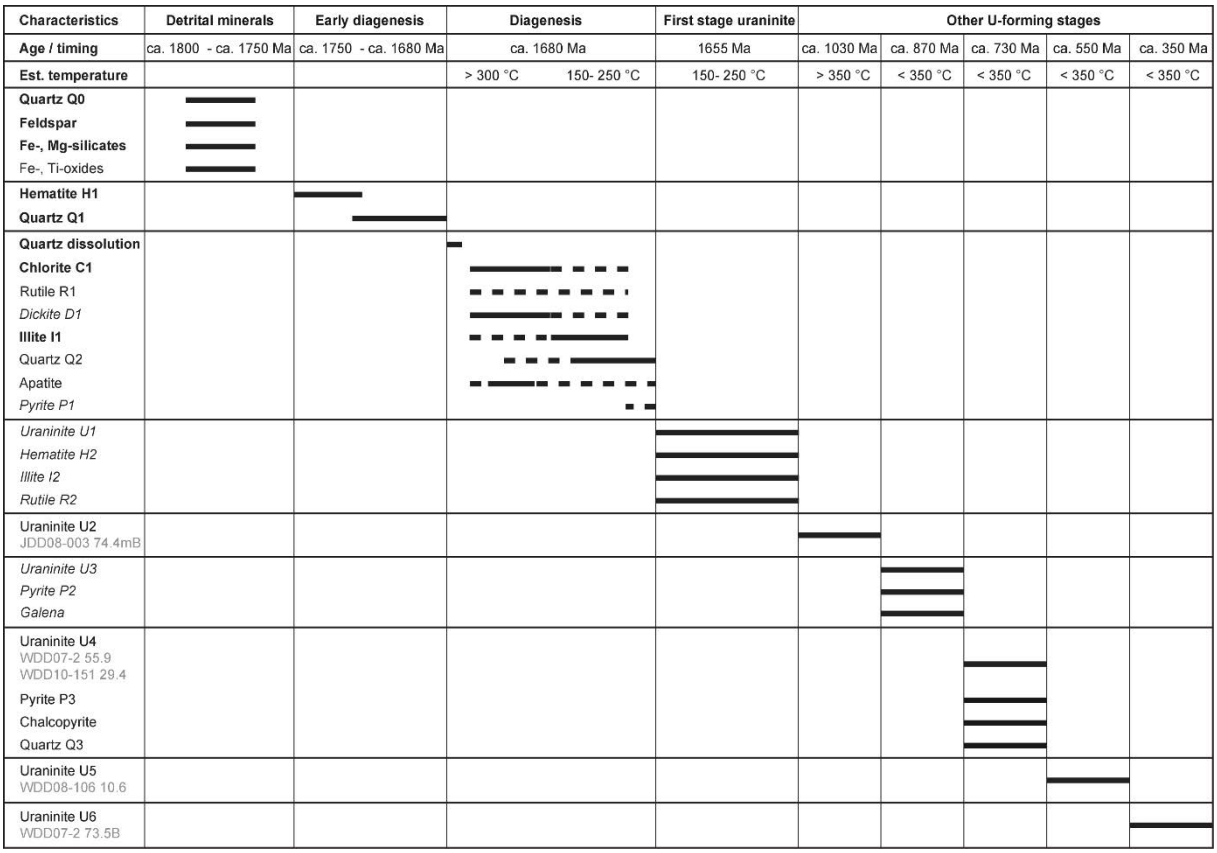

Figure 3-3: *Paragenesis of the Redtree and Junnagunna deposits (Polito et al. 2005a and this study). Ages are based on zircon U-Pb ages (Page et al., 2000) for the detrital minerals , on $^{207}Pb/^{204}Pb$ and $^{40}Ar/^{39}Ar$ ages from Polito et al. (2005a) and on U-Pb ages on apatite and uraninite from this study. Italic: data from the paragenesis presented by Polito et al. (2005a); regular: mineral sequence observed in this study; bold: mineral sequence observed in this study and by Polito et al. (2005a). The temperatures estimates are from chlorite and illite thermometry (Polito et al., 2005a and this study) and from the ∑REE (this study).*

(Figure 3-5g), filling voids. The mineral assemblage is similar for three last uranium generations, but the ages obtained state for the different generations.

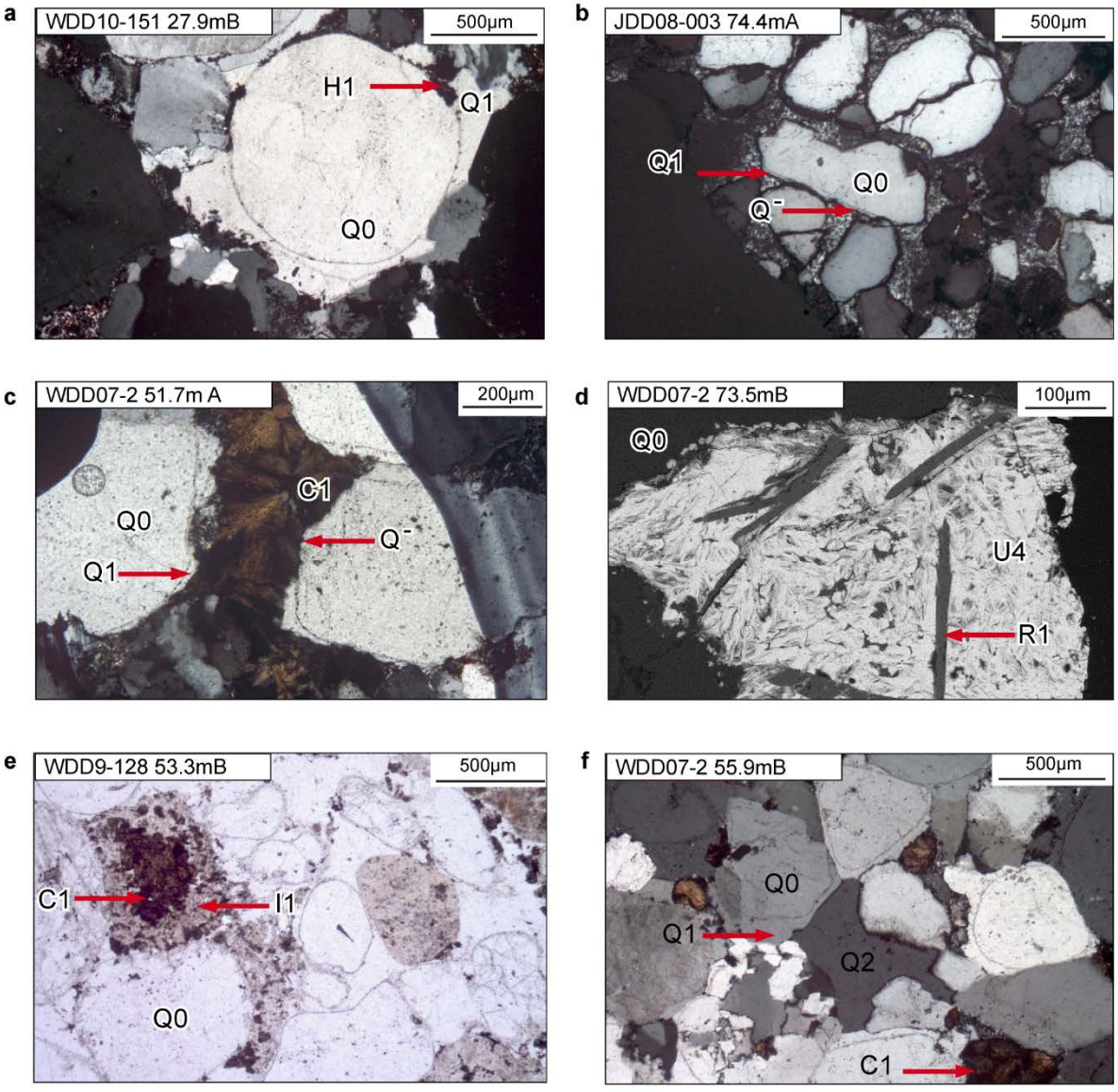

***Figure 3-4**: Diagenetic sequence for mineralized intercepts of the Redtree, Junnagunna and Huarabagoo U deposits (Westmoreland area, Australia). **a** Q0 detrital quartz grains coated by hematite (H1), and quartz overgrowths Q1. Optical microscopy, sample WDD10-151 27,9mB. **b** Quartz partial dissolution (Q^-) after Q1. Optical microscopy, sample JDD08-003 74,4mA. **c** Rosette of chlorite C1 after partial dissolution of Q0 and Q1. Optical microscopy, sample WDD07-2 51.7mA. **d** Diagenetic rutile R1 in a matrix formed by uraninite U4. Backscattered electron image, sample WDD07-2 73.5mB. **e** Illite as alteration on chlorite C1. Optical microscopy, sample WDD9-128 53.3mB. **f** Quartz Q2 after quartz Q1. Optical microscopy, sample WDD07-2 55.9mB.*

.

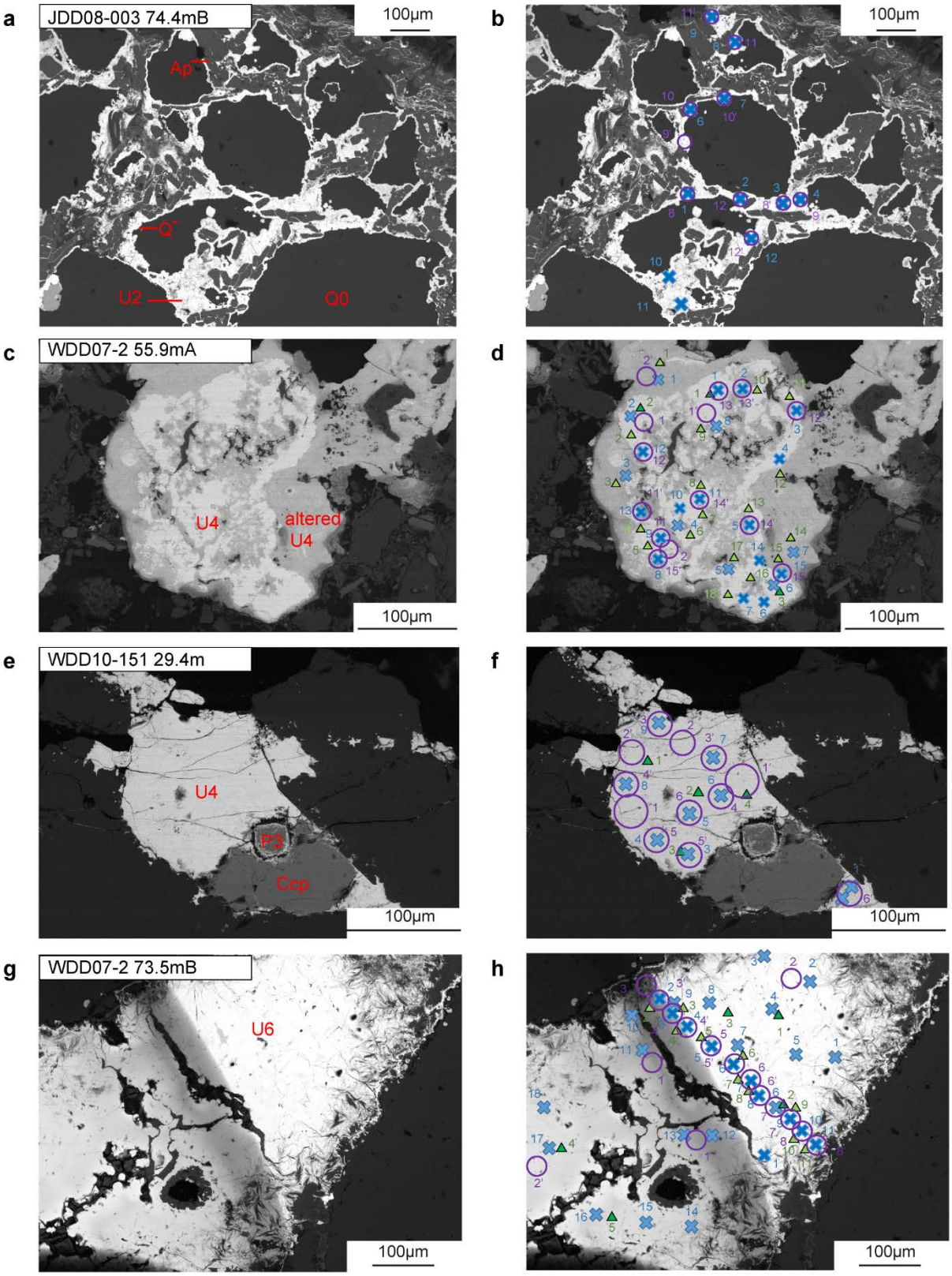

Figure 3-5: *Backscattered electron image images of uraninite mineral assemblages from the Redtree, Junnagunna and Huarabagoo U deposits (Westmoreland area, Australia).* ***a*** *Uraninite U2 as matrix around apatite grains (Ap), sample JDD08-003 74.4mB.* ***b*** *Location of the analyses: purple circle = LA-ICP-MS; blue cross = SIMS.* ***c*** *uraninite U4 with a altered zones, sample WDD07-2 55.9mA.* ***d*** *Location of the analyses: purple circle = LA-ICP-MS; blue cross = SIMS, dark green triangle = EPMA.* ***e*** *Uraninite U4 in vein associated with chalcopyrite and pyrite, sample WDD10-151 29.4m.* ***f*** *Location of*

the analyses: purple circle = LA-ICP-MS; blue cross = SIMS, dark green triangle = EPMA. ***g*** *Uraninite U6 associated with clay minerals sample WDD07-2 73.5mB.* ***h*** *Location of the analyses: purple circle = LA-ICP-MS; blue cross = SIMS, dark green triangle = EPMA.*

3.4.2. Chemical composition of the uranium oxides

The chemical composition of the different uranium oxides are reported in Supplementary Table 3-1 for the major elements and in Supplementary Table 3-2 for minor and trace elements. Figure 3-6 shows the chemical maps obtained by EPMA. On these maps, some elements concentration measured during punctual EPMA analyses are reported as scale.

Major elements

The U contents of the different generation of uranium oxides range from 59.3 to 88.6 wt%. The thorium content for all the uranium oxides is low with concentrations below the detection limits (0.1 wt% Th). The different uranium oxides are characterised by variable content in lead, either between samples or within an individual sample (Figure 3-6 and 3-7a). The maximum Pb content is 9.16 wt% PbO measured for the freshest zones of WDD07-2 55.9mA and B (U4) while the most altered zones of this sample have Pb content < 1 wt% PbO. In the other samples, the lead contents vary between 2.62 wt% PbO (freshest zones) and < 1940 ppm (most altered zones) for JDD08-003 74.4mB (U2), between 1.94 (freshest zones) and 1.01 (most altered zones) wt% PbO for WDD10-151 29.4m (U4), between 3.78 and 2.09 wt% PbO for WDD08-106 10.6m (U5) and between < 1940 ppm (most altered zones) and 3.56 wt% PbO (freshest zones) for WDD07-2 73.5mB (U6). The samples WDD10-151 29.4m (U4) and WDD08-106 10.6m (U5) have the most homogeneous Pb contents and can be considered as the least altered. The titanium content is below the detection limit (417 ppm Ti) except for samples JDD08-003 74.4mB (U2) with concentrations up to 1.39 wt% TiO_2, WDD07-2 73.5mB (U6) up to 1.25 wt% TiO_2 and WDD07-2 55.9mA and B (U4) up to 2.6 wt% TiO_2. The phosphorous content is lower than 2 wt% P_2O_5 in sample WDD07-2 73.5mB (U6), but can reach 6.93 wt% P_2O_5 in zones where U concentration are low for samples WDD07-2 55.9mA and B (U4). The calcium and silica contents are also highly variable, ranging from 0.98 to 4.16 wt% CaO with the highest values found in samples WDD07-2 55.9mA and B (U4) and JDD08-003 74.4mB (U2), and from < LOD (= 500 ppm Si) to 13.11 wt% SiO_2 in zones with low U concentrations. The Si content is higher than the Ca content for all the samples except WDD08-106 10.6m (U5). The alteration for samples WDD07-2 55.9m A and B (U4) and WDD07-2 73.5mB (U6) are marked by a loss in lead compensated by a gain in Si, Ca, Fe and P (Figure 3-7a), phenomenon which is not observed for the other samples.

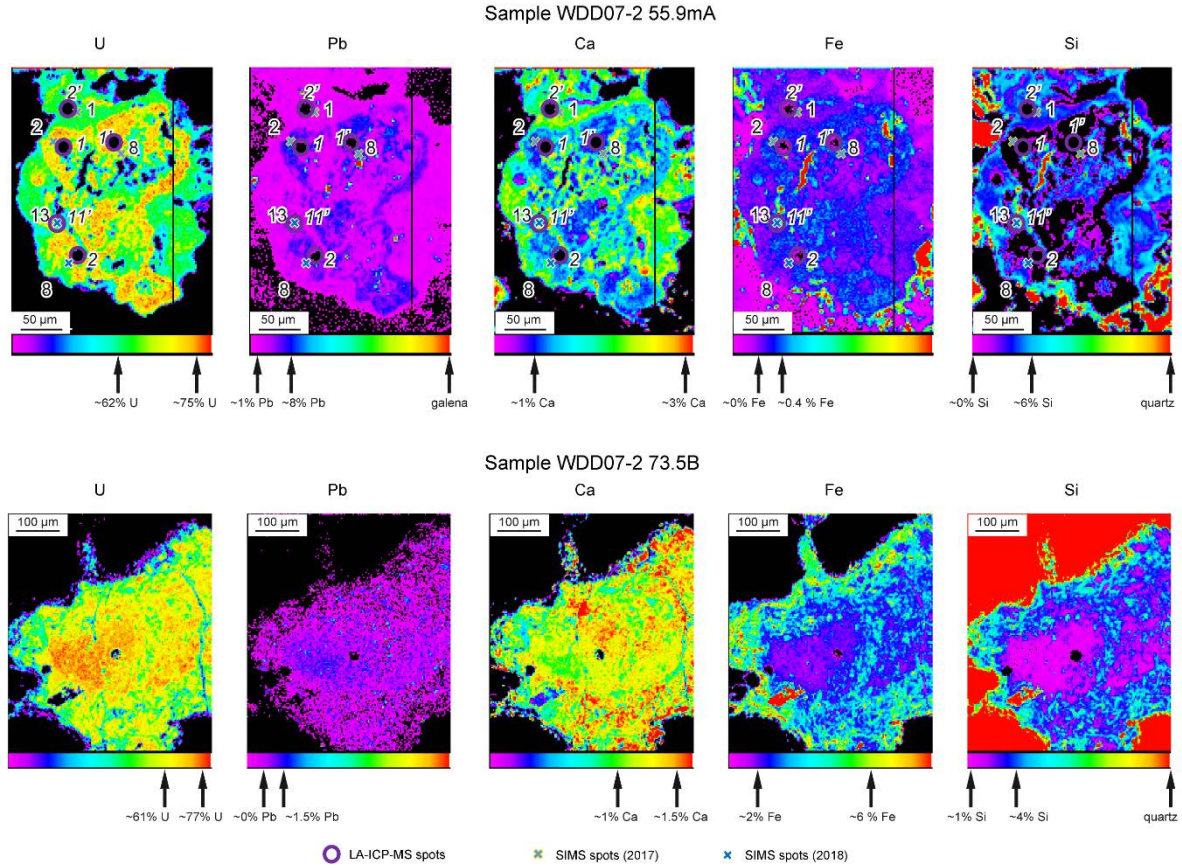

Figure 3-6: *EPMA Maps of distribution of U, Pb, Ca, Fe and Si in uraninite for two samples for samples WDD07-2 55.9mA (top) and WDD07-2 73.5B bottom (Westmoreland area, Australia). The U- and Pb-rich zones correlate with Ca- and Si-poor zones. The element concentration values (in wt%) are estimated from punctual EPMA analyses.*

Minor and trace elements

Among all the minor and trace elements measured by LA-ICP-MS, only 8 have contents below the limit of detection (LOD) for some of the analyses, with maximum LOD value calculated for each element considering all samples and all analyses of 29 ppm for Bi, 74 ppm for Cr, 4.3 ppm for Co, 620 ppm for Ni, 49 ppm for Cu, 23 ppm for Zn, 0.87 ppm for Ta and 0.6 ppm for Bi. When higher than LOD, the minor and trace elements content differs between the samples, with B ranging from 5.2 to 1090 ppm, Ti from 15.5 to 18 850 ppm, V from 469 to 16 510 ppm, Cr from 2.7 to 268 ppm, Mn from 194 to 5540 ppm, Co from 0.75 to 69 400 ppm, Ni from 45 to 23 800 ppm, Cu from 1.61 to 34 700, Zn from 0.12 to 86 ppm, Ga from 0.87 to 393 ppm, Sr from 0.4 to 830 ppm, Y from 36 to 20 750 ppm, Zr from 1.4 to 8680 ppm, Mo from 2 to 1322 ppm, Sb from 90 to 2280 ppm, Ta from 0.03 to 15.25, Bi from 0.1 to 504 ppm and Th from 0.05 to 535 ppm. The highest values measured for Ni and Co could correspond to micro inclusions within the analysed uraninites. The diagrams comparing the contents in As, Nb, W, Ba and V have been chosen because they demonstrate that the different uraninite

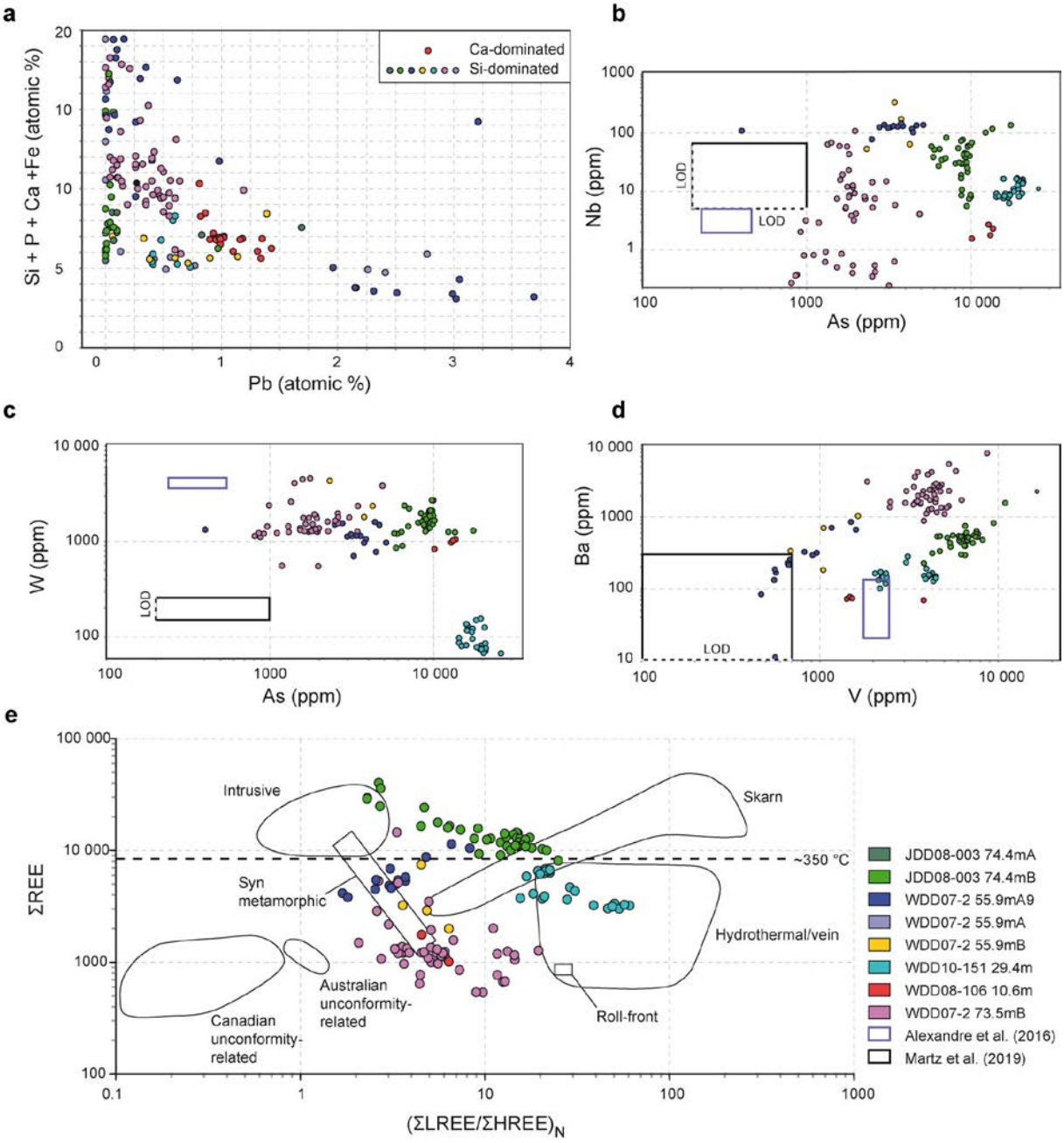

Figure 3-7: *Chemical compositions of the different uraninite generations from the Redtree, Junnagunna and Huarabagoo U deposits (Westmoreland area, Australia).* ***a*** *Pb vs Si + Ca + Fe.* ***b*** *Binary diagram of As vs Nb (in ppm).* ***c*** *Binary diagram of As vs W (in ppm).* ***d*** *Binary diagram of V vs Ba (in ppm).* ***e*** *Rare Earth Element abundance (ΣREE) vs. REE fractionation ($(\Sigma LREE/\Sigma HREE)_N$) from this study and from Mercadier et al. (2011b); Alexandre et al. (2016) and Martz et al. (2019). ΣREE and $(\Sigma LREE/\Sigma HREE)_N$ values are shown in Supplementary Table 3-2. Chondrite values are from Anders and Grevesse (1989).*

generations are chemically distinct. As content are low in sample for WDD07-2 73.5mB (U6, 807-4870 ppm), ranges between 2490 and 5130 ppm for WDD07-2 55.9mA (U4), and the highest values are obtained in sample JDD08-003 74.4mB (U2, 5750-17590 ppm), WDD10-151 29.4m (U4, 14300 and 25800 ppm) and WDD08-106 10.6m (U5, 10120-13130 ppm, Figure 3-7b and Supplementary Table 3-2). Nb content ranges between 1.56 and 2.7 ppm for

WDD08-106 10.6m (U5), between 0.24 and 108.8 ppm for WDD07-2 73.5mB (U6), between 6.3 and 16.9 ppm for WDD10-151 29.4m (U4), between 5.6 and 137 ppm for JDD08-003 74.4mB (U2), and between 78.2 and 147.8 ppm for WDD07-2 55.9mA (U4). W content ranges between 67.3 and 156.6 ppm for WDD10-151 29.4m (U4 in veins) and between 551 and 8350 ppm for the other samples. Ba content ranges between 69.4 and 77.6 ppm for WDD08-106 10.6m (U5), between 101 and 283 ppm for WDD10-151 29.4m (U4), between 227 and 2280 ppm for JDD08-003 74.4mB (U2), between 32.6 and 856 ppm for WDD07-2 55.9mA (U4), and between 584 and 7780 ppm for WDD07-2 73.5mB (U6). V content ranges between 469 and 1637 ppm for WDD07-2 55.9mA (U4), and between 1418 and 16510 ppm for WDD07-2 73.5mB (U6), JDD08-003 74.4mB (U2), WDD10-151 29.4m (U4) and WDD08-106 10.6m (U5).

Rare Earth Elements

The REE spectra of the uranium oxides from the different samples display variable patterns, but are all characterised by a relatively high concentrations in REEs (between 537 and 40169 ppm ∑REE, Figure 3-7e) and an enrichment in LREE and MREE compared to HREE. The REE patterns are globally constant between zones of uranium oxides for a considered sample, except for samples JDD08-003 74.4mB and WDD07-2 55.9mA and B (Figure 3-8). The sample JDD08-003 74.4mB (U2) is marked by a variation of MREE and HREE (1709 to 42014 ppm Gd and 154 to 6778 ppm Lu for example), whereas sample WDD07-2 55.9m A and B (U4) is marked by a variation for LREE (19 to 2493 ppm La for example). Some of the spectra of several samples display a negative Eu anomaly (WDD07-2 55.9mA and B, WDD10-151 29.4m, WDD07-2 73.5mB). The REE variations for WDD07-2 55.9mA and B are correlated to alteration processes with a gain in LREE correlated to the alteration, whereas this is not the case for MREE and HREE variations in sample JDD08-003 74.4mB.

Correlations between the elements

Some of the elements are correlated in all the samples, whereas some of them are only visible in some of the uraninite generations. The matrix correlation results are presented in Supplementary Tables 3-3 to 3-8. In all the samples the following elements have a positive correlation: Co and Ni; the REEs; and Ba and Ga. However, minor and trace elements in each sample show specific correlations. In sample JDD08-003 74.4mB, B is correlated to V, Zn, Ga and Ba; Mn is anti-correlated to the REEs; Bi is correlated to Co and Ni (Supplementary Table 3-3). In sample WDD07-2 55.9mA, V is correlated to Ba and the LREE; Mn to Sb; Cu to Ga, Sr and Ba (Supplementary Table 3-4). In sample WDD07-2 55.9mB, the REEs, Zr and Th are correlated; B is correlated to Mn and Sb, and anti-correlated to Sr (Supplementary Table 3-5).

In sample WDD07-2 73.5mB, Co is correlated to Cu and Ga; Ti to Nb; B to Co; Ba to Ga and Sr (Supplementary Table 3-6). In sample WDD08-106 10.6m, As is correlated to the HREE and W, and anti-correlated to V, Mn and Co; Mo is anti-correlated to the LREE (Supplementary Table 3-7). In sample WDD10-151 29.4m, B is correlated to the REEs but anti-correlated to V and Mn (Supplementary Table 3-8).

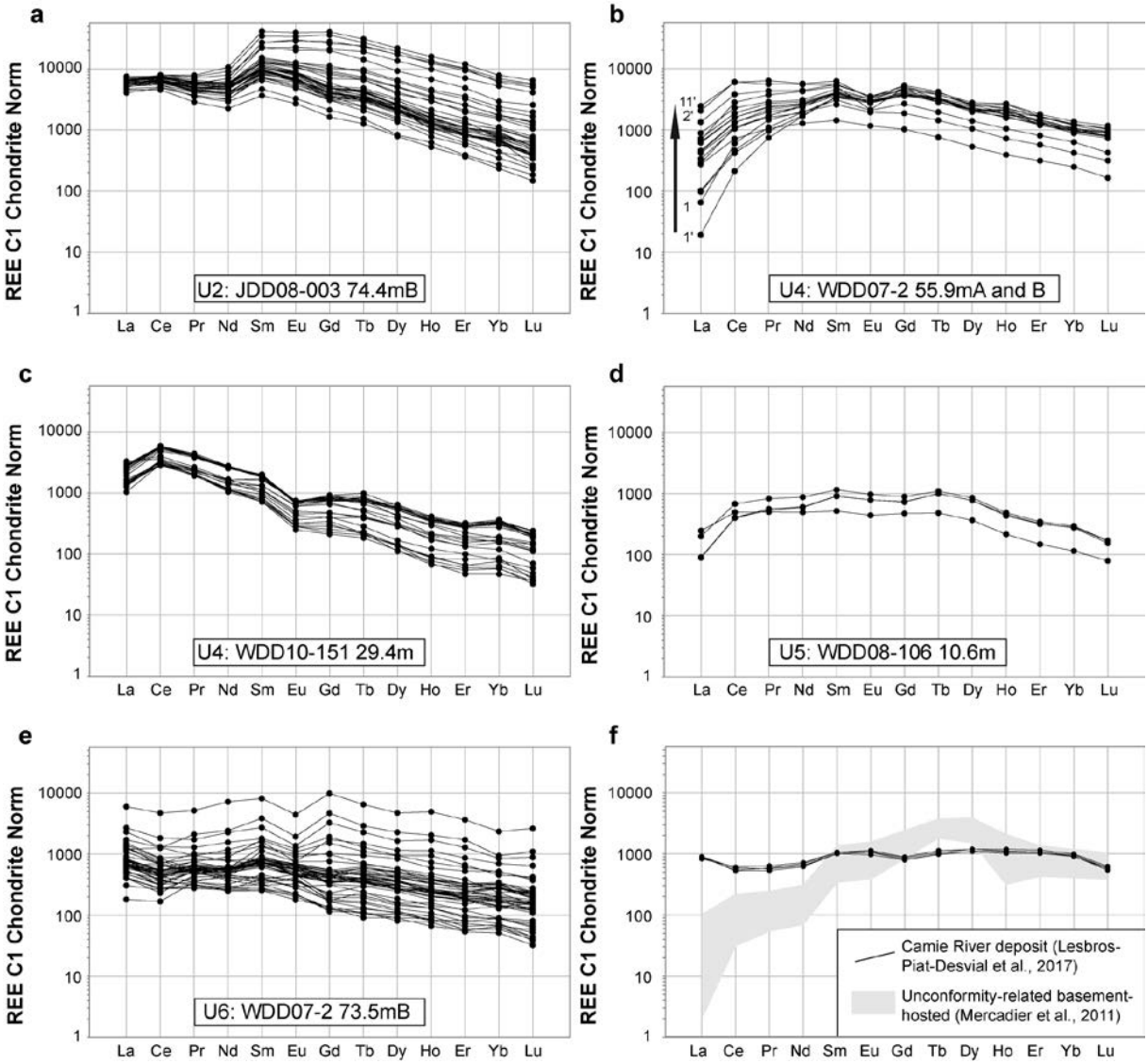

Figure 3-8: *Chondrite-normalised REE patterns of the different uraninite generations from the Redtree, Junnagunna and Huarabagoo U deposits (Westmoreland area, Australia). Each generation exhibiting a singular REE pattern indicating different chemical environments, as previously observed for the other minor and trace elements (Figure 3-7). The REE C1 Chondrite normalization is after Sun and McDonough (1989).* ***a*** *U2 generation. Sample JDD08-003 74.4mB.* ***b*** *U4 generation. The LREE enrichment indicated by the arrow is explained by the alteration corresponding to Pb loss. The numbers indicated to the left of the diagram corresponds to the LA-ICP-MS spots presented in Figure 3-5. Sample WDD07-2 55.9mA.* ***c*** *U4 generation. Sample WDD10-151 29.4m.* ***d*** *U5 generation. Sample WDD07-2 73.5mB.* ***e*** *U6 generation. Sample WDD08-106 10.6m.* ***f*** *Data from unconformity-related basement-hosted deposit in the ARUF (Mercadier et al., 2011b) and from uraninite from the Camie River deposit, Otish Basin, Canada (Lesbros-Piat-Desvial et al., 2017).*

3.4.3. Isotopic ages of apatite and uranium oxides

Apatite

The apatite predates the uranium oxides JDD08-003 74.4mB (Figure 3-9a). A significant number of analyses present anomalous U and/or Pb contents correlated to anomalous Pb/Pb or U/Pb ratios (Supplementary Table 3-9 and Figure 3-9b). These anomalous values are probably linked contribution from uraninite during the analyses of some apatites, due to the relatively small size of the apatite grains. When discarding such data, the eight remaining analyses (Supplementary Table 3-9) are marked by variable concentrations in common Pb and discordancy degree, with $^{204}Pb/^{206}Pb$ and $^{207}Pb/^{206}Pb$ ratios ranging respectively from 0.0015 to 0.0350 and 0.1281 to 0.5846. The analyses plot in a discordant position on a Tera-Wasserburg diagram with the calculated lower intercept giving a poorly defined age of 1685 ± 65 Ma (MSWD=1.4; 8 data).

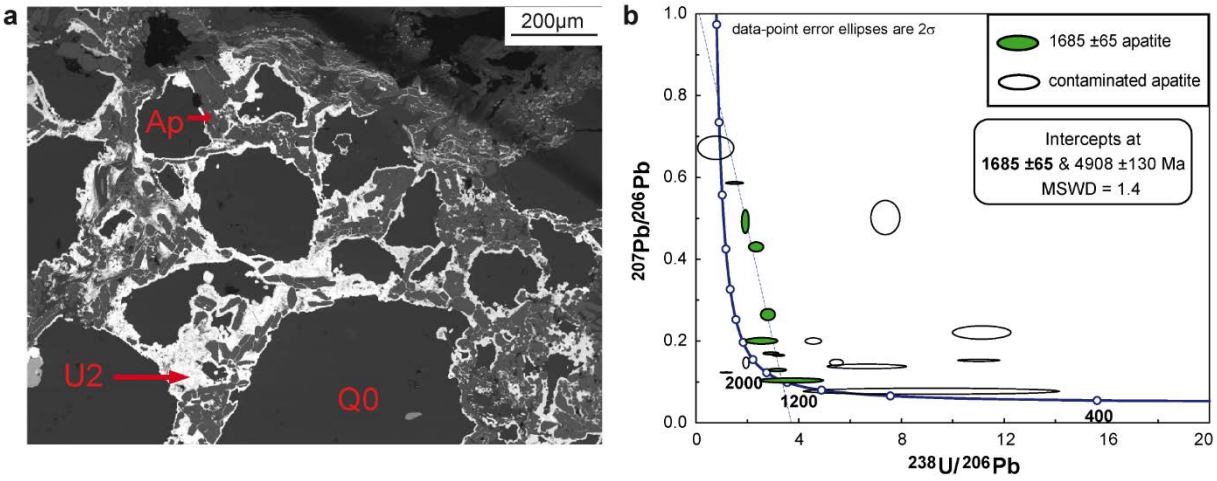

Figure 3-9: *$^{238}U/^{206}Pb$ and $^{207}Pb/^{206}Pb$ ratios measured and related age on diagenetic apatites from the sample JDD08-003 74.4mB (Junnagunna deposit, Westmoreland area, Australia).* ***a*** *Detrital quartz Q0 and diagenetic apatite in a uraninite U2 matrix (BSE image).* ***b*** *Tera–Wasserburg Concordia diagram.*

Uranium oxides

The data for the different uranium oxides dated in this study are given in Supplementary Table 3-10. The majority of the U-Pb isotopic ratios are discordant in the Wetherill Concordia diagram (Figure 3-10), indicating that all the uranium oxides suffered from post-crystallisation alteration, although the freshest zones (i.e. richest in Pb) were selected for the isotopic dating based on EPMA analyses and mapping (Figure 3-6). All the uranium oxides have a contribution of common lead, with $^{204}Pb/^{206}Pb$ ratios varying between 0.000001 and 0.001926. Sample WDD10-151 29.4m has the highest common lead contribution, with $^{204}Pb/^{206}Pb$ ratio between

0.000763 and 0.0011327, followed by samples JDD08-003 74.4mB (U2, $^{204}Pb/^{206}Pb$: 0.000002-0.001926), WDD07-2 55.9mA and B (U4, $^{204}Pb/^{206}Pb$: 0.000010-0.000171), WDD08-106 10.6m (U5, $^{204}Pb/^{206}Pb$: 0.000030-0.000057), and WDD07-2 73.5mB (U6, $^{204}Pb/^{206}Pb$: 0.000003-0.000122). All the analyses were corrected for common lead using the common lead contribution calculated at their crystallisation age: 1030 Ma for JDD08-003 74.4mB (U2), 730 Ma for WDD10-151 29.4m and WDD07-2 55.9mA and B (U4), 550 Ma for WDD08-106 10.6m (U5), and 350 Ma for WDD07-2 73.5mB (U6).

The 54 analyses for the uranium oxides from sample JDD08-003 74.4mB (U2) are moderately to strongly discordant and give an upper intercept at 1035 ± 57 Ma and a lower intercept at the origin, indicating a recent alteration event (Figure 3-10a). The data are scattered with a MSWD of 76, with a majority of analyses with U/Pb ratios close to the origin. The different uranium oxides from samples WDD07-2 55.9A and B (U4) give a global upper intercept age of 661 ± 39 Ma (49 analyses, lower intercept: 12 ± 11 Ma) but the data are highly scattered (MSWD = 170) and present highly variable discordancy behaviour, from almost concordant to strongly discordant (Figure 3-10b). When using the less discordant data (25 analyses), the data are less but still scattered (MSWD = 84), with an upper intercept age at 738 ± 44 Ma and a lower intercept of 79 ± 45 Ma. The 20 analyses from the uranium oxides from sample WDD10-151 29.4m (U4) are discordant but grouped (MSWD = 4.2) and give and upper intercept at 725 ± 23 Ma when anchoring the lower intercept at 0 ± 5 Ma (initial calculated lower intercept at –14 ± 6 Ma, Figure 3-10c). The 59 analyses from the uranium oxides from sample WDD08-106 10.6m (U5) are discordant but grouped (MSWD = 4.2) with an upper intercept of 554 ± 6 Ma when anchoring the lower intercept at 0 ± 5 Ma (initial calculated lower intercept at –16 ± 15 Ma, Figure 3-10d). The 85 analyses from the uranium oxides from sample WDD07-2 73.5mB (U6) are highly scattered (MSWD = 139) and present a variable discordancy degree, giving an upper intercept of 350 ± 21 Ma when anchoring the lower intercept at 0 ± 5 Ma (Figure 3-10e). All the samples except one (WDD07 2 55.9A and B) are characterised by a lower intercept at almost 0 Ma, indicating that the alteration of the different uranium oxides is recent.

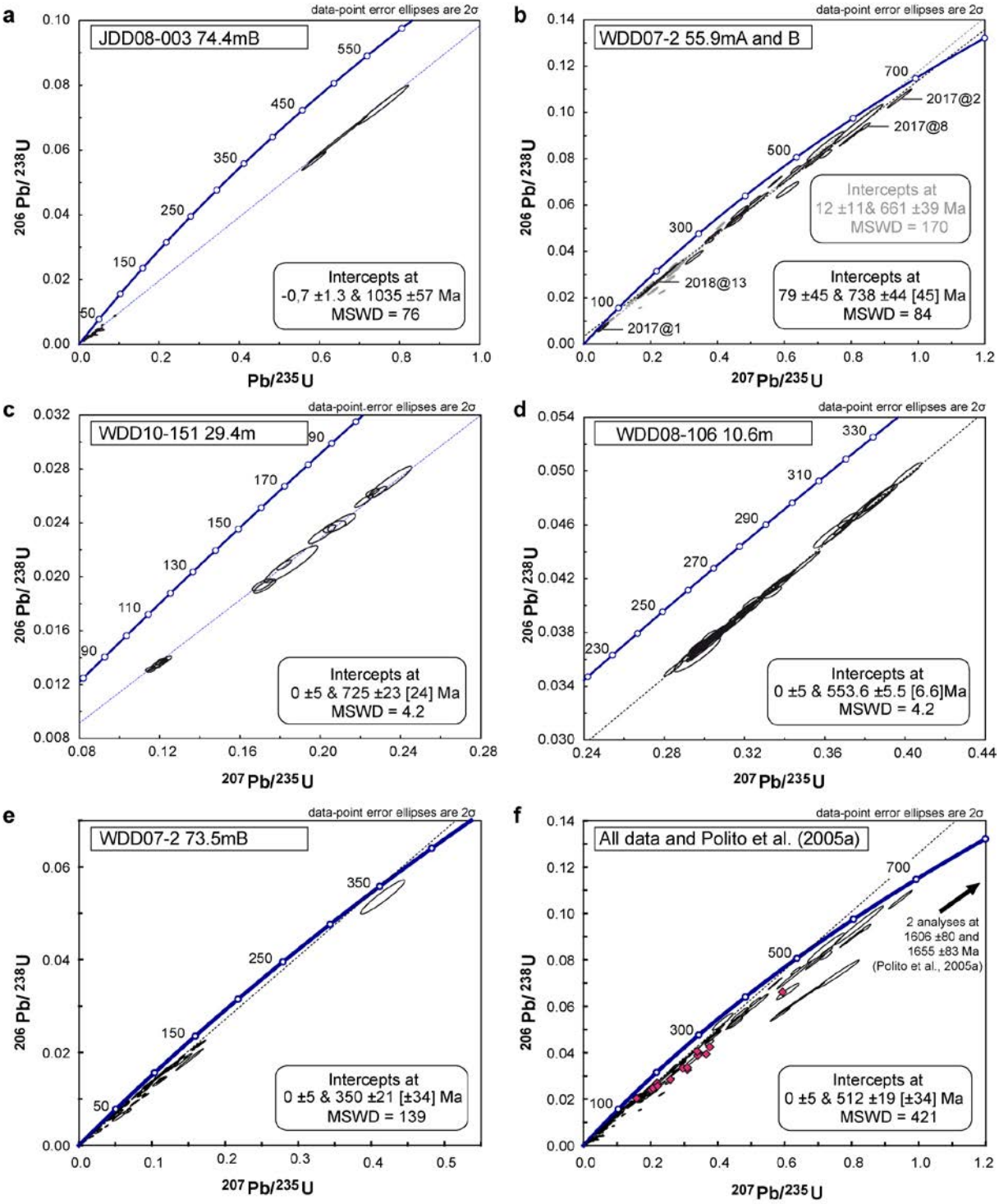

Figure 3-10: *U-Pb Concordia diagrams from in-situ isotopic analysis by SIMS of the different generations of uranium oxides from the Redtree, Junnagunna and Huarabagoo U deposits (Westmoreland area, Australia). Plots were constructed using ISOPLOT (Ludwig, 2007) from the isotope ratios presented in Supplementary Table 3-10. (**a**) Sample JDD08-003 74.4mB. (**b**) The black ellipses are the data obtained on a single uraninite and the grey ellipses are additional data from the same depth in the same drillcore. Samples WDD07-2 55.9mA and B. (**c**) Sample WDD10-151 29.4m anchored at 0 ±5 Ma. (**d**) Sample WDD08-106 10.6m anchored at 0 ±5 Ma. (**e**) Sample WDD07-2 73.5mB anchored at 0 ±5 Ma. (**f**) All data from this study (open circles, anchored at 0 ±5 Ma) and from Polito et al. (2005a, pink).*

3.4.4. Chlorite composition and crystallisation temperatures

All the analysed chlorites have a high iron content (30.26–45.31 wt% FeO) and a low magnesium content (2.01–11.99 wt% MgO), the two elements plot along the Fe^{2+}–Mg^{2+} chamosite–clinochlore substitution trend (Figure 3-11a). Silica content is comprised between 21.14 and 27.44 wt% SiO_2 and Al between 16.18 and 22.15 wt% Al_2O_3. Ti, Mn, Ca, Na and K contents are globally below the detection limits except when chlorite is mixed with illite (Supplementary Table 3-11). Chlorite has a chamositic composition (Figure 3-11b, this study and Polito et al. 2005a). To estimate their temperature, the model developed by Bourdelle et al. (2013) was used, This model was chosen because for it was designed for diagenetic to low-grade metamorphic conditions and it avoids the problem of estimating the oxidation state of iron in chlorite. Other thermometers were tested such as the ones developed by Cathelineau (1988) and by Jowett (1991). The results are presented in Supplementary Table 3-11, where the "Linear T°" column corresponds to the basic linear model for T°C < 350 °C, the “Quadratic T°" is based on a quadratic equation used above 350 °C, and the “Final T°" column gives the linear T° when it is <350 °C and the quadratic one for temperatures > 350 °C. On 99 analyses, 13 range between 159 and 300 °C, most of the calculated temperatures are above 300 °C and 42 analyses could not be calculated due to the sum of Si + Ti + Al + Fe^{2+} + Mn + Mg + Ca + Na + K - 4 (in *apfu*) higher than 6. The geothermometers of Cathelineau (1988) and Jowett (1991) also give calculated temperatures higher than 300 °C.

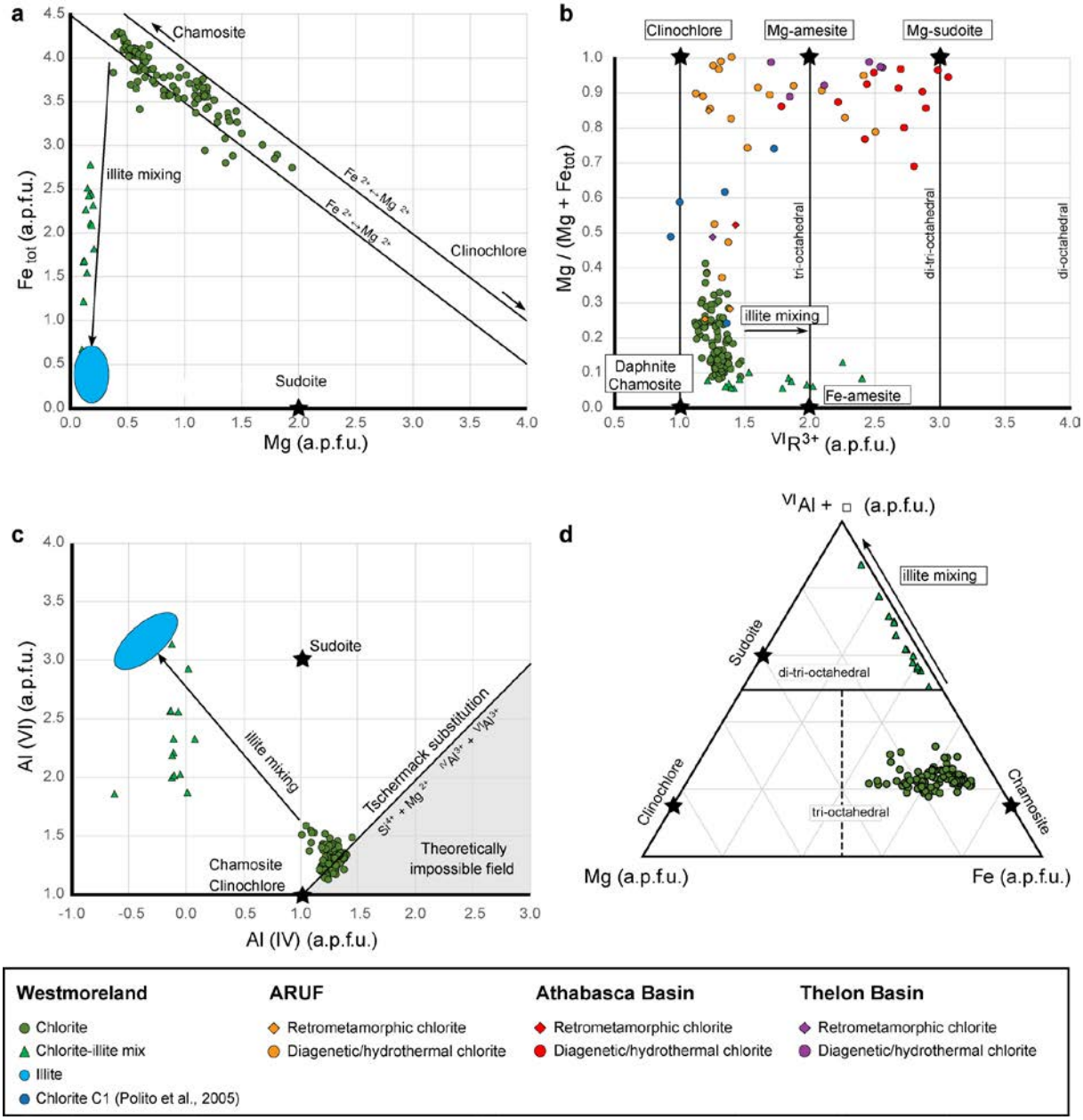

Figure 3-11: *Chlorite composition and nomenclature in Westmoreland area:* ***a*** *Fe-Mg diagram indicating that all Fe atoms are in the Fe^{2+} form in the ferromagnesian chlorites.* ***b*** *Classification diagram after Plissart et al. (2009).* ***c*** *Al^{VI}-Al^{IV} diagram for analysed chlorites. Structural formulas are calculated on the basis of 14 oxygens.* ***d*** *Classification diagram for rock-forming chlorites according to Zane and Weiss (1998). Compositions of chlorite from the Westmoreland area (this study and Polito et al., 2005a) are plotted together with chlorite from deposits from the ARUF (Beaufort et al., 2005; Gigon et al., 2019; Polito et al., 2004, 2005b), the Athabasca Basin (Billault et al., 2002; Kotzer and Kyser, 1995; Martz, 2017) and the Thelon Basin (Grare et al., submitted) for comparison. For data from the ARUF and the Canadian basin, the plotted data corresponds to the mean compositions for each sample or generation.*

3.5. Discussion

3.5.1. Timing of the U mineralisation in the Westmoreland area and its correlation to the geodynamic evolution of Australia

The paragenesis defined during this study was based on samples from the mineralised areas of the Redtree, Junnagunna and Huarabagoo U deposits, and should be combined with the one from Polito et al. (2005a), because the latter paragenetic sequence takes into account a larger diversity of samples from barren, altered and mineralised zones (Figure 3-3). Some of their mineral assemblages were not observed in our samples, and were kept unchanged. This concerns the Fe-, Ti-oxides in the detrital minerals, the dickite D1 and the pyrite P1 linked to the ca. 1680 Ma diagenetic event. These authors conducted also a study on the different clay minerals, and identified dickite and illite. In our study, the dickite was not identified and the clay mineral replacing chlorite C1 was named illite I1 by comparison with the paragenesis established by Polito et al. (2005a). Concerning uranium mineralisation, a first generation of micron-sized grains of uranium oxide U1 (referred to as “uraninite” in Polito et al. 2005a) is texturally associated with illite I2, hematite H2 and rutile R2. Polito et al. (2005a) described another generation of uranium oxide (noted U3 in the combined sequence) that crystallises in voids or in veins, with possible association with pyrite (Py2) and galena. These two generations were not observed in the present study.

The U-Pb isotopic ages for the different studied uranium oxides range from 1035 ± 57 Ma (sample JDD08-003 74.4mB) to 350 ± 21 Ma (WDD07-2 73.5mB), with 4 distinct stages at ca. 1035 Ma, ca. 730 Ma, ca. 550 Ma and ca. 350 Ma (Figure 3-10). These ages are younger than the oldest ages calculated for the Westmoreland area on micron-sized uranium oxides entrapped in hematite, with $^{207}Pb/^{206}Pb$ ages of 1606 ± 80 Ma and 1655 ± 83 Ma from two analyses obtained by LA-HR-ICPMS on very fine-grained intergranular uraninite inclusions U1 in hematite (6–8µm) at Redtree (“uraninite” in Polito et al. 2005a). The present ages correlate with the younger events of Polito et al. (2005a, Figure 3-10f). Although the common lead contribution in U1 was not measured, this old age is comparable to the 1680 ± 21 Ma $^{40}Ar/^{39}Ar$ age measured for diagenetic illite extracted from the Westmoreland Conglomerate (Polito et al., 2005b) and to the 1685 ± 65 Ma age measured for apatite in association with uranium oxides at the Junnagunna deposit (sample JDD08-03 74.4mB; Figure 3-9). Therefore, it can be confirmed that a fluid event responsible for a hydrothermal event during which clay minerals, apatite and a first stage of uranium oxide crystallised was active in the area at ca. 1680 Ma. From a geodynamic point of view, the ca. 1680 Ma period in the Westmoreland area can be correlated to the initiation of magmatism in the Warumpi Province (Scrimgeour et al., 2005)

and to a phase of rifting and intrusion of the 1678 Ma Carters Bore Rhyolite and the 1670 Ma syn-extensional Sybella Batholith in the Mount Isa Province (Gibson et al., 2016). This stage was followed by at least five successive events of U mineralisation at ca. 1035 Ma, ca. 870 Ma (Polito et al., 2005b), ca. 730 Ma, ca. 550 Ma and ca. 350 Ma. Hypotheses can be made to relate these events to the geodynamic evolution of the McArthur Basin or Australia in a more global view. The ca. 1035 Ma event could be related to the 1085–1040 Ma Giles Event, which included a failed east-trending intracontinental rift in the western Musgrave Province and the extensive 1075 Ma Warakurna Large Igneous Province (Ahmad and Munson, 2013; Evins et al., 2010; Howard et al., 2011; Wingate et al., 2004). The ca. 870 Ma event could correspond to the initiation of the Centralian Superbasin at about 840 Ma related to extension, rifting and crustal sagging that may have been an early expression of the breakup of the Neoproterozoic Rodinia Supercontinent (Greene, 2010; Lindsay, 2002). The 730 Ma phase corresponds to a period of tectonic quiescence, with little evidence for major tectonic events (Ahmad and Munson, 2013). The last two uraniferous events (ca. 550 and 350 Ma) take place when central Australia was affected by major intraplate tectonism, that dissected the Centralian Superbasin, exhumed rocks from deep crustal levels, and resulted in large amplitude east-trending gravity anomalies in central Australia (Ahmad and Munson, 2013). The first of these events, the Petermann Orogeny, was focused in the Musgrave Province at 580–530 Ma and could correspond to the ca. 550 Ma event. Then, the Alice Springs Orogeny was a major intraplate orogenic event that variably affected large areas of central Australia in the period 450–300 Ma and resulted in the exhumation of the Arunta Region (Collins and Teyssier, 1989; Haines et al., 2001) which could be related to the ca. 350 Ma mineralisation. The temporal correlation between the ages of the different uranium oxides in the Westmoreland area and of several successive geodynamic events having affected Australia demonstrates that these different events favoured fluid circulations in the McArthur Basin and related basement and uranium mobility during more than 1.3 Ga. However, none of the uraninite generation records the Isan Orogeny (1640–1490 Ma, with the peak around ca 1590 Ma, Murphy et al. 2011) that affected the Mount Isa Basin.

3.5.2. Geochemistry of the successive U mineralisation: changing physico-chemical conditions in the Westmoreland area

The chemical composition of the ca. 1680 Ma first stage of uranium oxide (“uraninite” in Polito et al. 2005a) is unknown, precluding comparison with later generations. The chemical composition of the different generations of uranium oxides identified during this study are

variable, either for REE patterns or for other minor and trace elements (Figures 3-7 and 3-8). Such results indicate at first order that the physico-chemical conditions for the formation of these different uranium oxides were different. Although the origin of this variability is not precisely constrained (i.e., the chemical composition of the mineralising fluids, the source(s) of the fluids or of the metals or the pressure-temperature conditions; see Mercadier et al. 2011b) such variability suggests that the physico-chemical conditions within the studied deposits have not been constant through time. The successive generations of uranium oxides do not show any U-Pb isotopic signatures which could indicate that they have been altered and/or remobilised by later fluid events, all the lower intercepts of the Discordia lines being younger than 100 Ma (Figure 3-10). This result, combined to the variability in the geochemical signatures of the different generations of uranium oxides, does not allow definitely defining if the current stock of U in the Westmoreland area was initially deposited at ca. 1680 Ma and after remobilised at local scale during the five posterior identified fluid events, or if each successive fluid event brought a new batch of uranium and related metals in the deposits. The last option could still be preferred, the remobilisation through time of the same initial stock of uranium in Canadian unconformity-related deposits leading to the formation of uranium oxides for which some of the geochemical markers, like REE spectra, are preserved across the generations (Martz et al., 2019; Mercadier et al., 2011a). The U mineralisation currently observed in the Westmoreland area is thus the result of a protracted history during at least 1.3 Ga (1.68–0.35 Ga) of fluid circulations for which the physico-chemical conditions have probably varied. The chemical compositions and ages of these different generations indicate that multiple hydrothermal events occurred in the area between ca. 1.7 Ga to the present time and that they were related to specific geodynamic events. The significant variations of the geochemical signatures of these different uranium oxides probably indicate new U inputs for each successive generation, or at least variable physico-chemical conditions. Each U-forming event in the Westmoreland area is characterised by a specific mineral assemblage that are a first indication of different formation conditions, or degree of post-ore alteration (Polito et al., 2011).

3.5.3. Chemical composition of the clay minerals and related temperature of crystallisation

Published data on C1 chlorite from the Westmoreland U deposits indicate that this unique generation of chlorite is Fe-dominated but has variable Al contents and Mg/Fe ratios depending on their location (Westmoreland Conglomerate and Seigal Volcanics), classifying them between the chamosite, clinochlore and Mg-amesite poles (Polito et al., 2005b). The Fe^{2+} in

the Fe-rich chlorite adjacent to the mafic dykes and volcanics or the mafic rocks themselves may have been the chemical reductant that reduced the hexavalent uranium to precipitate uraninite (International Atomic Energy Agency, 2018a; Wall, 2006). The variation of the chemical composition leads to variable calculated temperatures of formation from 196 °C to 364 °C (Polito et al., 2005b). All the new analysed C1 chlorite, whatever the location and deposit, lie in the chamosite field with related temperature of formation mostly above 300 °C (Figure 3-11 and Supplementary Table 3-11). Polito et al. (2005a) proposed that the Fe-rich composition of the chlorite giving the highest temperatures of crystallisation (364 °C) could be linked to the vicinity of the Seigal Volcanics which could have provided excess of Fe during the crystallisation of the chlorite. The distance between our samples and the Seigal Volcanics are unknown, but the same process could be considered for the high Fe contents measured and the related high temperature of crystallisation. Temperature estimates from fluid inclusions in the Redtree, Junnagunna and Huarabagoo deposits are lacking, but fluid inclusions were analysed from two related U deposits (Eva Mine and Jackson Pit) in the basement below the Westmoreland Conglomerate (Mernagh and Wygralak, 2011). The quartz veins in which the fluid inclusions were studied are genetically comparable to the Q_2 drusy vein described by Polito et al. (2005a) which are co-genetic or post-date C1 chlorite. Temperatures of homogenisation for the different types of fluid inclusions are between 99 to 380 °C, with two populations: 99–270 °C and 190–380 °C (Mernagh and Wygralak, 2011). Assuming that data obtained by Mernagh and Wygralak (2011) can be extrapolated to the Redtree, Junnagunna and Huarabagoo deposits, both chlorite and fluid inclusions indicate abnormally high thermal conditions (T>300 °C) at ca. 1680 Ma. Three most probable origin can be proposed. Firstly, the high temperatures could be due to a high regional geothermal gradient. Secondly, the fluids could be heated by the Seigal Volcanics whose age is not constrained but that could be correlated to ca. 1780 Ma volcanics (Mernagh and Wygralak, 2011). Thirdly, fluids can be heated in the basement before being injected in the basin. These high thermal conditions were probably short-lived because temperature estimates for illite I1 post-dating chlorite C1 during the ca. 1680 Ma diagenetic event and illite I2 co-genetic of U1 uranium stage at 1655 Ma range from 150 °C to 250 °C (Polito et al., 2005b). The temperature estimate and age of formation for this first U mineralising event are however loosely constrained and the possibility that this U stage formed at ca. 1680 Ma in direct relation with the emplacement of the Seigal Volcanics has to be reconsidered, in particular due to spatial correlation between the U mineralisation and the Seigal Volcanics (Figure 3-2) and the older supposed age of the volcanics. The implication of dyke emplacement in the formation of U mineralisation in Proterozoic basins similar to the McArthur Basin has been previously proposed for other basin-hosted mineralisation, like for the Matoush and Camie River U deposits (Otish Basin, Canada;

Alexandre et al. 2015; Lesbros-Piat-Desvial et al. 2017), with temperature of formation exceeding 300 °C. Such implication should be therefore studied in more details for the Westmoreland area.

No information regarding the type of alteration, the nature of the fluids or the temperature can be currently provided for the five generations of uranium oxides postdating the ca. 1680 Ma U1 of Polito et al. (2005a), as these generations are not genetically associated with clays or quartz for example. A first-order assessment could be proposed based the REE contents measured in the uranium oxides (Frimmel et al., 2014; Mercadier et al., 2011b), but must be considered with caution. As ∑REE for U2 (sample JDD08-003 74.4mB) formed at ca. 1030 Ma is above 1 wt% (Figure 3-6e), a temperature estimate > 350 °C is proposed, whereas the following generations of uranium oxides were probably formed at a temperature < 350 °C.

3.5.4. Comparison between the uranium deposits in the Westmoreland area and unconformity-related U deposits

Comparison at the scale of the McArthur Basin: Westmoreland area vs ARUF

The Alligator Rivers Uranium Field (ARUF) of the McArthur Basin hosts numerous unconformity-related U deposits such as Ranger, Nabarlek, Jabiluka and Koongarra (Cuney and Kyser, 2015; Jefferson et al., 2007; Polito et al., 2011, 2005c, 2004; Skirrow et al., 2016). They are located exclusively in the basement rocks, near the unconformity between an Archean to Paleoproterozoic basement complex and the McArthur Basin, and mostly grade above 0.1% U_3O_8 (Jackson et al., 2000; Rawlings, 1999). As these deposits and the ones in the Westmoreland area share similar first-order settings and are all associated with the McArthur Basin, it is critical to establish if they could be linked to the same ore-forming event and/or ore-forming processes.

The ARUF and the Westmoreland area were affected by a major event of diagenetic/hydrothermal fluid circulation at ca. 1680–1600 Ma (Figure 3-12). This common episode is attested by multiple isotopic ages measured on illites, apatite and uranium oxides for the two zones (Clauer et al., 2015; Maas, 1989; Polito et al., 2005b, 2005c, 2004; Skirrow et al., 2016). The fluids at the origin of the diagenetic/hydrothermal event in the ARUF and Westmoreland area at 1680–1600 Ma are basin-derived brines and low-salinity fluids (Derome et al., 2003a, 2007; Mernagh and Wygralak, 2011; Polito et al., 2004, 2005c, 2006b; Wilde et al., 1989; Ypma and Fuzikawa, 1980) . The isotopic and fluid inclusions data at Westmoreland show the involvement of NaCl-rich and $CaCl_2$-rich brines, comparable to the two brines related to the origin of the unconformity-related deposits in the ARUF and derived from evaporated

seawater (Derome et al., 2007). The mixing between low-salinity fluids and brines is a key process for ore deposition in both areas (e.g. Derome et al., 2003, 2007; Mernagh and Wygralak, 2011). Although contemporaneous and related to the same types of fluids, the episode of fluid circulations which started at 1680 Ma in the ARUF and Westmoreland area are considered as physico-chemically different based on the differences in the mineralogy and chemistry of the minerals which crystallised at that time in both zones. The most recent studies done on the unconformity-related U deposits from the ARUF, in particular for the Ranger U deposit, show significant differences with the deposits in the Westmoreland area for several key mineral phases, either for the composition of the chlorite (Gigon et al., 2019; Skirrow et al., 2016) or the presence and composition of hydrothermal tourmaline (Gigon et al., 2019). The chlorite in the Westmoreland area are dominantly chamosite, and no sudoite has been described although sudoite is a marker of unconformity-related deposits in the ARUF (Beaufort et al., 2005b; Polito et al., 2005c, 2004). The chlorite composition for the ARUF gives temperatures between 101 °C and 310 °C (Gigon et al., 2019; Polito et al., 2004), considerably lower than the > 300 °C calculated in this study. A striking difference between the two zones of the McArthur Basin is the absence of hydrothermal Mg-tourmaline with the uranium oxides in the Westmoreland area, whereas it is a fingerprint mineral of unconformity-related U deposits in the ARUF (Gigon et al., 2019; Skirrow et al., 2016). The unconformity-related U deposits formed in the ARUF at ca. 1680–1600 Ma are the consequence of a Mg- and B-metasomatism (Fisher et al., 2013; Gigon et al., 2019; Skirrow et al., 2016), but such metasomatism is lacking in the Westmoreland area. Another major difference for the uranium deposits between the north and south of the McArthur Basin is the location of the mineralisation: structurally-controlled in the basement to the North and spatially-related to volcanic dykes and sills in the basin to the South (Hein, 2002; Laramide Resources Ltd, 2019; Polito et al., 2005b; Skirrow et al., 2016).

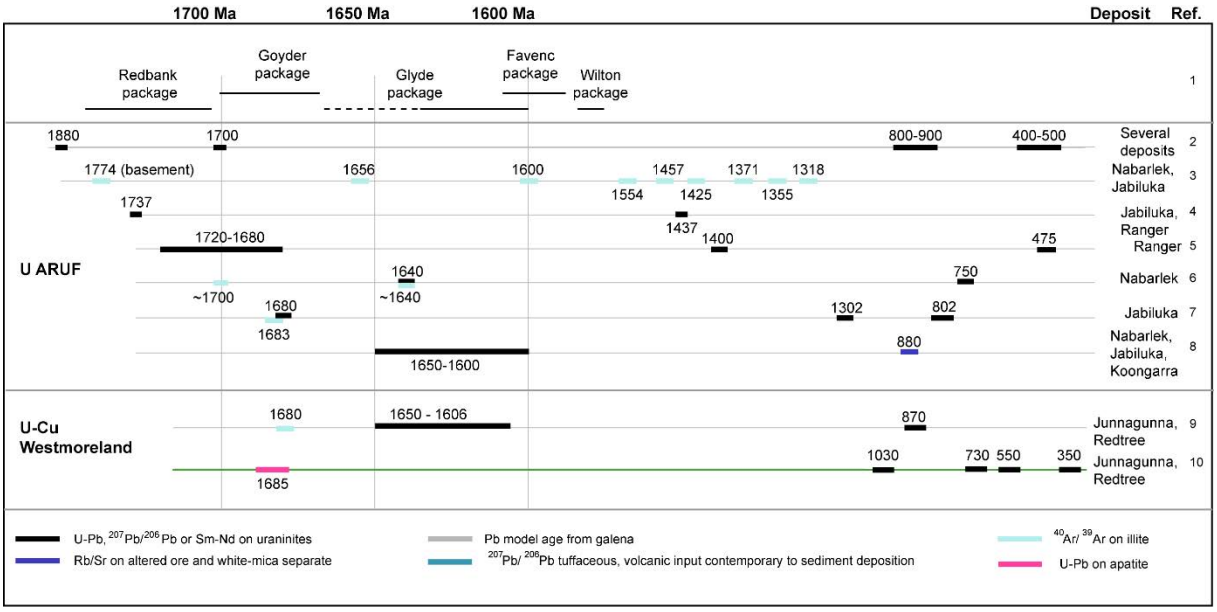

Figure 3-12: *Synthesis of the alteration and mineralisation ages obtained in the McArthur Basin in the U-rich ARUF and the Westmoreland area. 1: Ahmad and Munson (2013). 2: Hills and Richards (1976). 3: Clauer et al. (2015). 4: Ludwig et al. (1987). 5: Skirrow et al. (2016). 6: Polito et al. (2004). 7: Polito et al. (2005b). 8: Maas (1989). 9: Polito et al. (2005a). 10: this study.*

The present study identifies for the first time multiple U generations between 1035 and 350 Ma in two deposits of the Westmoreland area. The succession of fluid circulations also characterised the unconformity-related U deposits from the ARUF, with multiple ages from 1680 Ma to the present time measured on both uranium oxides and illites (Ahmad and Munson, 2013; Clauer et al., 2015; Hills and Richards, 1976; Ludwig et al., 1987; Maas, 1989; Polito et al., 2005c, 2004; Skirrow et al., 2016). These post 1680 Ma ages in the ARUF are mainly observed between 1600 and 1300 Ma for the clay minerals and some uranium oxides, but are dominantly younger than 900 Ma for the uranium oxides. Based on the available datasets, the post-1680 Ma ages measured for the ARUF do not totally correlate with the five post-1680 Ma ages measured at the Westmoreland area, which could induced partial temporal disconnection of the fluid circulations in the two zones from 1680 Ma to the present time.

The nature of the fluid(s) and physico-chemical conditions of these different events in the ARUF are barely known. Concerning the Westmoreland area, the ultimate origin of the different generations and the physico-chemical conditions prevailing between 1035 and 350 Ma have also to be constrained. REE patterns of UO_2, which are diagnostic features of deposit types, differ significantly between the ARUF and the Westmoreland area. The different generations of uranium oxides in the Westmoreland area do not exhibit the “bell-shape” (i.e. high concentrations of Tb and Dy) typical of unconformity-related U deposits from ARUF such as Nabarlek and Koongarra (Mercadier et al., 2011b). Even if some post crystallisation modification of the REE patterns may have contributed to the LREE enrichment (as described

in the Athabasca Basin by Mercadier et al. 2011a and Martz et al. 2019), such phenomenon is not sufficient to explain the major differences of the REE patterns between the two zones. The different uranium oxides from the Westmoreland area have significantly higher contents in common lead (Supplementary Table 3-10) when compared to typical uranium oxides from unconformity-related U oxides (Martz et al., 2019; Skirrow et al., 2016), which is also an indicator of differences in their conditions of formation compare to the ARUF. It can be concluded therefore that the formation conditions of the different U generations in the Westmoreland area did not correspond to those known for unconformity-related U deposits in ARUF. It is currently not possible to link the physico-chemical conditions for the U1 generation in the Westmoreland area with the one in unconformity-related deposits as no analyses have been performed. They could have been formed in a similar system, but under higher temperatures.

Comparison between U deposits in the Westmoreland area and U deposits in Canadian Proterozoic basins

Several Paleo- to Mesoproterozoic basins in Canada present U mineralisation, for which research works have been carried out: the Athabasca Basin (Saskatchewan), the Thelon Basin (Nunavut) and the Otish Basin (Québec). The present section compares at first order the deposits of these basins with those of the Westmoreland area.

The ca. 1680-1600 Ma diagenetic/hydrothermal episode defined in the Westmoreland area is documented in the Thelon Basin, where apatite is dated at 1667 ± 5.1 Ma (Davis et al., 2011). In the Athabasca Basin, this fluid event has been recorded by TIMS analyses of hydrothermal zircon tips (uranium-rich, thorium-depleted) in a leucogranite sampled 200 meters east of the McArthur River high-grade uranium deposit with ages from 1680 to 1550 Ma. This was interpreted as the approximate timing of the thermotectonic event(s) and associated fluids that produced the new zircon rich in uranium (Annesley et al., 2007). Such results confirm a global fluid event at 1680–1600 Ma affecting the Athabasca, Thelon and McArthur basins which could have belong to the same super basin at that time (Furlanetto et al., 2016). No U mineralisation has however been dated at 1680 Ma for the Athabasca and Thelon basins, with maximum ages at ca. 1590 Ma (Alexandre et al., 2009) and ca. 1500 Ma (Sharpe et al., 2015) respectively. No significant hydrothermal activity is also known at ca. 1680 Ma for the Otish Basin, with older age of fluid circulation and mineralisation at ca. 1725 Ma for the Camie River U deposit (Beyer et al., 2012; Lesbros-Piat-Desvial et al., 2017). The timing of formation of the Matoush deposit is loosely constrained (1695 ± 110 Ma; Alexandre et al. 2015). The U mineralisation in the Athabasca Basin are of unconformity-related type, like

those in the ARUF (Cuney and Kyser, 2015; Jefferson et al., 2007). Recent data on the U mineralisation in the Thelon Basin indicate that these deposits had a polyphased history over hundreds of Ma in which unconformity-related U mineralization formed from ca. 1500 Ma, followed by low-T and meteoric-related redox fronts (Chi et al., 2017; Grare et al., n.d.; Shabaga et al., 2017; Sharpe et al., 2015). Concerning the Otish Basin, the ca. 1725 Ma U mineralization at Camie River was initially interpreted to be unconformity-related type (Beyer et al., 2012), but recent research didn't support this interpretation because of a Paleoproterozoic, higher-temperature hydrothermal event, whose origin remains speculative (Lesbros-Piat-Desvial et al., 2017). The main characteristics of the Matoush U deposit, also located in the Otish Basin, do not infer an unconformity-related type, although the U-bearing fluids were oxidizing basinal fluids (Alexandre et al., 2015), like for the Westmoreland area.

The chemical composition of the different uranium oxides analysed for this study present major differences for minor and trace elements (including REEs) compared to typical unconformity-related U deposits from the Athabasca (Alexandre et al., 2016; Martz et al., 2019; Mercadier et al., 2011b) or Thelon basins (Grare et al., in review). This is particularly visible when comparing the REEs, as all the REE spectra of the different generations of uranium oxides from the Westmoreland area do not having the typical bell-shape pattern of the unconformity-related U deposits (Figure 3-8). Differences are also visible for numerous minor and trace elements like As, W, Ba and V (Figure 3-7c and d) compared with McArthur River and Cigar Lake U deposits of the Athabasca Basin for example (Alexandre et al., 2015; Martz et al., 2019). The majority of the minor and trace elements have significantly higher concentrations in the uranium oxides from the Westmoreland area, which could indicate a higher temperature of formation and/or different sources of metals.

The complete geochemistry of the uranium oxides from the Otish Basin is lacking, but the REE patterns of the ca. 1725 Ma uranium oxides from the Camie River are rather similar to those measured for different generations of uranium oxide from the Westmoreland area (Figure 3-8). Such results allow consideration that the physico-chemical conditions for the formation of the U mineralization in the Westmoreland area were probably more similar to those for the origin of Matoush or Camie River U deposits of the Otish Basin than those of the Athabasca and Thelon basins. The temperatures at the Matoush deposit (~300 ±50 °C, based on illite and chlorite crystal chemistry, Alexandre et al. 2015) and at the Camie River deposit (275 to 300 °C, Beyer et al. 2012 and 320 °C, Lesbros-Piat-Desvial et al. 2017) are consistent with the ones observed in the Westmoreland area, but are significantly higher than for the Athabasca and Thelon basins (e.g. Grare et al.; Kotzer and Kyser 1995; Richard et al. 2016; Chi et al. 2017). Other similarities with the U deposits from the Otish Basin are the lack of Mg-

rich minerals (sudoite, Mg-foitite) or alumino-phosphate-sulfate minerals, which are markers of unconformity-related U deposits. The Matoush and Camie River deposits are spatially related to dykes (Beyer et al., 2012; Alexandre et al. 2015; Lesbros-Piat-Desvial et al. 2017), which played a role as the reductant of uranium, because it was a source of Cr and Fe at Matoush (Alexandre et al., 2015). An equivalent process was proposed for the Westmoreland area with the implication of iron from the dykes as reductant (Polito et al., 2005b). The mafic activity in the Otish Basin and in the southern McArthur Basin (Westmoreland area) could thus have favoured the formation of atypical U deposits, although linked to the same types of fluids as unconformity-related U deposits.

3.6. Conclusions

The new data provided on different U mineralised intercepts from two deposits of the Westmoreland area (Queensland and Northern Territory, Australia) indicate that this zone of the McArthur Basin was affected by several episodes of fluid circulations between ca. 1680 Ma to the present time, which document a protracted mobility of uranium over more than 1.3 Ga. Based on published and new data, six different events of U mobility were conclusively active at ca. 1680 Ma, ca. 1035 Ma, ca. 850 Ma, 730 Ma, ca. 550 Ma and ca. 350 Ma. The ca. 1680 Ma mineralisation was formed due to the circulation and mixing of NaCl-rich, $CaCl_2$-rich basin-derived brines and low-salinity fluids, a timing and types of fluids comparable to the unconformity-related U deposits in the ARUF to the North of the McArthur Basin. The physico-chemical conditions for the formation of these contemporaneous uranium mineralisation are different between the two zones, with higher chlorite temperature (> 300 °C) for the Westmoreland area, the lack of Mg-rich minerals (such as Mg-chlorite and Mg-foitite) or alumino-phosphate-sulphate minerals which are markers of unconformity-related U systems. The U deposits that formed at ca. 1680 Ma in the Westmoreland area are not characterised by the Mg- and B-metasomatism that is typical of unconformity-related U deposits. Although the precise chemical composition of the uranium oxide formed at ca. 1680 Ma has not been measured, all the other U mineralisation found in the Westmoreland area are chemically different than the uranium oxides found in unconformity-related U deposits. They are specifically marked by high contents in numerous minor and trace elements, like REEs, which tend to confirm the higher temperature of crystallisation. Even if the timing and the types of fluids between the two parts of the basin were similar, the geological context was different at ca. 1680 Ma with either volcanic activity or mantle proximity in the Westmoreland area that is not recorded in the ARUF. This heat could be the trigger of fluid circulation in the Westmoreland area, and the dykes could provide the structural and chemical traps that focused the uranium-

bearing brines and favoured U deposition at ca. 1680 Ma. Such conditions appears rather similar to those known for the formation of U deposits in the Proterozoic Otish Basin (Québec, Canada). The physico-chemical conditions related to the successive U mineralisation between ca. 1035 and 350 Ma could not be determined, but the variable chemical compositions of the uranium oxide are not in favour of stable physico-chemical conditions through time. These conditions were different than those known in unconformity-related U deposits from the ARUF. On the basis of the studied samples, it is thus unlikely that significant unconformity-related U deposits are present in the Westmoreland area.

Acknowledgements

The Northern Territory Geological Survey provided logistical support for the sampling mission. Laramide Resources Ltd. provided authorisation, logistical support and guidance for sampling on the Westmoreland exploration camp (especially Adrian Buer). Alexandre Flammang and John Moine (GeoRessources Lab) as well as Thin Section Lab company staff are acknowledged for careful thin section preparation. Chantal Peiffert, Andreï Lecomte and Olivier Rouer (GeoRessources Lab) are acknowledged for support in LA-ICP-MS, SEM and EPMA analyses respectively. This research was funded by (i) a French Ministry of Higher Education and Research PhD salary Grant to J.G., (ii) a Région Lorraine-FEDER grant to J.M : « Rôle des phases fluides dans la distribution spatiale des ressources métalliques dans les bassins sédimentaires paléoproterozoiques australiens », (iii) OSU OTELo grants to J.M. : « Conditions de transport des métaux dans un mégabassin protérozoïque » and A.R. : « Transferts de fluides et métaux dans le bassin de McArthur (Australie) » and (iv) a CNRS-INSU-CESSUR grant to J.M. Transferts des fluides et métaux dans les méga-bassins paléoprotérozoïques.

Supplementary material

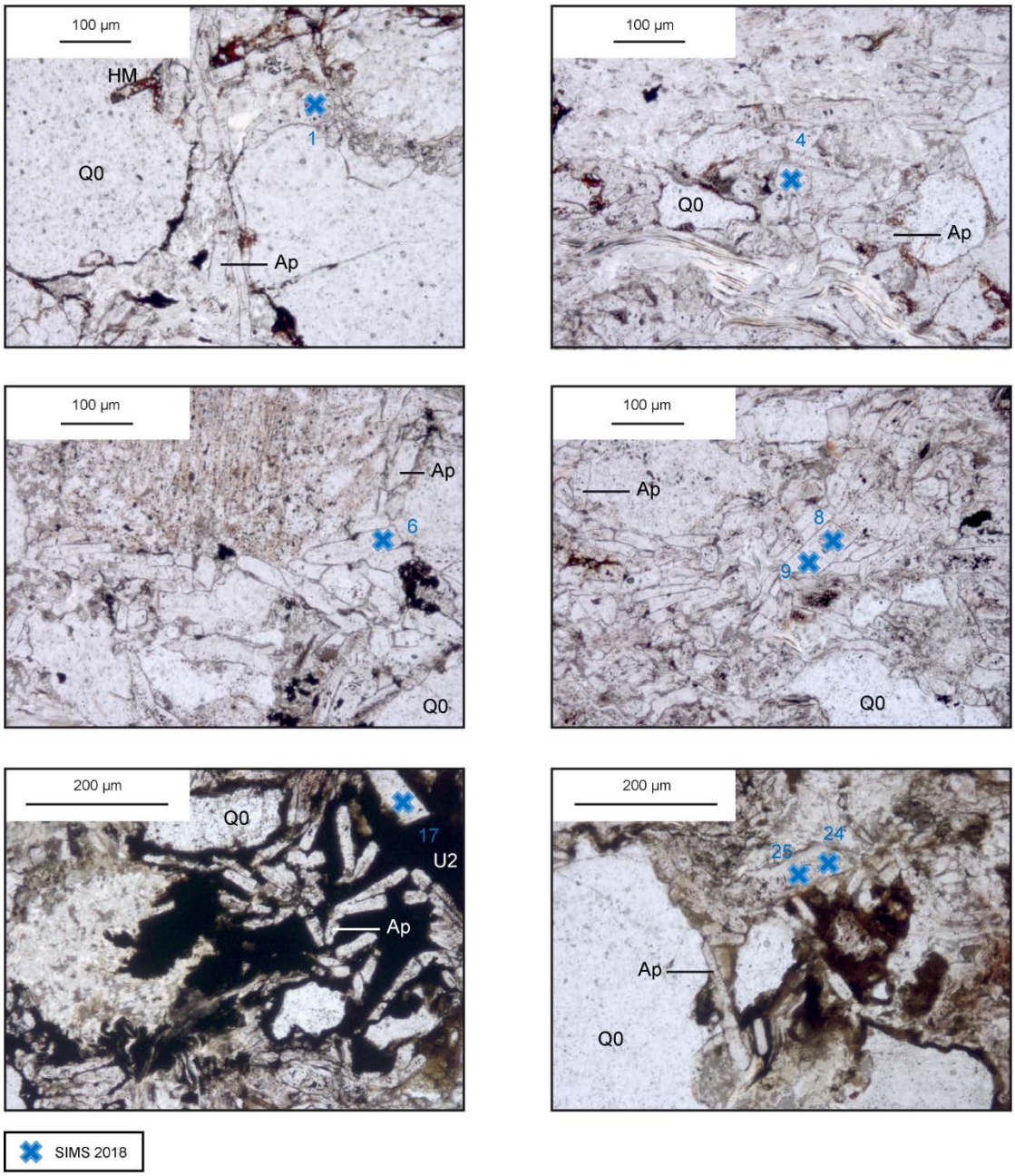

Supplementary Figure 3-1*: Location of the SIMS analyses on apatite. Sample JDD08-003 74.4mB, transmitted light.*

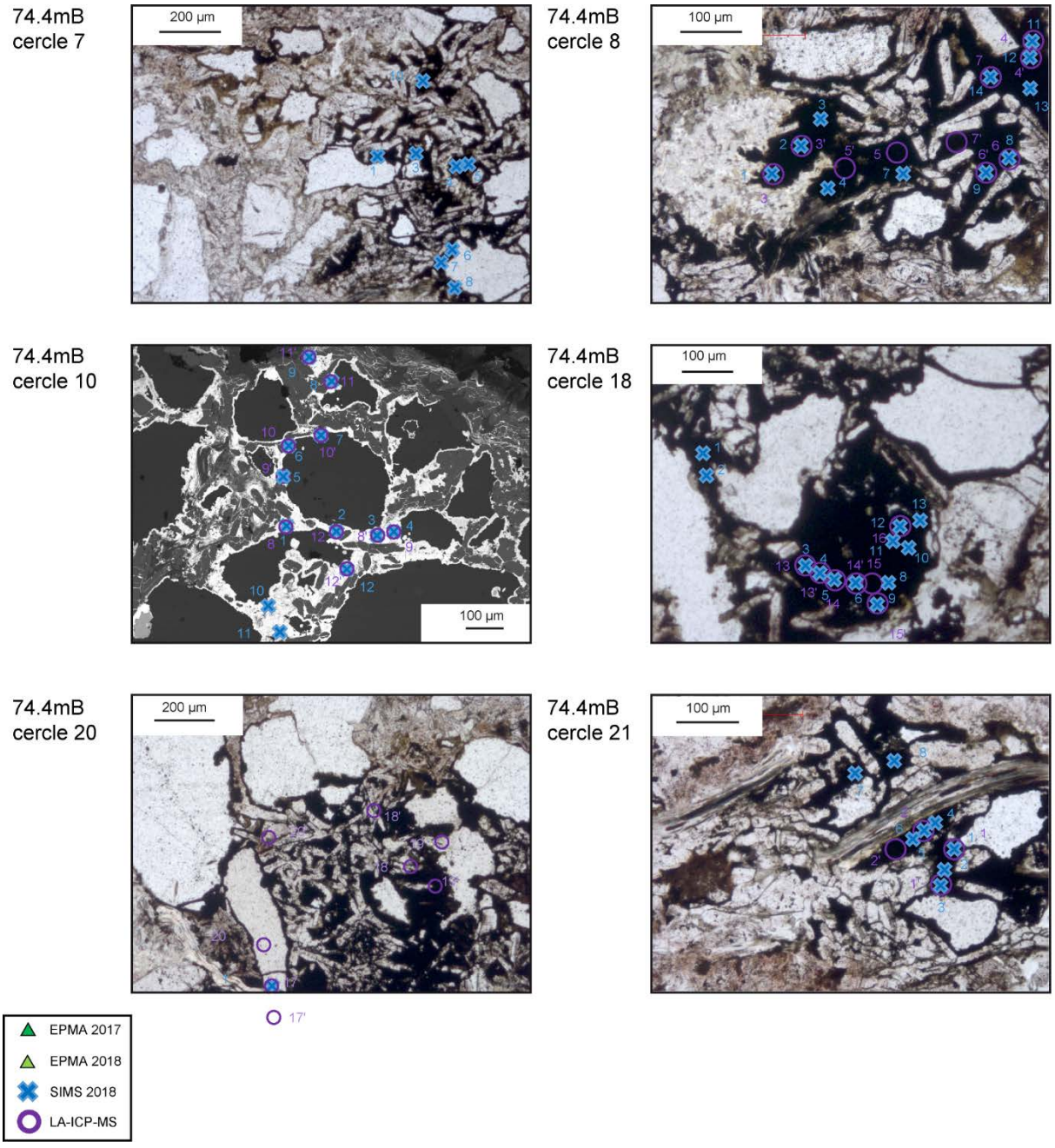

***Supplementary Figure 3-2**: Location of the EPMA, LA-ICP-MS and SIMS analyses on uraninite. Sample JDD08-003 74.4mB, transmitted light.*

55.9A cercle 7

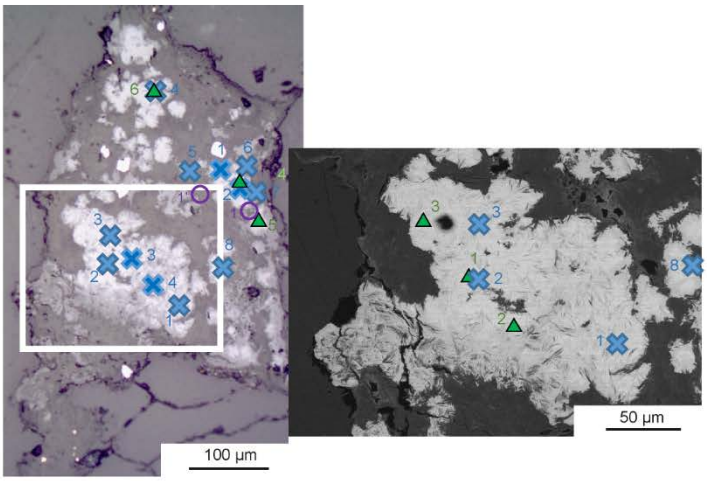

55.9A cercle 9

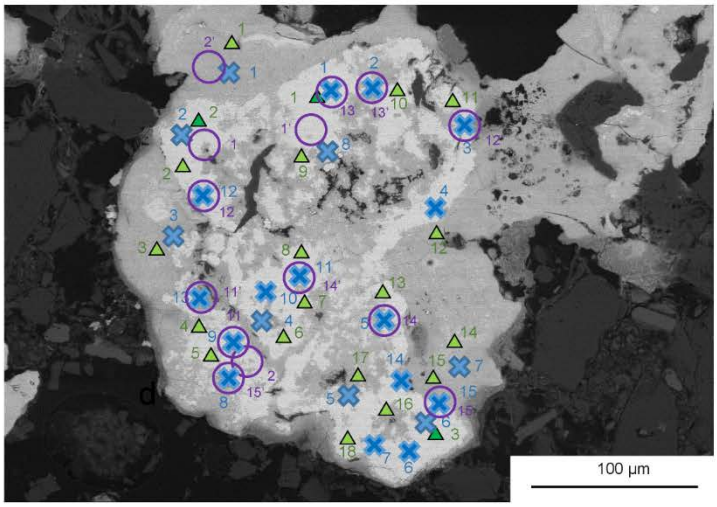

55.9A cercle 9

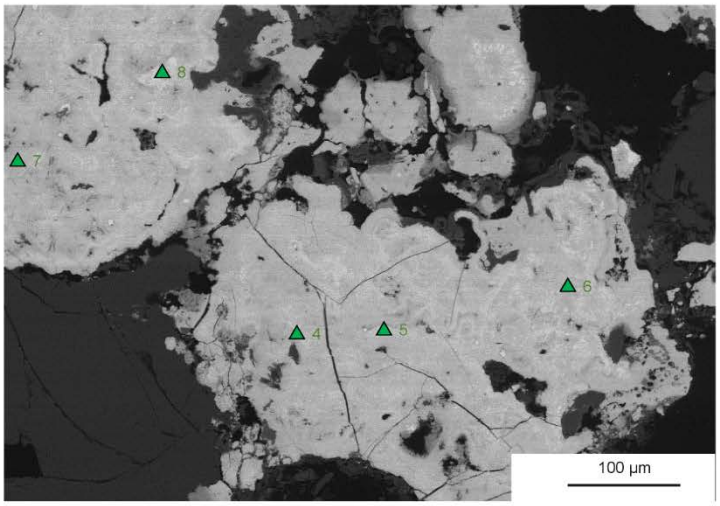

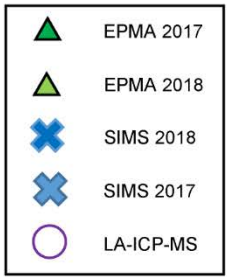

Supplementary Figure 3-3: *Location of the EPMA, LA-ICP-MS and SIMS analyses on uraninite. Sample WDD07-2 55.9mA, BSE images.*

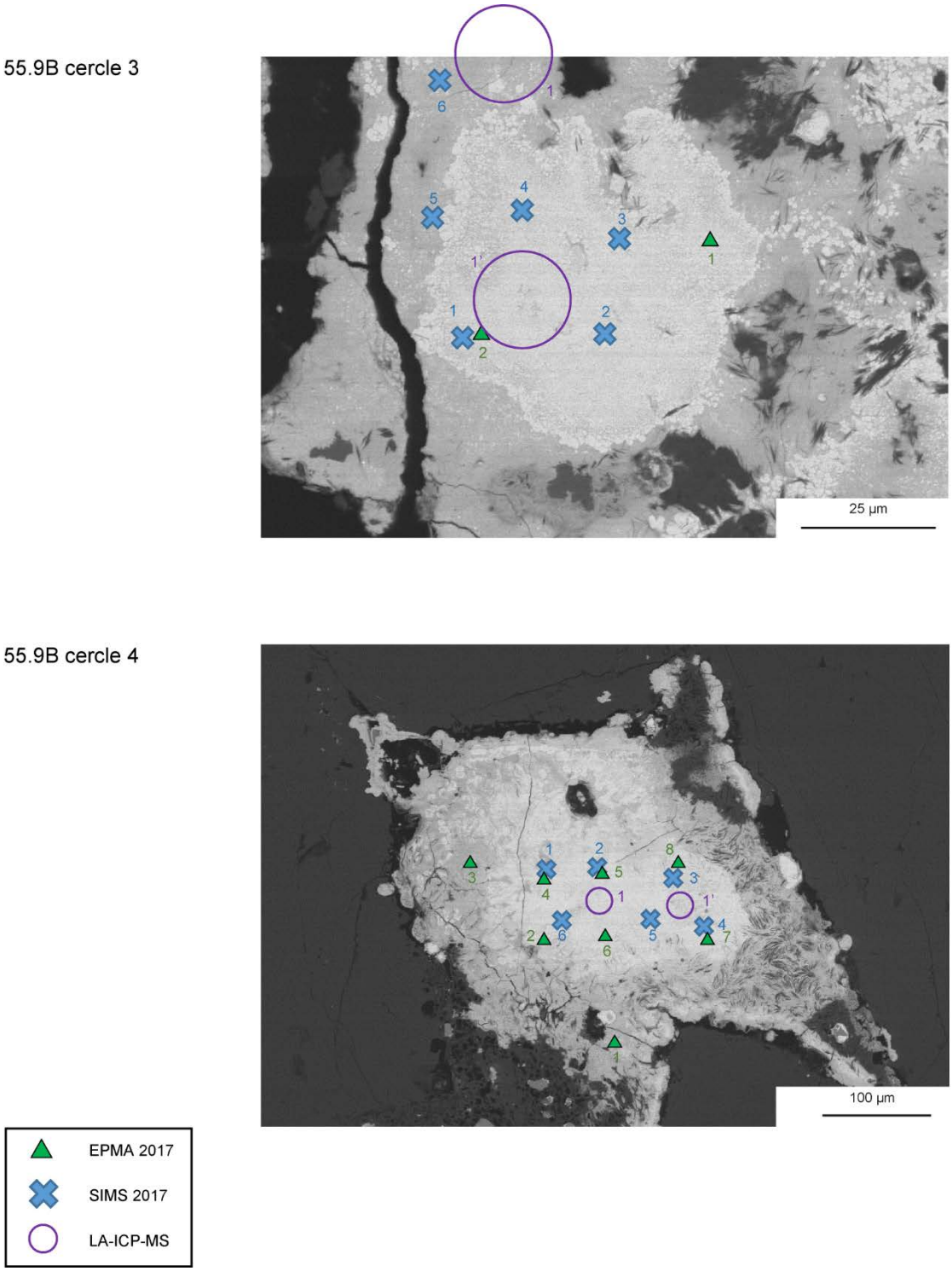

***Supplementary Figure 3-4**: Location of the EPMA, LA-ICP-MS and SIMS analyses on uraninite. Sample WDD07-2 55.9mB, BSE images.*

29.4 cercle 1

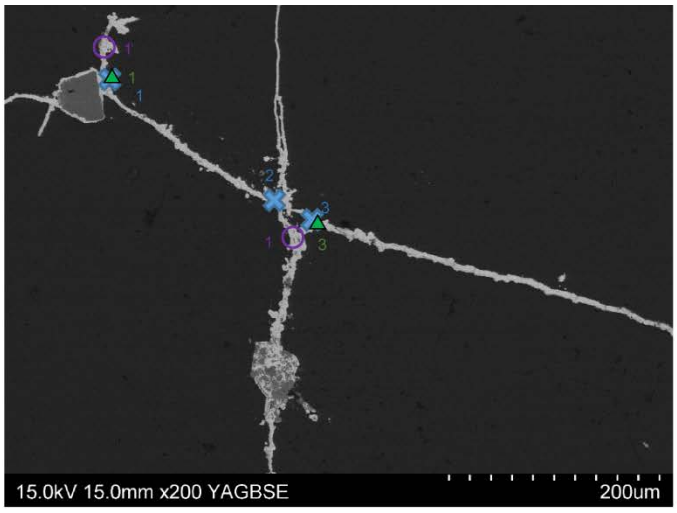

29.4 cercle 2

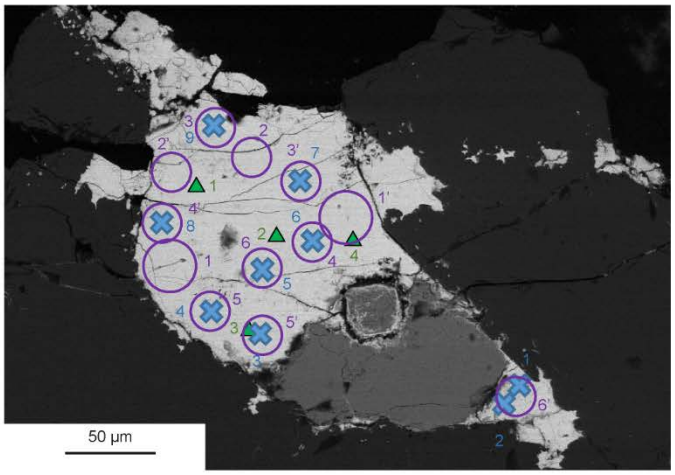

29.4 cercle 4

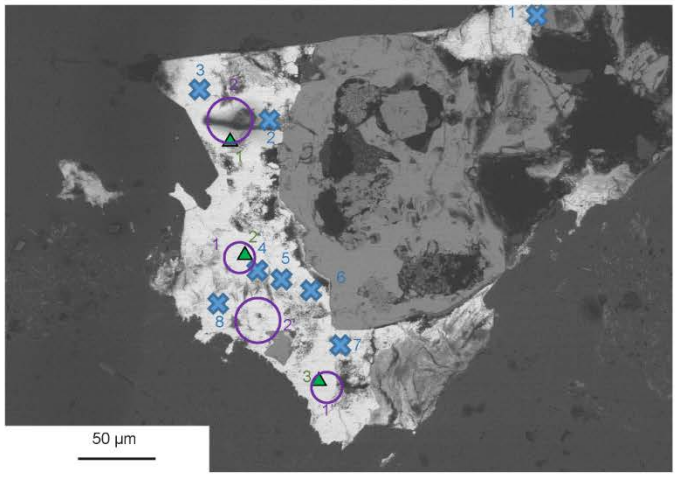

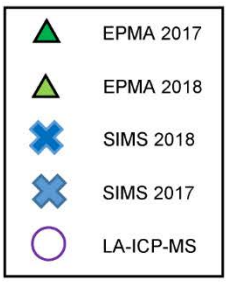

***Supplementary Figure 3-5**: Location of the EPMA, LA-ICP-MS and SIMS analyses on uraninite. Sample WDD10-151 29.4m, BSE images.*

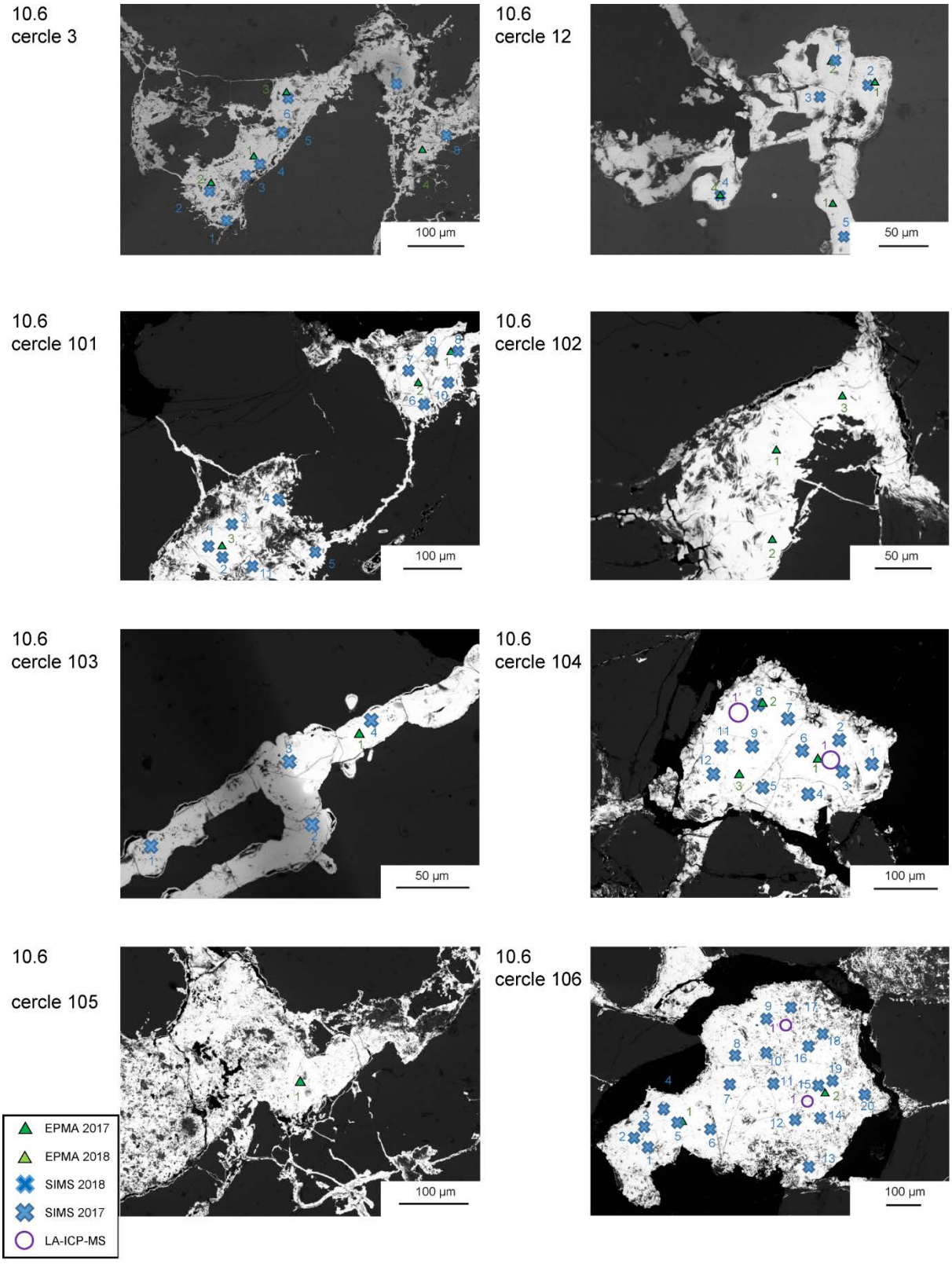

***Supplementary Figure 3-6**: Location of the EPMA, LA-ICP-MS and SIMS analyses on uraninite. Sample WDD08-106 10.6m, BSE images.*

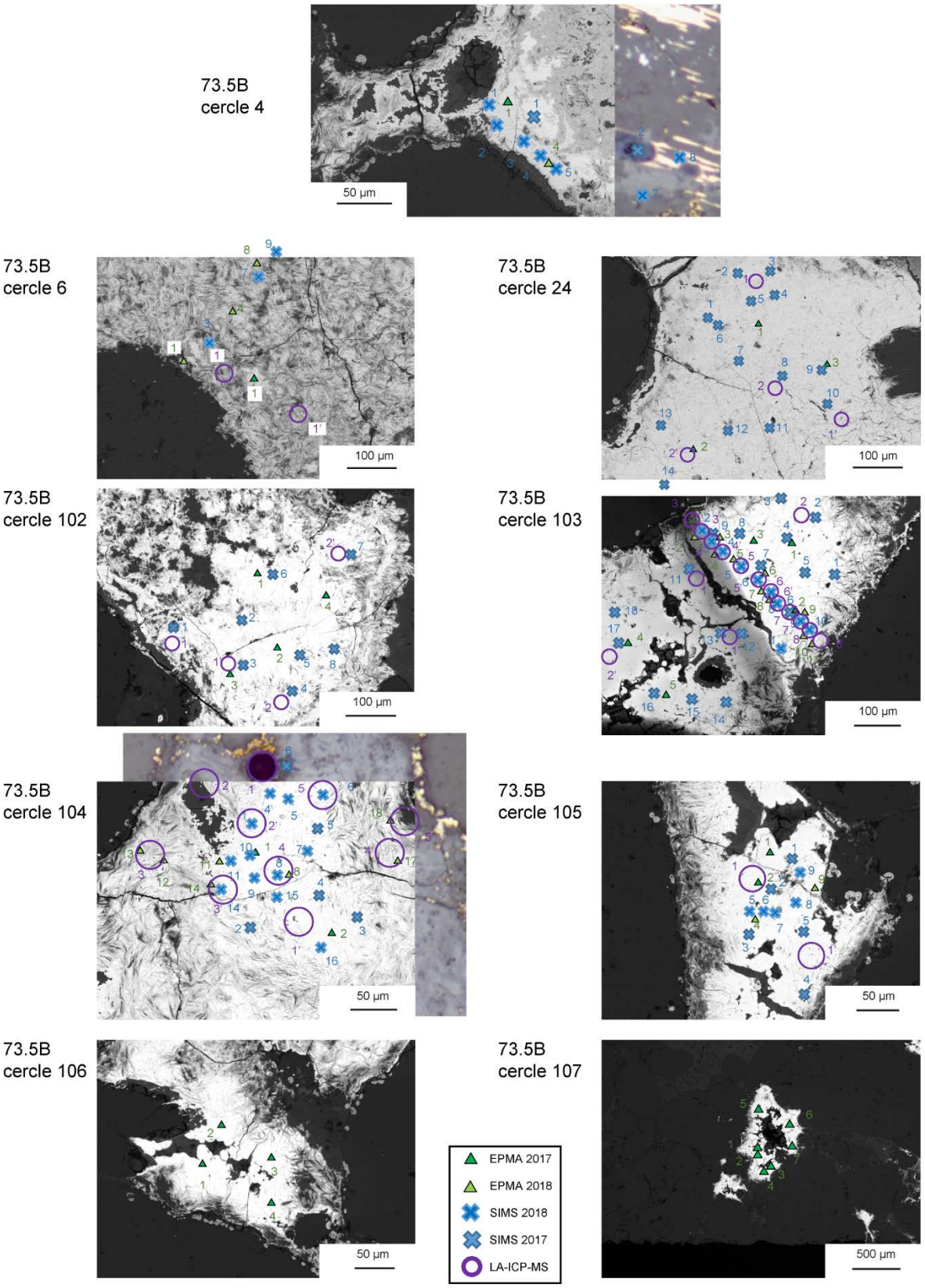

***Supplementary Figure 3-7**: Location of the EPMA, LA-ICP-MS and SIMS analyses on uraninite. Sample WDD07-2 73.5mB, BSE images except some reflective light images expanding the BSE images.*

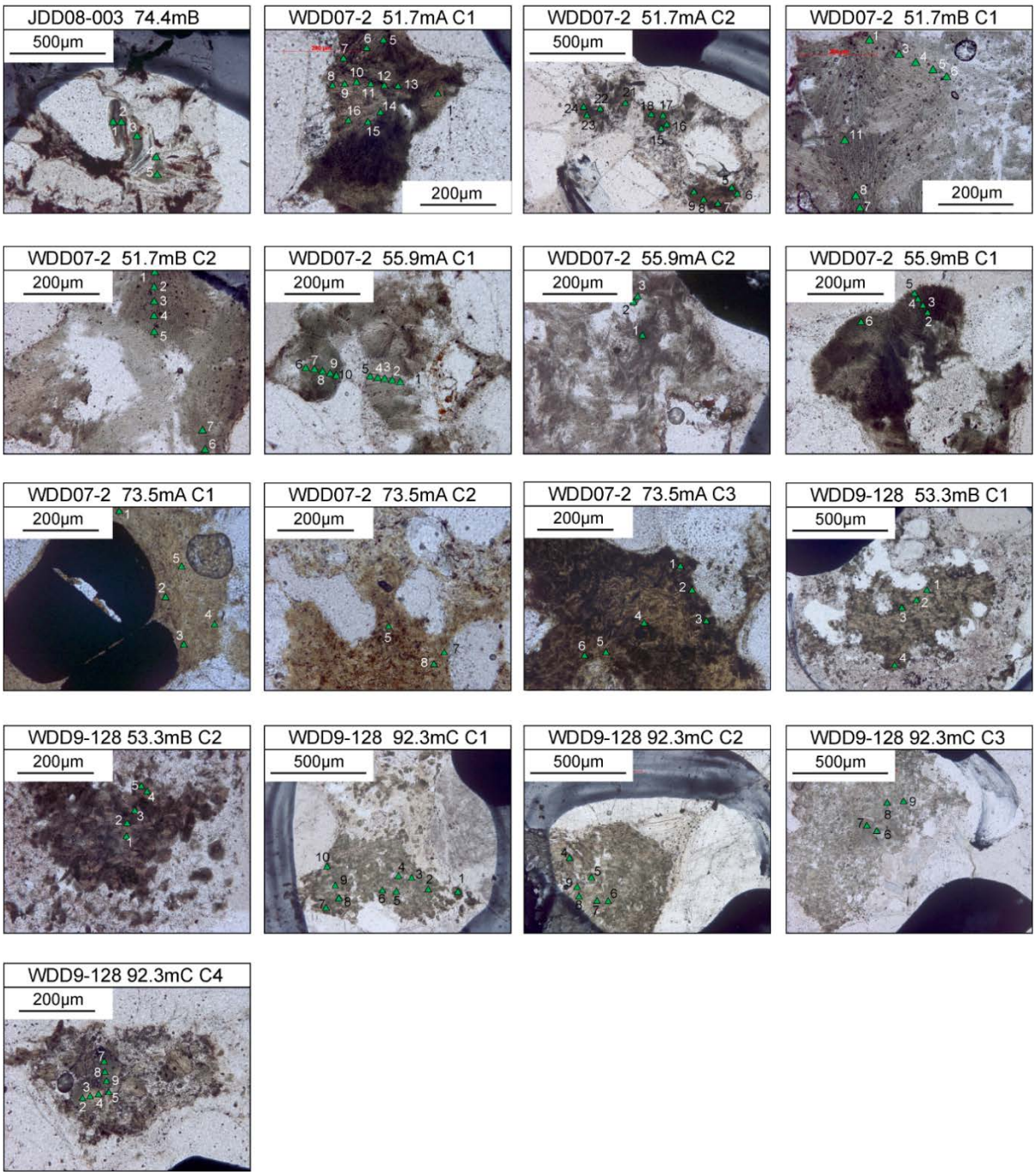

***Supplementary Figure 3-8**: Location of the EPMA analyses on chlorite. Samples JDD08-003 74.4mB, WDD07-2 51.7mA and B, 55.9mA and B, and 73.5mA; WDD9-128 53.3mB and 92.3mC, transmitted light.*

Supplementary Table 3-1: *Major elements composition on uraninite from the Westmoreland area obtained by EPMA.*

Year	Drillhole #	Depth (m)	Circle #	Analysis #	Si (wt%)	P (wt%)	Ca (wt%)	U (wt%)	Ti (wt%)	V (wt%)	Mn (wt%)	Fe (wt%)	Zr (wt%)	Y (wt%)	Pb (wt%)	Th (wt%)	Al (wt%)	O (wt%)	Total (wt%)
2017	WDD07-2	55.9A	9	1	0.2	0.02	1.45	75.25	0.17	0.07	0.2	0.3	0	-	7.25	0	0	11.79	96.69
2017	WDD07-2	55.9A	9	2	0.11	0.06	1	74.64	0.13	0.01	0.05	0.28	0	-	8.5	0	0	11.47	96.25
2017	WDD07-2	55.9A	9	3	0.18	0	1.2	77.61	0.4	0.01	0.17	0.42	0	-	5.18	0.04	0	11.97	97.18
2017	WDD07-2	55.9A	9	4	3.62	1.28	1.43	69.04	0.49	0.17	0.05	0.35	0.01	-	0.1	0.08	0.21	16.37	93.21
2017	WDD07-2	55.9A	9	5	6.05	1.95	2.15	62.72	0.2	0.05	0.03	0.26	0	-	0.35	0.02	0.54	19.46	93.79
2017	WDD07-2	55.9A	9	6	2.45	1.12	1.48	70.15	0.33	0.1	0	0.31	0	-	1.16	0	0.15	14.84	92.08
2017	WDD07-2	55.9A	9	7	4.1	1.64	1.92	66.87	0.2	0.05	0	0.25	0	-	0	0	0.22	16.96	92.21
2017	WDD07-2	55.9A	9	8	4	1.13	1.53	69.12	0.37	0.11	0.02	0.28	0	-	0.85	0.06	0.13	16.5	94.10
2017	WDD07-2	55.9A	7	1	0.47	0.09	1.21	77.93	0.36	0.17	0.15	0.64	0.03	-	1.9	0	0.02	12.34	95.32
2017	WDD07-2	55.9A	7	2	0.83	0.53	0.76	75.83	0.44	0.44	0.09	0.49	0	-	0.34	0	0.1	12.9	92.74
2017	WDD07-2	55.9A	7	3	0.67	0.07	1.13	77.94	0.5	0.19	0.15	0.82	0	-	1.39	0	0.02	12.6	95.49
2017	WDD07-2	55.9A	7	4	0.62	0.19	1.08	77.94	0.55	0.25	0.13	0.71	0	-	1.07	0.04	0.06	12.73	95.38
2017	WDD07-2	55.9A	7	5	0.48	0.08	1.1	79.47	0.57	0.16	0.2	0.72	0	-	1.32	0	0.09	12.67	96.85
2017	WDD07-2	55.9A	7	6	0.77	0.05	1.13	76.85	0.49	0.2	0.16	0.59	0.02	-	0.96	0	0.08	12.53	93.84
2017	WDD07-2	55.9A	6	1	0.34	0.13	1.22	76.06	0.48	0.09	0.12	0.66	0	-	5.57	0	0.01	12.29	96.96
2017	WDD07-2	55.9A	6	2	3.74	2.07	2.29	65.52	0.12	0.21	0	0.16	0	-	0.04	0.01	0.15	17.02	91.33
2017	WDD07-2	55.9A	6	3	0.79	0.27	1.25	75.45	0.47	0.1	0.09	0.32	0.04	-	7.19	0	0.05	12.98	98.99
2017	WDD07-2	55.9A	6	4	0.34	0.19	1.16	76.41	0.57	0.1	0.15	0.56	0	-	6	0	0.01	12.46	97.95
2017	WDD07-2	55.9A	5	1	2.48	0.55	1.21	72.51	0	0.14	0.03	0.29	0	-	0	0	0.19	14.1	91.51
2017	WDD07-2	55.9A	5	2	1.03	0.89	0.91	72.83	1.14	0.52	0	0.29	0	-	0	0.01	0.1	13.66	91.37
2017	WDD07-2	55.9A	5	3	5.73	2.61	2.75	60.53	0.14	0.01	0.04	0.07	0	-	0	0	0.27	19.5	91.64
2017	WDD07-2	55.9A	5	4	4.09	1.13	1.66	68.17	0.09	0.11	0.1	0.19	0.09	-	0	0	0.23	16.38	92.25
2017	WDD07-2	55.9A	5	5	3.28	0.92	1.47	69.16	0.23	0.12	0	0.27	0	-	0	0	0.2	15.27	90.92
2017	WDD10-151	29.4	4	1	0.34	0.42	0.82	77.69	0.07	0.39	0.23	0.95	0	-	1.54	0.03	0.19	12.57	95.24
2017	WDD10-151	29.4	4	2	0.07	0.78	0.7	77.23	0	0.4	0.22	0.85	0.01	-	1.8	0	0.08	12.45	94.58
2017	WDD10-151	29.4	4	3	0.54	1.19	0.89	71.01	0	0.29	0.06	0.96	0	-	1.45	0	0.15	12.72	89.26
2017	WDD10-151	29.4	2	1	0	0.73	0.8	75.15	0	0.16	0.12	1	0	-	0.94	0	0.01	11.84	90.74
2017	WDD10-151	29.4	2	2	0	0.76	0.77	76.01	0	0.12	0.17	0.9	0	-	0.97	0	0.06	11.99	91.75
2017	WDD10-151	29.4	2	3	0	0.73	0.76	76.46	0	0.16	0.14	1.1	0	-	0.95	0	0.01	12.04	92.34
2017	WDD10-151	29.4	2	4	0	0.79	0.91	75.28	0	0.14	0.11	1.08	0	-	0.98	0	0.05	12.03	91.37
2017	WDD10-151	29.4	1	1	0.92	0.74	0.97	74.81	0	0.21	0.19	1.29	0	-	1.55	0	0.04	13.13	93.87
2017	WDD10-151	29.4	1	3	0.09	0.91	1.19	76.65	0	0.21	0.13	1.11	0	-	1.2	0	0.08	12.68	94.25
2017	WDD08-106	10.6	8	1	0	0.92	0.9	74.26	0	0.12	0.13	1.52	0.02	-	2.37	0	0.06	12.3	92.59
2017	WDD08-106	10.6	8	2	0.31	0.85	0.89	74.49	0.03	0.12	0.23	1.56	0	-	2.36	0	0.23	12.8	93.88
2017	WDD08-106	10.6	8	3	0	0.96	0.95	75.18	0	0.16	0.1	1.55	0	-	2.34	0	0.07	12.52	93.83
2017	WDD08-106	10.6	8	4	0.02	0.9	0.9	75.25	0	0.09	0.18	1.62	0	-	2.35	0	0.07	12.46	93.84
2017	WDD08-106	10.6	103	1	0.01	0.73	0.9	76.35	0	0.08	0.23	1.44	0	-	2.71	0	0.06	12.35	94.85
2017	WDD08-106	10.6	104	1	0	0.72	0.87	71.94	0	0.31	0.16	1.9	0	-	2.82	0	0.03	11.93	90.68
2017	WDD08-106	10.6	104	2	0.08	0.52	1.06	76.36	0	0.19	0.26	1.47	0.07	-	3.24	0	0.04	12.35	95.63
2017	WDD08-106	10.6	104	3	0.02	0.44	0.93	76.68	0	0.21	0.32	1.57	0	-	3.26	0	0.01	12.17	95.62
2017	WDD08-106	10.6	105	1	0.71	0.93	0.81	70.08	0	0.19	0.04	1.69	0	-	2.22	0	0.53	12.98	90.17
2017	WDD08-106	10.6	106	1	0	0.96	0.95	75.43	0.04	0.09	0.18	1.69	0	-	2.55	0.06	0.04	12.61	94.61
2017	WDD08-106	10.6	106	2	0.01	0.93	0.97	75.39	0	0.17	0.1	1.6	0	-	2.45	0.03	0.08	12.58	94.32
2017	WDD08-106	10.6	26	1	0.01	0.56	0.97	75.76	0	0.14	0.29	1.77	0.12	-	3.51	0	0.01	12.28	95.41
2017	WDD08-106	10.6	26	2	0.16	0.61	1	74.56	0	0.15	0.15	1.73	0	-	3.32	0	0.03	12.29	94.00
2017	WDD08-106	10.6	26	3	0.01	0.92	0.98	75.36	0	0.12	0.19	1.62	0	-	2.54	0	0.07	12.56	94.37
2017	WDD08-106	10.6	101	1	0	0.87	0.98	74.91	0	0.12	0.15	1.61	0	-	2.88	0.01	0.09	12.45	94.08
2017	WDD08-106	10.6	101	2	0.01	0.92	0.89	75.13	0.02	0.12	0.12	1.42	0.02	-	2.45	0	0.08	12.43	93.60
2017	WDD08-106	10.6	101	3	0	0.94	0.96	74.92	0	0.12	0.23	1.55	0	-	2.46	0.02	0.05	12.47	93.72
2017	WDD08-106	10.6	102	1	0	0.91	0.94	74.7	0	0.16	0.19	1.57	0	-	2.23	0.05	0.05	12.4	93.19
2017	WDD08-106	10.6	102	2	1.66	0.93	0.83	68.82	0	0.15	0.14	2.25	0	-	2.43	0	1.55	15	93.76
2017	WDD08-106	10.6	102	3	0.5	0.89	1.04	72.81	0	0.11	0.11	1.73	0	-	2.13	0	0.37	12.98	92.65
2017	WDD07-2	73.5B	6	1	1.69	0.29	1.93	74.04	0	0.35	0.12	2.72	0	-	0.12	0	0.25	14.24	95.76
2017	WDD07-2	73.5B	4	1	2.23	0.11	1.61	70.27	0	0.38	0.17	4	0.01	-	0.37	0.04	0.48	14.61	94.29
2017	WDD07-2	73.5B	2	1	3.05	0.1	1.34	72.3	0	0.25	0.31	2.01	0	-	1.29	0.07	0.49	15.18	96.38
2017	WDD07-2	73.5B	2	2	1.58	0.13	1.15	76.07	0	0.21	0.27	2.4	0	-	1.25	0	0.17	13.77	97.00
2017	WDD07-2	73.5B	2	3	1.52	0.11	1.19	76.9	0	0.28	0.31	2.3	0	-	1.3	0	0.23	13.87	98.01
2017	WDD07-2	73.5B	103	1	1.74	0.05	1.11	75.32	0	0.33	0.3	2.11	0	-	1.52	0	0.14	13.71	96.33
2017	WDD07-2	73.5B	103	2	1.36	0.21	1.66	74.32	0	0.43	0.24	2.48	0.1	-	1.77	0	0.18	13.8	96.55
2017	WDD07-2	73.5B	103	3	1.68	0.03	1.33	76.36	0.01	0.33	0.38	1.73	0	-	1.64	0	0.1	13.74	97.34
2017	WDD07-2	73.5B	103	4	1.81	0	1.36	75.24	0.13	0.81	0.29	1.17	0.03	-	1.52	0.01	0.11	13.84	96.34
2017	WDD07-2	73.5B	103	5	1.96	0	1.16	74.14	0.08	0.7	0.27	1.48	0.01	-	1.33	0	0.12	13.75	95.00
2017	WDD07-2	73.5B	102	1	1.4	0.15	1.22	75.01	0.72	0.55	0.17	2.02	0.15	-	0.54	0	0.14	13.95	96.02
2017	WDD07-2	73.5B	102	2	0.58	0.05	0.95	78.73	0.71	0.37	0.25	1.59	0	-	1.68	0	0.07	13.05	98.03
2017	WDD07-2	73.5B	102	3	0.76	0.02	0.91	77.71	0.75	0.39	0.24	1.51	0	-	1.58	0	0.07	13.08	97.01
2017	WDD07-2	73.5B	102	4	2.84	0.26	1.3	67.31	0.58	0.58	0.05	3.4	0	-	1.97	0.01	1.03	15.86	95.18
2017	WDD07-2	73.5B	104	1	1.12	0.09	1.2	77.25	0	0.57	0.34	1.97	0.04	-	1.49	0.03	0.13	13.44	97.68
2017	WDD07-2	73.5B	104	2	1.21	0.04	1.53	76.61	0	0.57	0.05	2.44	0	-	1.11	0	0.08	13.49	97.15
2017	WDD07-2	73.5B	105	1	2.46	0.17	1.35	73.13	0	0.26	0.11	2.39	0	-	0.75	0	0.29	14.54	95.45
2017	WDD07-2	73.5B	105	2	2.27	0.13	1.59	72.61	0.01	0.4	0.14	2.4	0.08	-	1.17	0.01	0.32	14.48	95.60
2017	WDD07-2	73.5B	106	1	1.01	0.07	1.48	76.22	0	0.46	0.17	2.27	0	-	0.93	0	0.13	13.19	95.94
2017	WDD07-2	73.5B	106	2	1.06	0.08	1.42	77.18	0	0.41	0.38	1.95	0	-	1.33	0	0.1	13.31	97.21
2017	WDD07-2	73.5B	106	3	1.04	0.14	1.5	77.19	0	0.32	0.21	2.26	0	-	0.93	0	0.08	13.34	97.01
2017	WDD07-2	73.5B	106	4	1.31	0.1	1.66	75.57	0	0.44	0.13	2.92	0	-	0.28	0.06	0.23	13.77	96.46
2017	WDD07-2	73.5B	107	1	1.42	0.08	1.81	75.57	0	0.01	0.19	2.75	0.05	-	1.37	0	0.09	13.65	96.97
2017	WDD07-2	73.5B	107	2	1.53	0.08	1.89	75.78	0	0.06	0.23	2.74	0	-	0.72	0	0.11	13.82	96.95
2017	WDD07-2	73.5B	107	3	1.44	0.11	1.88	74.34	0	0.34	0.03	2.62	0	-	0.16	0	0.17	13.6	94.68
2017	WDD07-2	73.5B	107	4	1.81	0.11	1.76	73.54	0	0.36	0.12	2.6	0	-	0.91	0	0.3	14.08	95.59

Year	Drillhole #	Depth (m)	Circle #	Analysis #	Si (wt%)	P (wt%)	Ca (wt%)	U (wt%)	Ti (wt%)	V (wt%)	Mn (wt%)	Fe (wt%)	Zr (wt%)	Y (wt%)	Pb (wt%)	Th (wt%)	Al (wt%)	O (wt%)	Total (wt%)
2017	WDD07-2	73.5B	107	5	2.1	0.15	1.57	74.69	0	0.01	0.19	2.32	0.03	-	0.74	0	0.3	14.32	96.44
2017	WDD07-2	73.5B	107	6	2.08	0.12	1.59	74.57	0	0	0.3	2.11	0.11	-	1.37	0	0.2	14.21	96.66
2017	WDD07-2	73.5B	107	7	1.82	0.13	1.82	73.85	0	0.27	0.09	2.62	0	-	0.21	0	0.28	14.07	95.17
2017	WDD07-2	55.9B	3	1	0.79	0.25	1.04	75.96	0.68	0.15	0.06	0.46	0.13	-	2.89	0	0.06	12.85	95.33
2017	WDD07-2	55.9B	3	2	1.57	0.67	1.08	73.29	0.52	0.11	0.11	0.42	0	-	3.81	0	0.11	13.87	95.56
2017	WDD07-2	55.9B	4	1	4.42	2.07	2.32	64.95	0.05	0.1	0	0.17	0.13	-	0.1	0	0.22	17.74	92.25
2017	WDD07-2	55.9B	4	2	0.61	0.14	1.27	77.86	0.47	0.17	0.17	0.58	0.04	-	1.51	0	0.04	12.63	95.50
2017	WDD07-2	55.9B	4	3	3.55	2.24	1.86	66.03	1.56	0.14	0.04	0.19	0	-	0	0	0.13	17.85	93.60
2017	WDD07-2	55.9B	4	4	0.8	0.09	1.03	77.58	0.67	0.17	0.1	0.59	0	-	0.96	0.05	0.07	12.75	94.89
2017	WDD07-2	55.9B	4	5	0.79	0.68	1.13	76.59	0.51	0.29	0.06	0.57	0	-	0.89	0	0.24	13.46	95.19
2017	WDD07-2	55.9B	4	6	0.53	0.2	1.17	78.49	0.52	0.15	0.14	0.6	0.03	-	1.79	0.01	0.09	12.73	96.44
2017	WDD07-2	55.9B	4	7	0.55	0.07	1.51	78.54	0.27	0.1	0.13	0.48	0	-	2.22	0	0.03	12.47	96.35
2017	WDD07-2	55.9B	4	8	0.7	0.94	1.04	75.97	0.65	0.29	0.03	0.49	0	-	0.17	0	0.21	13.56	94.05
2017	JDD08-003	74.4A	10	1	0.14	0.35	2.05	74.2	0	0.49	0.25	0.57	0.09	-	0.16	0	0.01	11.93	90.24
2017	JDD08-003	74.4A	10	2	0.42	0.33	2.02	74.32	0.01	0.52	0.24	0.83	0	-	0.13	0	0.14	12.39	91.35
2017	JDD08-003	74.4A	10	3	0.42	0.2	2.04	71.04	0	0.49	0.38	1.04	0.08	-	4.2	0	0.19	12.26	92.35
2017	JDD08-003	74.4A	10	4	0.23	0.25	2.13	75.17	0	0.5	0.39	0.93	0	-	0.24	0	0.03	12.2	92.07
2017	JDD08-003	74.4A	10	5	0.26	0.1	2.78	74.67	0	0.43	0.63	1.21	0	-	0.16	0	0.03	12.34	92.61
2017	JDD08-003	74.4A	10	6	0.41	0.37	1.11	72.62	0.32	0.32	0.15	0.44	0.26	-	0	0	0.06	11.83	87.89
2017	JDD08-003	74.4A	10	7	0.31	0.06	2.75	75.71	0.01	0.44	0.54	1.27	0.15	-	0.27	0	0	12.52	94.04
2017	JDD08-003	74.4A	10	8	0.14	0.16	2.26	73.28	0.09	0.49	0.43	0.92	0.1	-	2.02	0.01	0	12	91.91
2018	JDD08-003	74.4B	18	1	0.57	0.54	1.91	71.61	0.6	0.53	0.22	0.68	-	0	0.04	0.2	0.32	12.95	90.16
2018	JDD08-003	74.4B	18	2	4.88	0.37	1.72	60.4	0.45	0.6	0.33	2.19	-	0	0	0.14	2.59	18.48	92.16
2018	JDD08-003	74.4B	18	3	1.75	0.42	1.83	70.48	0	0.72	0.25	1.12	-	0	0.12	0.13	0.87	14.28	91.98
2018	JDD08-003	74.4B	18	4	1.21	0.49	1.65	71.72	0.8	0.54	0.27	0.96	-	0	0	0.08	0.5	13.92	92.15
2018	JDD08-003	74.4B	18	5	0.27	0.5	1.52	71.69	0.83	0.33	0.14	0.35	-	0	0	0	0.03	12.07	87.73
2018	JDD08-003	74.4B	18	6	0.21	0.55	1.41	71.56	0.83	0.52	0.16	0.95	-	0	0.03	0	0	12.26	88.48
2018	JDD08-003	74.4B	18	7	0.54	0.51	1.1	70.76	0.78	0.45	0.21	0.69	-	0	2.43	0	0.2	12.59	90.27
2018	JDD08-003	74.4B	18	8	0.58	0.55	1.58	71.59	0.79	0.5	0.05	0.67	-	0	0.03	0	0.15	12.72	89.20
2018	JDD08-003	74.4B	18	9	0.75	0.42	1.82	74.34	0.05	0.63	0.28	0.74	-	0.01	0.1	0.07	0.29	13.02	92.52
2018	JDD08-003	74.4B	18	10	0.3	0.06	2.32	72.92	0.05	0.64	0.6	0.9	-	0	0.24	0.43	0.02	12.02	90.51
2018	JDD08-003	74.4B	18	11	0.24	0.51	1.62	72.5	0.77	0.52	0.18	0.42	-	0	0	0	0.01	12.26	89.03
2018	JDD08-003	74.4B	18	12	0.36	0.1	2.21	73.4	0.04	0.66	0.53	1.03	-	0.01	0.18	0	0.04	12.13	90.69
2018	JDD08-003	74.4B	18	13	0.26	0.48	1.63	73.08	0.77	0.58	0.18	0.39	-	0	0	0	0	12.34	89.72
2018	JDD08-003	74.4B	18	14	0.23	0.53	1.46	73.65	0.73	0.44	0.19	0.35	-	0	0	0	0.02	12.3	89.91
2018	JDD08-003	74.4B	18	15	0.25	0.54	1.49	71.51	0.77	0.44	0.2	0.46	-	0	0.02	0	0.01	12.12	87.81
2018	JDD08-003	74.4B	8	1	5.25	0.28	0.93	58.47	0	0.77	0.16	2.33	-	0	0.26	0	2.75	18.12	89.31
2018	JDD08-003	74.4B	8	8	1.73	0.32	1.46	70.66	0	0.87	0.38	1.23	-	0	0.15	0	0.96	14.2	91.96
2018	JDD08-003	74.4B	8	13	4.46	2.24	1.8	55.68	0.2	0.54	0.05	1.74	-	1.83	0.12	0.28	1.1	18.6	88.62
2018	WDD07-2	55.9A	9	1	4.73	1.68	1.9	62.78	0.14	0.12	0	0.07	-	0.05	0.12	0.09	0.22	17.16	89.06
2018	WDD07-2	55.9A	9	2	4.04	1.25	1.51	66.01	0.49	0.13	0.02	0.3	-	0	0.26	0	0.23	16.39	90.63
2018	WDD07-2	55.9A	9	3	4.99	1.92	2.2	61.7	0.05	0.17	0.04	0.14	-	0	1.24	0	0.19	17.77	90.42
2018	WDD07-2	55.9A	9	4	6.07	2.22	2.26	61.18	0.17	0.17	0.07	0	-	0.11	0.38	0	0.26	19.42	92.31
2018	WDD07-2	55.9A	9	5	2.56	0.31	0.8	70.97	0.61	0.14	0.03	0.27	-	0.01	0.71	0	0.18	13.95	90.55
2018	WDD07-2	55.9A	9	6	0.14	0	1.14	75.44	0.45	0.17	0.11	0.34	-	0.15	5.91	0	0	11.76	95.62
2018	WDD07-2	55.9A	9	7	0.35	0.02	0.9	75.24	0.45	0.17	0.05	0.42	-	0.07	5.08	0.06	0.01	11.84	94.67
2018	WDD07-2	55.9A	9	8	0.09	0	1.01	73.66	0.3	0	0.11	0.31	-	0.2	6.88	0.39	0	11.37	94.31
2018	WDD07-2	55.9A	9	9	4.4	2.19	2.09	62.98	0.2	0.06	0	0.13	-	0.07	1.05	0.21	0.16	17.61	91.15
2018	WDD07-2	55.9A	9	10	0.07	0.01	1.14	73.71	0.21	0	0.31	0.33	-	0.12	6.83	0.03	0.01	11.36	94.14
2018	WDD07-2	55.9A	9	11	2.84	0.74	1.21	67.58	0.29	0.1	0.06	0.4	-	0.05	2.8	0	0.13	14.48	90.69
2018	WDD07-2	55.9A	9	12	4.48	2.02	2.02	61.61	0.21	0.13	0.04	0.2	-	0.12	2.11	0	0.2	17.44	90.57
2018	WDD07-2	55.9A	9	13	0.14	0.03	1.13	74.97	0.52	0.06	0.07	0.33	-	0.09	5.39	0.27	0	11.7	94.71
2018	WDD07-2	55.9A	9	14	4.33	1.24	1.44	65.74	0.84	0.04	0.04	0.09	-	0.08	0.03	0.23	0.2	16.8	91.10
2018	WDD07-2	55.9A	9	15	6.13	2.5	2.57	60.73	0.04	0.13	0	0	-	0.21	0.28	0.06	0.24	19.79	92.68
2018	WDD07-2	55.9A	9	16	5.28	3.03	2.98	60.14	0.09	0.08	0	0.01	-	0.22	0.6	0.56	0.13	19.6	92.73
2018	WDD07-2	55.9A	9	17	3.45	1.42	1.61	57.91	0.37	0.08	0	0.11	-	0.14	9.88	0	0.15	15.45	90.58
2018	WDD07-2	55.9A	9	18	0.58	0.14	1.05	73.87	0.56	0	0.09	0.39	-	0.03	4.7	0	0	12.09	93.51
2018	WDD07-2	73.5B	103	2	1.78	0.08	1.06	73.63	0	0.26	0.13	2.38	-	0	0.74	0	0.14	13.49	93.70
2018	WDD07-2	73.5B	103	3	2.09	0.11	1.02	72.98	0.02	0.62	0.13	2.14	-	0	1.13	0	0.24	14	94.47
2018	WDD07-2	73.5B	103	4	1.94	0.07	1.03	72.22	0	0.24	0.36	1.96	-	0	3.3	0.08	0.31	13.75	95.28
2018	WDD07-2	73.5B	103	5	2.01	0.03	1	73.54	0	0.84	0.29	1.59	-	0	1.39	0.03	0.15	13.8	94.66
2018	WDD07-2	73.5B	103	6	2.25	0.09	1.27	72.97	0	0.29	0.29	1.49	-	0	1.55	0	0.17	13.92	94.29
2018	WDD07-2	73.5B	103	7	1.56	0.11	1.26	72.7	0.01	0.74	0.07	2.35	-	0	0.96	0	0.18	13.48	93.42
2018	WDD07-2	73.5B	103	8	1.45	0.09	1.44	73.19	0	0.57	0.05	2.21	-	0	0.39	0	0.08	13.21	92.70
2018	WDD07-2	73.5B	103	9	1.73	0.09	1.1	73.74	0	0.48	0.13	2.19	-	0.01	0.75	0	0.16	13.53	93.91
2018	WDD07-2	73.5B	103	10	2.7	0.13	1.38	65.42	0	0.55	0.04	5.1	-	0	1.13	0.03	0.71	15.04	92.23
2018	WDD07-2	73.5B	103	11	1.7	0.12	1.41	70.19	0	0.45	0.19	3.22	-	0	0.36	0.03	0.26	13.54	91.48
2018	WDD07-2	73.5B	4	4	1.74	0.06	1.44	72.73	0	0.59	0.11	2.29	-	0	0.29	0	0.18	13.56	92.99
2018	WDD07-2	73.5B	104	18	4.28	0.13	1.19	61.35	0	0.42	0	5.86	-	0	0.48	0	1	16.57	91.28
2018	WDD07-2	73.5B	104	17	3	0.04	1.44	67.76	0	0.4	0.09	3.63	-	0	0.03	0	0.45	14.82	91.67
2018	WDD07-2	73.5B	104	8	1.3	0.05	1.08	75.55	0	0.49	0.18	2.27	-	0	0.93	0	0.14	13.27	95.25
2018	WDD07-2	73.5B	104	14	2.52	0.03	1.46	67.53	0.08	0.57	0.06	4.39	-	0	0.89	0.02	0.45	14.64	92.65
2018	WDD07-2	73.5B	104	11	1.35	0.08	1.6	72.28	0.08	0.76	0.11	2.55	-	0	0.39	0.18	0.11	13.32	92.80
2018	WDD07-2	73.5B	104	12	3.63	0.05	1.29	64.88	0	0.23	0.05	5.07	-	0	0	0	0.84	15.75	91.78
2018	WDD07-2	73.5B	104	13	4.21	0.08	1.29	61.87	0	0.51	0.04	5.47	-	0	0.71	0	0.83	16.34	91.34
2018	WDD07-2	73.5B	105	9	1.12	0.23	1.91	72.75	0	0.55	0.15	2.43	-	0	0.09	0.17	0.09	13.22	92.72
2018	WDD07-2	73.5B	105	4	2.12	0.11	1.5	71.73	0	0.55	0.09	2.22	-	0	0.29	0	0.29	14	92.90
2018	WDD07-2	73.5B	6	1	4.02	0.07	1.72	63.04	0	0.27	0.03	5.27	-	0	0	0	0.9	16.27	91.58
2018	WDD07-2	73.5B	6	4	3.47	0.33	1.76	63.59	0	0.29	0.13	4.73	-	0.04	0.09	0	1.07	16.11	91.59
2018	WDD07-2	73.5B	6	8	4.33	0.14	1.41	59.13	0	0.28	0.16	6.52	-	0	0.13	0.12	1.64	17.16	91.02

***Supplementary Table 3-2**: Minor and trace elements composition on uraninites from the Westmoreland area obtained by LA-ICP-MS.*

Drillhole #	Depth (m)	Circle #	Analysis #	B (ppm)	Ti (ppm)	V (ppm)	Cr (ppm)	Mn (ppm)	Co (ppm)	Ni (ppm)	Cu (ppm)	Zn (ppm)	Ga (ppm)	As (ppm)	Sr (ppm)	Y (ppm)	Zr (ppm)	Nb (ppm)	Mo (ppm)	Sb (ppm)	Ba (ppm)
WDD07-2	55.9A	9	1	83	3340	469	< 8.8	1598	0.75	< 17	< 2.9	< 2.8	1.46	4380	17.9	2430	140	117.8	189	1905	84
WDD07-2	55.9A	9	1'	127	3780	562	< 10	2026	< 0.31	< 20	< 3.4	< 3.2	0.87	4660	14.7	2211	78.1	135.6	108.5	2280	32.6
WDD07-2	55.9A	9	2	84	4020	567	< 7.3	1037	3.6	< 17	< 3	3.9	4.5	3850	21.4	1961	378	132.3	50.2	1066	169
WDD07-2	55.9A	9	2'	47	1426	1496	< 10	222	5.2	< 25	< 4.2	< 3	22.3	402	24.4	2290	108	109.8	4.1	90	856
WDD07-2	55.9A	7	1	278	5380	8930	54	386	186	316	1096	36	171	1020	234	36.1	762	145.1	31.7	166	6750
WDD07-2	55.9A	7	1'	1090	5380	15400	< 74	457	415	700	1850	86	393	2940	283	67.7	1180	234	90	265	12700
WDD07-2	55.9A	9	11	90.7	3540	680	< 5.1	914	6.8	< 140	< 2.7	< 2.8	14.1	2970	22.3	2274	374	139	56.4	1016	257
WDD07-2	55.9A	9	11'	70	2360	1594	< 8.8	194	173	< 250	90	20	36.5	3250	28.6	3300	426	126.9	11.9	338	669
WDD07-2	55.9A	9	12	111.1	3600	959	< 5.6	908	31	< 160	< 3.1	5.2	17.1	3570	22.2	2362	381	129.5	64.3	1019	318
WDD07-2	55.9A	9	12'	90.4	4100	911	< 6.2	847	156	< 170	22.3	19.5	18.9	5130	22.7	2223	409	137.9	39.8	1112	296
WDD07-2	55.9A	9	13	94.2	3500	820	< 5.6	1079	0.85	< 110	< 2.8	< 2.8	18.3	2770	20.5	2420	223	126.1	80.1	1370	328
WDD07-2	55.9A	9	13'	76.9	2470	662	< 5.9	1217	2.94	< 140	8.1	< 4.8	13.2	2490	19.4	3378	68.3	78.2	170	1794	227
WDD07-2	55.9A	9	14	85.1	3778	670	< 5.2	906	11.1	< 120	4.2	< 4.2	9.9	3370	22	2109	302	132.5	37.5	1043	215
WDD07-2	55.9A	9	14'	116.8	3310	555	< 5.1	1364	2.43	< 120	< 2.8	< 4.1	7.2	3130	15.7	2944	87.4	123.4	69.6	1756	132.7
WDD07-2	55.9A	9	15	108	3110	1164	< 6.5	704	109	145	113	22.9	35.6	4450	36.2	3040	371	102.9	51.8	904	710
WDD07-2	55.9A	9	15'	90	4870	560	< 12	933	8.9	< 250	< 7.3	< 7.5	9.6	3760	25.1	2020	471	147.8	41	1096	187
WDD07-2	55.9B	3	1	65	3560	1050	< 11	526	80	238	< 4	< 5.6	17.5	3760	30.6	2660	1124	174.2	< 0.88	501	705
WDD07-2	55.9B	3	1'	87	7980	685	< 8.2	1164	< 0.47	< 26	< 3.1	< 4.4	9	3430	22.9	1106	527	338	< 0.69	1352	338
WDD07-2	55.9B	4	1	120	3440	1046	< 15	2046	< 0.59	< 39	< 5.9	< 4.5	4.55	4240	19.6	756	90	64.6	2.2	2050	183
WDD07-2	55.9B	4	1'	78	3600	1637	< 14	1334	< 0.55	< 38	< 5.4	< 4.2	28.6	2320	24.7	369	40	53.5	< 1.7	1048	1036
WDD07-2	55.9B	Minimum value		47	1426	469	54	194	0.75	145	4.2	3.9	0.87	402	14.7	36.1	40	53.5	2.2	90	32.6
		Maximum value		1090	7980	15400	54	2046	415	700	1850	86	393	5130	283	3378	1180	338	189	2280	12700
WDD08-106	10.6	104	1	< 3.1	128	3820	14.4	2573	350	< 6.7	8.9	13.5	1.98	10120	0.428	167	1.42	1.56	11.5	1066	69.4
WDD08-106	10.6	104	1'	< 2.9	21.2	1418	11.2	1905	18.8	< 6.4	19.6	16	2.25	13620	0.59	222.8	1.85	2.3	4.14	875	72.3
WDD08-106	10.6	106	1	< 4.6	670	1475	16.6	1805	21.7	< 7	5.3	22.2	2.49	12800	0.57	211.2	46.1	2.7	11.8	809	77.6
WDD08-106	10.6	106	1'	< 5.1	118	1519	12.5	1828	24.3	< 7.9	< 1.4	32.9	3.51	13130	0.96	209.4	20.2	1.78	12.4	845	73.8
WDD08-106	10.6	Minimum value		0	21.2	1418	11.2	1805	18.8	0	5.3	13.5	1.98	10120	0.428	167	1.42	1.56	4.14	809	69.4
		Maximum value		0	670	3820	16.6	2573	350	0	19.6	32.9	3.51	13620	0.96	222.8	46.1	2.7	12.4	1066	77.6
JDD08-003	74.4B		1	< 18	719	6680	32	4290	< 1.4	340	< 9.3	< 10	21.4	9360	242	608	928	30.8	283	622	472
JDD08-003	74.4B		1'	73	1070	7560	49	3360	8.3	< 350	< 8	17	25.3	9820	206	826	895	40.7	411	539	640
JDD08-003	74.4B		2	40	436	6640	18	4240	3.9	< 520	< 12	< 10	16.6	9370	301	766	801	29	270	652	487
JDD08-003	74.4B		2'	23.8	664	6740	41	3900	< 1.2	< 260	< 5.9	< 5.2	17.3	9420	234	568	1032	31.5	236	593	472
JDD08-003	74.4B		3	206	166	9420	130	2700	174	< 710	< 15	< 19	45.5	9970	95.7	879	185	8.1	467	567	826
JDD08-003	74.4B		3'	100	108	7520	111	2730	18.6	< 410	< 8.5	< 11	25.9	9750	130	952	201	7.5	493	534	591
JDD08-003	74.4B		4	108	3440	8180	80	1530	854	1860	< 16	< 25	25	5890	133	20750	624	38.8	220	288	481
JDD08-003	74.4B		4'	63	4090	7200	95	1689	544	1650	< 14	< 21	23.5	6440	153	17060	571	53.4	252	340	436
JDD08-003	74.4B		5	72	75	7660	119	2930	250	< 370	< 7.9	< 8.2	23.4	9430	97.2	933	178	5.6	434	585	528
JDD08-003	74.4B		5'	722	137	16510	268	3760	746	3000	48	83	131	9940	172	945	337	8.8	447	733	2280
JDD08-003	74.4B		6	73	328	7300	87	3280	94	< 380	< 9.2	< 6	20.3	9540	165	909	485	21.5	392	572	556
JDD08-003	74.4B		6'	43.7	741	6440	61	3120	31.9	< 300	< 7.4	< 4.8	22.6	8780	195	1039	447	29.8	400	548	549
JDD08-003	74.4B		7	87	158	7460	119	3480	155.5	< 390	< 9.6	< 6.4	20.9	8810	122	1006	278	10.7	405	618	532
JDD08-003	74.4B		7'	33.9	164	6700	79	3480	45.6	< 250	< 6.2	5.2	16.1	8750	158	802	320	8.6	352	578	477

Drillhole #	Depth (m)	Circle #	Analysis #	B (ppm)	Ti (ppm)	V (ppm)	Cr (ppm)	Mn (ppm)	Co (ppm)	Ni (ppm)	Cu (ppm)	Zn (ppm)	Ga (ppm)	As (ppm)	Sr (ppm)	Y (ppm)	Zr (ppm)	Nb (ppm)	Mo (ppm)	Sb (ppm)	Ba (ppm)
JDD08-003	74.4B		8'	38.7	4260	6010	61	2410	3.2	< 320	< 7.9	< 7.5	19.7	9220	360	3060	737	38.9	362	474	544
JDD08-003	74.4B		8'	44.4	2610	6240	55	2580	14.7	< 270	< 6.8	< 6.4	15.3	8790	257	4970	428	30.3	397	499	535
JDD08-003	74.4B		9'	38.2	1880	6180	40	2500	6.2	< 280	< 7.1	8	18.5	8720	152	3760	691	19	416	518	442
JDD08-003	74.4B		9	63	1530	6680	62	3320	51.5	390	< 9.9	< 9.3	19.8	9190	223	981	303	45.4	396	579	527
JDD08-003	74.4B		10	31.9	1670	6120	55	4620	4.5	< 240	< 7.4	< 6.9	14.6	9590	282	453	1179	60.2	145	663	521
JDD08-003	74.4B		10'	598	3900	10940	175	2870	152	< 580	< 18	< 17	77	9580	165	1103	778	58.1	379	504	1580
JDD08-003	74.4B		11	20	1290	6050	37	2820	4.4	< 340	< 11	< 9.6	15.8	8050	295	1790	978	30.2	428	517	475
JDD08-003	74.4B		11'	36	1260	6520	56	2400	23.9	< 370	< 12	< 10	13.1	6360	264	9420	861	27.4	363	454	395
JDD08-003	74.4B		12'	124	1850	6630	64	3840	117	< 1300	< 49	< 27	20.3	9500	830	2870	720	25.3	405	516	609
JDD08-003	74.4B		12'	37.5	1291	6110	47	2620	62	< 230	< 9.1	< 5	15.5	8720	264	3430	736	16.8	434	529	515
JDD08-003	74.4B		13	38.2	4720	5570	69	3112	1120	610	< 5.7	< 8.1	16.6	9890	254	701	3660	61.8	371	521	554
JDD08-003	74.4B		13'	38.5	5400	5180	94	3510	340	< 240	< 5.4	< 7.7	17.2	10130	284	608	4700	68.5	279	542	518
JDD08-003	74.4B		14	20	7830	4550	67	2360	16600	7600	< 11	< 12	17.7	12290	281	618	6890	102	332	766	537
JDD08-003	74.4B		14'	22	8530	4270	117	2270	64100	19300	< 17	< 17	10.4	13500	137	563	7640	118.8	297	1099	315
JDD08-003	74.4B		15	< 53	9530	3830	87	2090	69400	23800	< 49	< 42	< 5.4	17490	118	550	8680	137	399	1410	227
JDD08-003	74.4B		15'	30.5	6380	4720	72	2490	7.8	< 260	< 9.1	< 7.7	15.6	8910	258	645	5150	77.1	365	444	542
JDD08-003	74.4B		16	20.6	1150	5410	32	5500	2.1	390	< 5.9	< 5.6	8.9	6640	214	654	1908	34.8	54.4	670	386
JDD08-003	74.4B		16'	23.6	3010	5370	50	4710	< 1.1	< 190	< 5.8	< 5.5	11.8	8370	276	552	2490	55.1	181	639	438
JDD08-003	74.4B		17	94	585	6530	45	3350	10	< 230	< 7.5	11	28.7	8490	238	1297	566	31.1	435	529	754
JDD08-003	74.4B		17'	38.3	939	6190	48	3010	3	300	< 6.6	< 6.4	18.8	9030	205	953	484	42.9	428	503	537
JDD08-003	74.4B		18	< 29	500	6520	< 31	2640	< 3.9	< 620	< 23	< 23	11.1	5990	243	13200	394	52	269	417	296
JDD08-003	74.4B		18'	19	352	6470	29	2900	2.9	< 380	< 14	< 9.8	9	7000	276	10100	890	37.2	267	442	401
JDD08-003	74.4B		19	106	1390	6800	37	3120	30.9	< 290	< 11	17	22.6	8710	158.7	4400	177	73.5	406	549	532
JDD08-003	74.4B		19'	< 26	740	6200	< 26	2850	< 4.3	< 590	< 21	< 23	12.9	5750	227	12400	300	59.2	192	402	302
JDD08-003	74.4B		20	35	860	6810	39	3410	15.7	< 230	< 8.1	< 9.1	14.1	9480	239	1055	553	43.8	419	534	520
JDD08-003	74.4B		20'	27.5	456	4710	20.8	5540	< 1.5	< 200	< 7	< 7.9	10	7080	150	325	83	83.6	102	799	335
JDD08-003	74.4B	Minimum value		19	75	3830	18	1530	2.1	300	48	5.2	8.9	5750	95.7	325	83	5.6	54.4	288	227
		Maximum value		722	9530	16510	268	5540	69400	23800	48	83	131	17490	830	20750	8680	137	493	1410	2280
WDD10-151	29.4	2	3	< 10	180	2172	< 7.9	1358	1445	857	8.1	< 7	3.4	25800	1.24	267	12.3	11.1	77	480	101
WDD10-151	29.4	2	3'	< 9.9	133	2280	< 7.6	1574	324	239	< 6.3	< 6.7	7	19500	1.86	221	12.8	15.3	81	512	137
WDD10-151	29.4	2	4'	< 9.1	126	2336	< 5.5	1557	425	236	< 7.4	5.6	5	20820	1.06	202.4	16.5	14.4	71.2	520	118
WDD10-151	29.4	2	4	< 12	230	2240	< 7.2	1586	617	332	< 9.8	7.5	5.3	18910	1.15	207	15	16.4	70	509	150
WDD10-151	29.4	2	5	< 9.3	111	2260	< 5.6	1547	492	345	< 7.6	5.7	4.6	19300	1.1	206	12.8	12.8	66.3	504	147
WDD10-151	29.4	2	5'	< 9.1	97	2370	< 5.5	1531	510	415	< 7.5	7.1	5.1	18300	0.82	209	20.8	10	61.3	479	147
WDD10-151	29.4	2	6	< 16	116	2350	< 17	1561	500	351	< 8	0.12	5.1	20700	1.89	209	13.5	13.7	67.4	542	164
WDD10-151	29.4	2	6'	< 18	36	2190	< 19	1405	1220	930	42.9	0.77	8.2	19610	1.66	232	26.3	8.2	62.2	477	172
WDD10-151	29.4	4	3	< 8.2	261	4150	18.3	2170	3.1	< 110	59	17.8	8	15860	0.9	48.2	3.3	7.7	67.6	587	157
WDD10-151	29.4	4	3'	< 15	169	4060	< 18	1694	26.6	< 200	2740	16	9.9	17300	< 0.87	93	7.1	8.7	83	732	149
WDD10-151	29.4	4	4	13.7	678	4080	19	808	33	< 160	4210	45	10.5	15800	3.7	311	36.8	16.5	102	637	157
WDD10-151	29.4	4	4'	< 13	109	3840	18	1520	16.1	< 160	1660	25	9.6	14300	2.9	296	4.9	9.2	70	555	152
WDD10-151	29.4	4	5	< 11	89	4330	< 9.4	1770	1620	590	34700	35	7.3	17100	3.9	67.1	3.4	6.3	80	683	127
WDD10-151	29.4	4	5'	< 9.2	87	3920	8.6	1400	18.8	< 180	641	21	9.2	14300	1.59	245	8.3	8.1	76	516	138
WDD10-151	29.4	4	6	< 19	90	3960	21	1241	25.2	< 340	30000	21	10.5	14820	2.4	223	11.9	8.3	60	594	191

Drillhole #	Depth (m)	Circle #	Analysis #	B (ppm)	Ti (ppm)	V (ppm)	Cr (ppm)	Mn (ppm)	Co (ppm)	Ni (ppm)	Cu (ppm)	Zn (ppm)	Ga (ppm)	As (ppm)	Sr (ppm)	Y (ppm)	Zr (ppm)	Nb (ppm)	Mo (ppm)	Sb (ppm)	Ba (ppm)
WDD10-151	29.4	4	6'	< 9.9	101	4470	< 9.1	1860	10.1	< 180	326	29	8.1	16000	0.95	61.1	2.8	8.4	70	605	142
WDD10-151	29.4	4	2	5.2	343	4470	14.7	2062	2.69	< 6.1	89	17.8	5.55	16170	0.93	49.7	3.33	9.15	71.7	610	149.4
WDD10-151	29.4	4	2'	6.6	116	4440	8	1917	42.7	45	860	19.6	6.06	16870	1.48	68.4	2.66	7.9	81.4	639	142.7
WDD10-151	29.4	2	1	< 2.6	152	2230	< 2.7	1492	479	332	3.05	6.6	3.99	19100	1.85	197	13.1	16.9	70.3	508	150.9
WDD10-151	29.4	2	1'	< 2.6	132	2277	2.7	1474	532	420	< 1	4.8	3.81	20460	0.65	201.7	17.7	13.57	72.3	507	146.2
WDD10-151	29.4	4	1	< 7.6	302	4420	12.7	2041	7.1	< 12	251	22.8	5.32	20500	1.24	66.4	4.28	9.26	83.5	676	149
WDD10-151	29.4	4	1'	10.6	170	4260	13.9	1776	10.4	< 13	465	26.3	8.2	17250	1.4	176	4.31	8.92	72	610	166
WDD10-151	29.4	1	1	< 12	103	3050	< 9.6	1960	35.2	< 16	445	10.8	5.5	19400	2.75	131.2	28.8	11.1	76.7	621	233
WDD10-151	29.4	1	1'	< 22	139	3110	< 17	2070	46.4	< 28	1610	< 12	7.7	18200	5.6	113.9	18.7	11	78.4	682	283
WDD10-151	29.4	2	2	< 6	185	2130	6.8	1458	414	232	< 1.9	< 2.9	3.28	20700	1.85	195	13.5	16.1	63.9	500	132.5
WDD10-151	29.4	2	2'	< 7.5	234	2040	< 7.1	1447	677	353	< 2.3	5.4	2.52	20200	0.9	210	16.4	15.5	72	465	164
WDD10-151	29.4	Minimum value		5.2	36	2040	2.7	808	2.69	45	3.05	0.12	2.52	14300	0.65	48.2	2.66	6.3	60	465	101
		Maximum value		13.7	678	4470	21	2170	1620	930	34700	45	10.5	25800	5.6	311	36.8	16.9	102	732	283
WDD07-2	73.5B	103	3	419	109	5290	19.9	2008	< 1.8	< 410	< 8.7	< 5.5	277	3450	154.1	233.8	134	5.84	39.7	1925	5470
WDD07-2	73.5B	103	3'	85.4	144	3560	12.1	1621	< 0.6	< 140	< 3	< 1.9	97.6	2270	72.1	176.9	22.5	7.47	253	922	1993
WDD07-2	73.5B	103	4	145	223	3685	6.3	2114	< 0.54	< 130	< 2.6	< 1.7	76.7	1957	58.5	182.7	35.2	9.31	370	459	1593
WDD07-2	73.5B	103	4'	340	369	4148	6.9	2501	< 0.53	< 130	3.6	< 1.7	82.2	1912	59.8	164.7	58.8	11.71	421	397	1734
WDD07-2	73.5B	103	5	405	158	4230	< 2.5	3463	< 0.48	135	3.8	2.6	61.9	1823	56.9	80.9	81.8	8.64	170	141.5	1302
WDD07-2	73.5B	103	5'	537	152	4530	5.3	3538	< 0.53	< 130	< 2.6	< 1.6	55.3	2250	106.6	69.8	108	8.2	198	150.3	1165
WDD07-2	73.5B	103	6	263	333	4450	5.8	2572	< 0.53	< 130	3.8	< 1.6	74	1910	59.2	153.7	153	12.7	392	339	1625
WDD07-2	73.5B	103	6'	139.2	316	4480	9.9	2055	< 0.56	< 150	< 2.8	< 3.2	86.7	1767	60.8	154.6	49.6	12.03	421	510	1810
WDD07-2	73.5B	103	7	137.6	156	3540	6.4	2096	< 0.57	< 160	< 2.9	< 3.3	79.3	1804	62.3	153	11.6	8.02	253	530	1673
WDD07-2	73.5B	103	7'	167	106	3350	8.2	2670	< 0.49	< 130	< 2.4	< 2.8	72.3	1530	63.6	170.1	30	7.53	232	373	1490
WDD07-2	73.5B	103	8	53.3	64	4680	< 3	1560	< 0.65	< 180	< 3.2	< 3.7	128.1	1936	88.8	119.4	65.9	3.18	472	963	2680
WDD07-2	73.5B	103	8'	146	169	4030	18.1	1661	< 1	< 280	< 5	< 5.7	204	2600	117	152.6	147.3	7.53	145.7	1392	3920
WDD07-2	73.5B	4	1	103	195	4380	8.1	1096	< 0.88	< 250	< 4.4	< 5	98.5	1731	88.6	2420	163	5.35	297	878	2080
WDD07-2	73.5B	4	1'	90.6	141	4740	< 3.2	1275	1.6	< 210	4.1	< 4.2	108.5	1990	83.1	1121	116.4	4.17	627	637	2288
WDD07-2	73.5B	4	2	316	77	3413	12.4	770	7.8	< 490	< 9.9	< 9.2	183.9	1184	122.5	7740	221	2.92	9.6	382	3630
WDD07-2	73.5B	4	2	94.6	18850	1844	9	326	2.78	< 230	57.2	< 4.3	144.3	1970	85.8	1227	321	108.8	162	460	3120
WDD07-2	73.5B	104	2	94.2	< 14	3758	10.6	1501	< 0.73	< 230	< 4.5	< 4.2	97.9	2598	60.3	70.8	13.7	0.54	28.2	1543	2063
WDD07-2	73.5B	104	2'	82.9	1870	4830	39.8	1802	< 0.62	< 200	< 3.8	< 3.6	63.3	1600	61	39.6	1720	15.8	188	829	1352
WDD07-2	73.5B	104	3	86.7	< 14	4290	12.3	1523	< 0.72	< 230	< 4.4	< 4.2	119.1	2610	67.4	64.8	14.8	0.42	22.7	1462	2407
WDD07-2	73.5B	104	3'	66.4	2220	5300	35.2	1687	< 0.63	< 200	< 3.9	< 3.6	103.9	1652	82.8	39.9	2190	19.4	195	896	2322
WDD07-2	73.5B	104	4	140.8	187	4790	14.5	2404	< 0.59	< 210	< 3	< 3.3	64.4	987	61.7	41.8	80.9	3.17	350	454	1358
WDD07-2	73.5B	104	4'	75.2	28	4129	18	1535	< 0.65	< 230	< 3.3	< 3.6	111.1	2510	76.6	57.9	2.38	0.35	31.3	1529	2399
WDD07-2	73.5B	104	5	105.3	160	5010	19.9	1691	< 0.68	< 250	< 3.5	< 3.8	50.5	1870	59.6	47	70.9	3.85	180	997	1106
WDD07-2	73.5B	104	5'	486	1280	5790	36	2089	< 1.6	< 580	< 8.1	< 8.7	218	3050	93.4	57.6	220	14.9	24.6	1626	4400
WDD07-2	73.5B	105	2	597	840	8660	57	1920	11.3	< 1300	< 18	< 19	382	4870	201	100.4	1310	4.1	242	1598	7780
WDD07-2	73.5B	105	2	54.4	187	4420	12.7	1693	< 0.55	< 210	< 2.8	< 3	113.8	1900	92.6	118.1	14.8	0.4	314	1231	2554
WDD07-2	73.5B	105	3	43.5	210	3060	< 2.9	1591	< 0.49	< 190	< 2.5	< 2.7	99.5	1103	85.9	174.6	39	0.81	1120	768	2314
WDD07-2	73.5B	105	3'	66.4	208	4570	< 3.6	1635	< 0.58	< 220	< 3	< 3.2	121.5	1530	103.5	137.2	16.5	0.5	413	991	2752
WDD07-2	73.5B	105	4	53.3	437	4360	3.4	1613	< 0.47	< 190	< 2.4	< 2.6	118.6	1630	103.1	131.7	34.6	0.85	460	1029	2746
WDD07-2	73.5B	105	4'	54.5	234	4480	< 2.9	1501	< 0.49	< 180	< 2.9	< 2.9	125.5	807	101.1	179.7	14.9	0.27	922	783	2935

Drillhole #	Depth (m)	Circle #	Analysis #	B (ppm)	Ti (ppm)	V (ppm)	Cr (ppm)	Mn (ppm)	Co (ppm)	Ni (ppm)	Cu (ppm)	Zn (ppm)	Ga (ppm)	As (ppm)	Sr (ppm)	Y (ppm)	Zr (ppm)	Nb (ppm)	Mo (ppm)	Sb (ppm)	Ba (ppm)
WDD07-2	73.5B	6	1	153	20.8	3540	7.3	1270	1.66	< 20	5.8	< 4.3	115.1	3170	139	3990	23.5	0.243	80.3	1261	4230
WDD07-2	73.5B	6	1'	172	61	4230	13.8	1426	< 0.3	< 22	< 3.2	< 4.9	117.6	3420	131.8	607	49.4	0.63	46	1284	4240
WDD07-2	73.5B	105	1	48.9	125	4810	< 2.7	1460	< 0.21	< 11	< 1.3	< 2.7	70.7	872	94.6	168.5	14.3	0.373	1007	820	2830
WDD07-2	73.5B	105	1'	45.1	154	3370	< 2.9	1503	< 0.22	< 12	1.79	< 2.9	65.4	856	88.5	180.2	14.47	0.362	1176	921	2645
WDD07-2	73.5B	24	1	412	90.3	2470	12.3	3330	< 0.15	< 10	12.8	< 1.8	34.3	918	49.6	175.4	7.01	2.02	411	453	1376
WDD07-2	73.5B	24	1'	130	40.6	3440	13.2	1946	< 0.17	< 11	< 1.7	< 1.9	42.3	1302	63.5	193.3	5.13	0.92	386	916	1615
WDD07-2	73.5B	24	2	148	55.3	3015	5.1	2255	< 0.21	< 12	< 1.6	< 2.6	39.6	1294	56.2	182.3	5.4	0.62	441	782	1583
WDD07-2	73.5B	24	2'	295	43.7	2486	8.8	3028	< 0.19	< 11	11.4	< 2.3	40.8	963	56.3	183.3	3	0.8	462	505	1631
WDD07-2	73.5B	103	1	618	381	6240	5.7	2539	< 0.22	< 13	5.4	< 2.6	44	1801	62.2	130.9	298	23.1	553	318	1728
WDD07-2	73.5B	103	1'	587	747	5280	9	2989	< 0.22	< 12	1.61	< 2.5	35	2510	58.2	112.9	169.7	14.35	150.7	199	1427
WDD07-2	73.5B	103	2	226	15.5	3663	8	2172	< 0.23	< 14	2.7	< 2.4	36.9	1723	60.5	182.9	19.2	5.08	237	425	1534
WDD07-2	73.5B	103	2'	705	1313	7720	16.5	3088	< 0.21	< 13	< 1.7	< 2.2	14.7	1810	77.5	108.4	739	43.5	82.4	98.1	584
WDD07-2	73.5B	102	1	141	6850	3830	6.8	1863	< 0.31	< 15	272	< 2.1	25.6	1583	36.8	287	95.5	60	1077	1364	887
WDD07-2	73.5B	102	1'	118	5580	3960	< 6.9	1842	< 0.25	< 14	192.1	< 1.8	26.2	1760	41.6	474	42.2	58.8	1322	1286	1119
WDD07-2	73.5B	102	2	96	7880	3970	10.9	1327	< 0.29	< 16	41.8	< 2	46.9	1344	68.6	970	49.8	64.1	714	1007	1905
WDD07-2	73.5B	102	2'	146	7460	4080	9	1790	< 0.3	< 16	99.1	< 2.1	33	1413	52.3	269	188.9	68.6	1072	1076	1268
WDD07-2	73.5B	104	1	77	430	3804	18.6	1453	< 0.29	< 15	< 1.7	< 1.5	60.1	2520	69.2	63.4	820	5.3	68.2	1539	2302
WDD07-2	73.5B	104	1'	124	55.1	5150	< 7	1649	< 0.3	< 16	< 1.8	< 1.6	33.9	1912	59	50.4	18.1	0.54	389	781	1354
		Minimum value		43.5	15.5	1844	3.4	326	1.6	135	1.61	2.6	14.7	807	36.8	39.6	2.38	0.243	9.6	98.1	584
WDD07-2	73.5B	Maximum value		705	18850	8660	57	3538	11.3	135	272	2.6	382	4870	201	7740	2190	108.8	1322	1925	7780
All analyses		Minimum value		0	21.2	469	2.7	194	0.75	0	3.05	0.12	0.87	402	0.428	36.1	1.42	0.27	2.2	90	32.6
		Maximum value		1090	18850	16510	268	5540	69400	23800	34700	86	393	25800	830	20750	8680	338	1120	2280	12700

Drillhole #	Depth (m)	Circle #	Analysis #	La (ppm)	Ce (ppm)	Pr (ppm)	Nd (ppm)	Sm (ppm)	Eu (ppm)	Gd (ppm)	Tb (ppm)	Dy (ppm)	Ho (ppm)	Er (ppm)	Tm (ppm)	Yb (ppm)	Lu (ppm)	Ta (ppm)	W (ppm)	Bi (ppm)	Th (ppm)
WDD07-2	55.9A	9	1	23.3	257	91.1	800	529	169.7	864	123.4	646	109.9	275	33.7	201.6	23.6	5.13	1598	3.2	165
WDD07-2	55.9A	9	1'	4.57	130.4	71.2	781	539	175.6	828	116.7	602	99.8	234.2	30.8	184.7	19.6	4.66	1489	5.71	46.2
WDD07-2	55.9A	9	2	68	680	161	1190	608	169.6	797	106.7	547	89.4	217.5	27	159.7	19.8	6.6	1059	1.34	457
WDD07-2	55.9A	9	2'	490	3747	535	2598	834	204.9	950	107.9	534	91.1	206.6	25	150.8	18.7	4.63	1330	< 0.1	30.9
WDD07-2	55.9A	7	1	142	565	55	150	29.5	14.5	23.8	2.89	11.7	1.41	5	< 0.35	4.2	< 0.38	0.56	8350	< 0.25	8.1
WDD07-2	55.9A	7	1'	136	536	46.8	157	32	16.8	29	4.2	15.9	2.1	5.3	< 1.1	4.4	< 1.1	< 1.2	7840	< 0.75	10.8
WDD07-2	55.9A	9	11	147	980	231	1275	638	166.6	743	118	535	112.1	202	26.6	162.7	20.9	5.83	1126	1.28	455
WDD07-2	55.9A	9	11'	585	3690	608	2671	965	192	1108	157.4	658	149	276	33.7	214	26.9	5.14	706	< 0.22	290
WDD07-2	55.9A	9	12	152	987	222	1241	617	159.5	793	125	554	121.1	226.7	26.5	164.5	23	6.23	1140	1.11	498
WDD07-2	55.9A	9	12'	171.4	1158	258	1359	633	167.9	794	120.3	535	118	221.8	27.6	178	22.5	7.88	972	1.08	429
WDD07-2	55.9A	9	13	99.9	685	153.1	890	520	159.5	753	124.1	546	118.8	221	27.2	175.8	22.7	5.58	1548	3.14	221
WDD07-2	55.9A	9	13'	211	1410	275	1448	714	185.6	993	152.1	711	152.7	298.2	38.2	233.7	29.8	4.3	1504	4.96	44.3
WDD07-2	55.9A	9	14	104.3	809	205	1202	588	170.5	738	117.2	527	104.7	211.8	26.6	171.2	19.8	6.68	1149	1.07	432
WDD07-2	55.9A	9	14'	108.8	821	187	1100	649	184.9	933	141.2	654	131	266.7	33.8	209.8	26.9	4.53	1191	3.87	63.4
WDD07-2	55.9A	9	15	319	2340	415	2070	857	205.8	1056	141.2	674	124.8	274	34.8	214	26	5.96	778	0.55	331
WDD07-2	55.9A	9	15'	80	640	163	1130	559	175.1	763	110.8	502	95.3	198	23.8	162	20.3	7.5	966	0.98	535
WDD07-2	55.9B	3	1	161.6	1740	357	2000	791	124.6	1012	120.1	596	102.7	246.7	32.1	180.3	23.4	7.8	1802	0.21	385
WDD07-2	55.9B	3	1'	24.2	284	105.6	908	477	121.5	555	73.4	357	59.5	134.4	16.03	107.7	10.86	11.71	1238	2.05	190
WDD07-2	55.9B	4	1	15.5	370	139.2	934	399	112.9	385	53.8	266	41.1	94.9	12.6	72.1	8.02	1	2360	1.13	11.6
WDD07-2	55.9B	4	1'	65.2	441	100.3	602	220	67.8	211	28.5	135.7	22.3	52.1	6.71	42.5	4.19	0.61	4320	0.46	7.1
WDD07-2	55.9B	Minimum value		4.57	130.4	46.8	150	29.5	14.5	23.8	2.89	11.7	1.41	5	6.71	4.2	4.19	0.56	706	0.21	7.1
		Maximum value		585	3747	608	2671	965	205.8	1108	157.4	711	152.7	298.2	38.2	233.7	29.8	11.71	8350	5.71	535
WDD08-106	10.6	104	1	58.4	302	47.4	230	79.3	25.5	96.9	17.97	92.8	12.19	24.5	3.1	19.5	2.02	< 0.021	833	18.6	0.26
WDD08-106	10.6	104	1'	47.4	415	78.6	408	175.7	56.2	183	40.8	216.2	27.5	57.3	7.58	50	4.31	< 0.019	1052	11.15	0.057
WDD08-106	10.6	106	1	21.15	244.3	50.7	277.6	138.3	45.6	151.4	37.2	196.1	25.8	53.3	7.37	46.9	3.92	2.69	975	156	41.8
WDD08-106	10.6	106	1'	21.55	248	53.2	282	139.3	45.6	149.5	37.1	196.7	24.52	52.5	7.3	48	4.27	0.322	1026	103.5	20.62
WDD08-106	10.6	Minimum value		21.15	244.3	47.4	230	79.3	25.5	96.9	17.97	92.8	12.19	24.5	3.1	19.5	2.02	0.322	833	11.15	0.057
		Maximum value		58.4	415	78.6	408	175.7	56.2	183	40.8	216.2	27.5	57.3	7.58	50	4.31	2.69	1052	156	41.8
JDD08-003	74.4B		1	1403	3980	426	1783	1094	295	640	88.9	377	51.9	101.6	12.2	74	6.4	< 0.098	2015	12.3	1.98
JDD08-003	74.4B		1'	1553	4710	540	2510	1458	403	828	121.6	547	74.2	146	17.3	103	10.1	0.22	2103	29.4	1.48
JDD08-003	74.4B		2	1392	3900	453	1880	1105	318	720	91.8	406	62.3	115	13.2	75	8.6	< 0.26	1806	33	8.7
JDD08-003	74.4B		2'	1407	3870	421	1780	1003	280	633	77.4	345	44	93.5	11.2	58.8	5.82	0.39	2102	41.2	11.5
JDD08-003	74.4B		3	1561	4660	579	2700	1890	521	1015	161.3	668	90.7	183	23.1	142	12.7	< 0.24	2699	1.01	< 0.32
JDD08-003	74.4B		3'	1643	4790	575	2750	1885	520	1026	157.6	661	92	179	24.5	152	13.9	< 0.14	2707	0.45	0.47
JDD08-003	74.4B		4	1433	4870	749	4970	6290	2277	8260	1159	5540	903	1985	229	1339	164.7	< 0.33	857	< 0.6	14.9
JDD08-003	74.4B		4'	1475	4850	716	4260	5300	1970	7400	1006	4890	770	1700	201	1183	144.2	< 0.28	901	1.33	4.8
JDD08-003	74.4B		5	1528	4700	566	2541	1751	501	983	152.9	671	88.5	179.8	23.6	145.9	13.7	< 0.14	2066	1	1.29
JDD08-003	74.4B		5'	1260	4010	474	2160	1500	393	856	131	613	81	181	20.4	129	16.3	< 0.6	1860	1.7	< 0.58
JDD08-003	74.4B		6	1449	4430	520	2340	1621	447	918	140.1	610	86.8	166	19.9	138	12.7	< 0.072	2091	1.27	1.84
JDD08-003	74.4B		6'	1473	4340	523	2412	1633	456	1004	151.7	643	89.7	181.5	24.9	152	13.8	< 0.058	1764	1.06	4.58
JDD08-003	74.4B		7	1439	4380	515	2380	1521	409	990	136	570	78.3	159	18.1	124	12	< 0.22	1826	0.45	0.72
JDD08-003	74.4B		7'	1347	4170	470	2185	1437	383	855	123.9	521	74.6	137.5	19.7	110.1	10.9	< 0.14	1869	1.11	1.97

Drillhole #	Depth (m)	Circle #	Analysis #	La (ppm)	Ce (ppm)	Pr (ppm)	Nd (ppm)	Sm (ppm)	Eu (ppm)	Gd (ppm)	Tb (ppm)	Dy (ppm)	Ho (ppm)	Er (ppm)	Tm (ppm)	Yb (ppm)	Lu (ppm)	Ta (ppm)	W (ppm)	Bi (ppm)	Th (ppm)
JDD08-003	74.4B		8'	1536	4270	533	2570	1940	608	1670	248	1055	168	349	42.6	276	30.4	0.24	1360	1.38	5
JDD08-003	74.4B		8'	1575	4410	560	2710	2344	734	2300	334	1570	241	536	60.2	359	42.3	0.14	1452	< 0.1	11.1
JDD08-003	74.4B		9'	1503	4510	550	2740	2110	678	1904	274	1301	202	423	53.4	300	34.7		1508	< 0.16	10.87
JDD08-003	74.4B		9	1507	4160	484	2330	1424	384	919	118.9	569	75.4	139	18.3	99	9.8	< 0.19	1601	< 0.34	2.9
JDD08-003	74.4B		10	1233	3400	333	1360	714	189	436	57	211	35.4	64.6	7.3	45.8	4.68	0.15	2120	< 0.25	3.55
JDD08-003	74.4B		10'	1557	4490	518	2310	1435	393	857	109.3	498	73	143	17.9	99	11.1	< 0.34	1555	3.09	18.4
JDD08-003	74.4B		11	1622	4530	591	2650	1718	515	1203	152.8	682	100.5	227	23.1	128	15.4	0.43	1575	0.67	20.6
JDD08-003	74.4B		11'	1500	4860	672	3720	3430	1168	4110	532	2350	383	809	87.7	499	65.3	0.28	1258	1.32	5.3
JDD08-003	74.4B		12'	1790	4610	630	2610	1960	639	1440	250	980	174	323	33.6	260	26.6	< 0.7	1390	1.4	25.8
JDD08-003	74.4B		12'	1453	4400	531	2590	2000	664	1780	259	1270	191	429	50	294	33.8	0.59	1513	< 0.17	95.8
JDD08-003	74.4B		13	1347	3570	427	1897	1365	407	794	127.2	557	74.4	156.1	19.34	128	11.8	< 0.1	1522	21.2	94.4
JDD08-003	74.4B		13'	1292	3390	387	1677	1278	370	685	115.5	516	62.3	136.7	17.9	116	10.23	0.12	1655	75.4	64.3
JDD08-003	74.4B		14	1490	3740	436	1874	1441	413	739	123.9	535	66.5	135.5	17.3	114.1	9.4	0.5	1259	138	63.6
JDD08-003	74.4B		14'	1473	3760	409	1953	1275	380	751	118	519	71.3	129	19	114	10.1	< 0.34	1248	478	69.8
JDD08-003	74.4B		15	1364	3790	394	1910	1300	361	726	113	538	58.3	136	15.7	115	6.7		1300	504	86
JDD08-003	74.4B		15'	1407	3740	408	1870	1350	392	804	131.6	554	70.9	139	18.7	120.1	9.9	0.49	1277	1.4	107
JDD08-003	74.4B		16	964	3010	352	1460	1222	399	668	126.8	641	80.7	180	23.3	160	13.4		2373	33.3	40.5
JDD08-003	74.4B		16'	1117	3100	345	1492	1102	350	647	109.7	466	70.3	140	18.3	109.8	9.27	0.18	1975	2.58	10.32
JDD08-003	74.4B		17	1329	4060	450	2130	1601	501	1074	181	829	121.3	254	32.8	190	19.9	0.33	1611	0.69	10.1
JDD08-003	74.4B		17'	1388	4150	486	2210	1606	476	1011	168.8	765	104	206	27	177	18.4	0.77	1718	1.41	12.6
JDD08-003	74.4B		18	1265	3790	542	3260	4140	1670	5800	860	4410	700	1560	181	1090	140	< 0.42	1202	< 0.82	1.6
JDD08-003	74.4B		18'	1366	3940	540	2910	3380	1310	4320	720	3450	559	1170	146	890	105	0.53	1439	0.47	3.2
JDD08-003	74.4B		19	1369	3860	462	2410	2210	734	2102	361	1663	259	590	63.5	408	49.7	< 0.14	1499	0.61	1.15
JDD08-003	74.4B		19'	1201	3710	518	3290	4140	1740	5370	890	4360	727	1660	173	1030	128	< 0.19	1218	< 0.38	0.81
JDD08-003	74.4B		20	1396	3881	468	2139	1630	488	1013	163	775	102.4	208	29.9	174	17.6	0.46	1846	0.47	11.5
JDD08-003	74.4B		20'	1074	2790	273	1052	560	157	336	47.3	200	29.8	60.4	6.99	39.6	3.75	0.14	2210	0.81	0.92
JDD08-003	74.4B	Minimum value		964	2790	273	1052	560	157	336	47.3	200	29.8	60.4	6.99	39.6	3.75	0.12	857	0.45	0.47
		Maximum value		1790	4870	749	4970	6290	2277	8260	1159	5540	903	1985	229	1339	164.7	0.77	2707	504	107
WDD10-151	29.4	2	3	456	2981	361	1191	299	42.7	187	36.7	158	21.6	50.9	8.8	57.9	5.94	0.11	67.3	417	1.15
WDD10-151	29.4	2	3'	691	3590	421	1299	292	40.9	169	30.7	140.1	20.8	53.3	7.58	57.7	5.35	< 0.11	81.1	182.5	4.6
WDD10-151	29.4	2	4'	677	3530	405	1207	290	40.9	175	29.7	148	20.8	47.3	7.3	56.6	5.4	0.16	76.1	270	4.95
WDD10-151	29.4	2	4	630	3440	389	1254	296	38.8	189	31.8	146	20.5	50	8.2	59.3	6.1	< 0.15	77	379	3.3
WDD10-151	29.4	2	5	662	3490	402	1227	282	41	163	26.3	146	19.7	45.1	7.31	56.3	5.11	< 0.12	75.8	140.3	3.55
WDD10-151	29.4	2	5'	647	3460	385	1295	288	43	166	28.7	148.5	22.7	48.3	7.51	54.2	5.04	< 0.12	78.2	221	4.98
WDD10-151	29.4	2	6	669	3540	393	1287	288	42	178	26.3	143	20.3	46.7	6.9	55.8	5.34	0.053	85.7	220.4	3.88
WDD10-151	29.4	2	6'	520	3170	374	1230	308	40.6	185	28.4	163	23.3	52.5	6.97	62.3	5.08	0.17	74.3	123.7	6.5
WDD10-151	29.4	4	3	391	1876	194	521	111	16.4	46.4	7.7	34.4	3.98	7.8	1.41	8	0.93	< 0.47	136.6	< 0.23	1.7
WDD10-151	29.4	4	3'	334	1806	194	555	143	21	83	10.6	42.3	6.9	16.5	1.48	13.4	1.49	< 0.87	122	3.9	2.5
WDD10-151	29.4	4	4	246	1809	221	766	261	41.6	164	28.6	105.3	17.4	37.1	6.3	31.3	3.61	0.26	81.9	0.46	24.4
WDD10-151	29.4	4	4'	330	2090	226	771	249	43.5	168	24.8	110	16.6	32	5.54	32.6	3.9	< 0.2	86.9	0.8	3.4
WDD10-151	29.4	4	5	358	1800	181	531	119	18.6	63.3	7.8	34.8	4.88	13.5	1.18	14.6	0.97	< 0.2	113	116	1.21
WDD10-151	29.4	4	5'	316	1960	209	665	200	36	143	18.8	78.8	11.9	28	4.41	27.5	2.9	< 0.17	97.7	0.34	4.35
WDD10-151	29.4	4	6	300	2050	233	742	202	35.1	134	19.7	97	12.2	30.6	3.5	26.6	3.7	< 0.27	80.2	32.1	7.5

Drillhole #	Depth (m)	Circle #	Analysis #	La (ppm)	Ce (ppm)	Pr (ppm)	Nd (ppm)	Sm (ppm)	Eu (ppm)	Gd (ppm)	Tb (ppm)	Dy (ppm)	Ho (ppm)	Er (ppm)	Tm (ppm)	Yb (ppm)	Lu (ppm)	Ta (ppm)	W (ppm)	Bi (ppm)	Th (ppm)
WDD10-151	29.4	4	6'	367	1899	191.5	534	128	18.3	70.5	8.2	28.3	4.37	9.8	1.47	10	0.82	< 0.14	116.9	0.3	1.07
WDD10-151	29.4	4	2	366	1738	186.9	486	109.7	14.5	43.5	6.88	29.1	3.8	9.06	1.51	9.85	0.9	0.07	129.6	0.38	1.86
WDD10-151	29.4	4	2'	327	1743	184.1	512	118.6	16.41	51.9	8.31	36	4.97	10.93	1.59	10.89	1.07	< 0.046	119.9	6.8	1.24
WDD10-151	29.4	2	1	629	3380	370	1182	289	38.2	152.8	27.4	132.8	18.9	44.2	6.66	46.9	4.96	0.124	75	255.3	3.28
WDD10-151	29.4	2	1'	567	3340	368	1182	292	38.3	161.4	27.7	140.4	20.64	46.2	7.25	52.9	5.08	0.131	77.9	297.9	5.79
WDD10-151	29.4	4	1	363	1987	192.2	535	119.3	16.8	58.4	8.57	35.1	5.15	10.77	1.44	12.9	1.23	< 0.087	125.6	0.35	2.71
WDD10-151	29.4	4	1'	348	1985	215.1	648	172	29	97.4	14.5	71.9	10.19	21.8	3.38	20.2	1.78	0.121	95.6	0.103	2.29
WDD10-151	29.4	1	1	761	2430	252	783	171	26.5	95.3	15.4	75.3	11.33	25.2	3.98	29.1	3.08	< 0.078	155.6	14.8	0.93
WDD10-151	29.4	1	1'	777	2210	236	701	155	24.9	80	14.9	74.4	9.6	22.6	3.34	26.1	2.83	< 0.14	150	176	< 0.28
WDD10-151	29.4	2	2	638	3330	385	1178	302	39	156.3	27.4	134.2	19.6	46.2	6.97	51.5	4.67	0.089	70.7	272	3.97
WDD10-151	29.4	2	2'	595	3330	392	1215	276	39	152	27.2	152	20.2	50.5	7.08	57.2	5.25	0.089	68	486	4.04
WDD10-151	29.4	Minimum value		246	1738	181	486	109.7	14.5	43.5	6.88	28.3	3.8	7.8	1.18	8	0.82	0.053	67.3	0.103	0.93
		Maximum value		777	3590	421	1299	308	43.5	189	36.7	163	23.3	53.3	8.8	62.3	6.1	0.26	155.6	486	24.4
WDD07-2	73.5B	103	3	216.1	438	77.7	366	128	36	107.4	16.7	90.4	16.6	42.2	4.43	33.6	4.2	< 0.28	2356	< 0.19	9.1
WDD07-2	73.5B	103	3'	149.6	278	55.3	263	114.2	34	96	17.6	103.2	18.52	48.5	6.86	46.1	5.73	< 0.094	1282	< 0.064	4.62
WDD07-2	73.5B	103	4	154.1	271	54.9	270	131.5	39.2	104.1	22	126.8	21.6	53.4	8.93	52.8	6.08	< 0.084	1266	< 0.057	11.5
WDD07-2	73.5B	103	4'	168.4	300.4	55.5	268	139.2	37.8	102.8	21.7	133.4	21.2	54.1	8.56	58.4	6.18	0.089	1288	< 0.056	20.9
WDD07-2	73.5B	103	5	111.7	196	32.5	149	70	20.7	46.9	11.1	62.4	10.1	25.2	3.89	30.8	2.97	< 0.074	1510	< 0.049	10.5
WDD07-2	73.5B	103	5'	97	169	27	125	59	16.5	35.7	8.8	47.3	8.1	20.3	3.3	23.9	2.77	< 0.082	1611	< 0.053	8.24
WDD07-2	73.5B	103	6	162.6	300.2	55.8	276	126.6	37.2	92.4	22.4	117.4	21.03	49.1	7.8	55.2	5.76	0.144	1279	< 0.052	9.74
WDD07-2	73.5B	103	6'	158.6	273.7	50	254.6	113.3	36.6	84.2	19.57	103.8	19.7	43.2	6.74	46.2	5.52	0.076	1294	< 0.09	7.5
WDD07-2	73.5B	103	7	140.9	259.8	46.1	243	122.9	35.7	88.8	20.6	110.1	21.3	49.9	7.78	49.2	5.5	< 0.063	1287	0.117	0.27
WDD07-2	73.5B	103	7'	149.5	272.4	51.2	260	132.4	40	111.2	23.4	128.5	24.6	53.5	8.25	55.5	7.01	< 0.053	1376	< 0.077	1.46
WDD07-2	73.5B	103	8	152.6	232	35.7	193	61.5	16.8	64.6	8.87	40.2	8.99	19.8	2.52	15.2	2.05	< 0.071	1747	< 0.1	9.72
WDD07-2	73.5B	103	8'	154.6	306	52.6	281	99.7	27.2	85	14.2	70.4	13.8	30.2	4.29	27.3	3.74	< 0.11	1555	< 0.15	13.4
WDD07-2	73.5B	4	1	637	1116	164	1055	416	79	671	85.1	416	95.9	212	27.8	144	22.5	0.26	1767	2.55	16.3
WDD07-2	73.5B	4	1'	358	525	88.7	551	245	43.4	356	55	292	63.9	143	20.3	118.5	16.37	0.29	1376	0.76	18.5
WDD07-2	73.5B	4	2	1414	2880	490	3357	1244	256.7	2027	242.3	1197	278.9	602	75.8	398	66.6	< 0.093	557	0.25	20.2
WDD07-2	73.5B	4	2	549	800	122.2	724	275	70.7	393	48.3	239.9	53.1	109.9	14.02	77.3	10.67	15.25	551	69	175.6
WDD07-2	73.5B	104	2	305.1	472	50.2	213	58.9	26.9	39.5	7.2	37	7.38	15.1	2.43	15.2	1.69	< 0.042	1967	0.33	1.09
WDD07-2	73.5B	104	2'	159.9	228.4	29.2	124.9	42	13.1	23.6	4.19	20.5	4.3	8.9	1.59	8.7	0.82	1.45	1766	3.23	97
WDD07-2	73.5B	104	3	310.8	405	46.7	205.3	63.9	21.8	44.6	7.77	39.3	7.43	16	2.79	14.6	1.85	< 0.042	1791	0.146	1.26
WDD07-2	73.5B	104	3'	159.2	220.3	29.7	131.5	41.4	11.7	25.6	3.99	26.2	4.88	9.6	1.19	10	1.02	1.84	1520	4.29	214
WDD07-2	73.5B	104	4	95.7	165.5	26.2	120.3	38.8	12.5	27.1	3.41	23.2	4.89	9.5	1.51	11	1.11	< 0.042	2387	0.2	5.5
WDD07-2	73.5B	104	4'	295.1	437.2	46.1	191.5	54.4	21.8	37.3	6.22	32.5	6.14	13	1.94	15.2	1.59	< 0.046	1648	0.45	0.56
WDD07-2	73.5B	104	5	189.7	260	32.8	137.3	48.7	12.89	25.2	4.72	28.1	5.41	10.8	1.69	11.9	1.32	< 0.048	1926	0.63	2.41
WDD07-2	73.5B	104	5'	335.8	509	54.3	197	50.4	23.8	34.6	5.94	29.6	4.68	13.6	1.36	12.5	1.11	0.48	1785	0.47	11.8
WDD07-2	73.5B	105	2	406	785	90	366	101	32.3	66	11.2	78	14.2	30.7	4	24.5	3.4	0.41	3840	< 0.49	8.9
WDD07-2	73.5B	105	2	194.2	336	56.4	260	117	26	71.5	13.6	77.4	14.27	32	4.92	30.4	3.85	0.149	1349	< 0.078	2.14
WDD07-2	73.5B	105	3	181.5	281	52.4	263	102.4	24.9	83.1	13.32	66.1	13.49	31.2	4.27	23.7	3.96	0.161	1229	< 0.072	1.3
WDD07-2	73.5B	105	3'	191.2	324	59.7	271.4	117.3	26.6	75.6	12.62	77.4	14.1	33.7	4.69	32.1	3.84	< 0.041	1318	< 0.086	2.43
WDD07-2	73.5B	105	4	185.8	340.4	59.5	253.6	103.5	25.2	70.4	13.45	70.8	12.93	32.2	4.75	29.3	3.83	0.33	1284	< 0.072	3.65
WDD07-2	73.5B	105	4'	178.4	314.8	64.1	295	130	32.1	89.8	15	87.9	14.68	37.8	5.23	34.7	4.55	0.087	1140	< 0.069	2.91

Drillhole #	Depth (m)	Circle #	Analysis #	La (ppm)	Ce (ppm)	Pr (ppm)	Nd (ppm)	Sm (ppm)	Eu (ppm)	Gd (ppm)	Tb (ppm)	Dy (ppm)	Ho (ppm)	Er (ppm)	Tm (ppm)	Yb (ppm)	Lu (ppm)	Ta (ppm)	W (ppm)	Bi (ppm)	Th (ppm)
WDD07-2	73.5B	6	1	285.6	767	199.6	1131	588	112.1	960	108.4	577	115.6	284.1	31.5	159.7	27.8	< 0.048	1140	< 0.12	0.75
WDD07-2	73.5B	6	1'	159.3	422	96.8	482	207	57.6	203	26.3	144	26.8	63.1	7.52	40	6.3	< 0.055	1270	< 0.14	5.12
WDD07-2	73.5B	105	1	149.8	297	62.1	283.2	113.3	29	85	14.65	79.3	14.07	35.1	4.89	30.2	3.98	0.059	1113	< 0.022	1.65
WDD07-2	73.5B	105	1'	157.6	273.4	57.1	258.6	99.8	26.2	88.2	12.83	69	11.76	29.9	4.01	21.7	3.4	0.087	1227	< 0.024	1.49
WDD07-2	73.5B	24	1	112.3	188.9	50.7	237	110.4	32.7	91.8	15.09	80.5	12.76	31.8	4.42	28.7	3.2	0.051	1210	0.268	3.64
WDD07-2	73.5B	24	1'	118.3	243	56	264	109.5	28.6	94	14.4	79.8	13.36	33.9	4.83	33.9	4.11	0.03	1257	0.259	2.55
WDD07-2	73.5B	24	2	123.7	212.3	49.3	232.2	93	25.6	88.2	12.56	67.5	11.24	29.9	3.7	24.5	3	0.118	1442	0.126	5.7
WDD07-2	73.5B	24	2'	128.4	192.1	49.2	234	98.4	27.1	93.2	13.1	65.4	11.73	27.9	3.92	23.8	3.15	0.06	1436	0.132	0.72
WDD07-2	73.5B	103	1	154.8	324	59.7	250	109.1	31.7	72.1	15.08	90.9	13.7	38.7	6.05	47.8	4.91	0.372	1307	0.116	14.7
WDD07-2	73.5B	103	1'	162.3	335	62	249	112.5	34	68.1	15.15	92.1	14.15	36	6.59	46.7	4.78	1.44	1546	< 0.043	5.8
WDD07-2	73.5B	103	2	141.9	261	54.8	245.7	121	35.5	97	17.86	109.9	18.74	47.6	7.2	47.6	5.84	< 0.067	1267	0.116	0.88
WDD07-2	73.5B	103	2'	175.2	376	70.6	279	123.8	35.6	70.2	15.76	96.1	13.68	39.2	6.09	49.7	5.16	1.85	1315	0.159	5.12
WDD07-2	73.5B	102	1	42.8	102.7	33	213.3	171.7	43.4	156.4	25.4	144.7	22.4	54	7.88	55	4.76	1.28	4480	0.206	76.2
WDD07-2	73.5B	102	1'	96.3	141	42.7	270	202	52.2	211	35.4	213	33.6	87.3	13.4	88.7	9.5	1.42	4580	0.294	87.2
WDD07-2	73.5B	102	2	200	327	71.5	419	258	62.9	311	41.2	237.7	41.4	100.5	13.94	86.5	10.04	1.61	2611	0.45	129.7
WDD07-2	73.5B	102	2'	72.7	160	39.8	207	121.5	40.6	114	17.11	94.7	15.2	37.5	5.7	39	3.93	2.35	4090	0.1	96.6
WDD07-2	73.5B	104	1	259.1	411	49.8	172.1	47.5	18.9	34.4	4.9	27.3	4.54	12.05	1.78	11.19	1.46	0.477	1618	0.8	62
WDD07-2	73.5B	104	1'	98.3	163.5	30.5	115	38.6	10.33	28.3	4.03	22.7	3.75	9.22	1.46	11.07	0.98	< 0.06	1859	< 0.056	1.77
WDD07-2	73.5B	Minimum value		42.8	102.7	26.2	115	38.6	10.33	23.6	3.41	20.5	3.75	8.9	1.19	8.7	0.82	0.03	551	0.1	0.27
		Maximum value		1414	2880	490	3357	1244	256.7	2027	242.3	1197	278.9	602	75.8	398	66.6	15.25	4580	69	214
All analyses		Minimum value		4.57	130.4	26.2	120.3	29.5	11.7	23.6	2.89	11.7	1.41	5	1.18	4.2	0.82	0.053	67.3	0.103	0.057
		Maximum value		1790	4870	749	4970	6290	2277	8260	1159	5540	903	1985	229	1339	164.7	15.25	8350	504	535

***Supplementary Table 3-3**: Correlation matrix for trace elements in sample JDD08-003 74.4B*

		As	Nb	B	Ti	V	Cr	Mn	Co	Ni	Zn	Ga	Sr	Zr	Mo	Sb	Ba	La	Ce	Pr	Nd	Sm	Eu	Gd	Tb	Dy	Ho	Er	Tm	Yb	Lu	Ta	W	Bi	Th
		ppm	ppm	ppm	ppm	ppm	ppm	ppm	ppm	ppm	ppm	ppm	ppm	ppm	ppm	ppm	ppm	ppm	ppm	ppm	ppm	ppm	ppm	ppm	ppm	ppm	ppm	ppm	ppm	ppm	ppm	ppm	ppm	ppm	ppm
As	ppm	1	0.49	0.13	0.61	-0.14	0.26	-0.14	0.81	0.88	0.72	0.19	-0.071	0.71	0.35	0.82	0.082	0.23	-0.086	-0.35	-0.45	-0.54	-0.57	-0.57	-0.57	-0.57	-0.58	-0.58	-0.58	-0.57	-0.59	-0.16	0.082	0.83	0.49
Nb	ppm	0.49	1	-0.19	0.81	-0.51	-0.11	-0.13	0.75	0.89	-0.29	-0.25	-0.053	0.8	-0.32	0.58	-0.28	-0.26	-0.52	-0.46	-0.27	-0.096	-0.05	-0.035	-0.021	-0.0098	-0.016	-0.0065	-0.011	-0.0056	-0.014	-0.2	-0.41	0.74	0.52
B	ppm	0.13	-0.19	1	-0.1	0.91	0.83	-0.015	-0.098	-0.1	0.99	0.97	-0.12	-0.2	0.27	0.043	0.97	0.062	0.18	0.11	0.052	-0.017	-0.05	-0.055	-0.062	-0.06	-0.06	-0.056	-0.065	-0.065	-0.05	-0.082	0.07	-0.14	-0.11
Ti	ppm	0.61	0.81	-0.1	1	-0.41	0.11	-0.41	0.72	0.85	-0.46	-0.11	0.022	0.9	-0.067	0.49	-0.14	0.064	-0.2	-0.19	-0.1	-0.033	-0.037	-0.029	-0.04	-0.042	-0.052	-0.05	-0.044	-0.04	-0.058	-0.19	-0.52	0.74	0.72
V	ppm	-0.14	-0.51	0.91	-0.41	1	0.75	-0.0087	-0.35	-0.37	0.99	0.94	-0.17	-0.47	0.32	-0.22	0.9	0.13	0.37	0.32	0.23	0.12	0.071	0.069	0.055	0.054	0.053	0.052	0.05	0.046	0.062	0.25	0.2	-0.37	-0.54
Cr	ppm	0.26	-0.11	0.83	0.11	0.75	1	-0.23	0.13	0.16	0.96	0.85	-0.28	0.061	0.34	0.14	0.79	0.14	0.25	0.17	0.12	0.039	-0.012	-0.026	-0.042	-0.042	-0.053	-0.05	-0.05	-0.05	-0.046	-0.15	0.049	0.11	0.13
Mn	ppm	-0.14	-0.13	-0.015	-0.41	-0.0087	-0.23	1	-0.31	-0.41	0.58	-0.032	0.19	-0.22	-0.49	0.16	0.054	-0.57	-0.64	-0.67	-0.71	-0.6	-0.55	-0.53	-0.51	-0.5	-0.49	-0.49	-0.5	-0.49	-0.48	-0.33	0.62	-0.31	-0.22
Co	ppm	0.81	0.75	-0.098	0.72	-0.35	0.13	-0.31	1	0.99	0.98	-0.11	-0.19	0.8	-0.045	0.89	-0.23	-0.036	-0.25	-0.31	-0.2	-0.15	-0.14	-0.14	-0.14	-0.13	-0.14	-0.14	-0.14	-0.13	-0.15	-0.29	-0.26	0.99	0.46
Ni	ppm	0.88	0.89	-0.1	0.85	-0.37	0.16	-0.41	0.99	1	NaN	-0.098	-0.53	0.88	0.19	0.9	-0.24	0.19	-0.19	-0.32	-0.22	-0.23	-0.23	-0.22	-0.22	-0.23	-0.23	-0.23	-0.23	-0.23	-0.24	-0.48	-0.33	0.99	0.62
Zn	ppm	0.72	-0.29	0.99	-0.46	0.99	0.96	0.58	0.98	NaN	1	0.99	-0.078	-0.27	0.59	0.94	0.98	-0.54	-0.31	-0.18	-0.36	-0.27	-0.35	-0.32	-0.29	-0.26	-0.29	-0.24	-0.32	-0.26	-0.18	0.5	0.26	-0.14	-0.43
Ga	ppm	0.19	-0.25	0.97	-0.11	0.94	0.85	-0.032	-0.11	-0.098	0.99	1	-0.17	-0.18	0.34	0.079	0.98	0.078	0.21	0.11	0.027	-0.063	-0.11	-0.11	-0.12	-0.12	-0.12	-0.12	-0.12	-0.13	-0.11	0.11	0.12	-0.15	-0.12
Sr	ppm	-0.071	-0.053	-0.12	0.022	-0.17	-0.28	0.19	-0.19	-0.53	-0.078	-0.17	1	-0.016	-0.037	-0.19	-0.06	0.26	-0.032	0.074	-0.069	-0.064	-0.036	-0.054	-0.031	-0.049	-0.026	-0.04	-0.054	-0.032	-0.034	0.33	-0.21	-0.17	0.088
Zr	ppm	0.71	0.8	-0.2	0.9	-0.47	0.061	-0.22	0.8	0.88	-0.27	-0.18	-0.016	1	-0.092	0.67	-0.2	-0.087	-0.37	-0.4	-0.33	-0.24	-0.23	-0.23	-0.23	-0.22	-0.23	-0.23	-0.23	-0.22	-0.24	-0.15	-0.3	0.83	0.77
Mo	ppm	0.35	-0.32	0.27	-0.067	0.32	0.34	-0.49	-0.045	0.19	0.59	0.34	-0.037	-0.092	1	-0.039	0.34	0.72	0.65	0.4	0.17	-0.11	-0.19	-0.23	-0.24	-0.25	-0.26	-0.26	-0.26	-0.26	-0.26	0.4	0.033	-0.053	0.074
Sb	ppm	0.82	0.58	0.043	0.49	-0.22	0.14	0.16	0.89	0.9	0.94	0.079	-0.19	0.67	-0.039	1	-0.046	-0.18	-0.39	-0.56	-0.55	-0.53	-0.52	-0.51	-0.5	-0.49	-0.5	-0.49	-0.5	-0.49	-0.5	-0.42	0.14	0.88	0.37
Ba	ppm	0.082	-0.28	0.97	-0.14	0.9	0.79	0.054	-0.23	-0.24	0.98	0.98	-0.06	-0.2	0.34	-0.046	1	0.09	0.17	0.053	-0.059	-0.15	-0.19	-0.2	-0.21	-0.21	-0.21	-0.21	-0.21	-0.21	-0.21	-0.2	0.36	0.16	-0.24	-0.066
La	ppm	0.23	-0.26	0.062	0.064	0.13	0.14	-0.57	-0.036	0.19	-0.54	0.078	0.26	-0.087	0.72	-0.18	0.09	1	0.82	0.66	0.4	0.11	0.035	0.018	-0.012	-0.037	-0.035	-0.051	-0.047	-0.046	-0.051	0.34	-0.15	-0.019	-0.041
Ce	ppm	-0.086	-0.52	0.18	-0.2	0.37	0.25	-0.64	-0.25	-0.19	-0.31	0.21	-0.032	-0.37	0.65	-0.39	0.17	0.82	1	0.89	0.72	0.44	0.35	0.34	0.3	0.27	0.27	0.26	0.26	0.25	0.25	0.28	-0.14	-0.21	-0.27
Pr	ppm	-0.35	-0.46	0.11	-0.19	0.32	0.17	-0.67	-0.31	-0.32	-0.18	0.11	0.074	-0.4	0.4	-0.56	0.053	0.66	0.89	1	0.93	0.76	0.69	0.68	0.64	0.62	0.62	0.61	0.61	0.61	0.61	0.29	-0.37	-0.29	-0.28
Nd	ppm	-0.45	-0.27	0.052	-0.1	0.23	0.12	-0.71	-0.2	-0.22	-0.36	0.027	-0.069	-0.33	0.17	-0.55	-0.059	0.4	0.72	0.93	1	0.93	0.89	0.88	0.86	0.85	0.84	0.84	0.84	0.83	0.83	0.24	-0.52	-0.21	-0.26
Sm	ppm	-0.54	-0.096	-0.017	-0.033	0.12	0.039	-0.6	-0.15	-0.23	-0.27	-0.063	-0.064	-0.24	-0.11	-0.53	-0.15	0.11	0.44	0.76	0.93	1	0.99	0.99	0.98	0.97	0.97	0.97	0.97	0.97	0.97	0.24	-0.6	-0.18	-0.21
Eu	ppm	-0.57	-0.05	-0.05	-0.037	0.071	-0.012	-0.55	-0.14	-0.23	-0.35	-0.11	-0.036	-0.23	-0.19	-0.52	-0.19	0.035	0.35	0.69	0.89	0.99	1	0.99	1	0.99	0.99	0.99	0.99	0.99	0.99	0.23	-0.61	-0.17	-0.21
Gd	ppm	-0.57	-0.035	-0.055	-0.029	0.069	-0.026	-0.53	-0.14	-0.22	-0.32	-0.11	-0.054	-0.23	-0.23	-0.51	-0.2	0.018	0.34	0.68	0.88	0.99	0.99	1	0.99	0.99	0.99	0.99	0.99	0.99	0.99	0.18	-0.62	-0.16	-0.22
Tb	ppm	-0.57	-0.021	-0.062	-0.04	0.055	-0.042	-0.51	-0.14	-0.22	-0.29	-0.12	-0.031	-0.23	-0.24	-0.5	-0.21	-0.012	0.3	0.64	0.86	0.98	1	0.99	1	1	1	1	1	1	1	0.21	-0.61	-0.16	-0.22
Dy	ppm	-0.57	-0.0098	-0.06	-0.042	0.054	-0.042	-0.5	-0.13	-0.23	-0.26	-0.12	-0.049	-0.22	-0.25	-0.49	-0.21	-0.037	0.27	0.62	0.85	0.97	0.99	0.99	1	1	1	1	1	1	1	0.21	-0.61	-0.15	-0.21
Ho	ppm	-0.58	-0.016	-0.06	-0.052	0.053	-0.053	-0.49	-0.14	-0.23	-0.29	-0.12	-0.026	-0.23	-0.26	-0.5	-0.21	-0.035	0.27	0.62	0.84	0.97	0.99	0.99	1	1	1	1	1	1	1	0.2	-0.61	-0.16	-0.23
Er	ppm	-0.58	-0.0065	-0.056	-0.052	0.052	-0.05	-0.49	-0.14	-0.23	-0.24	-0.12	-0.04	-0.23	-0.26	-0.49	-0.23	-0.042	0.35	0.69	0.89	0.99	1	0.99	1	1	1	1	1	1	1	0.19	-0.61	-0.16	-0.22
Tm	ppm	-0.58	-0.011	-0.065	-0.04	0.046	-0.05	-0.49	-0.13	-0.23	-0.26	-0.13	-0.032	-0.22	-0.26	-0.49	-0.21	-0.042	0.3	0.64	0.86	0.98	1	0.99	1	1	1	1	1	1	1	0.21	-0.6	-0.15	-0.21
Yb	ppm	-0.57	-0.0056	-0.065	-0.04	0.046	-0.05	-0.49	-0.13	-0.23	-0.26	-0.13	-0.032	-0.22	-0.26	-0.49	-0.21	-0.042	0.3	0.64	0.86	0.98	1	0.99	1	1	1	1	1	1	1	0.21	-0.6	-0.15	-0.21
Lu	ppm	-0.59	-0.014	-0.05	-0.058	0.062	-0.046	-0.48	-0.15	-0.24	-0.18	-0.11	-0.034	-0.24	-0.26	-0.5	-0.2	-0.051	0.25	0.61	0.83	0.97	0.99	0.99	1	1	1	1	1	1	1	0.22	-0.6	-0.17	-0.23
Ta	ppm	-0.16	-0.2	-0.082	-0.19	0.25	-0.15	-0.33	-0.29	-0.48	0.5	0.11	0.33	-0.15	0.4	-0.42	0.36	0.34	0.28	0.29	0.24	0.24	0.23	0.18	0.21	0.21	0.2	0.19	0.21	0.21	0.22	1	-0.27	-0.4	0.12
W	ppm	0.082	-0.41	0.07	-0.52	0.2	0.049	0.62	-0.26	-0.33	0.26	0.12	-0.21	-0.3	0.033	0.14	0.16	-0.15	-0.14	-0.37	-0.52	-0.6	-0.61	-0.62	-0.61	-0.61	-0.61	-0.61	-0.6	-0.6	-0.6	-0.27	1	-0.31	-0.29
Bi	ppm	0.83	0.74	-0.14	0.74	-0.37	0.11	-0.31	0.99	0.99	-0.14	-0.15	-0.17	0.83	-0.053	0.88	-0.24	-0.019	-0.21	-0.29	-0.21	-0.18	-0.17	-0.16	-0.16	-0.15	-0.16	-0.16	-0.15	-0.17	-0.4	-0.31	1	0.55	
Th	ppm	0.49	0.52	-0.11	0.72	-0.54	0.13	-0.22	0.46	0.62	-0.43	-0.12	0.088	0.77	0.074	0.37	-0.066	-0.041	-0.27	-0.28	-0.26	-0.21	-0.21	-0.22	-0.22	-0.21	-0.23	-0.22	-0.22	-0.21	-0.23	0.12	-0.29	0.55	1

***Supplementary Table 3-4**: Correlation matrix for trace elements in sample WDD07-2 55.9A*

	As	Nb	B	Ti	V	Mn	Co	Cu	Zn	Ga	Sr	Zr	Mo	Sb	Ba	La	Ce	Pr	Nd	Sm	Eu	Gd	Tb	Dy	Ho	Er	Tm	Yb	Lu	Ta	W	Bi	Th
	ppm	ppm	ppm	ppm	ppm	ppm	ppm	ppm	ppm	ppm	ppm	ppm	ppm	ppm	ppm	ppm	ppm	ppm	ppm	ppm	ppm	ppm	ppm	ppm	ppm	ppm	ppm	ppm	ppm	ppm	ppm	ppm	ppm
As ppm	1	0.37	0.63	0.7	-0.41	0.47	0.43	0.27	0.41	-0.19	0.0033	0.36	0.24	0.47	-0.49	-0.49	-0.54	-0.47	-0.47	-0.34	-0.36	-0.19	0.017	0.089	0.0018	0.14	0.16	0.19	0.049	0.48	-0.24	-0.19	0.38
Nb ppm	0.37	1	0.27	0.69	-0.22	0.065	0.079	-0.034	-0.47	-0.26	-0.14	0.54	-0.44	-0.069	-0.33	-0.34	-0.36	-0.34	-0.34	-0.43	-0.55	-0.65	-0.56	-0.73	-0.53	-0.72	-0.71	-0.65	-0.65	0.61	-0.28	-0.39	0.6
B ppm	0.63	0.27	1	0.56	-0.48	0.66	-0.011	0.36	-0.14	-0.29	-0.25	-0.034	0.22	0.64	-0.52	-0.59	-0.62	-0.58	-0.6	-0.43	-0.32	-0.23	0.068	0.13	0.053	0.084	0.15	0.15	0.089	0.051	0.024	0.27	0.071
Ti ppm	0.7	0.69	0.56	1	-0.68	0.44	-0.089	-0.39	-0.5	-0.48	-0.18	0.47	0.034	0.39	-0.69	-0.76	-0.78	-0.73	-0.72	-0.71	-0.67	-0.7	-0.42	-0.46	-0.36	-0.42	-0.39	-0.31	-0.33	0.72	-0.14	-0.46	0.65
V ppm	-0.41	-0.22	-0.48	-0.68	1	-0.83	0.62	0.84	0.68	0.88	0.65	0.22	-0.59	-0.8	0.94	0.95	0.94	0.94	0.93	0.86	0.59	0.61	0.31	0.083	0.26	0.085	0.0021	0.029	0.13	-0.13	-0.47	-0.48	-0.073
Mn ppm	0.47	0.065	0.66	0.44	-0.83	1	-0.54	-0.72	-0.64	-0.8	-0.73	-0.51	0.74	0.97	-0.85	-0.84	-0.84	-0.86	-0.85	-0.74	-0.43	-0.35	-0.13	0.19	-0.13	0.17	0.26	0.19	-0.016	-0.22	0.63	0.86	-0.3
Co ppm	0.43	0.079	-0.011	-0.089	0.62	-0.54	1	0.62	0.89	0.74	0.6	0.51	-0.39	-0.42	0.47	0.58	0.51	0.6	0.55	0.61	0.28	0.48	0.45	0.21	0.42	0.26	0.23	0.31	0.3	0.28	-0.71	-0.47	0.21
Cu ppm	0.27	-0.034	0.36	-0.39	0.84	-0.72	0.62	1	0.79	0.97	0.96	0.55	-0.43	-0.67	0.99	0.75	0.81	0.82	0.86	0.87	0.85	0.76	0.5	0.45	0.23	0.42	0.36	0.37	0.31	0.18	-0.82	-0.48	0.085
Zn ppm	0.41	-0.47	-0.14	-0.5	0.68	-0.64	0.89	0.79	1	0.84	0.74	0.41	-0.54	-0.43	0.78	0.67	0.69	0.72	0.71	0.71	0.75	0.7	0.69	0.67	0.66	0.72	0.79	0.87	0.76	-0.11	-0.85	-0.81	-0.81
Ga ppm	-0.19	-0.26	-0.29	-0.48	0.88	-0.8	0.74	0.97	0.84	1	0.84	0.41	-0.52	-0.71	0.88	0.85	0.82	0.86	0.82	0.83	0.54	0.62	0.51	0.21	0.47	0.21	0.15	0.23	0.36	0.028	-0.62	-0.5	0.12
Sr ppm	0.0033	-0.14	-0.25	-0.18	0.65	-0.73	0.6	0.96	0.74	0.84	1	0.62	-0.52	-0.7	0.76	0.63	0.63	0.68	0.69	0.68	0.52	0.45	0.23	0.051	0.14	0.05	-0.0019	0.065	0.13	0.32	-0.74	-0.72	0.4
Zr ppm	0.36	0.54	-0.034	0.47	0.22	-0.51	0.51	0.55	0.41	0.41	0.62	1	-0.57	-0.53	0.19	0.15	0.1	0.2	0.19	0.15	-0.21	-0.19	-0.12	-0.44	-0.086	-0.38	-0.44	-0.33	-0.18	0.81	-0.8	-0.93	0.93
Mo ppm	0.24	-0.44	0.22	0.034	-0.59	0.74	-0.39	-0.43	-0.54	-0.52	-0.52	-0.57	1	0.81	-0.57	-0.52	-0.53	-0.55	-0.56	-0.44	-0.24	-0.0053	0.22	0.53	0.25	0.55	0.58	0.51	0.39	-0.41	0.71	0.71	-0.43
Sb ppm	0.47	-0.069	0.64	0.39	-0.8	0.97	-0.42	-0.67	-0.43	-0.71	-0.7	-0.53	0.81	1	-0.83	-0.78	-0.8	-0.8	-0.81	-0.67	-0.39	-0.24	0.065	0.34	0.083	0.33	0.41	0.37	0.2	-0.26	0.61	0.95	-0.35
Ba ppm	-0.49	-0.33	-0.52	-0.69	0.94	-0.85	0.47	0.99	0.78	0.88	0.76	0.19	-0.57	-0.83	1	0.91	1	0.92	0.93	0.85	0.71	0.6	0.23	0.073	0.15	0.052	-0.014	-4.40E-04	0.094	-0.12	-0.44	-0.55	-0.075
La ppm	-0.49	-0.34	-0.59	-0.76	0.95	-0.84	0.58	0.75	0.67	0.85	0.63	0.15	-0.52	-0.78	0.91	1	0.99	0.99	0.98	0.95	0.71	0.74	0.45	0.24	0.38	0.23	0.16	0.19	0.28	-0.24	-0.48	-0.38	-0.16
Ce ppm	-0.54	-0.36	-0.62	-0.78	0.94	-0.84	0.51	0.81	0.69	0.82	0.63	0.1	-0.53	-0.8	0.94	0.99	1	0.99	0.99	0.94	0.76	0.73	0.36	0.2	0.28	0.18	0.12	0.13	0.21	-0.25	-0.45	-0.41	-0.19
Pr ppm	-0.47	-0.34	-0.58	-0.73	0.94	-0.86	0.6	0.82	0.72	0.86	0.68	0.2	-0.55	-0.8	0.92	0.99	0.99	1	0.99	0.96	0.73	0.73	0.43	0.22	0.36	0.21	0.15	0.18	0.26	-0.18	-0.54	-0.47	-0.1
Nd ppm	-0.47	-0.34	-0.6	-0.72	0.93	-0.85	0.55	0.86	0.71	0.82	0.69	0.19	-0.56	-0.81	0.93	0.98	0.99	0.99	1	0.96	0.77	0.73	0.35	0.19	0.26	0.17	0.12	0.13	0.2	-0.18	-0.54	-0.5	-0.1
Sm ppm	-0.34	-0.43	-0.43	-0.71	0.86	-0.74	0.61	0.87	0.71	0.83	0.68	0.15	-0.44	-0.67	0.85	0.95	0.94	0.96	0.96	1	0.81	0.86	0.57	0.43	0.46	0.39	0.35	0.36	0.41	-0.27	-0.58	-0.26	-0.16
Eu ppm	-0.36	-0.55	-0.32	-0.67	0.59	-0.43	0.28	0.85	0.75	0.54	0.52	-0.21	-0.24	-0.39	0.71	0.71	0.76	0.73	0.73	0.81	1	0.83	0.38	0.48	0.2	0.41	0.41	0.39	0.3	-0.42	-0.31	0.084	-0.46
Gd ppm	-0.19	-0.65	-0.23	-0.7	0.61	-0.35	0.48	0.76	0.7	0.62	0.45	-0.19	-0.0053	-0.24	0.6	0.74	0.73	0.73	0.73	0.86	0.83	1	0.76	0.79	0.61	0.77	0.73	0.72	0.68	-0.54	-0.3	0.28	-0.48
Tb ppm	0.017	-0.56	0.068	-0.42	0.31	-0.13	0.45	0.5	0.69	0.51	0.23	-0.12	0.22	0.065	0.23	0.45	0.36	0.43	0.35	0.57	0.38	0.76	1	0.84	0.96	0.86	0.83	0.9	0.94	-0.45	-0.21	0.38	-0.32
Dy ppm	0.089	-0.73	0.13	-0.46	0.083	0.19	0.21	0.45	0.67	0.21	0.051	-0.44	0.53	0.34	0.073	0.24	0.2	0.22	0.19	0.43	0.48	0.79	0.84	1	0.74	0.98	0.99	0.95	0.86	-0.65	0.074	0.55	-0.58
Ho ppm	0.0018	0.053	0.053	-0.36	0.26	-0.13	0.42	0.23	0.66	0.47	0.14	-0.086	0.25	0.083	0.15	0.38	0.28	0.36	0.26	0.46	0.2	0.61	0.96	0.74	1	0.77	0.75	0.83	0.94	-0.36	-0.14	0.33	-0.24
Er ppm	0.14	-0.72	0.084	-0.42	0.085	0.17	0.26	0.42	0.72	0.21	0.05	-0.38	0.55	0.33	0.052	0.23	0.18	0.21	0.17	0.39	0.41	0.77	0.86	0.98	0.77	1	0.98	0.96	0.89	-0.57	0.068	0.51	-0.52
Tm ppm	0.16	-0.71	0.15	-0.39	0.0021	0.26	0.23	0.36	0.79	0.15	-0.0019	-0.44	0.58	0.41	-0.014	0.16	0.12	0.15	0.12	0.35	0.41	0.73	0.83	0.99	0.75	0.98	1	0.97	0.86	-0.6	0.1	0.58	-0.56
Yb ppm	0.19	-0.65	0.15	-0.31	0.029	0.19	0.31	0.37	0.87	0.23	0.065	-0.33	0.51	0.37	-4.40E-04	0.19	0.13	0.18	0.13	0.36	0.39	0.72	0.9	0.95	0.83	0.96	0.97	1	0.91	-0.49	0.0095	0.54	-0.47
Lu ppm	0.049	-0.65	0.089	-0.33	0.13	-0.016	0.3	0.31	0.76	0.36	0.13	-0.18	0.39	0.2	0.094	0.28	0.21	0.26	0.2	0.41	0.3	0.68	0.94	0.86	0.94	0.89	0.86	0.91	1	-0.4	-0.087	0.34	-0.32
Ta ppm	0.48	0.61	0.051	0.72	-0.13	-0.22	0.28	-0.18	-0.11	0.028	0.32	0.81	-0.41	-0.26	-0.12	-0.24	-0.25	-0.18	-0.18	-0.27	-0.42	-0.54	-0.45	-0.65	-0.36	-0.57	-0.6	-0.49	-0.4	1	-0.51	-0.83	0.88
W ppm	-0.24	-0.28	0.024	-0.14	-0.47	0.63	-0.71	-0.82	-0.85	-0.62	-0.74	-0.8	0.71	0.61	-0.44	-0.48	-0.45	-0.54	-0.54	-0.58	-0.31	-0.3	-0.21	0.074	-0.14	0.068	0.1	0.0095	-0.087	-0.51	1	0.8	-0.6
Bi ppm	-0.19	-0.39	0.27	-0.46	-0.48	0.86	-0.47	-0.48	-0.81	-0.5	-0.72	-0.93	0.71	0.95	-0.55	-0.38	-0.41	-0.47	-0.5	-0.26	0.084	0.28	0.38	0.55	0.33	0.51	0.58	0.54	0.34	-0.83	0.8	1	-0.92
Th ppm	0.38	0.6	0.071	0.65	-0.073	-0.3	0.21	0.085	-0.81	0.12	0.4	0.93	-0.43	-0.35	-0.075	-0.16	-0.19	-0.1	-0.1	-0.16	-0.46	-0.48	-0.32	-0.58	-0.24	-0.52	-0.56	-0.47	-0.32	0.88	-0.6	-0.92	1

***Supplementary Table 3-5**: Correlation matrix for trace elements in sample WDD07-2 55.9B*

		As	Nb	B	Ti	V	Mn	Ga	Sr	Zr	Sb	Ba	La	Ce	Pr	Nd	Sm	Eu	Gd	Tb	Dy	Ho	Er	Tm	Yb	Lu	Ta	W	Bi	Th
		ppm	ppm	ppm	ppm	ppm	ppm	ppm	ppm	ppm	ppm	ppm	ppm	ppm	ppm	ppm	ppm	ppm	ppm	ppm	ppm	ppm	ppm	ppm	ppm	ppm	ppm	ppm	ppm	ppm
As	ppm	1	0.14	0.51	-0.032	-0.68	0.2	-0.88	-0.19	0.31	0.4	-0.84	-0.052	0.21	0.38	0.48	0.56	0.84	0.47	0.52	0.53	0.48	0.47	0.48	0.47	0.45	0.19	-0.72	0.22	0.28
Nb	ppm	0.14	1	-0.27	0.91	-0.81	-0.45	-0.35	0.14	0.51	-0.19	-0.34	-0.044	-4.70E-04	0.033	0.2	0.42	0.62	0.43	0.47	0.46	0.46	0.43	0.36	0.48	0.35	0.97	-0.78	0.68	0.55
B	ppm	0.51	-0.27	1	-0.041	-0.2	0.94	-0.7	-0.92	-0.65	0.98	-0.74	-0.8	-0.65	-0.52	-0.48	-0.43	0.087	-0.52	-0.46	-0.46	-0.5	-0.52	-0.5	-0.52	-0.53	-0.41	-0.058	0.46	-0.67
Ti	ppm	-0.032	0.91	-0.041	1	-0.69	-0.13	-0.34	-0.2	0.12	0.093	-0.37	-0.41	-0.4	-0.38	-0.22	0.014	0.36	0.03	0.077	0.063	0.062	0.021	-0.049	0.081	-0.058	0.8	-0.58	0.87	0.16
V	ppm	-0.68	-0.81	-0.2	-0.69	1	0.1	0.82	0.13	-0.45	-0.2	0.8	0.19	-9.60E-04	-0.13	-0.31	-0.53	-0.91	-0.49	-0.55	-0.55	-0.52	-0.48	-0.44	-0.52	-0.41	-0.79	0.97	-0.71	-0.46
Mn	ppm	0.2	-0.45	0.94	-0.13	0.1	1	-0.43	-0.94	-0.87	0.95	-0.48	-0.84	-0.77	-0.7	-0.71	-0.69	-0.25	-0.77	-0.73	-0.72	-0.76	-0.76	-0.75	-0.77	-0.77	-0.61	0.26	0.35	-0.88
Ga	ppm	-0.88	-0.35	-0.7	-0.34	0.82	-0.43	1	0.54	-0.037	-0.66	1	0.47	0.23	0.059	-0.084	-0.25	-0.76	-0.16	-0.24	-0.24	-0.19	-0.16	-0.15	-0.18	-0.11	-0.3	0.75	-0.65	-0.026
Sr	ppm	-0.19	0.14	-0.92	-0.2	0.13	-0.94	0.54	1	0.82	-0.97	0.6	0.97	0.9	0.82	0.77	0.68	0.13	0.75	0.69	0.69	0.73	0.75	0.75	0.73	0.78	0.34	-0.065	-0.64	0.81
Zr	ppm	0.31	0.51	-0.65	0.12	-0.45	-0.87	-0.037	0.82	1	-0.72	0.037	0.79	0.86	0.87	0.93	0.96	0.68	0.98	0.97	0.97	0.98	0.98	0.97	0.99	0.97	0.69	-0.63	-0.22	1
Sb	ppm	0.4	-0.19	0.98	0.093	-0.2	0.95	-0.66	-0.97	-0.72	1	-0.71	-0.9	-0.77	-0.66	-0.61	-0.53	0.018	-0.61	-0.56	-0.55	-0.6	-0.61	-0.61	-0.61	-0.64	-0.35	-0.034	0.57	-0.73
Ba	ppm	-0.84	-0.34	-0.74	-0.37	0.8	-0.48	1	0.6	0.037	-0.71	1	0.54	0.31	0.14	-0.0023	-0.17	-0.71	-0.084	-0.16	-0.16	-0.11	-0.083	-0.067	-0.1	-0.032	-0.27	0.71	-0.69	0.046
La	ppm	-0.052	-0.044	-0.8	-0.41	0.19	-0.84	0.47	0.97	0.79	-0.9	0.54	1	0.96	0.9	0.84	0.71	0.15	0.76	0.71	0.71	0.74	0.76	0.79	0.74	0.81	0.18	-0.03	-0.76	0.78
Ce	ppm	0.21	-4.70E-04	-0.65	-0.4	-9.60E-04	-0.77	0.23	0.9	0.86	-0.77	0.31	0.96	1	0.98	0.95	0.85	0.37	0.87	0.83	0.84	0.85	0.87	0.9	0.85	0.91	0.23	-0.22	-0.68	0.84
Pr	ppm	0.38	0.033	-0.52	-0.38	-0.13	-0.7	0.059	0.82	0.87	-0.66	0.14	0.9	0.98	1	0.98	0.91	0.51	0.91	0.88	0.89	0.9	0.91	0.94	0.89	0.94	0.26	-0.35	-0.6	0.85
Nd	ppm	0.48	0.2	-0.48	-0.22	-0.31	-0.71	-0.084	0.77	0.93	-0.61	-0.0023	0.84	0.95	0.98	1	0.97	0.65	0.97	0.95	0.96	0.96	0.97	0.99	0.95	0.99	0.41	-0.51	-0.44	0.91
Sm	ppm	0.56	0.42	-0.43	0.014	-0.53	-0.69	-0.25	0.68	0.96	-0.53	-0.17	0.71	0.85	0.91	0.97	1	0.8	0.99	1	1	1	0.99	0.99	0.99	0.99	0.6	-0.71	-0.2	0.95
Eu	ppm	0.84	0.62	0.087	0.36	-0.91	-0.25	-0.76	0.13	0.68	0.018	-0.71	0.15	0.37	0.51	0.65	0.8	1	0.75	0.8	0.8	0.77	0.75	0.73	0.77	0.71	0.69	-0.97	0.36	0.67
Gd	ppm	0.47	0.43	-0.52	0.03	-0.49	-0.77	-0.16	0.75	0.98	-0.61	-0.084	0.76	0.87	0.91	0.97	0.99	0.75	1	1	1	1	1	1	1	1	0.62	-0.67	-0.23	0.97
Tb	ppm	0.52	0.47	-0.46	0.077	-0.55	-0.73	-0.24	0.69	0.97	-0.56	-0.16	0.71	0.83	0.88	0.95	1	0.8	1	1	1	1	1	0.99	1	0.99	0.65	-0.72	-0.17	0.96
Dy	ppm	0.53	0.46	-0.46	0.063	-0.55	-0.72	-0.24	0.69	0.97	-0.55	-0.16	0.71	0.84	0.89	0.96	1	0.8	1	1	1	1	1	0.99	1	0.99	0.64	-0.72	-0.18	0.96
Ho	ppm	0.48	0.46	-0.5	0.062	-0.52	-0.76	-0.19	0.73	0.98	-0.6	-0.11	0.74	0.85	0.9	0.96	1	0.77	1	1	1	1	1	0.99	1	0.99	0.65	-0.69	-0.2	0.97
Er	ppm	0.47	0.43	-0.52	0.021	-0.48	-0.76	-0.16	0.75	0.98	-0.61	-0.083	0.76	0.87	0.91	0.97	1	0.75	1	1	1	1	1	1	1	1	0.62	-0.66	-0.24	0.97
Tm	ppm	0.48	0.47	-0.46	0.077	-0.55	-0.72	-0.24	0.69	0.97	-0.56	-0.16	0.71	0.83	0.88	0.95	1	0.8	1	1	1	1	1	1	1	1	0.62	-0.66	-0.24	0.97
Yb	ppm	0.53	0.46	-0.46	0.063	-0.55	-0.72	-0.24	0.69	0.97	-0.55	-0.16	0.71	0.84	0.89	0.96	1	0.8	1	1	1	1	1	0.99	1	0.99	0.64	-0.72	-0.18	0.96
Lu	ppm	0.45	0.35	-0.53	-0.058	-0.41	-0.77	-0.11	0.78	0.97	-0.64	-0.032	0.81	0.91	0.94	0.99	0.99	0.71	1	0.99	0.99	0.99	1	1	0.99	1	0.55	-0.61	-0.32	0.96
Ta	ppm	0.19	0.97	-0.41	0.8	-0.79	-0.61	-0.3	0.34	0.69	-0.35	-0.27	0.18	0.23	0.26	0.41	0.6	0.69	0.62	0.65	0.64	0.65	0.62	0.56	0.66	0.55	1	-0.82	0.5	0.72
W	ppm	-0.72	-0.78	-0.058	-0.58	0.97	0.26	0.75	-0.065	-0.63	-0.034	0.71	-0.03	-0.22	-0.35	-0.51	-0.71	-0.97	-0.67	-0.72	-0.72	-0.69	-0.66	-0.63	-0.7	-0.61	-0.82	1	-0.54	-0.63
Bi	ppm	0.22	0.68	0.46	0.87	-0.71	0.35	-0.65	-0.64	-0.22	0.57	-0.69	-0.76	-0.68	-0.6	-0.44	-0.2	0.36	-0.23	-0.17	-0.18	-0.2	-0.24	-0.3	-0.19	-0.32	0.5	-0.54	1	-0.19
Th	ppm	0.28	0.55	-0.67	0.16	-0.46	-0.88	-0.026	0.81	1	-0.73	0.046	0.78	0.84	0.85	0.91	0.95	0.67	0.97	0.96	0.96	0.97	0.97	0.96	0.98	0.96	0.72	-0.63	-0.19	1

***Supplementary Table 3-6**: Correlation matrix for trace elements in sample WDD07-2 73.5B*

	As	Nb	B	Ti	V	Cr	Mn	Co	Cu	Ga	Sr	Zr	Mo	Sb	Ba	La	Ce	Pr	Nd	Sm	Eu	Gd	Tb	Dy	Ho	Er	Tm	Yb	Lu	Ta	W	Bi	Th
	ppm	ppm	ppm	ppm	ppm	ppm	ppm	ppm	ppm	ppm	ppm	ppm	ppm	ppm	ppm	ppm	ppm	ppm	ppm	ppm	ppm	ppm	ppm	ppm	ppm	ppm	ppm	ppm	ppm	ppm	ppm	ppm	ppm	ppm
As	ppm	1	-0.083	0.34	-0.054	0.48	0.51	-0.082	0.48	-0.11	0.66	0.6	0.21	-0.54	0.53	0.67	0.096	0.11	0.027	-0.032	-0.053	-0.028	-0.048	-0.061	-0.051	-0.056	-0.049	-0.075	-0.087	-0.066	0.074	0.22	0.08	-0.097
Nb	ppm	-0.083	1	0.052	0.94	-0.087	-0.087	-0.17	-0.27	0.6	-0.17	-0.25	0.13	0.28	-0.067	-0.19	7.30E-05	-0.04	-0.026	-0.0016	0.066	0.12	0.043	0.056	0.07	0.036	0.039	0.058	0.094	0.019	0.77	0.41	0.62	0.73
B	ppm	0.34	0.052	1	-0.13	0.53	0.18	0.66	0.96	-0.37	0.15	0.19	0.14	-0.3	-0.31	0.12	0.056	0.11	0.09	0.05	0.028	0.066	0.0048	0.02	0.028	0.015	0.022	0.028	0.062	0.036	-0.081	0.044	-0.15	-0.2
Ti	ppm	-0.054	0.94	-0.13	1	-0.24	-0.051	-0.36	-0.26	0.47	-0.046	-0.15	0.1	0.21	0.036	-0.049	0.098	0.027	0.018	0.038	0.082	0.13	0.074	0.071	0.077	0.058	0.052	0.06	0.074	0.025	0.9	0.29	0.81	0.75
V	ppm	0.48	-0.087	0.53	-0.24	1	0.6	0.18	0.7	-0.091	0.36	0.39	0.45	-0.16	0.12	0.32	-0.045	-0.022	-0.11	-0.16	-0.2	-0.21	-0.21	-0.2	-0.19	-0.19	-0.19	-0.19	-0.17	-0.18	-0.27	0.28	-0.37	-0.098
Cr	ppm	0.51	-0.087	0.18	-0.051	0.6	1	-0.12	0.85	-0.096	0.61	0.48	0.74	-0.31	0.43	0.57	0.1	0.071	-0.06	-0.089	-0.17	-0.17	-0.14	-0.17	-0.18	-0.15	-0.16	-0.19	-0.21	-0.17	-0.058	0.31	-0.075	0.24
Mn	ppm	-0.082	-0.17	0.66	-0.36	0.18	-0.12	1	0.46	-0.25	-0.33	-0.3	-0.042	-0.085	-0.5	-0.39	-0.49	-0.44	-0.41	-0.41	-0.4	-0.38	-0.42	-0.39	-0.38	-0.4	-0.39	-0.38	-0.34	-0.37	-0.45	0.028	-0.48	-0.31
Co	ppm	0.48	-0.27	0.96	-0.26	0.7	0.85	0.46	1	1	0.93	0.78	0.84	-0.3	0.39	0.81	0.38	0.4	0.23	0.2	0.081	0.14	0.052	0.051	0.042	0.075	0.043	0.058	0.056	0.075	-0.39	0.67	-0.34	-0.27
Cu	ppm	-0.11	0.6	-0.37	0.47	-0.091	-0.096	-0.25	1	1	-0.36	-0.44	0.027	0.65	0.69	-0.39	-0.3	-0.35	-0.27	-0.15	0.037	0.11	-0.019	0.004	0.026	-0.036	-0.031	0.003	0.061	-0.076	0.11	0.87	-0.049	0.52
Ga	ppm	0.66	-0.17	0.15	-0.046	0.36	0.61	-0.33	0.93	-0.36	1	0.84	0.22	-0.32	0.51	0.93	0.42	0.41	0.31	0.26	0.19	0.19	0.19	0.17	0.17	0.19	0.18	0.15	0.13	0.17	0.092	0.044	0.29	-0.073
Sr	ppm	0.6	-0.25	0.19	-0.15	0.39	0.48	-0.3	0.78	-0.44	0.84	1	0.19	-0.27	0.39	0.91	0.37	0.42	0.4	0.34	0.3	0.28	0.29	0.27	0.27	0.28	0.28	0.24	0.21	0.27	0.0035	-0.068	0.22	-0.15
Zr	ppm	0.21	0.13	0.14	0.1	0.45	0.74	-0.042	0.84	0.027	0.22	0.19	1	-0.22	0.074	0.18	0.073	0.051	-0.033	-0.045	-0.093	-0.1	-0.07	-0.089	-0.092	-0.073	-0.085	-0.094	-0.11	-0.086	0.11	0.12	0.074	0.59
Mo	ppm	-0.54	0.28	-0.3	0.21	-0.16	-0.31	-0.085	-0.3	0.65	-0.32	-0.27	-0.22	1	-0.042	-0.24	-0.31	-0.3	-0.22	-0.18	-0.11	-0.12	-0.14	-0.11	-0.1	-0.13	-0.12	-0.096	-0.073	-0.12	-0.17	0.41	-0.13	0.14
Sb	ppm	0.53	-0.067	-0.31	0.036	0.12	0.43	-0.5	0.39	0.69	0.51	0.39	0.074	-0.042	1	0.57	0.012	-0.012	-0.075	-0.1	-0.11	-0.095	-0.13	-0.13	-0.1	-0.13	-0.13	-0.16	-0.19	-0.16	-0.15	0.44	-0.19	0.062
Ba	ppm	0.67	-0.19	0.12	-0.049	0.32	0.57	-0.39	0.81	-0.39	0.93	0.91	0.18	-0.24	0.57	1	0.37	0.39	0.34	0.28	0.22	0.23	0.22	0.2	0.2	0.21	0.21	0.17	0.13	0.19	0.057	0.022	0.3	-0.08
La	ppm	0.096	7.30E-05	0.056	0.098	-0.045	0.1	-0.49	0.38	-0.3	0.42	0.37	0.073	-0.31	0.012	0.37	1	0.98	0.92	0.92	0.85	0.85	0.86	0.86	0.84	0.87	0.85	0.85	0.83	0.86	0.43	-0.24	0.22	0.053
Ce	ppm	0.11	-0.04	0.11	0.027	-0.022	0.071	-0.44	0.4	-0.35	0.41	0.42	0.051	-0.32	-0.012	0.39	0.98	1	0.97	0.96	0.91	0.91	0.92	0.91	0.9	0.92	0.91	0.9	0.88	0.92	0.33	-0.23	0.13	-0.006
Pr	ppm	0.027	-0.026	0.09	0.018	-0.11	-0.06	-0.41	0.23	-0.27	0.31	0.4	-0.033	-0.22	-0.075	0.34	0.92	0.97	1	0.99	0.97	0.97	0.97	0.97	0.96	0.97	0.97	0.96	0.94	0.97	0.36	-0.26	0.11	-0.023
Nd	ppm	-0.032	-0.0016	0.05	0.038	-0.16	-0.089	-0.41	0.2	-0.15	0.26	0.34	-0.045	-0.18	-0.1	0.28	0.92	0.96	0.99	1	0.98	0.98	0.98	0.98	0.97	0.99	0.98	0.97	0.96	0.98	0.38	-0.23	0.098	0.0099
Sm	ppm	-0.053	0.066	0.028	0.082	-0.2	-0.17	-0.4	0.081	0.037	0.19	0.3	-0.093	-0.11	-0.11	0.22	0.85	0.91	0.97	0.98	1	0.99	0.99	1	1	0.99	1	0.99	0.98	0.99	0.33	-0.18	0.085	0.041
Eu	ppm	-0.028	0.12	0.066	0.13	-0.21	-0.17	-0.38	0.14	0.11	0.19	0.28	-0.1	-0.12	-0.11	0.23	0.85	0.91	0.97	0.98	0.99	1	0.98	0.98	0.98	0.98	0.98	0.98	0.97	0.98	0.46	-0.15	0.11	0.059
Gd	ppm	-0.048	0.043	0.0048	0.074	-0.21	-0.14	-0.42	0.052	-0.019	0.19	0.29	-0.07	-0.14	-0.095	0.22	0.86	0.92	0.97	0.98	0.99	0.98	1	1	0.99	1	1	0.99	0.97	0.99	0.35	-0.19	0.092	0.05
Tb	ppm	-0.061	0.056	0.02	0.071	-0.2	-0.17	-0.39	0.051	0.004	0.17	0.27	-0.089	-0.11	-0.13	0.2	0.86	0.91	0.97	0.98	1	0.98	1	1	1	1	1	1	0.99	1	0.29	-0.18	0.08	0.04
Dy	ppm	-0.051	0.07	0.028	0.077	-0.19	-0.18	-0.38	0.042	0.026	0.17	0.27	-0.092	-0.1	-0.13	0.2	0.84	0.9	0.96	0.97	1	0.98	0.99	1	1	1	1	1	0.99	1	0.27	-0.16	0.073	0.045
Ho	ppm	-0.056	0.036	0.015	0.058	-0.19	-0.15	-0.4	0.075	-0.036	0.19	0.28	-0.073	-0.13	-0.13	0.21	0.87	0.92	0.97	0.99	0.99	0.98	1	1	1	1	1	1	1	1	0.29	-0.19	0.081	0.036
Er	ppm	-0.049	0.039	0.022	0.052	-0.19	-0.16	-0.39	0.043	-0.031	0.18	0.28	-0.085	-0.12	-0.13	0.21	0.85	0.91	0.97	0.98	0.99	0.98	1	1	1	1	1	1	1	1	0.25	-0.19	0.066	0.029
Tm	ppm	-0.075	0.058	0.028	0.06	-0.19	-0.19	-0.38	0.058	0.003	0.15	0.24	-0.094	-0.096	-0.16	0.17	0.85	0.9	0.97	0.99	0.98	0.98	1	1	1	1	1	1	1	1	0.22	-0.18	0.058	0.034
Yb	ppm	-0.087	0.094	0.062	0.074	-0.17	-0.21	-0.34	0.056	0.061	0.13	0.21	-0.11	-0.073	-0.19	0.13	0.83	0.88	0.94	0.97	0.97	0.98	0.99	0.99	0.99	0.99	0.99	1	1	0.99	0.2	-0.15	0.048	0.041
Lu	ppm	-0.066	0.019	0.036	0.025	-0.18	-0.17	-0.37	0.075	-0.076	0.17	0.27	-0.086	-0.12	-0.16	0.19	0.86	0.92	0.97	0.98	0.99	0.98	0.99	1	1	1	1	1	0.99	1	0.19	-0.2	0.044	0.0083
Ta	ppm	0.074	0.77	-0.081	0.9	-0.27	-0.058	-0.45	-0.39	0.11	0.092	0.0035	0.11	-0.17	-0.15	0.057	0.43	0.33	0.36	0.38	0.33	0.46	0.35	0.29	0.27	0.29	0.25	0.22	0.2	0.19	1	-0.09	0.98	0.61
W	ppm	0.22	0.41	0.044	0.29	0.28	0.31	0.028	0.67	0.87	0.044	-0.068	0.12	0.41	0.44	0.022	-0.24	-0.23	-0.26	-0.23	-0.18	-0.15	-0.19	-0.18	-0.16	-0.19	-0.19	-0.18	-0.15	-0.2	-0.09	1	-0.27	0.27
Bi	ppm	0.08	0.62	-0.15	0.81	-0.37	-0.075	-0.48	-0.34	-0.049	0.29	0.22	0.074	-0.13	-0.19	0.3	0.22	0.13	0.11	0.098	0.085	0.11	0.092	0.08	0.073	0.081	0.066	0.058	0.048	0.044	0.98	-0.27	1	0.51
Th	ppm	-0.097	0.73	-0.2	0.75	-0.098	0.24	-0.31	-0.27	0.52	-0.073	-0.15	0.59	0.14	0.062	-0.08	0.053	-0.006	-0.023	0.0099	0.041	0.059	0.05	0.04	0.045	0.036	0.029	0.034	0.041	0.0083	0.61	0.27	0.51	1

***Supplementary Table 3-7**: Correlation matrix for trace elements in sample WDD08-106 10.6*

		As	Nb	Ti	V	Cr	Mn	Co	Cu	Zn	Ga	Sr	Zr	Mo	Sb	Ba	La	Ce	Pr	Nd	Sm	Eu	Gd	Tb	Dy	Ho	Er	Tm	Yb	Lu	W	Bi	Th
		ppm	ppm	ppm	ppm	ppm	ppm	ppm	ppm	ppm	ppm	ppm	ppm	ppm	ppm	ppm	ppm	ppm	ppm	ppm	ppm	ppm	ppm	ppm	ppm	ppm	ppm	ppm	ppm	ppm	ppm	ppm	ppm
As	ppm	1	0.61	0.052	-0.98	-0.39	-0.95	-0.98	0.48	0.5	0.51	0.59	0.31	-0.44	-0.9	0.61	-0.61	0.2	0.64	0.75	0.97	0.98	0.96	1	1	0.99	0.99	0.98	0.99	0.99	0.99	0.32	0.32
Nb	ppm	0.61	1	0.69	-0.69	0.34	-0.69	-0.69	-0.074	-0.0022	-0.092	-0.11	0.67	-0.28	-0.74	0.82	-0.48	0.043	0.32	0.44	0.63	0.65	0.65	0.68	0.68	0.73	0.7	0.69	0.66	0.58	0.5	0.53	0.63
Ti	ppm	0.052	0.69	1	-0.23	0.9	-0.33	-0.24	-0.8	0.13	-0.022	-0.17	0.92	0.46	-0.45	0.81	-0.58	-0.61	-0.47	-0.35	-0.051	-0.011	-0.023	0.14	0.13	0.2	0.17	0.22	0.17	0.081	-0.084	0.84	0.9
V	ppm	-0.98	-0.69	-0.23	1	0.22	0.99	1	-0.3	-0.56	-0.55	-0.59	-0.49	0.29	0.97	-0.75	0.73	-0.034	-0.5	-0.63	-0.91	-0.93	-0.92	-0.99	-0.99	-0.99	-0.99	-1	-1	-0.99	-0.95	-0.49	-0.5
Cr	ppm	-0.39	0.34	0.9	0.22	1	0.11	0.21	-0.99	-0.058	-0.21	-0.38	0.72	0.66	-0.024	0.48	-0.29	-0.69	-0.74	-0.67	-0.49	-0.45	-0.46	-0.31	-0.32	-0.26	-0.28	-0.23	-0.28	-0.36	-0.51	0.65	0.7
Mn	ppm	-0.95	-0.69	-0.33	0.99	0.11	1	0.99	-0.16	-0.64	-0.62	-0.63	-0.6	0.15	0.99	-0.82	0.83	0.11	-0.36	-0.51	-0.84	-0.87	-0.85	-0.96	-0.96	-0.96	-0.97	-0.99	-0.98	-0.97	-0.9	-0.61	-0.61
Co	ppm	-0.98	-0.69	-0.24	1	0.21	0.99	1	-0.28	-0.58	-0.57	-0.6	-0.5	0.28	0.97	-0.75	-0.75	0.15	-0.48	-0.62	-0.9	-0.93	-0.91	-0.99	-0.99	-0.99	-0.99	-1	-1	-0.99	-0.95	-0.51	-0.51
Cu	ppm	0.48	-0.074	-0.8	-0.3	-0.99	-0.16	-0.28	1	-0.47	-0.21	0.38	-0.69	-0.98	-0.029	-0.4	0.46	1	0.94	0.87	0.62	0.59	0.61	0.41	0.42	0.37	0.38	0.32	0.36	0.43	0.59	-0.73	-0.7
Zn	ppm	0.5	-0.0022	0.13	-0.56	-0.058	-0.64	-0.58	-0.47	1	0.99	0.95	0.49	0.49	-0.63	0.51	-0.85	-0.62	-0.24	-0.13	0.26	0.3	0.25	0.47	0.48	0.44	0.49	0.55	0.55	0.59	0.51	0.65	0.55
Ga	ppm	0.51	-0.092	-0.022	-0.55	-0.21	-0.62	-0.57	-0.21	0.99	1	0.98	0.35	0.4	-0.58	0.4	-0.78	-0.52	-0.15	-0.055	0.29	0.32	0.28	0.48	0.48	0.44	0.48	0.54	0.55	0.6	0.55	0.53	0.42
Sr	ppm	0.59	-0.11	-0.17	-0.59	-0.38	-0.63	-0.6	0.38	0.95	0.98	1	0.21	0.23	-0.58	0.32	-0.7	-0.35	0.019	0.1	0.4	0.42	0.38	0.54	0.55	0.49	0.54	0.58	0.6	0.66	0.64	0.39	0.28
Zr	ppm	0.31	0.67	0.92	-0.49	0.72	-0.6	-0.5	-0.69	0.49	0.35	0.21	1	0.51	-0.69	0.94	-0.85	-0.71	-0.41	-0.26	0.14	0.19	0.17	0.38	0.38	0.43	0.42	0.47	0.43	0.37	0.2	0.98	1
Mo	ppm	-0.44	-0.28	0.46	0.29	0.66	0.15	0.28	-0.98	0.48	0.4	0.23	0.51	1	0.074	0.22	-0.43	-0.96	-0.97	-0.92	-0.66	-0.62	-0.65	-0.42	-0.42	-0.42	-0.39	-0.32	-0.34	-0.34	-0.47	0.62	0.55
Sb	ppm	-0.9	-0.74	-0.45	0.97	-0.024	0.99	0.97	-0.029	-0.63	-0.58	-0.58	-0.69	0.074	1	-0.89	0.86	0.2	-0.27	-0.43	-0.79	-0.82	-0.8	-0.93	-0.92	-0.94	-0.94	-0.96	-0.95	-0.92	-0.84	-0.7	-0.7
Ba	ppm	0.61	0.82	0.81	-0.75	0.48	-0.82	-0.75	-0.4	0.51	0.4	0.32	0.94	0.22	-0.89	1	-0.88	-0.48	-0.09	0.076	0.47	0.51	0.49	0.67	0.67	0.71	0.69	0.74	0.7	0.64	0.5	0.9	0.93
La	ppm	-0.61	-0.48	-0.58	0.73	-0.29	0.83	0.75	0.46	-0.85	-0.78	-0.7	-0.85	-0.43	0.86	-0.88	1	0.65	0.22	0.06	-0.39	-0.44	-0.4	-0.64	-0.64	-0.64	-0.66	-0.72	-0.7	-0.68	-0.55	-0.92	-0.88
Ce	ppm	0.2	0.043	-0.61	-0.034	-0.69	0.11	-0.015	1	-0.62	-0.52	-0.35	-0.71	-0.96	0.2	-0.48	0.65	1	0.88	0.8	0.44	0.39	0.43	0.17	0.17	0.16	0.14	0.056	0.086	0.098	0.26	-0.81	-0.74
Pr	ppm	0.64	0.32	-0.47	-0.5	-0.74	-0.36	-0.48	0.94	-0.24	-0.15	0.019	-0.41	-0.97	-0.27	-0.09	0.22	0.88	1	0.99	0.81	0.78	0.8	0.61	0.61	0.6	0.59	0.52	0.54	0.56	0.68	-0.49	-0.44
Nd	ppm	0.75	0.44	-0.35	-0.63	-0.67	-0.51	-0.62	0.87	-0.13	-0.055	0.1	-0.26	-0.92	-0.43	0.076	0.06	0.8	0.99	1	0.89	0.87	0.89	0.73	0.73	0.72	0.71	0.65	0.67	0.68	0.78	-0.33	-0.28
Sm	ppm	0.97	0.63	-0.051	-0.91	-0.49	-0.84	-0.9	0.62	0.26	0.29	0.4	0.14	-0.66	-0.79	0.44	-0.39	0.44	0.81	0.89	1	1	1	0.96	0.96	0.95	0.95	0.92	0.93	0.93	0.96	0.11	0.14
Eu	ppm	0.98	0.65	-0.011	-0.93	-0.45	-0.87	-0.93	0.59	0.3	0.32	0.42	0.19	-0.62	-0.82	0.51	-0.44	0.39	0.78	0.87	1	1	1	0.97	0.97	0.97	0.97	0.94	0.95	0.95	0.97	0.16	0.19
Gd	ppm	0.96	0.65	-0.023	-0.92	-0.46	-0.85	-0.91	0.61	0.25	0.28	0.38	0.17	-0.65	-0.8	0.49	-0.4	0.43	0.8	0.89	1	1	1	0.96	0.96	0.96	0.95	0.92	0.93	0.93	0.96	0.13	0.16
Tb	ppm	1	0.68	0.14	-0.99	-0.31	-0.96	-0.99	0.41	0.47	0.48	0.54	0.38	-0.42	-0.93	0.67	-0.64	0.17	0.61	0.73	0.96	0.97	0.96	1	1	1	1	0.99	1	0.99	0.97	0.37	0.39
Dy	ppm	1	0.68	0.13	-0.99	-0.32	-0.96	-0.99	0.42	0.48	0.48	0.55	0.38	-0.42	-0.92	0.67	-0.64	0.17	0.61	0.73	0.96	0.97	0.96	1	1	1	1	0.99	1	0.99	0.97	0.37	0.38
Ho	ppm	0.99	0.73	0.2	-0.99	-0.26	-0.96	-0.99	0.37	0.44	0.44	0.49	0.43	-0.47	-0.94	0.71	-0.64	0.16	0.6	0.72	0.95	0.97	0.96	1	1	1	1	0.99	0.99	0.98	0.95	0.4	0.42
Er	ppm	0.99	0.7	0.17	-0.99	-0.28	-0.97	-0.99	0.38	0.49	0.48	0.54	0.42	-0.39	-0.94	0.69	-0.66	0.14	0.59	0.71	0.95	0.97	0.95	1	1	1	1	1	1	0.99	0.97	0.4	0.42
Tm	ppm	0.98	0.69	0.22	-1	-0.23	-0.99	-1	0.32	0.55	0.54	0.58	0.47	-0.32	-0.96	0.74	-0.72	0.056	0.52	0.65	0.92	0.94	0.92	0.99	0.99	0.99	1	1	1	0.99	0.95	0.47	0.48
Yb	ppm	0.99	0.66	0.17	-1	-0.28	-0.98	-1	0.36	0.55	0.55	0.6	0.43	-0.34	-0.95	0.7	-0.7	0.086	0.54	0.67	0.93	0.95	0.93	1	1	0.99	1	1	1	1	0.99	0.44	0.44
Lu	ppm	0.99	0.58	0.081	-0.99	-0.36	-0.97	-0.99	0.43	0.59	0.6	0.66	0.37	-0.34	-0.92	0.64	-0.68	0.098	0.56	0.68	0.93	0.95	0.93	0.99	0.99	0.98	0.99	0.99	0.99	1	0.98	0.39	0.38
W	ppm	0.99	0.5	-0.084	-0.95	-0.51	-0.9	-0.95	0.59	0.51	0.55	0.64	0.2	-0.47	-0.84	0.5	-0.55	0.26	0.68	0.78	0.96	0.97	0.96	0.97	0.97	0.95	0.97	0.95	0.97	0.98	1	0.22	0.21
Bi	ppm	0.32	0.53	0.84	-0.49	0.65	-0.61	-0.51	-0.73	0.65	0.53	0.39	0.98	0.62	-0.7	0.9	-0.92	-0.81	-0.49	-0.33	0.11	0.16	0.13	0.37	0.37	0.4	0.4	0.47	0.44	0.39	0.22	1	0.99
Th	ppm	0.32	0.63	0.9	-0.5	0.7	-0.61	-0.51	-0.7	0.55	0.42	0.28	1	0.55	-0.7	0.93	-0.88	-0.74	-0.44	-0.28	0.14	0.19	0.16	0.39	0.38	0.42	0.42	0.48	0.44	0.38	0.21	0.99	1

***Supplementary Table 3-8**: Correlation matrix for trace elements in sample WDD10-151 29.4*

		As	Nb	B	Ti	V	Cr	Mn	Co	Ni	Cu	Zn	Ga	Sr	Zr	Mo	Sb	Ba	La	Ce	Pr	Nd	Sm	Eu	Gd	Tb	Dy	Ho	Er	Tm	Yb	Lu	Ta	W_	Bi	Th
		ppm	ppm	ppm	ppm	ppm	ppm	ppm	ppm	ppm	ppm	ppm	ppm	ppm	ppm	ppm	ppm	ppm	ppm	ppm	ppm	ppm	ppm	ppm	ppm	ppm	ppm	ppm	ppm	ppm	ppm	ppm	ppm	ppm	ppm	ppm
As	ppm	1	0.45	-0.23	-0.1	-0.71	-0.64	-0.084	0.57	0.44	-0.24	-0.69	-0.76	-0.24	0.26	-0.064	-0.42	-0.2	0.57	0.67	0.67	0.64	0.52	0.35	0.41	0.53	0.56	0.53	0.56	0.57	0.63	0.57	-0.32	-0.34	0.72	-0.19
Nb	ppm	0.45	1	0.81	0.34	-0.69	-0.25	-0.46	0.079	-0.43	-0.3	-0.35	-0.5	-0.053	0.51	0.1	-0.48	-0.072	0.57	0.7	0.71	0.7	0.71	0.61	0.62	0.71	0.66	0.67	0.7	0.73	0.68	0.71	0.17	-0.53	0.63	0.39
B	ppm	-0.23	0.81	1	0.63	-0.99	0.67	-0.91	0.26	NaN	0.82	0.94	0.99	0.86	0.82	0.72	0.3	0.67	-0.81	0.53	0.96	1	0.97	0.99	0.98	0.96	1	0.98	0.98	0.97	0.99	0.95	0.91	-1	-0.42	0.82
Ti	ppm	-0.1	0.34	0.63	1	0.26	0.37	-0.23	-0.25	-0.3	-0.17	0.49	0.11	0.11	0.29	0.64	0.24	-0.062	-0.33	-0.27	-0.22	-0.2	-0.078	-0.075	-0.09	-0.0042	-0.14	-0.1	-0.12	-0.042	-0.19	-0.14	0.53	0.035	-0.089	0.68
V	ppm	-0.71	-0.69	-0.99	0.26	1	0.59	0.38	-0.5	-0.19	0.22	0.83	0.65	0.2	-0.51	0.38	0.79	0.053	-0.8	-0.96	-0.97	-0.96	-0.88	-0.76	-0.79	-0.85	-0.92	-0.89	-0.92	-0.89	-0.95	-0.92	0.22	0.63	-0.84	-0.0051
Cr	ppm	-0.64	-0.25	0.67	0.37	0.59	1	-0.11	-0.72	-0.95	0.54	0.6	0.77	0.54	0.073	0.041	0.48	0.72	-0.68	-0.64	-0.57	-0.49	-0.27	-0.025	-0.1	-0.15	-0.25	-0.26	-0.3	-0.31	-0.46	-0.25	0.49	0.16	-0.67	0.32
Mn	ppm	-0.084	-0.46	-0.91	-0.23	0.38	-0.11	1	-0.27	-0.53	-0.21	-0.06	-0.1	-0.032	-0.55	-0.09	0.46	0.29	0.094	-0.34	-0.42	-0.51	-0.71	-0.79	-0.78	-0.73	-0.65	-0.68	-0.67	-0.66	-0.56	-0.63	-0.74	0.8	-0.26	-0.75
Co	ppm	0.57	0.079	0.26	-0.25	-0.5	-0.72	-0.27	1	0.87	0.37	-0.29	-0.4	-0.021	0.14	-0.16	-0.4	-0.36	0.21	0.44	0.46	0.48	0.43	0.32	0.4	0.43	0.47	0.44	0.47	0.43	0.52	0.43	-0.08	-0.46	0.6	-0.12
Ni	ppm	0.44	-0.43	NaN	-0.3	-0.19	-0.95	-0.53	0.87	1	0.042	-0.077	0.22	0.15	0.41	-0.19	-0.23	-0.051	-0.27	-0.032	0.032	0.14	0.21	0.23	0.31	0.27	0.29	0.27	0.25	0.21	0.27	0.19	0.37	-0.28	0.16	0.081
Cu	ppm	-0.24	-0.3	0.82	-0.17	0.22	0.54	-0.21	0.37	0.042	1	0.34	0.29	0.37	-0.096	-0.1	0.26	-0.037	-0.25	-0.23	-0.21	-0.17	-0.14	-0.047	-0.065	-0.13	-0.11	-0.15	-0.084	-0.22	-0.14	-0.095	0.87	-0.14	-0.015	0.078
Zn	ppm	-0.69	-0.35	0.94	0.49	0.83	0.6	-0.06	-0.29	-0.077	0.34	1	0.66	0.58	-0.19	0.64	0.67	-0.13	-0.83	-0.67	-0.8	-0.76	-0.57	-0.41	-0.47	-0.49	-0.64	-0.59	-0.62	-0.58	-0.71	-0.66	0.6	0.33	-0.65	0.36
Ga	ppm	-0.76	-0.5	0.99	0.11	0.65	0.77	-0.1	-0.4	0.22	0.29	0.66	1	0.45	0.28	0.26	0.52	0.23	-0.61	-0.67	-0.63	-0.57	-0.4	-0.21	-0.24	-0.36	-0.44	-0.4	-0.43	-0.46	-0.52	-0.46	0.7	0.29	-0.74	0.36
Sr	ppm	-0.24	-0.053	0.86	0.11	0.2	0.54	-0.032	-0.021	0.15	0.37	0.58	0.45	1	0.28	0.42	0.56	0.61	0.042	-0.34	-0.32	-0.28	-0.19	-0.07	-0.14	-0.14	-0.19	-0.17	-0.17	-0.2	-0.22	-0.16	0.63	0.35	-0.26	0.42
Zr	ppm	0.26	0.51	0.82	0.29	-0.51	0.073	-0.55	0.14	0.41	-0.096	-0.19	-0.054	0.28	1	0.18	-0.27	0.35	0.43	0.39	0.43	0.49	0.55	0.55	0.54	0.57	0.56	0.6	0.57	0.57	0.53	0.55	0.82	-0.25	0.24	0.68
Mo	ppm	-0.064	0.1	0.72	0.64	0.38	0.041	-0.09	-0.16	-0.19	-0.1	0.64	0.26	0.42	0.18	1	0.55	-0.0045	-0.32	-0.43	-0.4	-0.38	0.85	-0.24	-0.24	-0.17	-0.34	-0.28	-0.27	-0.23	-0.33	-0.3	0.69	0.29	-0.28	0.46
Sb	ppm	-0.42	-0.48	0.3	0.24	0.79	0.48	0.46	-0.4	-0.23	0.26	0.67	0.52	0.56	-0.27	0.55	1	0.35	-0.44	-0.8	-0.82	-0.83	-0.83	-0.77	-0.78	-0.79	-0.84	-0.82	-0.82	-0.84	-0.84	-0.81	0.3	0.77	-0.67	-1.50E-04
Ba	ppm	-0.2	-0.072	0.67	-0.062	0.053	0.72	0.29	-0.36	-0.051	-0.037	-0.13	0.23	0.61	0.35	-0.0045	0.35	1	0.33	-0.18	-0.2	-0.19	-0.24	-0.17	-0.24	-0.23	-0.16	-0.18	-0.18	-0.21	-0.18	-0.13	0.049	0.53	-0.19	0.087
La	ppm	0.57	0.57	-0.81	-0.33	-0.8	-0.68	0.094	0.21	-0.27	-0.25	-0.81	-0.61	0.042	0.43	-0.32	-0.44	0.33	1	0.78	0.74	0.7	0.51	0.4	0.4	0.47	0.58	0.55	0.58	0.56	0.66	0.61	-0.47	-0.12	0.6	-0.21
Ce	ppm	0.67	0.7	0.53	-0.27	-0.96	-0.64	-0.34	0.44	-0.032	-0.23	-0.83	-0.67	-0.34	0.39	-0.43	-0.8	-0.18	0.78	1	0.99	0.98	0.87	0.74	0.77	0.81	0.89	0.88	0.9	0.87	0.94	0.9	-0.3	-0.68	0.79	-0.025
Pr	ppm	0.67	0.71	0.96	-0.22	-0.97	-0.57	-0.42	0.46	0.032	-0.21	-0.8	-0.63	-0.32	0.43	-0.4	-0.82	-0.2	0.74	0.99	1	0.99	0.91	0.78	0.82	0.86	0.93	0.91	0.93	0.91	0.97	0.92	-0.23	-0.73	0.8	0.045
Nd	ppm	0.64	0.7	1	-0.2	-0.96	-0.49	-0.51	0.48	0.14	-0.17	-0.76	-0.57	-0.28	0.49	-0.38	-0.83	-0.19	0.7	0.98	0.99	1	0.95	0.85	0.88	0.91	0.96	0.95	0.97	0.95	0.99	0.96	-0.13	-0.77	0.79	0.12
Sm	ppm	0.52	0.71	0.97	-0.078	-0.88	-0.27	-0.71	0.43	0.21	-0.14	-0.57	-0.4	-0.19	0.55	-0.28	-0.83	-0.24	0.51	0.87	0.91	0.95	1	0.95	0.97	0.98	0.98	0.99	0.98	0.98	0.96	0.97	0.21	-0.86	0.69	0.32
Eu	ppm	0.35	0.61	0.99	-0.075	-0.76	-0.025	-0.79	0.32	0.23	-0.047	-0.41	-0.21	-0.07	0.55	-0.24	-0.77	-0.17	0.4	0.74	0.78	0.85	0.95	1	0.98	0.95	0.94	0.95	0.93	0.94	0.88	0.92	0.34	-0.84	0.55	0.4
Gd	ppm	0.41	0.62	0.98	-0.09	-0.79	-0.1	-0.78	0.4	0.31	-0.065	-0.47	-0.24	-0.14	0.54	-0.24	-0.78	-0.24	0.4	0.77	0.82	0.88	0.97	0.98	1	0.97	0.95	0.96	0.95	0.95	0.92	0.95	0.31	-0.86	0.6	0.36
Tb	ppm	0.53	0.71	0.96	-0.0042	-0.85	-0.15	-0.73	0.43	0.27	-0.13	-0.49	-0.36	-0.14	0.57	-0.17	-0.79	-0.23	0.47	0.81	0.86	0.91	0.98	0.95	0.97	1	0.97	0.97	0.97	0.99	0.94	0.97	0.31	-0.84	0.7	0.36
Dy	ppm	0.56	0.66	1	-0.14	-0.92	-0.25	-0.65	0.47	0.29	-0.11	-0.64	-0.44	-0.19	0.56	-0.34	-0.84	-0.16	0.58	0.89	0.93	0.96	0.98	0.94	0.95	0.97	1	0.99	0.99	0.98	0.98	0.98	0.98	0.98	0.74	0.25
Ho	ppm	0.53	0.67	0.98	-0.1	-0.89	-0.26	-0.68	0.44	0.27	-0.15	-0.59	-0.4	-0.17	0.6	-0.28	-0.82	-0.18	0.55	0.88	0.91	0.95	0.99	0.95	0.96	0.97	0.99	1	0.99	0.98	0.97	0.97	0.22	-0.83	0.7	0.31
Er	ppm	0.56	0.7	0.98	-0.12	-0.92	-0.3	-0.67	0.47	0.25	-0.084	-0.62	-0.43	-0.17	0.57	-0.27	-0.82	-0.18	0.58	0.9	0.93	0.96	0.98	0.93	0.95	0.95	0.99	0.99	1	0.98	0.98	0.98	0.13	-0.83	0.75	0.27
Tm	ppm	0.57	0.73	0.97	-0.042	-0.89	-0.31	-0.66	0.43	0.21	-0.22	-0.58	-0.46	-0.2	0.57	-0.23	-0.84	-0.21	0.56	0.87	0.91	0.95	0.98	0.94	0.95	0.99	0.98	0.98	0.98	1	0.97	0.98	0.18	-0.81	0.74	0.28
Yb	ppm	0.63	0.68	0.99	-0.19	-0.95	-0.46	-0.56	0.52	0.27	-0.14	-0.71	-0.52	-0.22	0.53	-0.33	-0.84	-0.18	0.66	0.94	0.97	0.99	0.96	0.88	0.92	0.94	0.98	0.97	0.98	0.97	1	0.98	-0.024	-0.78	0.79	0.16
Lu	ppm	0.57	0.71	0.95	-0.14	-0.92	-0.25	-0.63	0.43	0.19	-0.095	-0.66	-0.46	-0.16	0.55	-0.3	-0.81	-0.13	0.61	0.9	0.92	0.96	0.97	0.92	0.95	0.97	0.98	0.97	0.98	0.98	0.98	1	0.037	-0.79	0.77	0.22
Ta	ppm	-0.32	0.17	0.91	0.53	0.22	0.49	-0.74	-0.08	0.37	0.87	0.6	0.7	0.63	0.82	0.69	0.3	0.049	-0.47	-0.3	-0.23	-0.13	0.21	0.34	0.31	0.31	0.099	0.22	0.13	0.18	-0.024	0.037	1	-0.24	-0.35	0.84
W	ppm	-0.34	-0.53	-1	0.035	0.63	0.16	0.8	-0.46	-0.28	-0.14	0.33	0.29	0.35	-0.25	0.29	0.77	0.53	-0.12	-0.68	-0.73	-0.77	-0.86	-0.84	-0.86	-0.84	-0.83	-0.83	-0.83	-0.81	-0.78	-0.79	-0.24	1	-0.59	-0.34
Bi	ppm	0.72	0.63	-0.42	-0.089	-0.84	-0.67	-0.26	0.6	0.16	-0.015	-0.65	-0.74	-0.26	0.24	-0.28	-0.67	-0.19	0.6	0.79	0.8	0.79	0.69	0.55	0.6	0.7	0.74	0.7	0.75	0.74	0.79	0.77	-0.35	-0.59	1	-0.1
Th	ppm	-0.19	0.39	0.82	0.68	-0.0051	0.32	-0.75	-0.12	0.081	0.078	0.36	0.36	0.42	0.68	0.46	-1.50E-04	0.087	-0.21	-0.025	0.045	0.12	0.32	0.4	0.36	0.36	0.25	0.31	0.27	0.28	0.16	0.22	0.84	-0.34	-0.1	1

***Supplementary Table 3-9**: U-Pb isotopic composition on apatite from the Westmoreland area obtained by SIMS.*

Drillhole #	Depth (m)	Analysis #	$^{207}Pb/^{206}Pb$	±	$^{204}Pb/^{206}Pb$	±	$^{208}Pb/^{206}Pb$	±	$^{206}Pb/^{238}U$	±	$^{207}Pb/^{235}U$	±	Correl.err
JDD08-003	74.4B	1	0.1686	0.0012	0.0046	0.0002	0.1678	0.0032	0.3156	0.0243	4.620	0.028	0.85
JDD08-003	74.4B	4	0.5846	0.0009	0.0350	0.0001	1.2320	0.0024	0.2931	0.0525	4.413	0.056	0.94
JDD08-003	74.4B	6	0.4908	0.0117	0.0262	0.0007	0.9806	0.0302	0.3044	0.0292	6.342	0.144	0.20
JDD08-003	74.4B	8	0.2003	0.0021	0.0062	0.0003	0.2405	0.0060	0.3366	0.0390	5.378	0.045	0.86
JDD08-003	74.4B	9	0.4288	0.0046	0.0237	0.0004	0.8245	0.0122	0.2639	0.0337	3.874	0.082	0.41
JDD08-003	74.4B	17	0.1281	0.0014	0.0015	0.0001	0.0506	0.0041	0.3029	0.0230	4.497	0.027	0.84
JDD08-003	74.4B	24	0.2563	0.0011	0.0109	0.0002	0.3829	0.0038	0.2843	0.0224	4.232	0.027	0.82
JDD08-003	74.4B	25	0.1636	0.0007	0.0040	0.0001	0.1487	0.0013	0.2877	0.0150	4.311	0.017	0.89

Drillhole #	Depth (m)	Analysis #	Age 206/238	±	Age 207/235	±	Age 207/206	±	$^{238}U/^{206}Pb$	± abs	$^{207}Pb/^{206}Pb$	± abs	Correl.err
JDD08-003	74.4B	1	1768	37	1753	23	1734	27	2.939	0.124	0.169	0.001	0.855
JDD08-003	74.4B	4	1657	76	1715	45	1786	35	1.530	0.136	0.585	0.001	0.937
JDD08-003	74.4B	6	1713	44	2024	119	2359	223	1.924	0.056	0.491	0.012	0.203
JDD08-003	74.4B	8	1870	63	1881	38	1894	41	2.678	0.210	0.200	0.002	0.857
JDD08-003	74.4B	9	1510	45	1608	64	1740	131	2.377	0.123	0.429	0.005	0.411
JDD08-003	74.4B	17	1706	34	1730	22	1761	27	3.223	0.143	0.128	0.001	0.841
JDD08-003	74.4B	24	1613	32	1680	22	1766	28	2.913	0.111	0.256	0.001	0.825
JDD08-003	74.4B	25	1630	22	1695	14	1777	14	3.254	0.089	0.164	0.001	0.889

***Supplementary Table 3-10**: Isotopic composition of uraninites from the Westmoreland area obtained by SIMS*

Year	Drillhole #	Depth (m)	Circle #	Analysis #	$^{206}Pb/^{238}U$	±	$^{207}Pb/^{235}U$	±	Correl. Err.	$^{207}Pb/^{206}Pb$	±	$^{204}Pb/^{206}Pb$	±	Age 6/8	±	Age 7/5	±	Age 7/6	±
2018	JDD08-003	74.4	21	1	2.33E-03	1.96E-02	2.45E-02	2.11E-02	9.32E-01	7.84E-02	2.88E-04	1.59E-04	2.96E-05	15	0	25	1	1101	15
2018	JDD08-003	74.4	21	2	2.09E-03	1.09E-02	2.24E-02	1.35E-02	8.03E-01	8.00E-02	5.64E-04	1.58E-04	1.42E-05	13	0	22	0	1142	16
2018	JDD08-003	74.4	21	3	4.73E-03	4.67E-02	5.32E-02	4.79E-02	9.75E-01	8.31E-02	7.69E-04	1.27E-04	2.16E-05	30	1	53	2	1232	21
2018	JDD08-003	74.4	21	4	2.91E-03	2.20E-02	3.97E-02	7.07E-02	3.11E-01	1.13E-01	2.25E-03	1.02E-03	3.55E-04	19	0	40	3	1608	120
2018	JDD08-003	74.4	21	5	2.07E-03	1.29E-02	2.22E-02	2.26E-02	5.70E-01	8.07E-02	8.71E-04	2.06E-04	6.67E-05	13	0	22	0	1144	36
2018	JDD08-003	74.4	21	6	3.05E-03	1.22E-01	3.35E-02	1.26E-01	9.65E-01	8.18E-02	2.56E-03	1.52E-04	2.40E-05	20	2	33	4	1189	64
2018	JDD08-003	74.4	21	7	5.96E-03	1.24E-02	5.84E-02	1.67E-02	7.44E-01	7.61E-02	4.10E-04	3.59E-04	3.98E-05	38	0	58	1	960	23
2018	JDD08-003	74.4	21	8	2.10E-03	1.39E-02	2.10E-02	1.63E-02	8.48E-01	7.57E-02	1.38E-04	2.14E-04	3.65E-05	14	0	21	0	1006	17
2018	JDD08-003	74.4	10	1	1.65E-03	1.16E-02	1.80E-02	1.27E-02	9.12E-01	8.22E-02	2.34E-04	2.24E-04	1.97E-05	11	0	18	0	1175	10
2018	JDD08-003	74.4	10	2	8.79E-03	9.82E-03	8.98E-02	1.46E-02	6.75E-01	7.86E-02	6.87E-04	3.23E-04	2.15E-05	56	1	87	1	1043	22
2018	JDD08-003	74.4	10	3	1.51E-03	1.49E-02	1.71E-02	1.73E-02	8.62E-01	8.45E-02	5.08E-04	1.79E-04	2.88E-05	10	0	17	0	1247	17
2018	JDD08-003	74.4	10	4	1.55E-03	8.45E-03	1.75E-02	1.29E-02	6.54E-01	8.40E-02	5.29E-04	1.64E-04	3.43E-05	10	0	18	0	1241	19
2018	JDD08-003	74.4	10	5	1.69E-03	7.77E-03	1.92E-02	8.90E-03	8.74E-01	8.48E-02	1.62E-04	1.74E-04	1.85E-05	11	0	19	0	1256	8
2018	JDD08-003	74.4	10	6	2.16E-03	1.71E-02	2.31E-02	5.67E-02	3.01E-01	9.46E-02	1.33E-03	1.21E-03	2.30E-04	14	0	23	1	1135	104
2018	JDD08-003	74.4	10	7	3.18E-03	3.56E-02	3.83E-02	3.75E-02	9.48E-01	9.11E-02	8.89E-04	2.75E-04	2.83E-05	20	1	38	1	1369	23
2018	JDD08-003	74.4	10	8	2.75E-03	1.23E-02	2.93E-02	1.93E-02	6.36E-01	8.07E-02	8.91E-04	2.37E-04	4.07E-05	18	0	29	1	1132	29
2018	JDD08-003	74.4	10	9	1.66E-03	1.24E-02	1.80E-02	1.49E-02	8.35E-01	8.20E-02	3.97E-04	2.42E-04	2.91E-05	11	0	18	0	1164	16
2018	JDD08-003	74.4	10	10	1.68E-03	4.80E-03	1.77E-02	8.72E-03	5.51E-01	7.84E-02	2.97E-04	1.55E-04	2.74E-05	11	0	18	0	1102	14
2018	JDD08-003	74.4	10	11	1.85E-03	1.75E-02	1.97E-02	1.82E-02	9.59E-01	7.92E-02	2.53E-04	1.29E-04	1.79E-05	12	0	20	0	1132	10
2018	JDD08-003	74.4	10	12	1.63E-03	1.35E-02	1.85E-02	1.55E-02	8.73E-01	8.42E-02	3.89E-04	1.42E-04	2.80E-05	10	0	19	0	1252	15
2018	JDD08-003	74.4	7	1	2.45E-03	4.20E-02	2.84E-02	7.47E-02	5.62E-01	8.40E-02	5.19E-03	1.53E-06	1.17E-06	16	1	28	2	1294	116
2018	JDD08-003	74.4	7	3	3.55E-03	2.00E-02	3.44E-02	2.75E-02	7.26E-01	7.44E-02	6.78E-04	2.95E-04	6.72E-05	23	0	34	1	937	38
2018	JDD08-003	74.4	7	4	2.12E-03	1.02E-02	2.25E-02	1.55E-02	6.57E-01	7.84E-02	6.93E-04	1.06E-04	3.23E-05	14	0	23	0	1119	23
2018	JDD08-003	74.4	7	5	2.59E-03	1.21E-02	2.66E-02	1.78E-02	6.76E-01	7.72E-02	5.89E-04	1.83E-04	4.57E-05	17	0	27	0	1060	26
2018	JDD08-003	74.4	7	6	4.26E-03	8.64E-03	4.34E-02	1.59E-02	5.45E-01	7.81E-02	5.07E-04	3.07E-04	4.92E-05	27	0	43	1	1037	27
2018	JDD08-003	74.4	7	7	1.98E-03	1.02E-02	1.96E-02	1.68E-02	6.10E-01	7.50E-02	7.43E-04	2.22E-04	3.40E-05	13	0	20	0	983	27
2018	JDD08-003	74.4	7	8	2.73E-03	1.88E-02	2.68E-02	3.20E-02	5.87E-01	7.54E-02	8.12E-04	3.03E-04	9.76E-05	18	0	27	1	962	52
2018	JDD08-003	74.4	7	10	4.81E-03	1.16E-02	4.86E-02	2.35E-02	4.94E-01	7.75E-02	1.00E-03	2.94E-04	6.40E-05	31	0	48	1	1023	41
2018	JDD08-003	74.4	8	1	1.56E-03	5.85E-03	1.61E-02	1.35E-02	4.33E-01	8.03E-02	7.55E-04	3.83E-04	2.80E-05	10	0	16	0	1068	24
2018	JDD08-003	74.4	8	2	1.53E-03	7.30E-03	1.61E-02	1.45E-02	5.04E-01	8.03E-02	7.60E-04	2.68E-04	3.24E-05	10	0	16	0	1109	25
2018	JDD08-003	74.4	8	3	4.08E-03	3.49E-02	4.43E-02	3.75E-02	9.30E-01	8.00E-02	1.03E-03	9.79E-05	1.69E-05	26	1	44	2	1165	27
2018	JDD08-003	74.4	8	4	1.94E-03	9.83E-03	2.08E-02	1.32E-02	7.43E-01	7.97E-02	4.97E-04	1.65E-04	2.69E-05	13	0	21	0	1132	18
2018	JDD08-003	74.4	8	7	4.42E-03	2.52E-02	5.19E-02	8.57E-02	2.94E-01	1.12E-01	2.95E-03	1.93E-03	3.55E-04	28	1	51	4	1322	151
2018	JDD08-003	74.4	8	8	2.18E-03	9.70E-03	2.27E-02	1.66E-02	5.85E-01	7.87E-02	6.28E-04	2.17E-04	4.63E-05	14	0	23	0	1087	27
2018	JDD08-003	74.4	8	9	1.79E-03	1.27E-02	1.88E-02	1.68E-02	7.55E-01	7.85E-02	2.99E-04	1.67E-04	4.62E-05	12	0	19	0	1101	22
2018	JDD08-003	74.4	8	11	1.58E-03	1.25E-02	1.79E-02	2.13E-02	5.86E-01	8.22E-02	1.07E-03	-3.28E-05	5.26E-05	10	0	18	0	1252	33
2018	JDD08-003	74.4	8	12	1.10E-03	2.35E-02	1.31E-02	3.53E-02	6.66E-01	8.67E-02	1.98E-03	-2.25E-06	6.08E-05	7	0	13	0	1357	50
2018	JDD08-003	74.4	8	13	1.69E-03	5.56E-03	1.88E-02	1.42E-02	3.92E-01	8.22E-02	8.72E-04	1.10E-04	3.26E-05	11	0	19	0	1216	25
2018	JDD08-003	74.4	8	14	1.93E-03	1.08E-02	2.10E-02	1.60E-02	6.74E-01	8.13E-02	5.58E-04	1.56E-04	4.34E-05	12	0	21	0	1176	23
2018	JDD08-003	74.4	18	1	1.65E-03	1.32E-02	1.65E-02	1.92E-02	6.86E-01	7.52E-02	3.78E-04	1.85E-04	5.59E-05	11	0	17	0	1005	28
2018	JDD08-003	74.4	18	2	1.47E-03	1.26E-02	1.40E-02	1.89E-02	6.69E-01	7.17E-02	6.59E-04	2.06E-04	4.11E-05	9	0	14	0	894	29
2018	JDD08-003	74.4	18	3	2.39E-03	7.04E-03	2.29E-02	1.34E-02	5.24E-01	7.07E-02	6.70E-04	9.75E-05	2.38E-05	15	0	23	0	911	23
2018	JDD08-003	74.4	18	4	3.80E-03	1.30E-02	3.70E-02	1.58E-02	8.24E-01	7.20E-02	5.28E-04	9.88E-05	1.92E-05	24	0	37	1	949	18
2018	JDD08-003	74.4	18	5	6.34E-02	4.59E-02	6.47E-01	4.60E-02	9.99E-01	7.55E-02	1.22E-04	1.06E-04	5.06E-06	396	18	506	18	1042	4

Year	Drillhole #	Depth (m)	Circle #	Analysis #	$^{206}Pb/^{238}U$	±	$^{207}Pb/^{235}U$	±	Correl. Err.	$^{207}Pb/^{206}Pb$	±	$^{204}Pb/^{206}Pb$	±	Age 6/8	±	Age 7/5	±	Age 7/6	±
2018	JDD08-003	74.4	18	6	7.39E-02	3.38E-02	7.59E-01	3.42E-02	9.88E-01	7.59E-02	3.76E-04	1.04E-04	4.43E-06	460	15	573	15	1054	10
2018	JDD08-003	74.4	18	8	2.09E-03	1.82E-02	1.99E-02	2.15E-02	8.45E-01	7.19E-02	5.94E-04	1.97E-04	3.04E-05	13	0	20	0	902	24
2018	JDD08-003	74.4	18	9	2.75E-03	1.80E-02	2.61E-02	2.07E-02	8.69E-01	7.01E-02	6.24E-04	9.88E-05	1.74E-05	18	0	26	1	891	21
2018	JDD08-003	74.4	18	10	5.66E-02	2.07E-02	5.86E-01	2.09E-02	9.89E-01	7.69E-02	2.17E-04	1.31E-04	4.19E-06	355	7	468	8	1071	6
2018	JDD08-003	74.4	18	11	1.59E-03	1.01E-02	1.52E-02	1.28E-02	7.91E-01	7.06E-02	4.98E-04	9.50E-05	1.15E-05	10	0	15	0	907	16
2018	JDD08-003	74.4	18	12	2.75E-03	9.96E-03	2.22E-02	1.20E-02	8.30E-01	6.00E-02	3.48E-04	9.79E-05	1.02E-05	18	0	22	0	554	14
2018	JDD08-003	74.4	18	13	1.74E-03	1.94E-02	1.63E-02	2.23E-02	8.70E-01	7.01E-02	3.67E-04	1.35E-04	3.87E-05	11	0	16	0	876	23
2018	JDD08-003	74.4	18	14	1.80E-03	2.69E-02	1.69E-02	2.87E-02	9.37E-01	6.99E-02	5.29E-04	1.30E-04	2.44E-05	12	0	17	0	873	21
2018	JDD08-003	74.4	18	15	2.38E-03	2.01E-02	2.07E-02	2.13E-02	9.43E-01	6.47E-02	3.21E-04	1.20E-04	1.81E-05	15	0	21	0	708	15
2018	JDD08-003	74.4	20	1	1.95E-03	1.73E-02	2.23E-02	1.95E-02	8.87E-01	8.44E-02	5.74E-04	1.03E-04	2.68E-05	13	0	22	0	1271	17
2017	WDD10-151	29.4	4	1	2.09E-02	2.68E-02	1.86E-01	2.90E-02	9.26E-01	7.65E-02	4.72E-04	8.67E-04	2.97E-05	134	4	173	5	751	23
2017	WDD10-151	29.4	4	2	2.70E-02	1.80E-02	2.35E-01	1.91E-02	9.45E-01	7.58E-02	2.82E-04	9.04E-04	1.53E-05	172	3	214	4	708	13
2017	WDD10-151	29.4	4	3	2.63E-02	6.72E-03	2.29E-01	7.76E-03	8.66E-01	7.54E-02	1.16E-04	8.65E-04	1.26E-05	167	1	209	1	713	8
2017	WDD10-151	29.4	4	4	2.56E-02	7.81E-03	2.22E-01	8.59E-03	9.09E-01	7.53E-02	1.46E-04	8.87E-04	9.81E-06	163	1	203	2	700	8
2017	WDD10-151	29.4	4	5	2.40E-02	1.10E-02	2.11E-01	1.33E-02	8.25E-01	7.65E-02	1.36E-04	9.07E-04	2.70E-05	153	2	194	2	729	16
2017	WDD10-151	29.4	4	6	2.09E-02	7.26E-03	1.82E-01	8.40E-03	8.65E-01	7.61E-02	7.56E-05	9.04E-04	1.50E-05	133	1	170	1	716	9
2017	WDD10-151	29.4	4	7	2.32E-02	1.23E-02	2.01E-01	1.39E-02	8.84E-01	7.60E-02	1.45E-04	9.18E-04	2.23E-05	148	2	186	2	706	14
2017	WDD10-151	29.4	4	8	2.63E-02	4.34E-03	2.26E-01	5.94E-03	7.30E-01	7.53E-02	2.15E-04	9.07E-04	7.10E-06	167	1	207	1	688	9
2017	WDD10-151	29.4	1	1	2.37E-02	7.29E-03	2.07E-01	1.11E-02	6.58E-01	7.94E-02	2.28E-04	1.13E-03	2.77E-05	151	1	191	2	719	18
2017	WDD10-151	29.4	1	2	1.94E-02	9.48E-03	1.71E-01	1.22E-02	7.78E-01	7.95E-02	1.15E-04	1.09E-03	2.79E-05	124	1	160	2	742	16
2017	WDD10-151	29.4	1	3	1.93E-02	1.09E-02	1.72E-01	1.30E-02	8.38E-01	7.96E-02	2.39E-04	1.05E-03	2.25E-05	123	1	161	2	766	15
2017	WDD10-151	29.4	2	1	1.32E-02	5.68E-03	1.15E-01	8.26E-03	6.87E-01	7.47E-02	2.44E-04	7.93E-04	1.68E-05	84	0	111	1	724	13
2017	WDD10-151	29.4	2	2	1.31E-02	4.55E-03	1.16E-01	7.16E-03	6.36E-01	7.51E-02	1.52E-04	7.71E-04	1.88E-05	84	0	111	1	750	12
2017	WDD10-151	29.4	2	3	1.37E-02	4.73E-03	1.22E-01	6.90E-03	6.86E-01	7.54E-02	1.85E-04	7.63E-04	1.54E-05	88	0	117	1	764	11
2017	WDD10-151	29.4	2	4	1.36E-02	8.61E-03	1.20E-01	1.18E-02	7.29E-01	7.54E-02	2.65E-04	8.05E-04	2.58E-05	87	1	115	1	744	17
2017	WDD10-151	29.4	2	5	1.39E-02	6.33E-03	1.23E-01	8.46E-03	7.48E-01	7.53E-02	2.43E-04	7.70E-04	1.52E-05	89	1	118	1	757	12
2017	WDD10-151	29.4	2	6	1.37E-02	4.76E-03	1.20E-01	7.16E-03	6.65E-01	7.50E-02	2.11E-04	7.97E-04	1.54E-05	87	0	115	1	733	11
2017	WDD10-151	29.4	2	7	1.37E-02	6.16E-03	1.21E-01	8.55E-03	7.20E-01	7.53E-02	1.24E-04	8.10E-04	2.11E-05	88	1	116	1	738	13
2017	WDD10-151	29.4	2	8	1.38E-02	4.91E-03	1.21E-01	8.29E-03	5.92E-01	7.52E-02	1.46E-04	8.11E-04	2.35E-05	88	0	116	1	732	14
2017	WDD10-151	29.4	2	9	1.33E-02	4.54E-03	1.18E-01	7.89E-03	5.76E-01	7.53E-02	2.22E-04	7.75E-04	2.03E-05	85	0	114	1	754	14
2017	WDD07-2	55.9 B	3	1	3.04E-02	2.04E-02	2.63E-01	2.08E-02	9.80E-01	6.34E-02	2.49E-04	6.83E-05	3.07E-06	193	4	237	4	696	9
2017	WDD07-2	55.9 B	3	2	3.61E-02	7.85E-03	2.98E-01	1.04E-02	7.54E-01	6.06E-02	3.97E-04	6.70E-05	4.74E-06	229	2	264	2	596	15
2017	WDD07-2	55.9 B	3	3	3.25E-02	7.34E-03	2.74E-01	7.61E-03	9.65E-01	6.22E-02	1.17E-04	8.36E-05	1.65E-06	206	1	246	2	645	4
2017	WDD07-2	55.9 B	3	4	3.47E-02	9.29E-03	2.92E-01	9.75E-03	9.52E-01	6.18E-02	1.74E-04	6.63E-05	2.71E-06	220	2	260	2	642	6
2017	WDD07-2	55.9 B	3	5	2.15E-02	2.89E-02	1.80E-01	2.94E-02	9.85E-01	6.13E-02	2.93E-04	5.63E-05	5.03E-06	137	4	168	5	628	11
2017	WDD07-2	55.9 B	3	6	1.03E-02	4.48E-02	8.01E-02	4.74E-02	9.45E-01	5.69E-02	8.66E-04	4.43E-05	6.02E-06	66	3	78	4	469	34
2017	WDD07-2	55.9 B	4	1	2.81E-02	2.08E-02	2.58E-01	2.21E-02	9.42E-01	6.74E-02	4.81E-04	7.39E-05	5.08E-06	179	4	233	5	823	15
2017	WDD07-2	55.9 B	4	2	5.11E-02	1.22E-02	4.09E-01	1.26E-02	9.70E-01	5.92E-02	1.60E-04	9.04E-05	4.16E-06	321	4	348	4	532	7
2017	WDD07-2	55.9 B	4	3	3.14E-02	3.03E-02	2.69E-01	3.05E-02	9.91E-01	6.35E-02	2.44E-04	9.26E-05	4.32E-06	199	6	242	7	685	9
2017	WDD07-2	55.9 B	4	4	3.29E-02	1.05E-02	2.78E-01	1.08E-02	9.73E-01	6.25E-02	1.20E-04	9.16E-05	5.53E-06	209	2	249	2	653	5
2017	WDD07-2	55.9 B	4	5	3.29E-02	8.53E-03	2.61E-01	9.01E-03	9.46E-01	5.84E-02	1.54E-04	7.29E-05	3.55E-06	209	2	235	2	511	6
2017	WDD07-2	55.9 B	4	6	3.39E-02	1.63E-02	2.68E-01	1.65E-02	9.90E-01	5.80E-02	1.12E-04	6.58E-05	4.23E-06	215	3	241	4	501	5
2017	WDD07-2	55.9 A	9	1	6.77E-03	8.40E-02	5.49E-02	8.85E-02	9.50E-01	5.87E-02	1.63E-03	1.04E-05	4.40E-06	44	4	54	5	558	59
2017	WDD07-2	55.9 A	9	2	1.06E-01	1.55E-02	9.45E-01	1.57E-02	9.90E-01	6.49E-02	1.31E-04	3.40E-05	2.58E-06	650	10	675	8	760	5

Year	Drillhole #	Depth (m)	Circle #	Analysis #	$^{206}Pb/^{238}U$	±	$^{207}Pb/^{235}U$	±	Correl. Err.	$^{207}Pb/^{206}Pb$	±	$^{204}Pb/^{206}Pb$	±	Age 6/8	±	Age 7/5	±	Age 7/6	±
2017	WDD07-2	55.9	A	9	3	3.75E-02	3.25E-02	3.31E-01	3.34E-02	9.75E-01	6.45E-02	4.67E-04	5.02E-05	4.64E-06	237	8	290	8	739	16
2017	WDD07-2	55.9	A	9	4	8.54E-02	2.99E-02	7.23E-01	3.07E-02	9.72E-01	6.20E-02	4.41E-04	5.45E-05	8.97E-07	528	15	552	13	652	15
2017	WDD07-2	55.9	A	9	5	5.43E-02	3.09E-02	4.58E-01	3.11E-02	9.94E-01	6.16E-02	2.11E-04	4.04E-05	2.04E-06	341	10	383	10	646	8
2017	WDD07-2	55.9	A	9	6	8.38E-02	9.27E-03	7.24E-01	1.00E-02	9.28E-01	6.31E-02	2.32E-04	4.19E-05	1.31E-06	519	5	553	4	696	8
2017	WDD07-2	55.9	A	9	7	8.24E-03	5.59E-02	6.50E-02	6.12E-02	9.14E-01	5.76E-02	1.41E-03	4.04E-05	5.87E-06	53	3	64	4	500	54
2017	WDD07-2	55.9	A	9	8	9.37E-02	8.02E-03	8.40E-01	8.47E-03	9.47E-01	6.53E-02	1.73E-04	3.01E-05	1.65E-06	577	4	619	4	775	6
2018	WDD07-2	55.9	A	9	1	8.94E-02	1.80E-02	7.99E-01	1.80E-02	9.96E-01	6.53E-02	1.00E-04	3.75E-05	1.24E-06	552	10	597	8	769	3
2018	WDD07-2	55.9	A	9	2	6.66E-02	2.15E-02	6.09E-01	2.24E-02	9.57E-01	6.66E-02	4.31E-04	2.45E-05	8.98E-07	416	9	483	9	817	14
2018	WDD07-2	55.9	A	9	3	7.00E-02	1.47E-02	5.72E-01	1.48E-02	9.95E-01	6.02E-02	7.78E-05	6.87E-05	1.68E-06	436	6	459	5	577	3
2018	WDD07-2	55.9	A	9	4	5.69E-02	2.16E-02	4.66E-01	2.20E-02	9.78E-01	6.03E-02	2.65E-04	6.60E-05	2.80E-06	357	7	388	7	583	10
2018	WDD07-2	55.9	A	9	5	4.47E-02	1.12E-02	3.76E-01	1.40E-02	8.02E-01	6.18E-02	5.03E-04	6.03E-05	3.26E-06	282	3	324	4	639	18
2018	WDD07-2	55.9	A	9	6	6.21E-02	1.23E-02	5.13E-01	1.29E-02	9.55E-01	6.04E-02	2.21E-04	3.99E-05	3.08E-06	388	5	420	4	601	8
2018	WDD07-2	55.9	A	9	7	7.54E-02	8.87E-03	6.33E-01	9.46E-03	9.37E-01	6.17E-02	1.92E-04	6.14E-05	2.85E-06	469	4	498	4	635	7
2018	WDD07-2	55.9	A	9	8	9.50E-02	3.65E-02	8.21E-01	3.69E-02	9.89E-01	6.34E-02	3.18E-04	5.73E-05	6.17E-06	585	20	608	17	696	12
2018	WDD07-2	55.9	A	9	9	7.93E-02	1.68E-02	6.91E-01	1.70E-02	9.91E-01	6.38E-02	1.34E-04	4.73E-05	2.40E-06	492	8	533	7	715	5
2018	WDD07-2	55.9	A	9	10	5.32E-02	2.00E-02	4.52E-01	2.22E-02	9.02E-01	6.21E-02	5.82E-04	4.81E-05	3.45E-06	334	7	378	7	657	20
2018	WDD07-2	55.9	A	9	11	8.21E-02	9.17E-03	7.23E-01	1.04E-02	8.78E-01	6.43E-02	3.18E-04	3.75E-05	8.73E-07	509	4	552	4	737	11
2018	WDD07-2	55.9	A	9	12	6.14E-02	2.74E-02	5.16E-01	2.78E-02	9.85E-01	6.18E-02	2.86E-04	5.72E-05	2.20E-06	384	10	423	10	639	10
2018	WDD07-2	55.9	A	9	13	2.73E-02	1.14E-01	2.22E-01	1.14E-01	9.99E-01	6.00E-02	3.37E-04	7.29E-05	3.16E-06	174	19	204	21	567	13
2018	WDD07-2	55.9	A	9	14	7.37E-02	3.36E-02	6.29E-01	3.37E-02	9.95E-01	6.27E-02	2.14E-04	5.92E-05	1.22E-06	459	15	496	13	670	7
2018	WDD07-2	55.9	A	9	15	4.69E-02	2.58E-02	3.87E-01	2.61E-02	9.90E-01	6.07E-02	2.14E-04	6.77E-05	1.63E-06	295	7	332	7	597	8
2018	WDD07-2	55.9	A	7	1	1.98E-02	7.22E-02	1.55E-01	7.24E-02	9.98E-01	5.77E-02	2.30E-04	6.20E-05	6.15E-06	126	9	146	10	487	10
2018	WDD07-2	55.9	A	7	2	1.12E-02	7.37E-03	8.83E-02	8.91E-03	8.27E-01	5.78E-02	2.59E-04	5.96E-05	6.54E-06	72	1	86	1	489	11
2018	WDD07-2	55.9	A	7	3	1.87E-02	3.03E-02	1.46E-01	3.07E-02	9.87E-01	5.74E-02	2.42E-04	6.68E-05	8.18E-06	120	4	138	4	471	11
2018	WDD07-2	55.9	A	7	4	3.36E-03	1.70E-02	2.67E-02	1.98E-02	8.58E-01	6.01E-02	4.74E-04	1.71E-04	2.00E-05	22	0	27	1	518	22
2017	WDD07-2	55.9	A	7	1	3.29E-03	1.34E-02	2.71E-02	1.71E-02	7.88E-01	6.13E-02	5.36E-04	1.16E-04	1.86E-05	21	0	27	0	600	23
2017	WDD07-2	55.9	A	7	2	2.49E-02	3.71E-02	1.92E-01	3.72E-02	9.97E-01	5.66E-02	1.59E-04	6.18E-05	3.86E-06	159	6	178	6	448	7
2017	WDD07-2	55.9	A	7	3	9.01E-03	1.54E-02	7.34E-02	1.59E-02	9.71E-01	5.99E-02	1.76E-04	6.89E-05	8.16E-06	58	1	72	1	570	8
2017	WDD07-2	55.9	A	7	4	1.27E-02	1.32E-02	1.02E-01	1.34E-02	9.84E-01	5.91E-02	8.51E-05	6.22E-05	6.55E-06	82	1	99	1	544	5
2017	WDD07-2	55.9	A	7	5	1.57E-02	8.30E-03	1.69E-01	1.06E-02	7.82E-01	7.93E-02	4.98E-04	9.27E-05	6.34E-06	100	1	159	2	1153	13
2017	WDD07-2	55.9	A	7	6	2.25E-02	1.54E-02	2.34E-01	1.59E-02	9.67E-01	7.62E-02	2.84E-04	7.47E-05	5.59E-06	144	2	214	3	1079	8
2017	WDD07-2	55.9	A	7	7	2.29E-02	3.00E-02	2.07E-01	3.07E-02	9.78E-01	6.60E-02	3.92E-04	5.88E-05	8.44E-06	146	4	191	5	788	14
2017	WDD07-2	55.9	A	7	8	8.83E-03	9.44E-03	7.27E-02	1.36E-02	6.94E-01	6.04E-02	5.70E-04	5.95E-05	6.37E-06	57	1	71	1	595	21
2017	WDD08-106	10.6	104	1	4.53E-02	9.22E-03	3.63E-01	9.85E-03	9.36E-01	5.86E-02	1.96E-04	2.22E-06	5.86E-02	286	3	315	3	535	8
2017	WDD08-106	10.6	104	2	4.55E-02	8.25E-03	3.66E-01	8.43E-03	9.78E-01	5.89E-02	9.16E-05	2.51E-06	5.89E-02	287	2	317	2	547	4
2017	WDD08-106	10.6	104	3	4.98E-02	7.08E-03	4.01E-01	7.40E-03	9.57E-01	5.88E-02	1.14E-04	2.90E-06	5.88E-02	313	2	342	2	546	5
2017	WDD08-106	10.6	104	4	4.64E-02	4.76E-03	3.72E-01	5.58E-03	8.53E-01	5.85E-02	1.63E-04	2.31E-06	5.85E-02	292	1	321	2	535	6
2017	WDD08-106	10.6	104	5	4.12E-02	5.70E-03	3.33E-01	6.09E-03	9.35E-01	5.90E-02	1.21E-04	1.86E-06	5.90E-02	260	1	292	2	553	5
2017	WDD08-106	10.6	104	6	4.75E-02	1.11E-02	3.83E-01	1.15E-02	9.62E-01	5.88E-02	1.79E-04	1.95E-06	5.88E-02	299	3	329	3	547	7
2017	WDD08-106	10.6	104	7	3.70E-02	5.20E-03	2.97E-01	5.62E-03	9.24E-01	5.85E-02	1.22E-04	1.28E-06	5.85E-02	234	1	264	1	535	5
2017	WDD08-106	10.6	104	8	4.62E-02	8.16E-03	3.72E-01	8.28E-03	9.86E-01	5.88E-02	7.76E-05	1.32E-06	5.88E-02	291	2	321	2	545	3
2017	WDD08-106	10.6	104	9	4.64E-02	6.04E-03	3.74E-01	6.12E-03	9.88E-01	5.88E-02	5.13E-05	1.17E-06	5.88E-02	292	2	322	2	545	2
2017	WDD08-106	10.6	104	11	4.77E-02	5.07E-03	3.85E-01	5.45E-03	9.30E-01	5.90E-02	1.08E-04	2.58E-06	5.90E-02	301	1	331	2	552	4
2017	WDD08-106	10.6	104	12	4.12E-02	7.00E-03	3.33E-01	7.14E-03	9.81E-01	5.90E-02	7.66E-05	1.53E-06	5.90E-02	260	2	292	2	554	3

Year	Drillhole #	Depth (m)	Circle #	Analysis #	$^{206}Pb/^{238}U$	±	$^{207}Pb/^{235}U$	±	Correl. Err.	$^{207}Pb/^{206}Pb$	±	$^{204}Pb/^{206}Pb$	±	Age 6/8	±	Age 7/5	±	Age 7/6	±
2017	WDD08-106	10.6	6	1	4.16E-02	8.20E-03	3.37E-01	8.64E-03	9.49E-01	5.91E-02	1.55E-04	2.02E-06	5.91E-02	263	2	295	2	557	6
2017	WDD08-106	10.6	6	2	4.80E-02	8.90E-03	3.88E-01	9.18E-03	9.70E-01	5.90E-02	1.17E-04	3.25E-06	5.90E-02	302	3	333	3	551	5
2017	WDD08-106	10.6	6	3	4.20E-02	6.29E-03	3.40E-01	6.37E-03	9.87E-01	5.91E-02	5.03E-05	1.90E-06	5.91E-02	265	2	297	2	557	2
2017	WDD08-106	10.6	6	4	3.96E-02	5.82E-03	3.21E-01	5.90E-03	9.87E-01	5.92E-02	3.77E-05	2.41E-06	5.92E-02	250	1	282	1	556	2
2017	WDD08-106	10.6	6	5	4.80E-02	8.10E-03	3.87E-01	8.42E-03	9.62E-01	5.88E-02	1.25E-04	2.51E-06	5.88E-02	302	2	332	2	546	5
2017	WDD08-106	10.6	106	1	3.65E-02	7.32E-03	2.97E-01	7.56E-03	9.68E-01	5.94E-02	9.86E-05	2.85E-06	5.94E-02	231	2	264	2	567	4
2017	WDD08-106	10.6	106	2	3.71E-02	1.03E-02	3.01E-01	1.04E-02	9.92E-01	5.93E-02	7.21E-05	1.34E-06	5.93E-02	235	2	267	2	562	3
2017	WDD08-106	10.6	106	3	3.75E-02	9.77E-03	3.04E-01	9.88E-03	9.89E-01	5.92E-02	8.00E-05	1.98E-06	5.92E-02	237	2	270	2	562	3
2017	WDD08-106	10.6	106	4	3.94E-02	9.28E-03	3.19E-01	9.34E-03	9.94E-01	5.92E-02	5.31E-05	1.47E-06	5.92E-02	249	2	281	2	558	2
2017	WDD08-106	10.6	106	5	3.71E-02	1.13E-02	3.01E-01	1.16E-02	9.82E-01	5.92E-02	1.12E-04	3.34E-06	5.92E-02	235	3	267	3	559	5
2017	WDD08-106	10.6	106	6	3.76E-02	8.96E-03	3.04E-01	9.02E-03	9.93E-01	5.91E-02	3.46E-05	2.94E-06	5.91E-02	238	2	270	2	556	2
2017	WDD08-106	10.6	106	7	4.29E-02	1.08E-02	3.48E-01	1.09E-02	9.92E-01	5.93E-02	6.62E-05	2.61E-06	5.93E-02	271	3	303	3	562	3
2017	WDD08-106	10.6	106	8	4.09E-02	7.54E-03	3.31E-01	7.70E-03	9.79E-01	5.90E-02	7.54E-05	3.03E-06	5.90E-02	259	2	290	2	554	3
2017	WDD08-106	10.6	106	9	3.98E-02	7.65E-03	3.23E-01	7.86E-03	9.73E-01	5.93E-02	9.05E-05	3.16E-06	5.93E-02	252	2	284	2	562	4
2017	WDD08-106	10.6	106	10	3.96E-02	7.26E-03	3.21E-01	7.42E-03	9.79E-01	5.91E-02	8.37E-05	1.53E-06	5.91E-02	250	2	282	2	556	3
2017	WDD08-106	10.6	106	11	3.80E-02	8.79E-03	3.09E-01	8.92E-03	9.85E-01	5.93E-02	7.93E-05	2.56E-06	5.93E-02	240	2	273	2	564	3
2017	WDD08-106	10.6	106	12	3.53E-02	6.33E-03	2.84E-01	6.65E-03	9.51E-01	5.88E-02	1.06E-04	3.17E-06	5.88E-02	224	1	254	1	547	4
2017	WDD08-106	10.6	106	13	3.68E-02	5.63E-03	2.97E-01	6.40E-03	8.79E-01	5.90E-02	1.66E-04	3.50E-06	5.90E-02	233	1	264	1	550	7
2017	WDD08-106	10.6	106	14	3.70E-02	1.16E-02	3.01E-01	1.18E-02	9.78E-01	5.93E-02	1.32E-04	3.43E-06	5.93E-02	234	3	267	3	566	5
2017	WDD08-106	10.6	106	15	3.85E-02	7.15E-03	3.13E-01	7.40E-03	9.66E-01	5.93E-02	1.09E-04	1.51E-06	5.93E-02	244	2	277	2	565	4
2017	WDD08-106	10.6	106	16	3.89E-02	5.49E-03	3.16E-01	5.71E-03	9.60E-01	5.93E-02	8.27E-05	2.47E-06	5.93E-02	246	1	279	1	567	3
2017	WDD08-106	10.6	106	17	3.72E-02	5.91E-03	3.01E-01	6.46E-03	9.15E-01	5.90E-02	1.34E-04	4.08E-06	5.90E-02	235	1	267	2	552	6
2017	WDD08-106	10.6	106	18	3.78E-02	7.55E-03	3.05E-01	7.82E-03	9.65E-01	5.89E-02	1.09E-04	2.79E-06	5.89E-02	239	2	270	2	547	4
2017	WDD08-106	10.6	106	19	3.84E-02	6.18E-03	3.11E-01	6.39E-03	9.67E-01	5.90E-02	9.08E-05	1.65E-06	5.90E-02	243	1	275	2	557	4
2017	WDD08-106	10.6	106	20	3.71E-02	5.62E-03	3.00E-01	5.96E-03	9.43E-01	5.91E-02	1.15E-04	9.76E-07	5.91E-02	235	1	266	1	555	4
2017	WDD08-106	10.6	8	1	3.81E-02	9.51E-03	3.08E-01	9.74E-03	9.77E-01	5.91E-02	1.05E-04	3.65E-06	5.91E-02	241	2	272	2	554	5
2017	WDD08-106	10.6	8	2	3.73E-02	5.19E-03	3.03E-01	5.40E-03	9.62E-01	5.92E-02	7.43E-05	2.49E-06	5.92E-02	236	1	268	1	559	3
2017	WDD08-106	10.6	8	3	3.71E-02	4.07E-03	3.01E-01	4.29E-03	9.48E-01	5.92E-02	6.96E-05	2.28E-06	5.92E-02	235	1	267	1	560	3
2017	WDD08-106	10.6	8	4	3.73E-02	6.21E-03	3.02E-01	6.66E-03	9.33E-01	5.91E-02	1.37E-04	1.45E-06	5.91E-02	236	1	268	2	556	5
2017	WDD08-106	10.6	8	5	4.10E-02	4.41E-03	3.34E-01	5.35E-03	8.24E-01	5.97E-02	1.19E-04	7.89E-06	5.97E-02	259	1	293	1	570	7
2017	WDD08-106	10.6	8	6	3.64E-02	1.45E-02	2.96E-01	1.58E-02	9.13E-01	5.95E-02	3.72E-04	3.83E-06	5.95E-02	230	3	264	4	571	14
2017	WDD08-106	10.6	8	7	3.74E-02	4.43E-03	3.02E-01	5.36E-03	8.27E-01	5.90E-02	1.69E-04	2.49E-06	5.90E-02	237	1	268	1	551	7
2017	WDD08-106	10.6	8	8	3.82E-02	6.53E-03	3.10E-01	6.82E-03	9.57E-01	5.91E-02	9.04E-05	4.23E-06	5.91E-02	242	2	274	2	559	4
2017	WDD08-106	10.6	103	1	3.95E-02	9.47E-03	3.19E-01	9.58E-03	9.89E-01	5.89E-02	5.94E-05	3.24E-06	5.89E-02	250	2	281	2	548	3
2017	WDD08-106	10.6	103	2	4.02E-02	4.86E-03	3.24E-01	5.77E-03	8.43E-01	5.88E-02	1.75E-04	2.27E-06	5.88E-02	254	1	285	1	545	7
2017	WDD08-106	10.6	103	3	3.96E-02	5.87E-03	3.20E-01	6.47E-03	9.08E-01	5.90E-02	1.42E-04	3.92E-06	5.90E-02	250	1	282	2	553	6
2017	WDD08-106	10.6	103	4	3.98E-02	5.32E-03	3.23E-01	6.25E-03	8.51E-01	5.92E-02	1.83E-04	3.10E-06	5.92E-02	252	1	284	2	557	7
2017	WDD08-106	10.6	101	1	3.71E-02	4.87E-03	2.99E-01	5.36E-03	9.08E-01	5.89E-02	1.12E-04	3.88E-06	5.89E-02	235	1	266	1	550	5
2017	WDD08-106	10.6	101	2	3.69E-02	4.92E-03	2.97E-01	5.83E-03	8.43E-01	5.89E-02	1.63E-04	4.64E-06	5.89E-02	233	1	264	1	550	7
2017	WDD08-106	10.6	101	3	3.68E-02	3.86E-03	2.97E-01	5.01E-03	7.71E-01	5.88E-02	1.76E-04	3.21E-06	5.88E-02	233	1	264	1	546	7
2017	WDD08-106	10.6	101	4	3.74E-02	5.05E-03	3.01E-01	5.42E-03	9.33E-01	5.88E-02	9.84E-05	3.22E-06	5.88E-02	237	1	267	1	544	4
2017	WDD08-106	10.6	101	5	3.62E-02	4.36E-03	2.93E-01	5.23E-03	8.35E-01	5.90E-02	1.58E-04	3.19E-06	5.90E-02	230	1	261	1	553	6
2017	WDD08-106	10.6	101	6	3.62E-02	4.13E-03	2.92E-01	4.83E-03	8.56E-01	5.88E-02	1.39E-04	2.25E-06	5.88E-02	229	1	260	1	547	5
2017	WDD08-106	10.6	101	7	3.91E-02	3.58E-03	3.16E-01	4.21E-03	8.50E-01	5.90E-02	1.24E-04	2.02E-06	5.90E-02	247	1	279	1	551	5

Year	Drillhole #	Depth (m)	Circle #	Analysis #	$^{206}Pb/^{238}U$	±	$^{207}Pb/^{235}U$	±	Correl. Err.	$^{207}Pb/^{206}Pb$	±	$^{204}Pb/^{206}Pb$	±	Age 6/8	±	Age 7/5	±	Age 7/6	±
2017	WDD08-106	10.6	101	8	3.74E-02	4.40E-03	3.01E-01	4.63E-03	9.51E-01	5.88E-02	6.51E-05	3.02E-06	5.88E-02	237	1	267	1	543	3
2017	WDD08-106	10.6	101	9	3.78E-02	4.17E-03	3.02E-01	4.61E-03	9.04E-01	5.85E-02	8.37E-05	4.54E-06	5.85E-02	239	1	268	1	532	4
2017	WDD08-106	10.6	101	10	3.69E-02	5.39E-03	2.96E-01	5.81E-03	9.28E-01	5.87E-02	1.13E-04	3.07E-06	5.87E-02	233	1	263	1	539	5
2017	WDD08-106	10.6	101	11	3.66E-02	6.27E-03	2.96E-01	6.41E-03	9.78E-01	5.89E-02	4.99E-05	3.56E-06	5.89E-02	233	1	263	1	546	3
2017	WDD07-2	73.5	24	1	1.52E-02	1.35E-02	1.10E-01	1.36E-02	9.92E-01	5.27E-02	8.50E-05	1.36E-05	1.40E-06	97	1	106	1	316	4
2017	WDD07-2	73.5	24	2	2.10E-02	7.54E-03	1.56E-01	7.74E-03	9.75E-01	5.39E-02	8.18E-05	1.70E-05	2.37E-06	134	1	147	1	364	4
2017	WDD07-2	73.5	24	3	1.28E-02	1.26E-02	9.05E-02	1.26E-02	9.94E-01	5.13E-02	6.39E-05	1.39E-05	1.57E-06	82	1	88	1	254	3
2017	WDD07-2	73.5	24	4	1.91E-02	1.18E-02	1.41E-01	1.23E-02	9.57E-01	5.35E-02	1.88E-04	1.97E-05	1.31E-06	122	1	134	2	344	8
2017	WDD07-2	73.5	24	5	2.17E-02	1.21E-02	1.63E-01	1.27E-02	9.53E-01	5.45E-02	2.04E-04	1.89E-05	2.23E-06	139	2	153	2	387	9
2017	WDD07-2	73.5	24	6	1.89E-02	1.04E-02	1.41E-01	1.06E-02	9.75E-01	5.40E-02	1.25E-04	1.17E-05	1.33E-06	121	1	134	1	369	5
2017	WDD07-2	73.5	24	7	1.78E-02	4.65E-03	1.31E-01	5.29E-03	8.80E-01	5.34E-02	1.25E-04	1.63E-05	2.49E-06	114	1	125	1	343	6
2017	WDD07-2	73.5	24	8	1.75E-02	2.46E-02	1.31E-01	2.53E-02	9.70E-01	5.41E-02	3.31E-04	1.47E-05	2.16E-06	112	3	125	3	374	14
2017	WDD07-2	73.5	24	9	1.79E-02	8.52E-03	1.32E-01	8.79E-03	9.70E-01	5.33E-02	1.06E-04	1.58E-05	2.27E-06	115	1	126	1	340	5
2017	WDD07-2	73.5	24	10	1.29E-02	2.10E-02	9.18E-02	2.17E-02	9.68E-01	5.16E-02	2.76E-04	1.28E-05	2.30E-06	83	2	89	2	269	12
2017	WDD07-2	73.5	24	11	1.53E-02	5.57E-03	1.10E-01	6.12E-03	9.10E-01	5.23E-02	1.30E-04	1.53E-05	1.10E-06	98	1	106	1	297	6
2017	WDD07-2	73.5	24	12	1.73E-02	8.46E-03	1.27E-01	8.65E-03	9.77E-01	5.32E-02	8.95E-05	1.41E-05	2.05E-06	111	1	121	1	334	4
2017	WDD07-2	73.5	24	13	1.51E-02	3.87E-03	1.09E-01	4.62E-03	8.38E-01	5.23E-02	1.26E-04	1.19E-05	2.03E-06	97	0	105	0	300	6
2017	WDD07-2	73.5	24	14	1.64E-02	1.32E-02	1.18E-01	1.35E-02	9.76E-01	5.19E-02	1.49E-04	9.08E-06	1.86E-06	105	1	113	1	283	7
2017	WDD07-2	73.5	103	1	1.45E-02	1.79E-02	1.15E-01	2.19E-02	8.18E-01	5.76E-02	7.22E-04	1.33E-05	2.12E-06	93	2	110	2	513	27
2017	WDD07-2	73.5	103	2	1.37E-02	1.29E-02	9.77E-02	1.37E-02	9.41E-01	5.17E-02	2.36E-04	6.61E-06	1.97E-06	88	1	95	1	278	11
2017	WDD07-2	73.5	103	3	8.03E-03	1.31E-02	6.88E-02	1.47E-02	8.93E-01	6.20E-02	4.06E-04	8.12E-06	2.02E-06	52	1	68	1	678	14
2017	WDD07-2	73.5	103	4	2.22E-02	6.84E-03	1.67E-01	6.99E-03	9.78E-01	5.47E-02	7.39E-05	2.11E-05	1.57E-06	142	1	157	1	395	3
2017	WDD07-2	73.5	103	5	1.68E-02	3.76E-03	1.21E-01	4.62E-03	8.14E-01	5.23E-02	1.37E-04	1.11E-05	1.50E-06	107	0	116	1	301	6
2017	WDD07-2	73.5	103	6	1.12E-02	1.50E-02	7.96E-02	1.52E-02	9.88E-01	5.13E-02	1.12E-04	6.89E-06	1.96E-06	72	1	78	1	259	5
2017	WDD07-2	73.5	103	7	2.07E-02	3.78E-03	1.57E-01	4.19E-03	9.02E-01	5.51E-02	9.62E-05	2.19E-05	1.23E-06	132	0	148	1	410	4
2017	WDD07-2	73.5	103	8	1.61E-02	5.22E-03	1.17E-01	5.54E-03	9.41E-01	5.27E-02	8.89E-05	1.17E-05	2.36E-06	103	1	112	1	314	4
2017	WDD07-2	73.5	103	9	1.13E-02	7.49E-03	8.05E-02	8.89E-03	8.43E-01	5.18E-02	2.46E-04	6.36E-06	1.07E-06	72	1	79	1	279	11
2017	WDD07-2	73.5	103	11	1.48E-02	4.36E-03	1.05E-01	4.58E-03	9.52E-01	5.12E-02	6.78E-05	5.68E-06	1.23E-06	95	0	101	0	254	3
2017	WDD07-2	73.5	103	12	1.78E-02	4.18E-03	1.31E-01	4.43E-03	9.45E-01	5.35E-02	7.08E-05	1.49E-05	1.70E-06	114	0	125	1	347	3
2017	WDD07-2	73.5	103	13	1.90E-02	4.04E-03	1.41E-01	4.77E-03	8.47E-01	5.41E-02	1.34E-04	2.20E-05	1.40E-06	121	0	134	1	370	6
2017	WDD07-2	73.5	103	14	7.72E-03	8.79E-03	5.98E-02	1.31E-02	6.73E-01	5.60E-02	5.41E-04	3.39E-06	1.33E-06	50	0	59	1	460	21
2017	WDD07-2	73.5	103	15	1.70E-02	4.16E-03	1.25E-01	4.31E-03	9.66E-01	5.33E-02	5.63E-05	1.37E-05	1.03E-06	109	0	120	0	340	3
2017	WDD07-2	73.5	103	16	1.83E-02	4.07E-03	1.35E-01	4.60E-03	8.86E-01	5.37E-02	1.03E-04	1.68E-05	2.75E-06	117	0	129	1	357	5
2017	WDD07-2	73.5	103	17	2.17E-02	3.74E-03	1.65E-01	3.84E-03	9.74E-01	5.53E-02	3.42E-05	2.27E-05	2.01E-06	138	1	155	1	418	2
2017	WDD07-2	73.5	103	18	1.55E-02	5.13E-03	1.12E-01	5.76E-03	8.91E-01	5.24E-02	1.32E-04	1.29E-05	1.69E-06	99	1	108	1	300	6
2017	WDD07-2	73.5	102	1	9.66E-03	1.99E-02	8.02E-02	2.05E-02	9.71E-01	6.01E-02	2.90E-04	9.74E-06	1.79E-06	62	1	78	2	610	10
2017	WDD07-2	73.5	102	2	1.34E-02	1.24E-02	9.67E-02	1.35E-02	9.18E-01	5.25E-02	2.79E-04	2.21E-05	1.36E-06	86	1	94	1	299	12
2017	WDD07-2	73.5	102	3	2.21E-02	1.49E-02	1.67E-01	1.52E-02	9.76E-01	5.51E-02	1.77E-04	2.52E-05	1.62E-06	141	2	157	2	409	7
2017	WDD07-2	73.5	102	4	1.74E-02	8.30E-03	1.33E-01	1.04E-02	7.98E-01	5.56E-02	3.41E-04	2.65E-05	2.94E-06	111	1	127	1	429	14
2017	WDD07-2	73.5	102	5	1.83E-02	2.50E-02	1.40E-01	2.63E-02	9.51E-01	5.57E-02	4.47E-04	2.29E-05	3.18E-06	117	3	133	3	434	18
2017	WDD07-2	73.5	102	7	1.27E-02	1.13E-02	9.46E-02	1.27E-02	8.93E-01	5.39E-02	2.97E-04	1.70E-05	4.15E-06	82	1	92	1	366	13
2017	WDD07-2	73.5	102	8	1.93E-02	1.42E-02	1.49E-01	1.50E-02	9.48E-01	5.64E-02	2.55E-04	3.09E-05	4.11E-06	123	2	141	2	458	11
2017	WDD07-2	73.5	4	1	6.37E-03	1.86E-02	4.75E-02	2.14E-02	8.71E-01	5.40E-02	5.61E-04	8.67E-06	4.35E-06	41	1	47	1	376	24
2017	WDD07-2	73.5	4	2	1.08E-02	9.21E-03	8.31E-02	1.14E-02	8.07E-01	5.60E-02	3.62E-04	2.62E-05	5.37E-06	69	1	81	1	447	15

Year	Drillhole #	Depth (m)	Circle #	Analysis #	$^{206}Pb/^{238}U$	±	$^{207}Pb/^{235}U$	±	Correl. Err.	$^{207}Pb/^{206}Pb$	±	$^{204}Pb/^{206}Pb$	±	Age 6/8	±	Age 7/5	±	Age 7/6	±
2017	WDD07-2	73.5	104	2	1.08E-02	1.35E-02	8.96E-02	1.40E-02	9.63E-01	6.00E-02	2.15E-04	1.06E-05	3.87E-06	69	1	87	1	606	8
2017	WDD07-2	73.5	104	3	1.11E-02	1.16E-02	8.94E-02	1.22E-02	9.49E-01	5.82E-02	1.85E-04	8.26E-06	7.25E-06	71	1	87	1	541	8
2017	WDD07-2	73.5	104	4	1.22E-02	1.35E-02	9.27E-02	1.42E-02	9.47E-01	5.51E-02	2.43E-04	7.33E-06	3.35E-06	78	1	90	1	421	10
2017	WDD07-2	73.5	104	5	1.46E-02	4.38E-03	1.12E-01	5.90E-03	7.42E-01	5.56E-02	2.08E-04	1.19E-05	3.84E-06	93	0	108	1	440	9
2017	WDD07-2	73.5	105	1	8.99E-03	2.26E-02	6.63E-02	2.29E-02	9.85E-01	5.35E-02	1.83E-04	2.09E-05	5.93E-06	58	1	65	1	349	9
2017	WDD07-2	73.5	105	2	8.92E-03	6.63E-03	6.31E-02	7.69E-03	8.62E-01	5.13E-02	1.89E-04	1.40E-05	3.50E-06	57	0	62	0	255	9
2017	WDD07-2	73.5	105	3	7.98E-03	8.21E-03	5.85E-02	9.39E-03	8.75E-01	5.30E-02	2.35E-04	8.29E-06	2.82E-06	51	0	58	1	336	10
2017	WDD07-2	73.5	105	4	1.87E-02	5.10E-02	1.52E-01	5.12E-02	9.95E-01	5.88E-02	2.97E-04	1.11E-05	4.11E-06	119	6	143	7	563	11
2017	WDD07-2	73.5	105	5	1.52E-02	2.40E-02	1.11E-01	2.44E-02	9.83E-01	5.31E-02	2.32E-04	1.14E-05	3.55E-06	97	2	107	2	335	10
2018	WDD07-2	73.5	104	1	1.42E-02	1.96E-02	1.12E-01	2.00E-02	9.79E-01	5.70E-02	2.30E-04	9.50E-06	1.50E-06	91	2	107	2	487	9
2018	WDD07-2	73.5	104	4	1.39E-02	3.04E-02	1.10E-01	3.21E-02	9.49E-01	5.75E-02	5.76E-04	1.47E-05	2.56E-06	89	3	106	3	505	22
2018	WDD07-2	73.5	104	5	1.41E-02	1.42E-02	1.03E-01	1.46E-02	9.72E-01	5.32E-02	1.74E-04	2.24E-05	2.50E-06	90	1	99	1	325	8
2018	WDD07-2	73.5	104	6	1.10E-02	1.34E-02	9.30E-02	1.39E-02	9.64E-01	6.15E-02	2.24E-04	1.11E-05	1.43E-06	70	1	90	1	655	8
2018	WDD07-2	73.5	104	7	1.62E-02	1.14E-02	1.20E-01	1.44E-02	7.89E-01	5.38E-02	4.70E-04	1.75E-05	2.98E-06	104	1	115	2	356	20
2018	WDD07-2	73.5	104	8	1.39E-02	4.30E-02	1.01E-01	4.32E-02	9.95E-01	5.30E-02	2.15E-04	1.30E-05	2.53E-06	89	4	98	4	324	9
2018	WDD07-2	73.5	104	9	1.56E-02	5.41E-02	1.15E-01	5.44E-02	9.94E-01	5.34E-02	3.05E-04	2.02E-05	2.66E-06	100	5	110	6	337	13
2018	WDD07-2	73.5	104	10	1.64E-02	2.60E-02	1.20E-01	2.68E-02	9.72E-01	5.35E-02	3.27E-04	2.16E-05	3.03E-06	105	3	115	3	341	14
2018	WDD07-2	73.5	104	11	6.51E-03	7.41E-02	5.70E-02	7.68E-02	9.64E-01	6.35E-02	1.29E-03	5.01E-06	3.34E-07	42	3	56	4	723	43
2018	WDD07-2	73.5	104	14	9.18E-03	2.27E-02	7.48E-02	2.34E-02	9.70E-01	5.93E-02	3.31E-04	1.16E-05	2.71E-06	59	1	73	2	573	12
2018	WDD07-2	73.5	104	15	1.09E-02	3.04E-02	7.82E-02	3.06E-02	9.94E-01	5.22E-02	1.61E-04	1.53E-05	2.92E-06	70	2	76	2	288	7
2018	WDD07-2	73.5	104	16	1.13E-02	1.10E-02	8.46E-02	1.25E-02	8.82E-01	5.42E-02	3.16E-04	1.11E-05	1.81E-06	73	1	82	1	376	13
2018	WDD07-2	73.5	105	5	8.16E-03	2.60E-02	5.77E-02	2.63E-02	9.87E-01	5.14E-02	2.13E-04	1.16E-05	2.55E-06	52	1	57	1	252	10
2018	WDD07-2	73.5	105	6	5.54E-03	6.72E-03	3.88E-02	8.77E-03	7.67E-01	5.09E-02	2.72E-04	1.24E-05	4.56E-06	36	0	39	0	232	13
2018	WDD07-2	73.5	105	7	1.23E-02	4.53E-02	9.08E-02	4.70E-02	9.65E-01	5.34E-02	6.59E-04	5.87E-06	1.97E-06	79	4	88	4	344	28
2018	WDD07-2	73.5	105	8	4.06E-03	1.44E-02	2.88E-02	1.89E-02	7.61E-01	5.17E-02	6.27E-04	1.38E-05	3.73E-06	26	0	29	1	265	28
2018	WDD07-2	73.5	105	9	1.87E-03	3.89E-02	1.61E-02	3.93E-02	9.90E-01	6.32E-02	2.93E-04	5.01E-05	1.05E-05	12	0	16	1	694	12
2018	WDD07-2	73.5	4	3	3.28E-03	3.11E-02	2.84E-02	4.25E-02	7.32E-01	6.32E-02	1.80E-03	4.23E-05	7.72E-06	21	1	28	1	698	61
2018	WDD07-2	73.5	4	7	4.35E-03	2.41E-02	3.84E-02	2.51E-02	9.60E-01	6.43E-02	3.94E-04	2.72E-05	1.17E-05	28	1	38	1	741	15
2018	WDD07-2	73.5	4	9	2.19E-03	1.06E-02	1.94E-02	1.56E-02	6.78E-01	6.59E-02	5.41E-04	1.22E-04	2.85E-05	14	0	19	0	750	24
2018	WDD07-2	73.5	3	1	3.30E-03	6.29E-02	2.75E-02	7.57E-02	8.30E-01	6.06E-02	2.55E-03	1.74E-05	5.13E-06	21	1	28	2	619	89
2018	WDD07-2	73.5	3	2	2.14E-03	2.44E-02	1.92E-02	2.87E-02	8.51E-01	6.61E-02	9.32E-04	5.90E-05	1.54E-05	14	0	19	1	785	31
2018	WDD07-2	73.5	3	3	6.87E-03	7.88E-02	5.00E-02	8.02E-02	9.83E-01	5.29E-02	7.68E-04	1.00E-05	3.93E-06	44	3	50	4	320	33
2018	WDD07-2	73.5	3	4	6.12E-03	3.34E-02	4.50E-02	3.77E-02	8.87E-01	5.36E-02	9.14E-04	2.18E-05	6.57E-06	39	1	45	2	342	39
2018	WDD07-2	73.5	3	5	6.65E-03	3.72E-02	4.82E-02	3.81E-02	9.78E-01	5.27E-02	4.08E-04	1.10E-05	4.65E-06	43	2	48	2	310	18
2018	WDD07-2	73.5	3	7	7.41E-03	1.89E-02	5.60E-02	2.83E-02	6.67E-01	5.51E-02	1.15E-03	2.14E-05	5.11E-06	48	1	55	2	405	47
2018	WDD07-2	73.5	3	8	5.36E-02	2.82E-02	4.15E-01	2.97E-02	9.49E-01	5.62E-02	5.22E-04	7.16E-06	2.16E-06	337	9	353	9	460	21
2018	WDD07-2	73.5	103	2	7.50E-03	2.66E-02	6.72E-02	3.06E-02	8.71E-01	6.50E-02	9.73E-04	4.45E-06	1.67E-06	48	1	66	2	774	31
2018	WDD07-2	73.5	103	3	9.49E-03	1.55E-02	6.71E-02	1.72E-02	9.03E-01	5.13E-02	3.70E-04	8.14E-06	3.43E-06	61	1	66	1	252	17
2018	WDD07-2	73.5	103	4	1.43E-02	5.07E-03	1.04E-01	7.01E-03	7.23E-01	5.31E-02	2.47E-04	1.79E-05	3.36E-06	91	0	100	1	324	11
2018	WDD07-2	73.5	103	5	1.80E-02	3.02E-03	1.35E-01	3.95E-03	7.64E-01	5.47E-02	1.29E-04	1.99E-05	2.80E-06	115	0	128	0	388	6
2018	WDD07-2	73.5	103	6	1.66E-02	6.50E-03	1.27E-01	8.04E-03	8.08E-01	5.50E-02	2.43E-04	2.05E-05	4.84E-06	107	1	121	1	403	11
2018	WDD07-2	73.5	103	7	9.70E-03	5.24E-03	6.84E-02	7.41E-03	7.07E-01	5.13E-02	2.60E-04	1.18E-05	3.23E-06	62	0	67	0	247	12
2018	WDD07-2	73.5	103	8	9.57E-03	4.37E-03	6.62E-02	5.66E-03	7.73E-01	5.04E-02	1.58E-04	1.57E-05	4.87E-06	61	0	65	0	203	8
2018	WDD07-2	73.5	103	9	1.46E-02	1.29E-02	1.06E-01	1.39E-02	9.34E-01	5.31E-02	2.51E-04	1.92E-05	3.73E-06	93	1	103	1	323	11
2018	WDD07-2	73.5	103	10	6.43E-03	4.75E-02	5.27E-02	4.81E-02	9.88E-01	5.95E-02	4.31E-04	7.55E-06	3.09E-06	41	2	52	2	582	16

***Supplementary Table 3-11**: Major elements composition in chlorite C1 obtained by EPMA with the associated structural formulae and calculated temperatures*

Analysed mineral	Drillhole #	Depth (m)	Circle #	Analysis #	SiO_2 (wt%)	TiO_2 (wt%)	Al_2O_3 (wt%)	FeO (wt%)	MnO (wt%)	MgO (wt%)	CaO (wt%)	Na_2O (wt%)	K_2O (wt%)	Total (wt%)	Linear T(°C)	Quadratic T(°C)	Final T(°C)
Chlorite C1	WDD07-2	51.7B	2	6	22.72	0.01	18.03	34.53	0.11	4.45	0.15	0.08	0.13	80.21	248	258	248
Chlorite C1	WDD07-2	51.7B	2	7	22.98	0.03	18.65	38.22	0.11	4.25	0.10	0.11	0.01	84.46	413	340	340
Chlorite C1	WDD07-2	55.9A	1	1	21.77	0.02	18.77	39.93	0.17	2.52	0.14	0.00	0.01	83.33	551	383	383
Chlorite C1	WDD07-2	55.9A	1	2	23.22	0.01	18.49	41.83	0.05	3.39	0.06	0.03	0.01	87.09	-	-	-
Chlorite C1	WDD07-2	55.9A	1	3	22.17	0.02	17.53	39.84	0.00	3.02	0.03	0.04	0.01	82.66	644	405	405
Chlorite C1	WDD07-2	55.9A	1	4	23.14	0.00	19.22	44.19	0.00	2.48	0.04	0.00	0.02	89.09	-	-	-
Chlorite C1	WDD07-2	55.9A	1	5	22.46	0.03	20.09	43.37	0.16	2.70	0.02	0.02	0.03	88.88	-	-	-
Chlorite C1	WDD07-2	55.9A	1	6	23.61	0.00	19.37	41.94	0.15	3.33	0.08	0.00	0.01	88.49	512	372	372
Chlorite C1	WDD07-2	55.9A	1	7	23.24	0.04	18.70	41.15	0.06	2.89	0.04	0.00	0.00	86.12	366	321	321
Chlorite C1	WDD07-2	55.9A	1	8	24.13	0.00	19.38	43.27	0.04	3.37	0.02	0.01	0.01	90.23	609	397	397
Chlorite C1	WDD07-2	55.9A	1	9	23.30	0.00	20.17	45.31	0.07	2.41	0.00	0.00	0.00	91.26	-	-	-
Chlorite C1	WDD07-2	55.9A	2	10	22.72	0.03	22.15	41.00	0.25	3.57	0.04	0.01	0.02	89.79	654	407	407
Chlorite C1	WDD07-2	55.9A	2	1	21.78	0.02	18.16	42.04	0.07	2.31	0.07	0.04	0.02	84.51	-	-	-
Chlorite C1	WDD07-2	55.9A	2	2	21.38	0.04	18.12	40.03	0.11	2.63	0.09	0.06	0.02	82.48	-	-	-
Chlorite C1	WDD07-2	55.9A	2	3	22.27	0.01	18.91	43.18	0.02	2.54	0.04	0.00	0.02	86.99	-	-	-
Chlorite C1	WDD07-2	55.9B	1	2	23.47	0.00	19.46	42.85	0.00	3.30	0.02	0.01	0.01	89.12	1857	526	526
Chlorite C1	WDD07-2	55.9B	1	3	23.30	0.00	18.13	35.71	0.03	2.86	0.07	0.00	0.35	80.45	185	206	185
Chlorite C1	WDD07-2	55.9B	1	5	23.27	0.02	17.81	36.73	0.12	2.01	0.07	0.02	0.23	80.28	177	197	177
Chlorite C1	WDD07-2	55.9B	1	6	23.49	0.01	20.04	42.86	0.17	2.98	0.07	0.05	0.10	89.77	882	447	447
Chlorite C1	WDD9-128	53.3B	1	1	24.90	0.05	17.82	38.62	0.17	6.48	0.00	0.00	0.09	88.13	685	414	414
Chlorite C1	WDD9-128	53.3B	1	2	24.67	0.00	17.96	38.98	0.02	6.64	0.02	0.15	0.02	88.46	-	-	-
Chlorite C1	WDD9-128	53.3B	1	3	24.19	0.00	17.79	39.04	0.04	6.47	0.03	0.05	0.05	87.66	-	-	-
Chlorite C1	WDD9-128	53.3B	1	4	24.49	0.01	17.87	40.09	0.17	5.98	0.05	0.00	0.05	88.71	-	-	-
Chlorite C1	WDD9-128	53.3B	2	1	23.83	0.02	17.21	37.62	0.06	5.92	0.09	0.10	0.10	84.95	-	-	-
Chlorite C1	WDD9-128	53.3B	2	2	24.22	0.00	17.71	38.23	0.13	6.79	0.08	0.03	0.04	87.23	-	-	-
Chlorite C1	WDD9-128	53.3B	2	3	24.26	0.01	17.86	36.64	0.00	7.33	0.04	0.02	0.01	86.17	-	-	-
Chlorite C1	WDD9-128	53.3B	2	4	23.22	0.00	16.53	34.94	0.03	6.44	0.05	0.03	0.04	81.28	508	371	371
Chlorite C1	WDD9-128	53.3B	2	5	22.66	0.02	16.18	37.78	0.16	5.21	0.04	0.00	0.04	82.09	-	-	-
Chlorite C1	WDD9-128	92.3C	1	1	24.35	0.00	19.43	38.03	0.07	6.50	0.04	0.05	0.04	88.51	693	415	415
Chlorite C1	WDD9-128	92.3C	1	2	26.28	0.00	20.17	31.78	0.10	7.12	0.05	0.11	0.98	86.59	178	199	178
Chlorite C1	WDD9-128	92.3C	1	3	24.39	0.00	18.88	39.82	0.07	6.77	0.00	0.01	0.00	89.94	-	-	-
Chlorite C1	WDD9-128	92.3C	1	4	24.69	0.05	20.04	38.19	0.17	6.02	0.07	0.02	0.34	89.59	419	342	342
Chlorite C1	WDD9-128	92.3C	1	5	24.65	0.00	19.64	38.53	0.03	6.78	0.05	0.01	0.03	89.72	950	456	456
Chlorite C1	WDD9-128	92.3C	1	6	25.60	0.00	19.93	36.85	0.08	6.71	0.05	0.09	0.40	89.71	294	286	294
Chlorite C1	WDD9-128	92.3C	1	7	26.02	0.01	19.63	34.92	0.02	9.35	0.04	0.08	0.02	90.09	388	330	330
Chlorite C1	WDD9-128	92.3C	1	8	24.53	0.02	20.71	37.96	0.11	6.64	0.00	0.09	0.10	90.16	548	382	382
Chlorite C1	WDD9-128	92.3C	1	9	24.61	0.01	19.49	38.34	0.21	6.55	0.02	0.00	0.12	89.35	711	419	419
Chlorite C1	WDD9-128	92.3C	1	10	24.21	0.00	19.20	38.87	0.00	7.17	0.03	0.06	0.02	89.56	-	-	-
Chlorite C1	WDD9-128	92.3C	2	4	24.61	0.00	18.26	34.47	0.05	8.63	0.10	0.04	0.16	86.32	-	-	-
Chlorite C1	WDD9-128	92.3C	2	5	24.43	0.00	18.90	34.25	0.22	7.56	0.10	0.09	0.34	85.89	408	338	338
Chlorite C1	WDD9-128	92.3C	2	6	25.93	0.00	18.90	33.11	0.11	10.37	0.03	0.01	0.25	88.71	512	372	372
Chlorite C1	WDD9-128	92.3C	2	7	24.25	0.01	18.99	36.48	0.00	8.75	0.08	0.02	0.02	88.60	-	-	-
Chlorite C1	WDD9-128	92.3C	2	8	24.05	0.02	18.58	38.13	0.08	6.90	0.08	0.08	0.02	87.94	-	-	-
Chlorite C1	WDD9-128	92.3C	2	9	23.86	0.00	18.61	38.82	0.06	7.07	0.10	0.13	0.02	88.67	-	-	-

Analysed mineral	Drillhole #	Depth (m)	Circle #	Analysis #	SiO_2 (wt%)	TiO_2 (wt%)	Al_2O_3 (wt%)	FeO (wt%)	MnO (wt%)	MgO (wt%)	CaO (wt%)	Na_2O (wt%)	K_2O (wt%)	Total (wt%)	Linear T(°C)	Quadratic T(°C)	Final T(°C)
Chlorite C1	JDD08-003	74.4B	1	1	26.11	0.02	18.56	32.91	0.00	8.11	0.03	0.10	0.32	86.16	211	230	211
Chlorite C1	JDD08-003	74.4B	1	2	25.17	0.00	18.93	35.82	0.00	7.80	0.05	0.07	0.14	87.98	392	331	331
Chlorite C1	JDD08-003	74.4B	1	3	24.89	0.01	18.55	30.26	0.06	10.64	0.10	0.09	0.16	84.76	440	349	349
Chlorite C1	JDD08-003	74.4B	1	4	24.71	0.00	19.11	35.59	0.09	8.33	0.06	0.02	0.03	87.94	931	454	454
Chlorite C1	JDD08-003	74.4B	1	5	27.44	0.00	19.61	30.78	0.06	8.34	0.08	0.11	0.73	87.15	159	253	159
Chlorite C1	WDD07-2	51.7A	1	1	22.87	0.04	19.30	41.82	0.18	3.07	0.06	0.16	0.05	87.55	-	-	-
Chlorite C1	WDD07-2	51.7A	1	5	23.17	0.01	19.67	41.57	0.04	3.62	0.00	0.12	0.02	88.22	-	-	-
Chlorite C1	WDD07-2	51.7A	1	6	22.84	0.02	19.80	43.91	0.09	2.73	0.00	0.02	0.03	89.44	-	-	-
Chlorite C1	WDD07-2	51.7A	1	7	23.10	0.00	19.54	42.55	0.00	2.78	0.02	0.11	0.01	88.11	845	442	442
Chlorite C1	WDD07-2	51.7A	1	8	22.56	0.00	18.50	40.59	0.04	2.80	0.09	0.12	0.12	84.82	655	408	408
Chlorite C1	WDD07-2	51.7A	1	9	23.54	0.00	19.31	40.27	0.10	3.62	0.02	0.00	0.28	87.14	396	333	333
Chlorite C1	WDD07-2	51.7A	1	10	22.44	0.01	18.62	38.06	0.05	3.58	0.02	0.00	0.12	82.90	351	314	314
Chlorite C1	WDD07-2	51.7A	1	11	22.28	0.01	18.73	39.78	0.06	2.93	0.06	0.02	0.01	83.88	438	349	349
Chlorite C1	WDD07-2	51.7A	1	12	22.86	0.00	19.88	41.10	0.15	2.92	0.06	0.00	0.02	86.99	447	351	351
Chlorite C1	WDD07-2	51.7A	1	13	22.71	0.03	19.57	41.50	0.12	3.34	0.05	0.00	0.01	87.33	-	-	-
Chlorite C1	WDD07-2	51.7A	1	14	23.31	0.01	19.52	42.49	0.06	3.02	0.00	0.10	0.02	88.53	852	443	443
Chlorite C1	WDD07-2	51.7A	1	15	22.14	0.00	19.45	40.98	0.06	3.14	0.00	0.05	0.00	85.82	-	-	-
Chlorite C1	WDD07-2	51.7A	1	16	22.13	0.02	17.74	38.50	0.07	3.46	0.04	0.20	0.13	82.29	-	-	-
Chlorite C1	WDD07-2	51.7A	2	5	23.68	0.01	19.73	40.10	0.15	3.36	0.02	0.00	0.35	87.40	327	303	327
Chlorite C1	WDD07-2	51.7A	2	6	24.10	0.01	19.55	40.13	0.10	3.26	0.05	0.10	0.14	87.44	275	275	275
Chlorite C1	WDD07-2	51.7A	2	7	22.44	0.00	18.74	39.58	0.08	3.60	0.04	0.06	0.07	84.61	858	443	443
Chlorite C1	WDD07-2	51.7A	2	8	22.74	0.02	19.22	40.85	0.12	3.40	0.11	0.08	0.03	86.57	-	-	-
Chlorite C1	WDD07-2	51.7A	2	9	23.90	0.00	19.63	40.25	0.09	3.22	0.12	0.13	0.42	87.76	332	305	332
Chlorite C1	WDD07-2	51.7A	2	15	22.91	0.00	19.79	40.91	0.15	3.81	0.03	0.04	0.05	87.69	-	-	-
Chlorite C1	WDD07-2	51.7A	2	16	21.88	0.00	18.33	41.38	0.05	3.85	0.06	0.10	0.04	85.69	-	-	-
Chlorite C1	WDD07-2	51.7A	2	17	22.82	0.00	19.37	42.09	0.03	3.02	0.07	0.11	0.10	87.61	-	-	-
Chlorite C1	WDD07-2	51.7A	2	18	22.87	0.00	18.18	36.80	0.04	3.96	0.10	0.11	0.34	82.40	312	295	312
Chlorite C1	WDD07-2	51.7A	2	21	25.01	0.03	18.93	34.59	0.00	3.44	0.17	0.08	1.06	83.31	158	252	158
Chlorite C1	WDD07-2	51.7A	2	22	22.89	0.00	19.35	41.77	0.14	3.25	0.00	0.05	0.05	87.50	-	-	-
Chlorite C1	WDD07-2	51.7A	2	23	23.60	0.04	19.59	36.94	0.01	3.25	0.21	0.09	0.77	84.50	236	249	236
Chlorite C1	WDD07-2	51.7A	2	24	24.45	0.00	19.05	39.24	0.12	3.80	0.07	0.09	0.29	87.11	264	268	264
Chlorite C1	WDD07-2	51.7B	1	1	21.64	0.03	17.10	35.89	0.00	4.63	0.05	0.07	0.06	79.47	912	451	451
Chlorite C1	WDD07-2	51.7B	1	3	21.98	0.00	19.46	37.93	0.14	4.59	0.08	0.32	0.04	84.54	-	-	-
Chlorite C1	WDD07-2	51.7B	1	4	22.03	0.01	17.98	35.62	0.14	4.86	0.06	0.13	0.04	80.87	518	374	374
Chlorite C1	WDD07-2	51.7B	1	5	22.76	0.02	18.53	38.35	0.18	5.39	0.17	0.05	0.01	85.46	-	-	-
Chlorite C1	WDD07-2	51.7B	1	6	22.51	0.01	18.83	41.68	0.10	3.54	0.08	0.07	0.01	86.83	-	-	-
Chlorite C1	WDD07-2	51.7B	1	7	21.14	0.00	18.38	38.62	0.10	3.67	0.03	0.15	0.09	82.18	-	-	-
Chlorite C1	WDD07-2	51.7B	1	8	22.95	0.02	19.81	43.33	0.06	2.90	0.06	0.00	0.01	89.14	-	-	-
Chlorite C1	WDD07-2	51.7B	1	11	22.90	0.00	19.28	42.25	0.07	3.35	0.06	0.02	0.01	87.94	-	-	-
Chlorite C1	WDD07-2	51.7B	2	1	24.13	0.01	19.63	40.56	0.08	3.92	0.12	0.07	0.04	88.56	351	314	314
Chlorite C1	WDD07-2	51.7B	2	2	23.01	0.01	18.93	39.21	0.00	4.02	0.05	0.17	0.10	85.50	583	391	391
Chlorite C1	WDD07-2	51.7B	2	3	24.18	0.00	20.42	39.30	0.00	3.48	0.14	0.18	0.51	88.21	284	280	284
Chlorite C1	WDD07-2	51.7B	2	4	23.52	0.04	20.23	38.76	0.12	4.31	0.20	0.05	0.24	87.47	379	326	326
Chlorite C1	WDD07-2	51.7B	2	5	21.34	0.05	18.36	37.38	0.19	3.90	0.07	0.18	0.07	81.54	-	-	-

Analysed mineral	Drillhole #	Depth (m)	Circle #	Analysis #	SiO_2 (wt%)	TiO_2 (wt%)	Al_2O_3 (wt%)	FeO (wt%)	MnO (wt%)	MgO (wt%)	CaO (wt%)	Na_2O (wt%)	K_2O (wt%)	Total (wt%)	Linear T(°C)	Quadratic T(°C)	Final T(°C)
Chlorite C1	WDD9-128	92.3C	3	6	22.38	0.00	18.12	33.90	0.00	6.65	0.03	0.00	0.02	81.10	600	395	395
Chlorite C1	WDD9-128	92.3C	3	7	24.24	0.00	18.65	39.14	0.03	7.15	0.00	0.04	0.04	89.29	-	-	-
Chlorite C1	WDD9-128	92.3C	3	8	25.93	0.01	19.02	30.29	0.12	11.99	0.08	0.09	0.07	87.60	504	370	370
Chlorite C1	WDD9-128	92.3C	3	9	25.10	0.00	18.67	36.34	0.02	8.33	0.04	0.01	0.07	88.58	1643	515	515
Chlorite C1	WDD9-128	92.3C	4	2	24.24	0.02	20.26	38.21	0.08	6.78	0.03	0.04	0.02	89.68	-	-	-
Chlorite C1	WDD9-128	92.3C	4	3	24.25	0.02	19.28	37.99	0.12	6.99	0.03	0.06	0.04	88.78	-	-	-
Chlorite C1	WDD9-128	92.3C	4	4	24.21	0.02	19.47	38.23	0.14	7.21	0.03	0.01	0.01	89.33	-	-	-
Chlorite C1	WDD9-128	92.3C	4	5	24.98	0.00	20.06	37.27	0.10	7.25	0.00	0.00	0.04	89.70	425	344	344
Chlorite C1	WDD9-128	92.3C	4	7	24.87	0.00	19.89	35.78	0.10	8.53	0.04	0.02	0.08	89.31	1200	483	483
Chlorite C1	WDD9-128	92.3C	4	8	25.18	0.01	19.10	31.45	0.08	11.02	0.09	0.06	0.07	87.06	1128	476	476
Chlorite C1	WDD9-128	92.3C	4	9	27.15	0.02	20.06	32.18	0.00	8.88	0.09	0.18	0.58	89.14	200	220	200
Mix Illite - Chlorite C1	WDD07-2	73.5A	1	1	41.50	0.06	20.67	18.60	0.16	0.97	0.61	0.27	4.30	87.14			
Mix Illite - Chlorite C1	WDD07-2	73.5A	1	2	40.35	0.03	20.19	19.57	0.15	0.73	0.47	0.18	3.12	84.79			
Mix Illite - Chlorite C1	WDD07-2	73.5A	1	3	37.49	0.04	19.50	18.58	0.19	0.74	0.52	0.18	3.08	80.32			
Mix Illite - Chlorite C1	WDD07-2	73.5A	1	4	30.45	0.03	13.22	20.13	0.00	0.67	0.53	0.18	1.30	66.51			
Mix Illite - Chlorite C1	WDD07-2	73.5A	1	5	23.53	0.03	5.33	15.31	0.01	0.51	0.51	0.15	0.68	46.06			
Mix Illite - Chlorite C1	WDD07-2	73.5A	2	5	26.42	0.01	10.59	22.04	0.00	0.77	0.46	0.13	1.51	61.93			
Mix Illite - Chlorite C1	WDD07-2	73.5A	2	7	40.57	0.00	25.48	14.90	0.19	0.77	0.26	0.16	3.53	85.86			
Mix Illite - Chlorite C1	WDD07-2	73.5A	2	8	36.51	0.01	18.97	23.52	0.20	1.09	0.40	0.13	2.56	83.39			
Mix Illite - Chlorite C1	WDD07-2	73.5A	3	1	27.81	0.00	10.74	19.72	0.00	0.82	0.59	0.15	2.07	61.90			
Mix Illite - Chlorite C1	WDD07-2	73.5A	3	2	35.98	0.06	16.50	19.11	0.06	1.21	0.61	0.16	4.22	77.91			
Mix Illite - Chlorite C1	WDD07-2	73.5A	3	3	32.21	0.01	13.71	19.57	0.09	0.98	0.56	0.17	3.26	70.56			
Mix Illite - Chlorite C1	WDD07-2	73.5A	3	4	32.74	0.00	12.94	23.19	0.01	0.85	0.72	0.16	2.70	73.31			
Mix Illite - Chlorite C1	WDD07-2	73.5A	3	5	17.33	0.00	4.66	20.82	0.04	0.80	0.81	0.18	0.95	45.59			
Mix Illite - Chlorite C1	WDD07-2	73.5A	3	6	29.52	0.01	12.20	20.22	0.05	0.97	0.83	0.15	3.01	66.96			

Analysed mineral	Drillhole #	Depth (m)	Circle #	Analysis #	Si (apfu)	Ti (apfu)	Al (apfu)	Fe^{2+} (apfu)	Mn (apfu)	Mg (apfu)	Ca (apfu)	Na (apfu)	K (apfu)	Total (apfu)
Chlorite C1	JDD08-003	74.4B	1	1	2.924	0.002	2.450	3.082	0.000	1.354	0.004	0.022	0.046	9.883
Chlorite C1	JDD08-003	74.4B	1	2	2.806	0.000	2.487	3.339	0.000	1.296	0.006	0.015	0.020	9.968
Chlorite C1	JDD08-003	74.4B	1	3	2.808	0.001	2.466	2.855	0.006	1.789	0.012	0.020	0.023	9.979
Chlorite C1	JDD08-003	74.4B	1	4	2.755	0.000	2.511	3.318	0.008	1.385	0.007	0.004	0.004	9.994
Chlorite C1	JDD08-003	74.4B	1	5	2.991	0.000	2.519	2.806	0.006	1.355	0.009	0.023	0.102	9.811
Chlorite C1	WDD07-2	51.7A	1	1	2.671	0.004	2.657	4.084	0.018	0.535	0.008	0.036	0.007	10.019
Chlorite C1	WDD07-2	51.7A	1	5	2.671	0.001	2.672	4.007	0.004	0.622	0.000	0.027	0.003	10.007
Chlorite C1	WDD07-2	51.7A	1	6	2.629	0.002	2.686	4.227	0.009	0.469	0.000	0.004	0.004	10.030
Chlorite C1	WDD07-2	51.7A	1	7	2.682	0.000	2.673	4.130	0.000	0.481	0.002	0.025	0.001	9.995
Chlorite C1	WDD07-2	51.7A	1	8	2.717	0.000	2.625	4.087	0.004	0.503	0.012	0.028	0.018	9.994
Chlorite C1	WDD07-2	51.7A	1	9	2.733	0.000	2.642	3.910	0.010	0.627	0.002	0.000	0.041	9.966
Chlorite C1	WDD07-2	51.7A	1	10	2.729	0.001	2.669	3.871	0.005	0.649	0.003	0.000	0.019	9.945
Chlorite C1	WDD07-2	51.7A	1	11	2.702	0.001	2.677	4.033	0.006	0.530	0.008	0.005	0.002	9.962
Chlorite C1	WDD07-2	51.7A	1	12	2.672	0.000	2.738	4.017	0.015	0.509	0.008	0.000	0.003	9.961
Chlorite C1	WDD07-2	51.7A	1	13	2.652	0.003	2.693	4.052	0.012	0.581	0.006	0.000	0.001	10.000
Chlorite C1	WDD07-2	51.7A	1	14	2.690	0.001	2.654	4.100	0.006	0.519	0.000	0.022	0.003	9.995
Chlorite C1	WDD07-2	51.7A	1	15	2.633	0.000	2.726	4.076	0.006	0.557	0.000	0.012	0.000	10.009
Chlorite C1	WDD07-2	51.7A	1	16	2.733	0.002	2.582	3.975	0.007	0.637	0.005	0.048	0.020	10.009
Chlorite C1	WDD07-2	51.7A	2	5	2.736	0.001	2.687	3.874	0.015	0.579	0.002	0.000	0.052	9.945
Chlorite C1	WDD07-2	51.7A	2	6	2.777	0.001	2.654	3.866	0.010	0.560	0.006	0.022	0.021	9.917
Chlorite C1	WDD07-2	51.7A	2	7	2.692	0.000	2.650	3.971	0.008	0.644	0.005	0.014	0.011	9.995
Chlorite C1	WDD07-2	51.7A	2	8	2.675	0.002	2.664	4.018	0.012	0.596	0.014	0.018	0.005	10.003
Chlorite C1	WDD07-2	51.7A	2	9	2.753	0.000	2.664	3.876	0.009	0.553	0.015	0.029	0.062	9.961
Chlorite C1	WDD07-2	51.7A	2	15	2.652	0.000	2.700	3.961	0.015	0.658	0.004	0.009	0.007	10.006
Chlorite C1	WDD07-2	51.7A	2	16	2.624	0.000	2.591	4.150	0.005	0.688	0.008	0.023	0.006	10.095
Chlorite C1	WDD07-2	51.7A	2	17	2.666	0.000	2.667	4.111	0.003	0.526	0.009	0.025	0.015	10.021
Chlorite C1	WDD07-2	51.7A	2	18	2.784	0.000	2.608	3.746	0.004	0.719	0.013	0.026	0.053	9.952
Chlorite C1	WDD07-2	51.7A	2	21	2.954	0.003	2.635	3.417	0.000	0.606	0.022	0.018	0.160	9.814
Chlorite C1	WDD07-2	51.7A	2	22	2.671	0.000	2.661	4.076	0.014	0.565	0.000	0.011	0.007	10.007
Chlorite C1	WDD07-2	51.7A	2	23	2.790	0.004	2.729	3.651	0.001	0.573	0.027	0.021	0.116	9.911
Chlorite C1	WDD07-2	51.7A	2	24	2.817	0.000	2.587	3.781	0.012	0.653	0.009	0.020	0.043	9.921
Chlorite C1	WDD07-2	51.7B	1	1	2.739	0.003	2.550	3.798	0.000	0.874	0.007	0.017	0.010	9.997
Chlorite C1	WDD07-2	51.7B	1	3	2.620	0.000	2.733	3.780	0.014	0.816	0.010	0.074	0.006	10.053
Chlorite C1	WDD07-2	51.7B	1	4	2.724	0.001	2.620	3.683	0.015	0.896	0.008	0.031	0.006	9.984
Chlorite C1	WDD07-2	51.7B	1	5	2.682	0.002	2.573	3.779	0.018	0.947	0.021	0.011	0.002	10.036
Chlorite C1	WDD07-2	51.7B	1	6	2.655	0.001	2.617	4.111	0.010	0.622	0.010	0.016	0.002	10.044
Chlorite C1	WDD07-2	51.7B	1	7	2.622	0.000	2.687	4.006	0.011	0.679	0.004	0.036	0.014	10.059
Chlorite C1	WDD07-2	51.7B	1	8	2.642	0.002	2.687	4.171	0.006	0.498	0.007	0.000	0.001	10.014
Chlorite C1	WDD07-2	51.7B	1	11	2.664	0.000	2.643	4.110	0.007	0.581	0.007	0.005	0.001	10.018
Chlorite C1	WDD07-2	51.7B	2	1	2.746	0.001	2.633	3.860	0.008	0.665	0.015	0.015	0.006	9.948
Chlorite C1	WDD07-2	51.7B	2	2	2.717	0.001	2.634	3.872	0.000	0.708	0.006	0.039	0.015	9.992
Chlorite C1	WDD07-2	51.7B	2	3	2.749	0.000	2.736	3.736	0.000	0.590	0.017	0.040	0.074	9.940
Chlorite C1	WDD07-2	51.7B	2	4	2.694	0.003	2.731	3.713	0.012	0.736	0.025	0.011	0.035	9.960
Chlorite C1	WDD07-2	51.7B	2	5	2.650	0.005	2.687	3.882	0.020	0.722	0.009	0.043	0.011	10.029

Analysed mineral	Drillhole #	Depth (m)	Circle #	Analysis #	Si (apfu)	Ti (apfu)	Al (apfu)	Fe^{2+} (apfu)	Mn (apfu)	Mg (apfu)	Ca (apfu)	Na (apfu)	K (apfu)	Total (apfu)
Chlorite C1	WDD07-2	51.7B	2	6	2.809	0.001	2.627	3.569	0.012	0.820	0.020	0.019	0.020	9.897
Chlorite C1	WDD07-2	51.7B	2	7	2.736	0.003	2.617	3.805	0.011	0.754	0.013	0.025	0.002	9.966
Chlorite C1	WDD07-2	55.9A	1	1	2.669	0.002	2.712	4.093	0.018	0.461	0.018	0.000	0.002	9.974
Chlorite C1	WDD07-2	55.9A	1	2	2.725	0.001	2.557	4.104	0.005	0.593	0.008	0.007	0.001	10.000
Chlorite C1	WDD07-2	55.9A	1	3	2.741	0.002	2.554	4.118	0.000	0.557	0.004	0.010	0.002	9.986
Chlorite C1	WDD07-2	55.9A	1	4	2.678	0.000	2.622	4.277	0.000	0.428	0.005	0.000	0.003	10.012
Chlorite C1	WDD07-2	55.9A	1	5	2.599	0.003	2.740	4.197	0.016	0.466	0.002	0.004	0.004	10.032
Chlorite C1	WDD07-2	55.9A	1	6	2.716	0.000	2.626	4.034	0.015	0.571	0.010	0.000	0.001	9.972
Chlorite C1	WDD07-2	55.9A	1	7	2.748	0.004	2.606	4.068	0.006	0.509	0.005	0.000	0.000	9.946
Chlorite C1	WDD07-2	55.9A	1	8	2.729	0.000	2.583	4.092	0.004	0.568	0.002	0.002	0.001	9.982
Chlorite C1	WDD07-2	55.9A	1	9	2.635	0.000	2.688	4.285	0.007	0.406	0.000	0.000	0.000	10.021
Chlorite C1	WDD07-2	55.9A	2	10	2.554	0.003	2.935	3.854	0.024	0.598	0.005	0.002	0.003	9.978
Chlorite C1	WDD07-2	55.9A	2	1	2.664	0.002	2.617	4.299	0.007	0.421	0.009	0.009	0.003	10.032
Chlorite C1	WDD07-2	55.9A	2	2	2.660	0.004	2.657	4.165	0.012	0.488	0.012	0.014	0.003	10.016
Chlorite C1	WDD07-2	55.9A	2	3	2.643	0.001	2.645	4.286	0.002	0.449	0.005	0.000	0.003	10.035
Chlorite C1	WDD07-2	55.9B	1	2	2.690	0.000	2.629	4.107	0.000	0.564	0.002	0.002	0.001	9.997
Chlorite C1	WDD07-2	55.9B	1	3	2.884	0.000	2.645	3.696	0.003	0.528	0.009	0.000	0.055	9.821
Chlorite C1	WDD07-2	55.9B	1	5	2.906	0.002	2.621	3.836	0.013	0.374	0.009	0.005	0.037	9.802
Chlorite C1	WDD07-2	55.9B	1	6	2.673	0.001	2.687	4.078	0.016	0.506	0.009	0.011	0.015	9.995
Chlorite C1	WDD9-128	53.3B	1	1	2.822	0.004	2.380	3.660	0.016	1.095	0.000	0.000	0.013	9.990
Chlorite C1	WDD9-128	53.3B	1	2	2.790	0.000	2.394	3.687	0.002	1.120	0.002	0.033	0.003	10.031
Chlorite C1	WDD9-128	53.3B	1	3	2.770	0.000	2.401	3.738	0.004	1.104	0.004	0.011	0.007	10.039
Chlorite C1	WDD9-128	53.3B	1	4	2.782	0.001	2.392	3.808	0.016	1.013	0.006	0.000	0.007	10.025
Chlorite C1	WDD9-128	53.3B	2	1	2.811	0.002	2.392	3.710	0.006	1.041	0.011	0.023	0.015	10.011
Chlorite C1	WDD9-128	53.3B	2	2	2.777	0.000	2.393	3.666	0.013	1.161	0.010	0.007	0.006	10.032
Chlorite C1	WDD9-128	53.3B	2	3	2.790	0.001	2.420	3.523	0.000	1.257	0.005	0.004	0.001	10.002
Chlorite C1	WDD9-128	53.3B	2	4	2.836	0.000	2.380	3.569	0.003	1.173	0.007	0.007	0.006	9.981
Chlorite C1	WDD9-128	53.3B	2	5	2.795	0.002	2.352	3.896	0.017	0.958	0.005	0.000	0.006	10.031
Chlorite C1	WDD9-128	92.3C	1	1	2.733	0.000	2.570	3.570	0.007	1.088	0.005	0.011	0.006	9.990
Chlorite C1	WDD9-128	92.3C	1	2	2.914	0.000	2.635	2.946	0.009	1.177	0.006	0.024	0.139	9.850
Chlorite C1	WDD9-128	92.3C	1	3	2.718	0.000	2.480	3.711	0.007	1.125	0.000	0.002	0.000	10.043
Chlorite C1	WDD9-128	92.3C	1	4	2.738	0.004	2.619	3.541	0.016	0.995	0.008	0.004	0.048	9.974
Chlorite C1	WDD9-128	92.3C	1	5	2.729	0.000	2.563	3.567	0.003	1.119	0.006	0.002	0.004	9.993
Chlorite C1	WDD9-128	92.3C	1	6	2.806	0.000	2.575	3.378	0.007	1.097	0.006	0.019	0.056	9.944
Chlorite C1	WDD9-128	92.3C	1	7	2.801	0.001	2.490	3.143	0.002	1.501	0.005	0.017	0.003	9.962
Chlorite C1	WDD9-128	92.3C	1	8	2.692	0.002	2.678	3.483	0.010	1.086	0.000	0.019	0.014	9.984
Chlorite C1	WDD9-128	92.3C	1	9	2.739	0.001	2.556	3.568	0.020	1.087	0.002	0.000	0.017	9.990
Chlorite C1	WDD9-128	92.3C	1	10	2.697	0.000	2.521	3.621	0.000	1.191	0.004	0.013	0.003	10.050
Chlorite C1	WDD9-128	92.3C	2	4	2.790	0.000	2.440	3.268	0.005	1.459	0.012	0.009	0.023	10.006
Chlorite C1	WDD9-128	92.3C	2	5	2.786	0.000	2.540	3.266	0.021	1.285	0.012	0.020	0.049	9.979
Chlorite C1	WDD9-128	92.3C	2	6	2.820	0.000	2.423	3.011	0.010	1.682	0.003	0.002	0.035	9.987
Chlorite C1	WDD9-128	92.3C	2	7	2.700	0.001	2.492	3.396	0.000	1.452	0.010	0.004	0.003	10.057
Chlorite C1	WDD9-128	92.3C	2	8	2.729	0.002	2.484	3.618	0.008	1.167	0.010	0.018	0.003	10.038
Chlorite C1	WDD9-128	92.3C	2	9	2.696	0.000	2.478	3.667	0.006	1.191	0.012	0.028	0.003	10.081

Analysed mineral	Drillhole #	Depth (m)	Circle #	Analysis #	Si (apfu)	Ti (apfu)	Al (apfu)	Fe^{2+} (apfu)	Mn (apfu)	Mg (apfu)	Ca (apfu)	Na (apfu)	K (apfu)	Total (apfu)
Chlorite C1	WDD9-128	92.3C	3	6	2.722	0.000	2.597	3.448	0.000	1.206	0.004	0.000	0.003	9.981
Chlorite C1	WDD9-128	92.3C	3	7	2.716	0.000	2.463	3.668	0.003	1.195	0.000	0.009	0.006	10.059
Chlorite C1	WDD9-128	92.3C	3	8	2.814	0.001	2.432	2.748	0.011	1.940	0.009	0.019	0.010	9.984
Chlorite C1	WDD9-128	92.3C	3	9	2.786	0.000	2.442	3.373	0.002	1.378	0.005	0.002	0.010	9.999
Chlorite C1	WDD9-128	92.3C	4	2	2.682	0.002	2.642	3.535	0.007	1.118	0.004	0.009	0.003	10.001
Chlorite C1	WDD9-128	92.3C	4	3	2.716	0.002	2.544	3.557	0.011	1.167	0.004	0.013	0.006	10.020
Chlorite C1	WDD9-128	92.3C	4	4	2.695	0.002	2.555	3.559	0.013	1.197	0.004	0.002	0.001	10.028
Chlorite C1	WDD9-128	92.3C	4	5	2.743	0.000	2.596	3.422	0.009	1.187	0.000	0.000	0.006	9.962
Chlorite C1	WDD9-128	92.3C	4	7	2.726	0.000	2.569	3.279	0.009	1.394	0.005	0.004	0.011	9.997
Chlorite C1	WDD9-128	92.3C	4	8	2.773	0.001	2.479	2.896	0.007	1.809	0.011	0.013	0.010	9.998
Chlorite C1	WDD9-128	92.3C	4	9	2.911	0.002	2.535	2.885	0.000	1.419	0.010	0.037	0.079	9.879

Chapter 4. Halogens (Cl, Br, I) and noble gases (Ar, Kr, Xe) in fluid inclusions from the Alligator Rivers Uranium Field and the Westmoreland area (Australia)

Preamble

The previous chapters highlighted differences between unconformity-related uranium deposits in the ARUF and uranium deposits in the Westmoreland area in terms of age, temperature, trace elements in uraninite and mineralising styles. However, similarities in terms of salinity and homogenisation temperature from fluid inclusions are summarised in the introduction. Noble gases and halogens are a powerful tool to get more information on the origin of the fluids and their interaction with the basement or organic matter. This chapter presents a comparison between the two U-rich zones of the McArthur Basin, and with a study in a similar context in the Athabasca Basin (Canada), showing that the brines from evaporated seawater and the low-salinity fluids of meteoric origin play a role in the area.

Préambule

Les chapitres précédents ont montré des différences entre les gisements d'uranium de type discordance au nord et ceux de la zone de Westmorland au sud en terme d'âge, de température, de cortèges d'éléments traces dans les uraninites et de styles de minéralisations, mais des ressemblances en terme de fluides sont mises en évidence dans l'introduction. Pour étudier plus en détails les fluides, l'étude des gaz rares et des halogènes permet d'obtenir des informations cruciales sur leur origine et l'intensité de leur interaction avec le socle ou la matière organique. Ce chapitre présente une comparaison entre les deux zones uranifères du bassin de McArthur, ainsi qu'avec une étude réalisée dans un contexte similaire dans le bassin d'Athabasca (Canada), et montre que les saumures sont probablement issues de l'évaporation de l'eau de mer et qui les fluides peu salés sont d'origine météorique.

4.1. Geological setting and sampling

The studied samples are from the Paleo- to Mesoproterozoic McArthur Basin, located mostly in the Northern Territory and for a smaller part in Queensland (Australia), or from its basement (Pine Creek Orogen). Close to the unconformity between the basement and the basin, numerous uranium deposits or prospects occur and some of them are the focus of this study (Figure 4-1). The basement and the basin are described in the previous chapters.

4.1.1. Uranium occurrences

Most of the known major uranium deposits in the Alligator Rivers Uranium Field (ARUF) are hosted by pre-McArthur Basin metasedimentary basement rocks (Figure 4-2) and the main deposits are Ranger, Jabiluka, Nabarlek, and Koongarra.

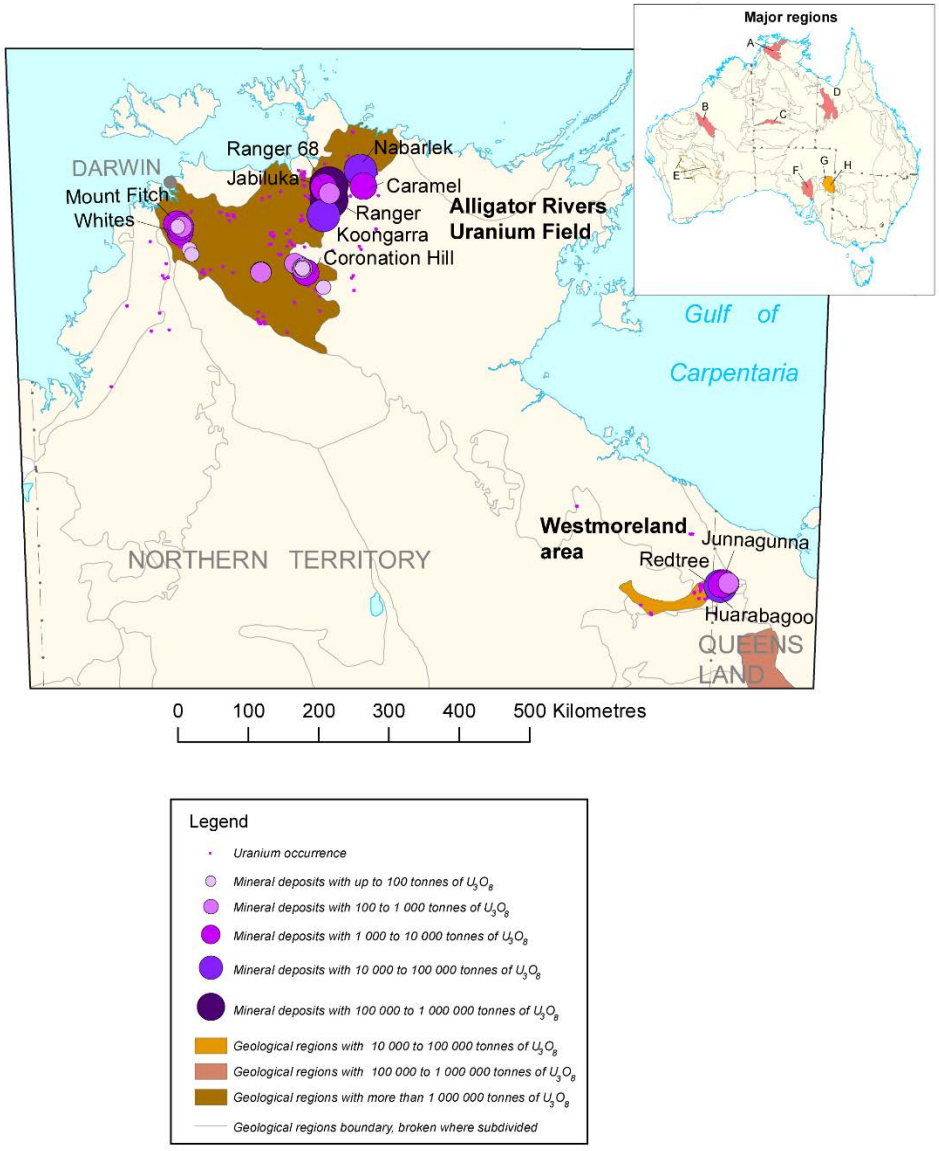

***Figure 4-1**: Location, grade of the uranium deposits or prospects and uranium-rich regions in the McArthur Basin and its basement (McKay et al., 2010).*

The Ranger deposit is one of the world's largest uranium deposits with resources estimated at 155.17 Mt of ore grading 0.09% U_3O_8 with past production of 49 194 t U_3O_8 from the Ranger 1 No 3 ore body (ERA, 2011) and 60 961t of U_3O_8 from the Ranger 1 No 1 ore body (Lally and Bajwah, 2006). It is described in more details in Chapter 2. The Caramal prospect is from unconformity-related type and the estimated resources are 0.944 Mt at 0.31% U_3O_8 (Alligator Energy, 2012) with primary uranium mineralisation occurring within an elongate zone, about 80 m wide in plan view. Mineralisation is hosted in altered metasedimentary schist and

carbonate rocks. The alteration is expressed by the replacement of biotite by chlorite and feldspar by sericite, identical to the 'outer alteration halo' described from other deposits of the East Alligator River region (McKay and Miezitis, 2001). Anomaly U-65 was studied by Derome et al. (2003). However, these authors did not observed U-mineralisation.

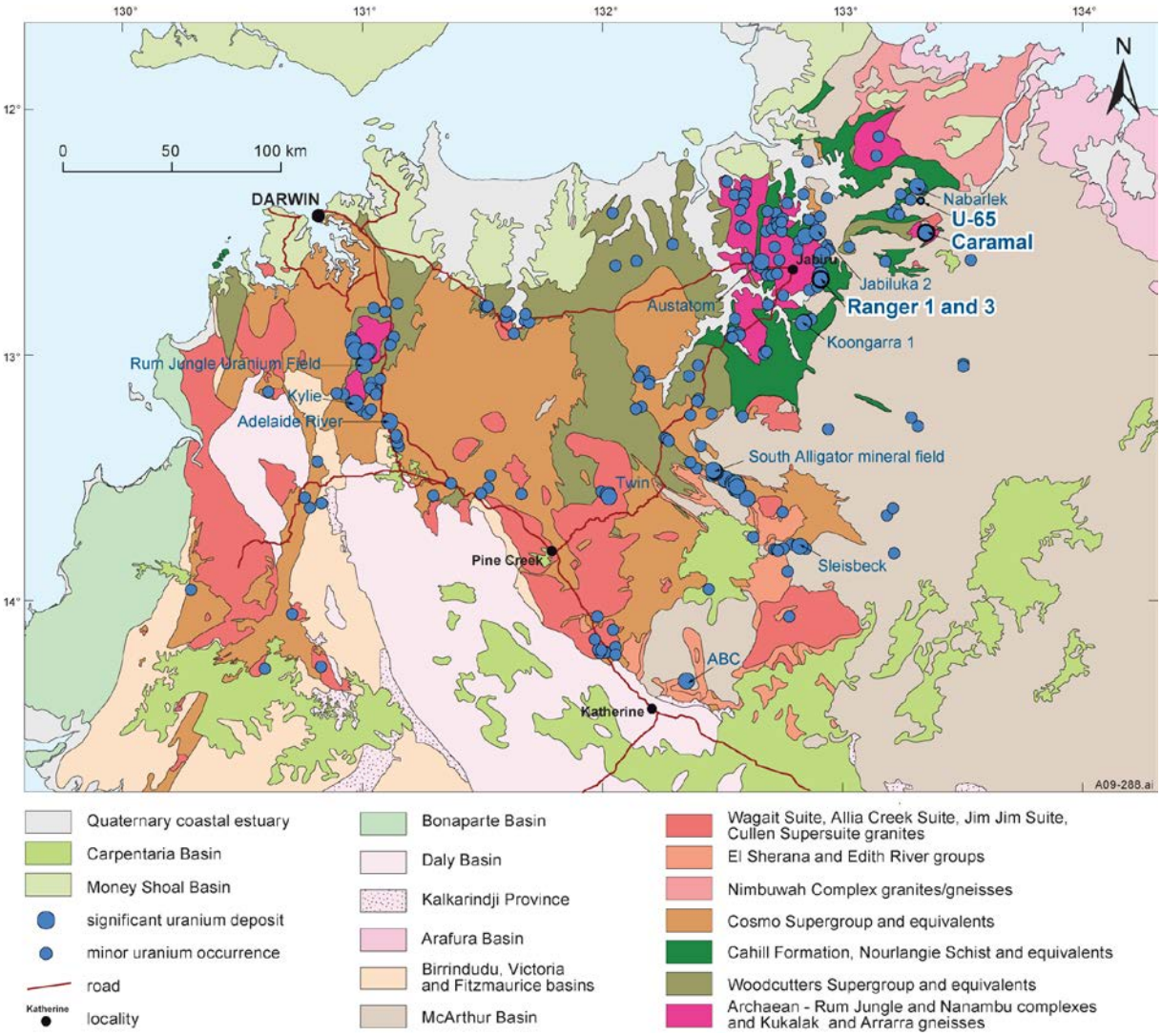

***Figure 4-2**: Schematic geological map of the Alligator Rivers Uranium Field, Northern Territory, Australia, where the Ranger and Caramal deposits and the U-65 location are represented. After Ahmad and Munson (2013).*

Small uranium-gold deposits are located in the Westmoreland Area, in the southern part of the McArthur Basin (Northern Territory and Queensland). Almost all of the occurrences are in the Westmoreland Conglomerate, the Seigal Volcanics, and in adjacent, unconformably underlying older rocks (Cliffdale Volcanics, Figure 4-3, Ahmad and Munson, 2013).

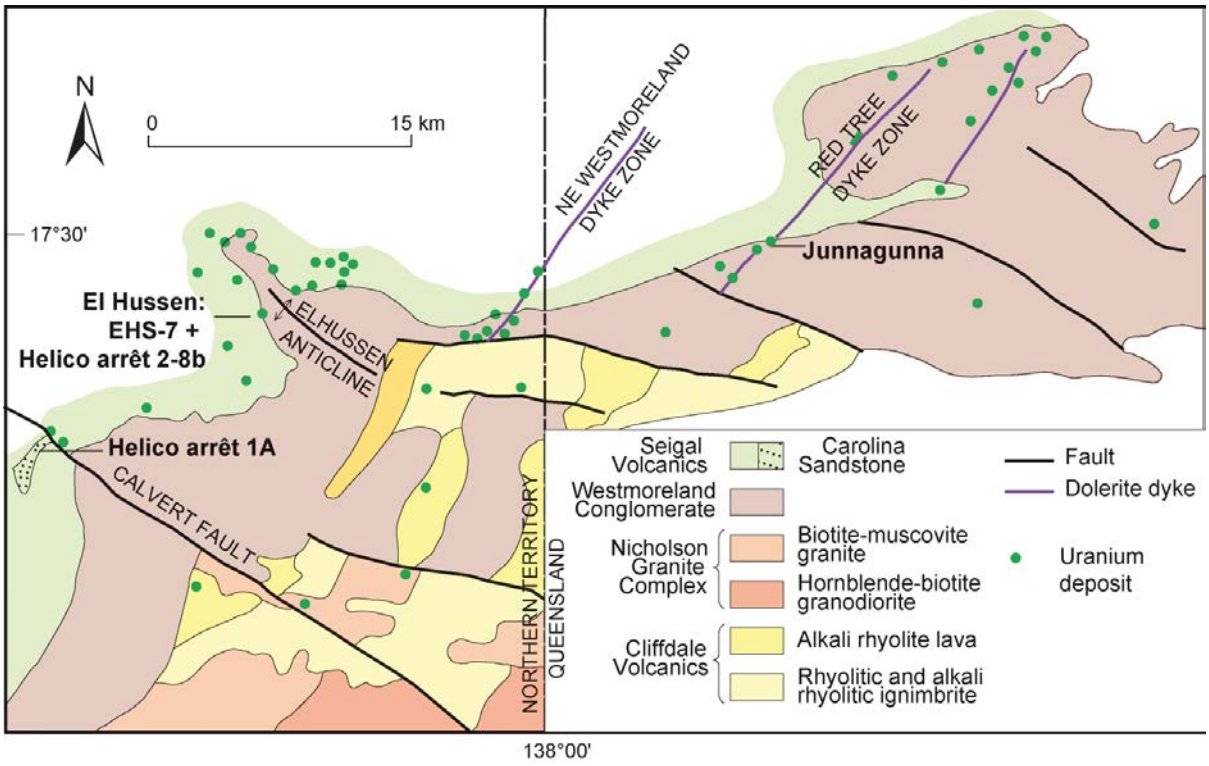

Figure 4-3: *Schematic geological map of the Westmoreland area, Northern Territory and Queensland, Australia. Simplified after Ahmad and Munson (2013).*

At the Junnagunna and Redtree deposits, uranium mineralisation occurs as sub-horizontal and sub-vertical lenses in the Westmoreland Conglomerate, adjacent to highly altered, generally subvertical dolerite dykes that may also be mineralised. Mineralisation is associated with three major northeast-trending lineaments, among them the Redtree and El Nashfa dyke zones containing the largest known uranium resources in the region. The Redtree dyke zone extends over a strike of 20 km, and hosts the Redtree (inferred resources: 10.2 Mt at 0.126% U_3O_8) and Junnagunna (inferred resources: 5400 t at 0.098% U_3O_8) prospects (Rheinberger et al., 1998). Uranium minerals are either interstitial to sand grains or occur as fracture coatings in sandstone and within haematite-quartz veins in dolerite. Mineralisation within the dyke zones is associated with a proximal alteration assemblage of quartz-sericite ± kaolinite in sandstone, and haematite-quartz in dolerite. Mineralisation distal to dyke zones is associated with chlorite and minor haematite alteration (Ahmad and Wygralak, 1989; Rheinberger et al., 1998). El Hussen prospect lies at the conformable contact between the Westmoreland Conglomerate and the Cliffdale or Seigal Volcanics. The overlying volcanics, Westmoreland Conglomerate, or both units may be mineralised adjacent to the contact. Mineralisation is seldom more than a few metres in width and only small-scale mining has taken place (Ahmad and Munson, 2013).

4.1.2. Sampling for the current study

Seven samples from the ARUF were selected for the current study (Table 4-1), that have already been studied or that are from the same generation than studied samples. In details, five are from Ranger (drillhole S3PD730 at 465.1m, 522.2m, and 628.9m depth; drillhole S3PD759 at 334.5m and 434m depth), one from Caramal (CA001 from Derome et al., 2007) and one from Ano U-65 (at 54.3m depth, Derome et al., 2003). The sample S3PD730 628.9m was sampled for its quartz and its carbonate as they occur in the same vein. For the Westmoreland area, two samples are from drillcores, and two samples are grab samples named Helico Arret 1A and Helico 2-8b. One sample is from the Junnagunna/Redtree area (drillhole JDD08-003 at 132.1m depth), two are from El Hussen deposit (drillhole EHS-6 at 119.3m depth and Helico 2-8b), and the sample named Helico Arret 1A is located in the Carolina Sandstone Member, which is a up to 20m thick sandstone interbed within the Seigal Volcanics (Ahmad and Wygralak, 1989). All samples are replaced in the paragenesis of Skirrow et al. (2016) for the Ranger deposit, Derome et al. (2003) for Ano U-65, Derome et al. (2007) for Caramal and Gigon et al., (in prep.) and Polito et al. (2005a) for the sample from Junnagunna/Redtree deposits. Samples from the El Hussen deposit and Helico arret1 are not from described deposits or areas.

The samples were selected from varying depths into the basement and the basin lithologies. Despite the close spatial association of the selected samples with mineralisation, none of the selected samples contain UO_2 ore within the hand-specimen sized section available from drill core. Barren samples were specifically selected to avoid possible artefacts related to post-entrapment production of nucleogenic noble gases modifying the fluid inclusions ^{36}Ar concentration.

Drillcore / Sample	Depth (m)	Deposit	Description	Link to mineralisation
S3PD730	465.1	Ranger	Quartz cementing breccia	Q3 from Skirrow et al. (2016)
S3PD730	522.2	Ranger	Late quartz vein with successive crystallisation generation	Later than Q3 from Skirrow et al. (2016)
S3PD730	628.9	Ranger	Coarse quartz-carbonate-pyrite vein	Later than Q3 from Skirrow et al. (2016)
S3PD759	334.5	Ranger	Quartz-chlorite-pyrite assemblage	Q2 from Skirrow et al. (2016)
S3PD759	434	Ranger	Quartz cementing breccia on metamorphosed clasts	Q3 from Skirrow et al. (2016)
CA001		Caramal	Late quartz	Q3 from Derome et al. (2007)
Ano U-65	54.3	Anomaly U-65	Two different generations, a first drusy one cementing breccia and a second late quartz	Q3 and Q4 from Derome et al. (2003)
EHS-6	119.3	El Hussen	Quartz vein	No information; probably late
Helico 2-8b		El Hussen	Quartz vein in sandstone	No information; probably late
JDD08-003	132.1	Junnagunna/ Redtree	Quartz cementing breccia	Q3 or late from Gigon et al. (in prep.)
Helico Arret1		-	Quartz cementing brecciated sandstone	No information; probably late

***Table 4-1**: Summary of the characteristics of the samples studied for noble gas and halogens in the McArthur basin or its basement.*

4.2. Methods

Thick sections were prepared and the different quartz overgrowths or fluids inclusions plans are currently analysed by microthermometry to get the ice melting temperature (Tm_{ice}) and the homogenisation temperature of the different assemblages. Based on the Tm_{ice}, the salinity of the fluids, and its equivalent Cl concentration are estimated. As an example, Figure 4-4 presents the thick section for sample Ano U-65 with the different quartz overgrowths visible in the thick section, on which two specific fluid inclusions plans are reported. When zooming at fluid inclusion scale, the plans contain both fluid inclusions with two phases, a liquid and a gaseous phase occupying 5–20% of the fluid inclusion. No daughter mineral was observed and the inclusions with various salinity present the same type on liquid-vapour ratios.

The halogens (Cl, Br, I), Ca, K and U were measured simultaneously with the naturally occurring noble gas isotopes of Ar, Kr and Xe using the noble gas method which is described in details by Kendrick (2012), Böhlke and Irwin (1992a) and Johnson et al. (2000). Fluid inclusion bearing quartz and carbonate samples of 30–110 mg were irradiated for 45 h in the central facility of the McClellan Research Reactor at UC Davis, California (irradiation designated RS#5 on the 23rd January 2018), to produce noble gas proxy isotopes ($^{38}Ar_{Cl}$, $^{80}Kr_{Br}$, $^{128}Xe_{I}$, $^{37}Ar_{Ca}$, $^{39}Ar_{K}$ and $^{134}Xe_{U}$) that are measured by noble gas mass spectrometry (Kendrick, 2012).The irradiated samples were loaded into modified Nupro® valves, baked under ultra-high vacuum at ~100 °C for 24–48 h to remove loosely adsorbed noble gases, and then analysed by in vacuum crushing. Short crushing experiments in Nupro® valves release naturally occurring and neutron-produced noble gas isotopes from fluid inclusions and contributions from the mineral matrix are negligible (Kendrick and Phillips, 2009). Each sample was analysed by multiple crushes, enabling compositional variations resulting from fluid inclusion heterogeneity to be assessed. The noble gas isotopes released by *in vacuo* crushing were purified by standard gettering procedures over a period of 20 min and measured in peak jumping mode on the MAP-215-50 noble gas mass spectrometer at the Australian National University. The isotopes of Ar where measured on a Faraday detector whereas the less abundant isotopes of Kr and Xe were measured on the more sensitive electron multiplier detector (Kendrick, 2012). Ratios of Cl to Br, I, Ca, K and U are obtained from the measured noble gas proxy isotopes and production ratios ($^{38}Ar_{Cl}$/Cl, $^{80}Kr_{Br}$/Br, $^{128}Xe_{I}$/I, $^{37}Ar_{Ca}$/Ca and $^{39}Ar_{K}$/K) monitored with the Hb_3Gr ^{40}Ar–^{39}Ar flux monitor and three scapolite standards (Kendrick, 2012; Kendrick et al., 2013). Standard corrections were made for Ar interference reactions based on K-glass and CaF_2 monitors and U-derived ^{84}Kr (Kendrick, 2012).

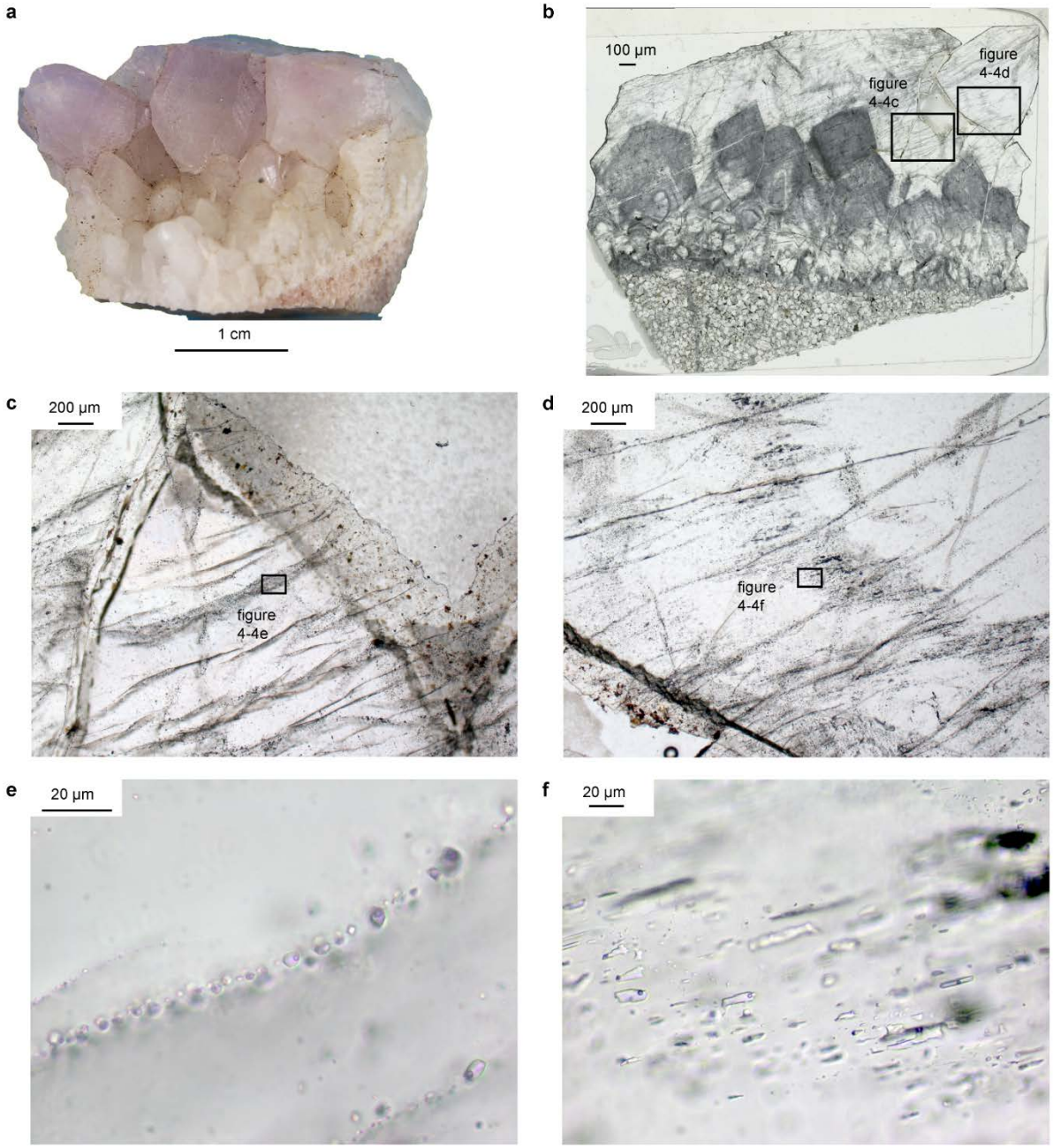

***Figure 4-4**: Example of material analysed for noble gas and halogens analyses: **a**: hand sample; **b**: associated thick section studied for noble gas and halogens; **c**: fluid inclusions plan with low salinities corresponding to Tm_{ice} between -4.1 and -5.9 °C; **d**: fluid inclusions plan with high salinities corresponding to Tm_{ice} between -25.3 and -29.7 °C; **e**: zoom on the low salinities fluid inclusions; **f**: zoom on the high salinities fluid inclusions. Sample Ano U-65.*

The noble gas method provides ppm detection limits for Cl and ppb detection limits for Br and I, and machine blanks for samples crushed in modified Nupro® valves are negligible typically accounting for <<1% of sample gas. Br/Cl and I/Cl ratio measurements have a long term repeatability of ~3% for Br/Cl and ~5% for I/Cl (1σ; see Kendrick, 2012 and Kendrick et al., 2013). The precision of the K/Cl, Ca/Cl and U/Cl measurements are more variable and were limited by the low abundance of the noble gas proxy isotopes ($^{39}Ar_K$, $^{37}Ar_{Ca}$ and $^{134}Xe_U$)

available for analysis in several of the current samples. The U measurements based on the $^{134}Xe_U$ proxy isotope are based on a ^{134}XeU/U production ratio calculated from the monitored neutron fluence and U cross section, and were not monitored directly. This means that real differences in the U concentration can be precisely monitored, but the absolute U values could be systematically over- or under-estimated by up to ~20% in all the samples. Fluid inclusion ^{36}Ar, ^{40}Ar and U concentrations have been calculated from the measured ratios (X/Cl). Finally, post entrapment modification of fluid inclusion Ar-isotope signatures are considered to be a minor artefact in this study. Firstly, the low K content of the samples means that despite the samples great age of 1.6 Ga (see introduction), post-entrapment production of radiogenic $^{40}Ar_R$ is negligible, necessitating a correction of less than 5% for the majority of samples. Secondly, we present data for samples situated >1 m from U ore, which minimises the possible influence of post-entrapment nucleogenic reactions modifying fluid inclusion ^{36}Ar concentrations, because neutrons have an attenuation distance of ~1 m in silicate rocks (Ballentine and Burnard, 2002; Hu et al., 2009).

4.3. Results

Microthermometry analyses are still running, but the first observations are consistent with what is summarised in the introduction, with large range of salinities depending on the fluid inclusions plans observed. In general, in quartz and in the carbonate from the sample S3PD730 628.9m the parameters are identical.

The halogen and noble gas results obtained by *in vacuo* crushing of quartz and carbonate hosted fluid inclusions are summarised in Table 4-2. Quartz and carbonate hosted fluid inclusions extracted by *in vacuo* crushing have molar Br/Cl values between (4.15 ± 0.04) × 10^{-3} and (9.60 ± 1) × 10^{-3}, and I/Cl values between (2.55 ± 0.2) × 10^{-6} and (40.3 ± 5.3) × 10^{-6} (Figure 4-5).

Deposit	Sample name	Sample weight (mg)	Extraction	Br/Cl ($\times 10^{-3}$)	±	I/Cl ($\times 10^{-6}$)	±	K/Cl	±	Ca/Cl	±	U/Cl	$^{40}Ar/^{36}Ar$ (1.6 Ga)	±	$F(^{84}Kr/^{36}Ar)_{air}$	±	$F(^{129}Xe/^{36}Ar)_{air}$	±	$Cl/^{36}Ar$ ($\times 10^6$)	±
Ranger	S3PD730-465.1	74.9	crush#1	5.91	0.077	2.70	0.1	0.07	0.006			4.024E-05	516	27	1.14	0.19	2.01	0.18	27.80	1.48
Ranger	S3PD730-465.1	74.9	crush#2	5.85	0.062	2.55	0.2	0.06	0.004				675	35	2.25	0.23	5.53	0.32	48.66	2.52
Ranger	S3PD730-465.1	74.9	crush#3	5.92	0.144	2.55	0.3					9.894E-05	892	212	2.19	0.55	5.84	1.42	70.26	16.76
Ranger	S3PD730-522.2	84.2	crush#1	7.69	0.069	3.50	0.1	0.06	0.003			3.607E-05	753	9	1.31	0.06	1.99	0.03	31.93	0.41
Ranger	S3PD730-522.2	84.2	crush#2	7.73	0.068	4.06	0.4	0.06	0.003	0.09	0.0	1.294E-04	828	13	4.13	0.19	9.79	0.17	39.32	0.63
Ranger	S3PD730-522.2	84.2	crush#3	7.64	0.035	3.09	0.2	0.05	0.005	0.12	0.1	1.158E-04	1076	53	5.30	0.38	13.11	0.74	58.77	2.91
Ranger	S3PD759-334.5	81.9	crush#1	6.85	0.059	5.97	0.3	0.17	0.007			5.780E-04	972	13	5.29	0.27	14.00	0.25	35.76	0.48
Ranger	S3PD759-334.5	81.9	crush#2	6.56	0.042	5.81	0.3	0.14	0.009	0.09	0.1	4.819E-04	1911	85	3.98	0.26	9.82	0.45	72.34	3.24
Ranger	S3PD759-334.5	81.9	crush#3	6.70	0.069	5.47	0.2	0.13	0.007			6.247E-04	1739	39	10.38	0.70	27.78	0.76	67.26	1.49
Ranger	S3PD759-434B	80.5	crush#1	5.70	0.045	2.86	0.4	0.08	0.006	0.20	0.1	4.062E-04	380	3	1.51	0.07	3.51	0.11	8.55	0.08
Ranger	S3PD759-434B	80.5	crush#2	5.26	0.071	5.18	0.3	0.12	0.021			3.340E-04	529	17	0.60	0.05	1.59	0.10	12.55	0.43
Ranger	S3PD759-434B	80.5	crush#3	5.14	0.113	7.03	0.7	0.12	0.036			5.775E-04	1319	96	0.74	0.09	2.46	0.33	16.16	1.22
Ranger	S3PD730-628.9qz	87.6	crush#1	8.24	0.076	3.44	0.4	0.05	0.006			6.494E-05	689	8	1.06	0.09	1.31	0.03	12.06	0.14
Ranger	S3PD730-628.9qz	87.6	crush#2	8.23	0.111	3.56	0.5	0.08	0.006			5.584E-05	695	27	1.08	0.10	1.82	0.22	16.17	0.62
Ranger	S3PD730-628.9qz	87.6	crush#3	7.87	0.089	3.56	0.3	0.05	0.010			3.218E-04	859	61	3.18	0.29	9.84	0.87	16.64	1.17
Ranger	S3PD730-628.9carb	87.6	crush#1	8.24	0.082	3.18	0.4	0.05	0.004	7.88	0.4	7.241E-05	547	7	0.96	0.09	1.32	0.07	11.16	0.14
Helico Stop	helico2-8b	84.9	crush#1	9.60	1.040	40.30	5.3						299	4	0.85	0.05	0.81	0.03	0.59	0.06
Helico Stop	helico2-8b	84.9	crush#2	7.73	0.195	22.46	0.6	0.14	0.042				296	2	0.73	0.03	0.49	0.04	1.44	0.04
Helico Stop	helico2-8b	84.9	crush#3	8.12	0.506	9.96	2.2	0.18	0.076				296	7	0.71	0.04	0.20	0.04	2.01	0.13
Helico Stop	helicoarret-1A	87.3	crush#1	6.98	0.161	32.03	1.6	0.33	0.019				294	2	0.75	0.05	0.93	0.03	1.26	0.03
Helico Stop	helicoarret-1A	87.3	crush#2	8.09	0.191	39.46	1.3	0.24	0.023				297	3	0.65	0.03	0.82	0.02	2.29	0.06
Helico Stop	helicoarret-1A	87.3	crush#3	8.41	0.291	29.67	1.1	0.13	0.042			1.228E-04	306	13	0.58	0.05	0.82	0.10	3.82	0.20
Ano U-65	U65-2-54.3mQ3	78.5	crush#1	6.30	0.049	22.30	0.3	0.04	0.002			1.670E-04	329	2	2.77	0.13	5.84	0.08	16.58	0.11
Ano U-65	U65-2-54.3mQ3	78.5	crush#2	6.25	0.056	27.85	0.3	0.03	0.001				356	8	2.91	0.18	7.29	0.19	23.97	0.49
Ano U-65	U65-2-54.3mQ3	78.5	crush#3	6.41	0.063	31.71	0.6	0.03	0.008			8.141E-05	386	31	2.12	0.25	5.90	0.54	34.61	2.58
Ano U-65	U65-2-54.2mQ4	82.1	crush#1	8.15	0.100	20.33	0.5					8.026E-05	345	21	1.34	0.15	2.52	0.22	15.92	0.89
Ano U-65	U65-2-54.2mQ4	82.1	crush#2	8.20	0.094	20.49	0.3	0.01	0.005				359	13	2.45	0.16	5.53	0.29	26.36	0.90
Ano U-65	U65-2-54.2mQ4	82.1	crush#3	7.83	0.076	26.12	0.3	0.04	0.003			7.891E-05	440	33	2.66	0.31	7.34	0.68	42.21	3.01
Caramal	CA001	82.8	crush#1	5.90	0.099	8.79	0.3	0.04	0.014			6.128E-05	322	25	1.22	0.16	2.20	0.30	13.92	1.01
Caramal	CA001	82.8	crush#2	5.91	0.087	7.07	0.4	0.15	0.007	11.4	0.6				1.08	0.26	2.67	0.44	19.48	1.84
Caramal	CA001	82.8	crush#3	6.54	0.155	11.24	0.5	0.19	0.029			1.017E-04	308	108	2.24	0.94	7.08	2.46	32.03	10.01
Junnagunna	JDD08-003-132.1m	67.1	crush#1	4.15	0.037	13.21	0.3	0.08	0.012	1.09	0.8	1.453E-04	369	28	2.40	0.26	6.62	0.62	22.65	1.58
Junnagunna	JDD08-003-132.1m	67.1	crush#2	4.27	0.071	10.80	0.3	0.07	0.014	1.16	0.2	6.323E-05	435	71	2.11	0.51	6.69	1.17	45.02	6.86
Junnagunna	JDD08-003-132.1m	67.1	crush#3	4.52	0.148	11.27	0.7			3.05	2.1		836	937	4.21	5.18	14.93	16.83	106.57	117.33
El Husein	EH5-6-119.3	80.3	crush#1	6.72	0.210	5.55	0.7						310	46	1.01	0.28	2.37	0.51	19.30	2.60
El Husein	EH5-6-119.3	80.3	crush#2	6.85	0.115	6.32	0.7	0.09	0.021			5.333E-05	352	54	1.25	0.33	2.13	0.60	24.73	3.45
El Husein	EH5-6-119.3	80.3	crush#3	6.94	0.220	4.19	0.4	0.14	0.031				337	174	0.78	0.96	0.92	1.66	39.28	18.29

***Table 4-2**: Summary of fluid inclusion noble gas, halogen and cation data for quartz and dolomite samples in uranium deposits and prospects (Pine Creek Orogen and McArthur Basin Basin), determined by in vacuo crushing. All ratios are molar. Fluid inclusion $F(^{84}Kr/^{36}Ar)_{air}$ versus $F(^{129}Xe/^{36}Ar)_{air}$ are defined as $F(X/^{36}Ar)_{air} = (X/^{36}Ar)sample/(X/^{36}Ar)_{air}$; reference values for air from Ozima and Podosek (2002).*

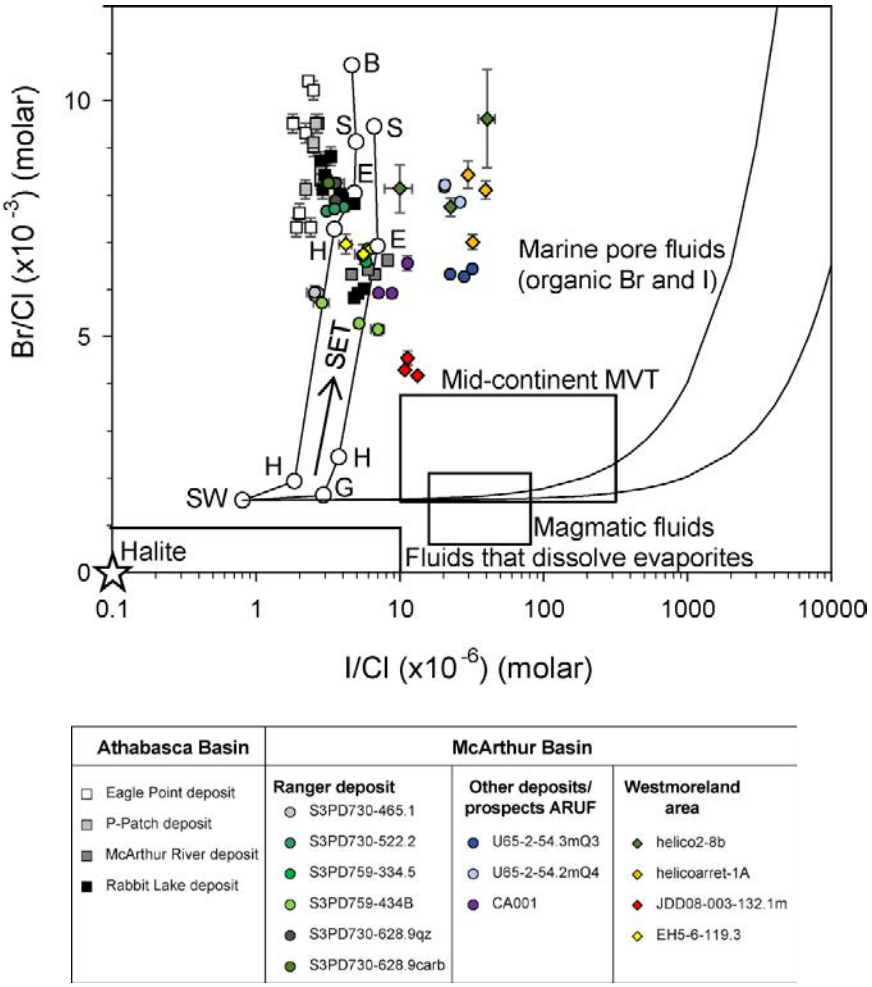

***Figure 4-5**: Fluid inclusion Br/Cl versus I/Cl molar ratios determined by in vacuo crushing in sample from the Athabasca Basin (Richard et al., 2014) and from this study. The composition of the seawater evaporation trajectory (SET); halite; fluids that dissolve evaporites; marine pore fluids; mid-continent MVT and magmatic fluids are based on Banks et al. (2000), Böhlke and Irwin (1992b), Fehn et al. (2005), Holser (1979), Kendrick et al. (2011, 2002a, 2002b, 2001), Muramatsu et al. (2007) and Zherebtsova and Volkova (1966); the complete list of references for all fields are given in Kendrick and Burnard (2013). Marine pore fluids are characterised by organic Br and I. Assuming an initial seawater Br/Cl value, most marine pore fluids acquire organic Br and I in a ratio of 0.5–2.5 (Kendrick et al., 2011).*

The fluid inclusion Cl/^{36}Ar values vary between (0.59 ± 0.06) × 10^6 and (72.34 ± 3.2) × 10^6 and ^{40}Ar/^{36}Ar$_{1.6Ga}$ between (294 ± 2) and (1911 ± 85). For every sample, repeat crushing analyses show a positive correlation between the two parameters, where the fluid inclusions with the highest salinity also have the highest ^{40}Ar/^{36}Ar values (Figure 4-6a). Some of the mixing lines converges on an end-member with low Cl/^{36}Ar and ^{40}Ar/^{36}Ar close to the modern atmospheric value of 296, but for other samples the end-member is clearly distinct from this value (Figure 4-6b).

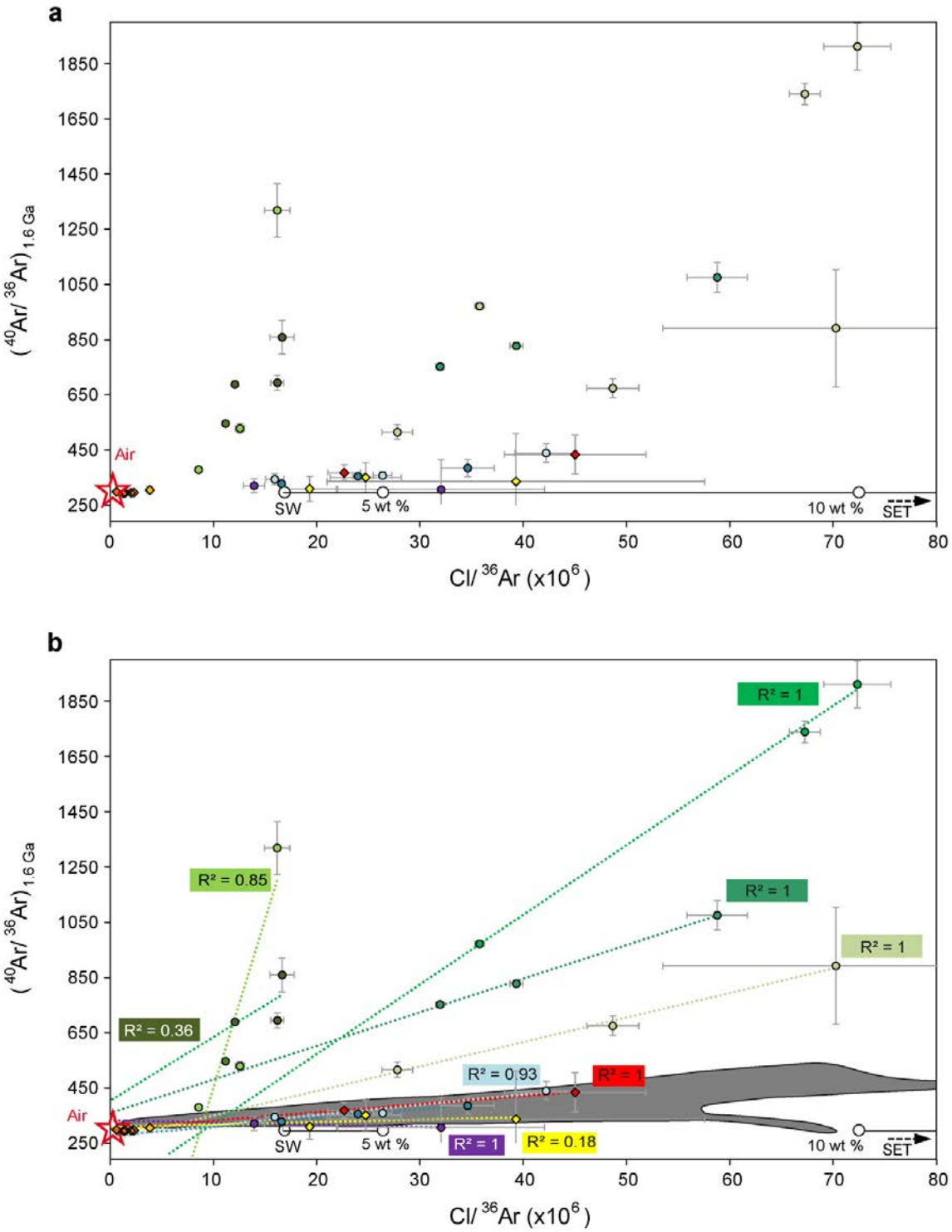

***Figure 4-6**: Fluid inclusion $Cl/^{36}Ar$ versus age-corrected (1.6 Ga) $^{40}Ar/^{36}Ar$ determined by in vacuo crushing. SW: seawater. SET: Seawater evaporation trajectory with salinity of evaporated seawater indicated in wt% salts (after Smith and Kennedy, 1983). **a**: All analyses for this study; **b**: regression lines of most of the samples. Note that the majority have coefficient close to 1. See Figure 4-5 for the legend.*

$F(^{84}Kr/^{36}Ar)_{air}$ values vary from 0.58 ± 0.05 to 10.38 ± 0.7, and $F(^{129}Xe/^{36}Ar)_{air}$ from 0.2 ± 0.04 to 27.78 ± 0.76. The results can be divided in three groups: the first one ("depleted") is depleted in ^{84}Kr and ^{129}Xe relative to ^{36}Ar compared to Air and air saturated meteoric water (ASMW), air saturated seawater (ASSW) and air saturated evaporated seawater or bittern brine (BB) from (Ozima and Podosek, 2002), the second one is consistent ("consistent") with these values and the third one is enriched ("enriched") in ^{84}Kr and ^{129}Xe relative to ^{36}Ar (Figure 4-7). The samples from Ranger are either in the consistent or the enriched group. Samples from the two Helico sampled are in the depleted group, the sample from the Redtree/Junnagunna deposit and some of the data from Ano U-65 and Caramal are in the enriched group.

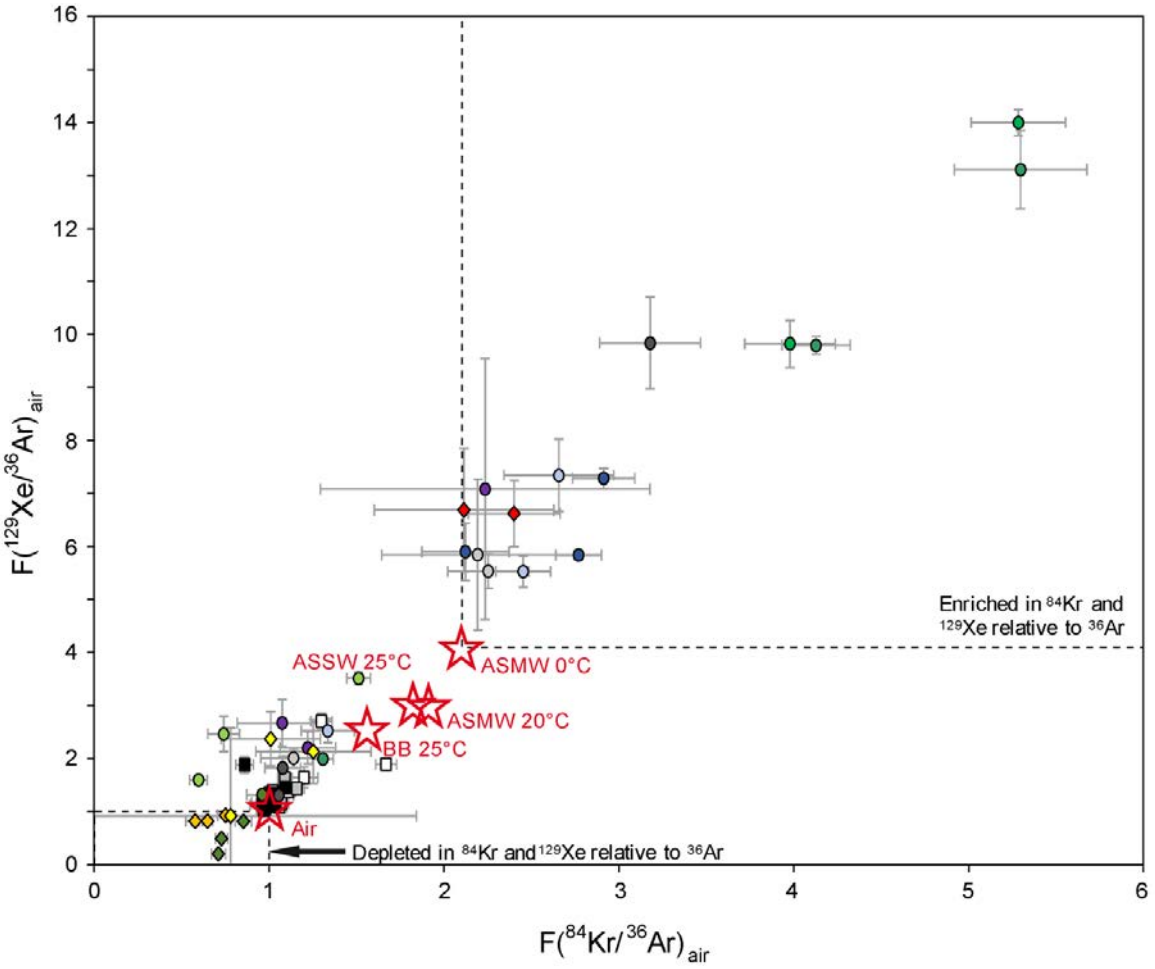

***Figure 4-7**: Fluid inclusion $F(^{84}Kr/^{36}Ar)_{air}$ versus $F(^{129}Xe/^{36}Ar)_{air}$ determined by in vacuo crushing. The fractionation values are defined as $F(X/^{36}Ar)_{air} = (X/^{36}Ar)_{sample}/(X/^{36}Ar)_{air}$. Reference values for Air and air saturated meteoric water (ASMW), air saturated seawater (ASSW) and air saturated evaporated seawater or bittern brine (BB) from (Ozima and Podosek, 2002). See Figure 4-5 for the legend.*

The *in vacuo* crushing data show fluid inclusion U/Cl values vary from 3.6×10^{-5} to 6.2×10^{-4} (Figure 4-8). Microthermometry has not been performed yet on all samples, but a range of U concentration can be estimated. Based on very low salinities fluid inclusions, the fluid inclusions are therefore indicated to contain between 0 and 3 ppm U, and when taking high-salinities brines with a salinity of 30 wt% U concentration in the brines range between 44 and 763 ppm. The value of 763 ppm is therefore the maximum U concentration, but it can be assumed that the concentration is around a few hundred ppm of U, which can be compared to the 3–170 ppm U obtained by Richard et al. (2014) for Canadian deposits.

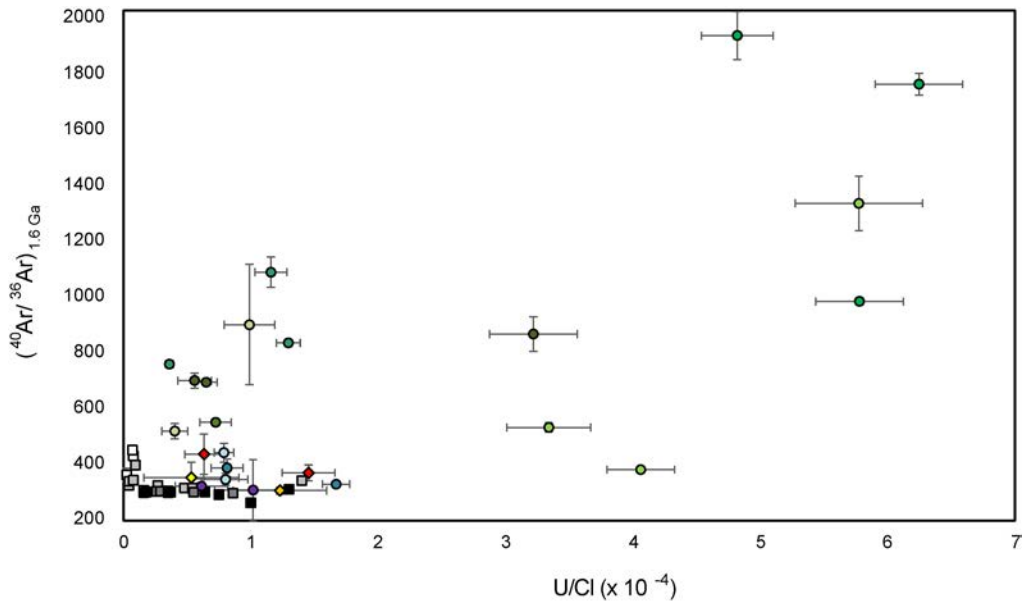

Figure 4-8: *Fluid inclusion U/Cl molar ratio versus age-corrected (1.6 Ga) $^{40}Ar/^{36}Ar$. See Figure 4-5 for the legend.*

A combined figure of fluid inclusion age-corrected (1.6 Ga) $^{40}Ar/^{36}Ar$ versus $F(^{129}Xe/^{36}Ar)_{air}$ is also plotted (Figure 4-9).

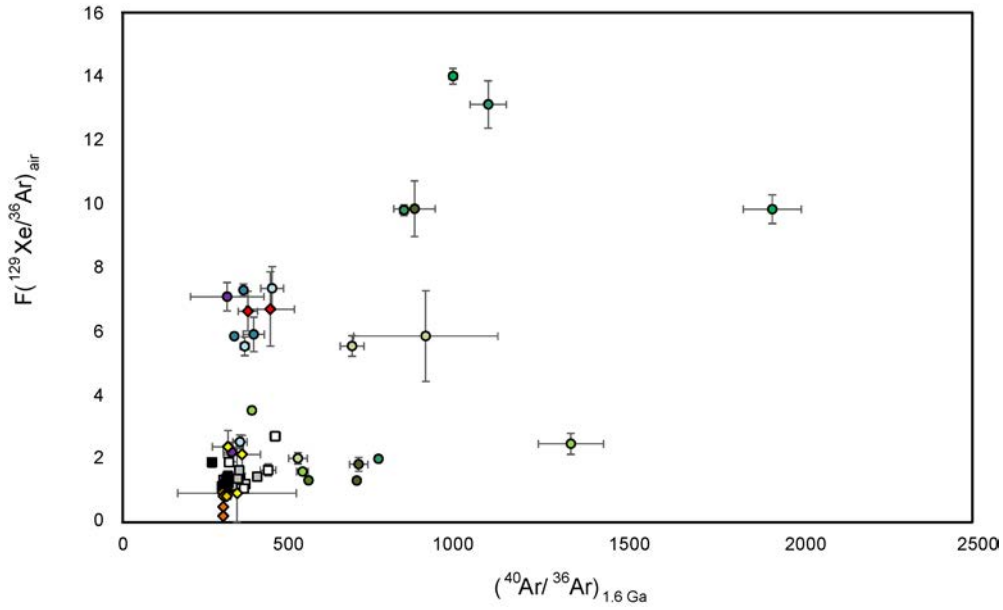

***Figure 4-9**: Fluid inclusion age-corrected (1.6 Ga) $^{40}Ar/^{36}Ar$ versus $F(^{129}Xe/^{36}Ar)_{air}$. See Figure 4-5 for the legend.*

4.4. Discussion and conclusions

As almost all data lie on the SET trends, the dominant source of halogens is seawater (Figure 4-5). Most of the analyses are beyond the halite saturation points. However, the preliminary fluid inclusions data and the known microthermometry data presented in the introduction suggest that the salinities range from 0 to 35 wt% eq $_{NaCl}$. Therefore, brines dilution is probably needed to explain the observed salinities. The low I/Cl values of most of the U-related fluids indicate very little interaction with organic-rich sediments or hydrocarbons, comparable with data from the Athabasca Basin (Richard et al., 2014). The only exceptions are data from the Junnagunna/Redtree area, the two Helico samples and Ano U-65 acquired in this study that have slightly higher I/Cl ratios. This can be due to a slightly higher interaction with organic-rich sediments or hydrocarbons.

Lines in the $Cl/^{36}Ar$ versus age-corrected (1.6 Ga) $^{40}Ar/^{36}Ar$ diagram (Figure 4-6) can be interpreted as contamination by the atmosphere during the processing of the samples, or as the contribution of two fluids: a low-salinity fluid and a brine, with variable fluid inclusions trapped in the samples and analysed. A low salinity fluid has small Cl content, and therefore a $Cl/^{36}Ar$ ratio close to 0. An atmospheric-component would move all data points in Figure 4-6 variable distances towards the point (0; 296) corresponding to the actual value for air. Here, the regression lines equations are specific for every sample and some of them do not converge to the modern atmospheric end-member, meaning that the contribution of two fluids is the favoured explanation. The presence of fluids with different salinities is known from the literature

(e.g. Derome et al., 2007, 2003; Mernagh and Wygralak, 2011) and from the first microthermometry data obtained for this study, and it can be proposed that in a single sample different crushes release fluids from variable salinity depending on the opened fluid inclusions. The low-salinity fluid would have been in equilibrium with the atmosphere, meaning that is correspond potentially to a meteoric fluid. Fluid inclusions from the Ranger deposit contain excess ^{40}Ar compared to what is expected from the Athabasca Basin, where age-corrected (1.6 Ga) $^{40}Ar/^{36}Ar$ were lower than 449 (Richard et al., 2014). Probable source of the excess ^{40}Ar component in the ore fluids is the basement contribution, as in the Athabasca Basin (Richard et al., 2014), a K-rich basin or a particularly old crustal component (basement or basin). ^{40}Ar values in basins are generally lower than in the basement because of the introduction of atmospheric gases in the basins. As the basements of the Athabasca and McArthur basins are from similar age, this is probably not the main factor influencing the high values. However, high $^{40}Ar/^{36}Ar$ values in this study are only reported in basement-hosted inclusions and the dominant source of the excess ^{40}Ar is probably the basement contribution. Strong basement influence during B-Mg metasomatism shortly before uranium main stage (Gigon et al., 2019) could therefore have extended until the later quartz veins develop.

In the $F(^{84}Kr/^{36}Ar)_{air}$ versus $F(^{129}Xe/^{36}Ar)_{air}$ diagram, the data enriched or depleted can reflect boiling, fluids mixing or fractionation between the different elements. No evidences of boiling was observed in the fluid inclusions assemblages. In order to choose between the two other explanations, a $^{40}Ar/^{36}Ar$ vs $F(^{129}Xe/^{36}Ar)_{air}$ graph has been drawn (Figure 4-9) because the $^{40}Ar/^{36}Ar$ ratio reflects sources and is not affected by any physical process (such as diffusion). As no correlation exists in this diagram, mixing could not explain the values obtained in the $F(^{84}Kr/^{36}Ar)_{air}$ versus $F(^{129}Xe/^{36}Ar)_{air}$ diagram. It means that in the analyses enriched and depleted in ^{84}Kr and ^{129}Xe relative to ^{36}Ar compared to Air and air saturated meteoric water (ASMW), air saturated seawater (ASSW) and air saturated evaporated seawater or bittern brine (BB) elements have been fractionated. It can be explain by the tortuosity of the pathways thought which the fluid has moved (Torgersen et al., 2004). As heavy elements such as ^{84}Kr and ^{129}Xe diffuse slower than the light ones (^{36}Ar), they remain in the sediments. Fluid compositions enriched in heavy elements could therefore correspond to fluids that have stayed longer in the rocks they went through, whereas compositions depleted in heavy elements could reflect fluids that have stayed for short time in the rocks. It could be interpreted either in term of fluid flux or of permeability of the host rocks.

The U/Cl ratio is highly variable between the samples, but Cl concentration was not yet obtained by microthermometry, so the high U/Cl ratios could be due either to high U content, or low Cl content. As demonstrated in Figure 4-8, U/Cl and age-corrected (1.6 Ga) $^{40}Ar/^{36}Ar$

are not correlated, even if the fluid inclusions with the highest U grade are also the one with the higher age-corrected (1.6 Ga) $^{40}Ar/^{36}Ar$. This suggests that there is no clear link between uranium leaching and the interaction of the fluid with the basement. The duration of the interaction, the uranium grade in the basement, or a uranium-rich basin can explain this distribution. If it is considered that the salinity is roughly the same in all samples, the fact that fluid inclusions with the highest U grade are also the one with the higher age-corrected (1.6 Ga) $^{40}Ar/^{36}Ar$ could show that the interaction with the basement (high age-corrected (1.6 Ga) $^{40}Ar/^{36}Ar$) could provide part of the uranium stock for the mineralisation.

In conclusion, noble gas and halogens confirm the seawater-derived origin for the fluid linked to uranium mineralisation in the ARUF and in the Westmoreland area, as well a low interaction with organic matter. The input of the basement is seen in some samples, and distinct U/Cl ratios depending on the samples. Further work on fluid inclusions (microthermometry to get the salinity and homogenisation temperature of the different fluid generations, LA-ICP-MS to get the metal content of single inclusions) will allow to better constraint the fluid generations and their salinity. Thanks to the Cl composition in fluid inclusions (and not from the samples) calculated from the salinities, the absolute concentrations in uranium for example can be estimated by the ratios plotted in the diagrams presented here.

Acknowledgments

Energy Resources Australia and in particular Greg Rogers are thanked for support in sampling at the Ranger mine site, and Laramide in the Junnagunna/Redtree area. Mark Kendrick is thanked for all the discussions and explanations that helped the understanding and the interpretation.

Chapter 5. Tracing metal sources for the giant McArthur River Zn-Pb deposit (Australia) using lead isotopes

Accepted in *Geology*

Joséphine Gigon[1]*, Etienne Deloule[2], Julien Mercadier[1], David L. Huston[3], Antonin Richard[1], Irvine R. Annesley[1], Andrew S. Wygralak[4], Roger G. Skirrow[3], Terrence P. Mernagh[5] & Kristian Masterman[6]

[1] Université de Lorraine, CNRS, GeoRessources lab, F-54500 Vandœuvre-lès-Nancy, France

[2] CRPG, UMR 7358 CNRS-UL, 15 rue Notre Dame des Pauvres, F-54501 Vandœuvre-lès-Nancy, France

[3] Geoscience Australia, GPO Box 378, Canberra, ACT 2601, Australia;

[4] Northern Territory Geological Survey, PO Box 2901, Darwin, NT 0801, Australia

[5] Research School of Earth Sciences, Australian National University, Acton, ACT 2601, Australia

[6] Glencore Australia Holdings Pty Ltd, Australia

Preamble

Base metal source(s) for the nowadays observed deposits can be previous sulphides, or for example Pb-rich minerals such as feldspars in the basement or the basin. The source(s) of lead are discussed in some papers and summarised hereafter. The high salinities of certain brines passing through the underlying mafic and felsic volcanic sequences would have been efficient in scavenging and transport of Pb, Zn and Cu at Walford Creek (Rohrlach et al., 1998a). Regarding the chemical properties of the Leichhardt and Calvert superbasins, Polito et al. (2006a, 2006b) consider the underlying clastic and volcanic successions belonging to theses basins as potential metal source rocks for the Century deposit and the discordant lodes. Finally, according to Cooke et al. (1998), Cu, Pb and Zn could have been almost entirely removed from the dolerite intruding the McArthur Basin. One argument for these suggestion is that as these mafic rocks are closer to the level at which base metal deposition occurred than the basement, they are a more accessible source of metals.

However, these propositions are based on the most plausible hypothesis, but at deeper study of the lead source(s) is needed to better constraint their possible location and model age. Based on the lead isotopes in galena, this chapter aims to identify possible stratigraphic levels containing the lead being mobilised to form the HYC world-class deposit. The trends observed in the lead isotope point to two different lead sources. Even if no precise unit can be identify as one of the lead sources, the mafic nature of the source can be discarded, and several units in the basement are proposed because of their felsic nature and age. The following chapter has been submitted to the international scientific journal *Geology*.

Préambule

Prédire l'approvisionnement en métaux pour les sociétés modernes demande des connaissances multiples, en particulier de comprendre comment les métaux s'accumulent dans la croûte terrestre jusqu'à former des gisements économiques. Les gisements géants hydrothermaux sont localisés là où des quantités importantes de métaux trouvent des conditions favorables pour leur précipitation à partir des fluides ayant lessivé les métaux à partir de roches sources ou de magmas. Cependant, dans la plupart des cas, l'origine ultime des métaux reste contestée. Ici, nous montrons pour la première fois que deux sources ont fourni en quantité comparable les 8 Mt de plomb et de zinc du gisement géant de plomb-zinc-argent de McArthur River (HYC, McArthur Basin, Australie). Grâce à des analyses par spectrométrie de masse des ions secondaires (SIMS) des isotopes du plomb dans la galène, nous avons déterminé que deux sources de métaux ont été impliquées de façon répétée pour

déposer les métaux dans les différentes lentilles minéralisées il y a environ 1640 Ma. De plus, les modèles de fractionnement des isotopes du plomb entre le manteau et les différents réservoirs crustaux indiquent que les sources majeures du plomb, lessivées par les fluides minéralisateurs, étaient probablement les roches felsiques du socle cristallin et les roches sédimentaires dérivées du socle dans le bassin. Cette étude fait la lumière sur l'importance cruciale du traçage des métaux comme prérequis pour contraindre les systèmes minéralisateurs à grande échelle. Elle appelle également à repenser la façon dont les systèmes hydrothermaux sont considérés comme capables de former des gisements géants: le lessivage de métaux de plusieurs sources pourrait en effet être un processus clé pour expliquer leur tonnage important.

La ou les source(s) des métaux de base dans les gisements actuels peuvent être des sulfures précédemment cristallisés, ou par exemple des minéraux riches en Pb comme des feldspaths, provenant du socle ou du bassin. La ou les source(s) du plomb sont discutées dans la littérature et résumés ci-après. Certaines saumures très salées traversant les roches volcaniques mafiques et felsiques sous-jacentes pourraient avoir lessivé et transporté Pb, Zn et Cu à Walford Creek (Rohrlach et al., 1998a). En se basant sur les propriétés chimiques des superbassins Leichhardt et Calvert, Polito et al. (2006a, 2006b) ont considéré les successions clastiques et volcaniques sous-jacentes comme potentielles sources de métaux pour le gisement de Century et les filons discordants. Enfin, selon Cooke et al. (1998), Cu, Pb et Zn pourraient avoir été entièrement extraits de la dolérite, intrusive dans le bassin de McArthur. Un argument pour cette hypothèse est que ces roches mafiques sont une source plus accessible car elles sont plus proches du niveau auquel la précipitation de métaux a eu lieu. Ces propositions sont basées sur les hypothèses les plus plausibles, mais une étude plus approfondie de la ou des source(s) du plomb est nécessaire pour pouvoir contraindre leur localisation possible et leur âge modèle. En se basant sur les isotopes du plomb dans la galène, ce chapitre a pour but d'identifier le nombre de source(s) du plomb et de proposer des niveaux stratigraphiques qui pourraient avoir contenu les métaux. Les allures des isotopes du plomb indiquent la mobilisation de deux sources du plomb. Bien qu'aucune unité ne puisse être identifiée précisément comme étant celle contenant une des sources du plomb, la nature mafique des sources peut être éliminée, et plusieurs unités du socle proposées au vu de leur nature felsique et de leur âge. Le chapitre qui suit a été soumis dans la revue internationale *Geology*.

Abstract

Giant hydrothermal ore deposits form where fluids carrying massive amounts of metals scavenged from source rocks or magmas encounter conditions favourable for their localised deposition. However, in most cases, the ultimate origin of metals remains highly disputed. Here, we show for the first time that two metal sources have provided in comparable amounts the 8 Mt of lead of the giant McArthur River zinc-lead deposit (McArthur Basin, Australia). By using high-resolution secondary ion mass spectrometry (SIMS) analysis of lead isotopes in galena, we demonstrate that the two metal sources have been repeatedly involved with the metal deposition in the different ore lenses ca. 1640 Ma ago. Modelling of lead isotope fractionation between mantle and crustal reservoirs implicates felsic rocks of the crystalline basement and the derived sedimentary rocks in the basin as the main lead sources that were leached by the ore-forming fluids. This sheds light on the crucial importance of metal tracing as a prerequisite to constrain large-scale ore-forming systems and calls for a paradigm shift in the way hydrothermal systems form giant ore deposits: leaching of metals from several sources may be key in accounting for their huge metal tonnage.

5.1. Introduction

Over a thousand giant ore deposits worldwide are recognized as containing exceptional accumulations of metals in restricted volumes (i.e. they store metals equivalent in 10^{11} tons of continental crust in mean crustal or “Clarke” concentration; Laznicka, 2014). Hydrothermal ore deposits are a specific class of metallic deposits that form by a combination of (i) metal extraction from a source rock or magma by a hydrothermal fluid, (ii) metal transport by a hydrothermal fluid from the source to a focused discharge where metals precipitate and accumulate and (iii) metal precipitation and accumulation (e.g. McCuaig and Hronsky, 2014). Giant hydrothermal ore deposits form only when all these processes are the most adequately combined in space and time (e.g. Richards, 2013) and when the volume of metalliferous fluid is sufficient. While the conditions for metal transport and precipitation are relatively well understood, thanks to, among others, fluid inclusion studies and metal speciation and mineral solubility experiments (e.g. Richard et al., 2012), the conditions under which metals are extracted from their source and more specifically the nature of the metal sources are still the most disputed aspect of many ore deposit models (e.g. Pettke et al., 2010). Several factors may underlie this controversy: (i) metal sources may occur at great distance from the ore deposit and may be hidden (e.g. Harlaux et al., 2018); (ii) metal sources will typically have large volumes but low concentrations of metal, meaning the mass balance studies required to

demonstrate large-scale metal mobilisation are highly challenging (e.g. Pitcairn et al., 2006); (iii) a single ore deposit may form from several metal sources (e.g. Mercadier et al., 2013); and (iv) fluid mixing may play a role in subsequent dilution of the geochemical signature of the primary metal source(s).

In order to address the number and the nature of metal source(s) involved with the formation of a true giant hydrothermal ore deposit, we have targeted the McArthur River Zn-Pb deposit (Northern Territory, Australia) and carried out a detailed *in situ* lead isotope study of galena. This widely used method is a powerful tool for tracing metal sources and ages based on model ages because it combines three radioactive decay systems ($^{238}U \rightarrow {}^{206}Pb$, $^{235}U \rightarrow {}^{207}Pb$ and $^{232}Th \rightarrow {}^{208}Pb$, e.g. Deloule et al., 1986).

5.2. Geological setting

The McArthur River Zn-Pb deposit is one of many giant hydrothermal ore deposits of the sediment-hosted massive sulphide (SHMS) category (e.g. Large et al., 1998; Leach et al., 2010). This deposit is situated in the Paleo- to Mesoproterozoic McArthur Basin, which unconformably overlies Paleoproterozoic crystalline basement units (Figure 5-1 and Supplementary Figure 5-1). This is one of the many giant ore deposits of the so-called “Carpentaria Zinc Belt” in the Northern Territory and Queensland (Large et al., 1998; McGoldrick et al., 2010) and one of the most important Zn-Pb deposits in the world (as of October 2018: 188 Mt @ 9.6% Zn, 4.5% Pb, 46g/t Ag, NTGS, 2018). The McArthur River deposit is located 2 km west of the Emu Fault, a major 10 km deep crustal structure (Rawlings et al., 2004) that potentially acted as a fluid conduit for upward migration of 150–250°C, oxidized, metal- and sulphate-rich basinal fluids (Cooke et al., 2000), in a sinistral strike-slip regime (McGoldrick et al., 2010). The eight ore lenses of the McArthur River deposit occur within the Pyritic Shale Member of the Barney Creek Formation, dated at 1639 ±2 Ma (Page and Sweet, 1998), that acted as a reduced geochemical trap for metal precipitation (Cooke et al., 2000). Most authors consider the formation of the McArthur River deposit as syn-sedimentary or sub-contemporaneous to the deposition of the upper Barney Creek Formation and therefore consider 1639 ± 2 Ma as a reasonable estimate of the age of metal deposition (Huston et al., 2006; Kunzmann et al., 2019).

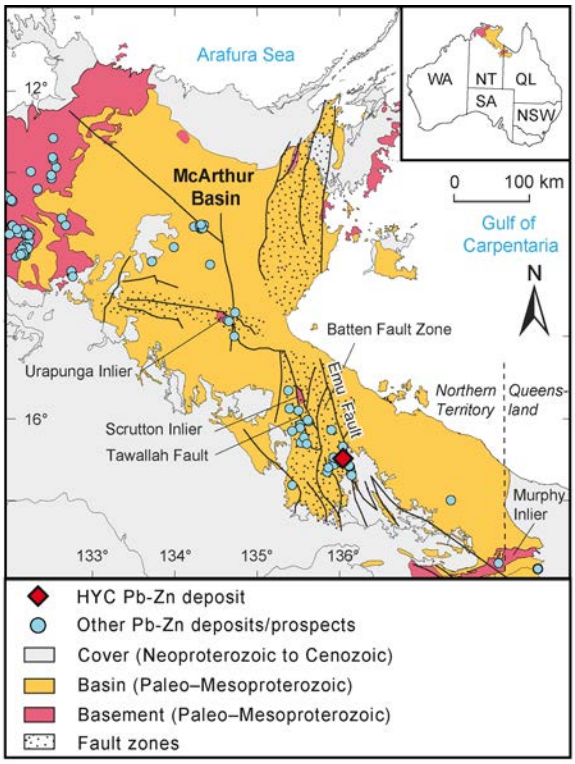

Figure 5-1: *Simplified geological map of the McArthur Basin (Northern Territory, Australia). Geological map with identification of the major lithostratigraphic units : the crystalline basement, the McArthur Basin and the more recent sedimentary cover (Ahmad et al., 2013a). The major faults and faults zones are indicated including the Emu Fault near the McArthur River Zn-Pb deposit. Other Zn-Pb deposits and prospects are indicated.*

5.3. Sampling and analytical methods

Samples span most of the ore sequence at the McArthur River mine site (136°098 E - 16°436 S – GDA 1994) and include five of the eight ore lenses and so called lens 0, a sub-economic lens located just below the main ore sequence (Figure 5-2). Petrographic investigation by reflected light optical microscopy and scanning electron microscopy (SEM) shows ores consist of sphalerite-galena-pyrite-rich bands interlayered with mudstones and quartz-carbonate turbidites (Figure 5-2, Large et al., 1998). 50 µm – 1mm galena crystals are typically poikilitic and contain numerous ~ 10 µm inclusions of pyrite, sphalerite and minor silicates and carbonates. No growth, recrystallization, zoning or alteration textures in galena were highlighted. Detailed mineral mapping using SEM was carried out in order to select the most favourable zones within galena grains (i.e. galena devoid of mineral inclusions) for *in situ* lead isotope analyses. The lead isotopes were measured by secondary ion mass spectrometry (SIMS) with a radiofrequence source whose analytical capacity allows an excellent sensitivity and a high spatial resolution with a spot size of 10 µm. Analytical methods are detailed in the Supplementary Information.

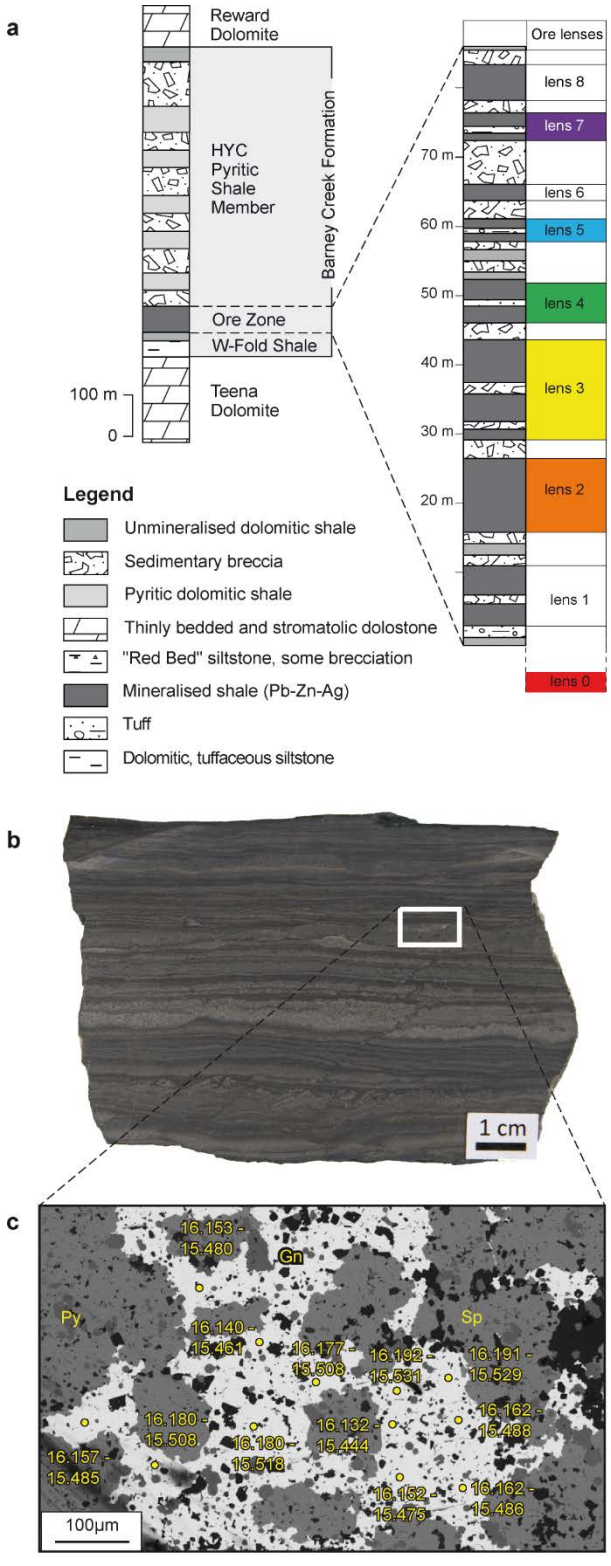

Figure 5-2: *Sample location in the McArthur River Zn-Pb deposit (Northern Territory, Australia) and description of a typical sample.* ***a****, Simplified stratigraphic succession of the McArthur River deposit with location of the different ore lenses (Large et al., 1998). The sampled ore lenses (0, 2, 3, 4, 5 and 7) are identified by different colours.* ***b****, Hand sample from the lens 2 with sulphide-rich laminae.* ***c****, SEM image of a sulphide-rich lamina showing the texture of galena (Gn), sphalerite (Sp), pyrite (Py) and carbonate (Cb) and the size and emplacement of the in situ lead isotope analyses by SIMS. For each SIMS spot, the lead isotopic ratios are indicated as follows:* $^{206}Pb/^{204}Pb$ - $^{207}Pb/^{204}Pb$*.Results*

The ranges of $^{206}Pb/^{204}Pb$, $^{207}Pb/^{204}Pb$ and $^{208}Pb/^{204}Pb$ ratios are 16.10–16.22, 15.43–15.57 and 35.42–36.57 respectively (Figure 5-3 and Supplementary Table 5-1). In a $^{207}Pb/^{204}Pb$ *vs* $^{206}Pb/^{204}Pb$ diagram, the data are distributed along a line whose slope is 1.42 with a mean square weighted deviation (MSWD) of 4.1 (Figure 5-3). Slopes are similar within the analytical error for the different lenses (Supplementary Figure 5-2). Lenses 0, 3, 4 and 5 show a similar distribution of $^{206}Pb/^{204}Pb$ and $^{207}Pb/^{204}Pb$ ratios with modes around 16.2 and 15.55 respectively, whereas lens 2 shows modes around 16.16 and 15.49, respectively. The lead isotope ratios exhibit similar variations at the grain and at lens scales (e.g. $^{206}Pb/^{204}Pb$ values of 16.192 and 16.132 for analytical spots 100 µm apart in a single grain, Supplementary Figures 5-3 to 5-8). Previous lead isotope compositions measured on mixed sulphides by thermal ionization mass spectrometry (TIMS) are clustered in the lower range of the $^{206}Pb/^{204}Pb$, $^{207}Pb/^{204}Pb$ and $^{208}Pb/^{204}Pb$ values obtained in this study (Supplementary Figure 5-9). Although they are compatible within error with the present data, they represent a mixed signature of several grains. The novelty here is that the *in situ* SIMS analyses have a high petrographic resolution and reveal the full range of lead isotope compositions.

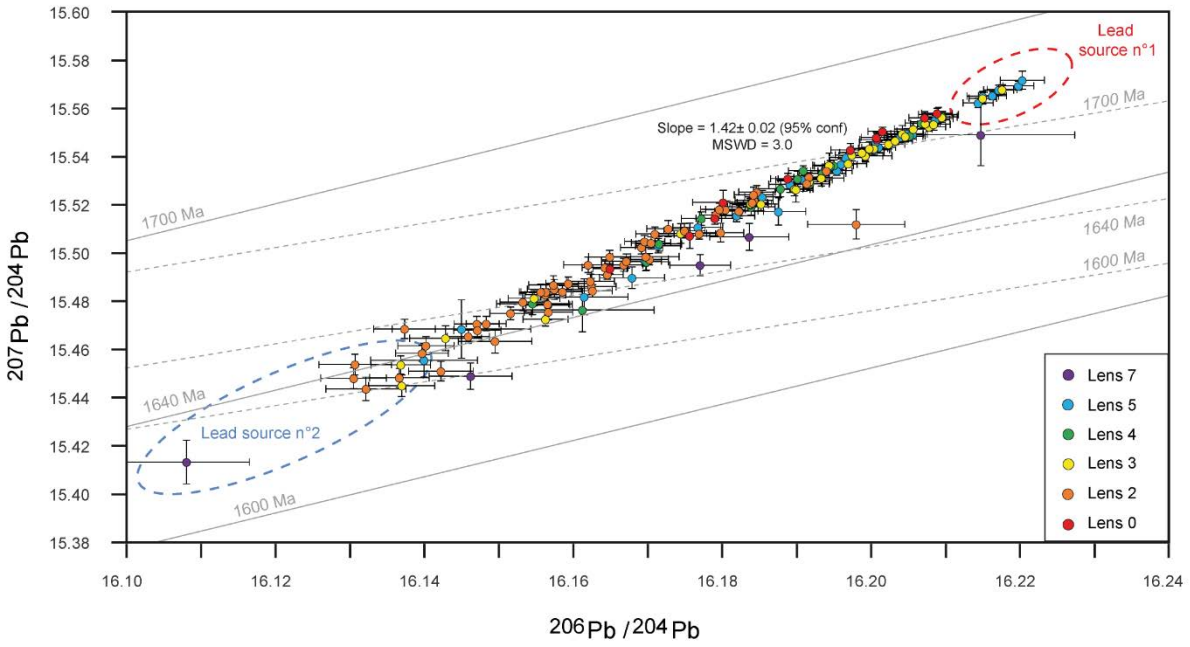

Figure 5-3: *Lead isotope composition of galena from the McArthur River Zn-Pb deposit (Northern Territory, Australia). The in situ SIMS data from the different ore lenses are identified by distinct colours as in Figure 5-2, and plotted with 1σ error bars. The slope of the line between all the analyses and the position of the ellipses corresponding to the probable ratios of Lead Sources 1 and 2 are reported. The isochrons (straight lines linking compositions of rocks or minerals having the same model age) from different models (solid lines, Sun et al., 1996 and dashed lines, Stacey and Kramers, 1975) are indicated.*

5.4. Discussion

5.4.1. Repeated mixing between two lead sources

The line between all the lead isotope data is discordant to isochrons linking rocks and minerals with the same model age (Figure 5-3, Stacey and Kramers, 1975; Sun et al., 1996). The most simple explanation is that the data lie along a mixing line between two distinct lead sources corresponding to two end-members of the data distribution that we name respectively Lead Source 1 ($^{207}Pb/^{204}Pb$ > 15.56 and $^{206}Pb/^{204}Pb$ > 16.21) and Lead Source 2 ($^{207}Pb/^{204}Pb$ < 15.46 and $^{206}Pb/^{204}Pb$ < 16.14, Figure 5-3). Assuming (i) the two lead sources have compositions similar to the extremes of the mixing line and (ii) the data are representative of the lead isotopic composition of the ore fluid at the time of sulphide deposition, the relative contribution from the two sources can be calculated. Considering the modes of $^{207}Pb/^{204}Pb$ and $^{206}Pb/^{204}Pb$ ratios in each lens, the relative proportion of lead derived from each source in the different ore lenses is between 38 and 83% for Lead Source 1 and between 17 and 62% for Lead Source 2 (Supplementary Figure 5-2). Thus, both lead sources have been repeatedly involved with the formation of the different ore lenses, and their relative proportions are of the same order of magnitude.

5.4.2. Isotope evolution models for lead sources

Models of lead isotope fractionation and evolution between the mantle and crustal reservoirs, together with existing chronostratigraphic constraints in the investigated area are helpful to identify the nature of Lead Sources 1 and 2. The usual local model for the North Australian Craton is based on the global “continuous growth-of-μ” model (where μ represents the $^{238}U/^{204}Pb$ ratio of a given reservoir, Cumming and Richards, 1975), and uses lead isotope ratios obtained by TIMS at the McArthur River deposit as a control point for the 1640 Ma isochron (Supplementary Figure 5-9, Sun et al., 1996). However, as the new *in situ* SIMS data presented here show considerably more scattering compared to previously-obtained bulk TIMS data, the local model should now be treated with caution. Alternative models are proposed and discussed below (Figure 5-4 and Supplementary Discussion for details).

The objective of the tested models is to account for distinct evolution of Lead Sources 1 and 2 that were both leached by the ore-forming fluids at ca. 1640 Ma, by adjusting the number and timing of crust formation and differentiation events, the age of crystallization of Pb-bearing minerals, as well as the μ values of the different lead reservoirs. As the composition

of Lead Source 2 lies close to the 1640 Ma isochron of the usual global and local models (Figure 5-3, Stacey and Kramers, 1975; Sun et al., 1996), we rely on the reasonable assumption that Lead Source 2 corresponds to a crustal reservoir that has evolved isotopically through ^{238}U, ^{235}U and ^{232}Th decay until the time of the McArthur River deposit formation (ca. 1640 Ma). Model A assumes that the model age of both lead sources is 1640 Ma. Back-calculation indicates the extraction of a crustal reservoir from the mantle at 3.83 Ga that evolved towards the composition of Lead Source 1 (μ_1 = 10.21), followed at 3.65 Ga by the extraction of another crustal reservoir from the mantle that evolved towards the composition of Lead Source 2 (μ_2 = 10.34, Figure 5-4a). Model B assumes a single episode of extraction of two crustal reservoirs from the mantle. These two reservoirs evolved towards the composition of Lead Sources 1 and 2 respectively (Figure 5-4b). Back-calculation indicates that this episode occurred at 3.65 Ga, which, in turn, imposes μ_1 = 11.12 and μ_2 = 10.34, and that lead isotope evolution of Lead Source 1 has ceased at 1764 Ma (i.e. was devoid of U and Th to avoid the production of radiogenic Pb). Model C assumes an initial extraction of a crustal reservoir from the mantle at 3.7 Ga, followed by an episode of differentiation into two crustal reservoirs that evolved towards the composition of Lead Sources 1 and 2 respectively (Figure 5-4c). Back-calculation indicates that crustal differentiation occurred between 3.65 and 3.0 Ga, which, in turn, imposes that lead isotope evolution of Lead Source 1 has ceased between 1895 and 1764 Ma, with μ_1 ranging between 11.12 and 12.92 and μ_2 ranging between 10.34 and 10.67.

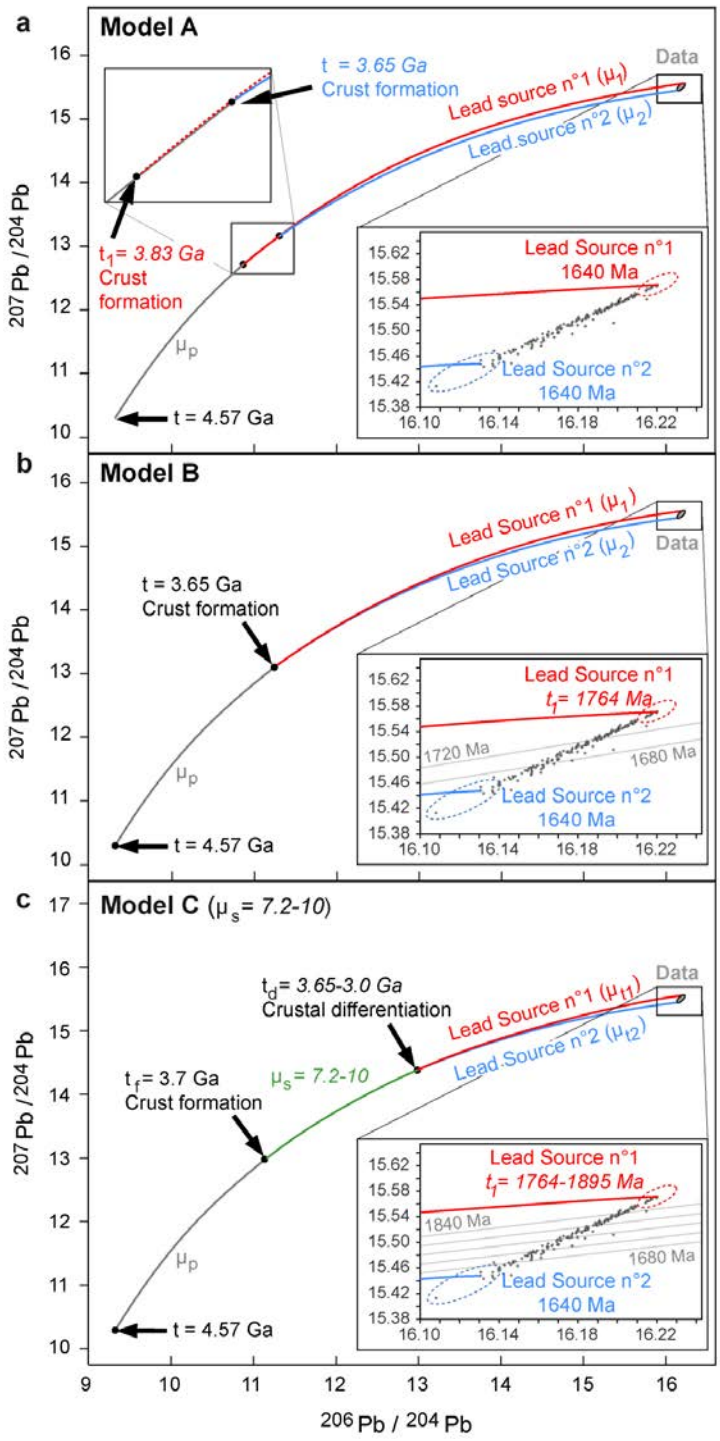

***Figure 5-4**: Lead isotope evolution models proposed for the origin of the two lead sources in the McArthur River Zn-Pb deposit (Northern Territory, Australia). See text for the description of the models. The evolution of the mantle, Lead Source 1, Lead Source 2 (Models A, B, C) and the crustal reservoir formed prior to crustal differentiation (Model C) are shown in grey, red, blue and green respectively. Values in italics are the calculated values after the models. μ_p, μ_s, μ_1 and μ_2 correspond to the $^{238}U/^{204}Pb$ ratio of: (i) the mantle (= 7.192), (ii) the first-formed crustal reservoir in Model C, (iii) Lead Source 1 and (iv) Lead Source 2 respectively. t_{f1} and t_{f2} correspond to the age of crust formation for Lead Source 1 and 2 respectively in Model A. t_f and t_d correspond to the ages of crust formation in Model B and to an episode of crustal differentiation after the crust formation at 3.7 Ga in Model C respectively. t_{c1} is the time from which the isotopic composition of the Lead Source 1 remained constant, corresponding to the crystallization of Pb-bearing, U- and Th-poor minerals in Models B and C.*

5.4.3. Potential candidates for lead sources

It is noteworthy that all scenarios require elevated μ values (between 10.2 and 12.92) for the crustal reservoirs in order to account for the composition of Lead Sources 1 and 2, ruling out mafic volcanics from the McArthur Basin as a plausible Pb source for the McArthur River deposit (e.g. Stacey and Kramers, 1975; Cooke et al., 1998; Hofmann, 2007). Models B and C require that Lead Source 1 would have stopped evolving isotopically between ca. 1895 and 1764 Ma. This is possible if Lead Source 1 consists of galena or Pb-bearing feldspar crystallized within this age span. However, only small galena deposits of this age are known in the basin or basement in the area and no felsic igneous rocks are recorded in the area between 1815 (oldest age in the basin) and 1730 Ma (Ahmad et al., 2013a). Therefore, according to Model C, Lead Source 1 should belong to or be derived from the youngest basement felsic units by erosion and sedimentation. Lead Sources 1 and 2 could actually belong to separate units or to the same unit if, in the latter, lead is alternatively leached from feldspar only or from all lead-bearing minerals including accessory uranium- and thorium-rich minerals. Several anorogenic felsic intrusive and volcanic units in the crystalline basement are plausible candidates for Lead Sources 1 and 2 as they meet the age constraints from the above models and have vertical (> 1 km) and lateral extension that could potentially account for the lead budget of the McArthur River deposit (Supplementary Table 5-3). This includes the ca. 1850 Ma Cliffdale and Scrutton volcanics located in the Murphy and Scrutton inliers respectively. Those anorogenic felsic units were likely among the sources of felsic-derived sediments in the McArthur Basin such as the black shales of the Barney Creek Formation, clastic units within carbonate-evaporite successions or the regionally extensive and permeable conglomerates and sandstones in the basal units of the McArthur Basin where framework alteration of detrital feldspar is documented (Davidson, 1998; Polito et al., 2011).

5.5. Conclusion

Altogether, the present *in situ* SIMS lead isotope data and isotope modelling provide for the first time a strong support for the previous assumption that the lead-rich products of anorogenic felsic magmatism contributed to the lead sources for some giant Proterozoic Zn-Pb deposits worldwide (Sawkins, 1989). More generally, the present work shows that if forming a giant hydrothermal ore deposit requires mobilizing metals from several sources, the current models for scales, geometries and dynamics of ore-forming hydrothermal systems should be revised. In turn, this would have a major impact on the estimation of metal endowment and

exploration strategies in world-class metallogenic provinces, as the volume of metal sources and their metal concentration define the total amount of metals available for ore deposits.

Acknowledgments

The Northern Territory Geological Survey provided logistical support for sampling. Glencore Australia Holdings Pty Ltd. and McArthur mine geologists team provided authorisation and guidance for sampling. The Ion Probe Team Nancy (CRPG-CNRS) provided technical support during SIMS analyses. The Service Commun de Microscopie Electronique et de Microanalyses (GeoRessources Lab) provided technical support during SEM analyses. This research was funded by (i) a French Ministry of Higher Education and Research PhD salary Grant to J.G., (ii) a Région Lorraine-FEDER grant to J.M : « Rôle des phases fluides dans la distribution spatiale des ressources métalliques dans les bassins sédimentaires paléoproterozoiques australiens », (iii) OSU OTELo grants to J.M. : « Conditions de transport des métaux dans un mégabassin protérozoïque » and A.R. : « Transferts de fluides et métaux dans le bassin de McArthur (Australie) », (iv) CNRS-INSU-CESSUR grants to J.M. Transferts des fluides et métaux dans les méga-bassins paléoprotérozoïques and A.R. « Traçage isotopique de migrations massives de métaux le long d'une faille d'échelle crustale (Emu Fault, bassin de McArthur, Australie) ». Reviews by Robert Scott and two anonymous reviewers greatly helped improving the manuscript.

5.6. Supplementary material

5.6.1. Methods

Optical and scanning electron microscopy (SEM)

Optical microscopy was carried out on thin sections or mounted polished sections in reflective light using a numerical microscope VHX-200F with a high resolution objective VH-Z500W for the whole sections and a Zeiss Axio Scope.A1 microscope for detailed petrography (GeoRessources Lab - Vandœuvre-les-Nancy, France). SEM images were obtained using backscattered electron detector (BSE) of a conventional tungsten source Tescan Vega3LM, with an acceleration voltage of 15 kV and beam current of around 1nA (GeoRessources Lab - Vandœuvre-les-Nancy, France).

Secondary ion mass spectrometry (SIMS)

Eight ore samples were selected from for *in situ* Pb isotope analysis on galena individual grains. 69 galena crystals were analysed from the different McArthur River deposit ore lenses with a total of 153 points. The analyses were performed on the Cameca IMS-1280 HR ion microprobe (CRPG-CNRS - Vandœuvre-les-Nancy, France) with an excellent sensitivity and a high spatial resolution thanks to the radiofrequence source (Deloule et al., 1986). The O^{2-} primary ion beam was accelerated at 13 kV, with an intensity that ranged between 72 and 74 nA. The size of the spot varied between 10 to 12 µm in diameter. Positive secondary ions were extracted with a 10 kV potential, and the spectrometer slits set for a Mass Resolving Power of ~2 500. The field aperture was set to 3 000 µm, and the transfer optic magnification adjusted to 107. Rectangular lenses were activated in the secondary ion optics to increase the transmission at high mass resolution (De Chambost et al., 1996). The energy window was opened at 50 eV, and its low energy side was positioned at 5 eV before the start of the energy distribution. ^{204}Pb, ^{206}Pb and ^{207}Pb were measured on multicollection mode with the FC (Farraday Cup) collector L1, C, and H1 respectively, with the ^{206}Pb in central position. ^{208}Pb was measured separately on the collector C by peak jumping. Each analysis consisted of 16 successive cycles, each cycle including the measurement of ^{204}Pb, ^{206}Pb, ^{207}Pb for 12 s, then that of ^{208}Pb for 8 s, with a waiting time of 1 s. Background on the FCs were measured before each analysis during the 120s of presputtering. Secondary beam centering and mass and energy calibrations were checked before each measurement. The instrumental mass fractionation was monitored using two CRPG internal standards Aloui and ISH9. The isotopic ratios are 18.125 for ^{206}Pb/^{204}Pb and 15.62 for ^{207}Pb/^{204}Pb for Aloui and 17.691 for ^{206}Pb/^{204}Pb and 15.436 for ^{207}Pb/^{204}Pb for ISH9 (Supplementary Table 5-2). The instrumental mass fractionation is of 2.6 ‰ /amu, and external errors on the reference galena is 0.14 for the ^{206}Pb/^{204}Pb ratio, 0.14 for the ^{207}Pb/^{204}Pb ratio and 0.18 for the ^{208}Pb/^{204}Pb ratio. The errors presented on Figure 5-3, Supplementary Figures 5-2 and 5-9 and Supplementary Table 5-1 correspond to 1σ errors.

5.6.2. Supplementary discussion

Three end-member scenarios of lead isotope evolution of crustal reservoirs accounting for the composition of Lead Sources 1 and 2 are shown and discussed below. The constants and parameters are as follows: λ_1 is the decay constant of ^{238}U ($\lambda_1 = 0.155125$ Ga^{-1}), λ_2 is the decay constant of ^{235}U ($\lambda_2 = 0.98485$ Ga^{-1}), $\left(\frac{^{206}Pb}{^{204}Pb}\right)_{4.57\ Ga}$ is the ^{206}Pb/^{204}Pb ratio of the mantle at 4.57 Ga (= 9.307, Tatsumoto et al., 1973), $\left(\frac{^{207}Pb}{^{204}Pb}\right)_{4.57\ Ga}$ is the ^{207}Pb/^{204}Pb ratio of the mantle at 4.57

Ga (= 10.294, Tatsumoto et al., 1973), the 1/137.88 ratio corresponds to the $^{235}U/^{238}U$ ratio (constant for all U of normal isotopic composition in the Earth at the present time, Halla, 2018), μ stands for the $^{238}U/^{204}Pb$ ratio of the mantle or a given crustal reservoir, μ_p is the $^{238}U/^{204}Pb$ ratio of the mantle (μ_p = 7.192, Tatsumoto et al., 1973), $\left(\frac{^{206}Pb}{^{204}Pb}\right)_{1.64\ Ga}$ is the $^{206}Pb/^{204}Pb$ ratio at 1640 Ma (16.131 for the Lead Source 2 and 16.220 for the Lead Source 1) and $\left(\frac{^{207}Pb}{^{204}Pb}\right)_{1.64\ Ga}$ is the $^{207}Pb/^{204}Pb$ ratio at 1640 Ma (15.448 for the Lead Source 2 and 15.572 for the Lead Source 1), both obtained in this study. The value of the lead isotope ratios for Lead Sources 1 and 2 has a significant influence on the final ages calculated and a sensitivity analysis is proposed for each model.

Model A

Model A (Figure 5-4a) assumes that the model ages for the two lead sources is 1640 Ma and that both the Lead Sources 1 and 2 were leached at 1640 Ma by the hydrothermal fluids. This Model involves the extraction from the mantle of a crustal reservoir that evolved towards the composition of Lead Source 1, followed by the extraction from the mantle of another crustal reservoir that evolved towards the composition of Lead Source 2. The parameters for this models are μ_1 and μ_2 which are the $^{238}U/^{204}Pb$ ratio for the Lead Sources 1 and 2 respectively, and t_{f1} and t_{f2} the timings of crust formation for Lead Sources 1 and 2 respectively. In order to calculate μ_1 and t_{f1}, the following two equations are used:

$$\left(\frac{^{206}Pb}{^{204}Pb}\right)_{1.64\ Ga} = \left(\frac{^{206}Pb}{^{204}Pb}\right)_{4.57\ Ga} + \mu_p \times (e^{\lambda_1 \times 4.57} - e^{\lambda_1 \times t_{f1}}) + \mu_1 \times (e^{\lambda_1 \times t_{f1}} - e^{\lambda_1 \times 1.64})$$

and

$$\left(\frac{^{207}Pb}{^{204}Pb}\right)_{1.64\ Ga} = \left(\frac{^{207}Pb}{^{204}Pb}\right)_{4.57\ Ga} + \frac{\mu_p}{137.88} \times (e^{\lambda_2 \times 4.57} - e^{\lambda_2 \times t_{f1}}) + \frac{\mu_1}{137.88} \times (e^{\lambda_2 \times t_{f1}} - e^{\lambda_2 \times 1.64})$$

Similarly, the μ_2 and t_{f2} values are given by:

$$\left(\frac{^{206}Pb}{^{204}Pb}\right)_{1.64\ Ga} = \left(\frac{^{206}Pb}{^{204}Pb}\right)_{4.57\ Ga} + \mu_p \times (e^{\lambda_1 \times 4.57} - e^{\lambda_1 \times t_{f2}}) + \mu_2 \times (e^{\lambda_1 \times t_{f2}} - e^{\lambda_1 \times 1.64})$$

and

$$\left(\frac{^{207}Pb}{^{204}Pb}\right)_{1.64\ Ga} = \left(\frac{^{207}Pb}{^{204}Pb}\right)_{4.57\ Ga} + \frac{\mu_p}{137.88} \times (e^{\lambda_2 \times 4.57} - e^{\lambda_2 \times t_{f2}}) + \frac{\mu_2}{137.88} \times (e^{\lambda_2 \times t_{f2}} - e^{\lambda_2 \times 1.64})$$

Solving the two systems of two equations and two unknowns yields t_{f1} = 3.83 Ga, t_{f2} = 3.65 Ga, μ_1 = 10.21 and μ_2 = 10.343. When shifting by 0.01 the ^{206}Pb / ^{204}Pb of a given lead source,

its calculated extraction age is shifted by ca. 10–11 Ma. When shifting by 0.01 the ^{207}Pb / ^{204}Pb value of a given lead source, its calculated extraction age is shifted by ca. 20–25 Ma.

According to this model, Lead Sources 1 and 2 have high μ values that are incompatible with mafic volcanics as a source of lead for the McArthur River deposit despite the strong alteration of mafic rocks in the McArthur Basin (Cooke et al., 1998).

Model B

Model B (Figure 5-4b) assumes a single episode of extraction from the mantle of two crustal reservoirs that evolved towards the composition of Lead Sources 1 and 2 respectively, similarly to the model of Stacey and Kramers (1975). However, if the Lead Source 2 corresponds the ca. 1640 Ma age of mineralisation, the Stacey and Kramers (1975) model must be adjusted as the Lead Source 2 does not lie on the 1640 Ma isochron (Figure 5-3). The parameters for this models are μ_1 and μ_2 which are the $^{238}U/^{204}Pb$ ratios for Lead Sources 1 and 2 respectively, t_f the corresponding age of crust formation for both Lead Sources (in Ga) and t_{c1} the time from which the isotopic composition of the Lead Source 1 remained constant. In order to calculate μ_2 and t_f, the following two equations are used:

$$\left(\frac{^{206}Pb}{^{204}Pb}\right)_{1.64\ Ga} = \left(\frac{^{206}Pb}{^{204}Pb}\right)_{4.57\ Ga} + \mu_p \times (e^{\lambda_1 \times 4.57} - e^{\lambda_1 \times t_f}) + \mu_2 \times (e^{\lambda_1 \times t_f} - e^{\lambda_1 \times 1.64})$$

and

$$\left(\frac{^{207}Pb}{^{204}Pb}\right)_{1.64\ Ga} = \left(\frac{^{207}Pb}{^{204}Pb}\right)_{4.57\ Ga} + \frac{\mu_p}{137.88} \times (e^{\lambda_2 \times 4.57} - e^{\lambda_2 \times t_f}) + \frac{\mu_2}{137.88} \times (e^{\lambda_2 \times t_f} - e^{\lambda_2 \times 1.64})$$

Solving the system of two equations and two unknowns yields t_f = 3.65 Ga and μ_2 = 10.343. Accordingly, $\left(\frac{^{206}Pb}{^{204}Pb}\right)_{3.65\ Ga} = 11.250$ and $\left(\frac{^{207}Pb}{^{204}Pb}\right)_{3.65\ Ga} = 13.094$ where $\left(\frac{^{206}Pb}{^{204}Pb}\right)_{3.65\ Ga}$ and $\left(\frac{^{207}Pb}{^{204}Pb}\right)_{3.65\ Ga}$ are respectively, the ^{206}Pb /^{204}Pb and ^{207}Pb /^{204}Pb ratio of Lead Source 2 at 3.65 Ga.

The age of crust formation (3.65 Ga) allows calculating μ_1 and t_{c1} using the following two equations:

$$\left(\frac{^{206}Pb}{^{204}Pb}\right)_{t_1} = \left(\frac{^{206}Pb}{^{204}Pb}\right)_{3.65\ Ga} + \mu_1 \times (e^{\lambda_1 \times 3.65} - e^{\lambda_1 \times t_{c1}})$$

$$\left(\frac{^{207}Pb}{^{204}Pb}\right)_{t_1} = \left(\frac{^{207}Pb}{^{204}Pb}\right)_{3.65\ Ga} + \frac{\mu_1}{137.88} \times (e^{\lambda_2 \times 3.65} - e^{\lambda_2 \times t_{c1}})$$

Solving the system of two equations and two unknowns yields μ_1 = 11.122 and t_{c1} = 1764 Ma (Figure 5-4b). When shifting by 0.01 the ^{206}Pb / ^{204}Pb value of a given lead source, its calculated extraction age is shifted by ca. 8 Ma. When shifting by 0.01 the ^{207}Pb / ^{204}Pb of a given lead source, its calculated extraction age is shifted by ca. 15–16 Ma.

The lead isotope evolution for the Lead Source 1 has to be stopped at ca. 1764 Ma, indicating that it was devoid of uranium and thorium to avoid the production of radiogenic lead. Galena would be a suitable candidate, and Spinks et al. (2016) identified evidences of sphalerite mineralisation with minor galena in the Wollogorang Formation (1730 ± 3 Ma - 1723 ± 4 Ma, Jackson et al., 1997), and of sphalerite on the McDermott Formation (~ 1780 Ma, Spinks et al., 2016), perhaps of primary sedimentary origin. However, the amount of lead in these units is unknown and probably too small to account for a large lead tonnage at the McArthur River deposit. Another suitable source is feldspar, as the ionic properties of Pb allows it to substitute for Ca in plagioclase and for K in K-feldspar in roughly equal amounts in both minerals (Heier, 1962), and as they are abundant in the basin and the basement. The high μ_1 and μ_2 values favour a felsic reservoir. However no felsic event is recorded in the McArthur Basin between 1815 (oldest age in the basin) and 1730 Ma (Ahmad et al., 2013a). Therefore, Model B is probably not suitable to account for the present data.

Model C

For the Model C (Figure 5-4c) the timing of crust formation is imposed at 3.7 Ga according to the Stacey and Kramers (1975) model and a crustal differentiation occurs later at t = t_d. The $^{238}U/^{204}Pb$ ratio (μ_s) of the first-formed crustal reservoir can vary from 7.192 (mantle ratio) to 10 (for higher μ_s values, the equations below cannot be solved). After crustal differentiation, μ_1 is the $^{238}U/^{204}Pb$ ratio for the Lead Source 1 and μ_2 is the $^{238}U/^{204}Pb$ ratio for the Lead Source 2. The following two equations are used to calculate t_d and μ_2:

$$\left(\frac{^{206}Pb}{^{204}Pb}\right)_{1.64\ Ga} = \left(\frac{^{206}Pb}{^{204}Pb}\right)_{3.7\ Ga} + \mu_s \times (e^{\lambda_1 \times 3.7} - e^{\lambda_1 \times t_d}) + \mu_{t2} \times (e^{\lambda_1 \times t_d} - e^{\lambda_1 \times 1.64})$$

$$\left(\frac{^{207}Pb}{^{204}Pb}\right)_{1.64\ Ga} = \left(\frac{^{207}Pb}{^{204}Pb}\right)_{3.7\ Ga} + \frac{\mu_s}{137.88} \times (e^{\lambda_2 \times 3.7} e^{\lambda_2 \times t_d}) + \frac{\mu_{t2}}{137.88} \times (e^{\lambda_2 \times t_d} - e^{\lambda_2 \times 1.64})$$

Solving the system of two equations and two unknowns (as μ_s is fixed, with μ_s = 10 in the following example) yields t_d = 3 Ga and μ_2 = 10.405. Accordingly, $\left(\frac{^{206}\mathrm{Pb}}{^{204}\mathrm{Pb}}\right)_{3\ \mathrm{Ga}} = 12.979$ and $\left(\frac{^{207}\mathrm{Pb}}{^{204}\mathrm{Pb}}\right)_{3\ \mathrm{Ga}} = 14.380$ where $\left(\frac{^{206}\mathrm{Pb}}{^{204}\mathrm{Pb}}\right)_{3\ \mathrm{Ga}}$ and $\left(\frac{^{207}Pb}{^{204}Pb}\right)_{3\ Ga}$ are respectively the ^{206}Pb /^{204}Pb and ^{207}Pb /^{204}Pb ratios of Lead Source 2 at 3 Ga.

The age of crust differentiation (t_d = 3 Ga) allows calculating the μ_1 value of the Lead Source 1 and the time t_{c1} from which the composition of the Lead Source 1 remained constant using the following two equations:

$$\left(\frac{^{206}Pb}{^{204}Pb}\right)_{t_1} = \left(\frac{^{206}Pb}{^{204}Pb}\right)_{3\ Ga} + \mu_1 \times (e^{\lambda_1 \times 3} - e^{\lambda_1 \times t_{c1}})$$

$$\left(\frac{^{207}\mathrm{Pb}}{^{204}\mathrm{Pb}}\right)_{t_1} = \left(\frac{^{207}\mathrm{Pb}}{^{204}\mathrm{Pb}}\right)_{3\ \mathrm{Ga}} + \frac{\mu_1}{137.88} \times (\mathrm{e}^{\lambda_2 \times 3} - \mathrm{e}^{\lambda_2 \times \mathrm{t_{c1}}})$$

Solving the system of two equations and two unknowns yields μ_1 = 12.92 and t_{c1} = 1895 Ma (Figure 5-4c). As 7.192 < μ_s ≤ 10, the application of this model leads to a range of possibilities comprised between 3.65 (equivalent to the model B) to 3 Ga for the crustal differentiation, and between 1895 Ma and 1764 Ma for t_{c1} (Figure 5-4c). The influence of lead isotope composition of Lead Sources 1 and 2 for the model calculation is presented hereafter with μ_s = 10 because it is the one where the larger shift is observed. When shifting by 0.01 the ^{206}Pb / ^{204}Pb of a given lead source, its calculated extraction age is shifted by ca. 11-12 Ma. When shifting by 0.01 the ^{207}Pb / ^{204}Pb of a given lead source, its calculated extraction age is shifted by ca. 23-26 Ma.

Depending on the μ_s value, the lead can be sourced from different stratigraphic levels. In this model too, the high μ values correspond to felsic rocks and as no felsic event is recorded in the McArthur Basin between 1815 and 1730 Ma (Ahmad et al., 2013a), the t_{c1} ages (up to 1895 Ma) have to correspond to basement units. To better constraint the age of the lead source, it is possible to rely on the timing of the crustal differentiation t_d, between 3.7 and 3.0 Ga (Figure 5-4c). Only one detrital zircon older than 3000 Ma is recorded in the McArthur River deposit area. It is dated at 3074 ±58 Ma (Page, 2018) in the Mallapunyah Formation (sedimentary siliciclastic) and could correspond to the age of the suspected crustal differentiation event. According to this model, the Lead Source 1 crystallised around 1875 Ma. In the basement, several units were emplaced at this time. In the Scrutton Inlier, which outcrops nowadays 70 kms from the McArthur River deposit, the Scrutton Volcanics (rhyolites, dacites and sedimentary units) have an age of 1851 ±7 Ma (Page et al., 2000) and a thickness of more than 1 km (Supplementary Table 5-2). Other basement units in the Murphy Inlier (south of the

McArthur basin, 200 km from the McArthur River deposit) and the Urapunga Inlier (200 km to the North-Est) have approximately the same age and present felsic lithologies that could be suitable candidates (Supplementary Table 5-2, Ahmad et al., 2013). For example, the Cliffdale Volcanics contain between 8 and 42 ppm Pb and have a vertical extent of more than 4 km (Orth, 2010). The most possible option for Model C is therefore a crustal differentiation around 3070 Ma and the crystallisation of feldspars from felsic volcanics or intrusives in the basement around 1850 Ma. It is not possible to firmly establish which specific unit was involved as a source, but several basement units having significant Pb contents (in feldspars), being thick (> 1 km) and extending over large areas could be proposed, such as the Cliffdale and Scrutton volcanics.

5.6.3. Supplementary tables

Supplementary Table 5-1*: Analytical results for lead isotope composition of galena in the McArthur River zinc-lead deposit (Northern Territory, Australia) as determined by secondary ion mass spectrometry (SIMS). The circle n° indicate the different analysed zones presented in Supplementary Figures 5-3 to 5-8 where the analysis n° is also indicated.*

Sample n°	Lens	Drill core or sample name	Depth (m)	Circle n°	Analysis n°	^{206}Pb / ^{204}Pb	Error (1σ)	^{207}Pb / ^{204}Pb	Error (1σ)	^{208}Pb / ^{204}Pb	Error (1σ)	^{206}Pb / ^{204}Pb	Error (1σ)
164-6@1	7	MRM2012-03	164.6	-	1	16.146	0.006	15.449	0.005	35.853	0.117	0.957	0.00005
164-6@2	7	MRM2012-03	164.6	-	2	16.177	0.004	15.495	0.004	35.423	0.190	0.958	0.00006
164-6@3	7	MRM2012-03	164.6	-	3	16.184	0.005	15.507	0.006	35.622	0.182	0.958	0.00006
164-6@4	7	MRM2012-03	164.6	-	4	16.215	0.013	15.549	0.013	35.747	0.132	0.959	0.00013
164-6@5	7	MRM2012-03	164.6	-	5	16.108	0.008	15.413	0.009	35.569	0.064	0.957	0.00010
E5-1-C1@01	5	E5		C1	1	16.191	0.004	15.530	0.005	36.289	0.067	0.959	0.00009
E5-1-C1@2	5	E5		C1	2	16.216	0.002	15.565	0.002	36.261	0.083	0.960	0.00003
E5-1-C1@3	5	E5		C1	3	16.201	0.002	15.544	0.002	36.073	0.064	0.959	0.00004
E5-1-C1@4	5	E5		C1	4	16.197	0.002	15.539	0.002	36.151	0.108	0.959	0.00003
E5-1-C1@5	5	E5		C1	5	16.220	0.003	15.572	0.004	36.209	0.037	0.960	0.00007
E5-1-C2@01	5	E5		C2	1	16.205	0.002	15.549	0.002	36.104	0.111	0.960	0.00004
E5-1-C2@02	5	E5		C2	2	16.214	0.002	15.562	0.002	36.344	0.205	0.960	0.00003
E5-1-C2@03	5	E5		C2	3	16.215	0.002	15.565	0.002	36.045	0.050	0.960	0.00003
E5-1-C2@04	5	E5		C2	4	16.177	0.003	15.511	0.004	35.994	0.082	0.959	0.00005
E5-1-C2@05	5	E5		C2	5	16.204	0.002	15.548	0.002	36.325	0.080	0.960	0.00004
E5-1-C2@06	5	E5		C2	6	16.209	0.002	15.556	0.002	36.280	0.095	0.960	0.00003
E5-1-C2@07	5	E5		C2	7	16.196	0.002	15.537	0.002	36.251	0.097	0.959	0.00005
E5-1-C2@08	5	E5		C2	8	16.194	0.003	15.534	0.003	36.028	0.163	0.959	0.00004
E5-1-C2@09	5	E5		C2	9	16.195	0.002	15.534	0.002	35.932	0.226	0.959	0.00003
E5-1-C2@10	5	E5		C2	10	16.206	0.002	15.549	0.002	36.057	0.100	0.960	0.00003
E5-1-C2@11	5	E5		C2	11	16.220	0.002	15.569	0.002	36.213	0.024	0.960	0.00003
E5-1-C3@01	5	E5		C3	1	16.140	0.007	15.455	0.007	35.915	0.146	0.958	0.00005
E5-1-C3@02	5	E5		C3	2	16.161	0.006	15.482	0.007	35.571	0.112	0.958	0.00015
E5-1-C3@03	5	E5		C3	3	16.168	0.004	15.490	0.005	36.427	0.170	0.958	0.00004
E5-1-C3@04	5	E5		C3	4	16.188	0.004	15.517	0.006	36.200	0.172	0.959	0.00012
E5-1-C3@05	5	E5		C3	5	16.145	0.009	15.468	0.012	36.022	0.257	0.958	0.00021
E5-1-C4@01	5	E5		C4	1	16.182	0.002	15.515	0.003	36.101	0.209	0.959	0.00005
E5-1-C4@02	5	E5		C4	2	16.170	0.002	15.497	0.002	36.067	0.307	0.958	0.00004
E5-1-C4@03	5	E5		C4	3	16.217	0.002	15.568	0.002	36.265	0.076	0.960	0.00003
E5-1-C4@4	5	E5		C4	4	16.185	0.002	15.523	0.003	36.168	0.085	0.959	0.00005
E5-1-C5@01	5	E5		C5	1	16.189	0.003	15.528	0.003	35.988	0.078	0.959	0.00006
E5-1-C6@01	5	E5		C6	1	16.201	0.002	15.546	0.002	36.107	0.081	0.960	0.00004
E5-1-C7@01	5	E5		C7	1	16.200	0.002	15.543	0.002	36.217	0.110	0.959	0.00004
E5-1-C7@02	5	E5		C7	2	16.209	0.002	15.555	0.002	36.290	0.084	0.960	0.00003
E5-1-C8@01	5	E5		C8	1	16.157	0.003	15.478	0.004	36.292	0.246	0.958	0.00011
E5-1-C8@02	5	E5		C8	2	16.171	0.003	15.503	0.003	35.943	0.076	0.959	0.00004
176-2-C1@01	4	MRM2012-03	176.2	C1	1	16.161	0.010	15.476	0.009	35.946	0.089	0.958	0.00005
176-2-C1@2	4	MRM2012-03	176.2	C1	2	16.192	0.003	15.529	0.003	35.907	0.160	0.959	0.00004
176-2-C1@3	4	MRM2012-03	176.2	C1	3	16.205	0.002	15.548	0.002	36.098	0.062	0.959	0.00005
176-2-C2@01	4	MRM2012-03	176.2	C2	1	16.172	0.003	15.504	0.003	36.111	0.051	0.959	0.00005
176-2-C2@2	4	MRM2012-03	176.2	C2	2	16.155	0.005	15.479	0.005	35.799	0.070	0.958	0.00004
176-2-C2@3	4	MRM2012-03	176.2	C2	3	16.190	0.003	15.531	0.003	36.332	0.129	0.959	0.00007
176-2-C2@4	4	MRM2012-03	176.2	C2	4	16.193	0.003	15.533	0.003	36.313	0.239	0.959	0.00004
176-2-C3@01	4	MRM2012-03	176.2	C3	1	16.170	0.003	15.496	0.003	35.861	0.053	0.958	0.00006
176-2-C3@2	4	MRM2012-03	176.2	C3	2	16.195	0.003	15.536	0.002	35.897	0.089	0.959	0.00004
176-2-C4@01	4	MRM2012-03	176.2	C4	1	16.195	0.002	15.536	0.002	36.188	0.061	0.959	0.00005
176-2-C4@2	4	MRM2012-03	176.2	C4	2	16.184	0.003	15.519	0.003	36.194	0.131	0.959	0.00004
176-2-C4@3	4	MRM2012-03	176.2	C4	3	16.191	0.002	15.534	0.002	36.044	0.093	0.959	0.00003
176-2-C4@4	4	MRM2012-03	176.2	C4	4	16.184	0.002	15.520	0.002	36.204	0.089	0.959	0.00003
176-2-C5@01	4	MRM2012-03	176.2	C5	1	16.207	0.002	15.554	0.002	36.059	0.050	0.960	0.00004
176-2-C6@01	4	MRM2012-03	176.2	C6	1	16.188	0.003	15.527	0.003	36.159	0.101	0.959	0.00006
176-2-C7@01	4	MRM2012-03	176.2	C7	1	16.210	0.002	15.557	0.002	36.345	0.076	0.960	0.00003
176-2-C7@2	4	MRM2012-03	176.2	C7	2	16.177	0.003	15.514	0.003	35.839	0.105	0.959	0.00004
191-C1@01	3	MRM2012-03	191	C1	1	16.182	0.002	15.517	0.003	36.072	0.155	0.959	0.00005
191-C1@2	3	MRM2012-03	191	C1	2	16.194	0.002	15.536	0.002	35.841	0.182	0.959	0.00004
191-C1@3	3	MRM2012-03	191	C1	3	16.215	0.002	15.564	0.002	36.145	0.044	0.960	0.00003
191-C1@4	3	MRM2012-03	191	C1	4	16.200	0.002	15.543	0.003	36.249	0.131	0.959	0.00005
191-C1@5	3	MRM2012-03	191	C1	5	16.199	0.002	15.540	0.003	36.349	0.115	0.959	0.00005
191-C1@6	3	MRM2012-03	191	C1	6	16.202	0.002	15.545	0.002	36.088	0.036	0.959	0.00003
191-C2@01	3	MRM2012-03	191	C2	1	16.199	0.004	15.540	0.005	35.803	0.125	0.959	0.00010
191-C2@2	3	MRM2012-03	191	C2	2	16.203	0.002	15.547	0.002	35.995	0.163	0.959	0.00004

Sample n°	Lens	Drill core or sample name	Depth (m)	Circle n°	Analysis n°	^{206}Pb / ^{204}Pb	Error (1σ)	^{207}Pb / ^{204}Pb	Error (1σ)	^{208}Pb / ^{204}Pb	Error (1σ)	^{206}Pb / ^{204}Pb	Error (1σ)
191-C3@01	3	MRM2012-03	191	C3	1	16.197	0.002	15.541	0.002	36.157	0.095	0.959	0.00004
191-C3@2	3	MRM2012-03	191	C3	2	16.190	0.002	15.526	0.002	36.383	0.102	0.959	0.00005
191-C4@01	3	MRM2012-03	191	C4	1	16.199	0.003	15.542	0.003	36.007	0.122	0.959	0.00005
191-C4@2	3	MRM2012-03	191	C4	2	16.197	0.002	15.537	0.002	36.091	0.103	0.959	0.00003
195-9Ac1@1	3	MRM2012-03	195.9A	C1	1	16.209	0.003	15.557	0.003	36.184	0.140	0.960	0.00005
195-9Ac1@2	3	MRM2012-03	195.9A	C1	2	16.155	0.003	15.481	0.003	35.795	0.104	0.958	0.00004
195-9Ac1@3	3	MRM2012-03	195.9A	C1	3	16.174	0.003	15.508	0.004	36.111	0.064	0.959	0.00007
195-9Ac2@1	3	MRM2012-03	195.9A	C2	1	16.137	0.004	15.454	0.004	35.803	0.102	0.958	0.00004
195-9Ac2@2	3	MRM2012-03	195.9A	C2	2	16.156	0.003	15.472	0.003	35.880	0.075	0.958	0.00003
195-9Ac3@1	3	MRM2012-03	195.9A	C3	1	16.190	0.002	15.526	0.003	35.924	0.315	0.959	0.00007
195-9Ac3@2	3	MRM2012-03	195.9A	C3	2	16.200	0.003	15.543	0.003	36.111	0.164	0.959	0.00005
195-9Ac3@3	3	MRM2012-03	195.9A	C3	3	16.204	0.003	15.549	0.003	36.093	0.165	0.960	0.00008
195-9Ac4@1	3	MRM2012-03	195.9A	C4	1	16.184	0.003	15.520	0.003	36.032	0.107	0.959	0.00003
195-9Ac4@2	3	MRM2012-03	195.9A	C4	2	16.210	0.002	15.556	0.002	36.288	0.123	0.960	0.00004
195-9Ac5@1	3	MRM2012-03	195.9A	C5	1	16.137	0.004	15.445	0.004	35.604	0.032	0.957	0.00006
195-9Ac5@2	3	MRM2012-03	195.9A	C5	2	16.200	0.002	15.543	0.002	36.162	0.180	0.959	0.00003
195-9Ac6@1	3	MRM2012-03	195.9A	C6	1	16.143	0.005	15.465	0.005	35.800	0.041	0.958	0.00007
195-9Ac6@2	3	MRM2012-03	195.9A	C6	2	16.185	0.002	15.520	0.003	36.164	0.128	0.959	0.00005
195-9Ac7@1	3	MRM2012-03	195.9A	C7	1	16.193	0.003	15.531	0.003	36.372	0.178	0.959	0.00005
195-9Ac7@2	3	MRM2012-03	195.9A	C7	2	16.206	0.003	15.551	0.003	36.220	0.127	0.960	0.00006
195-9Bc1@1	3	MRM2012-03	195.9B	C1	1	16.208	0.002	15.552	0.002	36.178	0.121	0.960	0.00003
195-9Bc1@2	3	MRM2012-03	195.9B	C1	2	16.205	0.002	15.548	0.002	36.269	0.134	0.959	0.00004
195-9Bc2@1	3	MRM2012-03	195.9B	C2	1	16.207	0.002	15.554	0.002	36.222	0.106	0.960	0.00003
195-9Bc2@2	3	MRM2012-03	195.9B	C2	2	16.192	0.003	15.529	0.003	36.091	0.167	0.959	0.00004
195-9Bc3@1	3	MRM2012-03	195.9B	C3	1	16.218	0.002	15.568	0.002	36.292	0.074	0.960	0.00003
195-9Bc4@1	3	MRM2012-03	195.9B	C4	1	16.208	0.002	15.553	0.002	36.146	0.077	0.960	0.00005
E11-1-C1@01	2	E11		C1	1	16.169	0.003	15.502	0.003	35.902	0.086	0.959	0.00003
E11-1-C1@02	2	E11		C1	2	16.131	0.005	15.454	0.004	36.021	0.115	0.958	0.00005
E11-1-C1@03	2	E11		C1	3	16.179	0.002	15.516	0.002	36.087	0.101	0.959	0.00004
E11-1-C1@04	2	E11		C1	4	16.167	0.003	15.495	0.003	36.030	0.112	0.958	0.00004
E11-1-C1@05	2	E11		C1	5	16.185	0.002	15.525	0.003	36.125	0.062	0.959	0.00005
E11-1-C1@06	2	E11		C1	6	16.159	0.003	15.487	0.003	36.005	0.069	0.958	0.00004
E11-1-C1@07	2	E11		C1	7	16.198	0.007	15.512	0.006	35.965	0.063	0.958	0.00005
E11-1-C1@08	2	E11		C1	8	16.184	0.003	15.524	0.003	36.059	0.139	0.959	0.00007
E11-1-C1@09	2	E11		C1	9	16.184	0.002	15.521	0.002	35.948	0.082	0.959	0.00003
E11-1-C1@10	2	E11		C1	10	16.146	0.003	15.465	0.003	36.045	0.245	0.958	0.00005
E11-1-C1@11	2	E11		C1	11	16.157	0.003	15.479	0.003	36.097	0.077	0.958	0.00005
E11-1-C1@12	2	E11		C1	12	16.137	0.004	15.448	0.004	35.787	0.060	0.957	0.00004
E11-1-C1@13	2	E11		C1	13	16.159	0.003	15.484	0.002	35.904	0.070	0.958	0.00004
E11-1-C1@14	2	E11		C1	14	16.156	0.003	15.483	0.002	35.948	0.083	0.958	0.00003
E11-1-C1@15	2	E11		C1	15	16.170	0.003	15.497	0.002	35.928	0.087	0.958	0.00005
E11-1-C5@01	2	E11		C5	1	16.167	0.003	15.497	0.003	35.832	0.132	0.959	0.00004
E11-1-C5@02	2	E11		C5	2	16.162	0.003	15.495	0.003	36.110	0.201	0.959	0.00004
E11-1-C5@03	2	E11		C5	3	16.170	0.004	15.498	0.006	35.812	0.133	0.959	0.00007
E11-1-C5@04	2	E11		C5	4	16.156	0.003	15.484	0.003	35.964	0.125	0.958	0.00004
E11-1-C5@05	2	E11		C5	5	16.147	0.003	15.470	0.003	35.849	0.161	0.958	0.00005
E11-1-C5@06	2	E11		C5	6	16.180	0.003	15.518	0.003	36.163	0.124	0.959	0.00004
E11-1-C5@07	2	E11		C5	7	16.170	0.003	15.505	0.003	35.966	0.054	0.959	0.00003
E11-1-C5@08	2	E11		C5	8	16.149	0.005	15.463	0.005	35.786	0.032	0.958	0.00005
E11-1-C5@09	2	E11		C5	9	16.157	0.003	15.487	0.004	35.854	0.084	0.958	0.00003
E11-1-C5@10	2	E11		C5	10	16.170	0.003	15.504	0.002	36.102	0.117	0.959	0.00004
E11-1-C5@11	2	E11		C5	11	16.142	0.004	15.451	0.004	35.697	0.050	0.957	0.00004
E11-1-C5@12	2	E11		C5	12	16.131	0.004	15.448	0.004	35.880	0.086	0.958	0.00003
E11-1-C5@13	2	E11		C5	13	16.175	0.003	15.509	0.003	36.158	0.105	0.959	0.00005
E11-1-C5@14	2	E11		C5	14	16.156	0.003	15.484	0.003	35.884	0.064	0.958	0.00009
E11-1-C5@15	2	E11		C5	15	16.173	0.003	15.510	0.003	35.957	0.111	0.959	0.00005
E11-1-C5@16	2	E11		C5	16	16.157	0.003	15.475	0.003	35.924	0.049	0.958	0.00005
E11-1-C5@17	2	E11		C5	17	16.147	0.003	15.468	0.003	35.885	0.205	0.958	0.00005

Sample n°	Lens	Drill core or sample name	Depth (m)	Circle n°	Analysis n°	^{206}Pb / ^{204}Pb	Error (1σ)	^{207}Pb / ^{204}Pb	Error (1σ)	^{208}Pb / ^{204}Pb	Error (1σ)	^{206}Pb / ^{204}Pb	Error (1σ)
E11-1-C5@18	2	E11		C5	18	16.164	0.003	15.494	0.003	36.003	0.191	0.959	0.00004
E11-1-C5@19	2	E11		C5	19	16.140	0.004	15.458	0.003	35.843	0.095	0.958	0.00004
E11-1-C5@20	2	E11		C5	20	16.194	0.002	15.534	0.002	36.085	0.032	0.959	0.00003
E11-1-C6@01	2	E11		C6	1	16.157	0.004	15.485	0.004	35.735	0.107	0.958	0.00007
E11-1-C6@02	2	E11		C6	2	16.180	0.003	15.508	0.004	35.834	0.139	0.959	0.00008
E11-1-C6@03	2	E11		C6	3	16.180	0.003	15.518	0.004	35.926	0.088	0.959	0.00008
E11-1-C6@04	2	E11		C6	4	16.153	0.003	15.480	0.004	35.849	0.116	0.958	0.00008
E11-1-C6@05	2	E11		C6	5	16.165	0.003	15.498	0.003	35.940	0.190	0.959	0.00004
E11-1-C6@06	2	E11		C6	6	16.140	0.004	15.461	0.004	36.139	0.166	0.958	0.00005
E11-1-C6@07	2	E11		C6	7	16.177	0.002	15.508	0.002	36.225	0.176	0.959	0.00006
E11-1-C6@08	2	E11		C6	8	16.192	0.002	15.531	0.002	36.102	0.046	0.959	0.00003
E11-1-C6@09	2	E11		C6	9	16.132	0.005	15.444	0.005	35.678	0.052	0.957	0.00007
E11-1-C6@10	2	E11		C6	10	16.152	0.003	15.475	0.003	35.942	0.095	0.958	0.00003
E11-1-C6@11	2	E11		C6	11	16.162	0.003	15.486	0.003	36.001	0.075	0.958	0.00004
E11-1-C6@12	2	E11		C6	12	16.162	0.003	15.488	0.003	35.788	0.078	0.958	0.00005
E11-1-C6@13	2	E11		C6	13	16.191	0.002	15.529	0.002	36.111	0.055	0.959	0.00004
E11-1-C6@14	2	E11		C6	14	16.171	0.003	15.508	0.003	35.995	0.099	0.959	0.00006
E11-1-C6@15	2	E11		C6	15	16.165	0.002	15.491	0.002	36.012	0.138	0.958	0.00006
E11-1-C6@16	2	E11		C6	16	16.163	0.003	15.484	0.003	35.801	0.088	0.958	0.00003
E11-1-C6@17	2	E11		C6	17	16.184	0.003	15.522	0.002	36.042	0.091	0.959	0.00004
E11-1-C6@18	2	E11		C6	18	16.148	0.003	15.471	0.003	35.919	0.043	0.958	0.00005
E11-1-C6@19	2	E11		C6	19	16.137	0.004	15.468	0.004	35.817	0.174	0.958	0.00004
E11-1-C6@20	2	E11		C6	20	16.182	0.003	15.517	0.003	36.067	0.049	0.959	0.00003
209-7-C1@01	0	MRM2012-03	209.7	C1	1	16.189	0.002	15.531	0.002	36.114	0.096	0.959	0.00004
209-7-C2@01	0	MRM2012-03	209.7	C2	1	16.180	0.004	15.521	0.005	36.030	0.082	0.959	0.00008
209-7-C2@2	0	MRM2012-03	209.7	C2	2	16.201	0.002	15.547	0.002	36.057	0.141	0.960	0.00004
209-7-C2@3	0	MRM2012-03	209.7	C2	3	16.197	0.003	15.543	0.003	35.940	0.163	0.960	0.00003
209-7-C2@4	0	MRM2012-03	209.7	C2	4	16.207	0.002	15.556	0.003	36.572	0.197	0.960	0.00005
209-7-C2@5	0	MRM2012-03	209.7	C2	5	16.201	0.002	15.548	0.002	36.158	0.084	0.960	0.00004
209-7-C3@01	0	MRM2012-03	209.7	C3	1	16.209	0.002	15.558	0.002	36.187	0.072	0.960	0.00003
209-7-C3@2	0	MRM2012-03	209.7	C3	2	16.202	0.002	15.550	0.002	36.162	0.117	0.960	0.00003
209-7-C4@01	0	MRM2012-03	209.7	C4	1	16.179	0.003	15.514	0.002	35.823	0.308	0.959	0.00004
209-7-C5@01	0	MRM2012-03	209.7	C5	1	16.176	0.004	15.507	0.005	36.033	0.104	0.959	0.00010
209-7-C5@2	0	MRM2012-03	209.7	C5	2	16.165	0.002	15.493	0.002	36.126	0.107	0.958	0.00006

***Supplementary Table 5-2**: Analytical results for lead isotope composition of the two standards of galena (ISH9 and Aloui) as determined by secondary ion mass spectrometry (SIMS).*

Sample n°	^{206}Pb / ^{204}Pb	Error (1σ)	^{207}Pb / ^{204}Pb	Error (1σ)	^{208}Pb / ^{204}Pb	Error (1σ)	^{206}Pb / ^{204}Pb	Error (1σ)
Gal_ISH9@1	17.617	0.0049	15.331	0.0049	37.868	0.0155	0.870208	0.00007
Gal_ISH9@2	17.622	0.0030	15.339	0.0030	37.866	0.0183	0.870334	0.00007
Gal_ISH9@3	17.622	0.0053	15.336	0.0050	37.899	0.0100	0.870287	0.00005
Gal_ISH9@4	17.612	0.0036	15.327	0.0036	37.881	0.0087	0.870259	0.00006
Gal_ISH9@5	17.619	0.0032	15.334	0.0034	37.885	0.0105	0.870340	0.00005
Gal_ISH9@6	17.614	0.0023	15.330	0.0031	37.862	0.0113	0.870263	0.00005
Gal_ISH9@7	17.624	0.0035	15.339	0.0033	37.899	0.0090	0.870378	0.00006
Gal_ISH9@8	17.612	0.0023	15.332	0.0026	37.885	0.0119	0.870441	0.00004
Gal_ISH9@9	17.620	0.0051	15.338	0.0050	37.882	0.0145	0.870539	0.00004
Gal_ISH9@10	17.616	0.0031	15.337	0.0030	37.878	0.0153	0.870545	0.00004
Gal_ISH9@11	17.618	0.0040	15.336	0.0037	37.875	0.0101	0.870505	0.00005
Gal_ISH9@12	17.614	0.0023	15.331	0.0021	37.832	0.0109	0.870420	0.00004
Gal_ISH9@13	17.622	0.0049	15.337	0.0048	37.873	0.0142	0.870357	0.00004
Gal_ISH9@14	17.624	0.0037	15.339	0.0038	37.872	0.0124	0.870298	0.00005
Gal_ISH9@15	17.638	0.0048	15.350	0.0044	37.887	0.0117	0.870327	0.00005
Gal_ISH9@16	17.634	0.0030	15.346	0.0032	37.899	0.0146	0.870282	0.00004
Gal_ISH9@17	17.625	0.0025	15.337	0.0024	37.870	0.0106	0.870230	0.00004
Gal_ISH9@18	17.626	0.0045	15.339	0.0044	37.864	0.0129	0.870287	0.00004
Gal_ISH9@19	17.634	0.0029	15.349	0.0027	37.898	0.0080	0.870416	0.00004
Gal_ISH9@20	17.624	0.0037	15.340	0.0032	37.928	0.0183	0.870421	0.00003
Gal_ISH9@21	17.621	0.0024	15.339	0.0022	37.870	0.0082	0.870552	0.00003
Gal_ISH9@22	17.620	0.0046	15.339	0.0043	37.839	0.0160	0.870543	0.00005
Gal_ISH9@23	17.615	0.0029	15.337	0.0036	37.833	0.0221	0.870565	0.00004
Gal_ISH9@24	17.623	0.0029	15.341	0.0029	37.864	0.0122	0.870492	0.00004
Gal_ISH9@25	17.629	0.0022	15.346	0.0031	37.868	0.0113	0.870449	0.00005
Gal_ISH9@26	17.636	0.0040	15.352	0.0041	37.879	0.0156	0.870465	0.00005
Gal_ISH9@27	17.629	0.0031	15.343	0.0029	37.869	0.0108	0.870330	0.00004
Gal_ISH9@28	17.628	0.0029	15.343	0.0028	37.874	0.0169	0.870378	0.00003
Gal_ISH9@29	17.617	0.0044	15.331	0.0039	37.853	0.0199	0.870241	0.00005
Gal_ISH9@29	17.622	0.0044	15.335	0.0039	37.862	0.0199	0.870241	0.00005
Gal_ISH9@30	17.622	0.0026	15.337	0.0026	37.864	0.0172	0.870292	0.00004
Gal_ISH9@31	17.621	0.0048	15.338	0.0041	37.868	0.0123	0.870579	0.00005
Gal_ISH9@32	17.620	0.0032	15.341	0.0029	37.844	0.0153	0.870675	0.00004
Gal_ISH9@33	17.631	0.0046	15.348	0.0042	37.872	0.0153	0.870527	0.00004
Gal_ISH9@34	17.634	0.0031	15.351	0.0030	37.884	0.0163	0.870534	0.00005
Gal_ISH9@35	17.633	0.0044	15.349	0.0042	37.866	0.0098	0.870492	0.00004
Gal_ISH9@36	17.625	0.0018	15.342	0.0020	37.855	0.0133	0.870475	0.00005
Gal_ISH9@37	17.639	0.0029	15.353	0.0033	37.883	0.0135	0.870387	0.00005
Gal_ISH9@38	17.638	0.0042	15.349	0.0043	37.854	0.0132	0.870385	0.00004
Gal_ISH9@39	17.633	0.0038	15.346	0.0041	37.893	0.0176	0.870451	0.00005
Gal_ISH9@40	17.638	0.0044	15.357	0.0046	37.930	0.0162	0.870529	0.00004

Sample n°	^{206}Pb / ^{204}Pb	Error (1σ)	^{207}Pb / ^{204}Pb	Error (1σ)	^{208}Pb / ^{204}Pb	Error (1σ)	^{206}Pb / ^{204}Pb	Error (1σ)
Gal_Aloui@1	18.019	0.0043	15.477	0.0043	37.900	0.0117	0.858987	0.00006
Gal_Aloui@2	18.017	0.0048	15.475	0.0046	37.903	0.0124	0.858900	0.00005
Gal_Aloui@3	18.026	0.0041	15.487	0.0048	37.923	0.0418	0.859038	0.00005
Gal_Aloui@4	18.032	0.0041	15.483	0.0036	37.922	0.0163	0.858882	0.00003
Gal_Aloui@5	18.017	0.0046	15.475	0.0046	37.884	0.0120	0.858936	0.00005
Gal_Aloui@6	18.013	0.0047	15.475	0.0038	37.897	0.0096	0.858963	0.00004
Gal_Aloui@11	18.024	0.0058	15.482	0.0053	37.889	0.0121	0.859011	0.00004
Gal_Aloui@12	18.029	0.0036	15.487	0.0034	37.889	0.0139	0.858943	0.00006
Gal_Aloui@13	18.020	0.0039	15.479	0.0036	37.889	0.0124	0.858996	0.00004
Gal_Aloui@14	18.024	0.0032	15.485	0.0026	37.895	0.0094	0.859029	0.00005
Gal_Aloui@15	18.018	0.0042	15.479	0.0039	37.867	0.0133	0.859034	0.00004
Gal_Aloui@16	18.021	0.0067	15.481	0.0061	37.888	0.0210	0.859010	0.00004
Gal_Aloui@17	18.009	0.0051	15.470	0.0047	37.862	0.0135	0.859019	0.00005
Gal_Aloui@17	18.015	0.0051	15.475	0.0047	37.874	0.0135	0.859019	0.00005
Gal_Aloui@18	18.032	0.0067	15.490	0.0065	37.896	0.0096	0.859017	0.00005
Gal_Aloui@19	18.022	0.0039	15.481	0.0036	37.885	0.0175	0.859002	0.00005
Gal_Aloui@20	18.044	0.0048	15.499	0.0042	37.894	0.0191	0.858946	0.00004
Gal_Aloui@21	18.031	0.0032	15.489	0.0027	37.895	0.0150	0.859026	0.00004
Gal_Aloui@22	18.023	0.0024	15.482	0.0027	37.884	0.0130	0.859011	0.00004
Gal_Aloui@23	18.026	0.0041	15.486	0.0034	37.893	0.0135	0.859014	0.00005
Gal_Aloui@24	18.027	0.0049	15.485	0.0045	37.862	0.0193	0.859005	0.00004
Gal_Aloui@25	18.018	0.0040	15.477	0.0039	37.876	0.0216	0.858991	0.00004
Gal_Aloui@26	18.013	0.0036	15.473	0.0034	37.853	0.0179	0.859023	0.00005
Gal_Aloui@27	18.015	0.0040	15.475	0.0042	37.877	0.0142	0.859035	0.00005
Gal_Aloui@28	18.028	0.0037	15.489	0.0030	37.908	0.0144	0.859062	0.00003
Gal_Aloui@29	18.025	0.0034	15.486	0.0037	37.901	0.0097	0.859027	0.00006
Gal_Aloui@30	18.023	0.0023	15.481	0.0024	37.880	0.0155	0.859063	0.00004
Gal_Aloui@31	18.020	0.0040	15.480	0.0034	37.889	0.0109	0.859102	0.00005
Gal_Aloui@32	18.015	0.0046	15.477	0.0044	37.858	0.0171	0.859108	0.00005
Gal_Aloui@33	18.005	0.0027	15.469	0.0029	37.842	0.0149	0.859047	0.00004
Gal_Aloui@34	18.009	0.0032	15.472	0.0030	37.863	0.0107	0.859073	0.00004
Gal_Aloui@35	18.015	0.0060	15.482	0.0050	37.912	0.0611	0.859388	0.00003
Gal_Aloui@36	18.029	0.0029	15.485	0.0031	37.896	0.0140	0.859017	0.00004
Gal_Aloui@37	18.023	0.0029	15.483	0.0024	37.894	0.0112	0.859083	0.00004
Gal_Aloui@38	18.016	0.0033	15.477	0.0029	37.847	0.0162	0.859073	0.00004
Gal_Aloui@39	18.016	0.0030	15.475	0.0027	37.952	0.0778	0.858998	0.00004
Gal_Aloui@40	18.026	0.0045	15.488	0.0037	37.882	0.0125	0.859112	0.00005

***Supplementary Table 5-3**: Location, age and composition and thickness of different felsic basement units of the McArthur Basin (Ahmad et al., 2013a; Page et al., 2000).*

Formation	Location	Age (Ma)	Lithology	Thickness	Reference
Cliffdale Volcanics	Murphy Inlier	coeval with Nicholson Granite complex	rhyolite, alkali rhyolite, dacitic lavas, ignimbrites and intrusions	> 4 km	Ahmad et al., 2013
Nicholson Granite complex	Murphy Inlier	1856 ±3; 1845 ±3	granite, quartz monzonite, granodiorite, monzonite, alkali granite	?	Page et al., 2000
Connellys Volcanics	Murphy Inlier	equivalent to Cliffdale Volcanics	rhyolite or rhyodacite	?	Ahmad et al., 2013
Murphy Metamorphics	Murphy Inlier	> ~ 1850	greenschist-facies metamorphosed shale and greywacke	?	Ahmad et al., 2013
Scrutton Volcanics	Scrutton Inlier	1851 ±7	volcanic rocks of rhyolitic to dacitic composition; sandstone and mudstone	> 1 km	Page et al., 2000
Urapunga Granite	Urapunga Inlier	1858 ±7	granite	?	Page et al., 2000
Mount Reid Rhyolite	Urapunga Inlier	1847 ±6	rhyolite	?	Page et al., 2000

5.6.4. Supplementary figures

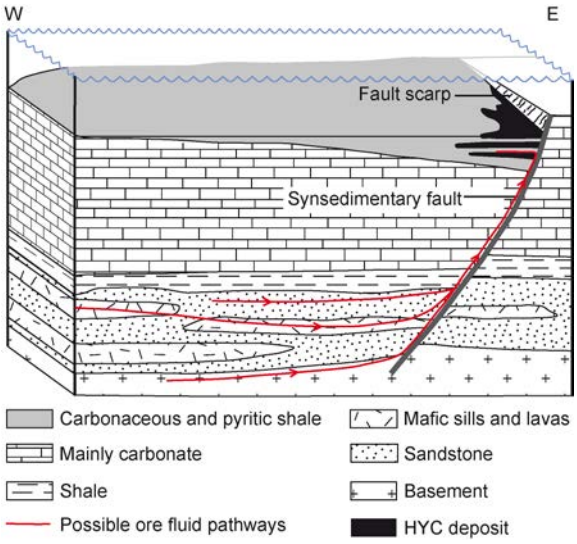

Supplementary Figure 5-1*: Schematic cross-section through the McArthur River deposit area. Cross section through the McArthur River deposit and Emu Fault at the time of deposit formation (1640 Ma). The units that potentially acted as metal source as well as the possible ore fluid pathways are represented. Modified after Large et al. (1998), Rawlings et al. (2004), Huston et al. (2006) and Wilkinson (2014).*

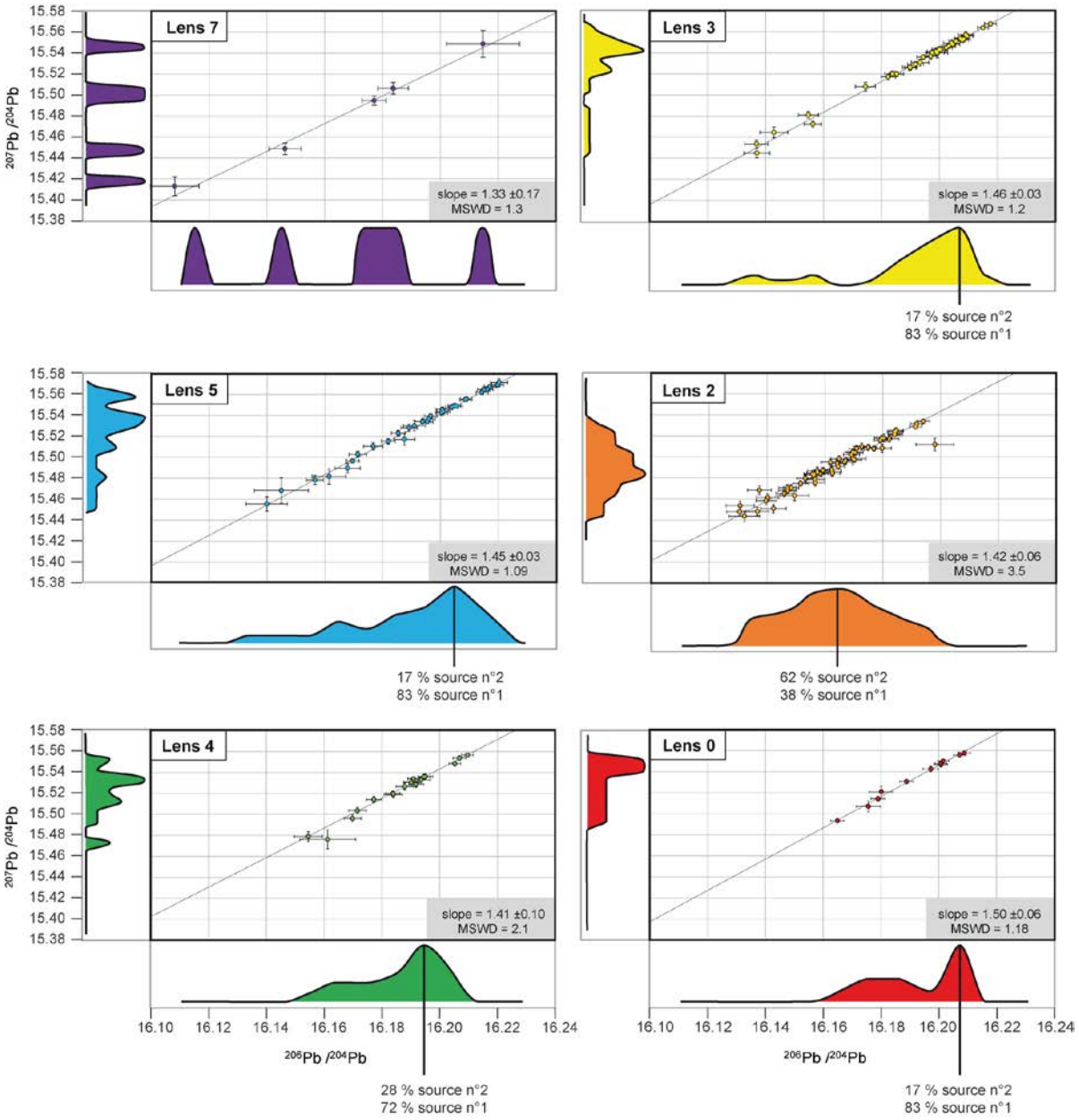

Supplementary Figure 5-2*: Lead isotope ratios plotted with 1σ error bars in the different lenses with the associated distribution fits. For each lens, the slope of the line is indicated as well as the mean square of weighted deviates (MSWD). According to the mode of the distribution fits, the contribution of each source can be calculated, based on the hypothesis that the Lead Source 1 isotopic ratios are 16.22 for $^{206}Pb/^{204}Pb$ and 15.572 for $^{207}Pb/^{204}Pb$, and 16.131 for $^{206}Pb/^{204}Pb$ and 15.448 for $^{207}Pb/^{204}Pb$ for Lead Source 2. For lens 7, there is not enough data to draw realistic distribution fits.*

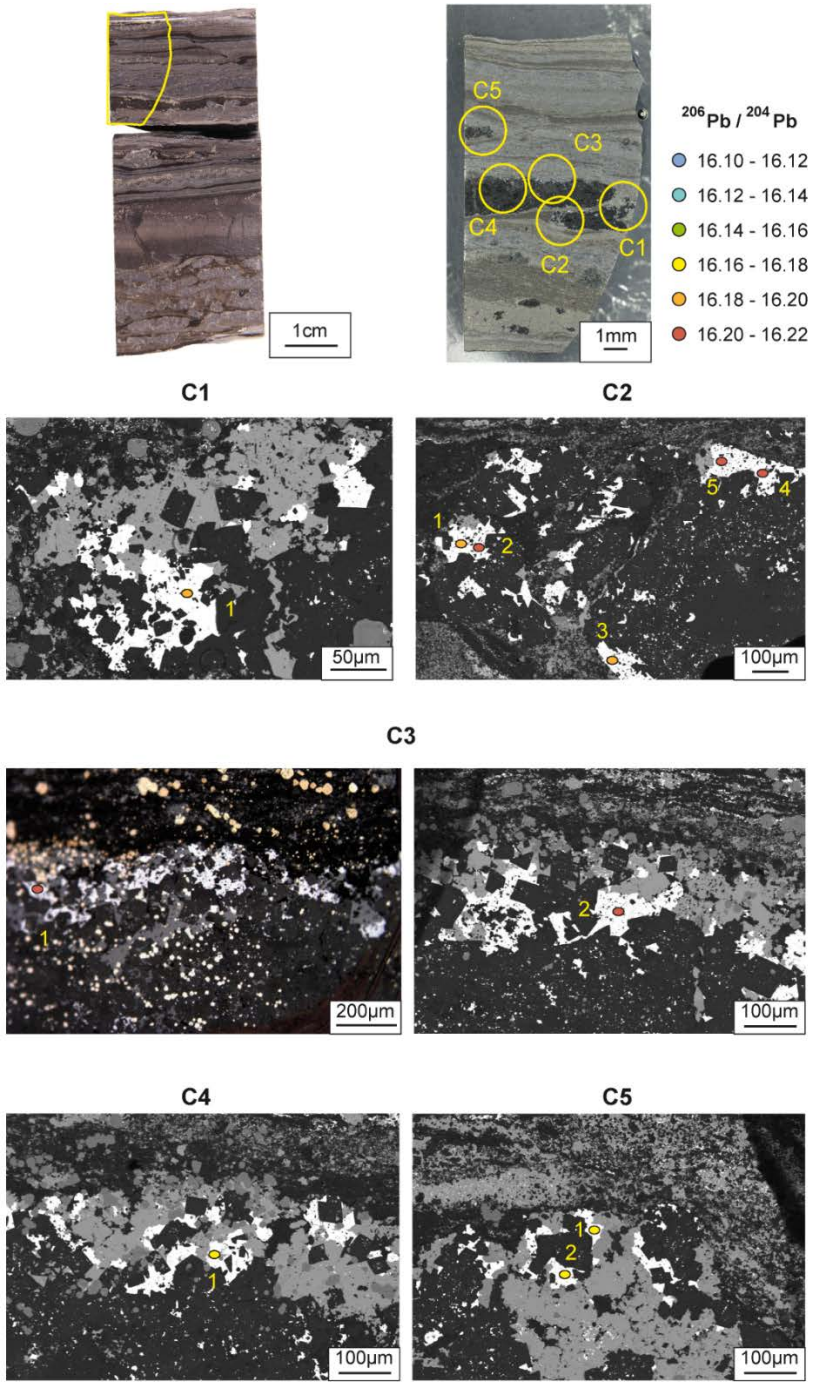

***Supplementary Figure 5-3**: Emplacement of the analysis in lens 0. The hand sample is presented, as well as the studied mounted section with the emplacement of the analysed circles. For each circle, analysed spots are plotted on SEM images (except the middle left image in reflective light by optical microscopy) with the corresponding $^{206}Pb/^{204}Pb$ ratio. Note that some ellipses representing the analysis spots have been enlarged compared to their real size.*

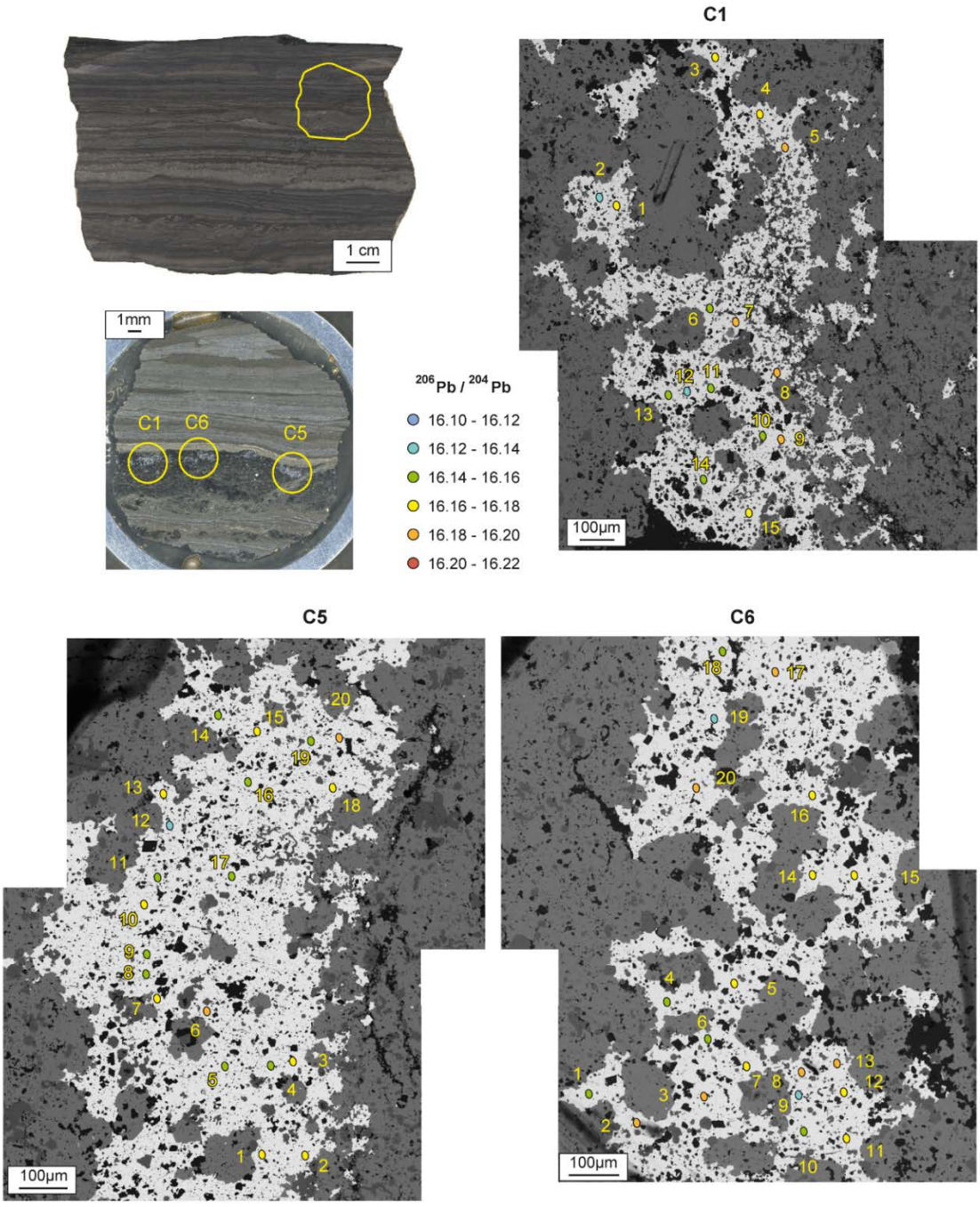

***Supplementary Figure 5-4**: Emplacement of the analysis in lens 2. The hand sample is presented, as well as the studied mounted section with the emplacement of the analysed circles. For each circle, analysed spots are plotted on SEM images with the corresponding $^{206}Pb/^{204}Pb$ ratio. Note that the ellipses representing the analysis spots have been enlarged compared to their real size.*

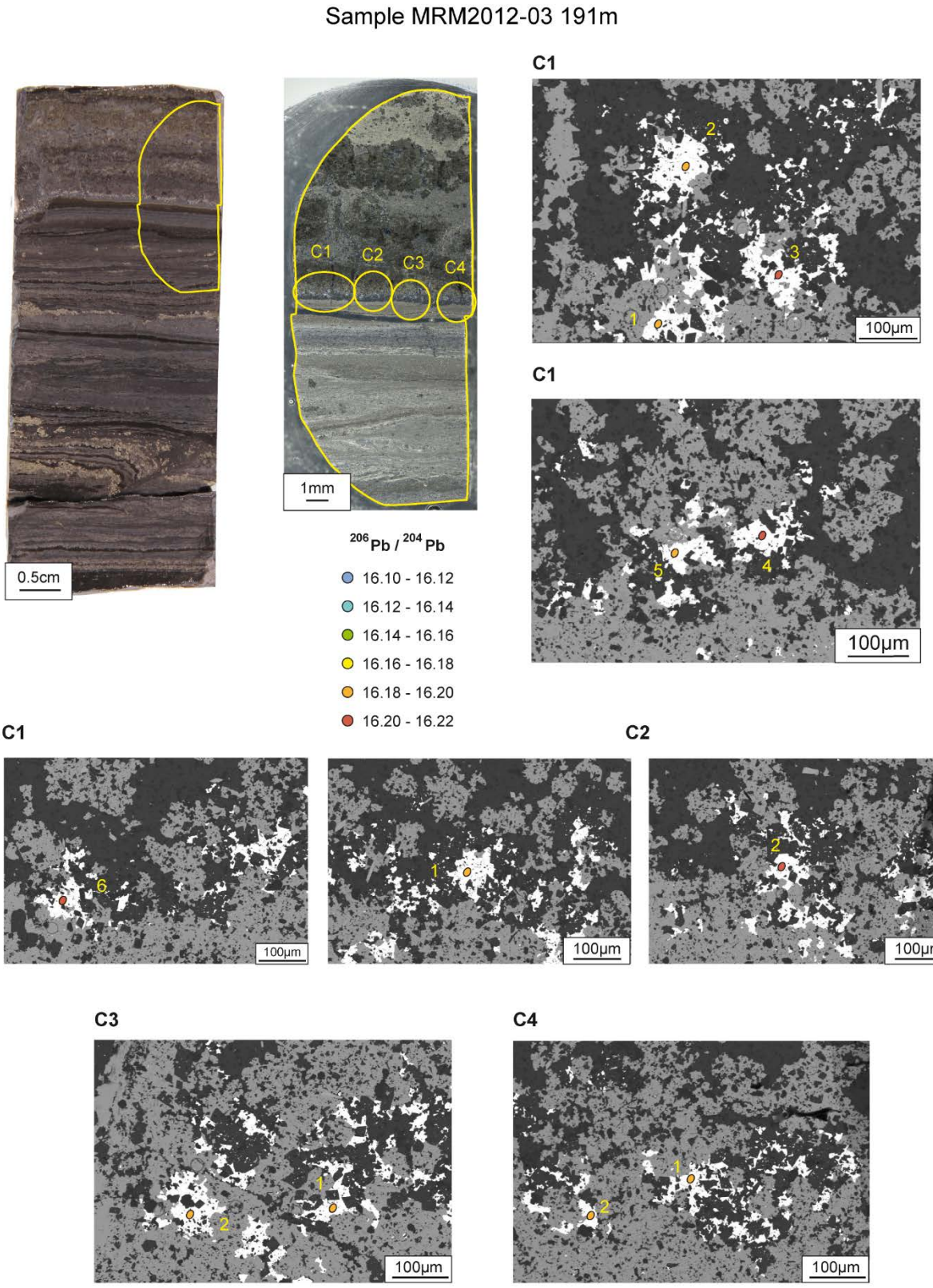
Sample MRM2012-03 191m
C1
C2
C3
C4
0.5cm
1mm
$^{206}Pb / ^{204}Pb$
16.10 - 16.12
16.12 - 16.14
16.14 - 16.16
16.16 - 16.18
16.18 - 16.20
16.20 - 16.22
100µm

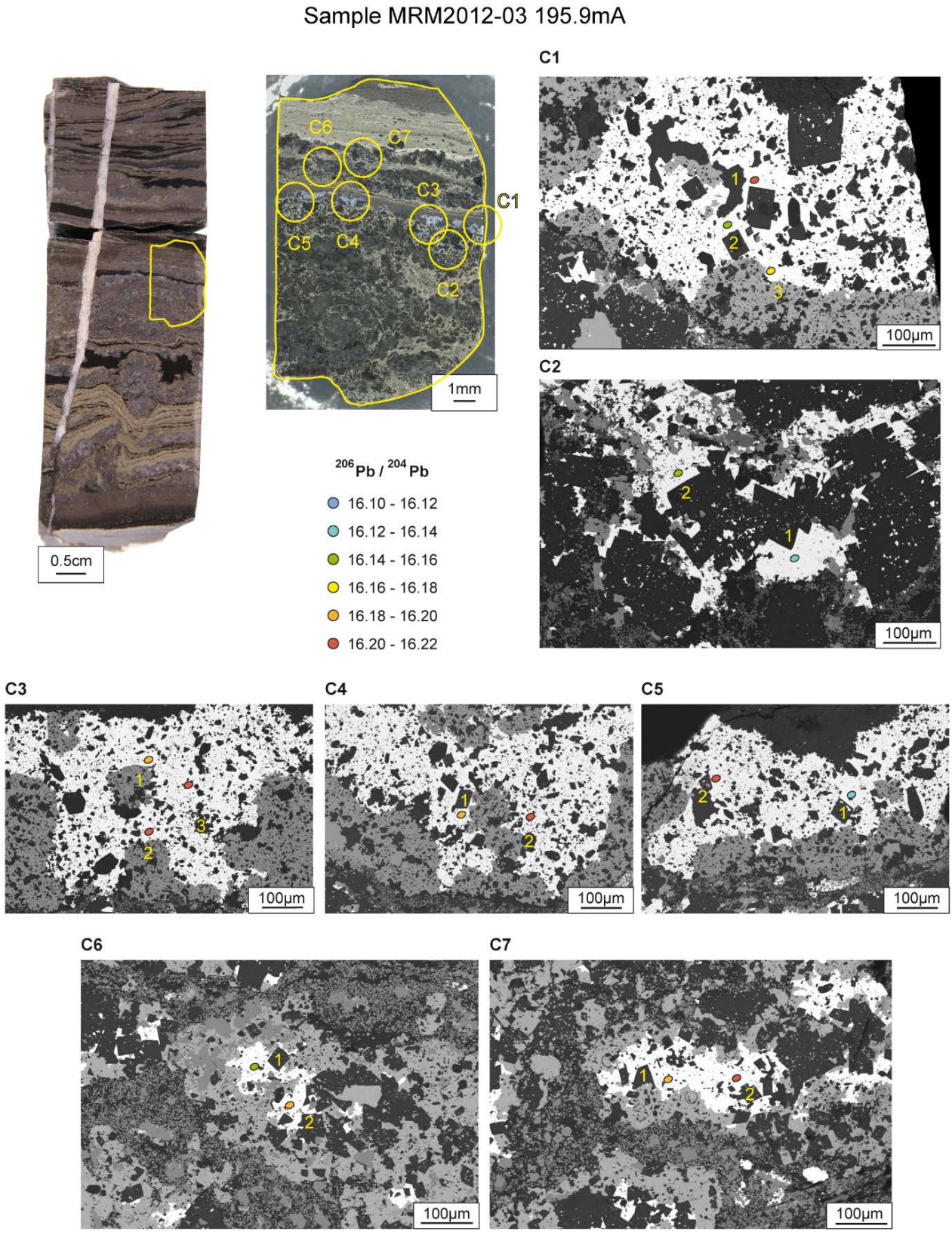
Sample MRM2012-03 195.9mA
0.5cm
C6
C7
C3
C1
C5
C4
C2
1mm
$^{206}Pb / ^{204}Pb$
16.10 - 16.12
16.12 - 16.14
16.14 - 16.16
16.16 - 16.18
16.18 - 16.20
16.20 - 16.22
C1
C2
C3
C4
C5
C6
C7
100µm

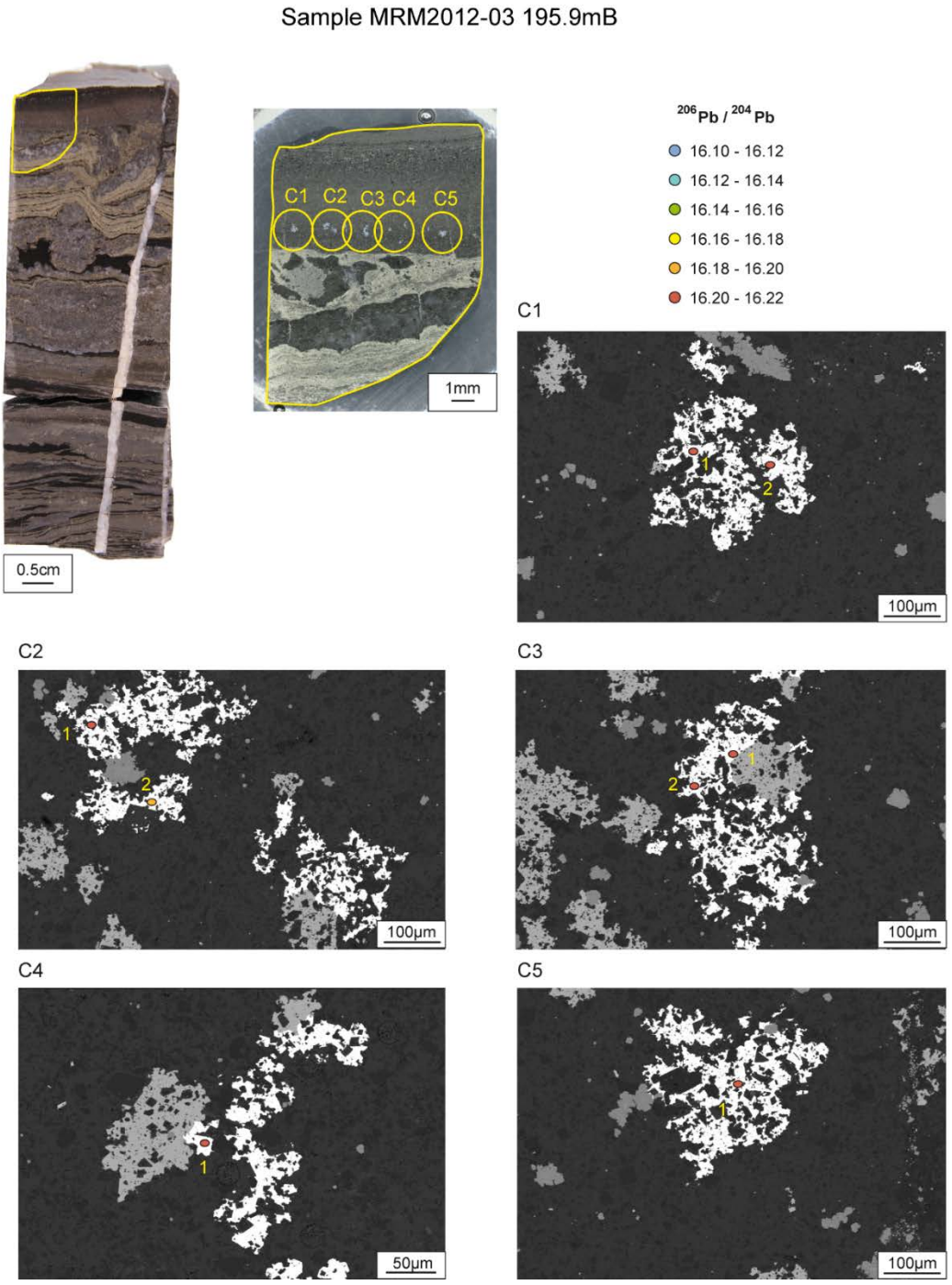

***Supplementary Figure 5-5**: Emplacement of the analysis in of samples MRM2012-3 191m, 195.9A and 195.9B in lens 3. For each sample, the hand sample is presented, as well as the studied mounted section with the emplacement of the analysed circles. For each circle, analysed spots are plotted on SEM images with the corresponding $^{206}Pb/^{204}Pb$ ratio.*

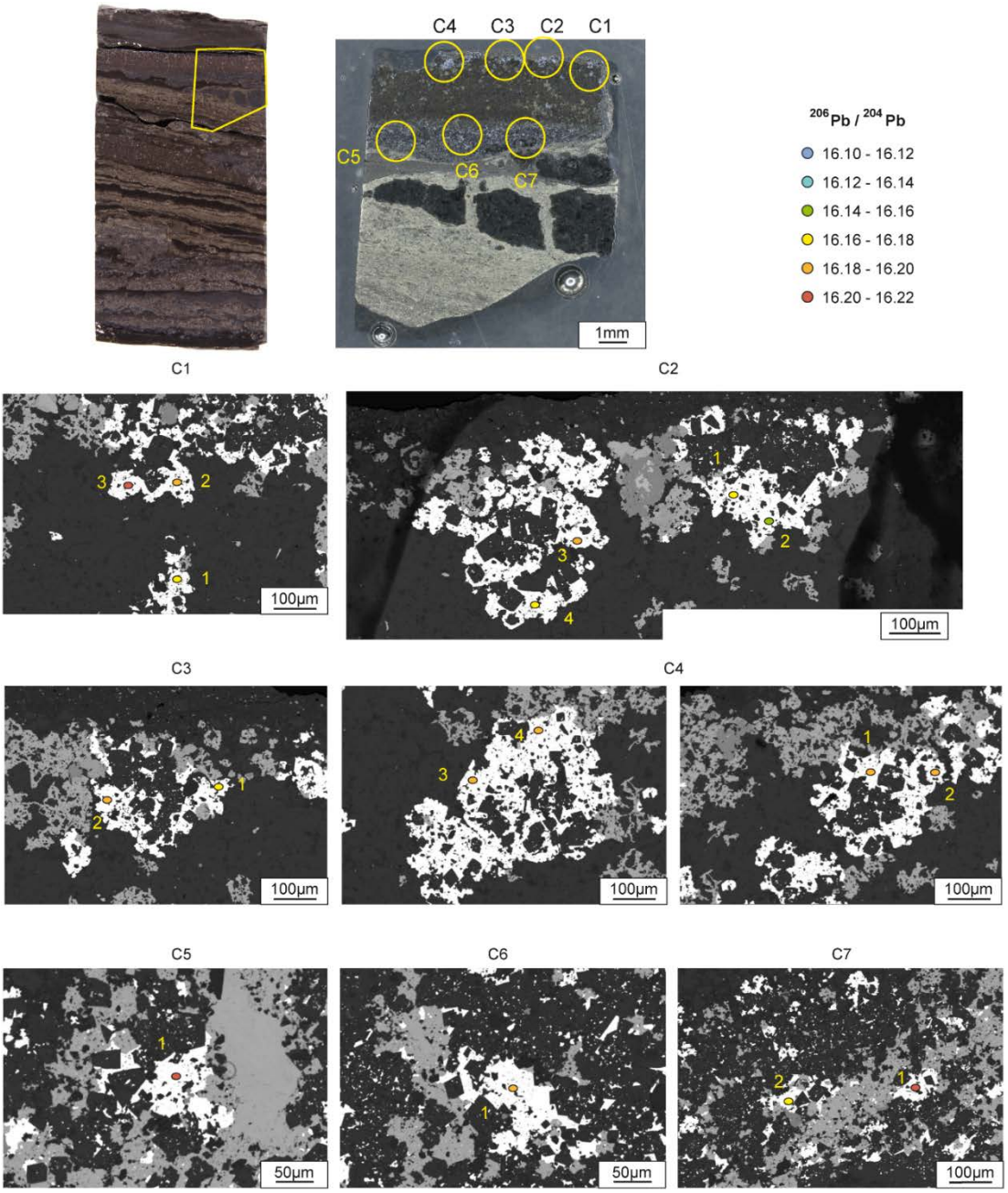

***Supplementary Figure 5-6**: Emplacement of the analysis in lens 4. The hand sample is presented, as well as the studied mounted section with the emplacement of the analysed circles. For each circle, analysed spots are plotted on SEM images with the corresponding $^{206}Pb/^{204}Pb$ ratio. Note that some ellipses representing the analysis spots have been enlarged compared to their real size.*

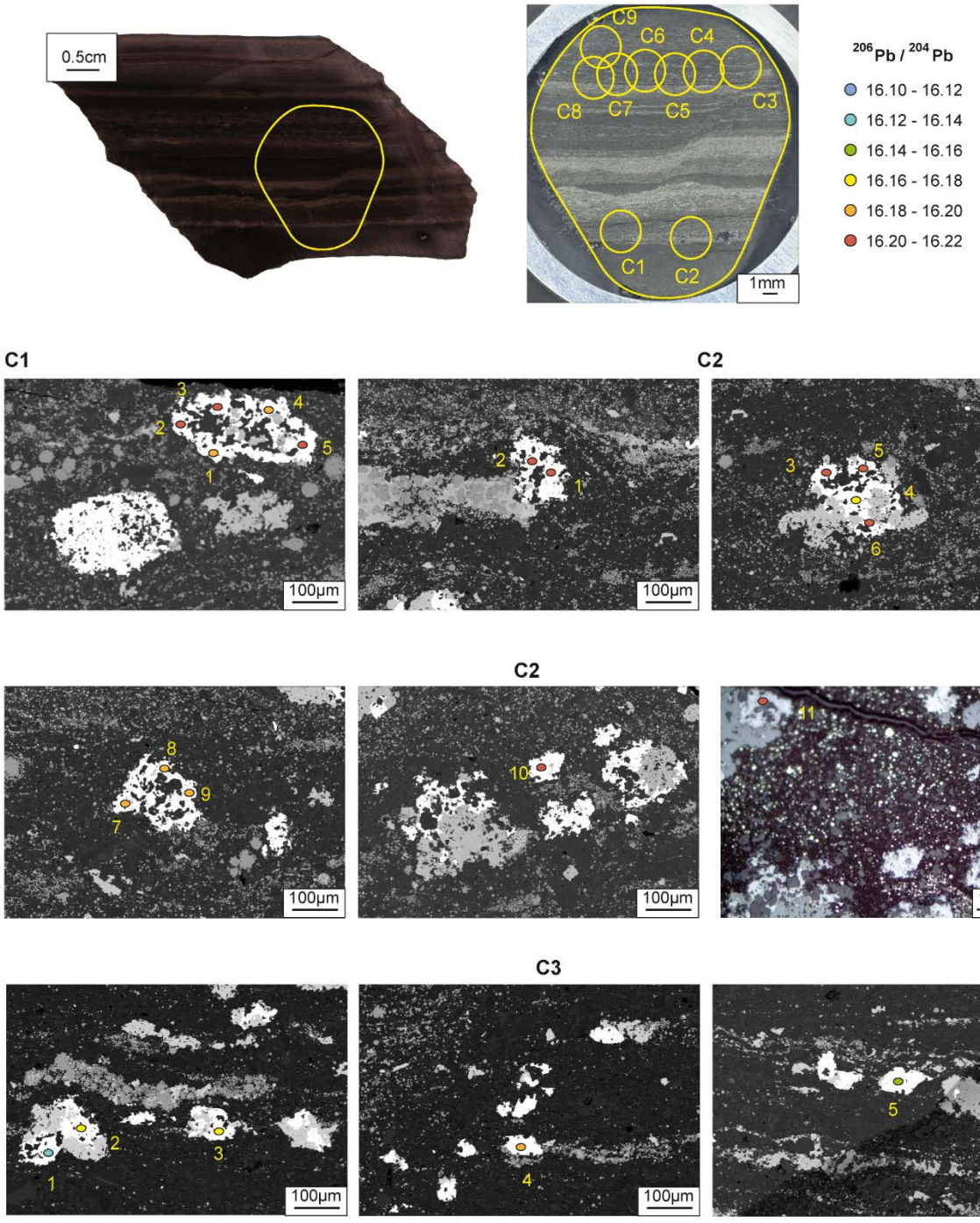
0.5cm
C9
C6
C4
C8
C7
C5
C3
C1
C2
1mm
^{206}Pb / ^{204}Pb
16.10 - 16.12
16.12 - 16.14
16.14 - 16.16
16.16 - 16.18
16.18 - 16.20
16.20 - 16.22
C1
C2
C2
C3
100µm

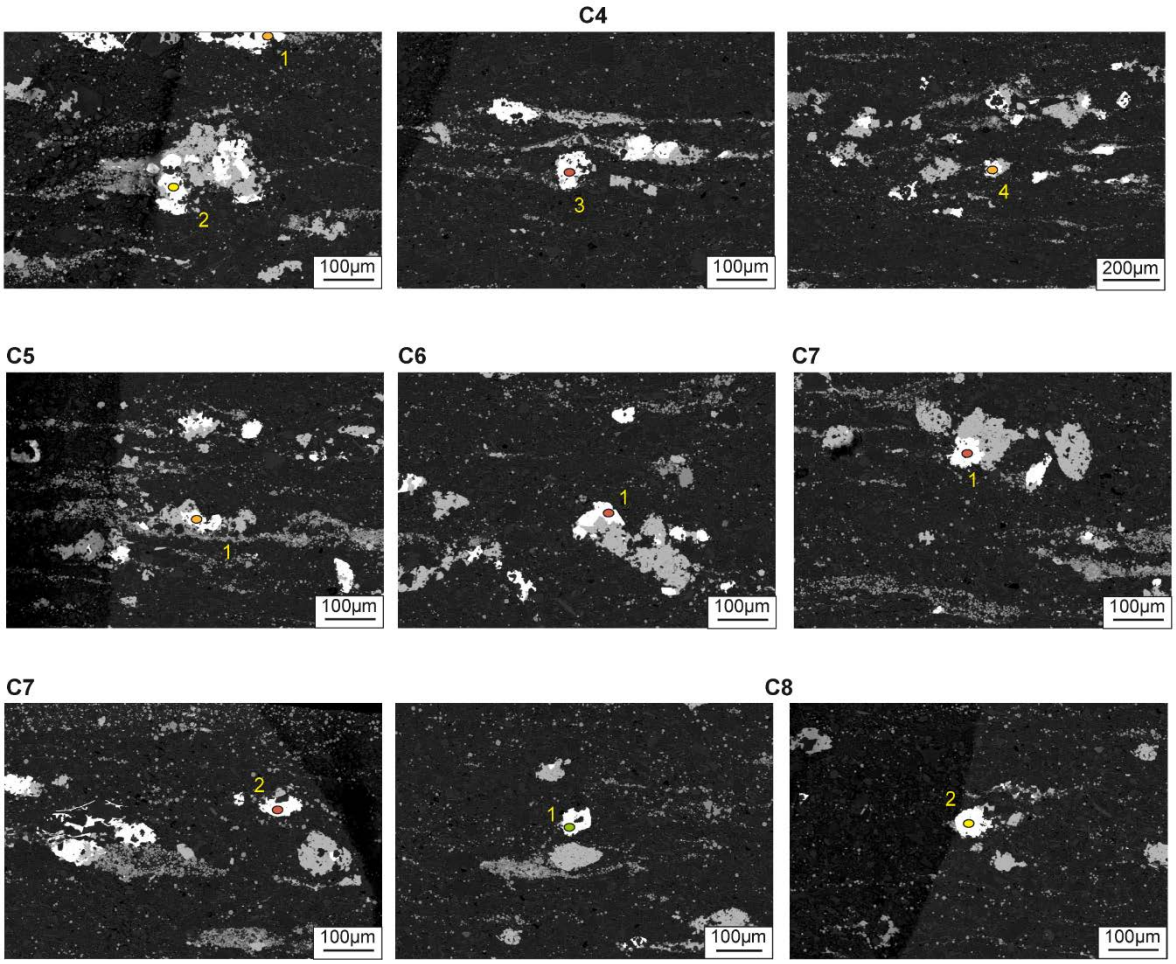

***Supplementary Figure 5-7**: Emplacement of the analysis in lens 5. The hand sample is presented, as well as the studied mounted section with the emplacement of the analysed circles. For each circle, analysed spots are plotted on SEM images (except the image for C2 to the left, reflective optical microscopy) with the corresponding $^{206}Pb/^{204}Pb$ ratio.*

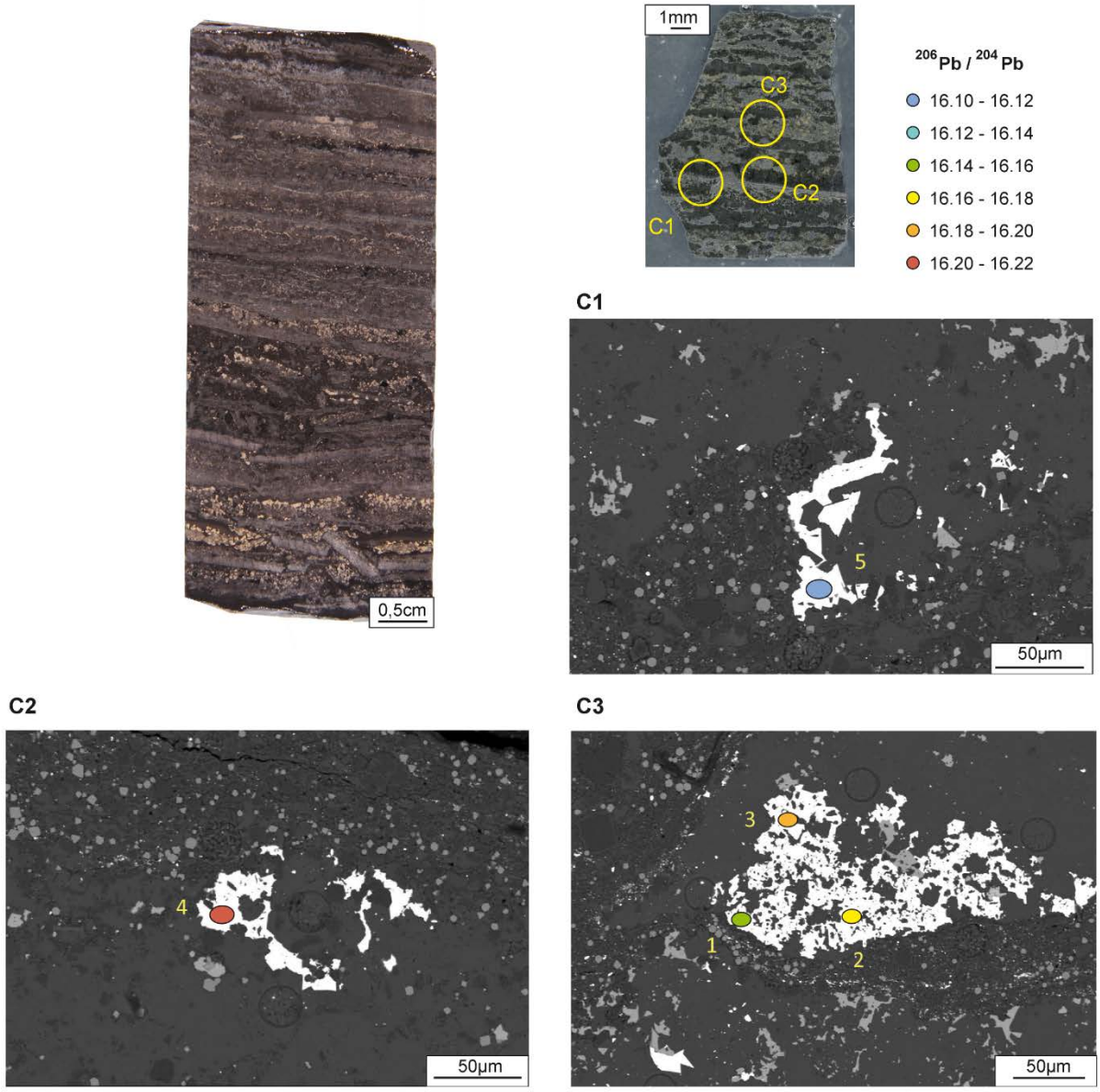

***Supplementary Figure 5-8**: Emplacement of the analysis in lens 7. The hand sample is presented, as well as the studied mounted section with the emplacement of the analysed circles. For each circle, analysed spots are plotted on SEM images with the corresponding $^{206}Pb/^{204}Pb$ ratio. Note that the mounted section was on the other side of the hand sample and can therefore not be represented on the hand specimen image.*

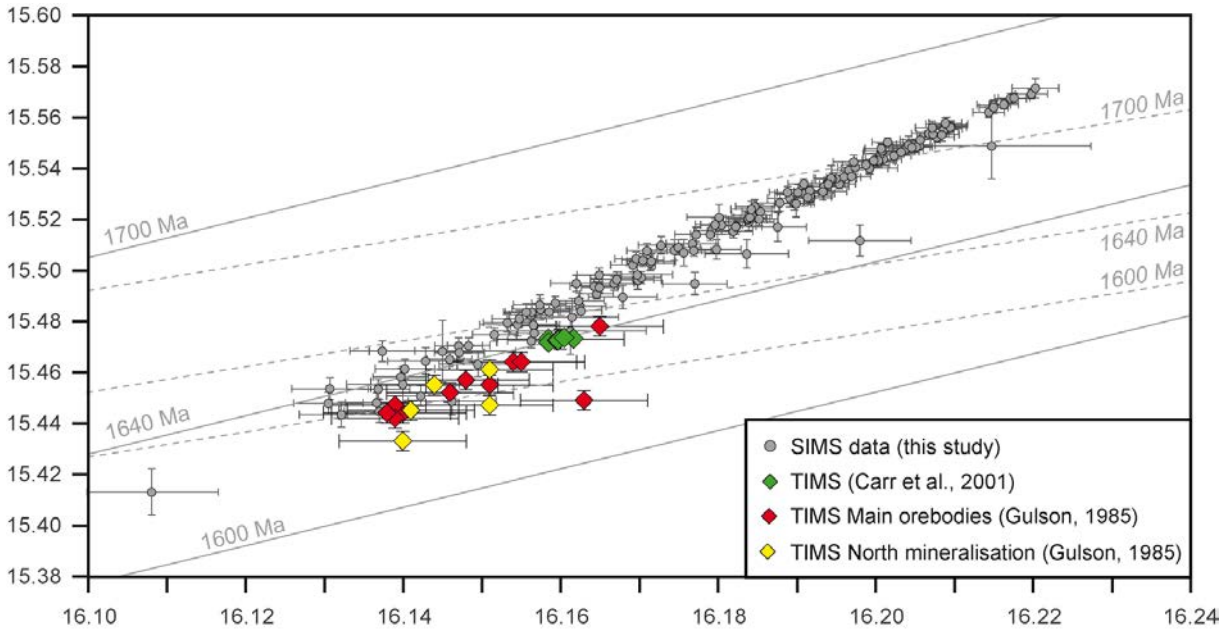

***Supplementary Figure 5-9**: TIMS and SIMS lead isotope composition of galena from the McArthur River zinc-lead deposit (Northern Territory, Australia). The in situ SIMS data from this study are in grey and bulk isotopic compositions of galena obtained by TIMS in coloured diamonds (Carr et al., 2001b; Gulson, 1985), all plotted with 1σ error bars. The isochrones (straight lines linking isotopic ratios corresponding to rocks or mineral having the same age) from different models (solid lines, Sun et al., 1996 and dashed lines, Stacey and Kramers, 1975) are indicated.*

Chapter 6. Proterozoic Pb-Zn mineralisation in the Batten Fault Zone and Lawn Hill Platform (Australia): insights from Pb isotopes and trace elements in sphalerite and galena

In preparation for *GCA*

Joséphine Gigon [1], Antonin Richard[1], Julien Mercadier[1], Etienne Deloule[2], Irvine R. Annesley[1], Andrew S. Wygralak[3], Roger G. Skirrow[4], Kristian Masterman[5], Nick Hayward[6], and Dan Johnson[7]

[1] Université de Lorraine, CNRS, GeoRessources Lab, F-54500 Vandœuvre-lès-Nancy, France

[2] CRPG, F-54501 Vandœuvre-lès-Nancy, France

[3] Northern Territory Geological Survey, PO Box 2901, Darwin, NT 0801, Australia

[4] Geoscience Australia, GPO Box 378, Canberra, ACT 2601, Australia;

[5] Glencore Australia Holdings Pty Ltd, Australia

[6] Teck Australia Pty Ltd. L2, 35 Ventnor Av., West Perth, WA 6005, WA 6872

[7] Aeon Metals, 51 Commercial Rd, Ryan, Mount Isa, QLD 4825

Preamble

In the previous chapter, the use of lead isotopes in galena to define the number of lead source(s) and their model ages has been demonstrated. In this chapter, this method is applied to deposits located at different distance from major faults, and even to a deposit located in another correlated basin. The analysed sulphides are from diverse paragenesis (stratiform/early diagenetic to late veins) and give insights on the range of mineralising events. This confirms the importance to get information on metal sources and timing, performed by the study of lead isotopes in galena from several deposits and prospects. The results reveal the input of at least three lead sources and the importance of a younger event (~1300 Ma) in deposits close to the major faults. Minor and trace elements in sphalerite and galena, in addition to being economically capital to be extracted as by-products, give precious insights on the conditions of sulphides formation. The temperature estimates decrease with time from 220 °C to less than 100 °C (minimum calibration).

This chapter corresponds to an article in preparation for *GCA.*

Préambule

Dans le chapitre précédent, l'utilisation des isotopes du plomb pour définir le nombre de source(s) du plomb et leur âge modèle a été démontrée. Dans ce chapitre, cette méthode est appliquée à des gisements situés à des distances variables des failles majeures (Caranbirini et Myrtle), ainsi qu'à un gisement d'un autre bassin corrélé stratigraphiquement (Walford Creek), situé dans la plateforme protérozoïque de Lawn Hill. Les sulfures analysés présentent des paragenèses variées (de stratiforme/diagénétique précoce à des veines tardives) et montrent la variété d'épisodes minéralisateurs. Ceci confirme l'importance d'obtenir des informations sur les sources des métaux et leur âge, grâce à l'étude des isotopes du plomb dans les galènes de plusieurs gisements ou indices. Les sulfures ont été analysés pour la première fois par LA-ICP-MS pour déterminer leur contenu en éléments mineurs et traces, et par SIMS pour leur composition isotopique. Les isotopes du plomb sur les galènes montrent la contribution d'au moins trois sources du plomb mobilisées lors d'évènements successifs. A HYC et Myrtle, les deux mêmes sources de plomb sont impliquées dans la minéralisation, alors qu'à Caranbirini et Walford Creek, proches des failles majeures, des évènements plus récents (~1300 Ma) impliquent une troisième source de plomb. En résumé, le premier évènement serait soit la cristallisation du socle vers 1850 Ma, soit la cristallisation de galène vers 1780 - 1760 Ma. Par la suite, un épisode minéralisateur majeur vers 1640 Ma a remobilisé cette première source de plomb ainsi qu'une autre provenant d'un réservoir crustal différent.

Enfin, un dernier évènement remobilisant le plomb des galènes formées vers 1640 Ma ainsi que du plomb provenant du même réservoir que celui qui les a formées a conduit à la cristallisation des derniers métaux de base. Entre 1640 et 1300 Ma, d'autres épisodes minéralisateurs pourraient avoir eu lieu, remobilisant le plomb de ce même réservoir, ou alors les données observées pourraient résulter uniquement d'un mélange entre deux sources du plomb mentionnées précédemment. Il semble y avoir un lien entre les sources du plomb et certains éléments mineurs et traces. Par exemple, Ag, As et Sb ont précipité du fluide transportant préférentiellement le plomb provenant d'une certaine source, qui transportait aussi de plus grandes quantités de métaux. Le contenu relatif en métaux des différents fluides peut être expliqué par des propriétés particulières des fluides, par la variabilité dans le temps et dans l'espace des conditions lors de la cristallisation des métaux et par les différents trajets qu'ils ont emprunté. Les températures semblent décroître avec le temps, de 220 °C à moins de 100 °C (limite inférieure de calibration). La composition en éléments traces confirme leur potentiel comme source de métaux critiques. La comparaison entre les données des différentes lentilles minéralisées à HYC et des autres gisements montre des dynamiques de minéralisation variables dans la zone d'étude. Les gisements situés à proximité des failles majeures enregistrent des évènements récents, mais la minéralisation stratiforme n'est plus visible, alors qu'à HYC par exemple la minéralisation stratiforme n'a pas été remobilisée par ces évènements plus jeunes, ce qui explique peut-être sa richesse en métaux.

Ce chapitre correspond à un article en préparation pour *GCA.*

Abstract

Besides their economic significance as potential by-products, minor and trace elements in sphalerite and galena can be useful indicators for ore-forming processes in Pb-Zn mineral systems. In addition, lead isotopes in galena provide valuable constraints on the number, nature and age of the lead source(s) as well as on the timing of lead mineralisation. Here, sphalerite and galena from the giant HYC deposit and nearby prospects or deposits (Caranbirini and Myrtle) of the Batten Fault Zone in the Proterozoic McArthur Basin, and from the Walford Creek deposit in the nearby Proterozoic Lawn Hill Platform (Australia) have been analysed for the first time by *in situ* Laser Ablation – Inductively Coupled Plasma – Mass Spectrometry (LA-ICP-MS) in order to determine their minor and trace element content, and by Secondary Ions Mass Spectrometry (SIMS) for their lead isotopic composition. Lead isotopes in galena indicate the involvement of at least three lead sources mobilised during successive events. At HYC and Myrtle, the same two lead sources are involved with the mineralisation, whereas at Caranbirini and Walford Creek, in close proximity to the major faults, younger events at ~1300 Ma involve a third lead source in addition to the two other sources identified at HYC and Myrtle. In summary, the first event would be either the crystallisation of the felsic basement around 1850 Ma or galena precipitation around 1780–1760 Ma. This was followed by the major mineralising event at 1640 Ma mobilising lead from this first lead source but also from another crustal reservoir. Finally, a last event remobilising lead from 1640 Ma galena and lead from the same reservoir they originate occurred to form the last base metal sulphides. Between 1640 and 1300 Ma, more events could have taken place mobilising lead from the same reservoir, or the observed data may result only from a mixing between two lead sources. There seems to be a link between the lead source and some of the minor and trace elements. For example, the Ag, As and Sb are precipitated from the fluid carrying preferentially the lead from Lead Source n°2, which also carried more metals. The relative metal content can be explained by different fluid properties, the variability of the conditions at the time of metal crystallisation in time and space, and the distinct fluid pathways. The geochemical signature of the sphalerite and galena from these lead-zinc deposits or prospects states decreasing formation temperature in the successive episodes (approximately from 220 °C to less than 100 °C). The composition of trace elements in sulphides highlights the potential critical element resources. The comparison between data from the different ore lenses at HYC and the other prospect and deposits indicate variable dynamics of the ore-forming systems in the study area. The deposits close to major fault zones have recorded later events and the stratiform mineralisation is no more observed, whereas at HYC for example the stratiform mineralisation was not overprinted by younger events, maybe explaining its metal abundance.

Keywords: Pb-Zn mineralisation, Proterozoic, Australia, lead isotopes, lead sources, minor and trace elements, sphalerite geothermometer

6.1. Introduction

Minor and trace elements in sphalerite and galena and lead isotopes in galena are precious forensic indicators to better understand the metals formation conditions (i.e. the source(s) of metals, composition and temperature of the ore-forming fluids) and can be extracted as by-products of Zn and Pb respectively. Having a precise idea of the minor and trace elements concentration and repartition in the host mineral is crucial for the mining companies to enhance their recovery. Some of them (e.g. Ga, Ge, In in sphalerite) are essential for green technologies and have been classified as critical raw materials by many countries because of their high risks of supply shortage and impact on the economy (Hayes and McCullough, 2018). Minor and trace elements in sphalerite are known to be highly variable and characteristics of the deposit type (Frenzel et al., 2016). Sphalerite incorporates many metals (Cu^{2+}, Ni^{2+}, Co^{2+}, Fe^{2+}, Mn^{2+}, Ge^{2+}, and Cd^{2+}) into its structure as they have a Z/R ratio of close to Zn^{2+}. However, more complex substitution are common, implying for example Ag, In, Ga, Sn or Tl (Belissont et al., 2014; Bonnet et al., 2016; Cook et al., 2009; Johan, 1988; Ye et al., 2011). The more common substitutions in galena are $2Ag^{+} = Pb^{2+}$ and coupled substitutions of $Ag^{+} + Sb^{3+}$, $Ag^{+} + Bi^{3+}$, and $Ag^{+} + As^{3+}$ (Renock and Becker, 2011). Instead of Ag, the substitution can also occur with Au and Cu. In a compilation of analyses from different deposit styles, George et al. (2015) highlighted a clear correlation between (Bi + Sb) and (Ag + Cu + Tl).

The lead isotopes results and their distribution in a sample provide insights on the number of lead sources and on their timing. In the HYC deposit, Gigon et al. (submitted) identified two lead sources mobilised to form this world-class-deposit. This present study expands the framework to see if the same sources were implied in different deposits and at different distances from major faults, and if minor and trace elements on one side and lead isotopes on the other side are correlated. A resultant question is if every metal-rich fluid, carrying lead from a specific lead source, has transported precise metals.

All the studied areas are within the Carpentaria Zinc Belt which hosts several world-class base metals deposits: Mount Isa, Hilton, George Fisher and Century in Queensland and HYC in the Northern Territory (Ahmad and Munson, 2013). The studied areas for this study are unmetamorphosed according to the metamorphic facies of Blake (1987), refined by the description of Foster and Rubenach (2006). The Paleo- to Mesoproterozoic McArthur Basin (Northern Territory, Australia) is exposed over an area of about 180 000 km² and is a favoured

target for the study because of the abundance of mineralisation from different styles: it hosts world-class and minor Pb-Zn resources that belong to the stratiform Sediment Hosted Massive Sulphide (SHMS) and vein categories, especially within the Batten Fault Zone (Ahmad and Munson, 2013). To the South, just across the Murphy Inlier, the Lawn Hill Platform, equivalent to the McArthur Basin, is also sulphide-rich area. In an attempt to document the minor and trace element variability of Pb-Zn occurrences located at different places in a major fault system, the HYC and Myrtle deposits and the Caranbirini prospect located in the Batten Fault Zone have been sampled (Figure 6-1), as well as the Walford Creek deposit in the Lawn Hill Platform. These deposits or prospects were favoured because their mineralisation style is variable and corresponds to successive mineralising events. The primary mineralisation is thought to be synsedimentary or early diagenetic, and probably formed at ca. 1640 Ma, the age of the host sequences (Page et al., 2000, 1994; Page and Sweet, 1998). The HYC deposit is exploited and its timing is bracketed, but the timing of younger events such as late veins is not constraint. Moreover, the deposits in the Batten Fault Zone are in the same sub-basin but at specific distances from a major fault zone that could have played a role in the deposition and remobilisation of some of the mineralised zones. This study aims to better characterise the sulphides hosting minor and trace elements, as well as their grade in the host mineral.

6.2. Geological settings and sampling

6.2.1. Regional geology

The McArthur and South Nicholson basins, and the Mount Isa Inlier (Northern Territory and Queensland, Australia), present spatial, stratigraphic and structural correlations, and could have corresponded to the same large sedimentary complex (Large et al., 2005a; Polito et al., 2006a; Southgate et al., 2006). The sedimentary basins unconformably overly the basement composed of Archean and Paleoproterozoic metamorphosed and deformed rocks such as the Murphy Province between the MacArthur Basin and the Mount Isa Inlier. The Murphy Inlier includes Paleoproterozoic metasedimentary, volcanic and felsic intrusive rocks. The comagmatic felsic intrusive and volcanic rocks were emplaced at 1860–1845 Ma (Ahmad and Munson, 2013; Page et al., 2000). The McArthur Basin is located in the north-eastern Northern Territory and contains a succession of sandstones, volcanic rocks, stromatolitic and evaporitic carbonate rocks and shale (Ahmad and Munson, 2013). Its deposition occurred in a variety of environments (lacustrine, fluvial, alluvial, deltaic, and shallow marine). The Lawn Hill Platform comprises sedimentary and volcanic strata.

The more recent study, based on deep seismic reflection imaging combined with geochronological, paleomagnetic and stratigraphic data in the Mount Isa Region indicate that the world class sediment-hosted Pb–Zn deposits of northern Australia are preferentially concentrated in the post-extensional syn-inversion fraction of the Calvert and Isa superbasins (Gibson et al., 2017). The origin of this tectonic context is linked to crustal shortening and supercontinent assembly leading to the reactivation of earlier-formed extensional faults, leading to upward expulsion of mineralising fluids at or close to the seafloor. Other authors favour an extensional faulting in a back-arc setting to create the trough (Betts et al., 2003). Several events postdating the basins emplacement could have affected these units. Most of them correspond to orogenesis occurring hundreds of kilometres away such as the 1330–1100 Ma Albany-Fraser and Musgravian orogenies (Myers et al., 1996), and the closest one to the studied areas is the Isan Orogeny (1640–1490 Ma, with the peak around ca 1590 Ma, Murphy et al., 2011).

The two areas which are the focus of this study are the Batten Fault Zone in the McArthur Basin and the Walford Creek deposit in the Lawn Hill Platform (Figure 6-1A).

6.2.2. The Batten Fault Zone of the McArthur Basin

From a structural point of view, the sampled Pb-Zn deposits/prospects in the McArthur Basin are located in the Batten Fault zone that corresponds to a north-south trending half graben, bounded by the Tawallah and Emu faults. Several sub-basins were identified by McGoldrick et al. (2010), corresponding to small individual depocenters during rock deposition. The sub-basins location was controlled by movement along ~north-south−trending faults. All the samples or this study are within 15 km from the Emu Fault, a major strike-slip basement-rooted crustal structure reaching 10 km in depth (Figure 6-1B, McGoldrick et al., 2010; Rawlings et al., 2004). The host formation of the primary stratiform mineralisation is the Barney Creek Formation and structural evidence suggests that the McArthur Basin was seismically active during its deposition (Garven et al., 2001). Zircons from three samples of tuffaceous sediments have yielded SHRIMP ages of 1640 ± 4, 1639 ± 3 and 1638 ± 7 Ma for this formation (Page et al., 2000; Page and Sweet, 1998). It has a wide regional extent, but thick sections are preserved only along the Emu Fault Zone (Logan et al., 2001). This fault and other major framing structures had the potential to act as fluid conduits to introduce basinal brines into the reduced sedimentary traps (Garven et al., 2001). Hydrologically, the Tawallah sandstones and Emu Fault Zone are key elements for ore genesis at HYC (Garven et al., 2001). In almost all the models proposed for fluid circulation in the studied area, fluids were moving down the Tawallah Fault (to the West) and up the Emu Fault (to the East, Garven et al., 2001). In more

details, these authors proposed three models for fluid circulation in the Batten Fault Zone: a topography-driven one, a density-driven hydrologic flow and a fault valve behaviour in which around 300–1000 major seismic events would be required to account for the total accumulation of ore at HYC. However, the tectonic settings along the Emu Fault at the time of the major mineralising event remains controversial.

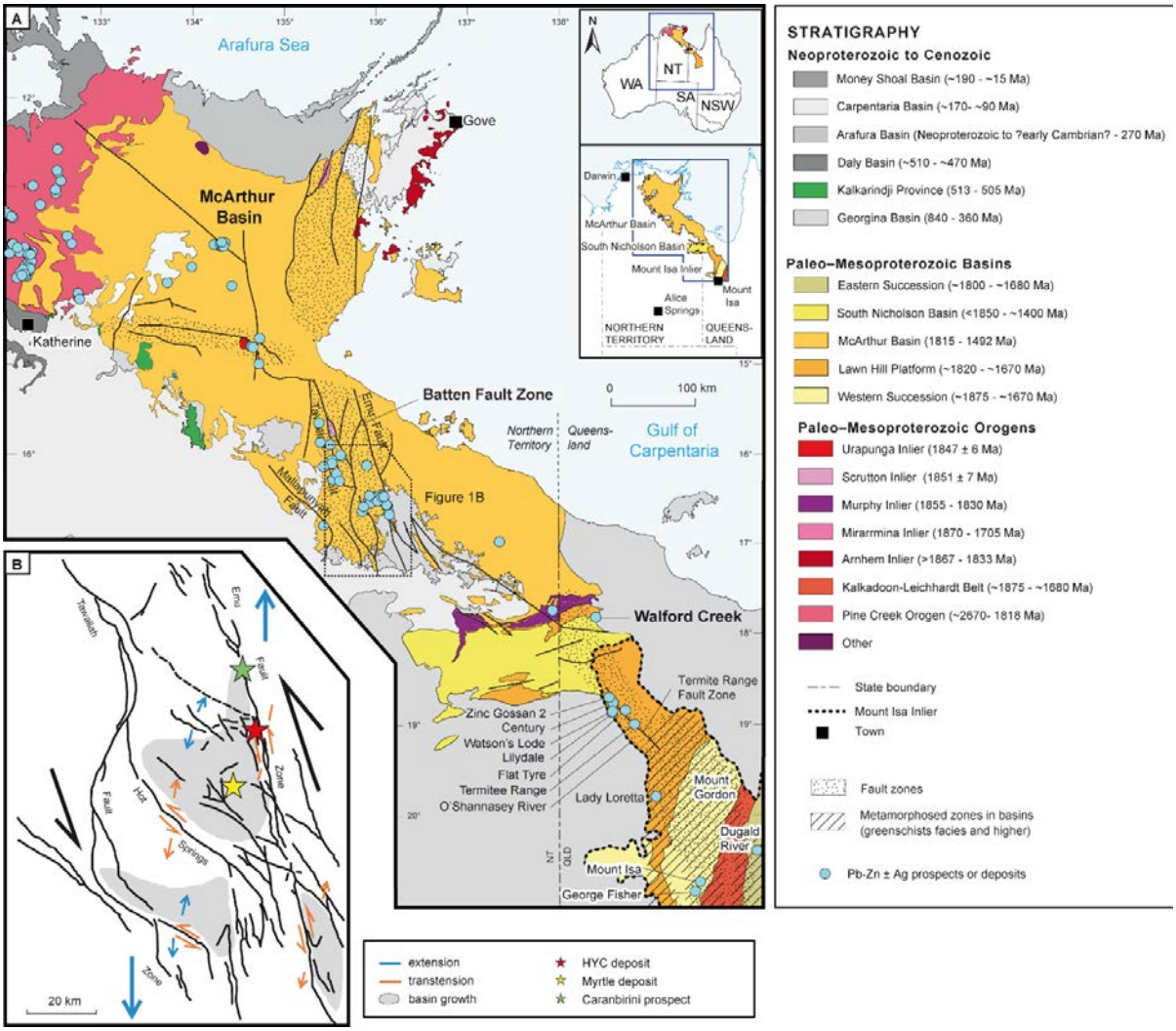

***Figure 6-1**: Location of the three studied deposits/prospects in the Batten Fault Zone and in the Lawn Hill Platform (**A**) Simplified geological map of the McArthur and South Nicholson basins, Lawn Hill Platform and Mount Isa Inlier (Northern Territory and Queensland, Australia). The crystalline basement, the Paleo-Mesoproterozoic basins, the more recent sedimentary cover and the major faults and faults zones are indicated including the Batten Fault Zone (one of the studied areas). Modified after Ahmad and Munson (2013). (**B**) Structural map of the Batten Fault Zone and emplacement of the sub-basins and sampled locations. After McGoldrick et al. (2010) and Mukherjee and Large (2017).*

6.2.3. The Lawn Hill Platform

The Lawn Hill Platform comprises sedimentary and volcanic strata. It is widely developed in the Lawn Hill region of Queensland and extends northwestward into the Northern Territory, where it occurs as narrow belts of east-trending outcrops separated by the South Nicholson Basin (Figure 6-1, Ahmad and Munson, 2013). A northern succession extends along the southern margin of the Murphy Inlier and a southern succession is exposed in areas along the southern margin of the South Nicholson Basin. The succession unconformably overlies mainly the Murphy Province and is unconformably overlain by the South Nicholson Basin. The term 'platform' implies that this terrane evolved under relatively stable tectonic conditions, even if it is known to be folded and faulted in the Queensland portion (Ahmad et al., 2013 and references herein). The host formation of the Walford Creek deposit is the Mount Les Siltstone that conformably overlies the Walford Dolostone and is disconformably overlain by the Doomadgee Formation (Sweet and Slater, 1975). The Mount Les Siltstone consists of dolostone, siltstone, shale and minor interbeds of flaggy dolostone with gypsum and pyrite pseudomorphs (Ahmad and Wygralak, 1989). Zircons from the tuffaceous bed have been dated by the SHRIMP U-Pb method at 1640 ± 7 Ma (Page et al., 1994).

6.2.4. Sampling strategy

The HYC deposit is the Pb-Zn world-class deposit of the McArthur Basin, and is therefore the privileged deposit to start the study. It has been evidenced that two lead sources were mobilised to form this deposit (Gigon et al., accepted). The Myrtle and HYC deposits shares the same sub-basin (McGoldrick et al., 2010) but the Myrtle deposit presents slightly different mineralising styles (see hereafter) whose timing is not constraint. However, it is of great interest to know if all the mineralisation occurred in a short period of time or if it is the results of several fluid events to enhance the exploration results. The Caranbirini prospect is also in the same sub-basin, directly on the Emu Fault and mineralisation is mostly younger in veins. This prospect could have recorded more mineralising events than the deposits at distance of the fault. This comparison gives insights on the importance of the distance to a major fault in a mineralising system. It has to be noted that the definition of sub-basins chosen here is the one of McGoldrick et al. (2010), but smaller divisions exist such as the sub-basins proposed by Walker et al. (1977).

After the comparison at sub-basin scale, an intrabasin study can give on the scale of the described events, and extend the stratigraphic correlation to basinal dynamic system. The Lawn Hill Platform was targeted with the Walford Creek deposit because of its vicinity to the McArthur Basin.

6.2.5. The HYC deposit

The HYC deposit is a world-class SHMS stratiform deposit with current JORC resource of 188 Mt @ 9.6% Zn, 4.5% Pb, 46g/t Ag ("Lead Zinc Silver factsheet and map," 2018). It is located 2 km from the Emu Fault and is composed of eight different finely laminated ore lenses in the HYC Pyritic Shale Member of the Barney Creek Formation (Figure 6-2, Large et al., 1998). Lot of studies have focused on HYC, but the genetic model is still debated. The arguments for a synsedimentary or a diagenetic model, based on different methods, have been summarised by Huston et al. (2006). More recently, Spinks et al. (2019) brought strong evidence for a diagenetic/epigenetic carbonate replacement origin for the HYC mineral system. If the mineralisation was syngenetic, the HYC Pyritic Shale Member would have acted as a chemical trap for metal deposition, and if it was diagenetic this unit would act as a physical trap for ascending metalliferous brines (Kunzmann et al., 2019). The evidence that mineralisation occurred shortly after sediment deposition is supported by paleomagnetic data in the Barney Creek Formation (Symons, 2007).

The sulphide crystallisation sequence is also not certain, but it has also been demonstrated that ore fluid reacted with sedimentary organic matter during ore formation (Logan et al., 2001). For some authors, base metal deposition occurred after pyrite crystallisation from H_2S, and there are sulphur isotopic evidences that the mechanism is not direct replacement of pyrite by base metals (Eldridge et al., 1993). Others involve repeating paragenetic sequence of galena/sphalerite → pyrite → nodular carbonate → sphalerite → pyrite (Ireland et al., 2004b). Another model is that hydrothermal fluids penetrated the pyritic zones or other metal-bearing sediments by dissolution and/or replacement, precipitating sphalerite, galena, secondary pyrite, and other ore-stage minerals with pyrrhotite and magnetite inclusions to form an epigenetic ore deposit (Symons, 2007). Biomarker data point to a marine environment of deposition (Logan et al., 2001). The study of polycyclic aromatic hydrocarbons abundances and their isomer distributions and geochemical, geological, paleobiological and mineralogical lines of evidence indicates that the ore formed within partially lithified sediments under marine conditions (Chen et al., 2003) and mass flow sedimentology show that base metal mineralisation is confined to the upper metre of unconsolidated seafloor sediment (Ireland et al., 2004a). Based on remanent magnetisation, relative dating using the apparent polar wander path and vitrinite reflectance values, time-temperature calculations indicate that the ore lenses have been heated to 310 ± 30 °C for ~10^5yr (Symons, 2007). In the deposit, a Pb/Zn zoning is observed: as the fluid moves and cools the amount of lead drops, and the Pb/Zn ratio decreases therefore from the feeder zone (Logan et al., 2001). Moreover, a zoning between the mineralisation types is observed, from laminated sphaleritic siltstones, to nodular

carbonate and then pyritic siltstones (Ireland et al., 2004b). In addition to this metal zoning, several halos from different composition are present at HYC: an extensive Zn–Pb–Tl halo is surrounded by a ferroan dolomite/ankerite halo, itself in a manganese carbonate halo whose extension is traceable for 15 to 23 km west of the deposit (Large et al., 2000). In this study, five of the eight ore lenses were sampled together with one sample located below the main ore sequence (named lens 0), covering most of the ore sequence at HYC (Figure 6-2). The samples are either grab samples (samples E5 and E11) or from the drillcore MRM2012-3 at several depths (164.6m, 176.2m, 191m, 195m and 209.7m). They all come from the Ore zone in the Barney Creek Formation.

6.2.6. The Myrtle deposit

The Myrtle deposit is located 19 km south-southwest of HYC. The inferred resources are 43.6 Mt @ 4.09% Zn and 0.95% Pb (Rox Resources, 2010). The zinc-lead mineralisation occurs within the Barney Creek Formation in the Myrtle Sub-basin, at depths of up to 500 m (Ahmad and Munson, 2013). Much of the resource mineralisation comprises stratiform laminated sulphides (sphalerite, galena and pyrite) layers, as well as disseminations in stratabound dolomite alteration lenses. The Myrtle deposit could have a different history than HYC (Nick Hayward and Rodney King, personal communication). First, very early diagenetic microeuhedral and fromboidal stratiform disseminated pyrite forming laminae and co-genetic carbonate nodules (with deformed bedding/laminae) crystallised. This was followed by crystallisation of early diagenetic dolomite sparry nodules along laminae and later coarser euhedral pyrite that may replace the edges of larger carbonate rims. Nodular hydrothermal dolomite is the result of the reaction forming the sulphides (Logan et al., 2001). Then, hydrothermal overprint results in early/mid diagenetic sphalerite and galena mineralisation coupled with anhedral pyrite overgrowth on earlier pyrite (apparently replacing carbonate cements) that are the main stage of mineralisation. Shortly after this event, mid/late diagenetic hydrothermal dolomitisation, broadly stratabound, texturally destructive, cross cuts the bedding and forms a range of overprinting textures (nodules, massive dolomite replacement, and hydrothermal rebrecciation). It is associated with replacement with sphalerite, galena and minor pyrite, maybe forming by fluid mixing when metalliferous fluids were still being pumped into the system, or by chemical remobilisation of stratiform mineralisation over short distances without affecting original Pb isotopic signature. Finally, late diagenetic (corresponding to basin inversion or syn-orogenic) quartz-calcite-dolomite-sulphide planar and cross-cutting veins with variable pyrite, sphalerite and galena emplace, and are probably younger than 1590 Ma (Nick Hayward, personal communication). For this study, one drillcore (MY16) was sampled at

several depths (170.7m, 172.9m, 177.5m, 190.0m, 195.5m, 195.9m and 205.3m) in the HYC Pyritic Shale Member of the Barney Creek Formation.

6.2.7. The Caranbirini prospect

The Caranbirini prospect is located on the Emu Fault, about 20 km north-northwest of the HYC deposit. In the studied drillholes, mineralisation was found in the Barney Creek Formation and in the overlying Reward Dolomite (Figure 6-2). The paragenesis of this deposit is more uncertain than the above deposits. Stratiform sulphides as well as sphalerite and galena in late carbonate veins have been sampled in three drillcores: DD82CA1 in the HYC Pyritic Shale Member of the Barney Creek Formation (565m, 679.2m and 734.9m) from which the best intersection is 0.5 m of 22.4% Zn and 2.5% Pb (Jenke, 1983), MANT79-3 (208.6m) and DD84CA4 (328.6m and 352.6m) located in the Reward Dolostone.

6.2.8. The Walford Creek deposit

The Walford Creek deposit is located in the Lawn Hill Platform (Figure 6-1). Most of the known paragenesis for Pb-Zn minerals was described by Rohrlach et al. (1998) and most of the descriptions below are from their work. The region was affected by multiple episodes of extensional and compressional deformation and a strong east-northeast grain is present. The Fish River Fault (Figure 6-2) is inferred to have been extensional growth fault active during deposition of the Mount Les Siltstone which is the host rock or mineralisation, as proven by the development of synsedimentary talus breccias interfingered with the Mount Les Siltstone. At Walford Creek, the Fish River Fault is assumed to have been a minor discharge zone at the time of mineralisation compared to bigger and deeper structures that would have focused most of the fluids (Yang et al., 2006).The Mount Les Siltstone contains abundant syndepositional pyrite within three stacked lenses in shale units (Stage I, Rohrlach et al., 1998). PY1 and PY3 massive pyrite lenses attain thickness of 40m in proximity to the Fish River Fault. They are currently located at shallow depth, PY1 from ~25m and PY3 from ~140m (Aeon Metals, 2019). Three temporally distinct phases of base metal mineralisation overprint the early massive pyrite lenses. Stage II is stratiform and cavity-filling Zn-Pb, stage III is cavity-filling and Cu-Pb-Zn veins and stage IV corresponds to Cu-Pb-Z veins. The timing of the late veins is thought to be ~1500 Ma at Walford Creek (Rohrlach et al., 1998b). Mineralisation is both structurally (Fish River Fault) and lithologically (PY1 and PY3) controlled. From a genetic point of view, the accepted model for Walford Creek is a SHMS event followed by Cu-Co hydrothermal fluids reacting with pyrite units and dropping out on the Fish River Fault (Aeon Metals, 2019). The resource occurs over 3.6km strike of the fault, which continues for more than 20kms. The

diagenetic fluids around Walford Creek likely had temperatures of about 200ºC at the time when the Zn-Pb deposits formed (Polito et al., 2006c). Six samples from three different drillcores in the Mount Les Siltstone were sampled: WFDD238 (140.5m and 141m), WFDD266 (110m, 130.8m and 271.4m) and WFDD272 (184.3m). All samples are from the PY3, except the one from drillcore WFDD266 at 110m and 130.8m that are in the PY1. The samples have been chosen for their galena and sphalerite content and because they present different sulphides assemblages. The paragenesis described by Rohrlach et al. (1998) was in a different area than the one sampled for this study and the samples used for the description of the paragenesis are no more available. The studied samples and the original paragenesis of Rohrlach et al. (1998) are therefore hardly to match.

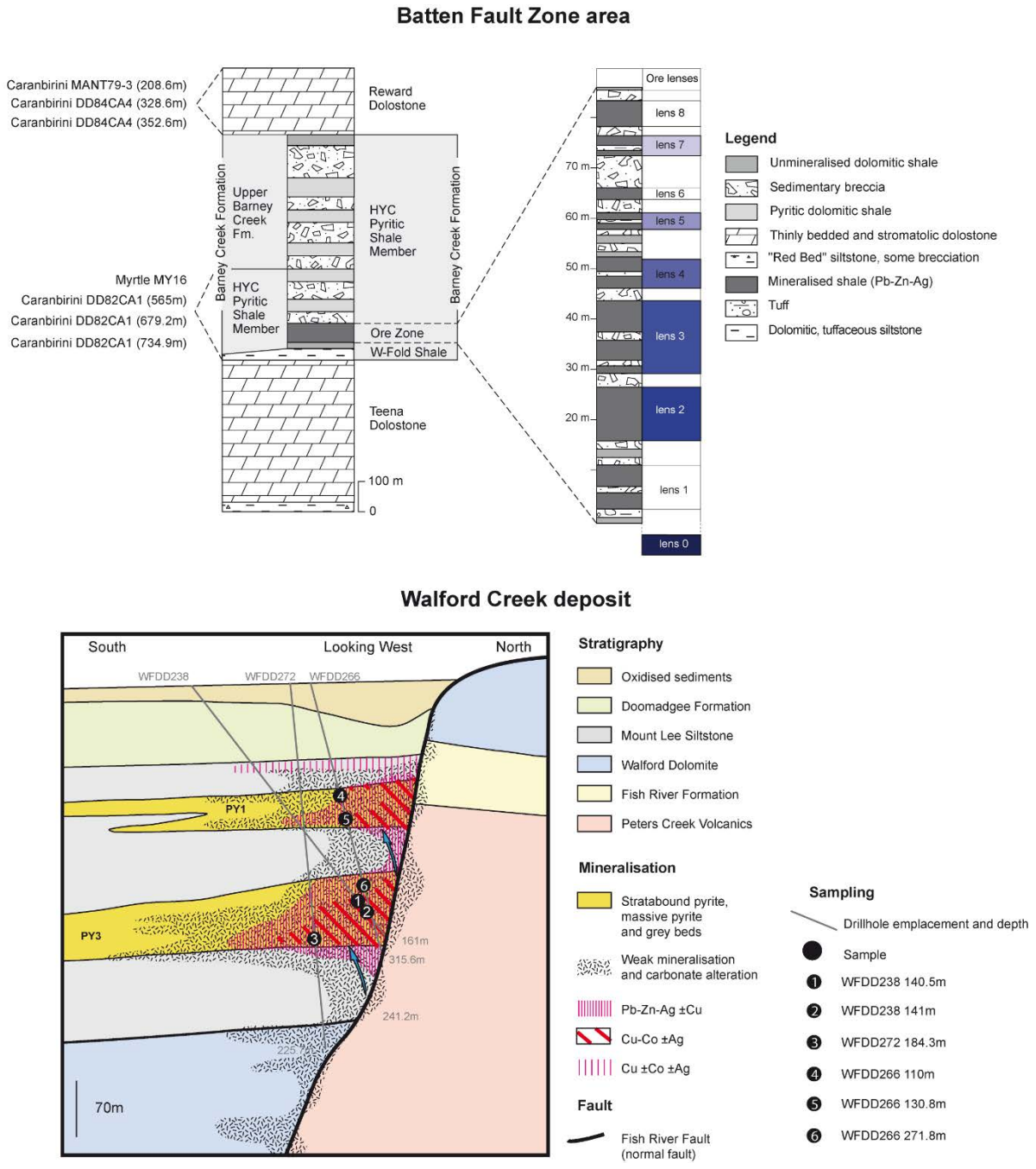

Figure 6-2: *Cross sections of the mineralised zones. Simplified stratigraphic succession of the Batten Fault Zone deposits deposit with location of the different ore lenses at HYC (top). The sampled ore lenses at HYC (lenses 0, 2, 3, 4, 5 and 7) are identified by different colours reported accordingly in the next figures. Note that all samples for galena analyses are from the Barney Creek Formation. After Large et al. (1998), Rox Resources Limited (2011) and Spinks et al. (2017). Simplified stratigraphic cross-section at Walford Creek with the mineralised zones and the emplacement of the samples studied here (bottom). After Aeon Metals (2019).*

6.3. Methods

All samples from HYC, Caranbirini and Walford Creek where polished mounted sections, and thin or thick sections where analysed at Myrtle. The samples were carbon coated for SEM and gold coated for SIMS analyses.

6.3.1. Optical and Scanning Electron Microscopy (SEM)

All petrographic and geochemical analyses were carried out at GeoRessources Lab (Vandœuvre-lès-Nancy, France). Petrographic investigation by was carried out using reflected light optical microscopy and SEM. Detailed mineral mapping was carried out in order to select the most favourable zones within the grains (i.e. large enough to avoid contamination by surrounding minerals and devoid of mineral inclusions). Optical microscopy was carried out on thin sections or mounted polished sections in reflective light using a numerical microscope VHX-200F with a high resolution objective VH-Z500W for the whole sections and a Zeiss Axio Scope.A1 microscope for detailed petrography (GeoRessources Lab - Vandœuvre-les-Nancy, France). SEM images were obtained using BackScattered Electron detector (BSE) of a conventional tungsten source Tescan Vega3LM (GeoRessources Lab - Vandœuvre-les-Nancy, France), with an acceleration voltage of 15 kV and beam current of around 1nA.

6.3.2. Electron Probe Microanalyses (EPMA)

Sulphides were first analysed by EPMA to establish major and minor element concentration including internal standards (Pb and Zn) for further LA-ICP-MS analysis. The quantitative measurements of major elements were performed using a CAMECA SX-100 electron microprobe analyses (GeoRessources laboratory, Nancy - Service Commun de Microscopie Electronique et Microanalyses). The microprobe is equipped with five wavelength-dispersion spectrometers (WDS), four of which contain classic crystal analysers (TAP, LiF, PET), and one of which is equipped with a large crystal (LiF and LPET). The calibration was based on natural and synthetic oxides and/or alloys The following elements, monochromators, standards, and limits of detection in galena, and in sphalerite were used: S (PET, pyrite, 721 and 744 ppm), Fe (LIF, pyrite, 1621 and 920 ppm), Co (LIF, Co, 1224 and 849 ppm), Ni (LIF, Ni, 1257 and 824 ppm), Cu (LIF, Cu, 1645 and 1295 ppm), Ag (PET, Ag, 3094 and 2169 ppm), Mg (TAP, forsterite, 550 and 676 ppm), Zn (LIF, sphalerite, 1896 and 1867 ppm), Si (TAP, albite, 435 and 501 ppm), Se (TAP, PbSe, 1328 and 1640 ppm), Pb (LPET, galena, 1834 and 1846 ppm), Ca (PET, andradite, 754 and 546 ppm), Cr (PET, chromite, never detected and 750 ppm), Mn (LIF, $MnTiO_3$, 1244 and 926 ppm), Cd (LPET, Cd, never detected and 999 ppm) and Sb (LPET,

stibnite, 2155 and 1410 ppm).The analytical conditions were 20 nA current, accelerating voltage of 20 kV, counting time of 10 s and spot size of about 1µm².

6.3.3. Secondary Ion Mass Spectrometry (SIMS)

21 ore samples were selected from for in situ Pb isotope analysis on galena individual grains with a total of 501 points. The analyses were performed on the Cameca IMS-1280 HR ion microprobe (CRPG-CNRS - Vandœuvre-les-Nancy, France) with an excellent sensitivity and a high spatial resolution thanks to the radiofrequence source (Deloule et al., 1986). The O^{2-} primary ion beam was accelerated at 13 kV, with an intensity that ranged between 72 and 74 nA. The size of the spot varied between 10 to 12 µm in diameter. Positive secondary ions were extracted with a 10 kV potential, and the spectrometer slits set for a MRP of ~2 500. The field aperture was set to 3 000 µm, and the transfer optic magnification adjusted to 107. Rectangular lenses were activated in the secondary ion optics to increase the transmission at high mass resolution (De Chambost et al., 1996). The energy window was opened at 50 eV, and its low energy side was positioned at 5 eV before the start of the energy distribution. ^{204}Pb, ^{206}Pb and ^{207}Pb were measured on multicollection mode with the FC (Farraday Cup) collector L1, C, and H1 respectively, with the ^{206}Pb in central position. ^{208}Pb was measured separately on the collector C by peak jumping. Each analysis consisted of 16 successive cycles, each cycle including the measurement of ^{204}Pb, ^{206}Pb, ^{207}Pb for 12 s, then that of ^{208}Pb for 8 s, with a waiting time of 1 s. Background on the FCs were measured before each analysis during the 120s of presputtering. Secondary beam centering and mass and energy calibrations were checked before each measurement. The instrumental mass fractionation was monitored using two CRPG internal standards Aloui and ISH9. The isotopic ratios are 18.125 for $^{206}Pb/^{204}Pb$ and 15.62 for $^{207}Pb/^{204}Pb$ for Aloui and 17.691 for $^{206}Pb/^{204}Pb$ and 15.436 for $^{207}Pb/^{204}Pb$ for ISH9. The instrumental mass fractionation is of 4.1 ‰ /amu, and external errors on the reference galena is 0.25 for the $^{206}Pb/^{204}Pb$ ratio, 0.24 for the $^{207}Pb/^{204}Pb$ ratio and 0.29 for the $^{208}Pb/^{204}Pb$ ratio. The errors presented on Figures 6-6 to 6-10 and Supplementary Table 6-4 correspond to 2σ errors.

6.3.4. Laser Ablation – Inductively Coupled Plasma – Mass Spectrometry (LA-ICP-MS)

Trace element contents in the main sulphide minerals have been investigated through LA-ICP-MS *in situ* method to determine the major, minor and trace element concentration of sulphides. LA-ICP-MS analyses were performed at the GeoRessources laboratory (Vandœuvre-lès-Nancy, France). The LA-ICP-MS device is composed of a 193 nm MicroLas

Pro ArF Excimer coupled with the Agilent 7500cc quadrupole ICP-MS. Laser ablations were performed at a 5 Hz pulse rate during 30 s and a constant fluence of 7 J/cm^2 by focusing the beam at the sample surface. The transport gas was a mixture of He and Ar, at typical flow rates of 0.5 and 0.9 l.min^{-1} respectively. All data were acquired in raw counts using time resolved mode. The following isotopes were measured with a dwell time of 10 ms for ^{24}Mg, ^{51}V, ^{53}Cr, ^{55}Mn, ^{57}Fe, ^{58}Co, ^{60}Ni, ^{63}Cu, ^{66}Zn, ^{68}Ge, ^{72}Ga, ^{75}As, ^{85}Rb, ^{88}Sr, ^{111}Cd, ^{118}Sn and ^{208}Pb, of 20ms for ^{95}Mo, ^{107}Ag and ^{115}In and of 30ms for ^{121}Sb, ^{125}Te, ^{157}Au, ^{202}Hg, ^{205}Tl and ^{209}Bi. The certified reference materials SRM NIST 610 and 612 glasses (Jochum et al., 2011) and MASS-1 (synthetic polymetallic sulphide material, Wilson et al., 2002) were used as external standards for calibration of all analyses and the internal standards used are Pb and Zn contents from electron microprobe analyses for galena and sphalerite analyses, respectively. The spot size was from 24 to 44 µm for sphalerite and from 24 to 60 µm for galena, depending on the grain size and homogeneity of the minerals. Data reduction was carried out using Iolite V3 software, following Longerich et al. (1996) standard methods. The analytical precision is calculated for all analysed elements using standard deviation of recorded intensity and is better than ± 20%.The Limit of detection (LOD) varies for each element and each analysis as a function of signal intensity and was calculated for each ablation from signal intensities using the 3 σ criterion of Longerich et al. (1996). To allow a graphical representation of all the data, even for the ones <LOD, all data points <LOD were assigned the value of LOD/2 in Figures 6-4 and 6-5. In the Supplementary Tables 6-2 and 6-3 (sphalerite and galena concentrations), the results are presented with the true value or the calculated LOD when data are <LOD, and for each sample the percentage of data <LOD are reported.

6.4. Results

6.4.1. Sulphides petrography

No growth, recrystallisation, zoning or alteration textures in sphalerite and galena were observed in any of the samples. The mineralisation has been subdivided in different categories depending on its paragenetic features (Figure 6-3).

Synsedimentary/early diagenetic sulphides are found only at HYC. HYC samples consist of laminated sulphide-rich shales, with sphalerite-galena-pyrite rich bands interlayered with mudstones and quartz-carbonate turbidites (Large et al., 1998, Figure 6-3a). There is no evidence for deformation at HYC and the sulphides are very small-grained, ranging from 5 to 30µm in size. The coarser galena and sphalerite grains show a poikilitic texture where galena crystals up to 1 mm show smaller (10 µm) inclusions of pyrite, sphalerite, carbonates and

silicates. This coarser galena is concentrated in layers visible in the mounted polished section (Figure 6-3b,c). Considering the size of the other sulphides at HYC, the poikilitic galena have been preferred to smaller ones for analyses in this study when they were present.

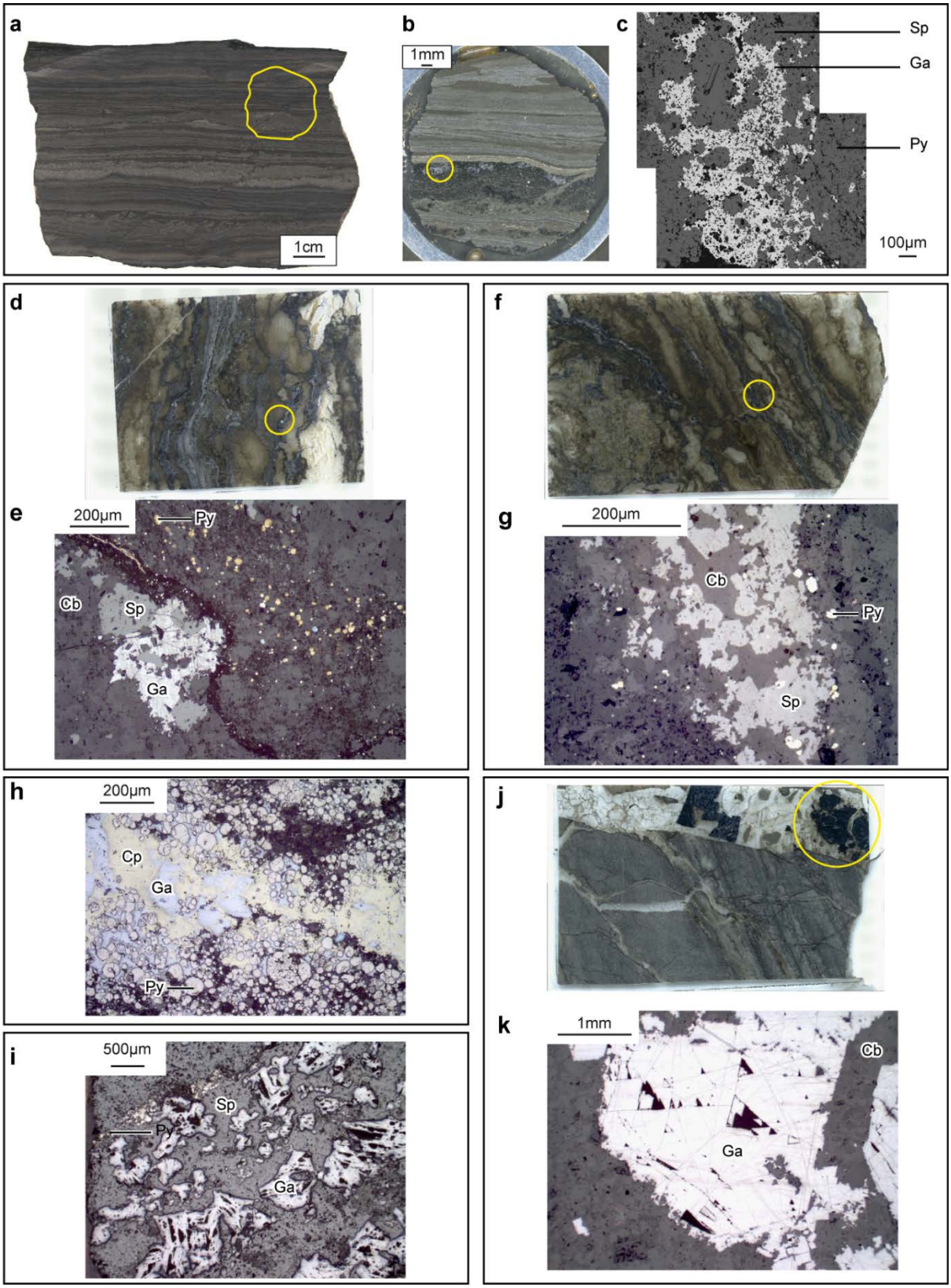

Figure 6-3: *Examples of galena and sphalerite assemblages from the different studied areas. (**a**) Hand sample of sulphide-rich laminations from synsedimentary/early diagenetic galena and sphalerite. Sample from Lens 2 at HYC. (**b**) Polished mounted section in reflective light showing the analysed galena, concentrated in specific layers. (**c**) SEM image of the poikilitic galena and sphalerite. (**d**) Thin section of early/mid diagenetic sphalerite and galena mineralisation and mid/late diagenetic hydrothermal dolomitisation. Sample MY16 205.3m at Myrtle. (**e**) Microscopic image in reflective light of sphalerite and galena at the border of nodular carbonate. (**f**) Thin section with sphalerite associated with hydrothermal texturally destructive dolomitisation. Sample MY16 172.9m at Myrtle. (**g**) Microscopic image in reflective light of the sphalerite associated with pyrite and carbonate. (**h**) Microscopic image in reflective light of poikilitic galena on early pyrite, with chalcopyrite replacement. Sample WFDD238 141m at Walford Creek. (i) Microscopic image in reflective light of sphalerite as matrix around coarse euhedral galena. Sample WFDD266 130.8m at Walford Creek. (**j**) Thin section of galena and carbonate late vein. Sample MY16 177.5m at Myrtle. (**k**) Microscopic image in reflective light on the coarse galena. Py = pyrite, Ga = galena, Sp = sphalerite, Cp = chalcopyrite, Cb = carbonate*

At Myrtle, the early phase of sphalerite mineralisation is overprinted by texturally destructive hydrothermal dolomite (Figure 6-3d,e). Galena and sphalerite can also directly be associated with the texturally destructive hydrothermal dolomite that replace early dolomite cement/nodule (Figure 6-3f,g). Because of the possible continuum between these two styles of mineralisation, they share common features and are not easily distinguishable. Generally, the sulphides are coarser than what is observed at HYC.

At Walford Creek, the authors identified the following paragenesis. The fine-grained fromboidal stratabound syn-sedimentary pyrite was described by Rohrlach et al. (1998). The next sulphides to crystallise are coarse galena ± sphalerite (seen in stratabound pyrite km out from the Fish River Fault). The galena can be up to 1mm, and is either poikilitic on pyrite (Figure 6-3h) or euhedral (Figure 6-3i). This is surrounded by sphalerite as matrix around coarse galena (Figure 6-3i). Sphalerite covers large zones and incorporate very-small inclusions of gangue minerals (mainly quartz and carbonates), giving a speckled aspect. Sphalerite can also be observed around galena, but without the micro inclusions. In some samples, there is textural evidence that galena is replaced by chalcopyrite (Figure 6-3h).

Finally, a late type of sulphide corresponds to mineralisation linked to polyphased dolomitisation or late veining. In the example shown in Figure 6-3j,k, the late carbonate-vein contains large euhedral galena crystals. At Walford Creek, late carbonate and galena/sphalerite veins could be followed by late chalcopyrite veining, which cross cut the previous assemblages. The timing of the late veins is thought to be at ~1500 Ma at Walford Creek (Rohrlach et al., 1998b) and <1590 Ma at Myrtle (Nick Hayward, personal communication).

6.4.2. Major elements results in sphalerite and galena

Major elements represent more than 1 wt% oxides in the analyses, minor elements between 0.1 and 1 wt% oxide and trace elements correspond to elements whose concentration is lower than 0.1 wt% oxide (i.e. equivalent to 1000 ppm).

Major elements in sphalerite and galena measured by EPMA are used for internal standardisation of the LA-ICP-MS analyses and are reported in Supplementary Table 6-1 and summarised in Table 6-1. S concentration varies from 28.89 to 34.54 wt% in sphalerite and from 11.58 to 14.39 wt% in galena. About 40% of the analysed sphalerite at HYC and Myrtle has between 1 and 3 wt% Cu and almost all the sphalerite at HYC avec Fe content between 1 and 5.33 wt% Fe. The question for these concentrations is whether they correspond to really high concentrations of these metals in sphalerite, or if are due to small inclusions of chalcopyrite and/or pyrite that would have been analysed at the same time as the sphalerite because of the small grain size in these deposits. As the EPMA spot size is about 1µm², and considering the size of the minerals in these deposits (see Figure 6-3), we can assume that Cu and Fe grades correspond to high concentrations of these elements in the sphalerite. The Pb and Zn content have been normalised to 100% because some of the analyses have totals ranging from 97 to 103 wt% and are noted as Zn_n and Pb_n in the Table 6-1 and Supplementary Table 6-1. The mean data and standard deviation are calculated for every sample and presented in Table 6-1. The metal grades are homogenous enough in a single sample to take the mean value as internal standard for LA-ICP-MS analyses for all the analyses in the sample. For the stoichiometric galena, the Pb content is 86.6wt% Pb. As the values measured by EPMA are close to this value, it has been chosen as internal standard for all the LA-ICP-MS analyses on galena. For sphalerite, the inter-samples variations are larger and for each sample the closer integer to the mean value has been chosen as concentration for internal standardisation. Except Pb, Zn, S, Cu and Fe, all measured elements (Co, Ni, Ag, Sb, Mg, Se, Cd, Ca, Mn, Ca, Cr and Si) have a maximum value of 1% in some selected samples.

Deposit	Mineralised lens or sample depth	Type	Galena		Sphalerite	
			Mean wt% Pb_n ± 1σ	Nb analyses	Mean wt% Zn_n ± 1σ	Nb analyses
HYC	lens 7	S	-	-	62.8 ±2.1	5
HYC	lens 5	S	85.0 ±0.8	4	63.0 ±2.2	5
HYC	lens 4	S	85.5 ±1.9	5	64.0 ±1.9	3
HYC	lens 3 (191m)	S	85.0 ±0.7	4	63.3 ±1.6	5
HYC	lens 2 (E11-1)	S	85.6 ±1.3	13	61.0 ±1.7	27
HYC	lens 2 (E11-2)	S	85.3 ±0.8	20	63.2 ±2.2	2
HYC	lens 2 (E4-2)	S	85.5	1	63.3 ±0.5	5
HYC	lens 0	S	85.1 ±0.9	3	62.1 ±0.9	4
Myrtle	MY16 170.7m	D	-	-	66.4 ±0.5	8
Myrtle	MY16 172.9m	D	-	-	66.4 ±0.4	8
Myrtle	MY16 177.5m	V	86.4 ±0.2	10	-	-
Myrtle	MY16 195.5m	E + V	-	-	65.3 ±1.1	14
Myrtle	MY16 197.7m	E + V	86.0 ±0.5	2	65.4 ±2.0	19
Myrtle	MY16 205.3m	E	86.5 ±0.2	15	65.5 ±0.6	4
Caranbirini	MANT79-3 208.6m	E	-	-	66.7 ±0.4	9
Caranbirini	DD82CA1 565m	V	86.0 ±0.1	5	-	-
Caranbirini	DD82CA1 679.2m	V	86.0 ±0.2	8	66.4 ±0.4	7
Caranbirini	DD82CA1 734.9m	V	86.0 ±0.2	5	-	-
Caranbirini	DD84CA4 328.6m	V	-	-	66.1 ±0.3	6
Caranbirini	DD84CA4 352.6m	V	-	-	66.8 ±0.4	6
Walford Creek	WFDD238 140.5m	M + P	86.2 ±0.2	5	67.0 ±0.3	5
Walford Creek	WFDD238 141m	P	86.1 ±0.2	5	-	-
Walford Creek	WFDD266 110m	M + G	86.2 ±0.3	3	66.4 ±0.3	4
Walford Creek	WFDD266 130.8m	H + G	85.1 ±0.5	5	65.7 ±0.8	5
Walford Creek	WFDD266 271.4m	H + V	86.3 ±0.1	5	66.4 ±0.6	4
Walford Creek	WFDD272 184.3m	P	86.0 ±0.3	4	-	-

***Table 6-1**: Mean values for wt% Pb_n in galena and wt% Zn_n in sphalerite obtained by EPMA. S = synsedimentary/ early diagenetic; E = early phase of sulphide mineralisation overprinted by texturally destructive hydrothermal dolomite; D = sulphides linked with late hydrothermal texturally destructive dolomite; M = Sphalerite as matrix around coarse galena; H = homogeneous sphalerite around galena; P = poikilitic galena on early pyrite; G = euhedral galena; V = linked to polyphased dolomitisation or late veining.*

6.4.3. Minor and trace element in sphalerite

Figure 6-4 shows the composition results for Ag and Sb (to get comparison with the Ag- and Sb-content in galena to determine the relative metal enrichment in the sulphides), Ga, Ge and In (economically strategic metals and used for temperature calculation), Mn and Fe (used for the temperature calculation) and Tl (due to the presence of a Tl anomaly at HYC). In addition, data from compilation of different Pb-Zn deposits types (MVT, SHMS and vein-type) are plotted for comparison (Frenzel et al., 2016). Supplementary Table 6-2 shows the data for the different deposits. The data indicate globally a large variability in the elements concentrations at a deposit scale, and even in the same sulphide grain. In general, the major, minor and trace elements content at HYC are similar between all the different lenses.

Fe content measured by LA-ICP-MS is high at HYC, with up to 60 000 ppm, consistent with the 5.3 wt% measured by EMPA. Three samples from the early phase of sulphide mineralisation overprinted by texturally destructive hydrothermal dolomite at Myrtle (samples MY16 195.5m, 195.9m and 197.7m) show the same content, whereas the other samples have Fe content below 10 000 ppm.

Ag content is relatively low at Myrtle and in the early mineralisation at Caranbirini (maximum of 5 ppm). In the other samples, the Ag concentration varies mostly between ~1 and ~1000 ppm. Caranbirini samples show distinctively high Ga content, between ~100 and ~1000 ppm, as well as sample WFDD266 271.4m at Walford Creek. Other deposits or samples show Ga values lower than ~100 ppm. Ge content is globally constant in all the samples, between ~10 and ~100 ppm. In values are mostly < LOD (~ 0.05 ppm) except at Walford Creek and in some samples at HYC, Myrtle and Caranbirini. The highest value is 136 ppm at Walford Creek, and sphalerite in veins contains more In than the other types of mineralisation. The Mn concentration ranges between ~10 and ~3000 ppm at HYC, and mostly between ~0.05 and ~100 ppm elsewhere. Sb present significant variations, mainly between the deposits. While HYC samples show Sb content between ~5 and ~100 ppm, Myrtle samples show systematically lower concentrations (~0.1 – ~10 ppm). Mn content at Walford Creek and Caranbirini show various patterns depending on the sample, and ranges from ~0.5 to ~1000 ppm. Tl concentrations are often < LOD (~0.01 - 0.1 ppm) except at HYC (~3 – ~100 ppm), Myrtle (~0.1 – ~30 ppm) and in samples WFDD266 130.8m and 271.4m at Walford Creek.

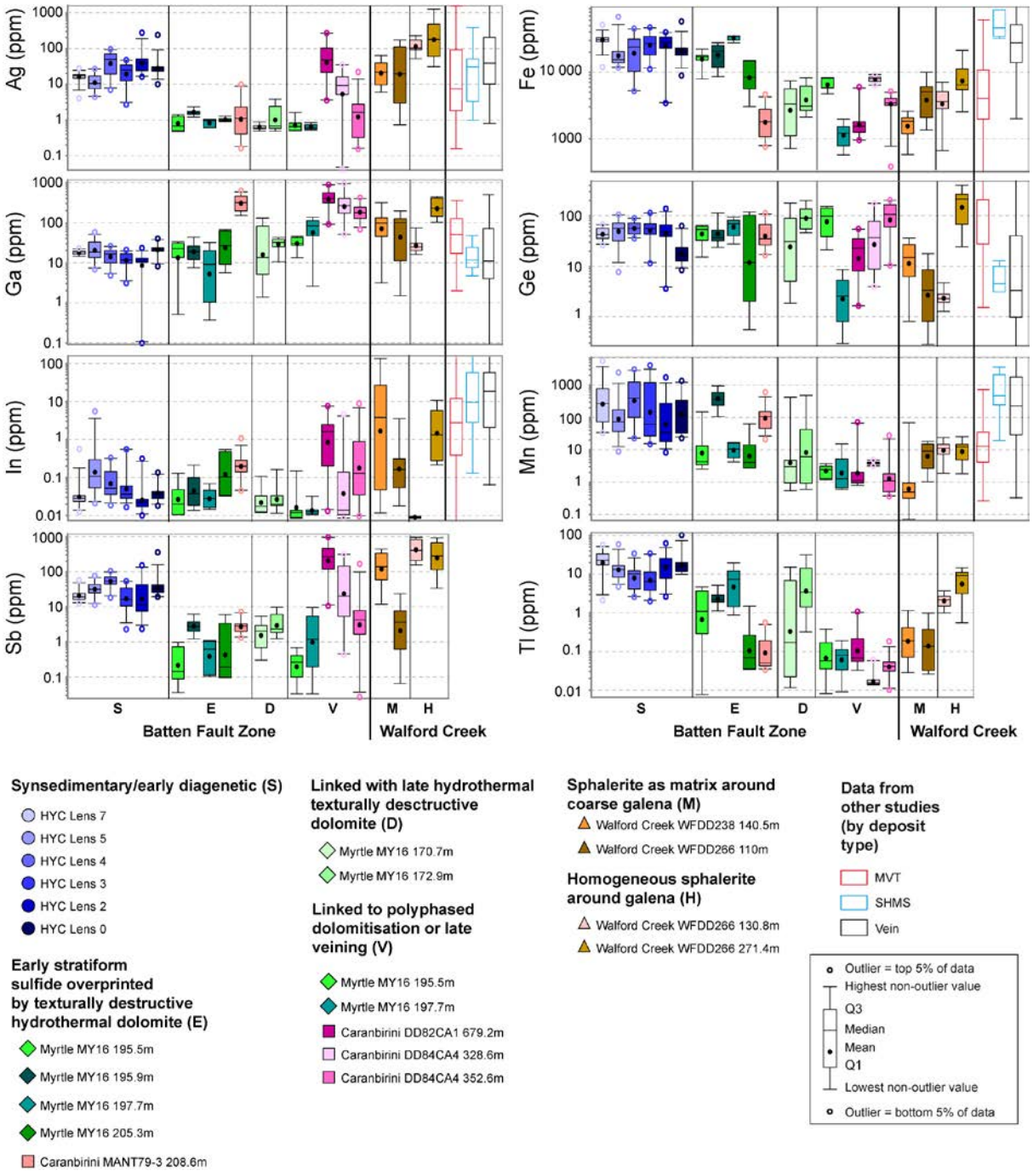

***Figure 6-4**: Box-and-whisker plots showing Ag, Fe, Ga, Ge, In, Mn, Sb and Tl concentration in sphalerite at the HYC, Myrtle and Walford Creek deposits and Caranbirini prospect (this study) and MVT, SHMS and vein-type deposits (Frenzel et al., 2016). Lower whiskers, bottoms of boxes, central lines, tops of boxes and upper whiskers represent 5th, 25th, 50th, 75th and 95th percentiles respectively; circle represent outlier. The black dots are for the mean.*

6.4.4. Minor and trace elements in galena

Minor and trace elements in galena are presented in Supplementary Table 6-3 and the ones in which most of the analyses are higher than the LOD are plotted on Figure 6-5. Galena at HYC shows high apparent concentrations of Fe (up to 4%) and Zn (up to 10%); probably due to minor contamination by small inclusions of sphalerite and pyrite during LA-ICP-MS analysis. Correlations are noted between Zn content and Cd, Ga, Ge and Hg concentrations, and between Fe content and As and Tl concentrations. This indicate that these elements concentrations must be interpreted with caution as they could result from the analyses of sphalerite or pyrite inclusions.

For most of the analysed elements, their concentration in galena show significant variations depending on the lenses or deposits. The highest Ag content are observed at Caranbirini and Walford Creek (~50–820 ppm Ag) whereas HYC and Myrtle values mostly range between 10 and 200 ppm. As concentrations are highly variable within the same deposit; with values ranging from 0.2 to 7660 ppm at HYC, except for Caranbirini where the values are all very low. High Bi values (>10 ppm) are present in three samples from Myrtle and one from Caranbirini, while the other samples present very low Bi content. The Cd content is globally homogeneous with a median value of 8 ppm. Cu varies a lot even in a single deposit, from ~0.1 to 20 400 ppm for example at HYC. The high values obtained at Walford Creek could be explained by chalcopyrite contamination. Mn has high content at HYC (~10–27 120 ppm), maybe due here too to contamination, and mostly low values elsewhere (~0.1–~100 ppm, with mean values around 1 ppm). Sb content varies depending on the samples, from 10 to 6400 ppm, and large variations are observed within one sample. Sn concentration are mostly between ~1 and ~10 ppm, except sample MY16 195.9m with up to 100 ppm Sn. Tl content is <LOD in one sample from HYC, but all the other samples from this deposit and Myrtle range between ~2 and ~200 ppm. At Caranbirini and Walford Creek, the values are lower than 10 ppm.

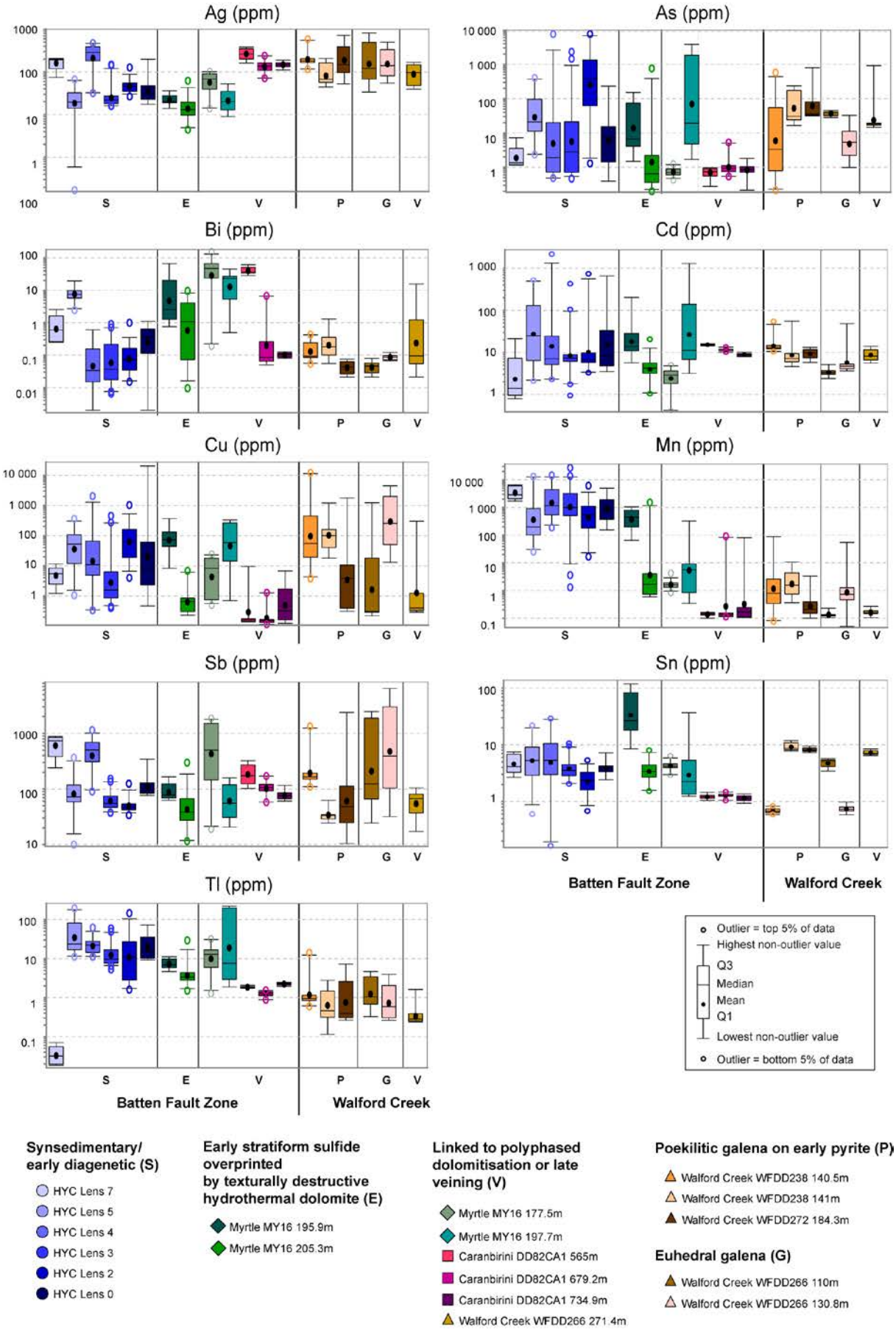
Ag (ppm)
As (ppm)
Bi (ppm)
Cd (ppm)
Cu (ppm)
Mn (ppm)
Sb (ppm)
Sn (ppm)
Tl (ppm)
S
E
V
P
G
V
Batten Fault Zone
Walford Creek
Outlier = top 5% of data
Highest non-outlier value
Q3
Median
Mean
Q1
Lowest non-outlier value
Outlier = bottom 5% of data
Synsedimentary/ early diagenetic (S)
HYC Lens 7
HYC Lens 5
HYC Lens 4
HYC Lens 3
HYC Lens 2
HYC Lens 0
Early stratiform sulfide overprinted by texturally destructive hydrothermal dolomite (E)
Myrtle MY16 195.9m
Myrtle MY16 205.3m
Linked to polyphased dolomitisation or late veining (V)
Myrtle MY16 177.5m
Myrtle MY16 197.7m
Caranbirini DD82CA1 565m
Caranbirini DD82CA1 679.2m
Caranbirini DD82CA1 734.9m
Walford Creek WFDD266 271.4m
Poekilitic galena on early pyrite (P)
Walford Creek WFDD238 140.5m
Walford Creek WFDD238 141m
Walford Creek WFDD272 184.3m
Euhedral galena (G)
Walford Creek WFDD266 110m
Walford Creek WFDD266 130.8m

***Figure 6-5**: Box-and-whisker plots showing Ag, As, Bi, Cd, Cu, Mn, Sb, Sn and Tl concentration in galena at the HYC, Myrtle and Walford Creek deposits and Caranbirini prospect (this study). Lower whiskers, bottoms of boxes, central lines, tops of boxes and upper whiskers represent 5th, 25th, 50th, 75th and 95th percentiles respectively; circle represent outlier. The black dots are for the mean.*

6.4.5. Lead isotopic results in galena

Lead isotope data are reported in Supplementary Table 6-4 and presented for all deposits in Figure 6-6. Globally, lead isotopes data at HYC and Myrtle are roughly similar, whereas Caranbirini and Walford Creek share common features. At HYC and Myrtle, lead isotopes ratios obtained in this study and by Gigon et al. (submitted) are globally distributed along a straight line. At Walford Creek and Caranbirini the data are more dispersed around another unique line. The lead isotope variation for individual deposits, and often for individual samples, is large.

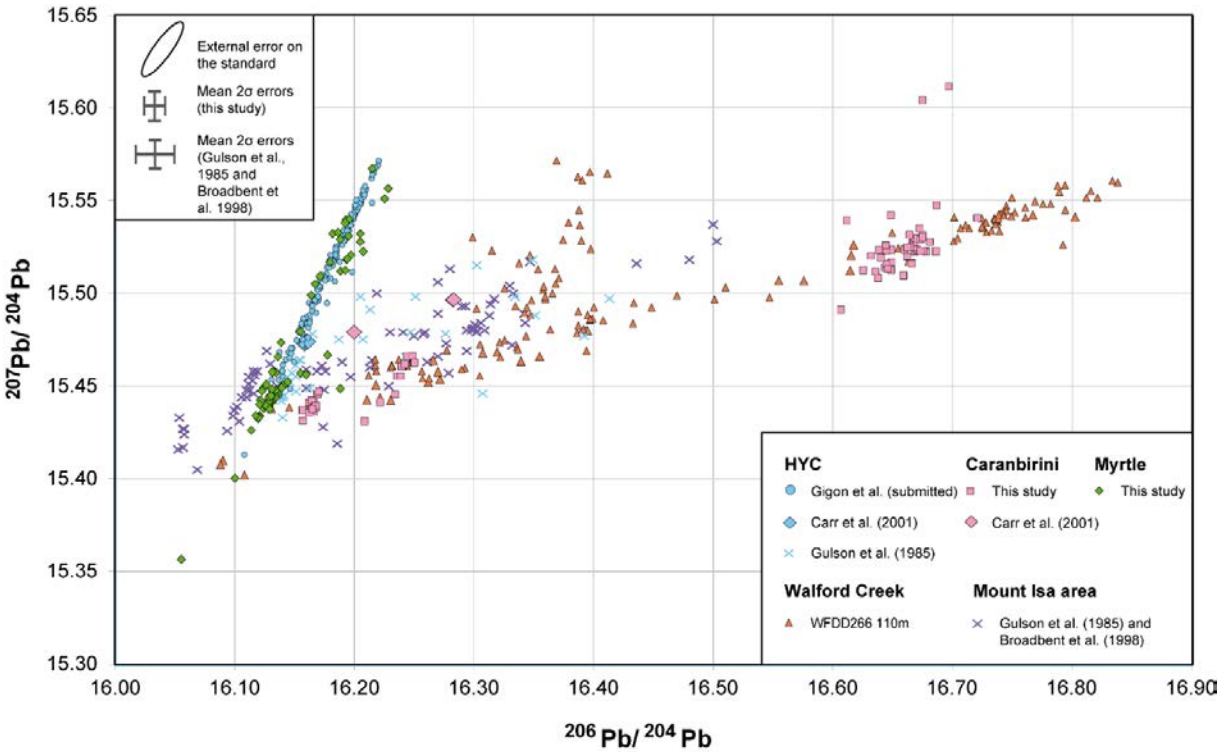

***Figure 6-6**: Lead isotopic composition of the galena from the HYC and Myrtle deposits and Caranbirini prospect (Northern Territory), Walford Creek deposit, and several deposits from the Mount Isa area (Queensland, Australia). Most of the data are from this study and from Gigon et al. (submitted), and data from Carr et al. (2001), Gulson (1985) and Broadbent et al. (1998) have been added. The external error on the standard and the mean 2σ errors for the samples are reported.*

The ranges of $^{206}Pb/^{204}Pb$ and $^{207}Pb/^{204}Pb$ ratios at HYC are 16.10–16.22, and 15.43–15.57 respectively. In a $^{207}Pb/^{204}Pb$ vs $^{206}Pb/^{204}Pb$ diagram (Figure 6-7), the data are distributed along a linear trend whose slope is 1.42 with a Mean Square of Weighted Deviates (MSWD) of 3. TIMS data from literature are either on the trend (Carr et al., 2001a; Gulson, 1985) or have

similar $^{207}Pb/^{204}Pb$ ratios but higher $^{206}Pb/^{204}Pb$ ratios (North mineralisation and veins, Gulson, 1985). A more detailed description of lead isotope data can be found in Gigon et al. (submitted).

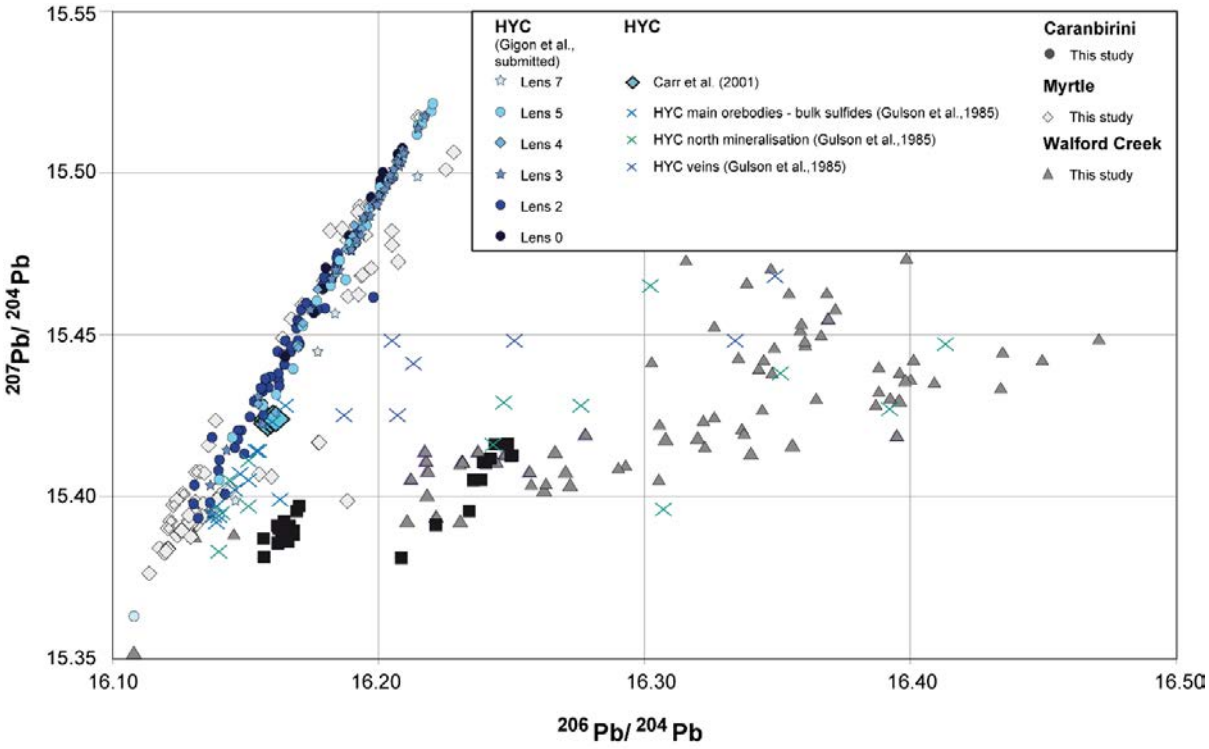

***Figure 6-7**: Lead isotopic composition of the galena from the HYC deposit (Northern Territory, Australia). Data from this study for Myrtle, Caranbirini and Walford Creek, and from (Carr et al., 2001a; Gigon et al., accepted; Gulson, 1985) for HYC.*

At Myrtle the pattern is identical to the one observed at HYC for the three samples with early stratiform mineralisation overprinted with nodular hydrothermal dolomite. The ranges of $^{206}Pb/^{204}Pb$ and $^{207}Pb/^{204}Pb$ ratios are 16.11–16.2, and 15.43–15.57 respectively. One analysis has very low ratios and is discarded from this range because it is clearly an outlier from a statistical point of view. In a $^{207}Pb/^{204}Pb$ vs $^{206}Pb/^{204}Pb$ diagram (Figure 6-8), the data are distributed along a linear trend whose slope is 1.33 with a MSWD of 3.3. In the galena analysed in the late carbonate vein (MY16 177.5m), all the values are close to the lower end-member presented above, with $^{206}Pb/^{204}Pb$ ratios of 16.133 ±0.013. The variations within this sample are the same that the external error on the standard, which means that all the analyses spots have in fact the same ratios and the mean value for the sample can be taken as reference.

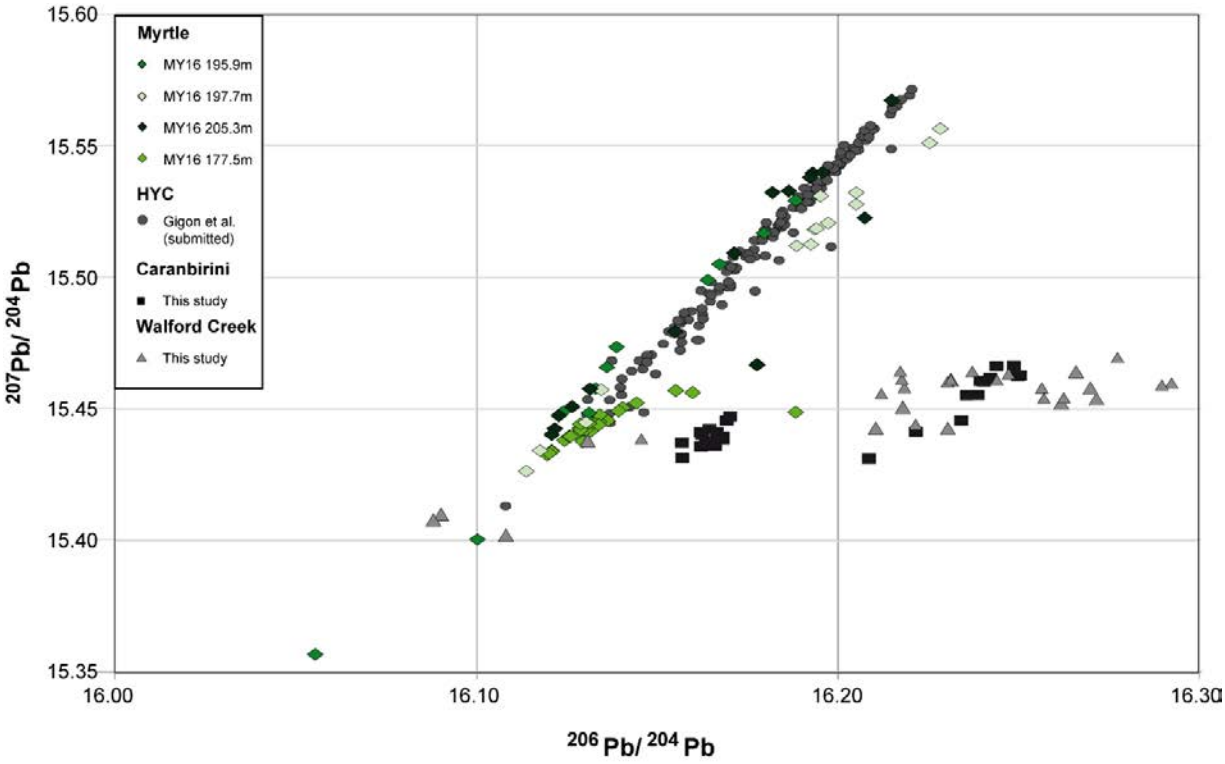

***Figure 6-8**: Lead isotopic composition of the galena from the Myrtle deposit (Northern Territory, Australia). Data from this study for Myrtle, Caranbirini and Walford Creek, and from Gigon et al. (submitted) for HYC.*

At Caranbirini, each sample has a specific isotopic signature. The less radiogenic sample is DD82CA1 565m with $^{206}Pb/^{204}Pb$ ratio of 16.165 ±0.004, followed by the 734.9m sample with ratios of 16.238 ±0.012, and the 679.2m with a 16.661 ±0.022 ratio. The slope between all the samples is 0.17 with a MSWD of 8.9 in a $^{207}Pb/^{204}Pb$ vs $^{206}Pb/^{204}Pb$ diagram (Figure 6-9). As explained for the sample MY16 177.5m, the variation in samples DD82CA1 565m and 734.9m are within the external error on the standard and a mean value can be taken as representative. The sample DD82CA1 679.2m has a wider extend but also larger errors, and almost all the analyses are also within the external error of the standard. Data from the literature for Caranbirini are three analyses (Carr et al., 2001a) that do not plot on the data trend of this study. However, the sample location and the errors are not known, making any comparison difficult.

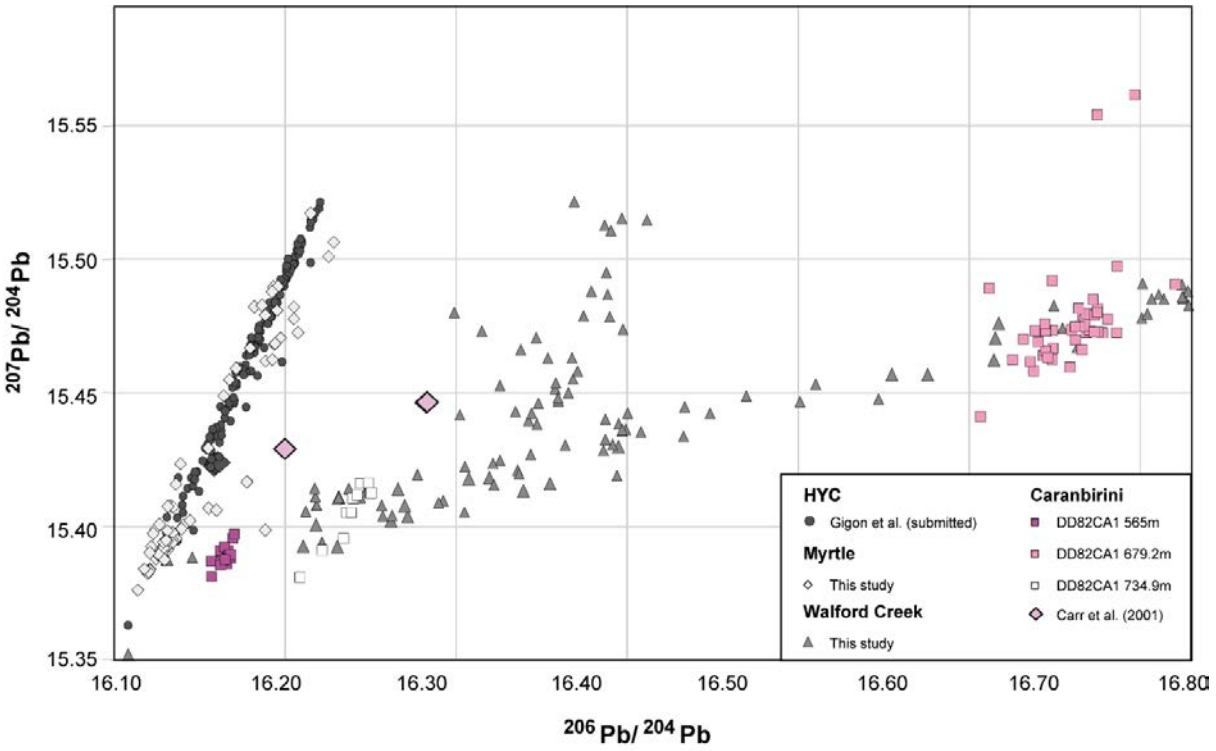

***Figure 6-9**: Lead isotopic composition of the galena from the Caranbirini prospect (Northern Territory, Australia). Data from this study for Myrtle, Caranbirini and Walford Creek, from (Carr et al., 2001a; Gigon et al., accepted) for HYC.*

At Walford Creek, in a $^{207}Pb/^{204}Pb$ vs $^{206}Pb/^{204}Pb$ diagram, the data are distributed along a linear trend whose slope is 0.17 with a MSWD of 6 (Figure 6-10). The less radiogenic end-member has $^{206}Pb/^{204}Pb$ ratio equal to 16.088 and $^{207}Pb/^{204}Pb$ equal to 15.408, the more radiogenic one with $^{206}Pb/^{204}Pb$ ratio equal to 16.837 and $^{207}Pb/^{204}Pb$ ratio to 15.560. The sample WDD238 140.5m data ranges between those two end-members, whereas the results for the others samples lie either close to one end-member (e.g. WFDD266 271.4m) or with more contribution on one of the end-members (e.g. WFDD266 130.8m). The exception is the sample WFDD238 141.0m with a steeper slope (= 0.64) and a poor MSWD of 39 between a less radiogenic end-member ($^{206}Pb/^{204}Pb$ = 16.322 and $^{207}Pb/^{204}Pb$ = 15.470) and a more radiogenic one ($^{206}Pb/^{204}Pb$ = 16.396 and $^{207}Pb/^{204}Pb$ = 15.563). Data in the literature (e.g. (Carr et al., 2001a) have low precision or were not from galena analysis and are therefore not reported on Figure 6-10.

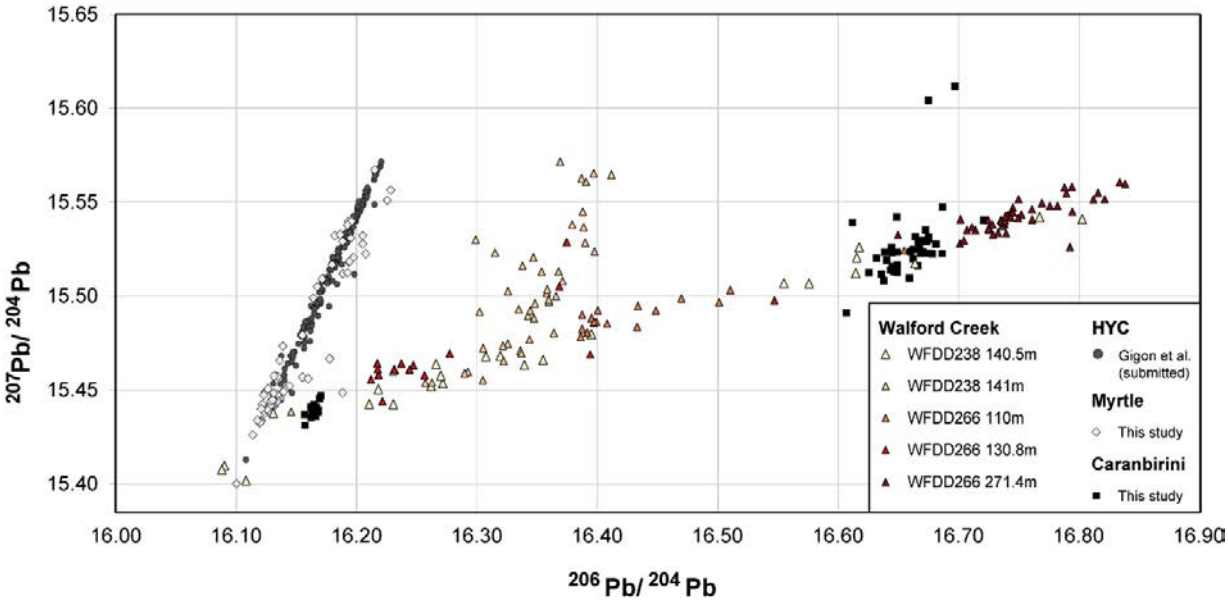

***Figure 6-10**: Lead isotopic composition of the galena from the Walford Creek deposit (Queensland, Australia). Data from this study for Myrtle, Caranbirini and Walford Creek, and from Gigon et al. (submitted) for HYC.*

6.5. Discussion

6.5.1. Lead sources

At HYC and Myrtle, the position and slope of the linear trend of all the lead isotope data cannot represent a secondary isochron (Stacey and Kramers, 1975; Sun et al., 1996). Therefore, the most simple explanation is that the data lie along a mixing trend between two lead sources corresponding to two end-members of the data distribution named respectively Lead Source n°1 ($^{207}Pb/^{204}Pb$ ~15.56 and $^{206}Pb/^{204}Pb$ ~16.21) and Lead Source n°2 ($^{207}Pb/^{204}Pb$ ~15.46 and $^{206}Pb/^{204}Pb$ ~16.14, Figure 6-11, Gigon et al., submitted). The two lead sources would have been mobilised by the ore-forming fluids at ~1640 Ma and mixed imperfectly prior to galena deposition. The late galena from the carbonate vein at Myrtle (sample MY16 177.5m) shows a signature typical of one of the end-members, therefore indicating that the galena in this sample has no significant input from the Lead Source n°1 and formed only with lead from Lead Source n°2.

Different models can be proposed to identify more precisely the lead sources. Lead Source n°2 is from a reservoir (in the basin or the basement) that evolved since crust formation and was leached at the time of mineralisation. For Lead Source n°1, several models are proposed by Gigon et al. (submitted). On one side, the crustal reservoir at its origin could have been extracted from the mantle at a timing different to the one at the origin of Lead Source n°2, explaining their distinct measured lead ratios. On the other side, minerals containing lead and

no uranium could have crystallised at the time indicated by the isochrons. For these minerals, galena would be a suitable candidate, and galena is present in the 1780–1730 Ma sediments in the basin (Spinks et al., 2016) but no leaching is recorded and the amount of lead that could have been leached in unknown. Another suitable lead source is feldspar, as the ionic properties of Pb allows it to substitute for Ca in plagioclase and for K in K-feldspar (Heier, 1962), and as they are abundant in the basin and the basement. The calculated μ values (where μ is the $^{238}U/^{204}Pb$ ratio of a given reservoir) indicate that the lithology hosting these feldspars has to be felsic.

A second trend is observed at Walford Creek only, with some of the data (mostly from sample WFDD238 141m) along a trend between two new source identified in this study (Lead Sources n°3 and 4), and poorly constrained. The straight line between these two end-members is approximately parallel to the isochrons (straight lines linking isotopic ratios corresponding to rocks or minerals having the same age) between 1500 and 1600 Ma, and could therefore correspond to an isochron.

At Caranbirini and Walford Creek, most of the samples lie along a straight line between Lead Source n°2 previously defined and a new source identified in this study (Lead Source n°5). The calculated model age of the Lead Source n°5 is 1315 Ma (Sun et al., 1996) or 1235 Ma (Stacey and Kramers, 1975, Figure 6-11). By analogy with the above discussion, a reservoir evolved until 1235-1315 Ma and was leached at that time.

The calculated μ values for Lead Sources n°2 and 5 are very close: 12.83 and 12.82 respectively with the Sun et al. (1996) model and 10.14 and 10.12 with the Stacey and Kramers (1975) one, and could be equivalent for Lead Source n°3. It could therefore be assumed that the same reservoir was leached three times, first at 1640 Ma, then at ~1500-1600 Ma and finally at ~1235–1313 Ma, or even more often. If lead is removed from a given crustal reservoir, its μ value should change, except if the quantity of the removed lead is negligible, which means leaching lead from different regions in the same reservoir, or a very large reservoir.

For the trend between Lead Sources n° 3 and 4, the most plausible explanation is that the reservoir leached to form Lead Sources n°2 and 5 was leached between 1500 and 1600 Ma (Lead Source n°3), together with another more radiogenic reservoir of unknown origin (Lead Source n°4). This timing correspond to the Isan Orogeny, and it can be supposed that the faults were reactivated at that time, mobilising several reservoirs.

To explain the trend between Lead Source n°2 and 5, a first possibility is that the observed pattern corresponds to a mixing at 1315–1235 Ma between fluid carrying lead from Lead Source n°5 and another fluid having remobilised the galena crystallised at ~1640 Ma. This possibility has to be favoured for samples whose isotopic results range between the two end-

members. It has to be noted that following this hypothesis the location of the analyses on the trend is function of the relative contribution of each source in the final lead budget, and cannot be interpreted in terms of age. The second possibility, favoured for samples with low dispersion, is that this reservoir was leached several time in its history, that lead was carried by a single fluid and that galena crystallised from a unique lead source. For example, for the sample DD82CA1 679.2m, the data could be explained by two different processes. First, the galena in this sample could have formed by mixing between lead carried by a fluid that has leached Lead Source n°5 (major component) and lead from galena crystallised at ca. 1640 Ma leached by another fluid. Alternatively, galena could have formed at 1330–1380 Ma (depending on the models) from lead extracted from the same reservoir than the one forming Lead Sources n°2, 3 and 5, implying a single lead source.

In most of the Mount Isa area deposits, the same pattern than the one described above occurs (Broadbent et al., 1998; Gulson, 1985).

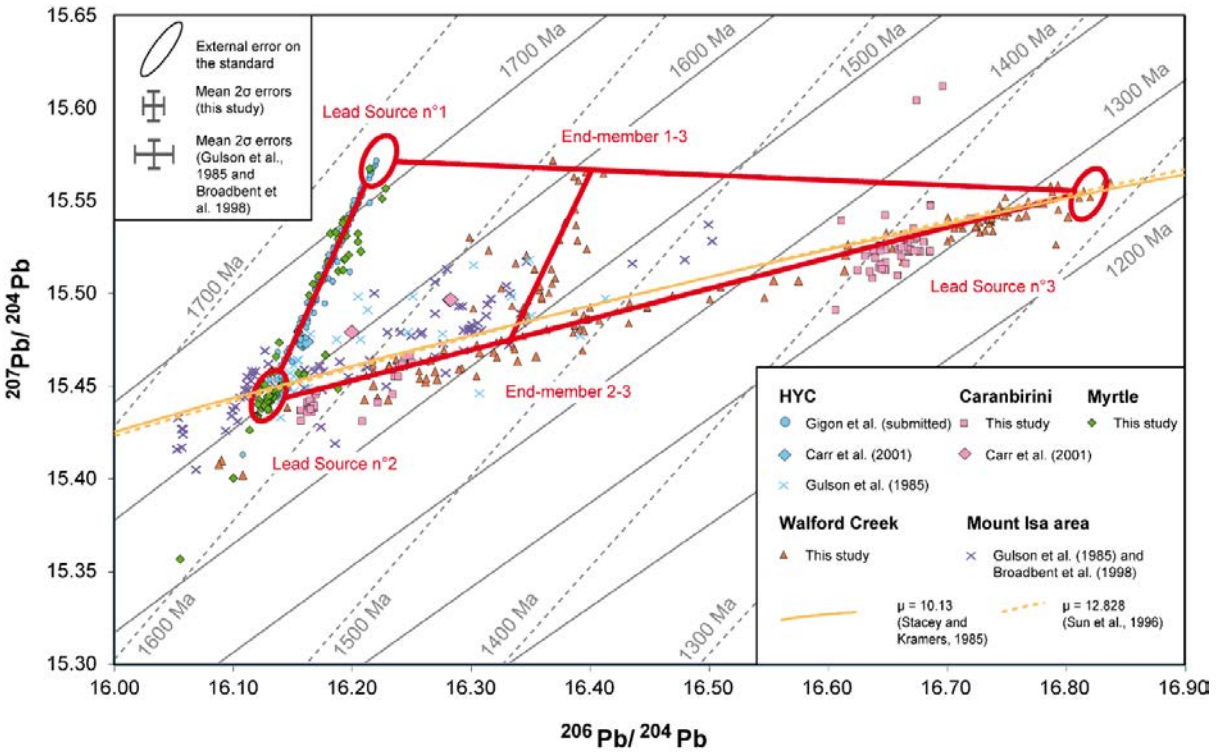

***Figure 6-11**: Lead isotopic interpretation based on the mixing between two lead sources at HYC and Myrtle, and a third one for Caranbirini and Walford Creek. Data from Gulson (1985) and Broadbent et al. (1998) are the only one represented for the Mount Isa region because they are the only published data where errors are indicated, with $^{206}Pb/^{204}Pb$ errors (2σ) = 0.1% * $^{206}Pb/^{204}Pb$ and $^{207}Pb/^{204}Pb$ errors (2σ) = 0.05 * $^{207}Pb/^{204}Pb$. The isochrones (straight lines linking isotopic ratios corresponding to rocks or mineral having the same age) from different models are indicated, with solid lines for the Stacey and Kramers (1975) model and dashed lines for the Sun et al. (1996) one. The growth curves with μ = 10.13 in the Stacey and Kramers (1975) model and μ = 12.828 for the Sun et al. (1996) one are plotted.*

6.5.2. Links between isotopic and chemical composition

A possibility would be that the fluid carrying lead from Lead Source n°1 has transported specific metals, distinct from the metals transported by the fluid carrying lead from Lead Source n°2. To check this hypothesis, LA-ICP-MS analyses have been performed exactly in the same holes than the SIMS ones. Figure 6-12A shows the $^{206}Pb/^{204}Pb$ ratio vs Ag, As, Mn and Sb concentrations for sample MY16 205.3m from Myrtle, and Figure 6-12B these diagrams for sample WFDD238 140.5m from Walford Creek. These samples were chosen because their lead isotopic data are scattered almost continually between end-members 1 and 2 for the first one, and 2 and 5 for the second one (the corresponding Lead Sources are reported at the top of the diagrams). Myrtle was favoured instead of HYC because of the major elements content in galena at HYC that could indicate a contamination by other sulphides, and therefore interfere with the trace elements content. No link between lead isotope content and Ag or Sb content has been observed in the sample from Myrtle. However, a possible correlation can be identified between the lead isotope ratio and As and Mn concentrations, which are the elements with the highest grade; this possible correlation extends therefore when comparing the isotope ratio and the sum of the minor and trace elements. As for example precipitated from the fluid carrying preferentially the lead from Lead Source n°1 and fluid carrying Lead Source n°1 could have carried a higher quantity of metals. In the sample from Walford Creek, for low $^{206}Pb/^{204}Pb$ ratios, corresponding to a higher input from fluid carrying Lead Source n°2, Ag, As and Sb concentrations are high and decrease when the isotope ratio increases. Ag, As and Sb are therefore precipitated from the fluid carrying preferentially the lead from Lead Source n°2, which also carried more metals. Concerning the metal grade in the fluids, it can be assumed that the fluid carrying lead from Lead Source n°2 had higher Ag, As, and Sb content. Ag content in the Walford Creek sample is ~300–600 ppm, whereas in the sample from Myrtle it is around 10 ppm. The relative metal content can be explained by different fluid properties, the variability of the conditions at the time of metal crystallisation in time and space, and the distinct fluid pathways.

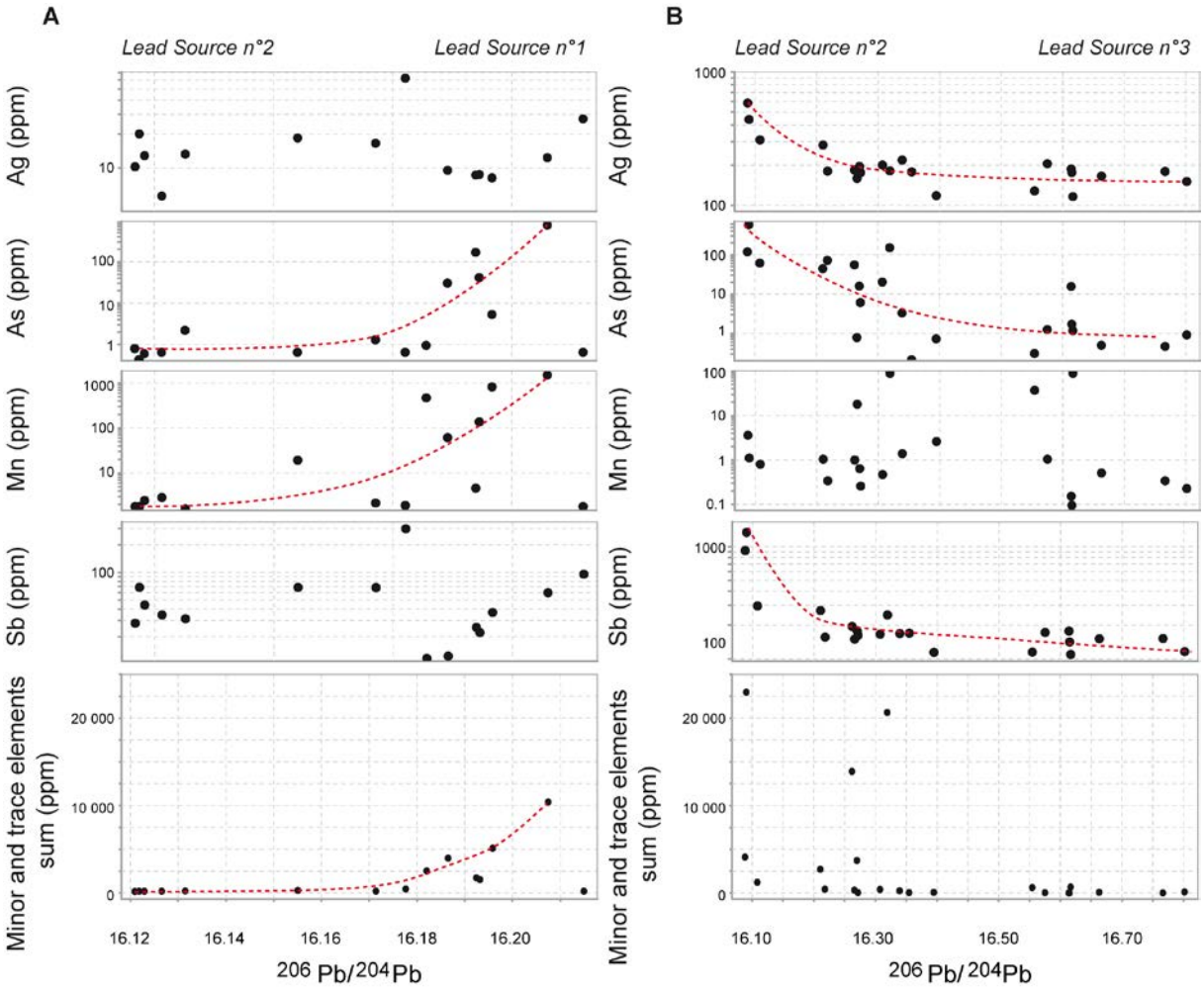

***Figure 6-12**: Lead isotopic ratios vs composition. (**A**) $^{206}Pb/^{204}Pb$ ratio vs Ag, As, Mn and Sb concentration, and sum of all the minor and trace elements analysed for sample MY16 205.3m from Myrtle. (**B**) $^{206}Pb/^{204}Pb$ ratio vs Ag, As, Mn and Sb concentration, and sum of all the minor and trace elements analysed for sample WFDD238 140.5m from Walford Creek.*

Another clue would be to consider samples recording only one lead source, and to look at the trace element content in galena, which should be constant at sample scale. Samples MY16 177.5m from Myrtle and WFDD266 271.4m from Walford Creek are the more homogeneous in lead composition. Even if the minor and trace elements content in these samples have globally a low dispersion, Ag and As content from other samples at Caranbirini and Walford Creek are higher than the two samples, while they should lie between the values if they are mixing between the two end-members. Sphalerite and galena are interpreted to be coprecipitated from the same fluid(s) at HYC and it is assumed that the contribution of each lead source in sphalerite is similar to their contribution in galena. The variations at the small scale are not negligible (Gigon et al., accepted) and multiplying the number of analysis would help to refine the proportion of each lead source.

6.5.3. Sulphide composition and temperatures estimates

Sphalerite compositions are constant in the stratiform HYC deposit, meaning constant conditions of ore formation. When comparing the different mineralisation types of sphalerite, the variation magnitude and the orders of magnitude are similar. The trace element in sphalerite are compared to Mississippi Valley-type (MVT), SHMS and vein-type deposits (Figure 6-4, Frenzel et al., 2016). For stratiform sphalerite at HYC, the grades obtained in this study are compatible with the one expected for Ag, Ga and Mn from SHMS deposits, slightly higher for Ge and lower for Fe and In. In vein-type sphalerite from this study, Ag content is within the expected range. Fe, In and Mn content are low compared to the generally > 10,000 ppm Fe and > 10 ppm Mn. On the contrary, Ga and Ge contents are high compared to the generally < 100 ppm Ga and < 300 ppm Ge.

Trace elements in galena can be compared to the ones in the Mount Isa deposit located in the adjacent sedimentary basin (George et al., 2015). Some elements in this study present very lower concentration compared to the ones measured at Mount Isa, such as Ag (693–2355 ppm) and Sb (888–3032 ppm), except from Walford Creek where the Sb content is in the same range. Bi concentration is lower than the 12–29 ppm at Mount Isa, except for two samples at Myrtle and one at Caranbirini. Sn content is similar at Mount Isa, HYC and Myrtle (3–12 ppm at Mount Isa) but some samples at Caranbirini and Walford Creek show lower content. Cd content is equivalent in almost all the analyses presented here and at Mount Isa (5–20 ppm). Cu content, < 6 ppm at Mount Isa, is equivalent at Caranbirini, higher at HYC and Myrtle and up to 10,000 times higher at Walford Creek, but a possible chalcopyrite contamination could explain this difference. Tl content (27–55 ppm at Mount Isa) is similar to the one observed at HYC and Myrtle. No clear relation between elements of corresponding valence such as between (Bi + Sb) and (Ag + Cu + Tl) observed by George et al. (2015) was highlighted here, but each sample seems to have its own substitution mechanism. Therefore, each sample probably underwent different substitution depending on the elements present in the environment at the time of crystallisation.

When comparing major, minor and trace elements in sphalerite and galena, there are 10 to 100 times more Ag in galena than in sphalerite, consistent with what is expected from substitution mechanisms (Belissont et al., 2014; Bonnet et al., 2016; Cook et al., 2009; Johan, 1988; Renock and Becker, 2011; Ye et al., 2011). Mn is more concentrated in galena at HYC, but in sphalerite at Caranbirini and Walford Creek. Sb can be up to 10 times more concentrated in galena (at HYC), but for example at Walford Creek the content can be similar in some selected samples.

Even if the concentration trace elements in sphalerite and galena at HYC is in the average of these kind of deposits, the tonnage is so significant that the total amount of trace elements may reach a large tonnage. For example, a potential stock of 10.9 kt Sb has been estimated at HYC (Yellishetty et al., 2017), consistent with the approximate values that can be calculated from the results present here and representing 3 times the 2018 production of Australia (U.S. Geological Survey, 2019).

The Tl halo at HYC surrounding the deposit and extending at least 250 m into the hangingwall and 100 m into the footwall of the Emu Fault (Large et al., 2000) is visible through the composition of sphalerite and galena, where Tl content is 2–200 ppm compared to 4–230 ppm in pyrite (Mukherjee and Large, 2017). This observation is conflicting the supposition of Spinks et al. (2019) who proposed that the Tl enrichment occurred prior to the deposition of base metal sulphides, and that Tl and Fe (forming the early pyrite) were transported in the same hydrothermal fluids.

Temperature of sphalerite precipitation was estimated thanks to the GGIMFis geothermometer using the Ga, Ge, Mn and In (in ppm) and Fe (in %) concentrations and the following equation (Frenzel et al., 2016):

$$T\ (°C) = (-54.4 \pm 7.3) \times ln\left(\frac{{C_{Ga}}^{0.22} * {C_{Ge}}^{0.22}}{{C_{Fe}}^{0.37} * {C_{Mn}}^{0.20} * {C_{In}}^{0.1}}\right) + (208\ \pm 10)$$

The GGIMFis geothermometer is calibrated between 100 and 400 °C. The temperatures fewer than 100 °C should not be taken into account, even if it can be assumed that the fluid carrying Zn was a low-temperature one. In this paragraph, the calculated values are nevertheless reported when they are lower than 100 °C for comparison between the different deposits. The calculated temperatures range from 134°C to 257 °C with a median value of 183 °C at HYC, from 40 °C to 211 °C with a median value of 118 °C at Myrtle, from 23 °C to 145 °C with a median value of 85 °C at Caranbirini and from 21 °C to 206 °C with a median value of 97 °C at Walford Creek (Figure 6-13 and Supplementary Table 6-2). The synsedimentary/early diagenetic sphalerite crystallised at higher temperatures (median = 183 °C), and a decrease of temperature is then observed in the following sulphides generations at Myrtle and Caranbirini. At Walford Creek, the sphalerite on early pyrite records low temperature (< 100 °C) whereas the sphalerite around coarse sphalerite has temperatures between 100 and 200 °C. Finally, sphalerite associated with late veining are around 100 °C, significantly higher than the veins in the Batten Fault Zone.

The temperatures at HYC are consistent with what is expected in this kind of deposits (Cooke et al., 2000; Huston et al., 2006; Large et al., 2005a; Rye and Williams, 1981), but higher than the 50–120 °C interpreted from the carbon and oxygen isotopes (Large et al., 2001)

and lower than the 310 ± 30 °C calculated from vitrinite reflectance (Symons, 2007). At Myrtle and Caranbirini, the low Fe, low In and high Ga content induce very low calculated temperatures. Even if some of the data are not in the calibration range, it is possible to infer a lower temperature at Myrtle and Caranbirini than at HYC.

This study highlights significant temperature variations in space and time. Differences between the deposits may relate to fluid temperature and fluid flux, which in turn may relate to how well feeder fault conduits tap deep fluid reservoirs, with a temperature decreasing with time.

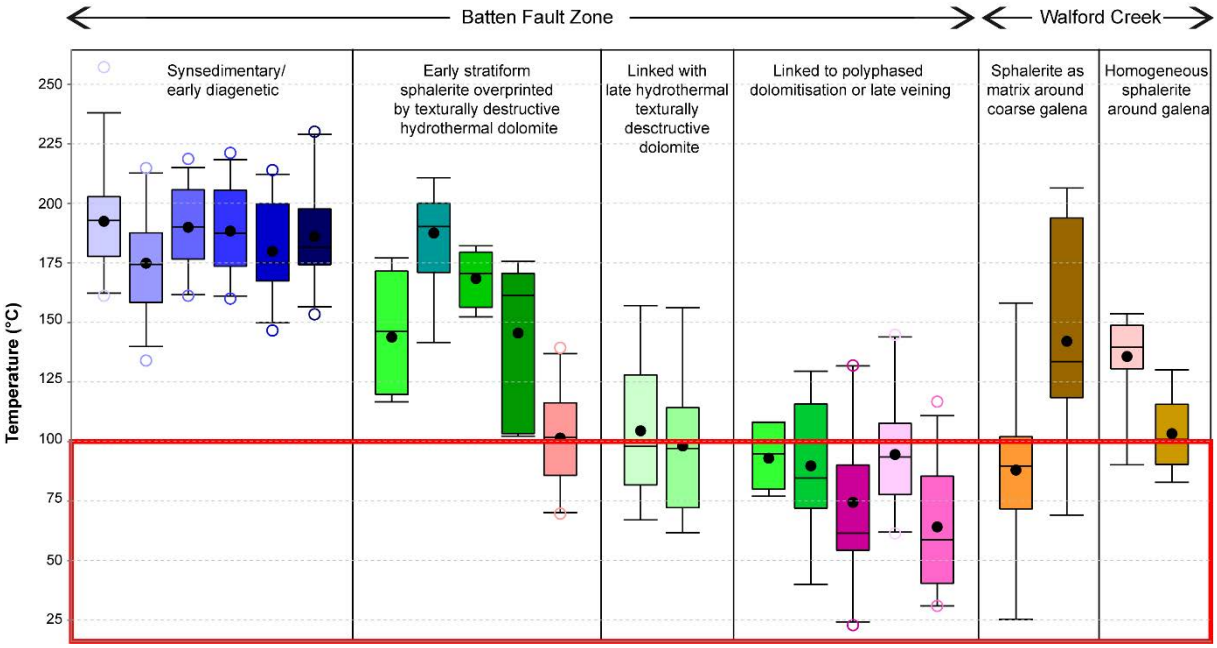

***Figure 6-13**: Estimated temperatures in sphalerites from HYC, Myrtle, Caranbirini and Walford Creek deposits calculated with the equation above (Frenzel et al., 2016). Temperatures below the calibration range are highlighted in red.*

6.5.4. Overall evolution and relation with regional tectonic context

The different paragenesis present in the deposits show a large variety of mineral assemblages, corresponding to different mineralising styles and timings. At 3.7 Ga, crust was extracted from the mantle and formed different crustal reservoirs, following a two-stage model as the one of Stacey and Kramers (1975). The different reservoirs were either formed exactly at the same time, or could result from different extracting event around 3.7 Ga. Each of this reservoirs evolved independently. The Sun et al. (1996) model proposes steady growth in μ through time, but was discarded by Gigon et al. (submitted) because the calculated model

ages did not correspond to any event in the basin. A detailed discussion about models for lead sources at HYC is presented in Gigon et al. (submitted).

The first possible event registered in the lead isotopic composition is the crystallisation of felsic rocks that will form the basement and the nowadays outcropping inliers. As they do not incorporate radioactive elements in their structure but only lead, the feldspars in these rocks record the lead isotopic composition at the time of crystallisation, at about 1860–1840 Ma (Figure 6-14A, Ahmad and Munson, 2013; Page et al., 2000). These feldspars can have remained in the basement or have been eroded to form the sedimentary rocks in the basin. At 1780–1730 Ma, galena crystallised in the basal sequence of the McArthur Basin (Spinks et al., 2016), here too recording the lead isotopic composition at this time (Figure 6-14B). The lead contained in the feldspars in the basement (that were then partly eroded in the basin) or in galena in the basin could then be mobilised at ~1640 Ma. As mentioned above, the basement- or basin-derivate contribution for Lead Source n°1 is not mandatory, if the preferred model is the one of different timing of crust extraction from the mantle.

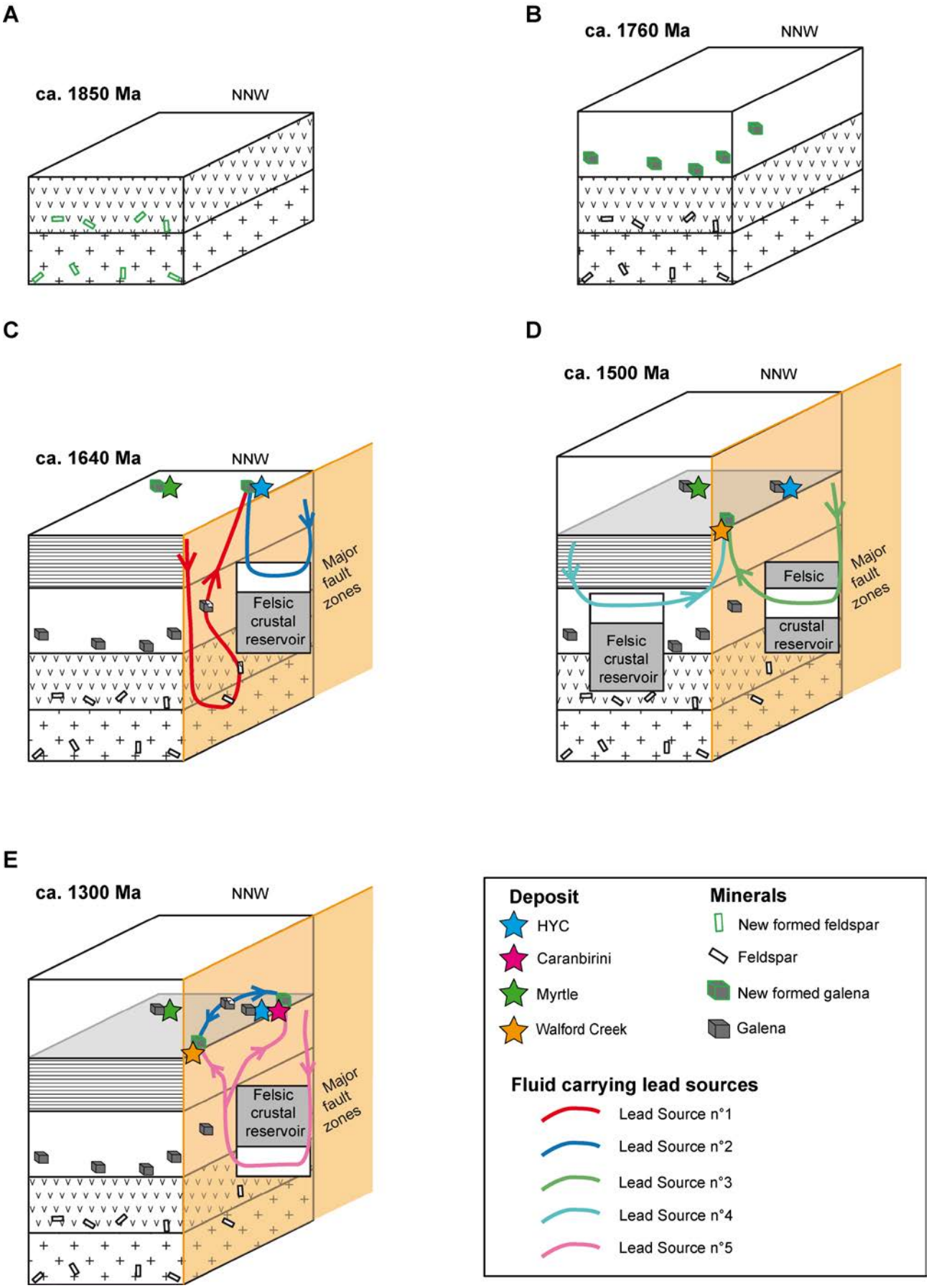
A
ca. 1850 Ma
NNW
B
ca. 1760 Ma
NNW
C
ca. 1640 Ma
NNW
Major fault zones
Felsic crustal reservoir
D
ca. 1500 Ma
NNW
Major fault zones
Felsic
crustal reservoir
Felsic crustal reservoir
E
ca. 1300 Ma
NNW
Major fault zones
Felsic crustal reservoir
Deposit
HYC
Caranbirini
Myrtle
Walford Creek
Minerals
New formed feldspar
Feldspar
New formed galena
Galena
Fluid carrying lead sources
Lead Source n°1
Lead Source n°2
Lead Source n°3
Lead Source n°4
Lead Source n°5

***Figure 6-14**: Schematic reconstruction of the fluid paths in the different reservoirs to explain the lead isotopes results in the studied deposits. **A**) At ca. 1850 Ma, feldspar crystallises in the basement (Gigon et al., accepted). **B**) At ca. 1760 Ma, galena crystallises in the Tawallah Group of the McArthur Basin (Spinks et al., 2016). **C**) At ca. 1640 Ma, a first fluid leaches the lead contained in the feldspar or in the galena (Lead Source n°1, red arrow), and a second fluid leaching a felsic crustal reservoir (Lead Source n°2, dark blue arrow), and the two fluids mix at the emplacement of the HYC and Myrtle deposits. **D**) At ca. 1500 Ma, during the Isan Orogeny, two fluids leach lead from two different felsic reservoirs. On reservoir is the same that was already leached at ca. 1640 Ma (Lead Source n° 3) and a new one poorly constrained (Lead Source n°4). These two fluids mix at the emplacement of the Walford Creek deposit. **E**) At ca. 1300 Ma, during the Musgrave Orogeny, a fluid leaches for the third time a felsic crustal reservoir (Lead Source n°5) and mixes with a fluids that leached galena crystallised at ca. 1640 Ma. The mixing happened at Caranbirini and Walford Creek.*

The second event recorded is the main crystallising event, at ~1640 Ma (Figure 6-14C). Lead Sources n°1 and 2 are mobilised at that time in almost all the samples from the HYC and Myrtle deposits, except the sample MY16 177.5m where only Lead Source n°2 is mobilised. Generally, at HYC and Myrtle, the mixing of the two lead sources is necessary and both brought approximately the same amount of lead in the deposit. The temperatures for this major mineralising event are 160–220 °C as recorded at HYC for the older galena. At Myrtle, the timing of the early stratiform sulphides overprinted by texturally destructive hydrothermal dolomite, compared to the sphalerite linked with this late hydrothermal dolomite cannot be confirmed by lead isotopes as all the youngest data are within the errors of the analyses at HYC. The temperature decreased rapidly at Myrtle between these two events, from 100–200 °C to <100–130 °C. The sample recording only Lead Source n°2 indicates that in some part of the deposit or at a specific timing, maybe slightly younger, only one lead source was leached and the temperature continued to decrease (< 100–120 °C). The tectonic settings around 1640 Ma could be either post-extensional syn-inversion fraction of the Calvert and Isa superbasins, linked to crustal shortening and supercontinent assembly (Gibson et al., 2017), or extensional faulting in a back-arc setting (Betts et al., 2003). Figure 6-15 presents the polar wander path for northern Australia, especially the tracks and bends, dated from >1700 Ma to youngest ages less constraint by U-Pb zircon dating. Major bends in the apparent polar wander path are associated with magnetic overprints related to episodes of fluid circulation, and three of them appear to be associated with the expulsion of metal rich brines that formed the world-class Broken Hill, Mt Isa and HYC Pb–Zn deposits (Idnurm, 2000). Rapid changes in the intraplate stress regime related to bends on this path may have been responsible for geologically instantaneous fluid expulsion and the migration of these fluids along faults (Southgate et al., 2006).

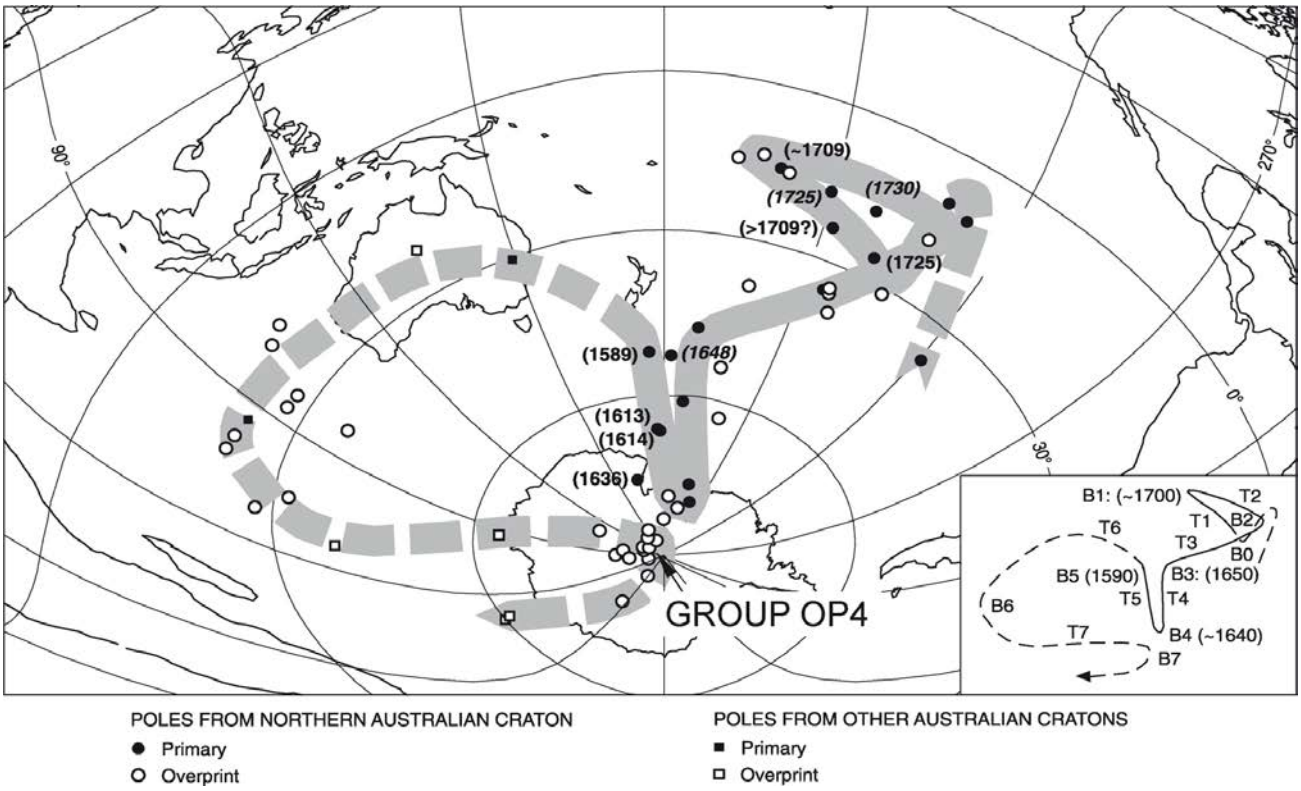

Figure 6-15*: Diagram of the Late Paleoproterozoic – Early Mesoproterozoic apparent polar wander path for northern Australia. Numbers in brackets after acronyms give U–Pb zircon ages in Ma. Parts of the apparent polar wander path regarded as tentative are shown by a broken band. Inset shows interpretation of apparent polar wander path in terms of tracks (T) and bends (B). Simplified after Idnurm (2000).*

The Isan Orogeny (1640–1490 Ma, with the peak around ca 1590 Ma, Murphy et al., 2011) did not disturb most of the lead isotopes in galena, and it can be assumed that its impact was negligible on the sulphide mineralisation in the Batten Fault Zone. However, its influence could be seen in one of the sample of Walford Creek whose lead isotopic ratio lie on the isochrons corresponding to the age of the Isan Orogeny. This could be interpreted as lead being mobilised from two different reservoirs during this major tectonic event (Figure 6-14D), one being the same reservoir than the one leached to form lead Source n°2, and another felsic crustal reservoir of unknown origin.

Following the hypothesis of several leaching events, the same reservoir than the one forming Lead Source n°2 had continued to evolve independently and could have been leached, and galena could have crystallised several times between 1640 and 1300 Ma (Figures 6-16 and 6-17).

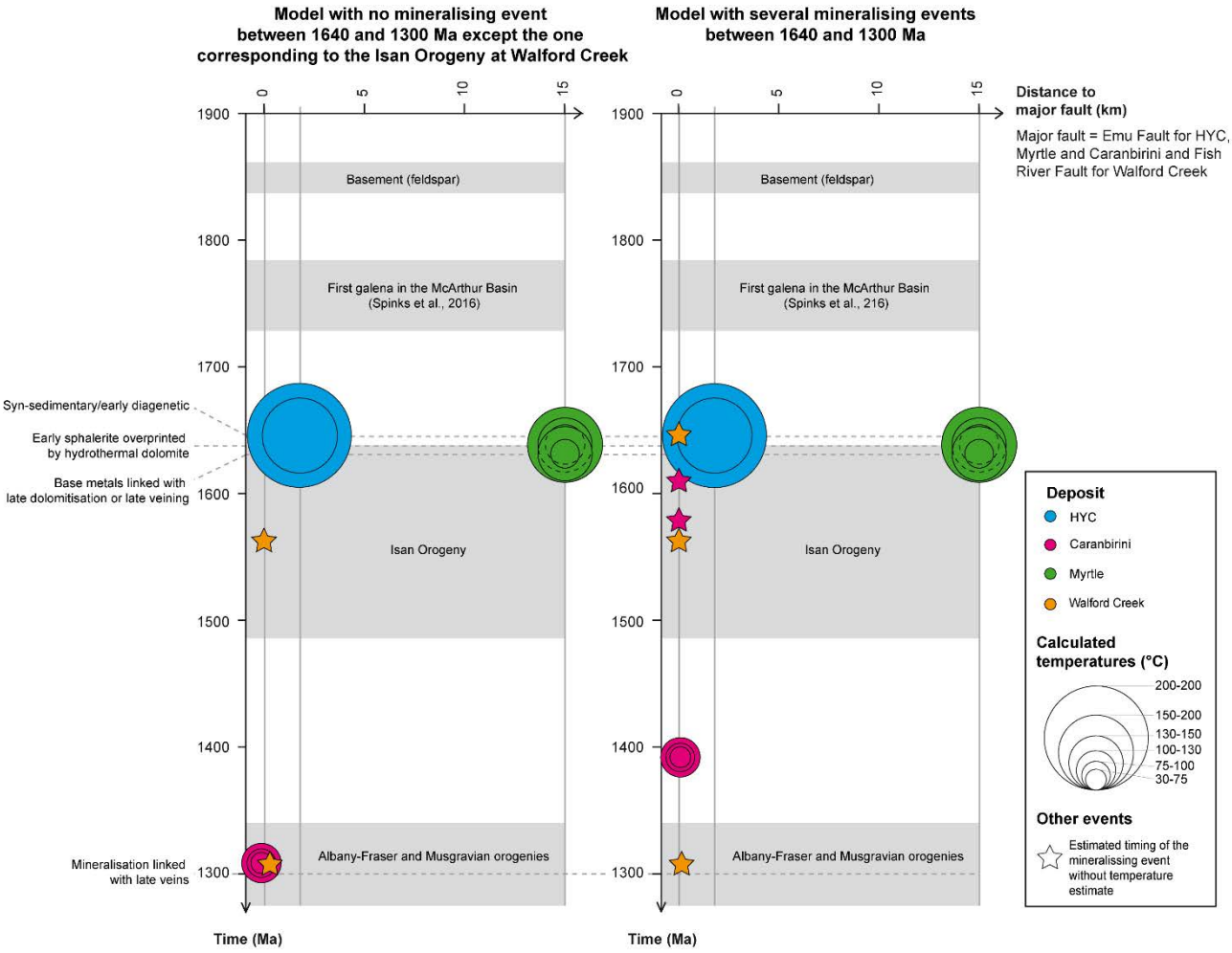

***Figure 6-16**: Synthesis of the fluid events and their associated temperature considering two models. The first one (to the left) without any mineralising event between 1640 and 1300 Ma (except the one corresponding to the Isan orogeny at Walford Creek), where all the lead isotopes ratios are explained by mixing. The second one (to the right) corresponds to several leaching and mineralising events of the same reservoir between 1640 and 1300 Ma. Note that the calculated temperature from sphalerite was reported when it was associated with dated galena.*

The model age of the event mobilising Lead Source n°5 is evaluated between 1315 Ma (Sun et al., 1996) and 1235 Ma (Stacey and Kramers, 1975). At that time, the same reservoir than the one from which Lead Source n°2 was leached had continued to evolve independently and was in turn leached. Based on the hypothesis of the mixing, it happened between this lead source and the Lead Source n°2 corresponding to a mineral crystallised at 1640 Ma and containing a uniform lead isotopic composition, likely galena crystallised at 1640 Ma from Lead Source n°2 only. This late event was at low temperature (< 100–120 °C) and didn't affect the HYC and Myrtle deposits that were maybe not reached by this fluid circulation because they are located at a distance from the Emu Fault. At Caranbirini on the contrary, no stratiform mineralisation is present, but there is evidence of the overprinting of a younger event. One hypothesis is that the primary base metal mineralisation was entirely remobilised at ~1300 Ma

in this prospect.

The following paragraphs give are an attempt to characterise the context for the circulation of the fluid carrying the Lead Source n°5. The ca. 1330–1100 Ma Albany-Fraser and Musgravian orogenies have been interpreted as the results of collision between the South Australian Craton and the North and West Australian Craton (Myers et al., 1996) or as an extensional intraplate event, accompanied by a high geothermal gradient and extensive melting of the lower crust (Smithies et al., 2011). Orogenesis involved two discrete events: the first one may have been an accretionary event characterised by high-temperature metamorphism between ca. 1330 and 1290 Ma, followed by final collision between 1220 and 1100 Ma (Betts and Giles, 2006). In the Northern Territory, the Musgrave Orogeny was recorded mostly in the Musgrave Province around 1200–1160 Ma, far from the McArthur Basin, and in the Arunta Region during the associated ca 1150 Ma Teapot event (Ahmad and Munson, 2013). K-Ar ages in the Lawn Hill Platform indicate a 1250 to 1150 Ma fluid-flow event mostly restricted in the northeast part of the platform and to the east of the Termite Range fault in the central Lawn Hill Platform and may be related to the assembly of the Rodinian supercontinent (Golding et al., 2006). In the McArthur-Mount Isa-Cloncurry minerals province, base metal deposits including Mount Isa, Lady Loretta, and Walford Creek show a similar multistage history, indicating that long-lived deep faults (such as the Termite Range fault) controlled basin-scale fluid flow and the location of major base metal deposits in the province.

A bend of specific interest in this study is the last one, noted as Overprinted 4 (OP4 in Figure 6-16). This event is mainly recorded throughout the Lawn Hill Platform, but also possibly in the Kombolgie Formation, extending the apparent polar wander path northward and indicating a prominent bend at OP4. The bend and overprint OP4 suggest a continuation of Mesoproterozoic tectonism and fluid movement in northern Australia after the Isan Orogeny (Idnurm, 2000). OP4 is therefore interpreted as Mesoproterozoic, but post-dating the gently folded South Nicholson and Roper Groups. The age of the Roper Group is constrained by a Rb-Sr determination of 1429 ± 31 Ma for diagenetic illite in one formation almost at the top of the McArthur Basin (Kralik, 1982), with a minimum age of 1324 ± 4 Ma from SHRIMP dating of baddeleyite from the Derim Derim Dolerite (Abbott et al., 2001). The age of OP4 would therefore be younger than 1429 Ma, and could correspond to the event during which the Lead Source n°5 was mobilised.

The reason why each deposit could have recorded or not the mineralising events could be linked to the vicinity to major faults and the partitioning of the basin in sub-basins where fluids can easily circulate or not. In addition, if we assume that stratiform mineralisation occurred everywhere, it could have been partly or entirely remobilised where it is no more expressed

today, such as Caranbirini for example. Following this hypothesis, the high metal content at HYC could be explained because this deposit has not been affected by younger event that would have remobilised the metals.

6.6. Conclusions

The lead isotopes data reveal a mixing between two lead sources at HYC and Myrtle, with the same end-members for these two deposits. At Caranbirini, in the same host rock formation, there is evidence for mixing between one of these lead sources and a younger one. The major distinction between all these deposits is the vicinity to the Emu Fault. At Caranbirini, the absence of lead in primary stratiform mineralisation and the evidence of the overprinting of a younger event can suggest that the primary lead was remobilised at ~1300 Ma. At Walford Creek and Caranbirini, the patterns are globally equivalent even if they lay hundreds of kilometres away. This homogeneity at regional scale confirms the genetic link between the McArthur Basin and the Lawn Hill Platform, where fluids circulated at the same period along deep faults. In addition, the lead isotope results in these two deposits highlight the remobilising of metals during at least a younger event (~1315–1235 Ma). The circulation of the fluid carrying this young lead source is possibly linked to a major orogenic event and could correspond to a major bend in the polar wander path of Northern Australia, similar to the one observed at ~1640 Ma where the major Pb-Zn deposits emplace. This study highlights the multistage history affecting the studied deposits. The long-lived deep faults controlled basin-scale fluid flow and the location of major base metal deposits in the province by allowing or not the remobilisation of sulphides several times in the history of the deposit. The sulphides composition provide also insights on the temperature of the mineralising events, with temperature dropping from 160–220°C in primary mineralisation to < 100 °C in some sulphide in late veins. The fluid carrying the different lead sources also carried distinct metals now found as minor and trace elements in the galena.

Acknowledgements

Glencore provided the samples for the HYC deposit, Teck for the Myrtle deposit, the Northern Territory Geological Survey for Caranbirini and Aeon Metals for the Walford Creek deposit. Nick Hayward and Rodney King (Teck) are thanked for the explanations on the Batten Fault Zone paragenesis, and Dan Johnson, Ed Jelicich-Kane and Jack Murday for the discussions on the Walford Creek deposit.

Supplementary material

Supplementary Table 6-1: *Major elements results obtained by SIMS on sphalerite and galena from the HYC, Myrtle and Walford Creek deposits and from the Caranbirini prospect.*

Deposit	Drillhole #/sample #	Depth (m)	Circle #	Analysis #	S (wt%)	Fe (wt%)	Cu (wt%)	Zn (wt%)	Zn_n (wt%)	Pb (wt%)	Pb_n (wt%)	Total (wt%)	Mean Zn_n (%)	Mean Pb_n (%)
HYC	E11-1		1	1	33.49	4.89	2.57	57.88	58.41	0.1		99.1	61.0	85.6
HYC	E11-1		1	2	33.16	5.17	2.24	58.00	58.63	0.14		98.93	1.7	1.3
HYC	E11-1		1	3	33.49	4.44	2.89	58.67	58.81	0.09		99.77		
HYC	E11-1		1	5	32.93	3.57	0	62.09	62.81	0.12		98.85		
HYC	E11-1		1	5	13.65	0	0	1.45		85.88	85.03	101		
HYC	E11-1		1	6	13.77	0	0	0.5		84.94	85.62	99.21		
HYC	E11-1		2	1	32.84	3.6	1.27	61.05	61.58	0.14		99.14		
HYC	E11-1		2	2	33.04	4.89	1.43	60.25	60.24	0.16		100.02		
HYC	E11-1		2	3	32.59	4.03	0.5	61.22	62.04	0.13		98.68		
HYC	E11-1		2	4	32.78	4.42	1.99	58.93	59.79	0.27		98.56		
HYC	E11-1		2	5	33.27	3.81	0.6	61.04	61.66	0.18		99		
HYC	E11-1		3	1	33.06	4.75	0.79	59.69	60.52	0.13		98.63		
HYC	E11-1		3	2	33.42	5.17	1.82	57.91	58.78	0.04		98.52		
HYC	E11-1		3	3	33.58	3.91	0.64	61.72	61.60	0.11		100.19		
HYC	E11-1		3	4	33.00	3.83	2.1	59.29	60.21	0.01		98.47		
HYC	E11-1		3	5	32.45	4.05	0.41	61.43	62.22	0.19		98.73		
HYC	E11-1		3	6	33.18	3.49	0.98	61.87	61.98	0.15		99.82		
HYC	E11-1		3	7	33.24	3.84	0.57	61.29	61.75	0.11		99.26		
HYC	E11-1		4	1	32.94	4.74	2.64	58.67	59.13	0.12		99.23		
HYC	E11-1		4	2	32.66	2.68	0.87	61.77	62.81	0.23		98.34		
HYC	E11-1		5	1	13.14	0	0	0.00		85.63	86.67	98.8		
HYC	E11-1		5	10	31.83	3.65	1.25	59.69	61.63	0.07		96.86		
HYC	E11-1		5	12	13.25	0	0	0.02		86.46	86.65	99.78		
HYC	E11-1		5	2	13.73	0	0	0.19		84.71	85.85	98.67		
HYC	E11-1		5	3	33.43	2.09	0.65	61.75	62.84	0.17		98.26		
HYC	E11-1		5	4	33.21	4.3	0.03	60.11	61.34	0.16		98		
HYC	E11-1		5	4	13.30	0	0	0		82.74	85.63	96.62		
HYC	E11-1		5	5	33.00	5.33	0.12	60.3	60.86	0.04		99.08		
HYC	E11-1		5	6	32.09	4.12	0.45	58.61	61.20	0.21		95.77		
HYC	E11-1		5	7	11.70	2.75	0	0.20		79.2	83.16	95.24		
HYC	E11-1		5	8	30.30	2.92	0.28	54.56	57.53	6.47		94.84		
HYC	E11-1		5	9	13.37	0	0	0.00		86.54	86.60	99.93		
HYC	E11-1		6	1	13.26	0	0	0.17		86.45	86.54	99.9		
HYC	E11-1		6	2	32.92	3.52	0.05	61.79	62.69	0.21		98.57		
HYC	E11-1		6	3	13.67	0	0	0.23		84.62	85.54	98.92		
HYC	E11-1		6	4	13.28	0.09	0	0.14		85.96	86.32	99.58		
HYC	E11-1		6	5	14.39	1.54	0	0.66		82.1	82.63	99.36		
HYC	E11-1		6	5	32.13	2.37	0.02	60.95	63.68	0.1		95.71		
HYC	E11-1		6	7	31.64	2.96	0.13	59.22	62.83	0.1		94.25		
HYC	E11-1		6	8	13.16	0	0	0.08		85.37	86.56	98.63		
HYC	E11-2		1	1	32.94	0.32	0	66	66.30	0		99.55	63.2	85.3
HYC	E11-2		1	2	33.34	0.24	0.05	65.78	65.81	0.11		99.96	2.2	0.8
HYC	E11-2		1	3	33.29	0.39	0	66.49	66.20	0.1		100.44		
HYC	E11-2		1	5	13.53	0	0	0.65		86.98	85.99	101.15		
HYC	E11-2		2	4	32.98	0.42	0	66.18	66.29	0.04		99.84		
HYC	E11-2		2	2	32.90	0.33	0	65.86	66.26	0.27		99.4		
HYC	E11-2		2	2	33.21	0.46	0.07	66.16	66.13	0.07		100.05		
HYC	E11-2		3	1	32.79	2.94	1.32	61.46	62.12	0.12		98.93		
HYC	E11-2		3	2	31.99	1.99	0.86	61.91	63.34	0.9		97.75		
HYC	E11-2		3	3	33.39	2.34	0.56	62.93	63.16	0.07		99.63		
HYC	E11-2		3	4	32.47	2.83	1.26	61.98	62.66	0.18		98.92		
HYC	E11-2		4	1	33.09	3.92	2.41	59.31	59.84	0.17		99.12		
HYC	E11-2		4	2	33.50	2.99	1.87	61.35	61.41	0.05		99.91		
HYC	E11-2		4	3	32.78	3.58	2.26	59.50	60.39	0.22		98.52		
HYC	E11-2		4	4	32.91	4.09	1.76	59.80	60.51	0.08		98.82		
HYC	E11-2		4	5	33.55	3.57	1.4	61.52	61.29	0.21		100.37		
HYC	E11-2		5	1	34.02	3.31	1.39	61.68	61.28	0.13		100.66		
HYC	E11-2		5	2	32.99	3.52	1.34	61.25	61.58	0.14		99.46		
HYC	E11-2		5	3	32.52	2.69	1.26	61.74	62.65	0.17		98.55		
HYC	E11-2		5	4	32.51	2.84	1.35	60.70	62.18	0.07		97.62		
HYC	E11-2		5	6	12.78	0	0	0.34		82.08	84.54	97.09		
HYC	E11-2		5	7	31.55	1.93	0.24	61.91	64.10	0.11		96.59		

Deposit	Drillhole #/sample #	Depth (m)	Circle #	Analysis #	S (wt%)	Fe (wt%)	Cu (wt%)	Zn (wt%)	Znn (wt%)	Pb (wt%)	Pbn (wt%)	Total (wt%)	Mean Znn (%)	Mean Pbn (%)
HYC	E11-3		1	1	13.46	0	0	0.45		83.6	85.67	97.58	62.5	85.6
HYC	E11-3		1	2	11.58	0	0	0.00		76.58	83.86	91.32	1.0	1.0
HYC	E11-3		1	3	32.35	1.92	0.46	62.44	63.86	0.15		97.78		
HYC	E11-3		2	1	13.47	0	0	0.04		84.7	86.09	98.39		
HYC	E11-3		2	2	13.89	0	0	1.89		83.6	84.08	99.43		
HYC	E11-3		2	3	13.72	0	0	0.06		82.38	85.58	96.26		
HYC	E11-3		3	1	13.22	0	0	0.00		85.06	86.43	98.42		
HYC	E11-3		3	2	13.26	0	0	0.00		84.51	86.20	98.04		
HYC	E11-3		3	3	13.32	0	0	0.39		85.57	86.18	99.29		
HYC	E11-3		4	1	33.04	1.95	0.62	60.87	62.41	0.94		97.53		
HYC	E11-3		4	2	32.71	2.14	0.21	61.37	62.47	1.7		98.24		
HYC	E11-3		4	2	13.55	0	0	1.08		81.61	84.75	96.29		
HYC	E11-3		4	3	13.29	0	0	0.06		86.36	86.61	99.71		
HYC	E11-3		4	3	33.93	2.75	0.36	59.56	60.99	0.88		97.66		
HYC	E11-3		4	4	13.37	0	0	0.51		86.81	86.17	100.74		
HYC	E11-3		4	5	32.42	2.48	0.44	60.61	62.69	0.42		96.68		
HYC	E4-2		1	1	32.82	2.03	0.88	62.76	63.47	0.19		98.88	63.3	83.5
HYC	E4-2		1	2	32.20	2.19	0.38	62.44	63.98	0.17		97.59	0.5	
HYC	E4-2		1	3	12.99	0	0	3.14		82.12	83.53	98.31		
HYC	E4-2		2	2	32.66	2.59	0.43	62.89	63.34	0.11		99.29		
HYC	E4-2		3	1	31.92	2.22	0.82	62.67	63.22	0.14		99.13		
HYC	E4-2		3	2	32.77	2.88	0.95	61.89	62.60	0.15		98.86		
HYC	E4-3		1	1	13.40	0	0	0.06		86.11	86.41	99.65	63.5	86.5
HYC	E4-3		1	3	13.50	0	0	0.51		86.81	86.09	100.84	0.4	0.3
HYC	E4-3		1	5	13.52	0	0	0.06		86.63	86.42	100.24		
HYC	E4-3		2	1	13.52	0	0	0.00		86.51	86.46	100.06		
HYC	E4-3		2	2	13.45	0	0	0.00		84.47	86.25	97.94		
HYC	E4-3		2	3	13.34	0	0	0.00		86.8	86.64	100.19		
HYC	E4-3		2	4	32.38	2.26	0.26	62.30	63.86	0.07		97.55		
HYC	E4-3		3	1	33.10	2.32	0.75	62.31	63.10	0.11		98.75		
HYC	E4-3		3	2	13.56	0	0	0.00		87.29	86.55	100.86		
HYC	E4-3		3	3	12.84	0	0	0.00		85.92	86.96	98.8		
HYC	E4-3		3	4	13.57	0	0	0.07		85.97	86.30	99.62		
HYC	E5-1			1	13.92	0	0	0.21		85.99	85.84	100.18	63.0	85.0
HYC	E5-1			2	34.11	3.12	0.79	64.67	62.89	0.08		102.83	2.2	0.8
HYC	E5-1			3	13.83	0	0	2.64		86.37	83.82	103.04		
HYC	E5-1			4	33.61	1.76	0.39	66.55	64.94	0.1		102.48		
HYC	E5-1			5	33.92	1.59	0.21	67.23	65.17	0.1		103.16		
HYC	E5-1			6	33.79	2.92	1.57	64.45	62.56	0.2		103.02		
HYC	E5-1			7	34.16	5.04	0.77	58.75	59.30	0.12		99.07		
HYC	E5-1			8	14.06	0	0	0.55		83.43	84.81	98.37		
HYC	E5-1			9	14.00	0.12	0	0		84.6	85.52	98.92		
HYC	MRM-2012-3	164.6		2	34.04	3.45	0.3	65.15	63.09	0.1		103.26	62.8	
HYC	MRM-2012-3	164.6		3	34.04	2.77	0.41	65.5	63.66	0.03		102.89	2.1	
HYC	MRM-2012-3	164.6		4	34.37	4.79	2.95	60.69	58.91	0.11		103.02		
HYC	MRM-2012-3	164.6		5	33.27	3.28	0.05	63.88	63.35	0.21		100.83		
HYC	MRM-2012-3	164.6		7	32.15	0.39	0.02	65.65	65.15	0.03		100.77		
HYC	MRM-2012-3	176.2		1	12.55	0	0	0		89.21	87.65	101.78	64.0	85.5
HYC	MRM-2012-3	176.2		2	33.31	0.94	0	66.89	65.99	0		101.36	1.9	1.9
HYC	MRM-2012-3	176.2		3	13.42	0	0	0.17		84.91	86.20	98.50		
HYC	MRM-2012-3	176.2		4	14.00	0	0	0		85.16	85.77	99.29		
HYC	MRM-2012-3	176.2		6	13.71	0	0	0		84.04	85.77	97.98		
HYC	MRM-2012-3	176.2		8	13.55	0	0	1.08		80.04	82.08	97.52		
HYC	MRM-2012-3	176.2		9	31.91	2.35	1.24	60.12	61.51	0.62		97.74		
HYC	MRM-2012-3	176.2		10	33.61	1.68	0.15	64.87	64.48	0.07		100.61		
HYC	MRM-2012-3	191		1	33.80	4.73	0.53	62.3	61.36	0.15		101.54	63.3	85.0
HYC	MRM-2012-3	191		2	34.28	4.41	0.4	63.27	61.65	0.07		102.62	1.6	0.7
HYC	MRM-2012-3	191		3	14.07	0	0	0.2		81.81	85.00	96.25		
HYC	MRM-2012-3	191		4	13.68	0	0	0.09		85.54	85.97	99.50		
HYC	MRM-2012-3	191		6	33.07	1.58	0.38	66.72	65.30	0		102.18		
HYC	MRM-2012-3	191		7	14.00	0	0	1.79		86.77	84.56	102.61		
HYC	MRM-2012-3	191		8	33.54	2.38	0.22	65.72	64.28	0.15		102.24		
HYC	MRM-2012-3	191		9	13.93	0	0	2.29		87.32	84.29	103.60		
HYC	MRM-2012-3	191		10	33.13	2.4	0.64	64.89	64.06	0.07		101.30		
HYC	MRM-2012-3	209.7		3	14.17	0	0	0.21		86.69	85.74	101.11	62.1	85.1
HYC	MRM-2012-3	209.7		4	13.89	0	0	0		84.24	85.66	98.34	0.9	0.9
HYC	MRM-2012-3	209.7		5	33.76	2.55	1.08	63.32	62.70	0.12		100.99		
HYC	MRM-2012-3	209.7		6	33.69	2.68	1.64	63.45	62.14	0.51		102.10		
HYC	MRM-2012-3	209.7		7	33.99	3.84	2.19	62.5	60.79	0.09		102.81		
HYC	MRM-2012-3	209.7		8	14.03	0	0	2.63		87.05	83.92	103.73		
HYC	MRM-2012-3	209.7		9	34.16	2.49	0.92	64.13	62.82	0.22		102.08		

Deposit	Drillhole #/sample #	Depth (m)	Circle #	Analysis #	S (wt%)	Fe (wt%)	Cu (wt%)	Zn (wt%)	Znn (wt%)	Pb (wt%)	Pbn (wt%)	Total (wt%)	Mean Znn (%)	Mean Pbn (%)
Myrtle	MY16	170.7	1	1	32.95	0.9	0	65.61	65.87	0.12		99.61	66.45	
Myrtle	MY16	170.7	1	2	33.06	0.94	0	66.26	66.04	0		100.33	0.47	
Myrtle	MY16	170.7	2	1	33.01	0.67	0	66.12	66.11	0.13		100.01		
Myrtle	MY16	170.7	2	2	32.39	0.49	0	65.89	66.63	0.07		98.89		
Myrtle	MY16	170.7	3	1	32.79	0.66	0	66.22	66.33	0.05		99.84		
Myrtle	MY16	170.7	3	2	32.89	0.36	0	66.12	66.42	0.05		99.55		
Myrtle	MY16	170.7	4	1	32.68	0.1	0	67.42	67.20	0.06		100.33		
Myrtle	MY16	170.7	4	2	32.73	0.1	0	66.8	66.99	0		99.71		
Myrtle	MY16	172.9	1	1	32.63	1.16	0.01	65.16	65.75	0.05		99.11	66.36	
Myrtle	MY16	172.9	1	2	32.27	0.38	0	66.01	66.78	0.06		98.84	0.38	
Myrtle	MY16	172.9	2	1	32.74	0.22	0	66.35	66.74	0.07		99.41		
Myrtle	MY16	172.9	2	2	32.94	0.33	0.03	66.11	66.40	0.03		99.56		
Myrtle	MY16	172.9	3	1	33.22	0.33	0.03	65.5	66.02	0.03		99.21		
Myrtle	MY16	172.9	3	2	32.88	0.45	0	65.42	66.05	0.17		99.05		
Myrtle	MY16	172.9	3	3	32.89	0.15	0	66.27	66.54	0.08		99.59		
Myrtle	MY16	172.9	3	4	32.59	0.39	0	66.04	66.60	0.07		99.16		
Myrtle	MY16	177.5	1	1	13.44	0	0	0		86.19	86.41	99.74		86.37
Myrtle	MY16	177.5	1	2	13.33	0	0	0		86.17	86.57	99.54		0.14
Myrtle	MY16	177.5	1	3	13.55	0	0	0		86.03	86.34	99.64		
Myrtle	MY16	177.5	1	4	13.35	0	0	0		86.13	86.56	99.5		
Myrtle	MY16	177.5	1	5	13.46	0	0	0		86.07	86.43	99.58		
Myrtle	MY16	177.5	1	6	13.67	0	0	0		85.95	86.25	99.65		
Myrtle	MY16	177.5	2	1	13.74	0	0	0		85.95	86.17	99.75		
Myrtle	MY16	177.5	2	2	13.59	0	0	0		87.09	86.46	100.73		
Myrtle	MY16	177.5	2	3	13.66	0	0	0		86.33	86.26	100.08		
Myrtle	MY16	177.5	2	4	13.72	0	0	0		85.96	86.23	99.69		
Myrtle	MY16	190	1	1	13.34	0	0	0		87.62	86.78	100.97		86.69
Myrtle	MY16	190	1	2	13.37	0	0	0		87.36	86.70	100.76		0.15
Myrtle	MY16	190	1	3	13.24	0	0	0		87.26	86.82	100.51		
Myrtle	MY16	190	1	4	13.65	0	0	0		87.39	86.48	101.05		
Myrtle	MY16	195.5	1	1	32.5	1.1	0.04	66.28	66.19	0		100.14	65.33	
Myrtle	MY16	195.5	1	2	32.4	1.23	0	66.43	66.24	0.15		100.29	1.13	
Myrtle	MY16	195.5	1	3	32.64	0.74	0.01	66.37	66.38	0.02		99.99		
Myrtle	MY16	195.5	1	4	32.86	0.62	0	66.26	66.31	0.09		99.93		
Myrtle	MY16	195.5	2	1	32.77	0.41	0	65.61	66.31	0		98.94		
Myrtle	MY16	195.5	2	2	32.76	0.59	0	66.03	66.28	0.03		99.63		
Myrtle	MY16	195.5	2	3	32.45	0.7	0	65.77	66.34	0.05		99.14		
Myrtle	MY16	195.5	2	4	32.83	0.99	0	64.8	65.57	0.08		98.83		
Myrtle	MY16	195.5	3	1	32.39	2.06	0.04	64.26	64.87	0.13		99.06		
Myrtle	MY16	195.5	3	2	33.05	3.23	0	62.64	63.18	0.06		99.15		
Myrtle	MY16	195.5	4	1	32.53	2.6	0	63.26	64.11	0.19		98.68		
Myrtle	MY16	195.5	4	2	32.56	2.82	0	63	63.87	0.09		98.64		
Myrtle	MY16	195.5	4	3	32.61	2.26	0	64.03	64.64	0.07		99.05		
Myrtle	MY16	195.5	4	4	32.48	2.57	0	63.76	64.31	0.08		99.14		
Myrtle	MY16	197.7	1	1	33.01	3.8	0	62.47	62.76	0.12		99.53	65.41	85.97
Myrtle	MY16	197.7	1	2	32.58	4.52	0.03	61.86	62.31	0.1		99.28	2.00	0.61
Myrtle	MY16	197.7	1	3	32.85	4	0	62.56	62.74	0.08		99.71		
Myrtle	MY16	197.7	1	4	32.76	3.87	0.05	63.14	62.98	0.25		100.25		
Myrtle	MY16	197.7	1	5	32.61	4.21	0	62.47	62.73	0.09		99.59		
Myrtle	MY16	197.7	2	1	33.01	2.62	0	64.47	64.31	0.08		100.25		
Myrtle	MY16	197.7	2	2	32.6	3.98	0	61.99	62.62	0.15		98.99		
Myrtle	MY16	197.7	3	1	32.62	0.12	0	67	66.91	0.13		100.14		
Myrtle	MY16	197.7	3	2	32.15	0.05	0	66.4	67.23	0.07		98.76		
Myrtle	MY16	197.7	3	3	32.72	0.79	0	65.5	66.02	0.08		99.21		
Myrtle	MY16	197.7	3	4	32.46	0	0	67.14	67.32	0.04		99.74		
Myrtle	MY16	197.7	4	1	32.54	0.14	0	66.94	67.07	0.05		99.81		
Myrtle	MY16	197.7	4	2	32.47	0.31	0	66.72	66.91	0		99.71		
Myrtle	MY16	197.7	5	1	32.47	0.15	0	66.36	66.92	0.03		99.17		
Myrtle	MY16	197.7	5	2	32.54	0.16	0	66.59	66.85	0.11		99.61		
Myrtle	MY16	197.7	5	3	32.51	0.08	0	66.08	66.80	0		98.92		
Myrtle	MY16	197.7	5	4	32.58	0.07	0	66.1	66.73	0.05		99.05		
Myrtle	MY16	197.7	5	5	32.8	0.11	0	66.61	66.80	0.06		99.71		
Myrtle	MY16	197.7	5	6	32.13	0.24	0	65.86	66.75	0.08		98.66		
Myrtle	MY16	197.7	5	7	13.31	0	0	0.22		86.25	86.40	99.83		
Myrtle	MY16	197.7	5	8	12.81	0	0	1.65		85.54	85.54	100		

Deposit	Drillhole #/sample #	Depth (m)	Circle #	Analysis #	S (wt%)	Fe (wt%)	Cu (wt%)	Zn (wt%)	Znn (wt%)	Pb (wt%)	Pbn (wt%)	Total (wt%)	Mean Znn (%)	Mean Pbn (%)
Myrtle	MY16	205.3	1	1	33.25	1.04	0	64.94	65.34	0.08		99.39	65.49	86.47
Myrtle	MY16	205.3	1	2	13.53	0	0	0		86.69	86.47	100.26	0.69	0.13
Myrtle	MY16	205.3	1	3	12.86	0	0	0		83.51	86.62	96.41		
Myrtle	MY16	205.3	1	4	32.8	1.57	0	63.59	64.72	0.11		98.26		
Myrtle	MY16	205.3	1	5	13.65	0	0	0.04		86.79	86.38	100.48		
Myrtle	MY16	205.3	1	6	32.76	1.26	0	65.24	65.53	0.14		99.55		
Myrtle	MY16	205.3	1	7	32.84	0.46	0	66.1	66.39	0.01		99.57		
Myrtle	MY16	205.3	2	1	13.37	0	0	0.02		87.38	86.67	100.82		
Myrtle	MY16	205.3	2	2	13.41	0	0	0		86.63	86.60	100.04		
Myrtle	MY16	205.3	2	3	13.55	0	0	0		87.38	86.54	100.97		
Myrtle	MY16	205.3	2	4	13.57	0	0	0		87.12	86.51	100.7		
Myrtle	MY16	205.3	3	2	13.27	0	0	0		86.36	86.64	99.68		
Myrtle	MY16	205.3	3	3	13.59	0	0	0		86.83	86.42	100.47		
Myrtle	MY16	205.3	3	4	13.46	0	0	0		86.13	86.48	99.6		
Myrtle	MY16	205.3	3	5	13.46	0	0	0.01		86.28	86.46	99.79		
Myrtle	MY16	205.3	4	1	13.53	0	0	0		86	86.41	99.53		
Myrtle	MY16	205.3	4	2	13.75	0	0	0		86.22	86.25	99.97		
Myrtle	MY16	205.3	4	3	13.57	0	0	0.07		86.05	86.28	99.73		
Myrtle	MY16	205.3	4	4	13.58	0	0	0		86.21	86.36	99.83		
Caranbirini	MANT79-3	208.6		1	33.65	0.25	0.01	69.18	66.92	0.03		103.37	66.75	
Caranbirini	MANT79-3	208.6		2	33.8	0.25	0.05	68.9	66.71	0.08		103.29	0.36	
Caranbirini	MANT79-3	208.6		3	33.3	0.29	0.03	69.34	67.08	0.03		103.37		
Caranbirini	MANT79-3	208.6		4	32.58	0.08	0	66.87	66.41	0.1		100.70		
Caranbirini	MANT79-3	208.6		5	33.79	0.05	0	70.12	67.31	0.12		104.18		
Caranbirini	MANT79-3	208.6		6	34.15	0.23	0	68.14	66.08	0.14		103.12		
Caranbirini	MANT79-3	208.6		7	33.88	0.27	0	69.52	66.82	0.12		104.04		
Caranbirini	MANT79-3	208.6		8	33.6	0.1	0.03	69.17	66.75	0		103.62		
Caranbirini	MANT79-3	208.6		10	33.54	0.03	0	68.25	66.64	0.16		102.41		
Caranbirini	DD84CA4	328.6		1	34.18	0.67	0.09	68.78	66.13	0.13		104.01	66.10	
Caranbirini	DD84CA4	328.6		2	34.52	0.9	0.09	68.78	65.74	0.11		104.63	0.29	
Caranbirini	DD84CA4	328.6		3	34.35	0.82	0	68.69	66.00	0.07		104.08		
Caranbirini	DD84CA4	328.6		4	33.97	0.82	0	68.78	66.31	0.07		103.73		
Caranbirini	DD84CA4	328.6		5	33.81	0.7	0	69.07	66.54	0.03		103.80		
Caranbirini	DD84CA4	328.6		6	33.84	1.03	0	67.82	65.89	0.02		102.93		
Caranbirini	DD84CA4	352.6		1	33.52	0.44	0	68.11	66.61	0.15		102.25	66.77	
Caranbirini	DD84CA4	352.6		2	33.58	0.37	0	68.36	66.76	0.09		102.40	0.41	
Caranbirini	DD84CA4	352.6		3	33.93	0.29	0	68.19	66.46	0.13		102.60		
Caranbirini	DD84CA4	352.6		4	28.89	0.38	0.04	64.65	67.60	0.15		95.64		
Caranbirini	DD84CA4	352.6		5	33.99	0.27	0.05	68.55	66.58	0.07		102.96		
Caranbirini	DD84CA4	352.6		6	34.12	0.28	0	68.79	66.63	0.01		103.24		
Caranbirini	DD82CA1	565		1	13.83	0	0	0		85.63	86.05	99.51		86.01
Caranbirini	DD82CA1	565		2	14.06	0	0	0		86.3	85.99	100.36		0.04
Caranbirini	DD82CA1	565		3	13.99	0	0	0		85.92	85.98	99.93		
Caranbirini	DD82CA1	565		4	13.97	0	0	0		85.55	85.96	99.52		
Caranbirini	DD82CA1	565		5	13.97	0	0	0		86.11	86.04	100.08		
Caranbirini	DD82CA1	679.2		1	33.69	0.08	0.22	66.49	65.79	0.16		101.06	66.41	86.05
Caranbirini	DD82CA1	679.2		2	33.52	0.12	0.01	67.81	66.68	0		101.70	0.41	0.16
Caranbirini	DD82CA1	679.2		3	13.85	0	0	0		85.41	86.01	99.30		
Caranbirini	DD82CA1	679.2		4	13.89	0	0	0		85.19	85.98	99.08		
Caranbirini	DD82CA1	679.2		5	33.86	0.1	0	68.15	66.45	0.01		102.56		
Caranbirini	DD82CA1	679.2		6	33.56	0.6	0.15	67.05	65.95	0.05		101.67		
Caranbirini	DD82CA1	679.2		7	13.74	0	0	0		86	86.22	99.74		
Caranbirini	DD82CA1	679.2		8	32.99	0.09	0.02	67.63	66.96	0.11		101.00		
Caranbirini	DD82CA1	679.2		9	13.99	0	0	0		85.67	85.94	99.69		
Caranbirini	DD82CA1	679.2		10	14.15	0	0	0		86.14	85.88	100.30		
Caranbirini	DD82CA1	679.2		11	14.01	0	0	0		85.51	85.91	99.54		
Caranbirini	DD82CA1	679.2		12	33.99	0.12	0.05	68.13	66.49	0.03		102.46		
Caranbirini	DD82CA1	679.2		13	33.58	0.15	0.18	68.1	66.56	0.01		102.32		
Caranbirini	DD82CA1	679.2		14	13.86	0	0	0		85.88	86.10	99.74		
Caranbirini	DD82CA1	679.2		15	13.77	0	0	0		86.94	86.32	100.72		
Caranbirini	DD82CA1	734.9		1	13.91	0	0	0		83.7	85.73	97.63		86.01
Caranbirini	DD82CA1	734.9		2	13.74	0	0	0		85.31	86.12	99.06		0.17
Caranbirini	DD82CA1	734.9		3	13.71	0	0	0		85.31	86.15	99.02		
Caranbirini	DD82CA1	734.9		4	13.89	0	0	0		85.62	86.03	99.52		
Caranbirini	DD82CA1	734.9		5	14	0	0	0		86.6	86.03	100.66		
Walford Creek	WFDD238	140.5		1	13.96	0	0	0		87.14	86.17	101.12	67.04	86.18
Walford Creek	WFDD238	140.5		2	13.78	0	0	0		87.32	86.35	101.12	0.32	0.12
Walford Creek	WFDD238	140.5		3	13.82	0	0	0		86.87	86.23	100.74		
Walford Creek	WFDD238	140.5		4	14.01	0	0	0		86.82	86.11	100.83		
Walford Creek	WFDD238	140.5		5	14.07	0	0	0		86.71	86.03	100.79		
Walford Creek	WFDD238	140.5		6	33.27	0.16	0	69.21	67.30	0.07		102.84		
Walford Creek	WFDD238	140.5		7	32.87	0.11	0	68.74	67.46	0.1		101.89		
Walford Creek	WFDD238	140.5		8	33.79	0.12	0.04	68.73	66.74	0.13		102.98		
Walford Creek	WFDD238	140.5		9	33.84	0.25	0	69.18	66.89	0.1		103.42		
Walford Creek	WFDD238	140.5		10	33.67	0.18	0.01	69.04	66.79	0.21		103.37		

Deposit	Drillhole #/sample #	Depth (m)	Circle #	Analysis #	S (wt%)	Fe (wt%)	Cu (wt%)	Zn (wt%)	Znn (wt%)	Pb (wt%)	Pbn (wt%)	Total (wt%)	Mean Znn (%)	Mean Pbn (%)
Walford Creek	WFDD238	141		1	14.05	0	0	0		87.99	86.22	102.05		86.10
Walford Creek	WFDD238	141		2	13.98	0	0	0		86.46	86.08	100.44		0.14
Walford Creek	WFDD238	141		3	13.78	0	0	0		85.96	86.18	99.75		
Walford Creek	WFDD238	141		4	13.79	0	0.08	0		86.35	86.16	100.22		
Walford Creek	WFDD238	141		5	14	0	0	0		85.99	85.87	100.14		
Walford Creek	WFDD266	110		2	14.13	0	0	0		85.53	85.81	99.67	66.44	86.21
Walford Creek	WFDD266	110		3	13.61	0	0	0		86.6	86.35	100.29	0.25	0.35
Walford Creek	WFDD266	110		4	33.9	0.81	0	68	66.12	0		102.85		
Walford Creek	WFDD266	110		5	13.59	0	0	0		86.99	86.48	100.59		
Walford Creek	WFDD266	110		9	33.73	0.7	0	68	66.37	0		102.45		
Walford Creek	WFDD266	110		10	33.39	0.58	0	67.95	66.59	0.02		102.05		
Walford Creek	WFDD266	110		11	33.4	0.29	0	67.94	66.68	0.14		101.89		
Walford Creek	WFDD266	130.8		1	14.15	0	0	0		83.34	85.42	97.56	65.73	85.06
Walford Creek	WFDD266	130.8		2	33.8	0.5	0.01	68.52	66.36	0.28		103.26	0.85	0.53
Walford Creek	WFDD266	130.8		3	34.54	0.86	0.2	65.99	64.58	0.41		102.18		
Walford Creek	WFDD266	130.8		4	34.1	0.51	0	67.22	65.72	0.34		102.28		
Walford Creek	WFDD266	130.8		5	14.38	0	0	0.17		81.11	84.75	95.70		
Walford Creek	WFDD266	130.8		6	14.31	0	0	0		83.18	85.32	97.49		
Walford Creek	WFDD266	130.8		7	14.23	0	0.23	0.01		81.65	84.29	96.87		
Walford Creek	WFDD266	130.8		8	32.14	0.64	0	66.26	66.72	0.16		99.31		
Walford Creek	WFDD266	130.8		9	14.04	0	0	0		82.96	85.53	97.00		
Walford Creek	WFDD266	130.8		10	33.85	0.79	0.1	66.22	65.28	0.42		101.44		
Walford Creek	WFDD266	271.4		1	13.94	0	0	0		87.48	86.20	101.48	66.45	86.32
Walford Creek	WFDD266	271.4		2	13.94	0	0	0		87.38	86.25	101.31	0.62	0.08
Walford Creek	WFDD266	271.4		3	13.84	0	0	0		87.88	86.39	101.72		
Walford Creek	WFDD266	271.4		4	13.78	0	0	0		87.25	86.35	101.04		
Walford Creek	WFDD266	271.4		5	13.85	0	0	0		87.95	86.38	101.82		
Walford Creek	WFDD266	271.4		6	33.12	0.42	0	69.21	67.16	0.21		103.05		
Walford Creek	WFDD266	271.4		8	33.22	0.53	0.15	68.52	66.59	0.15		102.90		
Walford Creek	WFDD266	271.4		9	33.45	1.3	0	67.32	65.67	0.44		102.52		
Walford Creek	WFDD266	271.4		10	33.03	0.74	0	67.94	66.37	0.66		102.37		
Walford Creek	WFDD272	184.3		1	14.33	0	0	0		86.71	85.82	101.04		86.00
Walford Creek	WFDD272	184.3		2	14.26	0	0	0		86.84	85.87	101.13		0.24
Walford Creek	WFDD272	184.3		3	14	0	0	0		86.03	85.95	100.09		
Walford Creek	WFDD272	184.3		4	13.84	0	0	0		87.55	86.34	101.40		

Supplementary Table 6-2: *Minor and trace elements results obtained by LA-ICP-MS on sphalerite from the HYC, Myrtle and Walford Creek deposits and from the Caranbirini prospect.*

Deposit	Lens # (HYC)	Drillhole #	Depth (m)	Analyse #	V (ppm)	Cr (ppm)	Mn (ppm)	Fe (ppm)	Co (ppm)	Ni (ppm)	Cu (ppm)	Ga (ppm)	Ge (ppm)	As (ppm)	Se (ppm)	Mo (ppm)	Ag (ppm)	Cd (ppm)	In (ppm)	Sn (ppm)	Sb (ppm)	Te (ppm)	Au (ppm)	Hg (ppm)	Tl (ppm)	Pb (ppm)	Bi (ppm)	Calculated temperature (°C)
HYC	7	MRM-2012-3	164.6	1	4.10	< 3.6	5600	51500	4.10	< 91	3930	19.2	26.3	605	< 90	< 0.94	11.6	750	0.56	9.90	15.50	< 5.2	< 0.21	42.00	2.10	241	< 0.056	257
HYC	7	MRM-2012-3	164.6	1'	10.30	< 3.3	2180	11860	1.68	< 82	272	18.4	67.4	5	< 83	< 0.85	4.1	623	< 0.066	4.90	57.90	< 4.7	< 0.19	55.30	4.08	104	< 0.051	191
HYC	7	MRM-2012-3	164.6	2	3.63	< 2.2	1770	35700	24.60	< 55	2266	18.6	56.8	772	< 52	< 0.51	17.4	646	< 0.042	6.40	22.40	< 3.5	< 0.15	24.80	43.20	980	< 0.046	211
HYC	7	MRM-2012-3	164.6	2'	4.40	< 3.7	310	30500	19.00	< 67	2380	16.7	31.4	550	< 70	< 0.65	14.2	673	< 0.076	5.20	17.50	< 4.6	< 0.15	16.40	17.30	1440	< 0.052	200
HYC	7	MRM-2012-3	164.6	3	1.74	< 2.1	820	28740	19.40	< 53	3130	21.5	63.6	745	< 64	0.51	17.2	646	< 0.062	6.10	19.20	< 2.5	< 0.13	27.10	44.20	3090	0.10	197
HYC	7	MRM-2012-3	164.6	3'	< 0.39	< 1.9	36	29900	22.50	< 54	2820	15.2	65.9	578	< 88	< 0.52	15.3	717	< 0.069	4.89	14.20	< 3.7	< 0.11	18.40	57.10	800	< 0.046	168
HYC	7	MRM-2012-3	164.6	4	15.70	< 2.7	660	31500	13.00	< 69	1950	17.9	48.5	671	< 75	< 0.63	28.0	637	< 0.057	3.78	40.70	< 4.5	< 0.091	37.90	37.30	1720	0.05	201
HYC	7	MRM-2012-3	164.6	4'	1.26	< 2.3	940	34100	19.30	< 48	2310	14.3	28.6	528	< 71	< 0.63	13.9	714	< 0.05	4.44	12.60	< 4.6	< 0.12	17.40	9.20	740	< 0.04	215
HYC	7	MRM-2012-3	164.6	5	0.45	< 1.8	33	27700	24.10	< 49	3370	21.2	63.9	940	< 71	< 0.6	21.2	693	< 0.06	4.75	19.20	< 3.9	< 0.13	18.70	47.40	4180	0.07	161
HYC	7	MRM-2012-3	164.6	5'	5.80	< 2.5	138	27900	18.30	< 56	2710	15.6	30.8	592	< 80	< 0.8	16.4	688	< 0.042	4.20	19.70	< 4.2	< 0.11	17.00	16.00	177	< 0.056	187
HYC	7	MRM-2012-3	164.6	6	10.40	< 2.2	710	35800	19.80	< 61	3000	15.1	34.6	642	< 78	< 0.93	20.6	569	< 0.083	2.85	27.90	< 3.7	< 0.14	18.80	20.00	2810	0.08	213
HYC	7	MRM-2012-3	164.6	6'	11.20	< 3.7	94	34100	18.80	< 61	2730	16.6	36.3	715	< 93	1.92	21.2	617	< 0.058	3.57	31.50	< 4.2	< 0.18	25.40	24.50	1890	< 0.049	186
HYC	7	MRM-2012-3	164.6	7	12.00	< 2.6	370	34300	24.90	< 59	2060	14.9	39.8	515	< 90	< 0.7	16.7	652	< 0.066	4.17	24.30	< 2.6	< 0.12	31.00	29.50	580	< 0.047	202
HYC	7	MRM-2012-3	164.6	7'	< 0.44	< 1.6	400	29200	21.40	< 38	3470	16.4	39.3	588	< 77	< 0.54	13.3	677	< 0.064	5.09	14.00	< 3.6	< 0.12	26.40	19.40	212	< 0.03	199
HYC	7	MRM-2012-3	164.6	8	2.09	< 2.3	54	30200	12.60	< 64	3170	15.5	28.8	451	< 110	< 0.54	12.2	708	< 0.067	4.52	15.00	< 4.9	< 0.11	21.90	5.33	86	< 0.055	182
HYC	7	MRM-2012-3	164.6	8'	1.20	< 2.6	41	28110	21.80	< 51	5100	20.1	61.4	725	< 88	< 0.57	19.7	737	< 0.044	4.98	17.70	< 2.5	< 0.13	18.60	38.50	420	< 0.039	163
HYC	7	MRM-2012-3	164.6	9	9.30	< 2.6	56	28100	21.70	< 58	2990	21.3	61.0	683	< 120	< 0.64	20.8	636	< 0.067	4.29	27.50	< 3.5	< 0.18	26.80	37.60	1040	< 0.069	168
HYC	7	MRM-2012-3	164.6	9'	5.60	< 2.9	211	30700	12.30	< 51	2610	17.4	29.0	522	< 140	< 0.42	15.6	715	0.06	3.76	18.20	< 2.2	< 0.14	17.20	5.92	13200	0.15	199
HYC	7	MRM-2012-3	164.6	10	8.60	< 2.3	850	31100	15.50	< 63	3030	17.6	36.8	594	< 140	< 0.64	16.2	656	< 0.063	4.69	22.80	< 3.7	< 0.14	28.50	23.40	274	< 0.039	208
HYC	7	MRM-2012-3	164.6	10'	< 0.31	< 0.95	49	31080	24.60	< 51	3760	19.4	41.1	700	< 120	< 0.38	15.6	682	< 0.03	5.79	14.20	< 3.1	< 0.11	13.20	17.60	300	< 0.035	170
HYC	7	MRM-2012-3	164.6	11	2.72	< 2.1	2460	36100	24.10	90	2700	18.4	44.7	738	< 200	< 0.46	17.6	629	< 0.055	3.90	23.40	< 2.5	< 0.15	14.40	27.30	4400	0.07	219
HYC	7	MRM-2012-3	164.6	11'	8.70	< 2.1	395	31700	20.50	< 75	2950	16.9	37.0	602	< 210	< 0.46	18.9	614	< 0.055	4.20	25.60	< 2.5	< 0.15	26.50	21.50	1700	< 0.041	200
HYC	7	MRM-2012-3	164.6	12X	5.52	< 1.9	94	31200	18.80	< 54	2600	18.3	43.6	620	< 190	0.54	17.2	631	< 0.054	5.04	22.70	< 3.3	< 0.12	23.40	18.20	890	< 0.054	181
HYC	7	MRM-2012-3	164.6	13	2.03	< 2.2	160	31400	22.40	< 60	3810	22.7	56.3	810	< 260	< 0.7	18.0	595	< 0.044	3.80	17.60	< 3.2	< 0.15	12.00	19.10	344	< 0.05	180
HYC	7	MRM-2012-3	164.6	13'	1.99	< 2.2	109	28440	18.70	< 65	3660	18.3	46.1	675	< 370	< 0.43	17.8	709	< 0.025	4.92	17.19	< 2.4	< 0.083	16.30	24.50	4300	< 0.036	176
HYC	7	MRM-2012-3	164.6	14	1.26	2.60	730	27790	19.70	< 57	2640	14.3	42.6	628	< 360	< 0.55	17.2	668	< 0.049	6.93	17.60	< 2.9	< 0.1	23.30	29.90	2030	< 0.04	203
HYC	7	MRM-2012-3	164.6	14'	6.70	< 2.3	270	30470	21.60	< 70	3140	17.2	38.9	608	< 490	< 0.85	17.5	642	< 0.045	7.40	22.10	< 3.7	< 0.15	22.90	18.90	750	< 0.065	193
HYC	7	MRM-2012-3	164.6	15	1.60	< 1.9	45	29880	26.10	< 65	2030	18.5	48.8	690	< 700	< 0.6	12.4	689	< 0.049	5.10	15.40	< 3.2	< 0.11	14.70	30.20	1580	< 0.036	170
HYC	7	MRM-2012-3	164.6	15'	18.70	< 2.7	105	32300	21.70	< 61	2070	21.3	46.4	660	< 1100	< 0.76	17.3	586	< 0.055	5.10	23.60	< 3.5	< 0.18	30.00	23.20	1630	< 0.049	180
Percentage of analyses > LOD					90	3	100	100	100	3	100	100	100	100	0	10	100	100	7	100	100	0	0	100	100	100	21	
HYC	5	E5-1		1	13.10	< 6	23	41500	10.40	< 120	2480	57.7	106.0	615	< 140	1.80	16.6	729	5.53	122.00	62.90	< 5.5	< 0.33	52.90	34.80	409	< 0.49	176
HYC	5	E5-1		1'	9.60	< 5.9	41	68000	13.50	< 74	17000	22.7	31.3	960	< 140	1.18	19.0	1000	1.61	72.40	41.00	< 5.9	< 0.33	21.50	59.90	477	0.23	211
HYC	5	E5-1		2	1.02	< 2.6	56	23100	0.95	< 35	9600	25.1	58.8	840	< 71	< 0.69	12.7	1057	2.54	74.00	24.10	< 3.4	< 0.11	19.60	12.60	165	< 0.054	186
HYC	5	E5-1		2'	7.10	< 2.7	593	20290	< 0.49	< 60	4310	11.4	54.4	< 3.3	< 76	< 0.64	4.4	875	< 0.063	7.46	19.50	< 4.5	< 0.15	31.80	16.56	359	< 0.044	196
HYC	5	E5-1		3	2.60	< 3.6	72	14500	< 0.34	< 74	1330	36.9	64.2	24	< 100	< 0.9	10.1	953	0.16	7.90	50.20	< 4.8	< 0.24	19.90	8.32	297	< 0.069	159
HYC	5	E5-1		3'	2.53	< 2.9	73	16310	0.66	< 59	4290	16.0	32.2	239	< 82	< 0.72	18.1	948	0.34	23.70	25.30	< 3.8	< 0.19	21.10	13.40	2440	0.15	184
HYC	5	E5-1		4	1.06	< 2.7	125	12650	< 0.34	< 54	1790	44.2	88.0	81	< 69	< 0.71	6.9	940	0.08	7.90	35.20	< 2.9	< 0.21	25.90	7.05	86	< 0.062	153
HYC	5	E5-1		4'	2.12	< 2.7	95	14960	< 0.33	< 53	2140	12.8	47.4	8	< 69	< 0.7	5.9	948	0.14	9.80	22.80	< 2.9	< 0.2	18.40	8.53	147	< 0.061	178
HYC	5	E5-1		5	2.42	< 2.8	69	13930	0.65	< 55	2570	13.3	66.7	31	< 72	< 0.73	15.2	929	0.24	15.10	30.10	< 3	< 0.21	22.40	16.42	165	0.10	172
HYC	5	E5-1		5'	5.18	< 3.2	144	14710	< 0.39	< 48	1954	30.3	86.8	12	< 80	< 0.47	9.5	857	0.05	10.30	38.30	< 3.9	< 0.19	25.70	12.82	145	< 0.054	160
HYC	5	E5-1		6	< 0.53	< 2.8	9	22500	< 0.37	< 55	10960	13.5	7.7	389	< 66	< 0.68	14.6	1062	0.06	7.50	13.50	< 3.1	< 0.12	18.80	8.94	1650	< 0.07	177
HYC	5	E5-1		6'	< 0.5	< 2.7	17	32300	< 0.35	< 52	12250	32.4	16.8	533	< 62	< 0.64	13.3	1275	0.47	16.50	11.40	< 2.9	< 0.11	13.40	17.20	304	< 0.066	183
HYC	5	E5-1		7	2.87	< 5.3	450	17500	1.80	< 76	1739	18.0	49.6	63	< 100	< 1	10.4	885	0.34	15.70	28.10	< 4	< 0.22	27.00	22.10	101	< 0.059	199
HYC	5	E5-1		7'	1.48	< 3.3	198	26300	4.90	< 47	2090	14.5	58.3	105	< 63	< 0.63	7.7	1019	< 0.042	5.20	38.30	< 2.5	< 0.13	17.00	20.60	500	< 0.036	183
HYC	5	E5-1		8	< 0.62	< 3.2	103	12180	0.32	< 57	1830	32.0	84.4	23	< 100	< 0.82	18.8	1060	0.12	11.40	45.40	< 4.2	< 0.13	7.30	12.80	78000	1.01	156
HYC	5	E5-1		8'	< 0.81	< 4.2	131	14700	0.83	< 74	2860	7.9	29.1	8	< 130	< 1.1	10.2	1090	< 0.1	7.40	35.70	< 5.4	0.37	5.39	16.60	84000	0.53	187
HYC	5	E5-1		9	< 0.65	< 2.2	224	15560	< 0.28	< 75	4770	8.5	38.3	4	< 85	< 0.9	5.6	987	< 0.069	9.70	17.06	< 3.9	< 0.13	19.50	8.77	63	< 0.04	188
HYC	5	E5-1		9'	1.18	< 3.2	26	13490	< 0.58	< 46	4030	24.7	61.6	189	< 87	4.49	22.1	916	0.36	22.90	53.00	< 4.2	< 0.17	23.40	13.20	6000	0.55	156
HYC	5	E5-1		10	< 0.55	< 3.2	61	11900	< 0.58	< 46	1820	33.0	70.8	12	< 89	< 0.64	9.2	902	< 0.065	11.20	50.60	< 4.2	< 0.17	24.20	10.32	187	< 0.042	145

Deposit	Lens # (HYC)	Drillhole #	Depth (m)	Analyse #	V (ppm)	Cr (ppm)	Mn (ppm)	Fe (ppm)	Co (ppm)	Ni (ppm)	Cu (ppm)	Ga (ppm)	Ge (ppm)	As (ppm)	Se (ppm)	Mo (ppm)	Ag (ppm)	Cd (ppm)	In (ppm)	Sn (ppm)	Sb (ppm)	Te (ppm)	Au (ppm)	Hg (ppm)	Tl (ppm)	Pb (ppm)	Bi (ppm)	Calculated temperature (°C)
HYC	5	E5-1		10'	0.78	< 3.1	167	13440	<0.57	< 45	2330	33.3	75.3	13	< 88	< 0.62	9.3	962	0.09	12.90	29.50	< 4.1	< 0.16	24.40	7.87	275	0.04	163
HYC	5	E5-1		11	0.58	< 3.8	28	21000	3.02	< 49	2030	34.5	96.9	97	< 88	2.65	26.2	983	0.11	13.70	77.00	< 4	< 0.14	18.60	31.70	890	0.20	150
HYC	5	E5-1		11'	< 0.39	< 3.1	394	17800	<0.21	< 40	4410	6.8	28.2	< 2.1	< 73	< 0.42	4.7	989	<0.05	7.40	15.60	< 3.3	< 0.11	18.70	6.44	153	< 0.035	202
HYC	5	E5-1		12	< 0.43	< 2.3	544	18000	0.97	< 50	4510	12.9	51.0	44	< 98	0.55	12.6	981	0.11	12.20	28.40	< 3.5	< 0.13	27.70	14.00	153	0.06	199
HYC	5	E5-1		12'	2.74	< 3	59	13720	0.46	< 53	2830	16.3	49.0	94	< 100	< 0.54	13.4	899	0.23	16.80	29.40	< 3.1	< 0.15	32.10	13.37	372	< 0.053	171
HYC	5	E5-1		13	8.00	< 2.5	38	14300	1.04	< 70	2920	18.0	29.1	275	< 120	6.20	27.0	904	0.28	17.20	53.40	< 3.7	< 0.17	15.90	14.60	10700	0.92	173
HYC	5	E5-1		13'	3.90	2.40	32	15140	0.58	< 65	3680	17.9	36.7	260	< 120	2.02	22.6	897	0.18	20.30	37.30	< 3.5	< 0.16	27.20	15.30	11200	0.41	167
HYC	5	E5-1		14	< 0.51	< 2.3	119	15560	< 0.41	< 43	3140	18.8	62.5	3	< 88	< 0.64	5.4	1004	0.07	8.00	26.90	< 3.7	< 0.13	22.10	7.05	1030	< 0.041	170
HYC	5	E5-1		14'	1.92	< 4.1	2460	19000	< 0.45	< 68	1002	13.9	30.7	3	< 130	< 0.8	10.4	882	< 0.066	7.60	27.00	< 6.4	< 0.17	24.00	4.76	485	< 0.048	215
HYC	5	E5-1		15	< 0.57	< 3	34	11700	< 0.33	< 49	1540	46.0	102.0	12	< 97	< 0.58	9.3	968	0.07	7.23	42.80	< 4.7	0.14	24.50	6.16	144	0.04	134
HYC	5	E5-1		15'	1.63	< 2.7	40	15000	1.90	< 52	2010	30.9	62.7	25	< 95	< 0.76	5.3	872	0.10	8.30	33.40	< 3.6	< 0.15	32.90	17.60	174	< 0.046	153
Percentage of analyses > LOD					67	3	100	100	50	0	100	100	100	93	0	23	100	100	77	100	100	0	7	100	100	100	40	
HYC	4	MRM-2012-3	172.6	1	10.60	< 3.1	1520	8600	< 0.65	< 87	231	9.4	46.2	4	51	< 1.1	13.1	1934	0.09	2.90	75.40	< 3.9	< 0.21	56.60	3.78	77	< 0.063	199
HYC	4	MRM-2012-3	172.6	1'	5.34	< 4	2010	7100	1.97	< 80	156	5.9	37.4	135	33	< 0.97	8.8	1737	< 0.074	3.60	45.60	< 5.1	< 0.23	60.90	2.71	36	< 0.1	201
HYC	4	MRM-2012-3	172.6	2	2.81	< 3.3	1163	9550	< 0.46	< 65	330	7.7	46.9	6	0	< 0.78	20.0	1725	< 0.06	3.63	66.50	< 4.1	< 0.18	36.60	4.88	135	< 0.081	194
HYC	4	MRM-2012-3	172.6	2'	8.70	< 4.7	1730	9400	< 0.29	< 110	173	4.8	38.7	< 4.7	67	< 0.7	16.9	1754	< 0.081	3.80	50.60	< 4.8	< 0.24	42.30	2.58	66	< 0.083	208
HYC	4	MRM-2012-3	172.6	3	18.60	< 4.3	620	26900	12.00	< 98	398	12.3	72.7	165	0	< 0.64	15.4	1780	0.14	5.26	72.30	< 4.4	< 0.22	44.90	11.22	298	0.42	206
HYC	4	MRM-2012-3	172.6	3'	9.80	< 4.2	890	16300	3.24	< 69	352	10.0	63.4	24	110	< 0.74	22.6	1749	0.25	4.54	69.40	< 3	< 0.18	42.10	12.70	87	< 0.037	207
HYC	4	MRM-2012-3	172.6	4	5.50	< 2.5	363	5330	< 0.42	< 87	273	12.3	50.0	< 3.3	130	< 0.6	21.8	1812	0.27	4.71	87.20	< 4.2	< 0.18	35.00	4.42	132	< 0.086	176
HYC	4	MRM-2012-3	172.6	4'	4.50	< 3.5	3070	9900	< 0.54	< 93	269	12.4	44.0	6	740	< 0.89	24.0	1888	< 0.099	3.38	104.80	< 4.4	< 0.24	50.20	3.80	96	< 0.076	203
HYC	4	MRM-2012-3	172.6	5	6.38	< 3.4	1117	10440	1.85	< 90	183	5.9	44.2	68	50000	< 0.86	6.9	1752	< 0.096	3.97	35.70	< 4.2	< 0.23	47.80	4.20	39	< 0.073	202
HYC	4	MRM-2012-3	172.6	5'	2.68	< 3	432	5210	< 0.46	< 79	203	8.5	43.5	< 4.2	0	< 0.75	16.8	1794	< 0.083	4.09	70.00	< 3.7	< 0.2	38.80	3.19	68	< 0.064	173
HYC	4	MRM-2012-3	172.6	6	< 0.68	< 3	23	32690	< 0.25	< 58	14360	18.8	35.6	1620	< 98	< 0.71	36.8	2906	0.05	5.67	18.30	< 3.3	< 0.16	14.39	10.95	177	< 0.064	171
HYC	4	MRM-2012-3	172.6	6'	< 0.45	< 2.8	23	30530	< 0.41	< 59	13140	24.8	41.6	1970	< 79	< 0.76	42.9	2940	0.04	4.49	22.50	< 3.1	< 0.15	14.67	11.14	199	< 0.046	164
HYC	4	MRM-2012-3	172.6	7	< 0.44	< 2.7	26	32270	< 0.4	< 58	22880	16.8	61.5	4560	< 78	< 0.74	91.4	2513	< 0.037	5.23	49.20	< 3	< 0.14	12.70	9.24	1180	< 0.045	162
HYC	4	MRM-2012-3	172.6	7'	< 0.43	< 3.6	26	31110	< 0.33	< 57	19950	20.1	59.1	3640	< 100	< 0.85	70.3	2758	< 0.049	5.05	39.80	< 4.9	< 0.19	13.00	10.71	181	< 0.051	161
HYC	4	MRM-2012-3	172.6	8	< 0.43	< 3.6	25	28130	< 0.33	< 56	19270	22.0	60.6	4120	< 100	< 0.84	79.5	1859	0.15	7.50	40.40	< 4.9	< 0.19	13.60	10.72	308	< 0.051	167
HYC	4	MRM-2012-3	172.6	8'	1.94	< 3.1	246	28120	< 0.43	< 54	17920	25.0	72.7	5340	< 87	< 0.8	94.9	1821	0.33	10.30	57.90	< 3.7	< 0.11	16.10	12.24	455	< 0.031	193
HYC	4	MRM-2012-3	172.6	9	< 0.57	< 3.4	24	26870	< 0.43	< 61	17640	17.1	43.4	2523	< 86	< 0.86	56.0	2577	0.31	8.30	26.50	< 3.6	< 0.19	13.28	7.94	413	< 0.034	177
HYC	4	MRM-2012-3	172.6	9'	1.29	< 3.4	272	24900	< 0.44	< 62	13680	23.6	43.4	1413	< 89	< 0.88	44.6	2417	< 0.05	4.69	27.10	< 3.7	< 0.19	16.04	9.79	789	< 0.035	184
HYC	4	MRM-2012-3	172.6	10	< 0.58	< 2.8	830	44300	< 0.37	< 64	11650	15.8	88.9	4400	< 100	< 0.57	75.5	2397	< 0.065	5.42	51.20	< 4	< 0.16	19.20	2.84	118	< 0.042	206
HYC	4	MRM-2012-3	172.6	10'	< 0.59	< 2.9	107	45000	< 0.38	< 65	9450	19.0	89.6	5030	< 110	< 0.58	89.2	2384	< 0.066	6.00	53.00	< 4.1	< 0.16	11.10	3.09	95	< 0.043	182
HYC	4	MRM-2012-3	172.6	11	12.80	8.00	1870	22800	2.40	< 99	840	10.0	71.2	22	< 190	< 1.1	15.8	1620	< 0.11	8.70	62.90	< 6.2	< 0.26	29.30	10.70	122	< 0.086	212
HYC	4	MRM-2012-3	172.6	11'	5.60	< 2.9	241	20510	0.51	< 43	10150	26.1	65.1	1909	< 100	< 0.65	57.7	1918	0.20	7.10	49.50	< 3.3	< 0.12	22.80	11.42	546	< 0.049	184
HYC	4	MRM-2012-3	172.6	12	5.69	< 3.2	276	21250	1.64	< 47	10720	19.0	86.3	2590	< 110	< 0.71	71.6	1964	0.08	6.23	75.80	< 3.6	< 0.14	15.12	16.70	20400	< 0.054	182
HYC	4	MRM-2012-3	172.6	12'	6.30	< 5.2	740	32100	6.90	< 76	4170	14.0	66.8	774	< 190	2.30	65.6	1739	< 0.11	6.90	92.90	< 6	< 0.22	16.60	34.40	16900	< 0.088	206
HYC	4	MRM-2012-3	172.6	13	4.02	< 3.7	920	15080	0.63	< 68	4680	7.3	53.9	46	< 140	< 0.65	36.2	1652	< 0.055	4.87	71.00	< 4.3	< 0.12	22.30	16.77	39300	< 0.056	200
HYC	4	MRM-2012-3	172.6	13'	1.64	< 3.3	185	16300	< 0.31	< 80	8670	16.7	51.1	1450	< 120	0.90	60.0	1859	0.12	4.89	63.50	< 3.5	< 0.16	19.00	16.45	20700	< 0.054	182
HYC	4	MRM-2012-3	172.6	14	8.00	< 3.7	254	16970	1.37	< 91	4600	16.6	65.4	1020	< 140	1.39	57.0	1748	0.11	5.44	78.30	< 4	< 0.18	25.30	21.60	10190	< 0.062	183
HYC	4	MRM-2012-3	172.6	14'	2.48	< 3.1	82	26300	2.52	< 75	11120	20.0	41.6	3370	< 120	< 0.53	68.1	1897	0.25	9.00	50.10	< 3.3	< 0.15	13.90	17.50	8500	< 0.051	187
HYC	4	MRM-2012-3	172.6	15	< 1.2	< 5	2720	40100	0.55	< 120	17610	19.5	83.1	3380	< 290	< 0.72	70.2	2000	< 0.13	9.10	51.90	< 7.9	< 0.23	18.80	4.87	103	< 0.075	219
HYC	4	MRM-2012-3	172.6	15'	< 0.71	< 2.9	1850	36300	< 0.28	< 70	23790	22.9	86.3	4660	< 170	< 0.41	89.1	2344	< 0.077	4.77	55.30	< 4.6	< 0.13	16.11	6.10	169	< 0.043	207
Percentage of analyses > LOD					67	3	100	100	40	0	100	100	100	90	23	10	100	100	47	100	100	0	0	100	100	100	3	
HYC	3	MRM-2012-3	195.9A	1	< 0.58	< 2.5	20	25250	< 0.41	< 53	16420	14.8	45.1	4100	300	< 0.7	39.4	2248	0.22	10.90	16.32	< 3	< 0.11	18.00	8.69	710	< 0.052	173
HYC	3	MRM-2012-3	195.9A	1'	10.20	< 2.7	1990	14810	< 0.41	< 65	1700	9.4	64.8	219	1100	< 1.1	34.8	1699	0.07	3.94	52.90	< 5.1	< 0.18	61.90	14.18	230	< 0.057	207
HYC	3	MRM-2012-3	195.9A	2	2.79	< 3.2	1900	11860	< 0.5	< 79	2333	9.8	49.9	273	< 8300	< 1.3	34.3	1669	0.06	3.84	45.00	< 6	< 0.22	63.50	9.71	215	< 0.068	204
HYC	3	MRM-2012-3	195.9A	2'	7.01	< 3.3	23	16030	< 0.54	< 85	2100	6.3	42.2	< 7.3	< 3300	< 1.3	3.4	1798	< 0.071	3.68	5.80	< 4.2	< 0.23	38.10	3.51	20	< 0.04	167
HYC	3	MRM-2012-3	195.9A	3	22.10	< 2.9	1199	17940	< 0.74	< 100	1813	12.5	112.6	< 6	< 3800	< 0.93	2.7	1600	< 0.079	4.00	16.00	< 8.8	< 0.32	67.40	5.91	28	< 0.093	193
HYC	3	MRM-2012-3	195.9A	3'	1.47	< 2.1	1129	14500	< 0.53	< 76	2190	9.9	114.0	< 4.4	< 2100	< 0.67	9.6	1448	< 0.057	3.70	16.70	< 6.3	< 0.23	41.40	2.42	44	< 0.067	188

Deposit	Lens # (HYC)	Drillhole #	Depth (m)	Analyse #	V (ppm)	Cr (ppm)	Mn (ppm)	Fe (ppm)	Co (ppm)	Ni (ppm)	Cu (ppm)	Ga (ppm)	Ge (ppm)	As (ppm)	Se (ppm)	Mo (ppm)	Ag (ppm)	Cd (ppm)	In (ppm)	Sn (ppm)	Sb (ppm)	Te (ppm)	Au (ppm)	Hg (ppm)	Tl (ppm)	Pb (ppm)	Bi (ppm)	Calculated temperature (°C)
HYC	3	MRM-2012-3	195.9A	4	9.70	8.20	1470	20000	< 1.1	< 160	3090	9.0	89.1	< 9.3	< 3400	< 1.4	6.2	1500	< 0.12	4.70	24.90	< 13	< 0.48	62.90	11.10	55	< 0.14	206
HYC	3	MRM-2012-3	195.9A	4'	11.00	< 2.7	2690	18800	< 0.69	< 99	1520	8.3	49.0	131	< 1900	< 0.87	29.3	1760	< 0.074	4.30	46.30	< 8.2	< 0.29	28.80	9.60	194	< 0.087	217
HYC	3	MRM-2012-3	195.9A	5	< 0.62	< 2.4	30	25480	< 0.51	< 58	18160	10.3	45.7	1830	< 510	< 0.77	26.7	2723	0.55	11.70	11.75	< 2.7	< 0.25	15.10	3.27	509	< 0.055	187
HYC	3	MRM-2012-3	195.9A	5'	< 0.63	< 3.3	23	25030	< 0.44	< 68	15680	15.7	48.6	3620	< 630	< 1.1	38.2	2039	0.55	18.20	16.20	< 3.3	< 0.16	20.20	8.60	348	< 0.045	178
HYC	3	MRM-2012-3	195.9A	6	8.40	< 3.7	2160	20580	1.48	< 88	3320	11.4	73.4	73	< 700	< 1.4	12.2	1560	< 0.075	4.90	22.90	< 5.9	< 0.23	49.60	6.96	77	< 0.075	208
HYC	3	MRM-2012-3	195.9A	6'	6.35	< 3.4	1300	14900	< 0.51	< 81	3570	10.4	64.2	84	< 600	< 1.3	18.6	1581	< 0.069	4.90	34.20	< 5.4	< 0.21	42.30	12.00	270	< 0.069	198
HYC	3	MRM-2012-3	195.9B	1	< 0.75	< 2.6	1190	31600	< 0.35	< 56	12340	18.8	32.4	2424	< 280	< 0.81	29.6	2227	< 0.08	5.80	12.80	< 3.6	< 0.12	19.40	21.61	396	< 0.065	214
HYC	3	MRM-2012-3	195.9B	1'	< 0.82	< 4.8	400	27400	< 0.54	< 81	19800	19.0	64.9	2294	< 320	< 0.75	36.0	2570	< 0.11	5.90	17.14	< 3.3	< 0.2	12.80	6.09	1107	< 0.063	193
HYC	3	MRM-2012-3	195.9B	2	< 0.66	< 3.7	100	31800	< 0.49	< 67	20800	10.1	56.1	1459	< 270	< 0.84	22.2	2460	0.11	6.20	12.00	< 4.3	< 0.18	10.10	2.16	76	< 0.047	193
HYC	3	MRM-2012-3	195.9B	2'	< 1.1	< 4.4	200	26600	< 0.67	< 92	19210	13.9	65.1	2450	< 340	< 1.7	31.6	2710	< 0.11	6.10	17.40	< 5.1	< 0.15	10.10	5.57	489	< 0.12	188
HYC	3	MRM-2012-3	195.9B	3	< 0.65	< 2.6	34	35300	< 0.4	< 56	20640	3.1	11.5	340	< 190	< 1	11.6	3226	< 0.068	4.90	2.29	< 3.1	< 0.089	9.40	2.91	480	< 0.071	210
HYC	3	MRM-2012-3	195.9B	3'	< 0.55	< 2.2	32	25900	< 0.34	< 48	15420	16.8	55.1	1434	< 150	< 0.85	23.1	2791	0.15	7.32	11.09	< 2.6	< 0.075	13.10	3.84	560	< 0.06	173
HYC	3	MRM-2012-3	195.9B	4	< 0.66	< 2.7	16	47000	< 0.41	< 58	5510	17.9	47.1	2201	< 180	< 1	29.9	2740	< 0.07	8.50	9.53	< 3.1	< 0.091	9.80	10.48	126	< 0.072	171
HYC	3	MRM-2012-3	195.9B	4'	< 0.51	< 2.6	38	32800	< 0.36	64	13810	12.1	33.6	1404	< 140	< 0.73	19.5	3164	< 0.058	5.70	7.84	< 4.4	< 0.18	11.00	5.20	340	< 0.058	180
HYC	3	MRM-2012-3	191	1	< 0.68	< 2.3	26	40710	0.53	< 56	6870	16.7	112.6	4890	< 130	< 0.58	46.9	1731	< 0.054	5.80	53.70	< 3.4	< 0.13	14.10	2.39	84	< 0.034	162
HYC	3	MRM-2012-3	191	1'	0.03	< 2.4	36	46010	< 0.63	< 92	7950	9.7	63.5	3920	< 150	0.00	39.0	2252	< 0.099	5.38	41.50	< 5.9	< 0.15	12.11	5.53	98	< 0.077	184
HYC	3	MRM-2012-3	191	2	9.70	< 3.9	792	15510	0.76	< 85	5320	9.9	67.9	971	< 130	< 0.84	30.2	1505	< 0.049	5.90	40.70	< 3.7	< 0.19	30.50	11.59	580	< 0.06	191
HYC	3	MRM-2012-3	191	2'	6.60	< 4.8	291	11100	< 0.43	< 100	940	6.4	61.1	< 5.7	< 150	< 1	3.8	1457	< 0.06	5.20	10.40	< 4.5	< 0.23	33.70	3.91	27	< 0.073	181
HYC	3	MRM-2012-3	191	3	< 0.62	< 2.6	101	27600	0.62	< 74	6790	16.6	50.2	1003	< 100	< 0.74	20.6	1678	< 0.033	5.16	14.21	< 3.3	< 0.19	17.70	32.20	525	< 0.055	176
HYC	3	MRM-2012-3	191	3'	8.20	< 9.5	4080	28800	0.42	< 320	5170	20.9	70.0	1196	< 510	0.08	29.4	1560	< 0.25	6.20	35.50	< 26	0.00	42.80	34.60	10030	1.02	221
HYC	3	MRM-2012-3	191	4	< 0.68	< 2.8	31	28700	1.13	< 66	8800	17.8	28.5	940	< 89	< 0.62	22.1	1775	< 0.049	4.87	14.05	< 4.8	< 0.092	14.00	24.50	1000	< 0.041	172
HYC	3	MRM-2012-3	191	4'	< 0.47	< 1.8	29	31100	< 0.6	< 53	9930	16.6	24.5	598	< 110	< 0.79	16.4	1750	< 0.064	4.75	8.66	< 3	< 0.14	9.20	14.23	1140	< 0.044	177
HYC	3	MRM-2012-3	191	5	0.55	< 1.9	17	40970	< 0.63	< 57	5800	17.7	84.1	3450	< 110	< 0.83	43.0	1833	< 0.068	5.83	34.40	< 3.1	< 0.15	9.90	7.10	128	< 0.047	162
HYC	3	MRM-2012-3	191	5'	< 0.63	< 2.4	15	35210	< 0.34	< 66	4769	14.4	72.1	3734	< 98	< 0.57	47.4	1816	< 0.054	5.92	34.30	< 3.9	< 0.18	12.90	4.26	103	< 0.045	160
HYC	3	MRM-2012-3	191	6	< 0.61	< 2.3	16	45200	0.81	< 65	3600	8.1	32.1	927	< 92	< 0.55	13.3	2322	< 0.052	4.80	9.80	< 3.8	< 0.18	10.60	3.79	69	< 0.044	182
HYC	3	MRM-2012-3	191	6'	< 0.58	< 2.2	37	44900	0.32	< 62	1722	3.7	12.0	260	< 85	< 0.52	5.6	2458	< 0.05	5.50	4.38	< 3.6	< 0.17	10.00	2.00	29	< 0.042	212
Percentage of analyses > LOD					44	3	100	100	25	3	100	100	100	84	6	3	100	100	22	100	100	0	0	100	100	100	3	
HYC	2	E11-1		1	< 0.12	< 0.94	29	38690	3.78	< 0.41	12350	9.3	58.4	1361	< 15	< 0.14	50.5	2840	0.03	4.52	5.94	< 0.62	< 0.056	7.67	25.70	244	0.02	177
HYC	2	E11-1		Z1	0.61	< 1.2	28	27790	8.13	< 0.62	10900	11.2	34.2	635	< 18	< 0.13	37.8	2137	< 0.024	3.95	8.55	< 0.84	< 0.061	10.43	25.30	656	< 0.023	169
HYC	2	E11-1		Z2	4.07	1.27	130	26840	8.42	< 0.58	8680	11.6	42.5	663	< 17	< 0.12	37.2	1922	0.03	3.53	11.76	< 0.79	< 0.057	19.90	29.90	840	< 0.022	187
HYC	2	E11-1		1	< 0.18	< 1.5	8	39060	8.43	< 0.87	4116	23.3	73.9	900	< 27	< 0.25	31.0	2683	< 0.031	4.45	2.33	< 1.5	< 0.098	18.60	63.10	716	< 0.027	147
HYC	2	E11-1		1'	0.43	< 1.6	19	39700	9.33	< 0.58	6190	10.4	30.5	473	< 22	< 0.17	21.5	2385	< 0.034	4.74	4.49	< 1.3	< 0.096	18.40	16.70	176	< 0.029	177
HYC	2	E11-1		2	1.51	< 2.2	570	31600	7.98	< 0.8	7450	9.8	50.4	193	< 31	< 0.24	19.1	2134	< 0.046	4.02	5.38	< 1.8	< 0.13	25.50	33.78	416	< 0.04	205
HYC	2	E11-1		2'	0.33	< 1.5	46	27250	6.83	< 0.56	9480	10.5	46.5	222	< 22	< 0.17	24.7	2255	< 0.033	3.75	6.94	< 1.3	< 0.093	22.20	26.10	219	< 0.028	173
HYC	2	E11-1		1	0.29	< 1.1	49	33060	8.02	< 0.57	8000	10.2	52.4	330	< 14	< 0.16	23.5	2252	< 0.02	3.81	4.07	< 0.77	< 0.058	9.53	36.40	195	< 0.02	174
HYC	2	E11-1		1	1.73	< 1.8	36	27950	8.78	< 0.72	7850	11.3	38.8	808	< 29	< 0.3	40.5	1950	< 0.049	3.51	10.90	< 1.5	< 0.11	24.10	28.60	2010	< 0.036	175
HYC	2	E11-1		1'	0.64	< 1.6	39	31350	8.93	< 0.64	12340	11.2	40.6	876	< 26	< 0.27	44.0	2037	< 0.044	4.49	8.46	< 1.3	< 0.1	16.20	21.88	325	< 0.032	177
HYC	2	E4-2		1	8.26	1.79	150	20420	4.00	2	3560	14.4	98.2	61	< 24	0.24	31.4	1626	0.04	4.65	83.90	< 1.2	< 0.072	103.10	5.74	150	< 0.026	172
HYC	2	E4-2		1'	15.00	< 2.1	292	22540	0.65	< 0.86	5250	13.3	138.4	34	< 31	< 0.29	17.8	1686	< 0.043	4.30	42.50	< 1.5	< 0.093	85.90	5.53	131	< 0.033	175
HYC	2	E4-2		1	13.42	< 2.8	1730	29350	14.20	1	5990	11.6	102.7	3130	41	< 0.23	16.2	1692	0.05	3.79	37.20	< 1.6	< 0.097	79.80	5.36	297	< 0.031	210
HYC	2	E4-2		1'	1.67	< 2.8	381	18390	2.84	< 1	7240	11.3	67.4	537	57	< 0.23	43.6	1811	< 0.048	2.84	52.30	< 1.6	< 0.098	52.80	16.57	1700	< 0.031	185
HYC	2	E4-2		1	0.42	< 2.4	223	24200	2.71	20	10600	9.5	63.9	293	< 33	< 0.42	22.6	1750	0.31	8.00	49.40	< 1.8	< 0.12	44.30	10.20	810	< 0.043	202
HYC	2	E4-2		1'	5.61	< 1.5	311	21950	0.61	< 0.8	10300	9.0	74.9	145	< 21	< 0.26	22.0	1579	0.22	8.90	42.50	< 1.1	< 0.074	56.60	5.90	319	< 0.027	200
HYC	2	E11-2		1	< 0.09	< 1	33	3431	< 0.058	< 0.35	73	0.1	3.6	3	30	< 0.094	276.0	949	0.01	4.46	117.10	< 0.64	< 0.036	26.73	2.63	671	< 0.011	214
HYC	2	E11-2		1'	< 0.12	< 0.77	24	3593	< 0.052	< 0.36	179	0.1	4.2	4	< 14	< 0.16	118.9	850	0.02	3.54	153.30	< 0.68	< 0.048	21.20	3.61	824	< 0.011	208
HYC	2	E11-2		1	2.81	< 1.4	17	2442O	9.90	1	13290	11.6	58.4	622	< 24	0.36	63.7	1971	0.03	4.76	37.90	< 0.83	< 0.069	21.10	15.94	2990	0.04	159
HYC	2	E11-2		1'	1.48	< 2.3	22	26000	5.80	< 1	10810	14.2	48.1	586	< 38	< 0.32	58.3	2030	< 0.041	3.50	25.40	< 1.3	< 0.11	10.44	15.70	960	< 0.038	162
HYC	2	E11-2		2	0.79	< 2.4	18	27000	8.10	< 1.1	14180	12.0	47.6	830	< 26	< 0.28	51.3	2090	< 0.034	4.47	13.80	< 1.9	< 0.13	8.30	25.10	1240	< 0.027	161
HYC	2	E11-2		2'	4.46	< 3.6	19	22600	6.50	< 1.7	10700	13.4	74.6	863	< 40	< 0.42	72.9	1870	< 0.052	4.10	50.30	< 2.8	< 0.19	34.50	16.19	1570	< 0.04	154

Deposit	Lens # (HYC)	Drillhole #	Depth (m)	Analyse #	V (ppm)	Cr (ppm)	Mn (ppm)	Fe (ppm)	Co (ppm)	Ni (ppm)	Cu (ppm)	Ga (ppm)	Ge (ppm)	As (ppm)	Se (ppm)	Mo (ppm)	Ag (ppm)	Cd (ppm)	In (ppm)	Sn (ppm)	Sb (ppm)	Te (ppm)	Au (ppm)	Hg (ppm)	Tl (ppm)	Pb (ppm)	Bi (ppm)	Calculated temperature (°C)
HYC	2	E11-2		1	< 0.12	< 1	16	35360	6.48	< 0.39	21800	12.2	37.5	885	< 18	< 0.21	42.1	2045	0.02	5.11	7.17	< 0.83	< 0.067	9.31	20.47	401	< 0.022	170
HYC	2	E11-2		1	1.00	< 2.5	358	33700	7.63	< 1.1	18270	11.7	39.2	784	< 23	< 0.28	39.2	1898	< 0.037	4.24	10.68	< 1.4	< 0.11	15.10	14.07	366	< 0.032	201
HYC	2	E11-2		1'	0.98	< 2.5	710	29170	3.33	< 1.2	14040	13.9	58.4	609	< 24	< 0.29	34.0	1988	< 0.038	4.29	16.90	< 1.4	< 0.11	21.60	7.17	392	< 0.034	199
HYC	2	E11-2		1	< 0.21	< 1.9	14	32970	6.41	< 0.68	19910	10.6	39.7	814	< 24	< 0.21	39.3	2093	< 0.035	5.19	9.48	< 1.7	< 0.096	22.30	13.18	653	< 0.024	167
HYC	2	E11-2		1'	1.26	< 2.4	17	34400	7.74	< 0.87	19020	16.4	49.7	1077	60	< 0.27	51.1	2087	< 0.045	6.02	10.46	< 2.1	< 0.12	18.70	18.10	550	< 0.031	162
HYC	2	E11-2		1	< 0.15	< 1.2	16	33700	9.82	1	18690	11.8	32.7	740	< 19	< 0.16	39.6	1992	0.03	6.15	8.88	< 0.58	< 0.059	12.62	18.80	621	< 0.017	172
Percentage of analyses > LOD					75	7	100	100	93	18	100	100	100	100	14	7	100	100	39	100	100	0	0	100	100	100	7	
HYC	0	MRM-2012-3	209.7	1	1.52	< 2.4	1120	23800	1.26	< 60	11290	39.7	21.2	1590	< 130	< 0.93	27.2	1450	< 0.049	3.90	25.10	< 4.5	< 0.19	13.90	10.60	1600	< 0.059	201
HYC	0	MRM-2012-3	209.7	1'	< 0.64	< 2.8	330	28900	0.45	< 51	17800	36.0	29.1	2980	< 120	< 0.91	33.3	1650	< 0.069	3.65	26.00	< 4.3	< 0.15	12.60	9.90	250	< 0.041	191
HYC	0	MRM-2012-3	209.7	2	12.60	< 2.9	1350	17400	1.16	< 72	4100	18.6	26.4	304	< 160	< 0.78	35.0	1146	0.11	4.60	71.10	< 4.4	< 0.23	29.80	24.50	950	< 0.048	211
HYC	0	MRM-2012-3	209.7	2'	9.80	< 4.1	23	8900	< 0.48	< 61	1269	10.9	49.6	511	< 130	3.90	240.0	1380	0.13	4.40	357.00	< 4	< 0.17	15.50	103.40	100800	0.45	153
HYC	0	MRM-2012-3	209.7	3	< 0.61	4.40	30	20800	0.71	< 51	11600	19.0	12.4	1035	< 100	< 0.75	22.7	1700	< 0.053	3.30	19.30	< 4	< 0.13	10.00	15.30	860	< 0.056	175
HYC	0	MRM-2012-3	209.7	3'	< 0.62	2.90	30	19800	0.51	90	10920	21.5	17.2	1132	< 110	< 0.72	28.9	1664	< 0.055	2.00	25.90	< 3.8	< 0.11	14.50	15.20	7100	< 0.027	168
HYC	0	MRM-2012-3	209.7	4	2.40	2.80	29	27300	0.66	< 36	14170	22.1	28.4	1910	< 83	< 0.82	26.3	1524	0.11	3.59	19.80	< 5	< 0.13	12.10	10.74	292	< 0.056	176
HYC	0	MRM-2012-3	209.7	4'	1.63	4.20	36	21200	4.80	< 52	8440	19.6	16.4	1000	< 130	< 0.66	33.7	1560	< 0.036	4.13	46.10	< 3.9	< 0.15	7.90	21.90	19200	< 0.055	171
HYC	0	MRM-2012-3	209.7	5	13.60	< 4.5	341	14960	0.88	< 46	4010	20.9	40.8	325	< 91	< 0.73	20.9	1128	0.07	4.70	44.00	< 3.5	< 0.18	22.40	15.75	163	< 0.063	184
HYC	0	MRM-2012-3	209.7	5'	0.82	< 4	36	19160	0.79	< 41	9360	24.3	16.3	1070	< 81	< 0.66	32.0	1402	0.07	4.57	35.20	< 3.1	< 0.16	16.20	16.00	4550	< 0.057	174
HYC	0	MRM-2012-3	209.7	6	< 0.93	8.70	151	21000	1.27	< 70	10940	19.4	13.1	740	< 110	< 0.88	26.8	1700	< 0.078	4.00	32.50	< 4.6	< 0.19	7.50	10.90	67000	< 0.063	194
HYC	0	MRM-2012-3	209.7	6'	< 0.61	< 2.1	28	21400	0.54	< 47	13720	35.6	21.2	1880	< 91	< 0.83	26.7	1540	< 0.046	3.15	23.40	< 4	< 0.18	14.60	10.92	223	< 0.048	160
HYC	0	MRM-2012-3	209.7	7	3.26	< 2	51	21800	2.26	< 45	7700	22.9	13.6	967	< 85	< 0.79	25.6	1508	< 0.044	4.30	33.40	< 3.8	< 0.18	17.10	20.00	3800	< 0.046	177
HYC	0	MRM-2012-3	209.7	7'	1.47	2.60	280	23500	1.83	< 44	10390	19.7	12.2	1090	< 83	< 0.78	25.1	1590	< 0.044	2.92	22.80	< 3.8	< 0.17	14.50	19.80	4920	< 0.046	200
HYC	0	MRM-2012-3	209.7	8	4.20	< 4.8	910	58000	13.40	< 85	7830	20.2	17.1	870	< 170	< 1.4	27.5	1380	< 0.081	7.60	28.20	< 5.8	< 0.23	7.80	53.90	5540	< 0.051	230
HYC	0	MRM-2012-3	209.7	8'	7.10	< 4	33	22600	2.70	< 71	7500	32.9	20.3	922	< 140	< 1.2	21.9	1540	< 0.068	6.50	19.40	< 4.9	< 0.19	13.40	9.90	216	< 0.043	166
HYC	0	MRM-2012-3	209.7	9	< 0.83	< 2.2	460	20300	0.99	< 52	7880	20.0	8.4	671	< 92	< 0.99	32.7	1452	< 0.085	4.50	31.70	< 7.2	< 0.16	9.20	12.60	20000	< 0.059	210
HYC	0	MRM-2012-3	209.7	9'	1.72	< 2.4	115	20300	1.51	< 49	10890	19.5	13.0	794	< 88	< 0.75	28.9	1356	< 0.082	4.83	32.00	< 5.2	< 0.19	12.70	17.20	1020	< 0.049	190
HYC	0	MRM-2012-3	209.7	10x	2.42	< 2.6	73	18400	1.74	< 53	6550	19.8	15.4	971	< 93	< 0.81	27.2	1548	< 0.089	3.01	34.90	< 5.6	< 0.21	16.50	22.30	13600	< 0.053	181
HYC	0	MRM-2012-3	209.7	11	1.87	4.10	58	16500	0.69	< 34	7080	20.3	12.7	712	< 59	< 0.82	29.7	1490	< 0.057	2.73	44.00	< 2.5	< 0.13	11.50	17.00	29200	< 0.038	176
HYC	0	MRM-2012-3	209.7	11'	1.22	< 2.7	291	19400	0.77	< 55	9900	22.1	10.9	1238	< 87	< 0.83	23.7	1487	< 0.065	2.35	23.70	< 4	< 0.18	17.20	12.71	569	< 0.051	199
HYC	0	MRM-2012-3	209.7	12	< 0.55	< 2.2	290	17700	0.80	< 37	7570	20.6	12.5	767	< 69	< 0.53	24.3	1480	< 0.071	3.11	30.30	< 5.1	< 0.15	13.50	13.80	2570	< 0.048	197
HYC	0	MRM-2012-3	209.7	12'	5.40	< 2.3	33	18300	0.89	< 38	8070	22.0	13.0	836	< 71	0.86	31.4	1571	< 0.074	3.17	39.20	< 5.3	< 0.15	15.90	14.90	11000	< 0.05	172
HYC	0	MRM-2012-3	209.7	13	14.70	< 3.4	279	17000	0.86	< 62	5150	13.7	39.5	96	< 100	< 0.76	18.6	1085	< 0.072	5.80	50.20	< 5.6	< 0.16	29.10	20.10	6300	< 0.072	187
HYC	0	MRM-2012-3	209.7	13'	3.30	< 6.6	978	26400	< 0.73	< 95	20600	8.1	16.9	113	< 140	< 1.4	21.0	1202	< 0.11	6.30	33.50	< 5.7	< 0.3	13.60	9.91	719	< 0.07	228
HYC	0	MRM-2012-3	209.7	14	8.70	< 4.9	402	15820	1.59	< 71	4440	18.0	63.0	< 3.9	< 100	< 1.1	10.0	1125	< 0.082	5.61	43.10	< 4.3	< 0.22	27.00	14.66	86	< 0.053	181
HYC	0	MRM-2012-3	209.7	14'	13.90	< 4.6	53	18470	4.30	< 56	6100	25.1	13.8	776	< 98	< 0.71	26.6	1405	< 0.079	4.50	41.10	< 6.9	< 0.2	19.10	19.90	18800	< 0.071	176
HYC	0	MRM-2012-3	209.7	15	12.80	< 4.4	164	25100	7.50	< 54	8520	24.8	16.6	999	< 92	< 0.68	21.7	1405	< 0.076	6.50	33.80	< 6.6	< 0.19	19.60	24.90	3800	< 0.068	192
HYC	0	MRM-2012-3	209.7	15'	2.73	< 3.4	29	19760	2.70	< 41	7770	21.8	10.2	937	< 70	< 0.53	25.3	1535	< 0.058	5.56	26.90	< 5.1	< 0.15	12.00	17.10	3510	< 0.052	174
Percentage of analyses > LOD					76	24	100	100	93	3	100	100	100	97	0	7	100	100	17	100	100	0	0	100	100	100	3	
Myrtle		MY16	170.7	1	< 0.18	< 1.3	4	7440	5.12	< 0.5	254	119.9	105.7	< 3.3	< 22	< 0.18	0.7	937	< 0.029	6.04	3.13	< 1.1	< 0.07	197.00	< 0.02	9	0.04	80
Myrtle		MY16	170.7	1'	< 0.28	< 1.8	2	6510	3.47	< 0.5	405	129.1	178.6	< 4.6	< 43	< 0.21	0.6	914	< 0.035	5.74	0.83	< 1.2	< 0.08	141.00	< 0.03	2	0.04	67
Myrtle		MY16	170.7	2	< 0.21	< 2.3	5	3280	1.93	< 0.5	98	13.5	43.1	< 4.1	< 37	< 0.23	0.6	618	< 0.037	4.33	1.87	< 1.2	< 0.07	84.00	15.20	57	< 0.024	105
Myrtle		MY16	170.7	2'	0.52	< 1.7	423	3670	11.10	2	139	13.5	54.6	62	< 25	< 0.38	0.7	600	< 0.079	3.52	5.43	< 1.7	< 0.14	141.00	10.60	60	0.04	157
Myrtle		MY16	170.7	1	< 0.14	< 1.1	< 1.1	3390	16.45	< 0.5	14	4.2	1.9	< 2.4	< 21	< 0.18	0.9	984	< 0.024	3.47	0.64	< 1	< 0.07	86.60	0.16	5	0.02	131
Myrtle		MY16	170.7	1'	< 0.21	< 0.97	< 1.6	2060	12.37	< 0.7	82	26.0	22.1	< 3.4	< 22	< 0.15	0.7	818	0.11	3.82	2.45	< 1.2	< 0.07	78.00	0.18	4	0.01	86
Myrtle		MY16	170.7	1	0.17	< 1.8	2	716	4.24	< 0.5	16	1.4	3.1	< 2.4	< 20	< 0.17	0.5	416	< 0.024	3.28	0.30	< 1	< 0.05	82.70	0.10	7	< 0.021	118
Myrtle		MY16	170.7	1'	< 0.29	< 1.3	5	900	3.05	< 0.5	88	9.2	21.0	< 4.6	< 42	< 0.28	0.6	803	< 0.035	2.98	2.23	< 1.7	< 0.06	87.50	1.85	14	< 0.037	91
Percentage of analyses > LOD					25	0	75	100	100	13	100	100	100	13	0	0	100	25	13	100	100	0	0	100	75	100	63	
Myrtle		MY16	172.9	1	2.34	< 3.7	480	8240	7.73	2	341	42.8	153.4	31	< 43	0.60	3.8	508	0.16	9.50	9.70	< 2	< 0.18	295.00	19.13	130	0.12	156
Myrtle		MY16	172.9	1'	< 0.17	< 2.3	52	6080	3.36	< 1.1	381	29.5	201.0	39	< 27	< 0.27	3.2	343	< 0.039	6.40	7.83	< 1.3	< 0.11	145.10	32.13	181	0.06	115
Myrtle		MY16	172.9	1	< 0.18	< 1.2	9	3130	2.97	< 0.5	146	23.6	92.5	6	< 19	< 0.17	0.6	561	0.04	5.00	2.09	< 0.9	< 0.07	63.80	2.12	15	< 0.02	98

Deposit	Lens # (HYC)	Drillhole #	Depth (m)	Analyse #	V (ppm)	Cr (ppm)	Mn (ppm)	Fe (ppm)	Co (ppm)	Ni (ppm)	Cu (ppm)	Ga (ppm)	Ge (ppm)	As (ppm)	Se (ppm)	Mo (ppm)	Ag (ppm)	Cd (ppm)	In (ppm)	Sn (ppm)	Sb (ppm)	Te (ppm)	Au (ppm)	Hg (ppm)	Tl (ppm)	Pb (ppm)	Bi (ppm)	Calculated temperature (°C)
Myrtle		MY16	172.9	1'	< 0.23	< 1	23	2110	3.10	< 0.6	155	10.6	69.2	6	< 21	< 0.22	0.6	473	< 0.036	5.14	1.79	< 0.9	< 0.1	76.00	1.80	13	< 0.026	110
Myrtle		MY16	172.9	1	0.40	< 1.1	4	6200	5.18	< 0.6	111	37.2	88.6	28	< 23	0.26	0.5	471	< 0.039	4.97	2.36	< 0.9	< 0.11	81.50	5.96	23	0.03	96
Myrtle		MY16	172.9	1'	0.53	< 1.2	3	2870	3.35	< 0.6	114	31.6	97.0	9	< 24	< 0.25	0.7	540	< 0.041	4.79	2.32	< 1	< 0.12	91.70	5.50	52	0.03	76
Myrtle		MY16	172.9	2	< 0.21	< 1.4	< 1.2	2616	5.02	< 0.7	30	38.4	46.2	< 3.5	< 24	< 0.18	0.6	580	< 0.023	4.12	1.24	< 0.9	< 0.07	77.40	0.32	5	0.03	62
Myrtle		MY16	172.9	2'	< 0.23	< 1.5	< 1.3	3053	5.46	< 0.7	102	33.1	50.6	6	< 27	0.24	1.1	550	0.03	4.81	2.87	< 1	< 0.08	74.40	1.30	65	0.03	71
Percentage of analyses > LOD					38	0	75	100	100	13	100	100	100	88	0	38	100	100	38	100	100	0	0	100	100	100	75	
Myrtle		MY16	195.5	1	< 0.17	< 1.4	4	8170	0.65	< 0.6	204	28.7	98.1	3	< 22	< 0.2	1.6	2110	< 0.027	4.65	0.40	< 0.9	< 0.08	75.90	0.06	13	< 0.018	100
Myrtle		MY16	195.5	1'	< 0.16	< 1.3	1	8250	0.48	< 0.6	71	13.3	38.7	6	< 21	< 0.19	0.5	1270	< 0.026	4.21	< 0.066	< 0.8	< 0.08	63.20	0.38	4	< 0.017	108
Myrtle		MY16	195.5	2	< 0.2	< 1.9	2	5800	0.63	< 0.6	197	45.4	153.1	< 2.5	< 23	< 0.21	0.7	2411	< 0.024	3.96	0.26	< 0.9	< 0.07	65.90	0.17	12	< 0.022	77
Myrtle		MY16	195.5	2'	< 0.21	< 2	2	5800	0.81	< 0.6	180	36.1	141.4	< 2.5	< 23	< 0.21	0.6	2000	< 0.024	3.96	0.26	< 0.9	< 0.07	65.50	0.13	10	0.03	80
Myrtle		MY16	195.5	1	< 0.17	< 1.5	3	5840	0.67	< 0.5	165	27.2	141.8	< 2.5	< 23	< 0.16	0.5	1558	< 0.017	4.24	0.10	< 0.8	< 0.06	82.00	0.04	2	< 0.018	83
Myrtle		MY16	195.5	1'	< 0.18	< 1.6	3	7470	1.13	< 0.5	64	42.0	62.1	< 2.6	< 25	< 0.17	0.5	2089	< 0.018	4.03	0.17	< 0.9	< 0.06	85.50	0.04	3	< 0.019	95
Myrtle		MY16	195.5	2	< 0.14	< 0.95	1	4750	2.00	< 0.4	75	30.3	21.1	< 1.7	< 20	< 0.17	0.8	1428	0.15	6.07	0.69	< 0.8	< 0.06	85.90	< 0.02	5	0.01	108
Myrtle		MY16	195.5	2'	< 0.13	< 0.93	3	7940	0.89	< 0.4	159	28.1	61.4	< 1.6	< 19	< 0.17	1.2	1163	0.13	7.05	0.98	< 0.8	< 0.06	78.50	< 0.02	5	0.02	117
Myrtle		MY16	195.5	1	< 0.23	< 1.3	4	17820	1.25	< 0.5	142	33.0	55.4	20	< 20	< 0.23	0.6	2945	< 0.021	4.68	0.14	< 0.9	< 0.07	52.70	1.08	106	0.04	120
Myrtle		MY16	195.5	1'	< 0.24	< 1.4	3	15130	2.50	< 0.5	31	0.5	15.2	6	< 21	< 0.23	0.5	1203	< 0.021	4.38	< 0.072	< 0.9	< 0.07	54.00	0.29	20	< 0.019	177
Myrtle		MY16	195.5	1	< 0.23	< 2.1	13	22390	1.09	< 0.7	78	22.3	53.6	26	< 31	< 0.31	0.5	2201	< 0.04	3.25	0.09	< 1.2	< 0.09	40.20	3.69	22	< 0.036	146
Myrtle		MY16	195.5	1'	< 0.22	< 2	150	17640	1.58	< 0.7	123	16.5	52.2	28	< 29	< 0.3	1.4	1850	< 0.038	3.89	0.11	< 1.1	< 0.08	51.60	4.67	28	< 0.034	172
Myrtle		MY16	195.5	2	< 0.2	< 1.4	7	16400	1.70	< 0.6	86	13.5	32.6	8	< 23	< 0.2	1.3	1997	0.05	4.67	0.72	< 0.8	< 0.09	52.50	1.05	14	0.02	150
Myrtle		MY16	195.5	2'	< 0.21	< 1.5	4	17020	1.19	< 0.6	174	30.3	64.5	26	< 25	< 0.21	0.7	2418	0.03	3.55	0.61	< 0.9	< 0.1	45.10	1.44	8	< 0.019	125
Percentage of analyses > LOD					0	0	100	100	100	0	100	100	100	57	0	0	100	100	29	100	86	0	0	100	86	100	36	
Myrtle		MY16	195.9	1	1.38	< 0.92	495	11800	0.41	< 0.7	342	38.0	113.8	15	< 5	< 0.19	1.77	1880	0.212	17.3	3.33	< 1	20.00	8.1	1.35	2550	0.038	170
Myrtle		MY16	195.9	1'	2.23	< 1.2	940	20400	0.24	< 0.9	180.8	25.4	50.6	22.2	< 7	< 0.26	1.21	1350	0.127	10.9	1.22	< 1.3	830.00	7.1	1.99	880	0.045	200
Myrtle		MY16	195.9	2	0.29	< 0.93	593	27710	0.473	< 0.6	248	7.4	38.2	20.5	< 5	< 0.23	1.54	1225	0.027	3.83	1.87	< 1	127.00	8.26	2.18	1280	0.102	211
Myrtle		MY16	195.9	2'	0.26	< 0.74	296	20780	0.32	< 0.6	154.6	18.88	23.8	20.4	< 5	< 0.24	1.67	1596	< 0.027	4.48	2.7	< 1	130.00	6.19	2.75	500	0.035	188
Myrtle		MY16	195.9	3	0.231	< 0.74	238	25540	0.391	< 0.6	286	12.09	36.5	27.5	< 5	< 0.24	1.6	1725	0.037	3.38	4.65	< 1	33.00	5.19	4.09	3490	0.096	196
Myrtle		MY16	195.9	3'	< 0.12	< 0.71	209	19180	0.29	< 0.6	128.1	13.14	26.6	15.3	< 5	< 0.23	1.43	1411	0.031	3.54	2.02	< 1	33.00	5.43	1.91	460	0.03	190
Myrtle		MY16	195.9	4	1.38	1.95	351	21600	0.21	< 1.1	162.1	25.8	36.4	23.5	< 7	< 0.35	1.73	1500	0.054	7.6	2.94	< 1.3	270.00	5.82	2.44	570	0.067	189
Myrtle		MY16	195.9	4'	1.33	< 0.81	597	8910	< 0.1	< 0.8	196.2	18.06	52.1	3.02	< 4	< 0.25	1.61	1620	< 0.033	5.00	2.76	< 1.2	81.00	5.96	1.89	1230	0.071	171
Myrtle		MY16	195.9	5	1.69	1.03	903	23600	0.39	< 0.9	147.7	19.7	33.0	259	< 4	< 0.28	1.42	1480	< 0.037	4.2	2.28	< 1.3	240.00	7.39	5.14	420	0.057	200
Myrtle		MY16	195.9	6	2.48	1.35	106.4	8560	< 0.12	< 0.6	363	43.3	112.2	4.22	< 6	< 0.23	2.34	1638	0.1	6.29	6.16	< 1.4	23.00	11.3	1.11	490	0.081	142
Myrtle		MY16	195.9	6'	0.3	< 0.73	342	25200	0.32	< 0.5	310	11.19	31.8	19.3	< 5	< 0.19	2.2	1566	0.076	5.1	3.73	< 1.1	134.00	5.47	2.9	245	0.039	206
Percentage of analyses > LOD					91	27	100	100	82	0	100	100	100	100	0	0	100	100	73	100	100	0	100	100	100	100	100	
Myrtle		MY16	197.7	1	< 0.4	< 3.1	17	33000	0.26	< 1.7	223	2.9	94.5	18	< 43	< 0.35	0.6	1990	< 0.062	6.00	0.13	< 1.9	< 0.16	49.90	2.30	11	< 0.041	177
Myrtle		MY16	197.7	1'	< 0.26	< 2	15	34480	0.20	< 1.1	312	9.0	71.5	134	< 28	< 0.23	1.0	2083	0.07	7.01	0.96	< 1.2	< 0.1	49.00	19.61	78	0.03	171
Myrtle		MY16	197.7	Z1	< 0.17	< 1.5	11	34800	0.09	< 0.6	250	12.3	58.9	54	< 24	< 0.14	1.0	2340	0.03	4.60	0.62	< 1	< 0.08	21.70	7.30	36	0.02	160
Myrtle		MY16	197.7	1	< 0.18	< 1.4	4	27640	< 0.09	< 0.6	186	0.4	69.6	11	< 23	< 0.19	0.6	1512	< 0.029	3.88	0.10	< 0.9	< 0.05	37.30	0.88	14	< 0.019	182
Myrtle		MY16	197.7	1'	< 0.22	< 1.7	8	34980	< 0.12	< 0.7	234	31.9	27.6	78	< 29	< 0.24	1.0	3229	< 0.036	4.67	1.11	< 1.1	< 0.06	30.90	7.53	29	< 0.023	152
Myrtle		MY16	197.7	1'	< 0.19	< 1.8	< 1.7	1970	0.93	< 0.6	23	47.0	0.7	13	< 19	< 0.3	0.9	3476	< 0.026	3.29	0.68	< 1	< 0.09	80.60	0.16	9	< 0.026	108
Myrtle		MY16	197.7	1'	< 0.18	< 1.7	4	764	0.20	< 0.6	37	104.9	5.3	< 2.2	< 18	< 0.28	0.6	1775	< 0.025	2.90	6.05	< 0.9	< 0.9	73.10	0.07	8	< 0.024	72
Myrtle		MY16	197.7	2	0.52	< 1.9	2	854	0.22	< 0.8	95	114.5	5.2	< 2.6	< 25	< 0.29	0.8	1376	0.03	3.37	9.64	< 0.9	< 0.1	70.40	0.08	16	< 0.025	73
Myrtle		MY16	197.7	2'	< 0.18	< 1.7	< 1.3	673	0.16	< 0.7	53	136.5	8.6	< 2.3	< 22	< 0.26	0.6	1362	< 0.022	2.85	5.67	< 0.8	< 0.09	71.60	0.11	10	< 0.022	40
Myrtle		MY16	197.7	1	< 0.17	< 1.6	< 1.2	1262	< 0.12	< 0.6	10	2.6	0.7	< 2.1	< 20	< 0.24	0.7	1920	< 0.021	3.47	0.10	< 0.8	< 0.08	60.10	< 0.02	1	< 0.021	129
Myrtle		MY16	197.7	1'	< 0.18	< 1.6	2	1850	< 0.12	< 0.6	142	107.0	6.9	< 2.2	< 21	< 0.25	0.7	2655	< 0.021	4.08	4.69	< 0.8	< 0.08	58.50	0.11	12	< 0.021	77
Myrtle		MY16	197.7	1	0.13	< 2.2	< 1.2	1226	< 0.12	< 0.5	5	136.4	2.6	< 2	< 29	< 0.18	0.5	2713	< 0.023	3.13	0.13	< 1.1	< 0.08	57.40	0.05	1	< 0.021	66
Myrtle		MY16	197.7	1'	< 0.12	< 2.2	13	1541	0.19	< 0.5	38	46.7	2.3	< 2	< 29	< 0.18	0.7	2573	< 0.023	3.05	1.29	< 1.1	< 0.08	54.90	0.08	48	0.02	118
Myrtle		MY16	197.7	2	0.31	< 1.8	15	1202	0.23	< 0.9	28	87.4	4.1	6	< 27	< 0.3	0.6	2184	< 0.034	6.86	1.25	< 1.5	< 0.08	55.10	0.19	165	< 0.03	103
Myrtle		MY16	197.7	2'	< 0.19	< 1.5	< 1.6	1144	0.31	< 0.8	25	78.4	2.6	3	< 22	< 0.25	0.5	2644	< 0.028	3.06	1.13	< 1.2	< 0.06	53.60	0.09	59	< 0.025	75
Myrtle		MY16	197.7	3	< 0.16	< 1.7	< 1.4	1444	0.34	< 0.5	14	49.3	1.3	< 1.7	26	< 0.18	0.6	2952	< 0.026	2.77	0.96	< 1	< 0.07	53.30	0.03	3	0.03	92
Myrtle		MY16	197.7	3'	< 0.17	< 1.8	6	572	0.19	< 0.5	26	23.4	< 0.59	< 1.8	< 27	< 0.19	0.6	1760	< 0.028	2.70	< 0.066	< 1.1	< 0.07	51.20	< 0.03	1	< 0.027	123
Percentage of analyses > LOD					18	0	65	100	71	0	100	100	94	47	6	0	100	100	18	100	94	0	0	100	88	100	24	

Deposit	Lens # (HYC)	Drillhole #	Depth (m)	Analyse #	V (ppm)	Cr (ppm)	Mn (ppm)	Fe (ppm)	Co (ppm)	Ni (ppm)	Cu (ppm)	Ga (ppm)	Ge (ppm)	As (ppm)	Se (ppm)	Mo (ppm)	Ag (ppm)	Cd (ppm)	In (ppm)	Sn (ppm)	Sb (ppm)	Te (ppm)	Au (ppm)	Hg (ppm)	Tl (ppm)	Pb (ppm)	Bi (ppm)	Calculated temperature (°C)
Myrtle		MY16	205.3	1x	< 0.37	< 1.8	8.6	3040	0.71	< 1.4	28.5	5.64	< 1.1	5.9	< 11	< 0.62	1.02	1858	< 0.069	1.04	5.97	< 3.1	< 0.18	9.19	< 0.07	21.3	< 0.089	176
Myrtle		MY16	205.3	2x	< 0.37	< 2.3	64	9780	< 0.32	< 1.5	120	26.7	18.1	5.4	< 11	< 0.51	0.97	1448	0.126	7.08	2.78	< 2.3	< 0.23	8.1	0.147	18	< 0.094	168
Myrtle		MY16	205.3	3	< 0.34	< 1.9	2.75	14530	< 0.2	< 1.4	61	26.51	3.11	1.78	< 10	< 0.72	1.27	1523	< 0.065	3.9	0.23	< 2.9	< 0.26	7.36	< 0.07	8.2	< 0.085	155
Myrtle		MY16	205.3	3'	< 0.49	< 2.4	5.7	15100	0.74	< 1.8	74.1	10.65	7.78	25.7	< 10	< 0.59	1.03	1335	0.084	6.68	< 0.19	< 2.8	< 0.22	7.46	1.48	40	< 0.1	169
Myrtle		MY16	205.3	4	< 0.35	< 2.2	2.91	7180	< 0.29	< 1.5	304.4	66.6	119.5	< 1.5	< 10	< 0.69	0.94	1306	0.547	18.2	< 0.2	< 3.2	< 0.19	6.14	< 0.11	2.1	< 0.075	102
Myrtle		MY16	205.3	4'	< 0.44	< 4.3	2.79	6910	< 0.51	< 2.5	281	60.6	97.6	< 2.3	< 15	< 0.75	0.89	1264	0.46	14.92	< 0.32	< 3.9	< 0.35	6.71	< 0.17	11	< 0.17	104
Percentage of analyses > LOD					0	0	100	100	33	0	100	100	83	67	0	0	100	100	67	100	50	0	0	100	33	100	0	
Caranbirini		DD82CA1	679.2	1	< 0.42	< 2.2	< 2.2	1241	< 0.34	< 45	1296	393.0	22.7	39	< 59	< 0.48	225.0	4550	0.66	46.30	808.00	< 2.4	< 0.07	44.40	0.29	157	< 0.04	56
Caranbirini		DD82CA1	679.2	1'	0.74	< 1.8	< 1.6	955	< 0.41	< 55	754	378.0	33.0	14	< 51	< 0.44	53.8	3056	1.94	61.20	263.00	< 2	< 0.07	44.60	< 0.09	55	0.02	49
Caranbirini		DD82CA1	679.2	2	< 0.45	< 2.3	71	5980	< 0.53	< 70	1287	527.0	25.3	22	< 64	< 0.59	127.3	3301	0.76	32.80	537.00	< 2.6	< 0.09	53.50	0.22	92	< 0.025	129
Caranbirini		DD82CA1	679.2	2'	< 0.31	< 1.4	< 2.4	1661	< 0.35	< 54	948	564.0	35.8	15	< 57	0.53	38.7	3135	1.56	47.80	232.00	< 2.2	< 0.1	43.50	< 0.13	180	< 0.045	58
Caranbirini		DD82CA1	679.2	3	0.57	< 1.7	< 2.9	3300	0.63	< 66	1250	479.0	40.2	28	< 69	1.08	114.0	4710	1.15	69.90	523.00	< 2.7	< 0.13	32.70	0.58	304	0.08	72
Caranbirini		DD82CA1	679.2	3'	< 0.4	< 1.8	8	1290	< 0.44	< 55	748	405.0	24.7	14	< 54	0.51	31.0	3095	2.29	78.40	209.40	< 2.8	< 0.09	35.80	< 0.11	34	< 0.038	84
Caranbirini		DD82CA1	679.2	4	< 0.41	< 1.8	2	1273	< 0.45	< 55	814	400.0	14.4	17	< 53	0.55	64.5	3058	2.55	43.30	281.00	< 2.9	< 0.09	39.80	< 0.12	56	< 0.039	77
Caranbirini		DD82CA1	679.2	4'	< 0.4	< 1.2	< 2.3	2020	< 0.37	< 43	1679	450.0	31.4	42	< 50	0.73	270.0	4470	0.78	81.40	966.00	< 2.1	< 0.05	39.10	1.07	220	0.02	62
Caranbirini		DD82CA1	679.2	5	0.65	< 1.2	< 2.3	1810	< 0.37	< 43	673	320.3	22.7	18	< 50	0.78	61.7	2393	0.12	4.69	273.00	< 2.1	< 0.05	45.70	0.20	64	0.03	57
Caranbirini		DD82CA1	679.2	5'	< 0.37	< 1.3	< 1.9	1760	< 0.32	< 45	1186	583.0	44.4	21	< 51	< 0.75	45.9	1898	1.70	127.60	316.00	< 1.8	< 0.11	38.20	0.23	43	0.03	54
Caranbirini		DD82CA1	679.2	6	< 0.36	< 1.3	< 1.9	1213	< 0.32	< 45	296	235.0	2.8	< 4.5	< 50	< 0.74	5.2	1716	2.42	11.90	36.50	< 1.8	< 0.11	35.40	< 0.12	21	< 0.02	92
Caranbirini		DD82CA1	679.2	6'	< 0.38	< 2.1	18	1649	< 0.35	< 60	480	342.2	< 3.4	6	< 53	< 0.62	13.8	2044	2.48	12.40	97.60	< 2.7	< 0.06	43.20	< 0.14	26	0.04	132
Caranbirini		DD82CA1	679.2	7	< 0.37	< 2	< 2.1	1501	< 0.34	< 58	213	105.0	< 3.3	< 3.9	< 52	< 0.6	6.6	2144	7.41	48.70	37.20	< 2.7	< 0.06	36.90	< 0.13	20	< 0.032	120
Caranbirini		DD82CA1	679.2	7'	< 0.34	< 1.1	< 1.9	2100	< 0.48	< 56	181	91.2	< 3.6	< 4	< 49	< 0.54	3.6	2050	7.60	48.50	10.63	< 2.9	< 0.07	38.30	< 0.11	15	< 0.033	126
Caranbirini		DD82CA1	679.2	8	< 0.35	< 1.1	< 2	1374	< 0.48	< 57	1025	870.0	12.0	6	< 49	< 0.54	19.4	1473	2.02	33.80	106.90	< 2.9	< 0.07	34.30	< 0.11	19	< 0.033	61
Caranbirini		DD82CA1	679.2	8'	< 0.38	< 1.2	< 2.3	1210	< 0.29	< 37	752	437.0	7.8	16	< 40	< 0.45	50.1	1968	2.50	38.70	266.00	< 2.4	< 0.04	33.30	0.14	54	< 0.025	75
Caranbirini		DD82CA1	679.2	9	< 0.38	< 1.2	11	1560	< 0.28	< 36	1760	881.0	55.0	34	< 39	0.70	137.0	1374	0.08	4.15	742.00	< 2.4	< 0.04	31.70	0.08	83	0.05	54
Caranbirini		DD82CA1	679.2	9'	< 0.26	< 1.8	< 1.6	1431	< 0.31	< 41	589	309.0	14.5	16	< 42	< 0.45	74.7	2166	0.14	3.38	292.00	< 2.1	< 0.07	37.30	0.12	66	0.05	55
Caranbirini		DD82CA1	679.2	10	< 0.26	< 1.9	< 1.6	986	< 0.32	< 41	880	658.9	44.5	12	< 42	< 0.44	28.4	1453	0.09	4.30	171.30	< 2.2	< 0.07	28.90	< 0.07	27	0.04	23
Caranbirini		DD82CA1	679.2	10'	< 0.36	< 1.1	< 1.9	1578	< 0.3	< 51	440	285.0	9.0	9	< 43	< 0.49	32.9	3925	< 0.026	2.60	166.00	< 2.6	< 0.1	34.30	< 0.07	37	0.04	53
Percentage of analyses > LOD					15	0	25	100	5	0	100	100	85	85	0	35	100	100	95	100	100	0	0	100	45	100	50	
Caranbirini		DD84CA4	328.6	1	< 0.23	< 0.71	4	6390	0.33	< 20	869	247.1	177.8	4	< 19	< 0.3	8.6	2286	< 0.024	2.53	230.70	< 1.4	< 0.05	44.00	< 0.03	88	0.04	61
Caranbirini		DD84CA4	328.6	1'	< 0.2	< 0.66	4	6736	0.58	< 16	439	446.1	33.3	< 2	< 21	< 0.18	7.1	2011	< 0.028	2.50	19.04	< 0.5	< 0.05	40.10	< 0.04	14	< 0.014	76
Caranbirini		DD84CA4	328.6	2	< 0.19	< 0.65	3	7240	0.66	< 16	840	950.0	41.0	2	< 21	< 0.17	5.4	2210	0.14	2.68	7.49	< 0.5	< 0.05	36.00	< 0.04	6	< 0.014	77
Caranbirini		DD84CA4	328.6	2'	< 0.13	< 0.62	4	8030	0.50	< 20	979	671.1	103.3	< 2	< 17	< 0.27	12.4	2441	4.64	16.22	71.30	< 0.9	< 0.04	34.00	< 0.03	48	0.01	94
Caranbirini		DD84CA4	328.6	3	< 0.13	< 0.63	4	7920	0.61	< 20	1187	478.2	144.0	6	< 17	< 0.27	24.0	2847	0.52	5.87	285.60	< 0.9	< 0.04	31.80	< 0.03	135	0.04	80
Caranbirini		DD84CA4	328.6	3'	< 0.17	< 0.61	3	7170	0.27	< 17	713	291.3	81.6	4	< 17	< 0.23	16.7	2495	0.03	2.07	226.10	< 1.3	< 0.04	29.70	< 0.03	99	0.03	75
Caranbirini		DD84CA4	328.6	4	< 0.17	< 0.61	4	8210	0.59	< 18	648	394.4	68.4	< 2.3	< 17	< 0.23	14.4	2586	< 0.02	1.94	113.40	< 1.3	< 0.04	27.50	< 0.03	48	< 0.018	72
Caranbirini		DD84CA4	328.6	4'	< 0.16	< 0.66	4	8170	0.45	< 20	717	225.0	44.7	< 1.8	< 19	< 0.26	16.7	2299	0.14	3.43	44.50	< 0.7	< 0.03	28.90	< 0.04	46	< 0.013	98
Caranbirini		DD84CA4	328.6	5	< 0.17	< 0.67	5	8760	0.53	< 20	675	354.0	56.7	3	< 20	< 0.27	22.9	2426	0.05	2.97	158.20	< 0.7	< 0.03	26.10	< 0.04	53	0.01	86
Caranbirini		DD84CA4	328.6	5'	< 0.21	< 0.73	5	8520	0.29	< 24	1264	408.3	146.0	6	< 20	< 0.28	35.5	2515	0.25	7.05	317.10	< 1.5	< 0.07	30.30	0.06	117	0.04	83
Caranbirini		DD84CA4	328.6	6	< 0.18	< 0.62	4	7990	0.39	< 20	452	286.4	40.7	< 2.3	< 17	< 0.24	12.1	2248	< 0.017	2.26	82.70	< 1.3	< 0.06	27.00	< 0.04	33	0.01	81
Caranbirini		DD84CA4	328.6	6'	< 0.18	< 0.73	4	7440	0.48	< 16	232	222.3	10.7	< 2.6	< 20	< 0.25	9.8	2092	< 0.02	1.86	3.85	< 0.7	< 0.04	24.30	< 0.03	7	< 0.019	98
Caranbirini		DD84CA4	328.6	7	< 0.18	< 0.72	4	8300	0.50	< 16	163	143.6	7.9	< 2.5	< 20	< 0.25	8.0	2581	< 0.02	2.12	10.28	< 0.7	< 0.04	24.40	< 0.03	12	< 0.019	110
Caranbirini		DD84CA4	328.6	7'	< 0.16	< 0.63	4	8510	0.55	< 20	275	241.5	15.9	< 2.2	< 19	< 0.23	11.8	2564	< 0.028	2.37	21.60	< 0.7	< 0.03	24.70	< 0.03	13	< 0.008	97
Caranbirini		DD84CA4	328.6	8	< 0.16	< 0.62	5	9250	0.45	< 20	225	209.2	10.9	< 2.1	< 18	< 0.23	5.8	2779	< 0.027	2.37	13.64	< 0.7	< 0.03	24.20	< 0.03	11	< 0.007	107
Caranbirini		DD84CA4	328.6	8'	< 0.22	< 0.5	4	8600	0.65	< 18	285	359.0	14.0	< 2	< 16	< 0.21	0.3	2432	< 0.018	2.15	5.78	< 1.2	< 0.03	23.10	< 0.03	5	< 0.015	92
Caranbirini		DD84CA4	328.6	9	< 0.24	< 0.55	4	8160	0.51	< 20	175	81.3	4.0	< 2.1	< 17	< 0.23	5.1	2737	0.40	6.00	5.28	< 1.3	< 0.04	27.00	< 0.03	11	< 0.017	145
Caranbirini		DD84CA4	328.6	9'	< 0.14	< 0.7	4	7760	0.76	< 22	167	159.6	8.2	< 1.9	< 19	< 0.33	0.6	2515	< 0.026	1.74	3.38	< 1.8	< 0.05	24.90	< 0.03	4	< 0.021	108
Caranbirini		DD84CA4	328.6	10	< 0.14	< 0.72	4	7290	0.53	< 23	79	73.0	4.8	< 2	< 20	< 0.34	0.4	2307	< 0.027	1.86	1.76	< 1.8	< 0.05	25.30	< 0.03	3	< 0.022	122
Caranbirini		DD84CA4	328.6	10'	< 0.13	< 0.69	4	6660	0.67	< 22	61	50.4	4.6	< 1.9	< 19	< 0.32	< 0.086	2133	< 0.026	1.97	0.43	< 1.8	< 0.05	23.10	< 0.03	2	< 0.021	125
Percentage of analyses > LOD					0	0	100	100	100	0	100	100	100	30	0	0	95	100	40	100	100	0	0	100	5	100	35	

Deposit	Lens # (HYC)	Drillhole #	Depth (m)	Analyse #	V (ppm)	Cr (ppm)	Mn (ppm)	Fe (ppm)	Co (ppm)	Ni (ppm)	Cu (ppm)	Ga (ppm)	Ge (ppm)	As (ppm)	Se (ppm)	Mo (ppm)	Ag (ppm)	Cd (ppm)	In (ppm)	Sn (ppm)	Sb (ppm)	Te (ppm)	Au (ppm)	Hg (ppm)	Tl (ppm)	Pb (ppm)	Bi (ppm)	Calculated temperature (°C)
Caranbirini		DD84CA4	352.6	1	< 0.23	< 0.97	1	3592	< 0.12	< 16.2	599	171.6	172.4	< 0.6	< 25	< 0.15	2.4	864	0.03	6.84	6.96	< 0.9	0.11	21.65	0.05	6	< 0.016	47
Caranbirini		DD84CA4	352.6	1'	< 0.16	< 0.5	1	3275	< 0.18	24	291	139.6	128.1	0	< 34	< 0.18	1.4	882	0.07	9.45	3.00	< 1.8	0.20	21.69	0.04	5	< 0.012	57
Caranbirini		DD84CA4	352.6	3x	< 0.34	< 1.22	2	3035	0.77	< 33.5	401	111.4	10.9	1	< 54	0.99	3.2	1960	8.83	163.44	36.24	< 2.2	< 0.08	33.40	0.04	15	< 0.021	117
Caranbirini		DD84CA4	352.6	4	< 0.23	< 0.9	< 1.2	383	< 0.23	< 22.3	383	100.4	10.4	7	< 31	< 0.23	22.0	3635	0.03	9.33	167.70	< 1.9	< 0.07	19.69	0.04	159	0.05	35
Caranbirini		DD84CA4	352.6	4'	< 0.31	< 1.42	< 1.3	3329	< 0.23	< 22.3	347	174.5	146.1	< 0.9	< 55	< 0.29	0.7	855	< 0.02	9.24	2.14	< 1.1	< 0.05	17.16	0.04	3	< 0.024	35
Caranbirini		DD84CA4	352.6	5	< 0.22	< 1.52	< 1	3193	0.11	< 28.4	396	224.2	148.6	< 0.9	< 35	< 0.19	2.0	888	0.11	11.55	7.00	< 1.3	0.12	15.94	0.05	6	< 0.023	41
Caranbirini		DD84CA4	352.6	5'	< 0.25	< 1.62	< 1.2	3171	< 0.11	< 26.4	444	119.4	113.1	< 0.7	< 41	< 0.22	2.6	818	0.08	7.59	5.86	< 1.4	< 0.09	16.24	< 0.03	8	< 0.03	52
Caranbirini		DD84CA4	352.6	6	< 0.16	< 0.92	3	2886	< 0.09	< 13.2	400	174.1	79.9	< 0.7	< 17	< 0.2	1.8	937	0.65	11.17	0.53	< 0.8	0.08	8.35	0.03	1	0.02	78
Caranbirini		DD84CA4	352.6	6'	< 0.19	< 1.42	2	3224	< 0.15	< 19.3	476	251.8	85.6	< 0.9	< 35	< 0.22	1.9	1177	0.08	4.83	5.04	< 1.4	< 0.1	7.72	0.03	3	< 0.021	58
Caranbirini		DD84CA4	352.6	7	< 0.12	< 0.74	3	3157	< 0.08	< 14.2	469	195.0	66.6	0	< 25	< 0.16	4.3	1156	0.28	7.11	1.71	< 0.7	0.08	9.37	0.04	4	0.02	77
Caranbirini		DD84CA4	352.6	7'	0.23	< 0.83	14	3122	0.27	< 15.2	479	209.8	83.0	0	< 23	< 0.2	5.5	1166	2.03	10.20	14.27	< 1	< 0.04	9.91	0.03	13	0.03	100
Caranbirini		DD84CA4	352.6	8x	< 0.17	< 0.95	2	3891	< 0.1	< 17.3	789	234.5	45.3	< 0.9	< 30	< 0.13	5.8	1345	1.18	56.75	10.96	< 1.1	0.10	7.26	0.18	5	0.02	86
Caranbirini		DD84CA4	352.6	9	< 0.13	< 0.72	1	4494	< 0.1	< 12.2	340	167.3	23.2	< 0.5	< 23	< 0.18	0.8	1634	0.20	7.68	4.42	< 1	< 0.04	6.95	0.06	3	< 0.015	84
Caranbirini		DD84CA4	352.6	9'	< 0.14	< 0.83	2	4676	< 0.17	< 18.3	354	203.0	29.2	< 0.8	< 27	< 0.16	1.1	1718	1.44	11.23	5.16	< 1.2	0.07	7.34	0.04	9	< 0.019	97
Caranbirini		DD84CA4	352.6	10	0.85	0.98	28	3201	< 0.17	< 18.3	558	371.3	98.9	< 0.9	< 27	< 0.27	2.4	827	0.16	10.20	2.12	< 1.1	0.05	15.63	< 0.02	7	0.02	85
Caranbirini		DD84CA4	352.6	10'	< 0.31	< 1.62	14	3145	< 0.35	< 30.5	504	240.3	83.6	0	< 37	< 0.23	4.7	1073	1.53	10.18	4.08	< 1.3	< 0.05	10.45	0.02	6	0.02	97
Caranbirini		DD84CA4	352.6	11	< 0.13	< 0.59	1	4517	5.49	< 13.2	474	419.3	25.8	0	< 19	< 0.12	1.5	1192	0.80	18.68	16.14	< 0.7	0.10	10.52	0.03	12	0.03	83
Caranbirini		DD84CA4	352.6	11'	< 0.17	< 0.8	1	5147	2.49	< 19.3	550	292.4	76.7	< 0.6	< 23	< 0.3	1.9	1465	4.18	102.12	25.07	< 1.7	0.05	10.30	0.04	18	0.02	86
Caranbirini		DD84CA4	352.6	12	< 0.13	< 0.56	< 0.7	4073	< 0.07	< 13.2	316	141.2	202.7	< 0.4	< 18	< 0.14	0.2	748	< 0.02	3.09	< 0.05	< 0.7	0.10	5.71	0.04	1	0.02	30
Caranbirini		DD84CA4	352.6	12'	< 0.16	< 0.8	< 0.8	3924	0.02	< 18.3	301	128.7	167.3	< 0.7	< 23	< 0.14	0.3	895	0.04	3.86	0.43	< 0.7	3.76	5.67	0.05	1	< 0.021	42
Caranbirini		DD84CA4	352.6	13	< 0.13	< 0.7	1	4023	< 0.11	< 16.2	325	97.2	165.6	< 0.5	< 18	< 0.11	0.3	768	0.03	4.79	1.94	< 0.7	0.29	5.55	0.07	1	0.01	52
Caranbirini		DD84CA4	352.6	13'	< 0.16	< 1.02	< 1	3945	< 0.1	< 19.3	369	115.2	203.0	< 0.9	< 26	< 0.13	0.2	775	0.02	3.50	0.07	0.04	0.08	5.07	0.06	1	< 0.015	39
Caranbirini		DD84CA4	352.6	14	< 0.1	< 0.58	< 0.8	4629	< 0.12	< 16.2	304	66.8	147.9	< 0.6	< 20	< 0.15	0.3	599	0.25	61.52	4.78	< 0.9	0.08	6.78	0.03	1	< 0.014	65
Caranbirini		DD84CA4	352.6	14'	< 0.25	< 0.82	< 1	3596	< 0.19	< 17.3	394	323.0	174.8	< 1.1	< 27	< 0.14	0.2	953	0.04	6.88	1.54	< 0.6	< 0.03	4.93	0.05	1	< 0.015	31
Caranbirini		DD84CA4	352.6	15	< 0.12	< 0.7	< 0.8	3560	< 0.1	< 12.2	387	343.3	172.5	< 0.4	< 19	< 0.16	0.2	967	0.07	9.94	0.20	< 0.8	0.15	4.60	0.04	0	< 0.012	31
Caranbirini		DD84CA4	352.6	15'	< 0.13	< 0.67	1	3193	0.31	< 11.2	329	176.2	130.9	< 0.5	< 17	< 0.13	0.5	845	0.67	13.64	3.29	< 0.6	0.03	5.53	0.04	3	< 0.01	59
Percentage of analyses > LOD					8	4	62	100	27	4	100	100	100	23	0	4	100	100	92	100	96	4	65	100	92	100	42	
Caranbirini		MANT79-3	208.6	1	1.36	< 4.37	171	1401	< 0.67	< 162.4	298	461.9	36.3	< 5.7	< 132	< 1.22	2.3	1254	0.31	4.67	3.84	< 4.1	0.68	79.08	0.42	12	< 0.102	102
Caranbirini		MANT79-3	208.6	1'	< 0.9	< 3.35	101	2822	0.81	< 121.8	217	471.0	29.2	< 4.4	< 99	< 0.92	< 0.46	1277	0.35	5.08	2.46	< 3.1	0.41	57.76	0.20	18	< 0.08	113
Caranbirini		MANT79-3	208.6	2	< 0.82	< 3.05	128	1279	< 0.47	< 111.7	423	381.7	112.5	< 4	< 88	< 0.83	2.5	1240	0.15	3.96	2.06	< 2.8	1.54	47.31	0.20	8	< 0.072	81
Caranbirini		MANT79-3	208.6	2'	< 0.94	< 3.55	142	3959	0.86	< 132	320	453.8	55.9	< 4.6	< 101	< 0.96	1.9	1227	0.27	3.76	2.82	< 3.4	51.77	40.71	0.56	11	< 0.083	115
Caranbirini		MANT79-3	208.6	3	0.70	< 2.64	152	2599	< 0.41	104	399	247.0	71.2	< 3.5	< 73	< 0.71	1.9	1728	0.25	8.02	4.24	< 2.4	3.86	42.53	0.12	15	< 0.061	111
Caranbirini		MANT79-3	208.6	3'	1.45	< 3.86	332	4649	< 0.6	178	376	160.1	86.4	< 5.1	< 102	< 1.02	3.0	1885	0.28	12.28	6.45	< 3.7	0.67	53.60	0.18	18	< 0.09	135
Caranbirini		MANT79-3	208.6	4	< 0.69	< 2.64	116	3147	< 0.4	164	366	149.5	81.8	< 3.4	< 70	< 0.7	0.4	1890	0.26	5.79	3.30	< 2.4	3.54	46.09	< 0.07	14	< 0.06	117
Caranbirini		MANT79-3	208.6	4'	< 1.02	< 4.06	116	3106	< 0.4	< 142.1	343	149.5	68.9	< 3.4	< 80	< 0.72	0.5	1889	0.22	7.31	4.05	< 4.7	0.86	43.45	0.21	22	< 0.031	117
Caranbirini		MANT79-3	208.6	5	< 1.32	< 5.08	68	2000	< 0.49	< 182.7	265	264.7	46.8	< 4.2	< 98	< 0.9	< 0.44	1670	< 0.09	4.37	2.76	< 5.8	0.30	40.30	0.13	12	< 0.04	92
Caranbirini		MANT79-3	208.6	5'	< 1.32	< 4.97	66	996	< 0.49	< 182.7	186	332.5	33.9	< 4.1	< 96	< 0.89	0.6	1329	0.17	5.18	1.82	< 5.7	1.35	38.88	< 0.09	10	< 0.039	86
Caranbirini		MANT79-3	208.6	6	< 1.42	< 5.58	33	832	< 0.53	< 213.2	207	445.7	30.7	< 4.6	< 102	< 0.98	5.2	1359	0.11	3.45	1.31	< 6.3	0.38	30.76	< 0.09	10	0.06	70
Caranbirini		MANT79-3	208.6	6'	< 1.22	< 4.97	42	883	< 0.48	< 192.9	239	523.8	24.0	< 4.1	103	< 0.88	1.0	1185	0.17	4.06	1.41	< 5.7	0.36	36.24	< 0.08	10	< 0.038	77
Caranbirini		MANT79-3	208.6	7	< 1.32	< 5.28	41	814	< 0.5	< 213.2	262	548.2	17.5	< 4.3	< 95	< 0.92	0.8	1230	0.10	3.96	1.99	< 5.9	0.30	41.11	< 0.09	11	< 0.04	76
Caranbirini		MANT79-3	208.6	7'	< 1.32	< 5.18	32	934	< 0.49	< 213.2	295	626.3	19.5	< 4.2	< 91	< 0.9	< 0.43	1283	0.20	4.73	1.78	< 5.8	< 0.11	40.50	0.11	12	< 0.039	76
Caranbirini		MANT79-3	208.6	8	< 1.52	< 6.29	153	1431	< 0.59	< 274.1	299	402.0	31.7	< 5.1	< 112	< 1.12	1.8	1293	0.20	3.86	2.84	< 7	0.39	46.70	0.17	11	< 0.046	102
Caranbirini		MANT79-3	208.6	8'	< 1.32	< 5.38	21	760	< 0.51	< 243.6	204	484.9	16.5	< 4.4	< 92	< 0.94	1.9	1171	0.11	2.41	1.69	< 6	0.23	37.26	< 0.09	9	< 0.04	70
Caranbirini		MANT79-3	208.6	9	< 1.62	< 6.7	247	1563	< 0.62	< 304.5	280	377.1	44.3	< 5.4	< 112	< 1.12	< 0.56	1248	0.12	4.87	3.00	< 7.4	0.97	49.13	< 0.1	10	< 0.048	103
Caranbirini		MANT79-3	208.6	9'	< 1.73	< 7	90	1320	< 0.65	< 335	194	289.3	30.0	< 5.7	< 112	< 1.22	6.5	1386	0.16	7.61	3.83	< 7.8	10.96	47.81	0.17	17	0.09	98
Caranbirini		MANT79-3	208.6	10	3.25	< 6.5	157	1634	< 0.6	< 324.8	168	200.1	17.7	< 5.3	< 102	< 1.12	8.1	1407	0.16	3.32	2.95	< 7.2	8.22	46.39	< 0.1	10	< 0.046	119
Caranbirini		MANT79-3	208.6	10'	< 1.32	< 5.48	36	2203	< 0.5	< 284.2	356	268.3	61.6	< 4.4	< 86	< 0.93	0.5	1634	0.20	5.51	2.27	< 6	8.12	36.65	< 0.08	12	< 0.039	92
Caranbirini		MANT79-3	208.6	11	< 0.68	< 5.79	47	2751	0.00	< 345.2	506	187.1	105.7	< 3.1	< 84	< 1.42	0.4	1772	0.10	8.22	2.56	< 4.1	0.21	38.68	< 0.08	15	< 0.059	93
Caranbirini		MANT79-3	208.6	11'	< 0.73	< 6.29	138	2873	0.00	< 395.9	500	181.6	88.1	< 3.5	< 89	< 1.52	2.7	1800	0.31	17.56	2.90	< 4.4	2.17	43.55	< 0.08	16	< 0.064	114
Caranbirini		MANT79-3	208.6	12	< 0.87	< 7.72	204	2193	0.00	< 497.4	230	225.4	26.6	< 4.2	< 112	< 1.93	< 0.04	1672	0.15	7.41	2.96	< 5.3	3.55	51.67	0.35	9	< 0.076	121

Deposit	Lens # (HYC)	Drillhole #	Depth (m)	Analyse #	V (ppm)	Cr (ppm)	Mn (ppm)	Fe (ppm)	Co (ppm)	Ni (ppm)	Cu (ppm)	Ga (ppm)	Ge (ppm)	As (ppm)	Se (ppm)	Mo (ppm)	Ag (ppm)	Cd (ppm)	In (ppm)	Sn (ppm)	Sb (ppm)	Te (ppm)	Au (ppm)	Hg (ppm)	Tl (ppm)	Pb (ppm)	Bi (ppm)	Calculated temperature (°C)
Caranbirini		MANT79-3	208.6	12'	< 0.74	< 6.6	91	2365	0.00	< 446.7	271	217.6	25.8	< 3.6	< 90	< 1.62	2.0	1943	0.50	6.80	2.91	< 4.5	2.83	45.78	< 0.09	15	< 0.065	121
Caranbirini		MANT79-3	208.6	13	< 0.87	< 7.82	134	2507	0.00	< 558.3	240	160.4	28.3	< 4.3	< 102	< 1.93	1.2	1916	< 0.09	7.41	3.26	< 5.3	0.25	50.96	< 0.1	14	< 0.076	116
Caranbirini		MANT79-3	208.6	13'	< 0.69	< 6.29	36	2447	0.08	< 467	378	176.0	67.4	< 3.4	< 83	< 1.52	1.4	1781	1.08	13.81	3.11	< 4.3	1.44	43.45	< 0.08	16	< 0.06	107
Caranbirini		MANT79-3	208.6	14	< 0.68	< 6.29	109	1368	0.00	< 517.7	233	299.0	39.3	< 3.4	< 81	< 1.52	< 0.32	1398	0.22	5.18	1.99	< 4.3	0.22	46.60	< 0.08	11	< 0.059	99
Caranbirini		MANT79-3	208.6	14'	1.48	< 11.17	601	3756	0.36	< 974.5	331	337.0	39.7	< 6.1	< 142	< 2.74	9.7	1537	0.41	17.87	7.24	< 7.6	7.72	70.65	0.46	15	< 0.102	139
Caranbirini		MANT79-3	208.6	15	< 0.66	< 6.19	92	1101	0.00	< 568.5	241	431.4	24.0	< 3.4	< 77	< 1.52	0.7	1378	0.28	4.38	1.93	< 4.2	0.79	42.84	< 0.07	12	0.06	95
Caranbirini		MANT79-3	208.6	15'	< 1.62	< 8.83	78	893	< 0.75	< 873	298	479.2	29.0	< 9.1	< 112	< 1.93	< 1.22	1233	0.26	6.29	2.30	< 6.9	< 0.27	75.22	0.19	10	< 0.173	85
Percentage of analyses > LOD					17	0	100	100	13	10	100	100	100	0	3	0	77	100	93	100	100	0	93	100	47	100	10	
Walford Creek		WFDD238	140.5	1	0.49	< 1.02	1	1096	23.56	0	331	95.7	6.1	2	< 5	115.73	14.4	3085	136.23	0.48	79.59	< 1.1	2.13	7.12	0.19	2944	< 0.056	116
Walford Creek		WFDD238	140.5	1'	0.11	< 0.93	0	578	22.57	1	395	40.9	5.3	1	< 4	1.53	40.8	6152	83.34	0.61	174.00	< 1	5.89	12.27	0.26	4761	< 0.049	98
Walford Creek		WFDD238	140.5	2	< 0.12	< 0.65	< 0.1	736	8.46	< 0.4	702	97.9	16.6	2	< 5	< 0.18	63.5	509	0.09	0.61	371.55	< 0.8	0.57	16.17	1.15	97	< 0.043	21
Walford Creek		WFDD238	140.5	2'	< 0.1	< 0.71	0	2589	7.67	< 0.4	437	3.1	0.8	< 0.51	< 4	< 0.2	6.0	2559	0.56	0.68	11.78	< 0.8	0.87	28.85	0.05	23	< 0.044	158
Walford Creek		WFDD238	140.5	3	< 0.1	< 0.71	1	1860	25.08	< 0.4	373	22.9	9.1	< 0.51	< 4	< 0.2	22.8	2257	0.04	0.99	181.71	< 0.8	0.10	15.23	0.19	96	< 0.043	89
Walford Creek		WFDD238	140.5	3'	0.11	< 0.7	1	1803	22.27	< 0.4	863	171.6	16.9	2	< 4	< 0.2	54.1	1432	7.31	0.79	442.61	< 0.8	0.47	19.89	0.58	274	< 0.041	82
Walford Creek		WFDD238	140.5	4	< 0.13	< 0.69	68	2030	22.11	< 0.4	738	120.9	21.9	1	< 4	< 0.21	34.8	1082	< 0.02	0.74	353.17	< 1	< 0.06	16.27	0.38	147	< 0.038	103
Walford Creek		WFDD238	140.5	4'	< 0.14	< 0.88	1	1533	19.31	< 0.4	359	135.1	13.4	< 0.50	< 4	< 0.26	20.6	1817	5.58	4.06	111.67	< 1.4	< 0.09	11.46	0.18	33	< 0.042	90
Walford Creek		WFDD238	140.5	5	< 0.14	< 0.89	< 0.2	1643	23.01	< 0.4	864	312.8	28.7	2	< 5	< 0.26	33.8	1250	2.57	0.68	295.41	< 1.4	< 0.09	15.01	0.42	86	< 0.041	43
Walford Creek		WFDD238	140.5	5'	< 0.15	< 0.95	0	2083	26.96	< 0.5	324	108.4	34.0	1	< 5	< 0.28	8.1	1572	24.16	0.85	63.24	< 1.5	3.15	13.36	0.09	35	< 0.043	86
Walford Creek		WFDD238	140.5	6	< 0.12	< 0.86	0	2100	18.68	< 0.4	170	91.4	6.7	< 0.59	< 4	< 0.18	10.9	1113	0.03	0.91	57.76	< 0.8	< 0.07	33.54	0.06	13	< 0.03	68
Walford Creek		WFDD238	140.5	6'	< 0.12	< 0.88	1	2030	29.00	< 0.4	903	60.5	36.2	5	< 4	< 0.18	9.2	1076	27.71	0.81	40.20	< 0.9	< 0.07	12.90	0.03	20	< 0.029	95
Percentage of analyses > LOD					25	0	83	100	100	17	100	100	100	67	0	17	100	100	92	100	100	0	58	100	100	100	0	
Walford Creek		WFDD266	110	9	< 0.47	< 2.1	1.54	2080	0.62	< 1	136	144.8	17.7	17.1	< 16	< 0.4	16.68	1844	0.061	12.96	23.6	< 3	< 0.19	56.9	0.27	22	< 0.066	72
Walford Creek		WFDD266	110	10	< 0.46	< 1.9	12.33	6060	10.94	4.66	99.3	108.0	8.18	21.1	< 16	< 0.53	174.5	1240	0.125	10.94	8.02	< 3	< 0.24	41.2	0.762	266	< 0.076	133
Walford Creek		WFDD266	110	11	< 0.34	< 1.5	11.47	5080	< 0.2	< 0.8	7.5	87.9	7.98	14.2	< 12	< 0.57	146.8	1262	0.58	10.08	7.56	< 2.6	< 0.1	32.7	0.98	142.3	< 0.089	140
Walford Creek		WFDD266	110	12	< 0.36	< 1.9	3.39	3160	7.92	0.93	15.47	39.1	3.32	17.2	< 12	< 0.44	30.9	1385	0.309	10.41	1.78	< 2.3	< 0.14	26.9	0.35	38.4	< 0.092	133
Walford Creek		WFDD266	110	13	< 0.37	< 1.8	9.2	5570	0.37	< 1.1	3.57	125.5	8.52	15.3	< 8	< 0.54	110.2	1366	< 0.066	9.06	3.64	< 3.3	< 0.18	31.7	0.546	70.8	0.071	118
Walford Creek		WFDD266	110	21	< 0.25	< 1.4	2.7	1359	9.19	< 0.7	104.2	99.0	1.33	15.9	< 15	< 0.39	17.8	1715	2.01	10.33	3.73	< 2.9	< 0.1	33.7	0.066	49.3	< 0.063	124
Walford Creek		WFDD266	110	22	< 0.26	< 1.7	1.09	1690	0.4	< 0.9	148.6	121.8	11.46	13.8	< 16	< 0.48	19.4	2167	< 0.079	8.66	16.17	< 3.1	< 0.2	45.1	0.154	27.2	< 0.11	69
Walford Creek		WFDD266	110	23	< 0.28	< 1.1	7	5260	0.29	< 0.6	1.71	197.0	9.7	15.1	< 12	< 0.31	90.1	1151	< 0.036	6.86	2.19	< 2.3	< 0.11	37.8	0.371	31.3	< 0.059	104
Walford Creek		WFDD266	110	24	< 0.22	< 1.8	11.69	5260	17.73	< 0.6	11.66	8.84	< 0.61	14.8	< 15	< 0.35	1.03	1258	0.181	6.31	< 0.13	< 2.6	< 0.09	17.5	0.08	3.08	< 0.064	201
Walford Creek		WFDD266	110	25	< 0.22	< 1.1	17.83	6780	24.89	< 0.7	26.2	11.19	0.81	14.1	< 11	< 0.33	7.54	1295	0.126	6.24	1.2	< 2	< 0.08	18.36	< 0.05	15.2	< 0.06	194
Walford Creek		WFDD266	110	26	< 0.36	< 1.4	18.19	9980	29.9	< 1	27.2	18.02	< 0.84	15.7	< 21	< 0.56	3.01	1402	0.195	5.72	0.617	< 3	< 0.17	22.2	< 0.06	11.4	< 0.11	206
Walford Creek		WFDD266	110	27	< 0.27	< 1.1	15.69	9610	31.6	< 0.8	34.7	6.16	1.69	15.5	< 16	< 0.36	0.73	1143	0.258	23.13	< 0.13	< 2.5	< 0.11	20.3	< 0.06	2.82	< 0.066	202
Walford Creek		WFDD266	110	28	< 0.28	< 1.4	15.11	3659	9.98	< 0.8	45.9	102.1	2.22	17.7	< 14	< 0.36	155.0	1278	0.162	5.28	5.98	< 2.3	< 0.13	22.68	0.134	88.2	< 0.057	142
Walford Creek		WFDD266	110	29	< 0.3	< 1.8	7.2	2181	5.69	< 0.8	50.6	135.1	4.8	17.4	< 21	< 0.56	57.1	1373	3.54	5.29	5.13	< 3.1	< 0.15	28.8	0.119	74	< 0.081	128
Walford Creek		WFDD266	110	30	< 0.22	< 1.3	1.02	1483	9.7	< 0.9	9.04	1.5	< 0.57	18.6	< 14	< 0.42	2.49	1131	0.054	4.62	0.51	< 2.7	< 0.1	10.75	< 0.05	9.59	< 0.076	164
Percentage of analyses > LOD					0	0	100	100	93	13	100	100	80	100	0	0	100	100	80	100	87	0	0	100	73	100	7	
Walford Creek		WFDD266	130.8	1	0.284	< 0.57	11.99	3030	25.7	3.09	898	17.94	1.5	23.9	< 4	0.473	105.2	1989	< 0.019	0.689	583.8	< 0.5	0.49	13.85	2.49	1267	< 0.027	146
Walford Creek		WFDD266	130.8	1'	< 0.11	< 0.56	13	3570	41.1	0.93	1157	21.91	2.37	32.7	< 4	0.626	171.1	1419	< 0.019	0.88	923.00	< 0.5	2.00	13.12	3.11	1686	< 0.027	143
Walford Creek		WFDD266	130.8	2	< 0.11	< 0.58	13.5	4780	59.8	17.2	1300	22.84	2.08	47.4	< 4	0.229	97.1	1502	< 0.019	0.84	478.00	< 0.6	2.3	12.01	2.51	1614	< 0.028	150
Walford Creek		WFDD266	130.8	2'	< 0.11	< 0.58	10.09	3690	73.3	19.6	1021	28.9	2.21	36.9	< 4	0.226	99.5	846	< 0.019	0.771	298.5	< 0.5	14.00	11.84	2.185	3020	< 0.028	138
Walford Creek		WFDD266	130.8	3	< 0.08	< 0.48	18.1	5370	61.9	3.3	551	29.1	2.7	13.2	< 4	< 0.16	55.9	850	< 0.018	0.773	157.00	< 0.6	19.00	12.53	0.988	1680	< 0.028	149
Walford Creek		WFDD266	130.8	3'	0.099	< 0.48	7.5	2770	38.00	< 0.4	802	21.02	2.15	13	< 4	< 0.15	121.1	815	< 0.018	0.786	352.7	< 0.6	4.6	10.33	1.527	2770	< 0.028	133
Walford Creek		WFDD266	130.8	4	0.236	0.73	10.29	6340	72.8	2.31	1580	73.8	4.69	18.8	< 3	< 0.16	52.0	1049	< 0.018	0.747	213.2	< 0.6	< 0.05	15.00	1.377	1026	< 0.023	129
Walford Creek		WFDD266	130.8	4'	0.09	< 0.56	1.87	665	20.42	< 0.4	249	24.18	1.66	5.8	< 3	< 0.15	97.4	374	< 0.017	0.714	198.00	< 0.5	7.6	8.88	1.713	3100	< 0.022	90
Walford Creek		WFDD266	130.8	5	< 0.08	2.93	14.1	5030	57.7	1.76	800	35.6	3.12	11.89	< 3	< 0.18	97.8	1024	< 0.018	0.71	183.00	< 0.8	4.00	11.8	1.101	2890	< 0.028	141
Walford Creek		WFDD266	130.8	5'	0.093	< 0.64	17.43	4890	112.5	59.2	1237	17.92	2.48	101.8	< 3	< 0.18	189.4	1544	< 0.018	0.77	965.00	< 0.8	< 0.08	11.69	3.74	3077	< 0.028	154
Walford Creek		WFDD266	130.8	6	< 0.08	2.45	2.58	1068	15.08	< 0.5	1039.3	15.97	1.27	24.3	< 3	0.263	161.8	3020	< 0.018	0.869	806.00	< 0.8	8.4	8.38	2.069	1687	< 0.028	112
Walford Creek		WFDD266	130.8	6'	0.154	5.57	6.93	2846	33.5	3.75	1360	25.11	2.02	32.1	< 3	0.2	178.6	1466	< 0.018	0.812	829.00	< 0.8	3.6	9.62	2.609	2195	< 0.027	131
Walford Creek		WFDD266	130.8	7	1.29	0.79	9.87	3480	37.3	3.03	976	25.8	2.6	34.4	< 3	< 0.14	226.5	1009	< 0.017	0.86	843.00	< 0.8	0.09	10.46	2.93	4270	< 0.026	135
Walford Creek		WFDD266	130.8	7'	0.091	< 0.53	23.9	7030	110.8	32.3	1091	44.7	3.61	71.7	< 3	< 0.14	78.5	1232	< 0.017	0.777	321.00	< 0.7	1.6	12.4	2.156	1232	< 0.026	149
Percentage of analyses > LOD					0	0	100	100	33	0	100	100	83	67	0	0	100	100	67	100	50	0	0	100	33	100	0	

Deposit	Lens # (HYC)	Drillhole #	Depth (m)	Analyse #	V (ppm)	Cr (ppm)	Mn (ppm)	Fe (ppm)	Co (ppm)	Ni (ppm)	Cu (ppm)	Ga (ppm)	Ge (ppm)	As (ppm)	Se (ppm)	Mo (ppm)	Ag (ppm)	Cd (ppm)	In (ppm)	Sn (ppm)	Sb (ppm)	Te (ppm)	Au (ppm)	Hg (ppm)	Tl (ppm)	Pb (ppm)	Bi (ppm)	Calculated temperature (°C)
Walford Creek		WFDD266	271.4	1	< 0.26	< 1.6	2.83	5510	12.00	< 0.9	1482	101.5	69.6	36.8	< 14	< 0.43	140.0	2260	10.74	30.4	434.00	6.8	< 0.11	21.76	0.548	377	< 0.063	114
Walford Creek		WFDD266	271.4	2	< 0.31	< 1.3	12.51	7320	< 0.19	< 1.1	2706	445.0	232.9	13.8	< 9	< 0.42	399.0	2500	1.15	13.91	868.00	< 3.3	0.77	13.61	10.78	2049	< 0.067	92
Walford Creek		WFDD266	271.4	3	< 0.28	< 1.6	12.1	5340	1.04	< 1.1	983	205.0	205.0	4.92	< 14	< 0.46	232.0	707	3.46	11.86	130.9	< 2.9	22.5	10.00	5.97	2400	< 0.063	102
Walford Creek		WFDD266	271.4	5	< 0.28	< 1.6	5.9	10100	1.11	< 1.1	2060	266.0	65.5	12.5	< 13	< 0.38	78.4	1338	5.25	11.99	378.00	9.00	1.1	17.78	4.28	622	< 0.076	120
Walford Creek		WFDD266	271.4	6	< 0.3	< 1.5	1.82	2530	8.95	< 1.2	482	150.7	24.3	5.9	< 14	< 0.46	31.0	1630	7.7	11.67	78.3	< 2.9	15.1	17.63	1.182	248	< 0.062	100
Walford Creek		WFDD266	271.4	7	< 0.26	< 1.2	7.46	14880	2.59	< 0.8	1783	428.0	110.9	7.27	< 10	< 0.35	71.2	1700	1.1	10.84	209.4	5.7	0.9	11.42	10.29	704	< 0.049	110
Walford Creek		WFDD266	271.4	8	< 0.26	< 1.2	13.99	6350	0.232	< 0.8	2307	411.0	249.0	12.7	< 10	< 0.35	435.0	1902	0.292	8.29	922.00	< 2.6	0.35	8.29	12.26	2214	< 0.048	83
Walford Creek		WFDD266	271.4	9	< 0.31	< 1.5	16.06	6450	< 0.2	< 1.4	3349	254.0	336.0	12.6	< 13	< 0.44	636.0	1780	0.238	8.01	612.00	< 3.9	< 0.1	6.67	9.98	3370	< 0.086	86
Walford Creek		WFDD266	271.4	0	< 0.27	< 1	25.5	6470	< 0.15	< 1	1682	121.0	404.0	6.54	< 11	< 0.35	1267.0	405	0.215	8.33	155.00	< 2.1	< 0.1	5.1	8.56	5120	< 0.064	97
Walford Creek		WFDD266	271.4	4	< 0.24	< 1.6	14.51	21400	0.42	< 1.2	1042	151.0	223.0	6.01	< 10	< 0.48	35.3	277	1.54	10.08	33.7	< 3.3	< 0.12	7.1	14.59	863	< 0.086	130
Percentage of analyses > LOD					0	0	100	100	70	0	100	100	100	100	0	0	100	100	100	100	100	30	60	100	100	100	0	

Supplementary Table 6-3: *Minor and trace elements results obtained by LA-ICP-MS on galena from the HYC, Myrtle and Walford Creek deposits and from the Caranbirini prospect.*

Deposit	Lens # (HYC)	Drillhole #	Depth (m)	Analyse #	V (ppm)	Cr (ppm)	Mn (ppm)	Fe (ppm)	Co (ppm)	Ni (ppm)	Cu (ppm)	Zn (ppm)	Ga (ppm)	Ge (ppm)	As (ppm)	Se (ppm)	Mo (ppm)	Ag (ppm)	Cd (ppm)	In (ppm)	Sn (ppm)	Sb (ppm)	Te (ppm)	Hg (ppm)	Tl (ppm)	Bi (ppm)
HYC	7	MRM-2012-3	164.6	1	-	-	6600	24400	1.1	32	< 2.4	461	1.17	6.5	7	< 330	-	74.9	< 2.3	< 0.1	7.50	240.0	< 9.2	-	< 0.14	0.60
HYC	7	MRM-2012-3	164.6	2	-	-	2870	5700	< 0.28	7	< 5.1	37	0.42	< 2.5	< 2.7	< 450	-	207.4	1.4	< 0.079	2.67	735.0	< 5.4	-	< 0.042	2.54
HYC	7	MRM-2012-3	164.6	2'	-	-	5400	11570	0.3	< 5.1	6	115	0.46	< 2.2	< 2.3	< 440	-	188.9	2.5	< 0.067	6.20	617.0	< 4.6	-	< 0.036	0.25
HYC	7	MRM-2012-3	164.6	3	-	-	1690	2940	0.3	25	12	< 24	0.32	< 1.1	2	< 370	-	193.4	< 1.6	< 0.06	4.12	887.0	< 6.8	-	< 0.064	1.04
HYC	7	MRM-2012-3	164.6	3'	-	-	2530	3670	< 0.17	9	< 11	14580	0.38	3.2	< 2.4	< 610	-	194.2	21.2	< 0.083	3.99	820.0	< 9.4	-	< 0.088	0.27
Percentage of analyses > LOD					0	0	100	100	60.0	80	60	80	100	40	40	0	0	100	60	0	100	100	0	0	0	100
HYC	5		E5	1	-	-	157	1550	< 0.22	< 24	15	710	0.31	< 1.7	3	< 230	-	11.7	5.9	< 0.048	6.02	44.1	< 2.6	-	12.93	3.52
HYC	5		E5	1'	-	-	625	92400	21.1	< 51	21	257	7.50	11.8	250	< 460	-	11.3	2.1	< 0.1	12.60	51.9	< 5.3	-	121.20	12.60
HYC	5		E5	2	-	-	111	3610	0.4	< 25	52	9700	1.39	< 1.9	15	< 240	-	17.5	29.5	< 0.037	4.93	48.2	< 7.9	-	20.30	7.45
HYC	5		E5	2'	-	-	749	2990	< 0.24	< 24	125	6380	0.49	2.6	9	< 190	-	19.6	26.9	< 0.03	5.97	57.1	< 5.5	-	16.60	5.54
HYC	5		E5	3	-	-	25	4920	< 0.36	< 43	357	226000	5.10	21.6	19	< 340	-	20.6	525.0	< 0.062	15.60	65.0	< 5	-	14.91	9.75
HYC	5		E5	3'	-	-	47	8300	1.9	< 89	199	169000	5.10	14.7	69	< 690	-	12.1	328.0	0.12	22.00	69.4	0.00	-	18.60	6.74
HYC	5		E5	4''	-	-	973	9900	0.7	< 57	154	106000	0.64	6.8	17	< 470	-	14.8	206.0	< 0.1	8.40	50.5	< 13	-	22.50	4.51
HYC	5		E5	5	-	-	13100	40300	< 0.51	< 89	91	201900	8.00	27.4	< 4.7	< 640	-	17.4	436.0	< 0.1	14.50	85.1	< 13	-	12.50	9.47
HYC	5		E5	6	-	-	1680	21700	0.5	< 79	9	215	2.20	4.5	15	< 620	-	21.6	2.4	< 0.16	9.80	85.4	< 10	-	32.60	4.02
HYC	5		E5	6'	-	-	620	7800	4.3	< 46	5	14	0.73	< 2.2	26	< 390	-	10.9	4.8	< 0.062	7.40	72.2	< 7.8	-	16.14	5.97
HYC	5		E5	7	-	-	4180	12000	< 0.4	< 49	60	26600	0.96	10.0	4	450	-	17.0	110.0	< 0.059	5.00	60.2	< 5.7	-	11.12	7.00
HYC	5		E5	7'	-	-	3380	50400	16.0	2900	< 2.1	6100	< 0.2	< 3.2	400	< 520	-	< 0.34	17.0	< 0.067	< 1.2	10.0	< 6.5	-	153.00	4.30
HYC	5		E5	8	-	-	129	1990	< 0.27	< 39	73	6310	0.25	3.8	123	< 340	-	56.5	30.7	< 0.041	4.08	240.0	< 7.1	-	109.00	19.40
HYC	5		E5	8'	-	-	850	15800	5.2	< 72	38	11790	2.98	6.1	67	< 670	-	28.4	25.0	< 0.1	8.40	106.8	< 7.9	-	92.30	19.40
HYC	5		E5	9	-	-	157	1450	< 0.23	< 36	54	41	0.68	1.6	49	< 300	-	13.3	4.1	< 0.051	2.55	73.6	< 3.7	-	23.06	8.38
HYC	5		E5	9'	-	-	171	3250	1.3	< 41	140	59700	1.47	6.1	141	< 360	-	43.5	154.0	0.06	5.30	176.0	< 4.2	-	74.60	6.41
HYC	5		E5	9''	-	-	198	1170	< 0.26	< 34	84	34800	1.22	8.0	2	< 370	-	32.5	104.0	< 0.071	2.38	130.2	< 4.4	-	33.30	2.43
HYC	5		E5	10'	-	-	58	1150	0.2	< 17	19	4300	0.76	1.5	21	< 200	-	25.0	17.5	< 0.035	3.42	71.4	< 2.1	-	33.70	9.82
HYC	5		E5	10''	-	-	56	27900	18.6	< 61	205	93000	6.30	12.5	310	< 650	-	66.6	227.0	< 0.071	9.80	366.0	< 5	-	193.00	8.36
HYC	5		E5	11	-	-	520	2210	< 0.23	< 50	9	1040	1.35	< 2.1	5	< 550	-	16.1	9.9	< 0.057	4.00	64.9	< 4.1	-	16.90	6.80
HYC	5		E5	11'	-	-	442	1430	0.4	< 29	4	155	< 0.17	< 1.2	17	< 330	-	32.7	5.6	< 0.033	3.22	106.6	< 2.3	-	37.60	7.23
HYC	5		E5	11''	-	-	12180	43700	< 0.58	< 110	71	7700	< 0.69	< 3.6	75	< 1300	-	56.3	25.9	< 0.17	7.50	219.0	< 12	-	78.90	9.77
HYC	5		E5	12	-	-	123	810	< 0.13	< 24	6	3000	0.99	1.1	19	< 300	-	16.5	10.5	< 0.036	2.57	71.6	< 2.7	-	20.80	12.03
HYC	5		E5	12'	-	-	74	18700	11.5	< 19	39	810	< 0.11	0.6	184	< 230	-	40.6	7.0	< 0.028	2.13	136.4	< 2.1	-	83.40	9.21
HYC	5		E5	13	-	-	93	720	0.4	< 22	28	2900	< 0.13	< 0.87	50	< 320	-	22.4	12.1	< 0.04	2.47	84.0	< 1.8	-	23.60	13.40
Percentage of analyses > LOD					0	0	100	100	56.0	4	96	100	80	68	96	4	0	96	100	8	96	100	0	0	100	100
HYC	4	MRM-2012-3	176.2	1'	-	-	383	1700	< 0.17	< 8.7	< 370	< 1400	< 0.18	< 1.1	< 1.3	200	-	277.0	7.0	< 0.071	5.36	373.0	< 5.6	-	28.40	< 0.19
HYC	4	MRM-2012-3	176.2	1''	-	-	2170	4450	< 0.51	< 35	60	20	< 0.48	16.0	< 3.7	2700	-	322.0	< 4.6	< 0.11	22.00	532.0	< 11	-	19.40	0.00
HYC	4	MRM-2012-3	176.2	2	-	-	7040	37000	< 0.52	< 40	4	< 5.7	< 0.5	< 2.7	5	160	-	351.0	< 4.8	< 0.12	8.60	576.0	< 11	-	29.40	0.07
HYC	4	MRM-2012-3	176.2	2'	-	-	10240	51800	1.4	< 64	7	23	< 0.75	5.3	172	120	-	265.0	< 7.2	< 0.18	12.70	405.0	< 17	-	18.20	0.00
HYC	4	MRM-2012-3	176.2	2''	-	-	750	2800	0.6	< 23	8	12	0.59	2.1	< 2	90	-	276.0	5.1	< 0.062	4.35	389.0	< 5.8	-	21.90	0.01
HYC	4	MRM-2012-3	176.2	3	-	-	7390	28100	< 0.61	116	< 2.5	690	2.58	< 3.2	< 4.5	90	-	45.2	15.7	< 0.14	5.30	123.5	< 13	-	15.40	0.21
HYC	4	MRM-2012-3	176.2	3'	-	-	463	2500	< 0.27	29	12	< 2.9	< 0.25	1.0	< 2	0	-	419.0	8.0	< 0.059	< 0.56	757.0	< 5.6	-	33.10	0.00
HYC	4	MRM-2012-3	176.2	3''	-	-	14420	71500	< 0.83	< 82	6	< 8.9	< 0.78	< 4.3	< 6	0	-	422.0	< 7.4	< 0.18	9.80	810.0	< 17	-	22.70	0.00
HYC	4	MRM-2012-3	176.2	4	-	-	651	5510	0.9	< 70	11	47	6.90	4.1	18	370	-	279.0	< 6	< 0.15	6.30	553.0	< 14	-	32.10	0.00
HYC	4	MRM-2012-3	176.2	4'	-	-	1700	2600	< 0.42	< 45	< 1.7	< 4.5	0.55	< 2.2	< 3.1	0	-	267.0	6.7	< 0.092	4.45	395.0	< 8.7	-	12.42	0.00
HYC	4	MRM-2012-3	176.2	4''	-	-	5200	23600	< 0.46	1000	30	< 4.9	< 0.43	< 2.3	< 3.3	0	-	474.0	7.4	< 0.099	17.00	802.0	< 9.4	-	26.90	0.00
HYC	4	MRM-2012-3	176.2	5	-	-	1269	5010	< 0.33	64	5	12600	< 0.31	< 1.7	< 2.4	120	-	382.0	50.1	< 0.071	4.27	533.0	< 6.7	-	14.09	0.00
HYC	4	MRM-2012-3	176.2	5'	-	-	560	3300	0.6	< 20	11	9	0.60	1.6	2	130	-	246.0	6.2	0.06	27.00	397.0	< 3.5	-	27.60	0.16
HYC	4	MRM-2012-3	176.2	6	-	-	384	1450	< 0.21	49	2	17	0.36	< 1.6	< 1.5	< 3800	-	293.0	6.2	< 0.056	2.62	486.0	< 5.1	-	20.83	< 0.046
HYC	4	MRM-2012-3	176.2	6''	-	-	375	3100	< 0.15	80	< 0.74	3600	< 0.15	< 1.1	< 1.1	50000	-	377.0	8.1	< 0.041	29.00	595.0	< 3.7	-	25.20	< 0.033
HYC	4	MRM-2012-3	176.2	7	-	-	1212	6330	< 0.24	37	89	109000	5.41	18.0	3	< 1600	-	323.0	537.0	< 0.062	4.93	588.0	< 5.7	-	22.50	< 0.051
HYC	4	MRM-2012-3	176.2	7'	-	-	643	1001	< 0.14	200	< 0.67	740	0.55	1.1	< 0.99	1600	-	275.0	7.6	< 0.036	< 0.52	403.0	< 3.3	-	11.16	< 0.03

Deposit	Lens # (HYC)	Drillhole #	Depth (m)	Analyse #	V (ppm)	Cr (ppm)	Mn (ppm)	Fe (ppm)	Co (ppm)	Ni (ppm)	Cu (ppm)	Zn (ppm)	Ga (ppm)	Ge (ppm)	As (ppm)	Se (ppm)	Mo (ppm)	Ag (ppm)	Cd (ppm)	In (ppm)	Sn (ppm)	Sb (ppm)	Te (ppm)	Hg (ppm)	Tl (ppm)	Bi (ppm)
HYC	4	MRM-2012-3	176.2	7''	-	-	1054	13600	37.0	< 44	6	62	3.60	6.9	7600	< 1600	-	358.0	5.9	< 0.082	5.80	686.0	< 7.5	-	28.00	< 0.067
HYC	4	MRM-2012-3	176.2	8	-	-	2520	10400	< 0.11	< 19	11	< 5.6	0.34	< 1.1	< 1.2	< 340	-	410.0	7.2	< 0.051	2.77	697.0	< 4.2	-	24.50	< 0.025
HYC	4	MRM-2012-3	176.2	8'	-	-	330	2200	< 0.1	440	11	< 5.1	< 0.13	< 0.98	< 1.1	5300	-	415.0	5.2	< 0.046	27.00	698.0	< 3.8	-	17.70	< 0.023
HYC	4	MRM-2012-3	176.2	8''	-	-	189	200	< 0.089	< 15	19	< 4.5	0.49	< 0.87	< 0.97	< 250	-	454.0	6.0	0.04	< 0.33	1143.0	< 3.4	-	61.90	0.03
HYC	4	MRM-2012-3	176.2	9	-	-	4210	19100	< 0.36	< 43	528	115900	3.62	13.0	136	< 710	-	47.6	397.0	< 0.074	6.40	133.7	< 11	-	14.12	0.61
HYC	4	MRM-2012-3	176.2	9'	-	-	2950	23500	0.7	< 60	2040	558000	12.00	54.6	355	< 940	-	74.0	2180.0	< 0.1	9.90	174.0	< 16	-	26.20	0.37
HYC	4	MRM-2012-3	176.2	10	-	-	1070	5880	< 0.31	< 37	276	63100	0.84	5.7	29	< 530	-	41.2	245.0	< 0.064	4.80	113.8	< 9.9	-	11.91	0.11
HYC	4	MRM-2012-3	176.2	10'	-	-	1110	6100	1.5	< 18	100	3480	0.33	1.6	13	< 240	-	31.9	22.2	< 0.031	2.88	90.4	< 4.8	-	12.00	0.06
HYC	4	MRM-2012-3	176.2	11	-	-	6830	41200	3.7	< 61	40	6250	1.07	3.8	113	< 750	-	34.2	33.0	< 0.051	3.00	106.8	< 9.1	-	14.40	0.30
Percentage of analyses > LOD					0	0	100	100	30.8	35	81	65	62	54	42	46	0	100	81	8	88	100	0	0	100	42
HYC	3	MRM-2012-3	191	1'	-	-	4010	22200	< 0.99	< 100	12	266	1.66	4.8	< 5	< 180	-	29.9	5.4	< 0.1	4.05	116.8	< 7	-	40.00	0.11
HYC	3	MRM-2012-3	191	4	-	-	4360	16200	< 0.42	< 41	< 1.6	28	0.71	2.6	7	< 77	-	49.1	6.5	< 0.06	4.34	153.2	< 4.1	-	48.60	0.05
HYC	3	MRM-2012-3	191	4'	-	-	2040	8700	< 0.49	< 48	< 1.9	13	0.77	< 1.7	< 2.5	< 93	-	19.2	5.2	< 0.07	4.48	75.1	< 4.8	-	16.88	< 0.046
HYC	3	MRM-2012-3	191	5	-	-	2150	8300	< 0.47	< 59	< 2.6	57	1.31	< 2.6	< 2.5	< 140	-	17.9	6.2	< 0.077	5.06	63.0	< 5.5	-	12.34	0.23
HYC	3	MRM-2012-3	191	5'	-	-	1100	6880	2.4	< 57	453	157000	3.63	29.1	143	< 140	-	27.3	430.0	< 0.075	7.10	82.3	< 5.4	-	16.55	0.52
HYC	3	MRM-2012-3	191	6	-	-	6480	13200	0.7	< 99	8	8310	2.93	8.3	< 2.9	< 290	-	30.3	38.4	< 0.14	6.70	135.3	0.00	-	41.90	< 0.12
Percentage of analyses > LOD					0	0	100	100	33.3	0	50	100	100	67	33	0	0	100	100	0	100	100	0	0	100	67
HYC	3	MRM-2012-3	195.9	1	-	-	585	1780	< 0.12	34	1	3	0.23	< 0.92	4	< 48	-	26.4	10.1	< 0.026	3.30	72.3	< 2.1	-	12.48	< 0.02
HYC	3	MRM-2012-3	195.9	1'	-	-	592	2030	< 0.15	< 21	< 0.89	3	1.71	< 1.1	< 1.1	< 58	-	26.9	6.6	< 0.03	3.31	47.1	< 2.5	-	8.48	< 0.023
HYC	3	MRM-2012-3	195.9	2	-	-	353	894	< 0.23	< 23	< 1.2	< 2.3	0.27	< 1.1	< 1.8	< 67	-	26.3	7.7	< 0.048	2.61	47.6	< 2.8	-	9.86	< 0.051
HYC	3	MRM-2012-3	195.9	2'	-	-	4410	11600	0.8	< 58	< 3	< 6.1	1.16	< 2.9	< 4.7	< 170	-	21.7	8.8	< 0.12	4.51	58.6	< 7.3	-	12.03	< 0.13
HYC	3	MRM-2012-3	195.9	2''	-	-	2742	7140	< 0.33	< 32	< 1.6	2600	< 0.21	< 1.6	< 2.6	112	-	21.2	16.7	< 0.067	3.44	42.6	< 4	-	7.54	< 0.072
HYC	3	MRM-2012-3	195.9	3	-	-	710	770	< 0.28	142	< 1.7	9	< 0.34	< 2.2	< 2	< 120	-	39.2	7.2	< 0.057	4.30	68.7	< 6.1	-	12.70	< 0.072
HYC	3	MRM-2012-3	195.9	3'	-	-	1860	3780	< 0.16	56	1	21	0.24	< 1.3	< 1.2	< 72	-	18.2	7.9	< 0.033	3.11	42.0	< 3.6	-	7.52	0.06
HYC	3	MRM-2012-3	195.9	4	-	-	599	2070	< 0.22	27	2	5	0.54	< 1.2	< 2.6	< 63	-	16.1	6.1	< 0.051	3.22	37.9	< 4.7	-	6.55	< 0.066
HYC	3	MRM-2012-3	195.9	4'	-	-	481	1730	< 0.23	41	< 1.6	< 2.6	< 0.21	< 1.3	< 2.8	< 68	-	21.7	8.4	< 0.054	3.68	56.2	< 5	-	8.76	< 0.07
HYC	3	MRM-2012-3	195.9	4''	-	-	593	2170	0.8	106	3	< 5.1	0.54	< 2	18	< 130	-	16.3	8.9	< 0.074	3.33	52.3	< 6.1	-	7.58	< 0.043
HYC	3	MRM-2012-3	195.9	5	-	-	371	660	< 0.11	< 12	1	< 2.1	< 0.11	< 0.8	< 0.93	136	-	18.2	6.3	< 0.03	2.05	37.2	< 2.5	-	5.28	0.18
HYC	3	MRM-2012-3	195.9	5'	-	-	147	721	0.3	< 14	< 0.79	< 2.5	0.35	< 0.91	< 1.1	155	-	22.3	9.9	< 0.034	2.28	45.3	< 2.8	-	8.00	< 0.02
HYC	3	MRM-2012-3	195.9	5''	-	-	1219	11200	< 0.34	63	< 2.1	< 6.5	1.74	2.7	5	243	-	16.4	7.3	< 0.09	3.36	66.5	< 7.4	-	7.50	< 0.052
HYC	3	MRM-2012-3	195.9	6	-	-	< 2.6	4300	4.6	75	227	25900	0.27	2.5	2328	< 100	-	141.7	71.2	< 0.068	4.45	121.1	< 2.4	-	17.05	0.55
HYC	3	MRM-2012-3	195.9	6'	-	-	4	26200	23.9	67	273	31100	0.37	4.2	1444	< 90	-	148.7	105.0	< 0.06	4.25	135.7	< 2.1	-	37.40	0.34
HYC	3	MRM-2012-3	195.9	6''	-	-	483	3000	2.5	52	7	148	< 0.11	< 0.76	9	< 54	-	34.5	8.0	< 0.036	2.82	77.9	< 1.2	-	20.80	0.04
HYC	3	MRM-2012-3	195.9	7	-	-	301	594	< 0.18	< 18	1	< 2.3	< 0.16	< 0.9	< 1.1	< 60	-	18.2	6.7	< 0.049	2.17	45.3	< 3.5	-	7.22	0.31
HYC	3	MRM-2012-3	195.9	7'	-	-	487	653	< 0.2	< 20	< 1.1	< 2.5	< 0.17	< 0.97	< 1.2	< 64	-	23.1	7.3	< 0.053	2.97	46.1	< 3.8	-	7.98	< 0.032
HYC	3	MRM-2012-3	195.9	8	-	-	881	2520	< 0.25	27	2	4	0.52	< 1.1	< 1.3	< 62	-	17.8	4.3	< 0.036	3.45	43.5	< 3.8	-	7.32	< 0.016
HYC	3	MRM-2012-3	195.9	8'	-	-	831	1870	< 0.23	< 18	< 1.1	< 2.8	< 0.13	< 1	< 1.2	< 56	-	19.3	8.1	< 0.033	2.73	42.9	< 3.4	-	7.65	0.08
HYC	3	MRM-2012-3	195.9	8''	-	-	1008	3300	< 0.37	< 29	< 1.8	7	0.83	< 1.6	< 1.9	< 89	-	17.4	6.7	< 0.053	3.65	48.8	< 5.6	-	7.86	< 0.024
HYC	3	MRM-2012-3	195.9	9	-	-	301	1150	0.3	30	2	< 2.6	0.26	< 0.9	4	< 50	-	17.9	7.2	< 0.03	2.19	51.9	< 3.1	-	6.99	< 0.013
HYC	3	MRM-2012-3	195.9	9'	-	-	766	2960	< 0.23	< 19	1	< 2.9	1.14	< 1	< 1.2	< 56	-	19.8	8.0	< 0.034	2.71	53.6	< 3.5	-	8.80	< 0.015
HYC	3	MRM-2012-3	195.9	9''	-	-	1380	2490	< 0.25	< 20	< 1.3	< 3.1	< 0.14	< 1.1	< 1.3	< 60	-	19.0	8.0	< 0.036	2.48	47.3	< 3.8	-	7.02	< 0.016
HYC	3	MRM-2012-3	195.9	10	-	-	788	5200	0.9	< 30	2	< 4.7	< 0.21	< 1.6	20	< 87	-	18.0	6.4	< 0.053	3.90	49.5	< 5.6	-	9.42	< 0.024
HYC	3	MRM-2012-3	195.9	10'	-	-	1009	5560	0.5	< 42	4	470	0.49	< 1.7	22	< 110	-	16.9	11.6	< 0.069	3.66	48.6	< 6.7	-	9.99	< 0.073
HYC	3	MRM-2012-3	195.9	10''	-	-	3480	8600	0.5	< 30	< 1.4	6	0.52	< 1.2	< 1.1	< 77	-	18.5	7.7	< 0.048	3.66	58.0	< 4.7	-	8.40	< 0.051
HYC	3	MRM-2012-3	195.9	11	-	-	1290	29900	6.2	< 51	38	764	< 0.28	3.1	242	< 120	-	22.0	12.9	< 0.08	2.60	54.4	< 7.7	-	59.20	0.10
HYC	3	MRM-2012-3	195.9	11'	-	-	2720	20700	5.8	< 41	18	655	< 0.22	< 1.5	182	< 97	-	24.1	8.8	< 0.062	2.95	46.4	< 6	-	26.20	< 0.066
HYC	3	MRM-2012-3	195.9	12	-	-	472	9300	3.3	< 41	7	< 6.3	< 0.27	< 1.9	126	< 100	-	20.4	7.4	< 0.038	3.43	44.8	< 4.5	-	23.30	0.12
HYC	3	MRM-2012-3	195.9	12'	-	-	3260	13000	3.9	< 59	6	33	< 0.38	< 2.7	109	< 140	-	15.9	5.4	< 0.055	4.19	61.0	< 6.4	-	14.01	< 0.071
HYC	3	MRM-2012-3	195.9	12''	-	-	812	30500	15.9	< 27	11	17	< 0.17	1.6	169	< 63	-	23.4	9.4	< 0.024	2.05	47.4	< 2.9	-	34.50	< 0.032
Percentage of analyses > LOD					0	0	97	100	46.9	38	59	53	53	16	44	13	0	100	100	0	100	100	0	0	100	28

Deposit	Lens # (HYC)	Drillhole #	Depth (m)	Analyse #	V (ppm)	Cr (ppm)	Mn (ppm)	Fe (ppm)	Co (ppm)	Ni (ppm)	Cu (ppm)	Zn (ppm)	Ga (ppm)	Ge (ppm)	As (ppm)	Se (ppm)	Mo (ppm)	Ag (ppm)	Cd (ppm)	In (ppm)	Sn (ppm)	Sb (ppm)	Te (ppm)	Hg (ppm)	Tl (ppm)	Bi (ppm)
HYC	3	MRM-2012-3	195.9B	1	-	-	3190	20400	0.8	< 56	< 6.1	< 2300	0.90	5.7	9	< 170	-	27.6	< 8.9	< 0.062	5.77	55.3	< 5.7	-	8.26	0.53
HYC	3	MRM-2012-3	195.9B	1'	-	-	7280	29800	< 0.52	< 59	< 6.4	< 2500	1.78	4.5	10	< 180	-	74.0	< 9.3	0.07	6.30	134.3	< 6	-	16.44	0.69
HYC	3	MRM-2012-3	195.9B	2	-	-	13770	59000	0.8	< 91	< 3.6	< 7	1.31	6.3	24	< 250	-	26.2	5.5	< 0.16	9.50	78.4	< 13	-	9.09	0.91
HYC	3	MRM-2012-3	195.9B	2'	-	-	10190	30100	< 0.69	< 89	< 3.5	< 6.9	1.69	4.7	12	< 250	-	29.0	< 3.5	< 0.16	7.90	80.7	< 13	-	10.77	0.68
HYC	3	MRM-2012-3	195.9B	3	-	-	4580	27000	2.3	< 130	7	< 9.8	2.74	7.3	98	< 500	-	23.8	1.0	< 0.17	6.00	57.2	< 21	-	11.66	0.71
HYC	3	MRM-2012-3	195.9B	3'	-	-	27120	83700	< 0.92	< 170	< 5.8	< 13	< 1.3	8.9	< 6.3	< 670	-	22.7	2.0	< 0.22	10.60	71.1	< 27	-	7.92	0.59
Percentage of analyses > LOD					0	0	100	100	50.0	0	17	0	83	100	83	0	0	100	50	17	100	100	0	0	100	100
HYC	2		E11-1	1	-	-	1245	12150	1.3	< 140	13	< 13	< 0.21	< 1.5	38	< 57	-	33.7	6.0	< 0.056	2.35	43.9	< 4.7	-	1.83	0.14
HYC	2		E11-1	1'	-	-	441	19200	8.3	< 150	75	< 14	< 0.23	< 1.6	451	69	-	45.6	8.9	< 0.06	1.52	46.0	< 5	-	14.40	1.00
HYC	2		E11-1	1''	-	-	708	13000	4.0	< 130	38	< 12	< 0.19	< 1.4	147	< 53	-	36.1	6.8	< 0.052	2.29	43.0	< 4.3	-	3.54	0.25
HYC	2		E11-1	2	-	-	598	5190	0.4	< 130	9	< 13	< 0.21	< 1.5	48	< 56	-	36.0	9.0	< 0.055	2.60	42.1	< 4.6	-	2.35	0.10
HYC	2		E11-1	2'	-	-	661	45000	15.7	< 120	139	< 12	< 0.2	2.3	787	< 53	-	36.0	6.5	< 0.052	2.64	54.0	< 4.3	-	20.90	0.03
HYC	2		E11-1	2''	-	-	542	42400	5.8	< 200	115	11	0.45	3.2	518	< 120	-	43.1	5.8	0.00	2.26	54.8	0.00	-	31.50	< 0.075
HYC	2		E11-1	3	-	-	723	40100	9.3	< 190	92	721	0.20	2.4	881	< 120	-	59.9	6.9	0.00	3.01	46.8	0.00	-	18.50	< 0.076
HYC	2		E11-1	3'	-	-	6100	24900	0.1	< 250	31	8	0.81	< 3.2	< 3.7	< 170	-	61.0	5.8	0.00	4.29	37.4	0.00	-	1.82	< 0.1
HYC	2		E11-1	3''	-	-	3521	15030	0.7	< 180	19	8	0.00	< 2.4	17	< 120	-	39.6	3.7	0.00	2.38	40.9	0.00	-	2.20	< 0.077
HYC	2		E11-1	4	-	-	1104	5390	0.0	< 150	7	5	0.00	< 2.2	< 2.6	< 120	-	33.3	5.6	0.00	2.24	40.6	0.00	-	1.93	0.13
HYC	2		E11-1	4'	-	-	1990	14300	0.8	< 130	15	< 4	0.00	< 2.1	62	< 110	-	34.6	8.9	0.00	1.89	38.2	0.00	-	2.79	< 0.069
HYC	2		E11-1	4''	-	-	958	4620	< 0.34	< 130	8	< 3.7	< 0.28	< 2.2	2	< 76	-	34.3	4.0	< 0.097	2.17	41.7	0.00	-	1.60	0.09
HYC	2		E11-1	5'	-	-	181	118200	41.0	< 160	477	292	0.56	4.1	3370	< 110	-	59.8	6.4	< 0.14	4.02	69.5	0.00	-	103.20	0.16
HYC	2		E11-1	5''	-	-	474	14500	4.5	< 120	65	8	< 0.32	< 2.6	200	< 89	-	32.9	4.5	< 0.11	2.72	46.2	0.00	-	5.71	0.06
HYC	2		E11-1	6	-	-	141	14250	4.7	< 67	44	4	< 0.086	2.0	377	< 72	-	33.1	8.0	< 0.067	3.81	48.8	< 5.4	-	10.68	< 0.056
HYC	2		E11-1	6'	-	-	179	3030	< 0.33	< 62	13	4	< 0.25	< 1.5	7	< 82	-	45.8	6.3	< 0.05	2.26	39.1	< 4.2	-	1.76	< 0.054
HYC	2		E11-1	6''	-	-	1146	16800	3.1	< 75	81	< 3.6	< 0.32	2.1	295	< 110	-	55.5	6.6	< 0.064	3.18	45.5	< 5.4	-	16.80	< 0.069
HYC	2		E11-1	7	-	-	755	7570	2.5	< 52	37	9	< 0.29	< 1.4	287	< 59	-	49.1	7.4	< 0.03	5.34	43.3	< 5.1	-	3.98	< 0.032
HYC	2		E11-1	7'	-	-	180	6500	0.8	< 49	14	< 2.4	< 0.29	< 1.4	75	< 58	-	42.0	5.9	< 0.03	4.61	48.9	< 5.1	-	3.58	< 0.032
HYC	2		E11-1	7''	-	-	237	54100	16.9	< 54	161	36	< 0.23	3.5	1168	< 70	-	53.0	5.9	< 0.031	3.81	46.0	< 3.2	-	26.90	0.07
HYC	2		E11-1	8''	-	-	1369	7050	1.3	< 39	25	< 2.7	< 0.23	1.7	63	< 73	-	38.3	3.3	< 0.067	2.69	45.6	< 2.4	-	4.42	0.10
HYC	2		E11-1	9	-	-	401	33500	9.0	< 35	92	< 2.6	0.25	2.2	656	< 70	-	47.2	6.0	< 0.062	3.55	49.8	< 2.3	-	11.00	0.12
HYC	2		E11-1	9'	-	-	90	6400	1.4	< 28	33	< 2.2	< 0.18	1.9	90	< 60	-	39.2	4.5	< 0.053	3.69	46.6	< 1.9	-	6.20	0.07
HYC	2		E11-1	9''	-	-	528	5350	< 0.22	< 40	4	5	0.16	1.9	19	< 76	-	33.0	7.8	< 0.045	3.10	46.9	< 3.6	-	1.72	0.07
HYC	2		E11-1	10'	-	-	408	34200	9.3	< 36	123	20800	0.71	5.1	934	< 76	-	49.5	83.0	< 0.044	3.72	52.0	< 3.5	-	18.40	< 0.03
HYC	2		E11-1	10''	-	-	751	4500	1.9	< 45	16	< 41	< 0.22	< 1.9	56	< 85	-	40.4	3.9	< 0.041	3.10	42.5	< 2.4	-	2.09	0.10
HYC	2		E11-1	11	-	-	1564	11700	1.8	< 24	44	3	0.30	< 2.7	121	< 150	-	56.0	9.8	< 0.039	2.85	48.7	< 1.5	-	7.15	< 0.035
HYC	2		E11-1	11'	-	-	486	16500	5.1	< 29	96	2	0.40	< 2.8	284	< 160	-	64.9	16.9	< 0.036	1.59	61.1	< 2.3	-	24.50	0.25
HYC	2		E11-1	12	-	-	1878	51300	15.1	< 49	212	79800	2.17	12.9	1031	< 420	-	74.1	562.0	< 0.076	2.20	54.0	< 4.2	-	25.80	0.09
HYC	2		E11-1	12'	-	-	86	152000	92.5	< 56	1030	124000	2.90	25.0	6840	< 570	-	127.0	740.0	< 0.085	3.26	124.7	< 4.7	-	145.40	0.35
HYC	2		E11-1	13	-	-	344	129000	46.1	< 42	529	9	0.63	4.8	3840	< 410	-	87.7	9.7	< 0.041	1.14	80.4	< 3.6	-	88.40	0.26
HYC	2		E11-1	14'	-	-	475	61100	18.7	< 45	103	12	1.14	5.3	1350	< 690	-	50.5	12.9	< 0.027	1.95	43.7	< 3.6	-	23.40	0.10
HYC	2		E11-1	15	-	-	41	94300	96.5	62	522	16	1.31	5.9	7660	< 1200	-	69.8	8.4	< 0.026	1.27	95.0	< 3.5	-	99.70	0.34
HYC	2		E11-1	15'	-	-	23	60400	38.1	< 38	404	< 2.6	0.26	8.5	5560	< 2400	-	54.5	8.2	< 0.025	1.16	79.2	< 4	-	103.80	0.35
HYC	2		E11-1	16	-	-	41	47100	29.1	< 30	239	830	0.25	< 2.8	3600	10	-	47.6	21.2	< 0.019	0.68	55.0	< 3	-	59.10	0.28
HYC	2		E11-1	16'	-	-	698	35000	18.4	< 38	64	4	0.16	< 3.1	1381	30	-	30.2	3.4	< 0.022	1.19	33.9	< 1.9	-	19.60	< 0.041
HYC	2		E11-1	17	-	-	395	11100	4.6	< 32	37	< 1.4	0.16	< 2.6	441	220	-	26.6	8.4	< 0.018	0.89	39.8	< 1.5	-	5.54	< 0.034
HYC	2		E11-1	18	-	-	1734	47400	27.3	< 59	350	78000	0.87	6.0	2190	0	-	30.6	367.0	< 0.054	0.86	47.5	< 2.1	-	31.70	0.04
HYC	2		E11-1	18'	-	-	17	39100	23.0	< 27	187	13	0.53	2.5	2110	0	-	52.5	9.8	< 0.028	0.85	52.5	< 1.6	-	38.30	0.26
Percentage of analyses > LOD					0	0	100	100	89.7	3	100	62	51	51	95	10	0	100	100	0	100	100	0	0	100	64

Deposit	Lens # (HYC)	Drillhole #	Depth (m)	Analyse #	V (ppm)	Cr (ppm)	Mn (ppm)	Fe (ppm)	Co (ppm)	Ni (ppm)	Cu (ppm)	Zn (ppm)	Ga (ppm)	Ge (ppm)	As (ppm)	Se (ppm)	Mo (ppm)	Ag (ppm)	Cd (ppm)	In (ppm)	Sn (ppm)	Sb (ppm)	Te (ppm)	Hg (ppm)	Tl (ppm)	Bi (ppm)
HYC	0	MRM-2012-3	209.7	1'	-	-	4610	15300	< 0.3	< 40	4	80	0.80	< 1.6	< 1.4	< 310	-	22.1	3.7	< 0.042	4.31	88.3	< 3.7	-	9.19	0.52
HYC	0	MRM-2012-3	209.7	2	-	-	1720	6810	1.6	< 37	3	< 2.7	1.35	< 1.4	65	< 220	-	19.0	8.0	< 0.032	2.42	92.0	< 4.7	-	10.18	0.49
HYC	0	MRM-2012-3	209.7	2'	-	-	1280	6260	0.8	< 45	2	< 3.2	0.79	1.8	11	< 250	-	32.0	4.1	< 0.038	3.92	100.1	< 5.6	-	11.52	1.11
HYC	0	MRM-2012-3	209.7	2''	-	-	1070	6060	< 0.14	< 27	< 0.93	< 1.9	0.99	1.0	< 0.78	< 140	-	47.1	7.3	< 0.023	3.89	170.0	< 3.4	-	49.20	0.40
HYC	0	MRM-2012-3	209.7	3	-	-	216	1550	< 0.17	< 33	1	8	0.59	< 1.2	6	< 160	-	23.2	5.1	< 0.028	3.87	79.3	< 4.1	-	12.41	0.57
HYC	0	MRM-2012-3	209.7	3'	-	-	1780	7100	< 0.15	32	60	930	0.44	< 1.1	2	< 130	-	37.2	10.7	< 0.025	4.20	126.1	< 3.6	-	31.10	0.76
HYC	0	MRM-2012-3	209.7	3''	-	-	276	874	< 0.13	< 25	62	< 1.8	1.12	< 0.95	10	< 110	-	30.1	7.6	< 0.022	3.60	78.4	< 3.2	-	14.39	0.85
HYC	0	MRM-2012-3	209.7	4	-	-	372	1450	< 0.2	< 37	23	5800	0.69	2.1	< 1.1	< 150	-	17.6	33.1	< 0.033	5.27	77.1	< 4.8	-	10.13	0.06
HYC	0	MRM-2012-3	209.7	4'	-	-	373	3770	0.4	< 30	2	11	1.43	1.4	10	< 120	-	24.3	4.1	< 0.026	4.21	91.8	< 3.8	-	10.19	0.73
HYC	0	MRM-2012-3	209.7	4''	-	-	431	5060	< 0.23	< 42	2	16	1.19	2.3	< 1.3	< 160	-	19.7	3.5	< 0.038	3.51	78.5	< 5.5	-	9.82	0.30
HYC	0	MRM-2012-3	209.7	5	-	-	820	2430	0.0	< 66	48	7600	< 0.4	< 2.9	< 4.3	< 270	-	46.5	32.0	< 0.071	2.78	136.5	0.00	-	50.30	0.12
HYC	0	MRM-2012-3	209.7	5'	-	-	3090	10300	0.0	< 67	13	8800	< 0.4	< 2.9	< 4.4	< 260	-	30.8	43.4	< 0.072	4.94	100.2	0.00	-	15.10	0.11
HYC	0	MRM-2012-3	209.7	5''	-	-	154	2120	0.7	< 43	2	13	0.71	< 1.9	10	< 160	-	48.3	8.4	< 0.046	3.08	175.2	0.00	-	25.90	0.00
HYC	0	MRM-2012-3	209.7	6	-	-	436	12900	3.6	< 81	1137	198000	2.44	11.0	232	< 280	-	198.0	658.0	< 0.089	7.20	342.0	0.00	-	72.10	0.31
HYC	0	MRM-2012-3	209.7	6'	-	-	2470	7680	3.1	< 52	5	219	< 0.32	< 2.3	124	< 170	-	40.4	7.7	< 0.057	3.74	94.9	0.00	-	17.21	0.08
HYC	0	MRM-2012-3	209.7	7	-	-	1450	29400	3.2	< 80	20400	128000	1.72	8.3	50	< 240	-	50.5	398.0	< 0.09	4.10	126.6	0.00	-	41.10	0.34
HYC	0	MRM-2012-3	209.7	7'	-	-	568	6010	0.0	< 55	4830	7310	< 0.35	< 2.5	< 3.8	< 160	-	47.8	33.2	< 0.062	3.40	86.7	0.21	-	34.10	0.24
HYC	0	MRM-2012-3	209.7	7''	-	-	4980	16490	1.0	< 49	33	4410	< 0.31	< 2.2	9	< 140	-	30.6	14.8	< 0.055	3.19	85.3	0.00	-	12.85	0.61
Percentage of analyses > LOD					0	0	100	100	44.4	6	94	78	72	39	61	0	0	100	100	0	100	100	6	0	100	100
Myrtle		MY16	177.5	1	-	-	< 2.3	< 26	< 0.24	< 15	14	11	< 0.19	< 1.4	< 1.2	< 100	-	57.5	1.9	< 0.032	6.38	503.0	< 3.2	-	13.48	85.50
Myrtle		MY16	177.5	1'	-	-	< 2.2	< 25	< 0.23	< 14	< 1.3	< 5	< 0.18	< 1.3	< 1.2	185	-	32.1	< 0.86	< 0.031	4.54	143.6	< 3.1	-	13.46	27.20
Myrtle		MY16	177.5	1''	-	-	< 2.6	< 29	< 0.27	< 16	3	< 5.9	< 0.21	< 1.5	< 1.4	205	-	59.2	4.1	< 0.036	5.66	432.0	< 3.7	-	18.48	54.90
Myrtle		MY16	177.5	2	-	-	< 2	< 22	< 0.2	< 12	18	< 4.4	< 0.16	< 1.2	< 1	< 94	-	90.3	3.0	< 0.027	4.12	1585.0	< 2.7	-	4.67	40.10
Myrtle		MY16	177.5	2'	-	-	< 2.2	< 24	< 0.22	< 13	< 1.3	< 4.8	< 0.17	< 1.3	< 1.1	143	-	41.9	< 0.83	< 0.03	4.07	187.6	< 3	-	20.67	28.30
Myrtle		MY16	177.5	2''	-	-	< 2.2	< 24	< 0.22	31	24	7	< 0.17	< 1.3	< 1.1	< 110	-	89.6	3.7	< 0.03	4.23	1534.0	< 3	-	4.08	5.49
Myrtle		MY16	177.5	3	-	-	< 1.7	< 19	< 0.17	< 9.4	9	9	< 0.14	< 0.98	< 0.86	122	-	28.2	4.5	< 0.023	4.04	96.9	< 2.3	-	12.83	18.99
Myrtle		MY16	177.5	3'	-	-	< 3.5	< 39	< 0.17	< 18	3	13	< 0.35	< 1.8	< 1.4	< 150	-	46.0	1.5	< 0.061	4.88	153.4	< 6.7	-	16.10	29.80
Myrtle		MY16	177.5	3''	-	-	< 4.2	< 47	< 0.21	< 21	20	< 5.3	< 0.41	< 2.2	< 1.7	< 180	-	100.8	2.6	< 0.073	3.96	1484.0	< 8	-	11.09	54.40
Myrtle		MY16	177.5	4	-	-	< 3.7	< 41	< 0.18	< 18	19	< 4.7	< 0.36	< 1.9	< 1.5	< 160	-	89.5	3.5	< 0.064	4.04	1413.0	< 7	-	9.64	47.50
Myrtle		MY16	177.5	4'	-	-	< 3.1	< 35	< 0.15	< 15	2	< 4	< 0.31	< 1.6	< 1.3	< 140	-	43.3	3.4	< 0.054	4.21	284.0	< 5.9	-	14.05	1.37
Myrtle		MY16	177.5	4''	-	-	< 3.8	< 42	< 0.19	41	< 1.4	< 4.8	< 0.37	< 1.9	< 1.5	< 170	-	36.6	3.2	< 0.065	3.84	147.2	< 7.2	-	16.91	0.24
Myrtle		MY16	177.5	5	-	-	4	49	0.5	< 17	< 1.4	193	< 0.36	< 1.9	< 1.5	< 180	-	14.7	4.0	< 0.064	3.91	19.1	< 7	-	6.66	106.80
Myrtle		MY16	177.5	5'	-	-	< 4.9	< 55	< 0.24	29	< 1.8	< 6.2	< 0.49	< 2.5	< 2	340	-	13.9	2.2	< 0.085	5.01	22.3	< 9.3	-	9.77	104.70
Myrtle		MY16	177.5	5''	-	-	< 4.7	< 52	< 0.23	< 21	3	10	< 0.46	< 2.4	< 1.9	< 240	-	84.7	4.7	< 0.081	4.62	292.7	< 8.9	-	19.91	4.55
Myrtle		MY16	177.5	6	-	-	< 3.1	< 28	< 0.21	< 13	18	< 2.9	< 0.25	< 1.6	< 2	178	-	68.3	2.9	< 0.034	3.95	1523.0	< 3.7	-	12.60	79.30
Myrtle		MY16	177.5	6'	-	-	< 3	< 27	< 0.2	< 12	18	< 2.8	< 0.24	< 1.5	< 1.9	175	-	91.0	5.1	< 0.033	3.64	1515.0	< 3.6	-	3.45	109.90
Myrtle		MY16	177.5	6''	-	-	< 4.3	< 65	< 0.39	< 24	13	< 5.6	< 0.34	< 2.9	< 2.3	< 300	-	73.2	< 3.8	< 0.25	4.62	1244.0	< 8.9	-	17.14	67.80
Myrtle		MY16	177.5	7	-	-	< 3.6	< 55	< 0.33	< 20	< 1.6	< 4.8	< 0.29	< 2.5	< 2	< 260	-	32.1	< 3.2	< 0.21	4.42	95.9	< 7.5	-	19.13	123.10
Myrtle		MY16	177.5	7'	-	-	< 4.6	< 70	< 0.43	< 25	16	< 6.1	< 0.37	< 3.1	< 2.5	< 330	-	83.2	< 4.1	< 0.27	3.87	1622.0	< 9.6	-	6.87	51.30
Myrtle		MY16	177.5	7''	-	-	< 3.9	< 59	< 0.36	< 21	23	< 5.1	< 0.31	< 2.6	< 2.1	< 280	-	101.7	< 3.5	< 0.22	4.60	1861.0	< 8.1	-	1.66	61.70
Myrtle		MY16	177.5	8	-	-	< 3.4	< 52	< 0.4	< 16	11	< 2.6	< 0.29	< 2.1	< 1.4	< 240	-	93.6	2.9	< 0.083	5.31	1266.0	0.00	-	6.95	42.20
Myrtle		MY16	177.5	8'	-	-	< 3.5	< 52	< 0.41	< 16	11	< 2.7	< 0.3	< 2.1	< 1.4	< 240	-	74.4	3.6	< 0.085	5.55	1174.0	0.00	-	5.26	45.60
Myrtle		MY16	177.5	8''	-	-	< 3.9	< 59	< 0.46	39	4	< 3	< 0.33	< 2.4	< 1.6	< 280	-	59.1	3.3	< 0.096	4.18	657.0	0.00	-	15.82	66.70
Myrtle		MY16	177.5	9	-	-	< 3.1	< 46	< 0.36	25	18	< 2.3	< 0.26	< 1.8	< 1.3	< 210	-	98.9	2.5	< 0.074	3.00	1668.0	0.00	-	5.34	67.90
Myrtle		MY16	177.5	9'	-	-	< 3.2	< 48	< 0.38	24	< 2.3	< 2.4	< 0.27	< 1.9	< 1.3	< 220	-	95.5	4.5	< 0.077	4.10	378.0	0.00	-	31.70	155.20
Myrtle		MY16	177.5	9''	-	-	< 3.3	< 33	< 0.22	48	< 1.3	< 2.5	< 0.17	< 1.7	< 1.4	< 200	-	21.5	1.7	< 0.046	4.03	81.5	< 4.3	-	13.82	23.03
Myrtle		MY16	177.5	10	-	-	< 2.5	< 24	< 0.17	51	20	< 1.9	< 0.12	< 1.3	< 1.1	< 150	-	78.5	4.4	< 0.034	4.33	1760.0	< 3.2	-	4.52	58.30
Myrtle		MY16	177.5	10'	-	-	< 3.2	< 32	< 0.22	43	< 1.3	< 2.5	< 0.16	< 1.7	< 1.4	< 190	-	37.7	3.0	< 0.045	4.37	126.0	< 4.2	-	15.00	0.19
Myrtle		MY16	177.5	10''	-	-	< 3.2	< 31	< 0.21	36	< 1.2	< 2.4	< 0.16	< 1.6	< 1.4	< 180	-	68.1	2.6	< 0.044	4.47	198.1	< 4.1	-	29.90	57.60
Myrtle		MY16	177.5	11	-	-	< 2.8	< 28	< 0.19	106	8	< 2.2	< 0.14	< 1.5	< 1.2	< 160	-	69.8	2.9	< 0.039	4.24	861.0	< 3.7	-	14.53	11.71
Myrtle		MY16	177.5	11'	-	-	< 3.3	< 33	< 0.22	70	14	< 2.5	< 0.17	< 1.7	< 1.4	< 180	-	96.8	< 1.4	< 0.046	3.52	1562.0	< 4.3	-	1.27	24.80
Myrtle		MY16	177.5	11''	-	-	< 2.6	< 25	< 0.17	90	< 0.99	< 1.9	< 0.13	< 1.3	< 1.1	< 140	-	42.8	1.4	< 0.035	2.91	120.6	< 3.3	-	9.48	42.30
Percentage of analyses > LOD					0	0	3	3	3.0	39	67	18	0	0	0	21	0	100	79	0	100	100	0	0	100	100

Deposit	Lens # (HYC)	Drillhole #	Depth (m)	Analyse #	V (ppm)	Cr (ppm)	Mn (ppm)	Fe (ppm)	Co (ppm)	Ni (ppm)	Cu (ppm)	Zn (ppm)	Ga (ppm)	Ge (ppm)	As (ppm)	Se (ppm)	Mo (ppm)	Ag (ppm)	Cd (ppm)	In (ppm)	Sn (ppm)	Sb (ppm)	Te (ppm)	Hg (ppm)	Tl (ppm)	Bi (ppm)
Myrtle		MY16	195.9	1	0.78	2.70	480	3200	0.3	4	220	5790	0.48	< 0.8	106	131	< 0.52	17.7	24.7	0.12	20.90	65.0	< 1.5	0.80	5.72	19.10
Myrtle		MY16	195.9	1'	1.13	3.90	65	820	0.4	2	49	106	0.27	< 1.1	54	88	< 0.55	30.7	5.7	0.06	29.00	70.5	< 2.2	1.07	11.20	66.20
Myrtle		MY16	195.9	2	0.83	2.20	122	2100	2.1	1	85	800	< 0.21	< 0.7	151	109	3.80	21.0	43.0	< 0.041	8.50	76.0	< 1.6	< 0.36	11.00	13.10
Myrtle		MY16	195.9	2'	1.86	4.40	230	2460	0.2	2	43	37900	1.30	1.5	66	85	< 0.39	19.9	202.0	0.06	11.69	62.7	< 1.3	0.59	6.77	23.90
Myrtle		MY16	195.9	4	1.64	3.70	432	2700	0.2	< 1	8	58	< 0.21	< 0.65	2	65	< 0.4	19.5	12.4	1.40	97.00	81.0	< 1.6	0.54	4.66	2.17
Myrtle		MY16	195.9	4'	0.49	10.00	460	1030	0.3	2	44	89	< 0.32	< 0.98	3	54	< 0.6	27.2	12.4	0.22	62.00	134.0	< 2.3	< 0.46	8.80	1.36
Myrtle		MY16	195.9	5	3.10	15.00	930	2600	0.5	7	61	180	0.51	< 1.4	7	83	< 0.86	36.0	14.9	0.51	119.00	166.0	3.40	< 0.59	9.34	0.76
Myrtle		MY16	195.9	5'	1.60	7.40	760	2180	0.8	3	94	69	0.29	< 0.97	5	78	< 0.58	22.0	13.7	< 0.068	24.40	121.0	2.10	< 0.39	6.90	1.04
Myrtle		MY16	195.9	6	1.04	11.00	380	2800	0.5	5	370	79	< 0.49	< 1.3	6	51	< 0.8	19.9	7.3	0.26	79.00	80.0	< 3	< 0.59	6.10	2.31
Myrtle		MY16	195.9	6'	4.50	6.50	1060	6600	0.5	16	110	140	< 0.45	< 1.2	5	61	< 0.73	14.0	14.0	0.09	21.00	70.0	< 2.7	< 0.54	5.88	2.77
Percentage of analyses > LOD					100	100	100	100	100.0	90	100	100	50	10	100	100	10	100	100	80	100	100	20	40	100	100
Myrtle		MY16	197.7	1	0.78	< 4.1	< 1.4	86	< 0.53	< 3.1	58	1900	< 0.48	< 2	< 3.4	55	< 1.1	19.4	9.4	< 0.12	2.58	29.6	< 4.3	< 0.83	2.86	35.20
Myrtle		MY16	197.7	2	1.35	< 3.4	10	230	< 0.59	< 2.4	60	2480	0.85	< 2.1	5	50	< 0.81	15.6	13.6	< 0.1	2.29	20.7	< 5.3	< 0.72	1.88	25.60
Myrtle		MY16	197.7	2'	4.23	< 6.7	259	1660	< 1.2	< 4.7	15	29	1.26	< 4.1	22	67	< 1.6	20.7	< 6.4	< 0.2	< 2.8	23.9	< 10	< 1.4	2.45	45.70
Myrtle		MY16	197.7	3	< 0.41	< 2.5	3	1950	2.0	4	330	29300	1.97	3.3	1430	23	5.42	32.4	104.0	0.38	5.32	100.9	< 3.3	0.69	174.30	20.03
Myrtle		MY16	197.7	3'	< 1	< 4.9	5	7890	3.5	5	194	442000	26.60	28.3	937	43	6.38	52.5	1299.0	2.72	37.20	115.1	< 6.7	4.06	107.40	26.71
Myrtle		MY16	197.7	4	< 0.62	< 3.1	7	60800	188.0	272	300	42900	2.43	5.8	3810	34	28.90	35.6	154.0	0.46	7.11	145.0	< 4.1	1.31	213.00	27.35
Myrtle		MY16	197.7	4'	< 0.61	< 3	6	38700	115.0	169	290	53300	3.30	5.5	3200	33	17.80	35.3	173.0	0.40	5.36	158.0	< 4.1	1.30	220.00	22.00
Myrtle		MY16	197.7	1	< 0.48	< 2.8	6	10200	24.5	34	116	7700	0.87	< 1.5	2000	28	16.30	33.8	30.3	< 0.11	2.21	120.7	< 4	< 0.62	205.60	24.66
Myrtle		MY16	197.7	6	0.49	< 2.1	< 0.69	138	0.6	< 1.6	14	39	< 0.42	< 1.2	4	30	< 0.76	12.9	8.0	< 0.093	1.23	53.0	< 3.1	< 0.58	4.66	0.49
Myrtle		MY16	197.7	6'	4.96	3.53	321	2070	0.6	< 2	16	37	0.93	< 1.9	17	49	< 0.74	9.0	8.2	< 0.082	1.30	34.5	< 5	< 0.55	3.18	7.48
Myrtle		MY16	197.7	7	0.58	< 2	1	180	0.4	< 1.8	13	23	< 0.32	< 1.7	6	< 15	< 0.66	13.3	6.3	< 0.073	1.34	57.2	< 4.4	< 0.5	8.16	3.40
Myrtle		MY16	197.7	7'	< 0.45	< 2.1	< 0.83	107	0.4	< 1.8	< 1.4	< 5.5	< 0.33	< 1.8	7	36	< 0.67	11.7	6.5	< 0.074	1.36	53.5	< 4.4	< 0.52	7.11	4.77
Percentage of analyses > LOD					50	8	75	100	75.0	42	92	92	67	33	92	92	42	100	92	33	92	100	0	33	100	100
Myrtle		MY16	205.3	1	-	-	469	1930	< 0.29	< 15	< 1.4	< 2.4	< 0.29	< 1.8	< 1.9	< 170	-	4.5	6.0	< 0.058	4.20	11.6	< 4.7	-	4.71	2.45
Myrtle		MY16	205.3	1'	-	-	137	1200	1.8	< 20	< 1.8	< 3.2	< 0.39	< 2.3	41	< 220	-	8.8	2.0	< 0.076	5.68	22.1	< 6.3	-	5.20	5.71
Myrtle		MY16	205.3	1''	-	-	5	1420	7.5	13	5	< 1.8	< 0.23	< 1.4	168	< 130	-	8.7	4.0	< 0.051	4.05	25.2	< 5.8	-	7.67	6.60
Myrtle		MY16	205.3	2'	-	-	1510	7890	5.2	< 21	7	6	< 0.41	< 2.5	763	< 210	-	12.4	< 3.5	< 0.089	6.50	60.1	< 10	-	8.68	9.60
Myrtle		MY16	205.3	2''	-	-	61	600	0.8	< 8.6	2	3200	< 0.15	0.9	30	< 86	-	9.6	20.6	< 0.03	4.45	12.3	0.00	-	1.51	2.62
Myrtle		MY16	205.3	3	-	-	< 5.7	< 53	< 0.31	< 19	< 1.9	< 11	< 0.31	< 1.9	< 1.3	< 170	-	5.7	3.9	< 0.063	3.91	34.4	0.54	-	29.30	< 0.095
Myrtle		MY16	205.3	3'	-	-	824	3920	< 0.94	84	< 2.8	< 9	3.05	< 4.6	5	< 410	-	8.2	< 4.7	0.00	8.00	36.7	0.00	-	3.20	4.73
Myrtle		MY16	205.3	4	-	-	< 3.2	80	0.7	26	< 1.3	< 2	< 0.16	< 2	2	< 130	-	13.3	5.0	< 0.04	3.42	31.3	< 4.2	-	2.71	6.93
Myrtle		MY16	205.3	4'	-	-	< 3.6	< 29	< 0.28	38	< 1.4	< 2.3	< 0.18	< 2.3	< 1.6	< 140	-	10.3	3.9	< 0.044	2.90	28.0	< 4.7	-	2.91	1.46
Myrtle		MY16	205.3	4''	-	-	< 1.7	< 16	< 0.18	< 7.5	< 0.59	< 1.1	< 0.1	< 0.89	< 0.4	< 61	-	11.0	5.9	< 0.028	2.70	27.3	< 2.1	-	2.38	3.67
Myrtle		MY16	205.3	5	-	-	< 3.6	< 34	< 0.38	< 17	< 1.3	< 2.4	< 0.21	< 1.9	< 0.86	< 130	-	20.1	5.7	< 0.06	3.61	68.7	< 4.5	-	4.09	0.14
Myrtle		MY16	205.3	5'	-	-	< 4.9	< 46	< 0.51	< 24	< 1.7	< 3.3	< 0.29	< 2.6	< 1.2	< 170	-	12.9	4.8	< 0.081	4.44	44.1	< 6.1	-	3.00	0.10
Myrtle		MY16	205.3	5''	-	-	< 1.4	< 16	< 0.12	< 9.3	< 0.58	< 1.8	< 0.14	< 0.77	< 0.66	< 38	-	12.6	6.0	< 0.035	3.39	36.2	< 3.5	-	4.46	0.28
Myrtle		MY16	205.3	6	-	-	< 1.4	63	< 0.11	< 9.9	< 0.58	< 1.8	< 0.14	< 0.76	< 0.65	< 35	-	11.0	5.5	< 0.034	3.12	24.6	< 3.4	-	2.01	4.13
Myrtle		MY16	205.3	6'	-	-	< 1.4	< 16	< 0.12	< 10	1	< 1.8	< 0.14	< 0.76	< 0.65	< 35	-	14.3	3.8	< 0.034	2.80	34.6	< 3.4	-	1.95	2.18
Myrtle		MY16	205.3	6''	-	-	< 1.7	< 13	0.2	< 13	< 0.62	< 1.5	< 0.11	< 0.69	< 0.81	< 44	-	7.6	4.8	< 0.012	2.83	17.4	< 2.7	-	2.15	4.06
Myrtle		MY16	205.3	7	-	-	< 1.9	< 15	< 0.098	< 16	< 0.73	< 1.8	< 0.13	< 0.81	< 0.96	< 49	-	12.3	4.5	< 0.014	2.46	33.6	< 3.2	-	2.26	0.90
Myrtle		MY16	205.3	7'	-	-	< 1.7	< 13	< 0.086	< 15	< 0.65	< 1.6	< 0.11	< 0.72	< 0.84	< 43	-	18.0	6.9	< 0.012	2.32	51.7	< 2.8	-	3.91	0.41
Myrtle		MY16	205.3	7''	-	-	2	< 14	< 0.075	< 12	< 0.67	< 1.6	< 0.11	< 0.74	< 0.52	< 35	-	20.8	6.6	< 0.024	2.68	55.4	0.00	-	3.78	1.30
Myrtle		MY16	205.3	8	-	-	19	126	< 0.19	< 34	< 1.7	< 4	< 0.26	< 1.8	< 1.3	< 84	-	18.5	3.0	< 0.059	4.29	68.6	0.00	-	3.40	< 0.069
Myrtle		MY16	205.3	8'	-	-	< 3.8	< 36	< 0.19	< 37	< 1.7	< 4.2	< 0.28	< 1.9	< 1.3	< 87	-	62.5	< 2.3	< 0.062	4.44	299.0	0.38	-	3.32	5.10
Myrtle		MY16	205.3	8''	-	-	< 3.6	< 33	< 0.18	< 37	< 1.6	< 3.9	< 0.26	< 1.8	< 1.3	< 80	-	27.3	< 2.1	< 0.058	4.79	95.6	0.00	-	4.44	0.11
Myrtle		MY16	205.3	9	-	-	< 1.3	13	< 0.044	< 17	< 0.53	< 1.5	< 0.11	< 0.74	< 0.8	< 34	-	22.9	3.2	< 0.015	2.62	104.3	< 1.3	-	3.98	0.05
Myrtle		MY16	205.3	9'	-	-	< 1.8	136	0.5	29	< 0.71	< 2	< 0.15	< 0.99	14	< 46	-	25.5	3.2	< 0.02	3.04	91.2	< 1.8	-	3.92	0.07
Myrtle		MY16	205.3	9''	-	-	< 4.3	< 38	< 0.14	< 62	< 1.7	< 4.9	< 0.36	< 2.4	< 2.6	< 110	-	16.6	5.1	< 0.049	4.06	68.3	< 4.2	-	3.86	< 0.061
Myrtle		MY16	205.3	10	-	-	< 1.3	17	< 0.044	40	< 0.53	< 1.5	< 0.11	< 0.73	2	< 33	-	19.4	4.9	< 0.015	1.73	62.3	< 1.3	-	3.16	< 0.019
Myrtle		MY16	205.3	10'	-	-	< 1.2	< 10	< 0.038	37	< 0.46	< 1.3	< 0.098	< 0.64	< 0.7	< 28	-	13.8	3.4	< 0.013	1.53	40.1	< 1.1	-	3.31	0.04
Myrtle		MY16	205.3	10''	-	-	< 1.2	< 10	< 0.039	43	< 0.46	< 1.3	< 0.099	< 0.65	< 0.7	< 28	-	19.5	3.4	< 0.013	1.63	64.8	< 1.1	-	2.98	0.19
Percentage of analyses > LOD					0	0	29	43	25.0	29	14	7	4	3.6	29	0	0	100.0	85.7	0	100	100.0	7	0	100	86

Deposit	Lens # (HYC)	Drillhole #	Depth (m)	Analyse #	V (ppm)	Cr (ppm)	Mn (ppm)	Fe (ppm)	Co (ppm)	Ni (ppm)	Cu (ppm)	Zn (ppm)	Ga (ppm)	Ge (ppm)	As (ppm)	Se (ppm)	Mo (ppm)	Ag (ppm)	Cd (ppm)	In (ppm)	Sn (ppm)	Sb (ppm)	Te (ppm)	Hg (ppm)	Tl (ppm)	Bi (ppm)
Caranbirini		DD82CA1	565	1	-	-	< 0.2	< 4.3	< 0.032	< 6.4	3	< 0.33	< 0.024	< 0.46	1	35	-	381.3	15.4	< 0.0067	1.45	325.4	< 0.33	-	1.73	39.83
Caranbirini		DD82CA1	565	1'	-	-	< 0.26	< 5.6	< 0.035	< 7.1	10	0	< 0.026	< 0.47	1	45	-	384.6	15.3	< 0.011	1.36	323.3	< 0.4	-	1.86	34.24
Caranbirini		DD82CA1	565	2	-	-	< 0.27	< 5.7	< 0.035	< 7.1	< 0.32	< 0.32	< 0.026	< 0.48	1	56	-	366.9	15.1	< 0.011	1.35	297.6	< 0.41	-	1.85	31.67
Caranbirini		DD82CA1	565	2'	-	-	< 0.23	< 5.1	< 0.043	< 6.5	< 0.27	< 0.31	< 0.017	< 0.54	1	49	-	352.2	15.7	< 0.01	1.22	276.7	< 0.39	-	1.94	35.86
Caranbirini		DD82CA1	565	3	-	-	< 0.24	< 5.3	< 0.045	< 6.7	< 0.28	< 0.32	< 0.017	< 0.56	1	55	-	331.3	15.2	< 0.01	1.29	249.2	< 0.4	-	1.77	35.75
Caranbirini		DD82CA1	565	3'	-	-	< 0.26	< 4.9	< 0.034	< 6.6	< 0.35	< 0.4	< 0.031	< 0.54	0	59	-	337.9	14.9	< 0.0052	1.13	246.1	< 0.53	-	1.84	42.24
Caranbirini		DD82CA1	565	4	-	-	< 0.27	< 5.1	< 0.036	< 6.6	3	0	< 0.032	< 0.56	1	81	-	279.4	14.5	< 0.0053	1.23	187.5	< 0.54	-	1.82	48.78
Caranbirini		DD82CA1	565	4'	-	-	< 0.26	< 5.9	< 0.045	< 7.9	< 0.3	< 0.49	< 0.034	< 0.47	1	132	-	259.4	15.5	< 0.0082	1.28	165.1	< 0.43	-	1.78	55.50
Caranbirini		DD82CA1	565	5	-	-	< 0.27	< 6.1	< 0.048	< 8	< 0.31	< 0.51	< 0.036	< 0.48	1	184	-	254.2	15.8	< 0.0083	1.19	157.1	< 0.44	-	1.83	57.11
Caranbirini		DD82CA1	565	5'	-	-	< 0.32	< 6	< 0.047	< 7.2	< 0.35	< 0.33	< 0.023	< 0.48	1	129	-	262.4	14.7	< 0.0065	1.25	154.9	< 0.69	-	1.79	62.25
Caranbirini		DD82CA1	565	6	-	-	< 0.32	< 6.2	< 0.049	< 7.1	< 0.34	< 0.34	< 0.024	< 0.48	1	125	-	208.7	16.0	< 0.0065	1.14	120.5	< 0.68	-	1.76	52.17
Caranbirini		DD82CA1	565	6'	-	-	< 0.29	< 6	< 0.04	< 6.7	< 0.34	< 0.27	< 0.036	< 0.51	1	107	-	197.6	14.5	< 0.0056	1.17	121.3	< 0.39	-	1.76	35.78
Caranbirini		DD82CA1	565	7	-	-	< 0.3	< 6.1	< 0.041	< 6.6	< 0.33	< 0.27	< 0.037	< 0.51	1	64	-	172.9	14.6	< 0.0056	1.07	106.7	< 0.38	-	1.81	28.44
Caranbirini		DD82CA1	565	7'	-	-	< 0.31	< 6.8	< 0.045	< 6.1	< 0.31	< 0.41	< 0.021	< 0.57	1	74	-	160.4	14.9	< 0.0054	1.04	102.2	< 0.34	-	1.96	31.61
Caranbirini		DD82CA1	565	8	-	-	< 0.3	< 6.6	< 0.044	< 5.8	< 0.29	< 0.39	< 0.021	< 0.54	1	111	-	194.1	15.1	< 0.0053	1.04	133.2	< 0.33	-	1.95	35.03
Caranbirini		DD82CA1	565	8'	-	-	< 0.29	< 5	< 0.045	< 5.8	< 0.27	< 0.35	< 0.034	< 0.42	< 0.56	70	-	249.0	16.0	< 0.0057	1.13	182.6	< 0.42	-	2.07	38.37
Percentage of analyses > LOD					0	0	0	0	0.0	0	19	13	0	0.0	94	100	0	100.0	100.0	0	100	100.0	0	0	100	100
Caranbirini		DD82CA1	679.2	11	-	-	91	1170	0.2	< 6.4	1	4	0.09	< 0.54	5	< 11	-	73.6	10.9	0.02	1.41	57.8	< 0.43	-	1.16	5.13
Caranbirini		DD82CA1	679.2	11'	-	-	16	710	0.5	< 8.5	1	7	0.11	< 0.71	2	< 15	-	80.7	10.2	< 0.011	1.48	62.1	< 0.56	-	1.11	5.14
Caranbirini		DD82CA1	679.2	12	-	-	< 0.23	< 6.4	< 0.046	< 6.6	< 0.34	1	< 0.034	< 0.52	1	< 12	-	232.3	11.3	< 0.0072	1.35	169.5	< 0.35	-	0.95	0.07
Caranbirini		DD82CA1	679.2	12'	-	-	1	9	< 0.077	< 7.7	< 0.38	1	< 0.046	< 0.75	1	< 15	-	239.0	11.7	< 0.0085	1.12	170.6	< 0.81	-	0.91	0.05
Caranbirini		DD82CA1	679.2	13	-	-	< 0.44	< 8.2	< 0.098	< 9.8	< 0.47	2	< 0.058	< 0.96	1	< 20	-	181.3	12.2	< 0.011	1.26	125.1	< 1	-	0.88	0.08
Caranbirini		DD82CA1	679.2	13'	-	-	< 0.28	< 5.7	< 0.054	< 7.3	< 0.3	1	0.04	< 0.54	1	< 12	-	183.0	11.9	< 0.006	1.25	127.1	< 0.49	-	1.04	0.25
Caranbirini		DD82CA1	679.2	14	-	-	< 0.28	< 5.6	< 0.054	< 7.3	< 0.3	1	< 0.034	< 0.54	1	< 12	-	151.2	11.5	< 0.006	1.29	105.6	< 0.49	-	1.26	0.05
Caranbirini		DD82CA1	679.2	14'	-	-	< 0.31	< 7.7	< 0.049	< 7.5	< 0.3	< 0.56	< 0.037	< 0.47	1	< 14	-	151.9	11.8	< 0.0088	1.35	107.1	< 0.65	-	1.22	0.06
Caranbirini		DD82CA1	679.2	15	-	-	< 0.3	< 7.5	< 0.047	< 7.3	< 0.3	1	< 0.036	< 0.46	1	< 14	-	155.5	11.8	< 0.0087	1.40	111.3	< 0.64	-	1.27	0.06
Caranbirini		DD82CA1	679.2	15'	-	-	< 0.29	8	< 0.061	< 7.5	< 0.28	< 0.48	< 0.033	< 0.55	1	< 14	-	120.5	11.9	< 0.0066	1.26	92.6	< 0.33	-	1.41	0.26
Caranbirini		DD82CA1	679.2	16	-	-	< 0.29	< 6	< 0.06	< 7.4	< 0.28	< 0.48	< 0.032	< 0.55	1	< 14	-	164.4	13.4	< 0.0066	1.23	121.4	< 0.33	-	1.21	0.06
Caranbirini		DD82CA1	679.2	16'	-	-	< 0.28	< 5.7	< 0.048	< 6.4	< 0.31	1	< 0.033	< 0.51	1	< 17	-	131.4	11.8	0.01	1.16	98.9	< 0.33	-	1.39	0.09
Caranbirini		DD82CA1	679.2	17	-	-	< 0.27	< 5.5	< 0.046	< 6.2	< 0.31	0	< 0.032	< 0.5	1	< 17	-	142.8	11.7	< 0.0065	1.23	112.1	< 0.33	-	1.29	0.08
Caranbirini		DD82CA1	679.2	17'	-	-	< 0.27	< 5.5	< 0.045	< 6.1	< 0.3	1	< 0.031	< 0.49	1	< 17	-	152.4	10.9	< 0.0065	1.19	120.5	< 0.33	-	1.19	0.08
Caranbirini		DD82CA1	679.2	18	-	-	< 0.25	< 5.7	< 0.049	< 5.3	< 0.26	< 0.37	< 0.032	< 0.52	1	< 15	-	87.5	12.8	< 0.0092	1.27	78.3	< 0.28	-	1.46	0.16
Caranbirini		DD82CA1	679.2	18'	-	-	< 0.25	< 5.6	< 0.048	< 5.2	< 0.25	0	0.03	< 0.51	1	< 15	-	129.5	12.4	< 0.009	1.29	115.8	< 0.27	-	1.44	0.07
Caranbirini		DD82CA1	679.2	19	-	-	< 0.25	< 4.9	< 0.05	< 6.2	< 0.26	0	< 0.027	< 0.49	1	< 13	-	116.9	11.0	< 0.0059	1.32	100.1	< 0.44	-	1.30	0.09
Caranbirini		DD82CA1	679.2	19'	-	-	< 0.25	< 5	< 0.05	< 6.2	< 0.27	< 0.38	< 0.027	< 0.5	1	< 13	-	111.2	11.0	< 0.0059	1.25	95.4	< 0.44	-	1.42	0.09
Caranbirini		DD82CA1	679.2	20	-	-	< 0.24	< 5.5	< 0.046	< 5	< 0.25	0	< 0.031	< 0.49	1	< 14	-	71.2	11.0	< 0.0087	1.05	62.1	< 0.27	-	1.53	6.74
Caranbirini		DD82CA1	679.2	20'	-	-	< 0.26	< 4.9	< 0.036	< 7	< 0.23	< 0.37	< 0.028	< 0.53	1	< 14	-	107.0	10.7	< 0.0065	1.23	99.3	< 0.35	-	1.54	4.73
Percentage of analyses > LOD					0	0	15	20	10.0	0	10	70	20	0.0	100	0	0	100.0	100.0	10	100	100.0	0	0	100	100
Caranbirini		DD82CA1	734.9	1	-	-	< 0.21	< 4	< 0.035	< 5.3	2	< 1.2	< 0.022	< 0.42	1	< 8.2	-	151.8	8.7	< 0.0094	1.36	65.8	< 0.51	-	1.95	0.11
Caranbirini		DD82CA1	734.9	1'	-	-	< 0.21	< 4.5	< 0.036	< 6.7	1	< 0.35	< 0.026	< 0.46	1	< 8.8	-	171.3	9.2	< 0.0038	1.35	73.8	< 0.36	-	2.15	0.11
Caranbirini		DD82CA1	734.9	2	-	-	< 0.22	< 4.7	< 0.038	< 7.2	0	< 0.37	< 0.028	< 0.5	1	< 9.6	-	190.3	9.6	< 0.004	1.19	87.4	< 0.39	-	2.08	0.11
Caranbirini		DD82CA1	734.9	2'	-	-	4	21	0.1	< 7.9	7	4	0.06	< 0.55	1	< 9	-	132.5	7.8	0.01	1.31	83.3	< 0.5	-	1.98	0.12
Caranbirini		DD82CA1	734.9	3	-	-	3	18	< 0.031	< 7.8	2	2	0.03	< 0.55	1	< 9.2	-	128.0	8.6	0.01	1.17	85.5	< 0.51	-	1.94	0.11
Caranbirini		DD82CA1	734.9	3'	-	-	< 0.25	< 4.2	< 0.034	< 6.3	2	2	0.04	< 0.47	1	< 10	-	139.1	8.9	0.01	1.27	88.7	< 0.87	-	2.10	0.12
Caranbirini		DD82CA1	734.9	4	-	-	< 0.26	< 4.3	< 0.035	< 6.3	< 0.25	< 0.32	< 0.025	< 0.48	< 0.43	< 11	-	173.5	9.4	< 0.0034	1.21	82.4	< 0.89	-	2.21	0.10
Caranbirini		DD82CA1	734.9	4'	-	-	< 0.22	< 4.9	< 0.031	< 6.2	< 0.27	< 0.34	< 0.028	< 0.53	1	< 10	-	181.4	9.3	< 0.0044	1.26	81.0	< 0.41	-	2.37	0.10
Caranbirini		DD82CA1	734.9	5	-	-	< 0.22	< 4.9	< 0.03	< 5.8	< 0.27	< 0.34	< 0.028	< 0.52	1	< 11	-	162.4	8.8	< 0.0044	1.33	63.0	< 0.4	-	2.32	0.08
Caranbirini		DD82CA1	734.9	5'	-	-	< 0.39	< 6.8	< 0.06	< 10	< 0.46	< 0.4	< 0.026	< 0.83	1	< 16	-	146.0	8.7	< 0.0076	1.16	60.5	0.00	-	2.29	0.09
Caranbirini		DD82CA1	734.9	6	-	-	< 0.39	< 6.9	< 0.06	< 9.6	< 0.47	< 0.41	< 0.026	< 0.83	1	< 17	-	138.4	9.6	< 0.0077	0.93	76.5	0.00	-	2.37	0.08

Deposit	Lens # (HYC)	Drillhole #	Depth (m)	Analyse #	V (ppm)	Cr (ppm)	Mn (ppm)	Fe (ppm)	Co (ppm)	Ni (ppm)	Cu (ppm)	Zn (ppm)	Ga (ppm)	Ge (ppm)	As (ppm)	Se (ppm)	Mo (ppm)	Ag (ppm)	Cd (ppm)	In (ppm)	Sn (ppm)	Sb (ppm)	Te (ppm)	Hg (ppm)	Tl (ppm)	Bi (ppm)
Caranbirini		DD82CA1	734.9	6'	-	-	< 0.28	59	0.1	< 8.2	4	10	0.04	< 0.64	2	< 15	-	164.3	8.8	< 0.0058	1.00	76.2	< 0.59	-	2.46	0.12
Caranbirini		DD82CA1	734.9	7	-	-	< 0.32	11	< 0.05	< 8.8	< 0.44	< 0.38	< 0.022	< 0.72	1	< 18	-	153.9	9.0	< 0.0066	1.06	66.4	< 0.66	-	2.39	0.10
Caranbirini		DD82CA1	734.9	7'	-	-	< 0.49	11	< 0.08	< 14	< 0.64	< 0.73	0.02	< 0.98	1	< 21	-	124.3	8.1	0.00	1.09	74.8	0.00	-	2.33	0.09
Caranbirini		DD82CA1	734.9	8	-	-	2	< 10	< 0.081	< 14	< 0.64	< 0.74	0.00	< 0.97	< 1.1	< 22	-	110.4	7.8	0.00	0.97	69.6	0.00	-	2.17	0.08
Caranbirini		DD82CA1	734.9	8'	-	-	< 0.33	< 6.2	< 0.048	< 6.7	< 0.32	< 0.29	< 0.045	< 0.51	1	< 15	-	144.8	8.9	< 0.0086	1.01	62.9	< 0.41	-	2.41	0.11
Caranbirini		DD82CA1	734.9	9	-	-	< 0.33	24	0.1	< 6.2	< 0.31	< 0.29	< 0.045	< 0.49	1	< 15	-	134.6	8.2	< 0.0085	1.04	96.3	< 0.39	-	2.08	0.11
Caranbirini		DD82CA1	734.9	9'	-	-	< 0.33	12	0.1	< 5.3	1	1	< 0.058	< 0.57	1	< 17	-	128.1	8.0	< 0.0089	1.06	74.6	< 0.56	-	2.34	0.09
Caranbirini		DD82CA1	734.9	10	-	-	81	433	< 0.054	< 6.1	0	< 0.49	< 0.071	< 0.69	1	< 20	-	159.0	10.1	< 0.011	1.13	116.5	< 0.66	-	2.28	0.12
Percentage of analyses > LOD					0	0	21	42	21.1	0	47	26	26	0	89	0	0	100	100	26	100	100	0	0	100	100
Walford Creek		WFDD238	140.5	1'	< 0.091	< 0.48	1	326	2.3	11	446	1940	0.13	0.4	44	< 2.4	< 0.14	282.2	23.6	0.12	0.83	269.2	< 0.65	< 0.1	1.15	0.09
Walford Creek		WFDD238	140.5	2'	< 0.13	< 0.67	1	220	1.0	20	350	46	< 0.08	0.3	61	< 3.3	0.46	309.0	12.7	0.03	0.67	296.0	< 0.9	< 0.14	3.24	0.08
Walford Creek		WFDD238	140.5	3	< 0.099	< 0.44	1	8400	8.4	29	12000	189	< 0.079	2.0	576	< 3.3	2.28	440.0	17.5	0.63	0.65	1340.0	< 0.58	0.68	14.00	0.24
Walford Creek		WFDD238	140.5	4	< 0.067	< 0.36	1	1700	3.8	18	2000	10200	0.61	0.6	55	< 2.2	< 0.12	183.3	54.8	0.97	0.76	194.2	< 0.43	0.19	0.76	0.11
Walford Creek		WFDD238	140.5	4'	< 0.077	< 0.42	0	11	0.2	2	41	17	< 0.069	0.3	6	< 2.5	< 0.13	175.6	12.4	< 0.014	0.74	162.2	< 0.5	< 0.15	0.86	0.08
Walford Creek		WFDD238	140.5	5	< 0.082	< 0.42	0	80	0.3	28	61	47	< 0.06	0.3	72	< 2.8	< 0.16	180.0	12.2	< 0.012	0.61	155.9	< 0.64	< 0.11	1.02	0.09
Walford Creek		WFDD238	140.5	5'	< 0.078	< 0.4	4	1080	3.1	25	1400	31	< 0.057	0.3	119	< 2.6	0.59	584.0	15.0	0.05	0.65	924.0	< 0.61	0.24	7.60	0.08
Walford Creek		WFDD238	140.5	6	< 0.09	< 0.63	1	1580	3.6	2	1720	417	< 0.077	0.4	16	< 3.8	2.12	195.5	14.5	0.03	0.82	177.2	< 0.66	< 0.13	0.84	0.09
Walford Creek		WFDD238	140.5	7	< 0.11	< 0.47	< 0.16	14	0.1	< 0.3	22	44	< 0.074	< 0.33	< 0.43	< 3.1	< 0.2	177.7	11.2	< 0.019	0.64	169.2	< 0.51	< 0.13	0.94	0.06
Walford Creek		WFDD238	140.5	7'	0.17	< 0.66	89	8500	25.6	17	9300	2360	0.16	0.9	151	< 4.3	2.40	180.9	19.5	0.29	0.83	246.0	< 0.72	0.29	1.14	0.10
Walford Creek		WFDD238	140.5	8	< 0.17	< 0.71	89	450	0.2	< 0.44	104	34	< 0.11	< 0.49	1	< 4.6	< 0.3	116.1	13.8	< 0.029	0.65	109.4	< 0.77	< 0.2	0.60	0.08
Walford Creek		WFDD238	140.5	8'	< 0.16	< 0.67	37	410	< 0.086	< 0.41	55	16	< 0.11	< 0.47	< 0.62	< 4.4	< 0.28	128.0	12.2	< 0.027	0.60	114.8	< 0.73	< 0.19	0.71	0.18
Walford Creek		WFDD238	140.5	9	< 0.12	< 0.68	3	24	< 0.093	< 0.34	32	17	< 0.1	< 0.48	1	< 3.4	< 0.16	118.1	11.4	< 0.024	0.68	114.2	< 0.74	< 0.16	0.68	0.06
Walford Creek		WFDD238	140.5	9'	0.23	< 0.67	18	92	0.1	< 0.34	43	19	< 0.099	< 0.48	1	9	< 0.16	159.0	13.4	< 0.023	0.70	149.8	< 0.74	< 0.16	0.67	0.05
Walford Creek		WFDD238	140.5	10	< 0.099	< 0.54	0	< 12	< 0.075	< 0.27	13	14	< 0.08	< 0.39	0	< 2.7	< 0.13	179.1	13.0	< 0.019	0.61	151.7	< 0.6	< 0.13	1.01	0.43
Walford Creek		WFDD238	140.5	10'	< 0.11	< 0.58	1	30	< 0.08	< 0.29	24	25	< 0.086	< 0.41	1	< 2.9	< 0.14	165.4	12.3	< 0.02	0.63	150.9	< 0.64	< 0.14	0.86	0.35
Walford Creek		WFDD238	140.5	11	< 0.1	< 0.55	0	< 12	< 0.077	< 0.27	4	5	< 0.082	< 0.4	1	< 2.8	< 0.13	150.5	10.4	< 0.019	0.60	116.0	< 0.61	< 0.13	0.87	0.39
Walford Creek		WFDD238	140.5	11'	< 0.1	< 0.56	< 0.19	< 13	< 0.078	1	7	15	< 0.083	< 0.4	2	< 2.9	< 0.14	176.1	12.0	< 0.019	0.59	141.4	< 0.62	< 0.13	0.95	0.25
Walford Creek		WFDD238	140.5	12	< 0.09	< 0.53	0	< 11	0.1	5	9	13	< 0.086	< 0.3	16	< 3	< 0.11	187.1	12.7	< 0.015	0.77	176.9	< 0.51	< 0.12	1.02	0.20
Walford Creek		WFDD238	140.5	12'	< 0.089	< 0.53	1	15	0.2	0	19	19	< 0.085	< 0.3	1	< 3	< 0.11	204.8	14.6	< 0.015	0.66	171.7	< 0.5	< 0.12	1.20	0.12
Walford Creek		WFDD238	140.5	13	< 0.094	< 0.56	0	38	0.3	7	70	141	< 0.09	< 0.32	20	< 3.2	< 0.12	200.0	13.3	0.03	0.73	165.6	< 0.53	< 0.13	0.89	0.09
Walford Creek		WFDD238	140.5	13'	< 0.065	< 0.46	1	< 10	0.3	1	78	82	< 0.077	< 0.27	3	< 3.2	< 0.16	218.2	13.0	0.02	0.68	168.0	< 0.51	< 0.13	0.98	0.09
Walford Creek		WFDD238	140.5	14	< 0.064	< 0.46	0	< 9.8	< 0.058	1	12	23	< 0.075	< 0.27	2	< 3.1	< 0.15	186.0	11.8	0.02	0.64	153.7	< 0.5	< 0.12	1.03	0.36
Percentage of analyses > LOD					9	0	91	74	69.6	65	100	100	13	39	91	4	22	100	100	43	100	100	0	17	100	100
Walford Creek		WFDD238	141	1	< 0.47	< 2	4	96	51.6	38	100	61	< 0.34	< 0.97	173	< 25	1.49	205.0	6.5	0.11	9.17	33.5	< 3.1	< 0.5	2.77	0.21
Walford Creek		WFDD238	141	2	1.40	< 2	6	220	129.0	35	160	69	< 0.34	< 0.96	234	< 24	1.53	162.7	5.9	< 0.068	7.97	34.4	< 3	< 0.5	1.46	0.32
Walford Creek		WFDD238	141	3	< 0.55	< 3.1	4	99	90.0	28	147	323	< 0.4	< 1.5	180	< 33	2.87	192.0	6.3	0.28	8.28	34.7	< 5.6	< 0.95	2.49	0.36
Walford Creek		WFDD238	141	4	< 0.46	< 2.6	< 0.73	< 53	< 0.32	< 1.7	18	< 5.2	< 0.38	< 0.94	16	< 21	< 0.7	67.6	7.2	0.07	7.76	62.5	< 3.6	< 0.54	0.46	< 0.11
Walford Creek		WFDD238	141	5	< 0.59	< 3.3	< 0.83	< 58	8.3	< 2.2	40	< 5.8	< 0.33	< 1.2	31	< 30	< 0.65	57.1	6.0	< 0.11	8.21	30.3	< 4.9	< 0.66	0.31	1.31
Walford Creek		WFDD238	141	6	< 1	< 4.4	11	900	2160.0	328	1210	18200	2.06	< 1.9	104	< 45	42.10	67.1	55.7	1.67	11.90	48.7	< 6.5	< 1	1.39	< 0.2
Walford Creek		WFDD238	141	7	< 1.2	< 5.8	< 2	< 110	6.8	< 4.8	112	160	< 0.96	< 2.7	29	< 56	< 1.6	72.0	8.4	0.17	11.40	34.2	< 9	< 1.3	0.30	< 0.23
Walford Creek		WFDD238	141	8	1.19	< 6.5	3	280	2.6	< 2.9	780	< 9.2	< 0.65	< 2.5	25	< 43	< 1.6	52.6	7.7	< 0.16	10.90	28.1	< 6.6	< 1.2	0.38	0.51
Walford Creek		WFDD238	141	9	< 1.3	< 8	< 3.1	< 170	1.1	< 7.4	25	< 20	< 1.8	< 3.8	24	< 72	< 1.8	44.5	< 9.3	< 0.18	9.00	24.4	< 10	< 1.5	0.59	< 0.36
Walford Creek		WFDD238	141	10	< 0.97	< 6.2	< 1.5	< 100	< 0.71	< 3.9	45	45	< 1.6	< 2.8	18	< 59	< 1.3	60.1	9.4	< 0.13	8.70	29.0	< 11	< 2.2	< 0.23	< 0.29
Walford Creek		WFDD238	141	11	< 0.62	< 5.3	< 1.6	780	51.0	10	69	1170	< 0.61	< 1.8	73	< 62	< 0.87	60.2	11.6	0.17	8.59	28.9	< 5.7	< 0.8	0.39	< 0.18
Percentage of analyses > LOD					18	0	45	55	81.8	45	100	64	9	0	100	0	36	100	91	55	100	100	0	0	91	45

Deposit	Lens # (HYC)	Drillhole #	Depth (m)	Analyse #	V (ppm)	Cr (ppm)	Mn (ppm)	Fe (ppm)	Co (ppm)	Ni (ppm)	Cu (ppm)	Zn (ppm)	Ga (ppm)	Ge (ppm)	As (ppm)	Se (ppm)	Mo (ppm)	Ag (ppm)	Cd (ppm)	In (ppm)	Sn (ppm)	Sb (ppm)	Te (ppm)	Hg (ppm)	Tl (ppm)	Bi (ppm)
Walford Creek		WFDD266	110	1	< 0.19	< 0.75	< 0.24	< 20	2.0	1	< 0.58	16	< 0.12	< 0.34	28	< 5.9	< 0.23	86.6	3.4	0.04	5.74	84.5	< 1.2	< 0.15	0.70	0.08
Walford Creek		WFDD266	110	2	< 0.16	< 0.76	< 0.26	< 24	0.5	< 0.45	< 0.54	2	< 0.11	< 0.3	29	< 6.2	< 0.22	103.3	3.7	< 0.024	5.50	107.5	< 1.8	< 0.15	0.68	0.07
Walford Creek		WFDD266	110	3	< 0.17	< 0.76	< 0.25	< 20	< 0.11	< 0.48	< 0.59	< 1.1	< 0.12	< 0.4	32	< 9.2	< 0.22	34.9	3.6	0.03	5.60	24.4	< 1.3	< 0.19	0.33	0.05
Walford Creek		WFDD266	110	4	< 0.17	< 1.1	< 0.28	< 27	0.2	< 0.6	16	< 1.4	< 0.16	< 0.44	32	< 9.5	< 0.26	620.0	5.2	< 0.026	5.42	1877.0	< 1.9	0.24	3.56	0.05
Walford Creek		WFDD266	110	5	< 0.14	< 0.81	< 0.26	< 21	0.4	< 0.61	< 0.67	2	< 0.13	< 0.35	33	< 6.1	< 0.21	71.0	3.1	< 0.033	5.23	71.5	< 1.5	< 0.18	0.46	0.06
Walford Creek		WFDD266	110	6	< 0.19	< 0.79	< 0.24	< 27	0.7	< 0.5	54	6	< 0.14	< 0.45	38	< 5.9	< 0.22	345.0	2.8	< 0.027	5.33	504.0	< 1.6	< 0.2	3.48	0.05
Walford Creek		WFDD266	110	7	< 0.19	< 0.78	< 0.24	130	10.5	4	1229	< 1.2	< 0.14	< 0.45	41	< 5.8	< 0.22	490.6	4.0	0.03	5.26	2142.0	< 1.6	< 0.2	3.43	0.04
Walford Creek		WFDD266	110	8	< 0.2	< 0.68	< 0.25	590	1.1	< 0.52	< 0.51	7	< 0.12	< 0.34	45	< 5.4	< 0.21	170.3	3.3	< 0.029	5.15	171.6	< 1.6	< 0.18	2.42	0.06
Walford Creek		WFDD266	110	14	< 0.21	< 1.1	< 0.36	< 22	< 0.15	< 0.47	20	6	< 0.13	< 0.54	43	< 6.6	< 0.26	820.0	3.0	< 0.032	4.16	2459.0	< 1.8	0.28	2.66	< 0.057
Walford Creek		WFDD266	110	15	< 0.25	< 1.6	< 0.46	< 39	< 0.21	< 1.2	18	< 4.5	< 0.21	< 0.49	41	< 7.8	< 0.39	775.0	3.8	< 0.068	3.88	2222.0	< 1.7	< 0.34	4.67	< 0.066
Walford Creek		WFDD266	110	16	< 0.18	< 0.85	< 0.27	< 21	< 0.091	< 0.57	< 0.57	< 1.4	< 0.13	< 0.32	40	< 6.3	< 0.26	33.5	3.0	< 0.028	3.45	28.4	< 1.6	< 0.19	0.34	< 0.044
Walford Creek		WFDD266	110	17	< 0.17	< 0.96	< 0.27	< 23	< 0.14	< 0.6	< 0.64	< 2.4	< 0.16	< 0.41	41	< 6.5	< 0.26	67.3	2.4	< 0.028	4.13	64.1	< 1.7	< 0.19	0.68	0.05
Walford Creek		WFDD266	110	18	< 0.17	< 0.7	< 0.23	< 20	< 0.11	< 0.44	< 0.44	< 1.4	< 0.13	< 0.31	40	< 5.8	< 0.24	67.7	3.4	< 0.024	4.04	66.1	< 1.7	< 0.18	0.84	0.04
Walford Creek		WFDD266	110	19	< 0.18	< 0.79	< 0.21	< 23	< 0.1	< 0.45	< 0.62	< 1.2	< 0.14	< 0.44	39	< 8.7	< 0.26	139.6	3.2	< 0.032	4.51	142.6	< 1.6	< 0.26	1.19	< 0.042
Walford Creek		WFDD266	110	20	< 0.23	< 0.85	< 0.24	< 24	< 0.13	< 0.43	< 0.62	< 1.9	< 0.18	< 0.43	41	< 7.1	< 0.25	121.0	3.3	< 0.033	4.14	122.7	< 1.9	< 0.17	1.04	< 0.054
Percentage of analyses > LOD					0	0	0	13	46.7	13	33	40	0	0	100	0	0	100	100	20	100	100	0	13	100	67
Walford Creek		WFDD266	130.8	1	0.66	1.13	1	189	0.5	1	1720	960	0.18	0.3	5	< 1.6	0.15	188.7	7.6	0.04	0.98	2100.0	< 0.34	0.14	0.55	0.12
Walford Creek		WFDD266	130.8	1'	0.38	0.32	5	170	0.8	1	324	162	0.10	< 0.14	6	< 1.9	0.08	103.8	4.9	0.03	0.84	350.0	< 0.39	0.15	0.30	0.10
Walford Creek		WFDD266	130.8	2	0.37	0.39	< 110	< 430	0.4	3	1380	250	0.09	0.2	14	< 1.4	< 0.095	336.5	4.8	0.02	0.80	2040.0	< 0.39	0.11	1.11	0.10
Walford Creek		WFDD266	130.8	2'	0.40	< 0.36	1	37	0.4	1	59	64	0.05	< 0.19	2	< 1.8	< 0.1	112.0	4.6	0.02	0.79	137.0	< 0.43	0.09	0.32	0.09
Walford Creek		WFDD266	130.8	3	0.14	< 0.33	1	23	0.1	0	106	55	< 0.036	< 0.18	1	< 1.7	< 0.094	77.2	4.1	0.01	0.74	117.0	< 0.39	0.09	0.30	0.12
Walford Creek		WFDD266	130.8	3'	0.17	< 0.36	1	53	0.1	< 0.23	35	660	0.07	0.2	1	< 1.9	< 0.1	62.7	5.4	0.01	0.87	72.4	< 0.43	0.09	0.26	0.09
Walford Creek		WFDD266	130.8	4	0.36	< 0.36	1	103	1.3	1	202	41	0.06	0.2	3	< 1.8	< 0.083	200.0	4.3	< 0.012	0.72	444.0	< 0.37	0.14	0.74	0.08
Walford Creek		WFDD266	130.8	4'	1.39	0.44	3	900	6.7	4	49	16230	1.91	0.5	5	< 1.7	1.45	99.1	48.4	< 0.011	0.71	109.5	< 0.33	0.65	0.70	0.10
Walford Creek		WFDD266	130.8	5	0.39	< 0.35	1	41	0.7	1	42	56	0.07	0.3	3	< 2	< 0.09	63.2	4.3	< 0.013	0.72	57.4	< 0.43	< 0.072	0.26	0.09
Walford Creek		WFDD266	130.8	5'	< 0.07	< 0.38	< 0.1	< 13	0.1	0	13	17	< 0.052	0.3	1	< 2.1	< 0.097	94.3	4.8	< 0.014	0.67	102.6	< 0.47	0.09	0.52	0.07
Walford Creek		WFDD266	130.8	6	0.36	< 0.46	1	590	3.0	2	2870	95	< 0.06	0.3	16	< 2.6	0.35	363.0	4.1	0.01	0.64	4490.0	< 0.44	0.12	3.34	0.07
Walford Creek		WFDD266	130.8	6'	0.49	0.56	0	32	0.8	10	3190	25	< 0.057	0.3	33	< 2.7	< 0.1	498.0	3.6	< 0.011	0.72	5440.0	< 0.44	< 0.13	3.94	0.08
Walford Creek		WFDD266	130.8	7	0.11	< 0.43	1	58	2.4	2	89	3700	0.22	0.3	6	4	< 0.11	54.6	15.8	< 0.012	0.62	31.7	< 0.49	< 0.15	0.30	0.09
Walford Creek		WFDD266	130.8	7'	0.37	0.65	0	27	1.1	1	446	67	< 0.077	0.3	4	< 2.4	< 0.15	176.0	5.0	< 0.015	0.79	776.0	< 0.58	0.17	0.62	0.07
Walford Creek		WFDD266	130.8	8	0.30	0.72	0	73	0.6	1	2086	194	< 0.063	0.3	7	< 2	< 0.12	391.0	3.8	< 0.012	0.59	3390.0	< 0.47	< 0.13	2.50	0.07
Walford Creek		WFDD266	130.8	8'	0.29	27.00	1	83	0.5	4	4460	12	< 0.073	0.3	13	< 2.3	< 0.14	329.6	4.1	< 0.014	0.74	6470.0	< 0.55	0.19	2.58	0.07
Percentage of analyses > LOD					94	50	88	88	100.0	94	100	100	56	81	100	6	25	100	100	44	100	100	0	75	100	100
Walford Creek		WFDD266	271.4	2	< 0.18	< 1	< 0.3	< 23	< 0.14	< 0.5	< 0.64	< 1.9	< 0.18	< 0.51	20	< 9.7	< 0.2	54.8	6.1	< 0.022	6.86	49.6	< 2	< 0.29	0.46	< 0.042
Walford Creek		WFDD266	271.4	3	< 0.21	< 0.92	< 0.3	< 23	< 0.15	< 0.58	< 0.75	< 1.8	< 0.13	< 0.42	19	< 7.7	< 0.25	153.7	11.8	0.03	6.83	76.4	< 1.8	< 0.22	0.24	0.05
Walford Creek		WFDD266	271.4	4	< 0.22	< 0.82	< 0.32	< 21	< 0.094	< 0.62	< 0.57	< 1.9	< 0.14	< 0.39	19	< 9.9	< 0.33	157.8	12.9	< 0.03	6.78	84.8	< 1.2	< 0.28	0.23	0.05
Walford Creek		WFDD266	271.4	5	< 0.24	< 1.4	< 0.29	< 23	< 0.13	< 0.56	< 0.83	< 2	< 0.18	< 0.4	18	< 12	< 0.43	166.9	13.1	< 0.043	7.07	82.3	< 2.6	< 0.26	0.26	0.06
Walford Creek		WFDD266	271.4	6	< 0.2	< 0.79	< 0.29	< 18	< 0.15	< 0.52	< 0.7	< 1.7	< 0.14	< 0.42	17	< 8.7	< 0.24	146.1	14.0	< 0.028	6.75	68.7	< 1.8	< 0.24	0.25	< 0.048
Walford Creek		WFDD266	271.4	7	< 0.17	< 0.65	< 0.22	< 22	< 0.13	< 0.62	< 0.62	< 1.6	< 0.13	< 0.37	18	< 7.5	< 0.23	146.9	11.3	< 0.025	6.71	71.4	< 1.6	< 0.22	0.26	0.06
Walford Creek		WFDD266	271.4	8	< 0.17	< 0.64	< 0.21	< 22	< 0.13	< 0.61	< 0.61	< 1.6	< 0.13	< 0.36	17	< 7.3	< 0.22	129.3	9.6	< 0.024	6.44	65.4	< 1.6	< 0.22	0.23	0.10
Walford Creek		WFDD266	271.4	9	< 0.22	< 1.2	< 0.29	< 22	< 0.14	< 0.64	< 0.75	< 2	< 0.15	< 0.51	19	< 7.8	< 0.27	120.5	6.3	< 0.038	7.98	104.6	< 2.1	< 0.27	0.41	0.07
Walford Creek		WFDD266	271.4	10	< 0.24	< 1.4	< 0.36	< 37	< 0.19	< 0.82	< 0.91	< 2.9	< 0.21	< 0.64	18	< 12	< 0.39	90.3	7.3	< 0.038	7.05	74.5	< 2.3	< 0.38	0.30	0.09
Walford Creek		WFDD266	271.4	11	< 0.27	< 1.4	< 0.37	< 22	< 0.22	< 1.3	< 0.76	< 2.4	< 0.18	< 0.47	19	< 11	< 0.39	102.7	6.5	< 0.044	7.94	83.2	< 2.8	< 0.33	0.34	0.18
Walford Creek		WFDD266	271.4	12	< 0.23	< 0.82	0	84	< 0.11	< 0.75	1	< 1.6	< 0.15	< 0.53	17	< 9.1	< 0.31	40.2	7.7	< 0.033	8.29	17.3	< 2.1	< 0.34	0.26	1.35
Walford Creek		WFDD266	271.4	13	< 0.26	< 1.1	< 0.4	< 29	< 0.18	< 0.96	1	< 2.4	< 0.22	< 0.58	17	< 9.8	< 0.55	45.5	7.1	< 0.043	7.50	22.1	< 2.6	< 0.27	0.25	0.89
Walford Creek		WFDD266	271.4	14	1.99	< 1.3	< 0.37	408	520.0	300	299	10	< 0.17	< 0.62	920	15	1460.00	68.5	5.6	< 0.05	8.41	43.9	< 2.5	< 0.32	1.61	15.68
Walford Creek		WFDD266	271.4	15	< 0.16	2.03	< 0.25	< 20	< 0.17	< 0.7	< 0.85	< 1.7	< 0.17	< 0.52	18	< 8.4	< 0.23	88.9	8.5	0.03	7.72	59.4	< 2.3	< 0.25	0.31	< 1.2
Walford Creek		WFDD266	271.4	16	0.79	< 1.5	< 0.41	1990	6.0	6	110	240	0.91	< 0.65	31	< 14	195.00	39.7	8.8	< 0.061	6.48	34.9	< 3	< 0.42	0.49	3.73
Walford Creek		WFDD266	271.4	17	< 0.23	< 1.2	< 0.32	42	< 0.12	< 0.71	70	19	< 0.24	< 0.51	15	< 11	< 0.34	41.6	8.0	< 0.048	6.86	30.7	< 2.4	< 0.33	0.31	4.82
Percentage of analyses > LOD					13	6	6	25	12.5	13	31	19	6	0	100	6	13	100	100	13	100	100	0	0	100	81

Deposit	Lens # (HYC)	Drillhole #	Depth (m)	Analyse #	V (ppm)	Cr (ppm)	Mn (ppm)	Fe (ppm)	Co (ppm)	Ni (ppm)	Cu (ppm)	Zn (ppm)	Ga (ppm)	Ge (ppm)	As (ppm)	Se (ppm)	Mo (ppm)	Ag (ppm)	Cd (ppm)	In (ppm)	Sn (ppm)	Sb (ppm)	Te (ppm)	Hg (ppm)	Tl (ppm)	Bi (ppm)
Walford Creek		WFDD272	184.3	1	< 0.17	< 0.69	0	< 16	< 0.1	< 0.54	59	< 2.3	< 0.13	< 0.36	36	< 9.6	< 0.24	339.0	10.3	< 0.028	7.25	208.0	< 1.4	< 0.23	0.64	0.06
Walford Creek		WFDD272	184.3	2	< 0.17	< 0.7	0	< 17	1.2	< 0.55	< 0.68	< 2.3	< 0.14	< 0.36	38	< 9.7	< 0.24	184.5	7.3	0.03	7.64	28.3	< 1.4	< 0.23	0.44	0.05
Walford Creek		WFDD272	184.3	3	< 0.19	< 1.1	< 0.32	< 24	0.4	< 0.67	5	1600	< 0.15	< 0.36	33	< 12	< 0.27	99.9	13.1	0.10	7.50	41.8	< 1.8	< 0.28	0.33	0.06
Walford Creek		WFDD272	184.3	4	< 0.16	< 0.84	< 0.25	< 20	< 0.1	< 0.56	4	270	< 0.12	< 0.38	33	< 9.3	< 0.23	95.5	11.2	0.05	8.16	55.7	< 1.7	< 0.24	0.28	0.08
Walford Creek		WFDD272	184.3	6	< 0.21	< 0.78	< 0.33	95	1.1	< 0.56	4	< 2.1	< 0.11	< 0.41	34	< 11	< 0.23	82.5	7.1	0.04	8.21	25.8	< 1.9	< 0.29	0.27	< 0.042
Walford Creek		WFDD272	184.3	7	< 0.16	1.80	3	2810	5.7	2	4	310	< 0.12	< 0.4	41	< 8.9	< 0.32	52.4	5.8	0.05	7.69	18.8	< 1.8	< 0.24	0.26	0.06
Walford Creek		WFDD272	184.3	8	< 0.17	< 0.92	< 0.33	33	< 0.13	1	1765	5	< 0.14	< 0.45	70	< 9.9	< 0.35	496.4	11.7	< 0.037	8.21	2390.0	< 2	< 0.27	2.06	< 0.052
Walford Creek		WFDD272	184.3	9	< 0.49	< 1.3	< 0.2	< 37	1.9	103	< 1.5	< 2.9	< 0.15	< 0.81	610	< 12	< 0.43	503.0	7.6	< 0.045	7.85	78.0	< 3.7	< 0.3	5.36	< 0.053
Walford Creek		WFDD272	184.3	10	< 0.4	< 1.6	0	720	0.8	28	9	430	< 0.29	< 0.68	124	< 16	< 0.38	356.0	13.2	0.10	7.87	10.4	< 4	< 0.29	5.12	< 0.071
Walford Creek		WFDD272	184.3	11	< 0.15	< 0.87	0	< 19	7.1	1	< 0.69	< 1.9	< 0.15	< 0.42	33	< 8.8	< 0.29	112.4	7.6	< 0.026	9.03	26.3	< 1.7	< 0.25	0.34	0.06
Walford Creek		WFDD272	184.3	12	< 0.13	< 0.77	< 0.23	< 17	29.5	6	< 0.62	< 1.7	< 0.13	< 0.38	32	< 7.8	< 0.26	118.6	7.6	0.02	7.77	21.2	< 1.5	< 0.23	0.35	0.07
Walford Creek		WFDD272	184.3	13	0.62	< 1.1	1	460	3.4	171	19	20	< 0.17	< 0.56	795	< 11	< 0.46	721.0	9.7	< 0.054	8.83	198.0	< 2.2	< 0.36	7.17	< 0.052
Walford Creek		WFDD272	184.3	14	< 0.34	< 1.2	< 0.43	< 27	< 0.19	< 0.97	< 0.9	< 2.4	< 0.2	< 0.65	36	< 13	< 0.54	96.9	9.8	< 0.063	9.44	72.3	< 2.6	< 0.42	0.31	< 0.06
Walford Creek		WFDD272	184.3	15	< 0.31	< 1.1	1	< 24	< 0.17	< 0.89	< 0.82	< 2.2	< 0.18	< 0.6	32	< 12	< 0.49	299.0	11.8	< 0.058	8.80	93.7	< 2.4	< 0.38	0.62	< 0.055
Percentage of analyses > LOD					7	7	50	36	64.3	50	57	43	0	0	100	0	0	100	100	50	100	100	0	0	100	50

***Supplementary Table 6-4**: Lead isotope results obtained by SIMS on galena from the HYC, Myrtle and Walford Creek deposits and from the Caranbirini prospect.*

Deposit	Lens # (HYC)	Drillhole #	Depth (m)	Circle #	Analyse #	$^{206}Pb/^{204}Pb$ standard corrected	Error (2σ)	$^{207}Pb/^{204}Pb$ standard corrected	Error (2σ)	$^{208}Pb/^{204}Pb$ standard corrected	Error (2σ)
HYC	Lens 7	MRM-2012-3	164.6		1	16.146	0.011	15.449	0.011	35.853	0.235
HYC	Lens 7	MRM-2012-3	164.6		2	16.177	0.008	15.495	0.009	35.423	0.381
HYC	Lens 7	MRM-2012-3	164.6		3	16.184	0.011	15.507	0.011	35.622	0.363
HYC	Lens 7	MRM-2012-3	164.6		4	16.215	0.025	15.549	0.026	35.747	0.264
HYC	Lens 7	MRM-2012-3	164.6		5	16.108	0.017	15.413	0.018	35.569	0.128
							Standard		Standard		Standard
					Minimum	16.108	deviation	15.449	deviation	35.423	deviation
					Mean	16.166	0.040	15.482	0.053	35.643	0.165
					Maximum	16.215		15.549		35.853	
HYC	Lens 5	E5-1		C2	1	16.205	0.004	15.549	0.004	36.104	0.221
HYC	Lens 5	E5-1		C2	2	16.214	0.004	15.562	0.004	36.344	0.411
HYC	Lens 5	E5-1		C2	3	16.215	0.004	15.565	0.004	36.045	0.101
HYC	Lens 5	E5-1		C2	4	16.177	0.007	15.511	0.007	35.994	0.165
HYC	Lens 5	E5-1		C2	5	16.204	0.004	15.548	0.005	36.325	0.160
HYC	Lens 5	E5-1		C2	6	16.209	0.004	15.556	0.004	36.280	0.189
HYC	Lens 5	E5-1		C2	7	16.196	0.004	15.537	0.005	36.251	0.195
HYC	Lens 5	E5-1		C2	8	16.194	0.005	15.534	0.005	36.028	0.325
HYC	Lens 5	E5-1		C2	9	16.195	0.004	15.534	0.004	35.932	0.453
HYC	Lens 5	E5-1		C2	10	16.206	0.004	15.549	0.004	36.057	0.199
HYC	Lens 5	E5-1		C2	11	16.220	0.004	15.569	0.004	36.213	0.047
HYC	Lens 5	E5-1		C1	1	16.191	0.008	15.530	0.010	36.289	0.135
HYC	Lens 5	E5-1		C1	2	16.216	0.004	15.565	0.004	36.261	0.166
HYC	Lens 5	E5-1		C1	3	16.201	0.005	15.544	0.005	36.073	0.129
HYC	Lens 5	E5-1		C1	4	16.197	0.004	15.539	0.004	36.151	0.216
HYC	Lens 5	E5-1		C1	5	16.220	0.006	15.572	0.007	36.209	0.075
HYC	Lens 5	E5-1		C3	1	16.140	0.014	15.455	0.014	35.915	0.293
HYC	Lens 5	E5-1		C3	2	16.161	0.012	15.482	0.015	35.571	0.225
HYC	Lens 5	E5-1		C3	3	16.168	0.009	15.490	0.009	36.427	0.340
HYC	Lens 5	E5-1		C3	4	16.188	0.007	15.517	0.011	36.200	0.344
HYC	Lens 5	E5-1		C3	5	16.145	0.019	15.468	0.024	36.022	0.514
HYC	Lens 5	E5-1		C4	1	16.182	0.005	15.515	0.005	36.101	0.418
HYC	Lens 5	E5-1		C4	2	16.170	0.004	15.497	0.004	36.067	0.614
HYC	Lens 5	E5-1		C4	3	16.217	0.004	15.568	0.004	36.265	0.153
HYC	Lens 5	E5-1		C4	4	16.185	0.005	15.523	0.005	36.168	0.171
HYC	Lens 5	E5-1		C5	1	16.189	0.006	15.528	0.007	35.988	0.155
HYC	Lens 5	E5-1		C6	2	16.201	0.004	15.546	0.005	36.107	0.163
HYC	Lens 5	E5-1		C7	1	16.200	0.004	15.543	0.004	36.217	0.219
HYC	Lens 5	E5-1		C7	2	16.209	0.004	15.555	0.004	36.290	0.168
HYC	Lens 5	E5-1		C8	1	16.157	0.006	15.478	0.008	36.292	0.493
HYC	Lens 5	E5-1		C8	2	16.171	0.006	15.503	0.006	35.943	0.151
							Standard		Standard		Standard
					Minimum	16.140	deviation	15.455	deviation	35.571	deviation
					Mean	16.192	0.022	15.530	0.032	36.133	0.170
					Maximum	16.220		15.572		36.427	
HYC	Lens 4	MRM-2012-3	176.2	C1	1	16.161	0.019	15.476	0.018	35.946	0.177
HYC	Lens 4	MRM-2012-3	176.2	C1	2	16.192	0.005	15.529	0.006	35.907	0.320
HYC	Lens 4	MRM-2012-3	176.2	C1	3	16.205	0.004	15.548	0.004	36.098	0.125
HYC	Lens 4	MRM-2012-3	176.2	C2	1	16.172	0.006	15.504	0.006	36.111	0.103
HYC	Lens 4	MRM-2012-3	176.2	C2	2	16.155	0.010	15.479	0.009	35.799	0.141
HYC	Lens 4	MRM-2012-3	176.2	C2	3	16.190	0.005	15.531	0.006	36.332	0.258
HYC	Lens 4	MRM-2012-3	176.2	C2	4	16.193	0.006	15.533	0.006	36.313	0.478
HYC	Lens 4	MRM-2012-3	176.2	C3	1	16.170	0.006	15.496	0.007	35.861	0.107
HYC	Lens 4	MRM-2012-3	176.2	C3	2	16.195	0.005	15.536	0.005	35.897	0.177
HYC	Lens 4	MRM-2012-3	176.2	C4	1	16.195	0.004	15.536	0.005	36.188	0.123
HYC	Lens 4	MRM-2012-3	176.2	C4	2	16.184	0.006	15.519	0.007	36.194	0.262
HYC	Lens 4	MRM-2012-3	176.2	C4	3	16.191	0.004	15.534	0.004	36.044	0.186
HYC	Lens 4	MRM-2012-3	176.2	C4	4	16.184	0.005	15.520	0.005	36.204	0.178
HYC	Lens 4	MRM-2012-3	176.2	C5	1	16.207	0.004	15.554	0.004	36.059	0.099
HYC	Lens 4	MRM-2012-3	176.2	C6	1	16.188	0.006	15.527	0.007	36.159	0.203
HYC	Lens 4	MRM-2012-3	176.2	C7	1	16.210	0.004	15.557	0.004	36.345	0.152
HYC	Lens 4	MRM-2012-3	176.2	C7	2	16.177	0.005	15.514	0.006	35.839	0.210
							Standard		Standard		Standard
					Minimum	16.155	deviation	15.476	deviation	35.799	deviation
					Mean	16.186	0.015	15.523	0.023	36.076	0.177
					Maximum	16.210		15.557		36.345	
HYC	Lens 3	MRM-2012-3	191	C1	1	16.182	0.005	15.517	0.006	36.072	0.311
HYC	Lens 3	MRM-2012-3	191	C1	2	16.194	0.004	15.536	0.004	35.841	0.363
HYC	Lens 3	MRM-2012-3	191	C1	3	16.215	0.004	15.564	0.003	36.145	0.087
HYC	Lens 3	MRM-2012-3	191	C1	4	16.200	0.005	15.543	0.005	36.249	0.262
HYC	Lens 3	MRM-2012-3	191	C1	5	16.199	0.005	15.540	0.005	36.349	0.231

&&

Deposit	Lens # (HYC)	Drillhole #	Depth (m)	Circle #	Analyse #	$^{206}Pb/^{204}Pb$ standard corrected	Error (2σ)	$^{207}Pb/^{204}Pb$ standard corrected	Error (2σ)	$^{208}Pb/^{204}Pb$ standard corrected	Error (2σ)
HYC	Lens 3	MRM-2012-3	191	C1	6	16.202	0.004	15.545	0.004	36.088	0.072
HYC	Lens 3	MRM-2012-3	191	C2	1	16.199	0.007	15.540	0.009	35.803	0.250
HYC	Lens 3	MRM-2012-3	191	C2	2	16.203	0.005	15.547	0.004	35.995	0.327
HYC	Lens 3	MRM-2012-3	191	C3	1	16.197	0.004	15.541	0.004	36.157	0.190
HYC	Lens 3	MRM-2012-3	191	C3	2	16.190	0.004	15.526	0.004	36.383	0.203
HYC	Lens 3	MRM-2012-3	191	C4	1	16.199	0.006	15.542	0.006	36.007	0.244
HYC	Lens 3	MRM-2012-3	191	C4	2	16.197	0.005	15.537	0.005	36.091	0.207
HYC	Lens 3	MRM-2012-3	195.9A	1	1	16.209	0.005	15.557	0.006	36.184	0.280
HYC	Lens 3	MRM-2012-3	195.9A	1	2	16.155	0.007	15.481	0.006	35.795	0.207
HYC	Lens 3	MRM-2012-3	195.9A	1	3	16.174	0.007	15.508	0.008	36.111	0.128
HYC	Lens 3	MRM-2012-3	195.9A	2	1	16.137	0.008	15.454	0.007	35.803	0.204
HYC	Lens 3	MRM-2012-3	195.9A	2	2	16.156	0.006	15.472	0.006	35.880	0.149
HYC	Lens 3	MRM-2012-3	195.9A	3	1	16.190	0.005	15.526	0.006	35.924	0.629
HYC	Lens 3	MRM-2012-3	195.9A	3	2	16.200	0.005	15.543	0.006	36.111	0.329
HYC	Lens 3	MRM-2012-3	195.9A	3	3	16.204	0.006	15.549	0.007	36.093	0.330
HYC	Lens 3	MRM-2012-3	195.9A	4	1	16.184	0.006	15.520	0.005	36.032	0.215
HYC	Lens 3	MRM-2012-3	195.9A	4	2	16.210	0.004	15.556	0.004	36.288	0.247
HYC	Lens 3	MRM-2012-3	195.9A	5	1	16.137	0.009	15.445	0.009	35.604	0.064
HYC	Lens 3	MRM-2012-3	195.9A	5	2	16.200	0.004	15.543	0.004	36.162	0.360
HYC	Lens 3	MRM-2012-3	195.9A	6	1	16.143	0.010	15.465	0.010	35.800	0.082
HYC	Lens 3	MRM-2012-3	195.9A	6	2	16.185	0.005	15.520	0.005	36.164	0.256
HYC	Lens 3	MRM-2012-3	195.9A	7	1	16.193	0.006	15.531	0.006	36.372	0.356
HYC	Lens 3	MRM-2012-3	195.9A	7	2	16.206	0.005	15.551	0.006	36.220	0.254
HYC	Lens 3	MRM-2012-3	195.9B	1	1	16.208	0.004	15.552	0.004	36.178	0.241
HYC	Lens 3	MRM-2012-3	195.9B	2	2	16.205	0.005	15.548	0.005	36.269	0.268
HYC	Lens 3	MRM-2012-3	195.9B	1	1	16.207	0.004	15.554	0.004	36.222	0.213
HYC	Lens 3	MRM-2012-3	195.9B	2	2	16.192	0.006	15.529	0.005	36.091	0.335
HYC	Lens 3	MRM-2012-3	195.9B	1	1	16.218	0.004	15.568	0.004	36.292	0.148
HYC	Lens 3	MRM-2012-3	195.9B	1	1	16.208	0.004	15.553	0.005	36.146	0.154
							Standard		Standard		Standard
					Minimum	16.137	deviation	15.445	deviation	35.604	deviation
					Mean	16.191	0.022	15.530	0.031	36.086	0.188
					Maximum	16.218		15.568		36.383	
HYC	Lens 2	E11-1		C1	1	16.169	0.006	15.502	0.005	35.902	0.171
HYC	Lens 2	E11-1		C1	2	16.131	0.010	15.454	0.009	36.021	0.229
HYC	Lens 2	E11-1		C1	3	16.179	0.004	15.516	0.005	36.087	0.202
HYC	Lens 2	E11-1		C1	4	16.167	0.005	15.495	0.005	36.030	0.223
HYC	Lens 2	E11-1		C1	5	16.185	0.005	15.525	0.005	36.125	0.125
HYC	Lens 2	E11-1		C1	6	16.159	0.006	15.487	0.005	36.005	0.137
HYC	Lens 2	E11-1		C1	7	16.198	0.013	15.512	0.012	35.965	0.127
HYC	Lens 2	E11-1		C1	8	16.184	0.005	15.524	0.006	36.059	0.278
HYC	Lens 2	E11-1		C1	9	16.184	0.004	15.521	0.004	35.948	0.165
HYC	Lens 2	E11-1		C1	10	16.146	0.006	15.465	0.006	36.045	0.490
HYC	Lens 2	E11-1		C1	11	16.157	0.007	15.479	0.007	36.097	0.153
HYC	Lens 2	E11-1		C1	12	16.137	0.008	15.448	0.008	35.787	0.120
HYC	Lens 2	E11-1		C1	13	16.159	0.005	15.484	0.005	35.904	0.139
HYC	Lens 2	E11-1		C1	14	16.156	0.005	15.483	0.005	35.948	0.166
HYC	Lens 2	E11-1		C1	15	16.170	0.005	15.497	0.005	35.928	0.174
HYC	Lens 2	E11-1		C5	1	16.167	0.007	15.497	0.006	35.832	0.264
HYC	Lens 2	E11-1		C5	2	16.162	0.007	15.495	0.006	36.110	0.402
HYC	Lens 2	E11-1		C5	3	16.170	0.009	15.498	0.012	35.812	0.266
HYC	Lens 2	E11-1		C5	4	16.156	0.007	15.484	0.007	35.964	0.250
HYC	Lens 2	E11-1		C5	5	16.147	0.006	15.470	0.006	35.849	0.322
HYC	Lens 2	E11-1		C5	6	16.180	0.005	15.518	0.005	36.163	0.247
HYC	Lens 2	E11-1		C5	7	16.170	0.005	15.505	0.005	35.966	0.108
HYC	Lens 2	E11-1		C5	8	16.149	0.010	15.463	0.010	35.786	0.065
HYC	Lens 2	E11-1		C5	9	16.157	0.007	15.487	0.008	35.854	0.168
HYC	Lens 2	E11-1		C5	10	16.170	0.005	15.504	0.005	36.102	0.233
HYC	Lens 2	E11-1		C5	11	16.142	0.009	15.451	0.008	35.697	0.100
HYC	Lens 2	E11-1		C5	12	16.131	0.009	15.448	0.009	35.880	0.173
HYC	Lens 2	E11-1		C5	13	16.175	0.006	15.509	0.006	36.158	0.210
HYC	Lens 2	E11-1		C5	14	16.156	0.006	15.484	0.007	35.884	0.128
HYC	Lens 2	E11-1		C5	15	16.173	0.006	15.510	0.007	35.957	0.221
HYC	Lens 2	E11-1		C5	16	16.157	0.007	15.475	0.007	35.924	0.097
HYC	Lens 2	E11-1		C5	17	16.147	0.006	15.468	0.006	35.885	0.410
HYC	Lens 2	E11-1		C5	18	16.164	0.006	15.494	0.006	36.003	0.382
HYC	Lens 2	E11-1		C5	19	16.140	0.007	15.458	0.007	35.843	0.190
HYC	Lens 2	E11-1		C5	20	16.194	0.004	15.534	0.004	36.085	0.064
HYC	Lens 2	E11-1		C6	1	16.157	0.007	15.485	0.008	35.735	0.214
HYC	Lens 2	E11-1		C6	2	16.180	0.006	15.508	0.008	35.834	0.278
HYC	Lens 2	E11-1		C6	3	16.180	0.005	15.518	0.007	35.926	0.177
HYC	Lens 2	E11-1		C6	4	16.153	0.006	15.480	0.007	35.849	0.231

Deposit	Lens # (HYC)	Drillhole #	Depth (m)	Circle #	Analyse #	$^{206}Pb/^{204}Pb$ standard corrected	Error (2σ)	$^{207}Pb/^{204}Pb$ standard corrected	Error (2σ)	$^{208}Pb/^{204}Pb$ standard corrected	Error (2σ)
HYC	Lens 2	E11-1		C6	5	16.165	0.006	15.498	0.005	35.940	0.380
HYC	Lens 2	E11-1		C6	6	16.140	0.008	15.461	0.008	36.139	0.332
HYC	Lens 2	E11-1		C6	7	16.177	0.004	15.508	0.004	36.225	0.352
HYC	Lens 2	E11-1		C6	8	16.192	0.004	15.531	0.004	36.102	0.093
HYC	Lens 2	E11-1		C6	9	16.132	0.011	15.444	0.010	35.678	0.103
HYC	Lens 2	E11-1		C6	10	16.152	0.006	15.475	0.005	35.942	0.191
HYC	Lens 2	E11-1		C6	11	16.162	0.007	15.486	0.007	36.001	0.150
HYC	Lens 2	E11-1		C6	12	16.162	0.006	15.488	0.006	35.788	0.156
HYC	Lens 2	E11-1		C6	13	16.191	0.004	15.529	0.004	36.111	0.110
HYC	Lens 2	E11-1		C6	14	16.171	0.005	15.508	0.006	35.995	0.199
HYC	Lens 2	E11-1		C6	15	16.165	0.004	15.491	0.004	36.012	0.276
HYC	Lens 2	E11-1		C6	16	16.163	0.005	15.484	0.005	35.801	0.175
HYC	Lens 2	E11-1		C6	17	16.184	0.005	15.522	0.005	36.042	0.183
HYC	Lens 2	E11-1		C6	18	16.148	0.005	15.471	0.006	35.919	0.086
HYC	Lens 2	E11-1		C6	19	16.137	0.008	15.468	0.008	35.817	0.348
HYC	Lens 2	E11-1		C6	20	16.182	0.007	15.517	0.006	36.067	0.098
							Standard		Standard		Standard
					Minimum	16.132	deviation	15.444	deviation	35.678	deviation
					Mean	16.165	0.018	15.494	0.024	35.946	0.146
					Maximum	16.192		15.531		36.225	
HYC	Lens 0	MRM-2012-3	209.7	C1	1	16.189	0.005	15.531	0.004	36.114	0.191
HYC	Lens 0	MRM-2012-3	209.7	C2	1	16.180	0.008	15.521	0.010	36.030	0.165
HYC	Lens 0	MRM-2012-3	209.7	C2	2	16.201	0.005	15.547	0.005	36.057	0.282
HYC	Lens 0	MRM-2012-3	209.7	C2	3	16.197	0.005	15.543	0.005	35.940	0.326
HYC	Lens 0	MRM-2012-3	209.7	C2	4	16.207	0.004	15.556	0.005	36.572	0.394
HYC	Lens 0	MRM-2012-3	209.7	C2	5	16.201	0.004	15.548	0.004	36.158	0.168
HYC	Lens 0	MRM-2012-3	209.7	C3	1	16.209	0.004	15.558	0.004	36.187	0.145
HYC	Lens 0	MRM-2012-3	209.7	C3	2	16.202	0.004	15.550	0.003	36.162	0.235
HYC	Lens 0	MRM-2012-3	209.7	C4	1	16.179	0.005	15.514	0.005	35.823	0.615
HYC	Lens 0	MRM-2012-3	209.7	C5	1	16.176	0.008	15.507	0.011	36.033	0.208
HYC	Lens 0	MRM-2012-3	209.7	C5	2	16.165	0.005	15.493	0.004	36.126	0.213
							Standard		Standard		Standard
					Minimum	16.165	deviation	15.493	deviation	35.823	deviation
					Mean	16.191	0.014	15.533	0.022	36.109	0.187
					Maximum	16.209		15.558		36.572	
Myrtle		MY16	177.5		1	16.131	0.009	15.446	0.009	35.775	0.033
Myrtle		MY16	177.5		2	16.129	0.007	15.444	0.008	35.784	0.022
Myrtle		MY16	177.5		3	16.121	0.007	15.434	0.007	35.769	0.028
Myrtle		MY16	177.5		4	16.133	0.009	15.446	0.010	35.804	0.026
Myrtle		MY16	177.5		5	16.121	0.005	15.434	0.005	35.768	0.026
Myrtle		MY16	177.5		6	16.129	0.007	15.442	0.007	35.772	0.029
Myrtle		MY16	177.5		7	16.130	0.008	15.444	0.008	35.760	0.032
Myrtle		MY16	177.5		8	16.130	0.006	15.443	0.006	35.770	0.024
Myrtle		MY16	177.5		9	16.124	0.007	15.438	0.008	35.771	0.027
Myrtle		MY16	177.5		10	16.132	0.008	15.445	0.008	35.808	0.037
Myrtle		MY16	177.5		11	16.155	0.008	15.457	0.008	35.843	0.048
Myrtle		MY16	177.5		12	16.188	0.034	15.449	0.008	35.755	0.122
Myrtle		MY16	177.5		13	16.140	0.009	15.451	0.009	35.796	0.035
Myrtle		MY16	177.5		14	16.139	0.007	15.449	0.007	35.799	0.016
Myrtle		MY16	177.5		15	16.136	0.008	15.446	0.007	35.801	0.029
Myrtle		MY16	177.5		16	16.131	0.007	15.442	0.008	35.792	0.024
Myrtle		MY16	177.5		17	16.129	0.008	15.441	0.008	35.767	0.025
Myrtle		MY16	177.5		18	16.134	0.006	15.446	0.007	35.784	0.037
Myrtle		MY16	177.5		19	16.134	0.006	15.448	0.007	35.843	0.050
Myrtle		MY16	177.5		20	16.125	0.008	15.440	0.008	35.763	0.028
Myrtle		MY16	177.5		21	16.134	0.008	15.444	0.009	35.742	0.052
Myrtle		MY16	177.5		22	16.119	0.006	15.433	0.006	35.759	0.027
Myrtle		MY16	177.5		23	16.120	0.007	15.433	0.007	35.758	0.035
Myrtle		MY16	177.5		24	16.130	0.008	15.442	0.009	35.772	0.027
Myrtle		MY16	177.5		25	16.131	0.006	15.445	0.006	35.761	0.028
Myrtle		MY16	177.5		26	16.128	0.007	15.443	0.007	35.782	0.026
Myrtle		MY16	177.5		27	16.144	0.009	15.452	0.007	35.846	0.026
Myrtle		MY16	177.5		28	16.128	0.008	15.440	0.008	35.772	0.043
Myrtle		MY16	177.5		29	16.129	0.006	15.442	0.006	35.768	0.030
Myrtle		MY16	177.5		30	16.129	0.007	15.444	0.007	35.783	0.021
Myrtle		MY16	177.5		31	16.160	0.011	15.456	0.010	35.857	0.063
Myrtle		MY16	177.5		32	16.126	0.006	15.440	0.006	35.757	0.061
Myrtle		MY16	177.5		33	16.129	0.007	15.438	0.008	35.762	0.022
							Standard		Standard		Standard
					Minimum	16.119	deviation	15.433	deviation	35.742	deviation
					Mean	16.133	0.013	15.444	0.006	35.783	0.029
					Maximum	16.188		15.457		35.857	

Deposit	Lens # (HYC)	Drillhole #	Depth (m)	Circle #	Analyse #	$^{206}Pb/^{204}Pb$ standard corrected	Error (2σ)	$^{207}Pb/^{204}Pb$ standard corrected	Error (2σ)	$^{208}Pb/^{204}Pb$ standard corrected	Error (2σ)
Myrtle		MY16	195.9		101	16.188	0.0043	15.529	0.0052	36.423	0.1459
Myrtle		MY16	195.9		102	16.180	0.0058	15.517	0.0067	36.378	0.2905
Myrtle		MY16	195.9		103	16.164	0.0103	15.499	0.0147	36.186	0.6241
Myrtle		MY16	195.9		104	16.131	0.0127	15.448	0.0170	35.811	0.6513
Myrtle		MY16	195.9		105	16.100	0.0066	15.400	0.0067	35.587	0.0940
Myrtle		MY16	195.9		106	16.124	0.0175	15.449	0.0218	36.047	0.4361
Myrtle		MY16	195.9		107	16.167	0.0230	15.505	0.0303	36.097	0.3123
Myrtle		MY16	195.9		108	16.136	0.0118	15.466	0.0158	36.145	0.5206
Myrtle		MY16	195.9		109	16.055	0.0082	15.356	0.0061	35.686	0.1843
Myrtle		MY16	195.9		110	16.139	0.0144	15.473	0.0206	35.918	0.5730
Myrtle		MY16	195.9		111	16.133	0.0090	15.458	0.0107	35.955	0.3495
							Standard		Standard		Standard
					Minimum	16.055	deviation	15.356	deviation	35.587	deviation
					Mean	16.138	0.038	15.464	0.051	36.021	0.264
					Maximum	16.188		15.529		36.423	
Myrtle		MY16	197.7		1	16.195	0.0152	15.531	0.0139	36.248	0.1689
Myrtle		MY16	197.7		2	16.226	0.0097	15.551	0.0098	36.529	0.5209
Myrtle		MY16	197.7		3	16.205	0.0281	15.528	0.0345	36.877	0.9970
Myrtle		MY16	197.7		4	16.229	0.0168	15.557	0.0199	36.970	0.9454
Myrtle		MY16	197.7		5	16.189	0.0155	15.512	0.0181	36.231	0.5248
Myrtle		MY16	197.7		6	16.193	0.0049	15.513	0.0062	36.149	0.2368
Myrtle		MY16	197.7		7	16.194	0.0042	15.518	0.0050	36.102	0.2632
Myrtle		MY16	197.7		8	16.198	0.0069	15.521	0.0081	36.209	0.3303
Myrtle		MY16	197.7		9	16.194	0.0048	15.519	0.0058	36.135	0.1721
Myrtle		MY16	197.7		10	16.205	0.0056	15.532	0.0075	36.526	0.2129
Myrtle		MY16	197.7		11	16.118	0.0055	15.434	0.0046	35.675	0.1090
Myrtle		MY16	197.7		12	16.130	0.0084	15.445	0.0091	35.617	0.2324
Myrtle		MY16	197.7		13	16.114	0.0068	15.426	0.0067	35.876	0.1438
Myrtle		MY16	197.7		14	16.135	0.0056	15.457	0.0056	35.831	0.0890
							Standard		Standard		Standard
					Minimum	16.114	deviation	15.426	deviation	35.617	deviation
					Mean	16.180	0.039	15.503	0.043	36.213	0.406
					Maximum	16.229		15.557		36.970	
Myrtle		MY16	205.3	C3	1	16.171	0.006	15.509	0.007	35.922	0.122
Myrtle		MY16	205.3	C3	2	16.215	0.005	15.567	0.005	36.164	0.107
Myrtle		MY16	205.3	C3	3	16.178	0.009	15.467	0.008	35.761	0.312
Myrtle		MY16	205.3	C3	4	16.155	0.012	15.480	0.012	36.180	0.675
Myrtle		MY16	205.3	C2	1	16.122	0.008	15.443	0.007	35.765	0.030
Myrtle		MY16	205.3	C2	2	16.123	0.008	15.448	0.010	35.715	0.188
Myrtle		MY16	205.3	C2	3	16.121	0.006	15.440	0.007	35.759	0.026
Myrtle		MY16	205.3	C2	4	16.131	0.006	15.458	0.006	35.656	0.176
Myrtle		MY16	205.3	C1	1	16.182	0.005	15.532	0.005	36.090	0.147
Myrtle		MY16	205.3	C1	2	16.193	0.004	15.540	0.004	36.183	0.248
Myrtle		MY16	205.3	C1	3	16.127	0.007	15.451	0.006	35.754	0.061
Myrtle		MY16	205.3	C1	4	16.207	0.007	15.523	0.007	36.112	0.118
Myrtle		MY16	205.3	C1	5	16.196	0.004	15.540	0.004	36.128	0.073
Myrtle		MY16	205.3	C1	6	16.192	0.008	15.538	0.008	36.356	0.345
Myrtle		MY16	205.3	C1	7	16.187	0.006	15.533	0.005	36.137	0.343
							Standard		Standard		Standard
					Minimum	16.121	deviation	15.440	deviation	35.656	deviation
					Mean	16.167	0.034	15.498	0.044	35.979	0.224
					Maximum	16.215		15.567		36.356	
Caranbirini		DD82CA1	565		101	16.157	0.0049	15.437	0.0060	35.809	0.0375
Caranbirini		DD82CA1	565		102	16.163	0.0045	15.440	0.0050	35.810	0.0431
Caranbirini		DD82CA1	565		103	16.169	0.0065	15.446	0.0063	35.823	0.0404
Caranbirini		DD82CA1	565		104	16.162	0.0036	15.441	0.0042	35.785	0.0385
Caranbirini		DD82CA1	565		105	16.167	0.0041	15.441	0.0048	35.801	0.0440
Caranbirini		DD82CA1	565		106	16.165	0.0043	15.442	0.0050	35.822	0.0380
Caranbirini		DD82CA1	565		107	16.166	0.0048	15.437	0.0041	35.829	0.0505
Caranbirini		DD82CA1	565		108	16.157	0.0043	15.431	0.0046	35.793	0.0299
Caranbirini		DD82CA1	565		109	16.167	0.0054	15.439	0.0049	35.813	0.0643
Caranbirini		DD82CA1	565		110	16.166	0.0070	15.438	0.0068	35.816	0.0337
Caranbirini		DD82CA1	565		111	16.166	0.0062	15.436	0.0060	35.807	0.0576
Caranbirini		DD82CA1	565		112	16.164	0.0044	15.437	0.0050	35.811	0.0289
Caranbirini		DD82CA1	565		113	16.162	0.0043	15.436	0.0042	35.801	0.0280
Caranbirini		DD82CA1	565		114	16.168	0.0057	15.438	0.0053	35.817	0.0496
Caranbirini		DD82CA1	565		115	16.168	0.0046	15.439	0.0041	35.810	0.0347
Caranbirini		DD82CA1	565		116	16.170	0.0057	15.447	0.0048	35.798	0.0233
Caranbirini		DD82CA1	565		117	16.165	0.0038	15.438	0.0042	35.819	0.0374
							Standard		Standard		Standard
					Minimum	16.157	deviation	15.431	deviation	35.785	deviation
					Mean	16.165	0.004	15.439	0.004	35.810	0.011
					Maximum	16.170		15.447		35.829	

Deposit	Lens # (HYC)	Drillhole #	Depth (m)	Circle #	Analyse #	$^{206}Pb/^{204}Pb$ standard corrected	Error (2σ)	$^{207}Pb/^{204}Pb$ standard corrected	Error (2σ)	$^{208}Pb/^{204}Pb$ standard corrected	Error (2σ)
Caranbirini		DD82CA1	679-2		101	16.676	0.0079	15.532	0.0102	36.350	0.3435
Caranbirini		DD82CA1	679-2		102	16.649	0.0056	15.517	0.0067	36.141	0.0745
Caranbirini		DD82CA1	679-2		103	16.649	0.0048	15.542	0.0045	36.218	0.1334
Caranbirini		DD82CA1	679-2		104	16.638	0.0058	15.508	0.0054	36.157	0.0445
Caranbirini		DD82CA1	679-2		105	16.644	0.0047	15.514	0.0047	36.189	0.0390
Caranbirini		DD82CA1	679-2		106	16.645	0.0069	15.516	0.0077	36.187	0.0461
Caranbirini		DD82CA1	679-2		107	16.669	0.0061	15.523	0.0054	36.179	0.0432
Caranbirini		DD82CA1	679-2		108	16.678	0.0055	15.523	0.0062	36.188	0.0359
Caranbirini		DD82CA1	679-2		109	16.678	0.0054	15.523	0.0055	36.175	0.0446
Caranbirini		DD82CA1	679-2		110	16.671	0.0050	15.524	0.0061	36.108	0.1468
Caranbirini		DD82CA1	679-2		111	16.649	0.0051	15.524	0.0040	36.148	0.1259
Caranbirini		DD82CA1	679-2		112	16.697	0.0062	15.612	0.0123	36.725	0.1865
Caranbirini		DD82CA1	679-2		113	16.607	0.0107	15.491	0.0101	36.016	0.0953
Caranbirini		DD82CA1	679-2		114	16.675	0.0273	15.604	0.0396	36.606	0.4646
Caranbirini		DD82CA1	679-2		115	16.636	0.0116	15.512	0.0129	36.155	0.0351
Caranbirini		DD82CA1	679-2		116	16.612	0.0090	15.539	0.0106	36.332	0.0973
Caranbirini		DD82CA1	679-2		117	16.721	0.0061	15.541	0.0051	36.234	0.0396
Caranbirini		DD82CA1	679-2		118	16.660	0.0041	15.524	0.0039	36.172	0.0401
Caranbirini		DD82CA1	679-2		119	16.668	0.0049	15.525	0.0048	36.168	0.0323
Caranbirini		DD82CA1	679-2		120	16.663	0.0040	15.520	0.0042	36.143	0.0291
Caranbirini		DD82CA1	679-2		121	16.667	0.0038	15.529	0.0041	36.135	0.0404
Caranbirini		DD82CA1	679-2		122	16.668	0.0046	15.527	0.0047	36.193	0.0324
Caranbirini		DD82CA1	679-2		123	16.687	0.0082	15.547	0.0075	36.149	0.3304
Caranbirini		DD82CA1	679-2		124	16.645	0.0048	15.523	0.0049	36.174	0.0340
Caranbirini		DD82CA1	679-2		125	16.669	0.0053	15.530	0.0052	36.129	0.0792
Caranbirini		DD82CA1	679-2		126	16.681	0.0052	15.528	0.0067	36.204	0.0287
Caranbirini		DD82CA1	679-2		127	16.687	0.0052	15.523	0.0053	36.196	0.0460
Caranbirini		DD82CA1	679-2		128	16.676	0.0058	15.523	0.0051	36.264	0.1818
Caranbirini		DD82CA1	679-2		129	16.671	0.0071	15.530	0.0072	36.196	0.0566
Caranbirini		DD82CA1	679-2		130	16.673	0.0046	15.535	0.0041	36.192	0.0723
Caranbirini		DD82CA1	679-2		131	16.665	0.0055	15.532	0.0063	36.209	0.0315
Caranbirini		DD82CA1	679-2		132	16.674	0.0064	15.529	0.0066	36.185	0.0367
Caranbirini		DD82CA1	679-2		133	16.675	0.0044	15.530	0.0051	36.216	0.0236
Caranbirini		DD82CA1	679-2		134	16.665	0.0046	15.525	0.0046	36.203	0.0280
Caranbirini		DD82CA1	679-2		135	16.663	0.0049	15.525	0.0059	36.190	0.0272
Caranbirini		DD82CA1	679-2		136	16.674	0.0057	15.523	0.0051	36.223	0.0489
Caranbirini		DD82CA1	679-2		137	16.666	0.0048	15.516	0.0038	36.199	0.0356
Caranbirini		DD82CA1	679-2		138	16.659	0.0079	15.510	0.0083	36.179	0.0505
Caranbirini		DD82CA1	679-2		139	16.649	0.0062	15.513	0.0062	36.199	0.0359
Caranbirini		DD82CA1	679-2		140	16.646	0.0081	15.513	0.0076	36.200	0.0507
Caranbirini		DD82CA1	679-2		141	16.641	0.0058	15.519	0.0051	36.144	0.0733
Caranbirini		DD82CA1	679-2		142	16.645	0.0042	15.526	0.0046	36.220	0.2143
Caranbirini		DD82CA1	679-2		143	16.639	0.0063	15.523	0.0052	36.189	0.0490
Caranbirini		DD82CA1	679-2		144	16.632	0.0076	15.520	0.0067	36.138	0.0411
Caranbirini		DD82CA1	679-2		145	16.626	0.0062	15.512	0.0050	36.158	0.0360
							Standard		Standard		Standard
					Minimum	16.607	deviation	15.491	deviation	36.016	deviation
					Mean	16.661	0.022	15.527	0.020	36.206	0.114
					Maximum	16.721		15.612		36.725	
Caranbirini		DD82CA1	734.9		101	16.209	0.0077	15.431	0.0076	35.806	0.0772
Caranbirini		DD82CA1	734.9		102	16.222	0.0040	15.441	0.0052	35.826	0.0778
Caranbirini		DD82CA1	734.9		103	16.234	0.0068	15.445	0.0075	35.723	0.2258
Caranbirini		DD82CA1	734.9		104	16.236	0.0037	15.455	0.0041	35.863	0.0343
Caranbirini		DD82CA1	734.9		105	16.239	0.0049	15.455	0.0056	35.878	0.0655
Caranbirini		DD82CA1	734.9		106	16.244	0.0038	15.466	0.0046	35.815	0.0632
Caranbirini		DD82CA1	734.9		107	16.241	0.0041	15.460	0.0043	35.897	0.0336
Caranbirini		DD82CA1	734.9		108	16.240	0.0047	15.460	0.0046	35.876	0.0244
Caranbirini		DD82CA1	734.9		109	16.242	0.0055	15.462	0.0050	35.914	0.0453
Caranbirini		DD82CA1	734.9		110	16.250	0.0044	15.462	0.0050	35.910	0.0313
Caranbirini		DD82CA1	734.9		111	16.249	0.0064	15.466	0.0066	35.921	0.1147
Caranbirini		DD82CA1	734.9		112	16.251	0.0055	15.463	0.0048	35.885	0.0356
							Standard		Standard		Standard
					Minimum	16.209	deviation	15.431	deviation	35.723	deviation
					Mean	16.238	0.012	15.456	0.011	35.860	0.058
					Maximum	16.251		15.466		35.921	
Walford Creek		WFDD238	140.5		201	16.131	0.0076	15.438	0.0096	35.772	0.1817
Walford Creek		WFDD238	140.5		202	16.210	0.0087	15.443	0.0052	35.836	0.0762
Walford Creek		WFDD238	140.5		203	16.230	0.0107	15.443	0.0113	35.774	0.0807
Walford Creek		WFDD238	140.5		204	16.108	0.0066	15.402	0.0101	35.664	0.1621
Walford Creek		WFDD238	140.5		205	16.090	0.0075	15.410	0.0068	35.985	0.4178
Walford Creek		WFDD238	140.5		206	16.262	0.0061	15.452	0.0061	35.879	0.1151

Deposit	Lens # (HYC)	Drillhole #	Depth (m)	Circle #	Analyse #	$^{206}Pb/^{204}Pb$ standard corrected	Error (2σ)	$^{207}Pb/^{204}Pb$ standard corrected	Error (2σ)	$^{208}Pb/^{204}Pb$ standard corrected	Error (2σ)
Walford Creek		WFDD238	140.5		207	16.271	0.0058	15.454	0.0053	35.921	0.0403
Walford Creek		WFDD238	140.5		208	16.218	0.0056	15.451	0.0040	35.842	0.1220
Walford Creek		WFDD238	140.5		209	16.088	0.0061	15.408	0.0055	35.752	0.3932
Walford Creek		WFDD238	140.5		210	16.270	0.0057	15.458	0.0041	35.946	0.0787
Walford Creek		WFDD238	140.5		211	16.355	0.0038	15.466	0.0041	35.997	0.0201
Walford Creek		WFDD238	140.5		212	16.319	0.0075	15.468	0.0073	36.001	0.1811
Walford Creek		WFDD238	140.5		213	16.617	0.0206	15.526	0.0056	36.221	0.0329
Walford Creek		WFDD238	140.5		214	16.554	0.0276	15.507	0.0056	36.198	0.0414
Walford Creek		WFDD238	140.5		215	16.395	0.0062	15.480	0.0041	36.040	0.0436
Walford Creek		WFDD238	140.5		216	16.266	0.0045	15.464	0.0054	35.967	0.1004
Walford Creek		WFDD238	140.5		217	16.766	0.0052	15.542	0.0047	36.407	0.0283
Walford Creek		WFDD238	140.5		218	16.663	0.0094	15.518	0.0054	36.305	0.0666
Walford Creek		WFDD238	140.5		219	16.802	0.0058	15.541	0.0043	36.437	0.0280
Walford Creek		WFDD238	140.5		220	16.615	0.0041	15.521	0.0043	36.285	0.0457
Walford Creek		WFDD238	140.5		221	16.614	0.0047	15.513	0.0043	36.245	0.0522
Walford Creek		WFDD238	140.5		222	16.575	0.0332	15.507	0.0061	36.180	0.0434
Walford Creek		WFDD238	140.5		223	16.307	0.0146	15.468	0.0040	35.923	0.0594
Walford Creek		WFDD238	140.5		224	16.339	0.0061	15.464	0.0062	35.917	0.1071
							Standard		Standard		Standard
					Minimum	16.088	deviation	15.402	deviation	35.664	deviation
					Mean	16.378	0.217	15.473	0.041	36.021	0.216
					Maximum	16.802		15.542		36.437	
Walford Creek		WFDD238	141		101	16.262	0.0049	15.454	0.0046	35.915	0.0437
Walford Creek		WFDD238	141		102	16.292	0.0048	15.460	0.0045	36.045	0.0896
Walford Creek		WFDD238	141		103	16.305	0.0073	15.456	0.0099	36.120	0.0488
Walford Creek		WFDD238	141		104	16.334	0.0049	15.493	0.0050	36.108	0.3620
Walford Creek		WFDD238	141		105	16.336	0.0053	15.471	0.0062	36.203	0.0970
Walford Creek		WFDD238	141		106	16.363	0.0040	15.481	0.0037	36.204	0.0468
Walford Creek		WFDD238	141		107	16.397	0.0078	15.524	0.0088	36.387	0.5177
Walford Creek		WFDD238	141		108	16.336	0.0055	15.470	0.0065	35.994	0.1330
Walford Creek		WFDD238	141		109	16.358	0.0064	15.502	0.0060	35.893	0.2484
Walford Creek		WFDD238	141		110	16.342	0.0069	15.490	0.0073	35.990	0.2614
Walford Creek		WFDD238	141		111	16.388	0.0041	15.537	0.0046	36.624	0.2529
Walford Creek		WFDD238	141		112	16.346	0.0100	15.521	0.0122	36.317	0.2331
Walford Creek		WFDD238	141		113	16.389	0.0094	15.529	0.0111	36.690	0.5662
Walford Creek		WFDD238	141		114	16.411	0.0079	15.565	0.0088	36.386	0.3671
Walford Creek		WFDD238	141		115	16.367	0.0107	15.513	0.0089	36.611	0.4851
Walford Creek		WFDD238	141		116	16.371	0.0058	15.508	0.0091	36.166	0.1888
Walford Creek		WFDD238	141		117	16.359	0.0151	15.497	0.0164	36.310	0.3876
Walford Creek		WFDD238	141		118	16.365	0.0079	15.500	0.0084	36.368	0.2825
Walford Creek		WFDD238	141		119	16.343	0.0053	15.477	0.0048	35.982	0.0722
Walford Creek		WFDD238	141		120	16.347	0.0064	15.488	0.0051	36.055	0.2186
Walford Creek		WFDD238	141		121	16.387	0.0083	15.545	0.0050	36.342	0.3157
Walford Creek		WFDD238	141		122	16.359	0.0076	15.498	0.0054	36.329	0.3924
Walford Creek		WFDD238	141		123	16.325	0.0057	15.475	0.0060	35.988	0.0357
Walford Creek		WFDD238	141		124	16.305	0.0073	15.473	0.0056	36.011	0.1231
Walford Creek		WFDD238	141		125	16.322	0.0062	15.466	0.0073	35.938	0.1461
Walford Creek		WFDD238	141		126	16.315	0.0189	15.523	0.0146	36.380	0.2522
Walford Creek		WFDD238	141		127	16.146	0.0071	15.439	0.0048	35.811	0.0657
Walford Creek		WFDD238	141		128	16.348	0.0049	15.496	0.0033	36.129	0.0758
Walford Creek		WFDD238	141		129	16.321	0.0046	15.474	0.0046	35.908	0.1122
Walford Creek		WFDD238	141		130	16.379	0.0077	15.538	0.0084	36.241	0.3085
Walford Creek		WFDD238	141		131	16.257	0.0067	15.454	0.0046	35.855	0.0542
Walford Creek		WFDD238	141		132	16.337	0.0052	15.516	0.0056	35.922	0.3269
Walford Creek		WFDD238	141		133	16.386	0.0039	15.563	0.0045	36.403	0.2018
Walford Creek		WFDD238	141		134	16.396	0.0041	15.566	0.0051	36.383	0.2236
Walford Creek		WFDD238	141		135	16.299	0.1199	15.479	0.1130	35.749	0.6269
Walford Creek		WFDD238	141		136	16.390	0.0069	15.561	0.0074	36.505	0.3611
Walford Creek		WFDD238	141		137	16.344	0.0101	15.493	0.0118	35.969	0.2847
Walford Creek		WFDD238	141		138	16.302	0.0101	15.492	0.0052	35.867	0.1603
Walford Creek		WFDD238	141		139	16.353	0.0046	15.513	0.0051	36.104	0.1569
Walford Creek		WFDD238	141		140	16.358	0.0098	15.504	0.0110	36.403	0.2883
Walford Creek		WFDD238	141		141	16.230	0.0081	15.460	0.0050	35.892	0.0914
Walford Creek		WFDD238	141		142	16.299	0.0323	15.530	0.0264	36.329	0.5984
Walford Creek		WFDD238	141		143	16.289	0.0057	15.459	0.0068	36.023	0.0928
Walford Creek		WFDD238	141		144	16.325	0.0121	15.503	0.0061	35.922	0.1900
Walford Creek		WFDD238	141		145	16.239	0.0892	15.449	0.0829	36.116	0.2681
Walford Creek		WFDD238	141		146	16.369	0.0081	15.572	0.0086	36.605	0.3313
							Standard		Standard		Standard
					Minimum	16.146	deviation	15.439	deviation	35.749	deviation
					Mean	16.335	0.051	15.500	0.035	36.163	0.243
					Maximum	16.411		15.572		36.690	

Deposit	Lens # (HYC)	Drillhole #	Depth (m)	Circle #	Analyse #	$^{206}Pb/^{204}Pb$ standard corrected	Error (2σ)	$^{207}Pb/^{204}Pb$ standard corrected	Error (2σ)	$^{208}Pb/^{204}Pb$ standard corrected	Error (2σ)
Walford Creek		WFDD266	110		1	16.387	0.0051	15.490	0.0056	36.044	0.0787
Walford Creek		WFDD266	110		2	16.408	0.0039	15.486	0.0037	36.067	0.0398
Walford Creek		WFDD266	110		3	16.433	0.0058	15.495	0.0050	36.094	0.0285
Walford Creek		WFDD266	110		4	16.448	0.0053	15.493	0.0046	36.116	0.0342
Walford Creek		WFDD266	110		5	16.469	0.0088	15.499	0.0053	36.136	0.0285
Walford Creek		WFDD266	110		6	16.395	0.0045	15.489	0.0043	36.045	0.0488
Walford Creek		WFDD266	110		7	16.386	0.0050	15.479	0.0058	36.036	0.0745
Walford Creek		WFDD266	110		8	16.391	0.0042	15.481	0.0042	36.039	0.0733
Walford Creek		WFDD266	110		9	16.387	0.0064	15.483	0.0072	36.063	0.0611
Walford Creek		WFDD266	110		10	16.510	0.0090	15.504	0.0052	36.167	0.0546
Walford Creek		WFDD266	110		11	16.432	0.0096	15.484	0.0074	35.928	0.4127
Walford Creek		WFDD266	110		12	16.500	0.0062	15.497	0.0048	36.142	0.0716
Walford Creek		WFDD266	110		13	16.400	0.0043	15.493	0.0046	36.034	0.0607
Walford Creek		WFDD266	110		14	16.397	0.0059	15.486	0.0060	36.069	0.0495
Walford Creek		WFDD266	110		15	16.399	0.0053	15.487	0.0053	36.179	0.1663
Walford Creek		WFDD266	110		16	16.397	0.0053	15.487	0.0053	36.086	0.0604
Walford Creek		WFDD266	110		17	16.654	0.0058	15.524	0.0058	36.301	0.0383
Walford Creek		WFDD266	110		18	16.724	0.0105	15.536	0.0054	36.362	0.0353
Walford Creek		WFDD266	110		19	16.437	0.0054	15.487	0.0060	35.948	0.0713
							Standard		Standard		Standard
					Minimum	16.386	deviation	15.479	deviation	35.928	deviation
					Mean	16.450	0.093	15.494	0.014	36.098	0.105
					Maximum	16.724		15.536		36.362	
Walford Creek		WFDD266	130.8		1	16.231	0.0085	15.461	0.0074	35.768	0.3745
Walford Creek		WFDD266	130.8		2	16.221	0.0049	15.444	0.0038	35.913	0.0610
Walford Creek		WFDD266	130.8		3	16.247	0.0045	15.463	0.0056	36.352	0.1941
Walford Creek		WFDD266	130.8		4	16.277	0.0056	15.470	0.0045	35.963	0.0521
Walford Creek		WFDD266	130.8		5	16.394	0.0158	15.469	0.0054	36.043	0.1047
Walford Creek		WFDD266	130.8		6	16.256	0.0045	15.458	0.0043	35.943	0.0707
Walford Creek		WFDD266	130.8		7	16.237	0.0044	15.464	0.0039	35.945	0.1357
Walford Creek		WFDD266	130.8		8	16.374	0.0542	15.529	0.0316	36.318	0.4271
Walford Creek		WFDD266	130.8		9	16.368	0.0388	15.505	0.0190	36.127	0.3757
Walford Creek		WFDD266	130.8		10	16.218	0.0066	15.458	0.0068	36.085	0.1387
Walford Creek		WFDD266	130.8		11	16.218	0.0053	15.461	0.0053	35.858	0.1468
Walford Creek		WFDD266	130.8		12	16.546	0.0181	15.498	0.0065	36.238	0.0589
Walford Creek		WFDD266	130.8		13	16.212	0.0069	15.456	0.0071	35.882	0.0918
Walford Creek		WFDD266	130.8		14	16.217	0.0055	15.464	0.0056	35.797	0.2291
Walford Creek		WFDD266	130.8		15	16.244	0.0109	15.461	0.0054	35.992	0.0971
							Standard		Standard		Standard
					Minimum	16.212	deviation	15.444	deviation	35.768	deviation
					Mean	16.284	0.095	15.471	0.022	36.015	0.179
					Maximum	16.546		15.529		36.352	
Walford Creek		WFDD266	271.4		101	16.701	0.0057	15.541	0.0063	36.346	0.0517
Walford Creek		WFDD266	271.4		102	16.713	0.0061	15.535	0.0060	36.365	0.0961
Walford Creek		WFDD266	271.4		103	16.700	0.0040	15.528	0.0050	36.330	0.0516
Walford Creek		WFDD266	271.4		104	16.703	0.0047	15.530	0.0044	36.368	0.0461
Walford Creek		WFDD266	271.4		105	16.725	0.0104	15.536	0.0049	36.393	0.0593
Walford Creek		WFDD266	271.4		106	16.738	0.0083	15.534	0.0060	36.380	0.0538
Walford Creek		WFDD266	271.4		107	16.728	0.0043	15.533	0.0044	36.365	0.0493
Walford Creek		WFDD266	271.4		108	16.737	0.0051	15.539	0.0048	36.399	0.0554
Walford Creek		WFDD266	271.4		109	16.732	0.0058	15.534	0.0054	36.374	0.0497
Walford Creek		WFDD266	271.4		110	16.736	0.0047	15.539	0.0055	36.386	0.0463
Walford Creek		WFDD266	271.4		111	16.751	0.0052	15.544	0.0051	36.426	0.0815
Walford Creek		WFDD266	271.4		112	16.748	0.0051	15.542	0.0047	36.405	0.0317
Walford Creek		WFDD266	271.4		113	16.735	0.0047	15.538	0.0045	36.372	0.0884
Walford Creek		WFDD266	271.4		114	16.737	0.0041	15.541	0.0038	36.398	0.0875
Walford Creek		WFDD266	271.4		115	16.737	0.0042	15.541	0.0044	36.368	0.0412
Walford Creek		WFDD266	271.4		116	16.734	0.0052	15.541	0.0060	36.372	0.0349
Walford Creek		WFDD266	271.4		117	16.735	0.0041	15.540	0.0040	36.391	0.0574
Walford Creek		WFDD266	271.4		118	16.741	0.0058	15.544	0.0051	36.404	0.0547
Walford Creek		WFDD266	271.4		119	16.740	0.0055	15.543	0.0050	36.406	0.0560
Walford Creek		WFDD266	271.4		120	16.735	0.0046	15.540	0.0053	36.380	0.0388
Walford Creek		WFDD266	271.4		121	16.738	0.0056	15.541	0.0056	36.392	0.0524
Walford Creek		WFDD266	271.4		122	16.744	0.0049	15.547	0.0047	36.383	0.0464
Walford Creek		WFDD266	271.4		123	16.738	0.0056	15.543	0.0061	36.413	0.0630
Walford Creek		WFDD266	271.4		124	16.760	0.0044	15.547	0.0052	36.400	0.0522
Walford Creek		WFDD266	271.4		125	16.744	0.0071	15.545	0.0072	36.402	0.0384
Walford Creek		WFDD266	271.4		126	16.749	0.0044	15.552	0.0046	36.411	0.0322
Walford Creek		WFDD266	271.4		127	16.742	0.0055	15.542	0.0045	36.402	0.0426
Walford Creek		WFDD266	271.4		128	16.815	0.0055	15.555	0.0051	36.472	0.0341
Walford Creek		WFDD266	271.4		129	16.788	0.0051	15.555	0.0049	36.436	0.0467

Deposit	Lens # (HYC)	Drillhole #	Depth (m)	Circle #	Analyse #	$^{206}Pb/^{204}Pb$ standard corrected	Error (2σ)	$^{207}Pb/^{204}Pb$ standard corrected	Error (2σ)	$^{208}Pb/^{204}Pb$ standard corrected	Error (2σ)
Walford Creek		WFDD266	271.4		130	16.820	0.0056	15.552	0.0048	36.457	0.0333
Walford Creek		WFDD266	271.4		131	16.781	0.0058	15.548	0.0060	36.466	0.0242
Walford Creek		WFDD266	271.4		132	16.787	0.0061	15.558	0.0051	36.460	0.0402
Walford Creek		WFDD266	271.4		133	16.793	0.0041	15.545	0.0041	36.452	0.0598
Walford Creek		WFDD266	271.4		134	16.710	0.0052	15.537	0.0048	36.370	0.0439
Walford Creek		WFDD266	271.4		135	16.724	0.0079	15.541	0.0065	36.381	0.0714
Walford Creek		WFDD266	271.4		136	16.727	0.0082	15.538	0.0048	36.356	0.0449
Walford Creek		WFDD266	271.4		137	16.706	0.0050	15.535	0.0057	36.493	0.0179
Walford Creek		WFDD266	271.4		138	16.649	0.0038	15.533	0.0043	36.297	0.0418
Walford Creek		WFDD266	271.4		139	16.760	0.0100	15.541	0.0062	36.477	0.0593
Walford Creek		WFDD266	271.4		140	16.724	0.0071	15.536	0.0041	36.381	0.0429
Walford Creek		WFDD266	271.4		141	16.793	0.0051	15.558	0.0059	36.432	0.0588
Walford Creek		WFDD266	271.4		142	16.837	0.0040	15.560	0.0039	36.460	0.0608
Walford Creek		WFDD266	271.4		143	16.768	0.0167	15.550	0.0045	36.455	0.0557
Walford Creek		WFDD266	271.4		144	16.775	0.0070	15.548	0.0054	36.450	0.0390
Walford Creek		WFDD266	271.4		145	16.791	0.0074	15.526	0.0060	36.382	0.0262
Walford Creek		WFDD266	271.4		146	16.811	0.0052	15.552	0.0044	36.490	0.0547
Walford Creek		WFDD266	271.4		147	16.833	0.0048	15.561	0.0046	36.497	0.0920
							Standard		Standard		Standard
					Minimum	16.649	deviation	15.526	deviation	36.297	deviation
					Mean	16.749	0.038	15.543	0.008	36.406	0.045
					Maximum	16.837		15.561		36.497	

Chapter 7. General discussion, conclusions, and perspectives

7.1. Multi-stage and long-lived mineralisation in the McArthur Basin

All the mineralizing event ages for the McArthur Basin, obtained from the literature and those acquired during this study, are reported in Figure 7-1. This compilation shows several episodes of U and Pb-Zn mineralisation. The oldest events are essentially equivalent to the onset of basin deposition (1815 Ma, Ahmad and Munson, 2013), whereas the most recent event is recorded at ca. 350 Ma in the Westmoreland area (see Chapter 3). It should be noted that there is an important contrast in preservation and/or remobilisation of the metals between the different deposits and prospects. At McArthur River the preservation is optimal; that is, it is not affected by younger events other than the synsedimentary/early diagenetic mineralisation. Late remobilisation ages (events) are recorded close to major faults, and these could be indicative of either a metal loss if fluids leached the metals, or a new style of mineralisation (vein-style). In uranium deposits of the Westmoreland area, the REE-patterns do not clearly witness multiple remobilisation of old uranium. In summary, the first major mineralising event is at ca. 1720–1680 Ma, followed by the 1650–1600 Ma event which affected both U and Pb-Zn mineralisation. Between 1400 and 350 Ma, each mineralising event is observed mainly at a single place within the basin. The major faults have been reactivated several times throughout the basin history.

7.2. Variation in mineralisation at basin scale

From a geochemical perspective, two mechanisms can lead to the metal zoning observed within the basin. The first mechanism occurs when the fluid carrying the metals undergoes a temperature drop, which results in a U solubility decrease, followed by the copper solubility, and finally by the Zn solubility. Alternatively, an oxidised fluid being reduced leads to a similar sequence of ordered uranium – copper – lead crystallisation. Both of the above scenarios can explain the zoning observed within the basin with respect to the hypothesis of a single fluid carrying the three metals. Increasing the reducing state can be accomplished by a mixing with a more reduced fluid, with minerals such as pyrite and organic-rich formations such as the Barney Creek Formation.

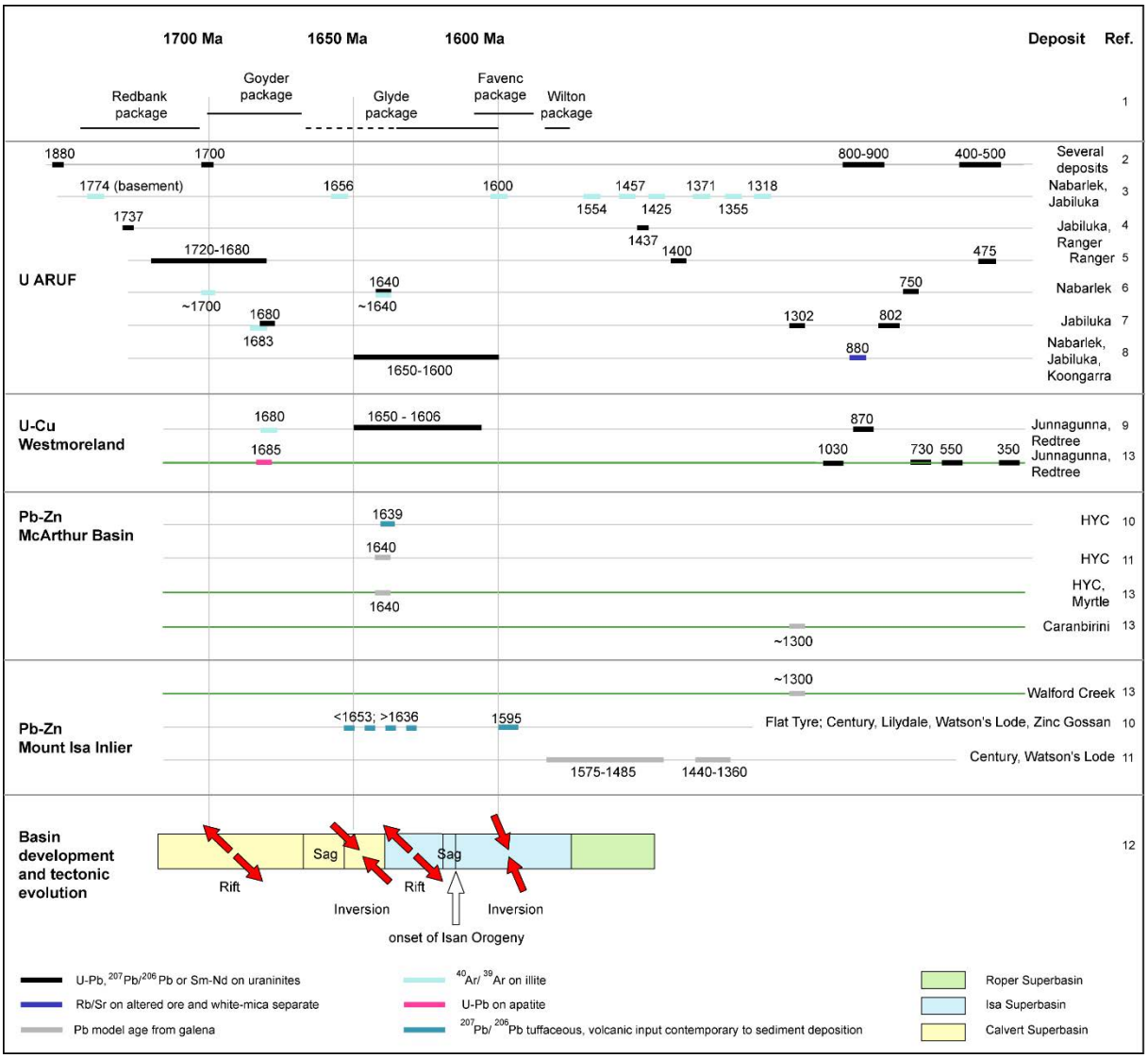

***Figure 7-1**: Synthesis of the geochronological data available in the McArthur Basin and in the unmetamorphosed part of Mount Isa Basin, from the literature and with new data acquired during this PhD. 1: Ahmad and Munson (2013). 2: Hills and Richards (1976). 3: Clauer et al. (2015). 4: Ludwig et al. (1987). 5: (Skirrow et al., 2016). 6: Polito et al. (2004). 7: Polito et al. (2005b). 8: Maas (1989). 9: Polito et al. (2005a). 10: Page and Sweet (1998); 11: Carr et al. (2001). 12: Gibson et al. (2017) ; 13 : (Gigon et al., in prep. for Mineralium Deposita and in prep. for GCA).*

In addition to the metal zoning, deposits of the same metal can be different from each other in terms of temperature and age at a basin scale. As documented in Chapter 3, uranium deposits in the northern and the southern parts of the basin were deposited from a distinct fluid(s) and/or under different physicochemical conditions, and mineralising stages occurred at various times. Considering the size of the basin, this is not surprising. However, as the fluids were shown to share common characteristics, it could be postulated that there was greater homogeneity. The present study highlights the necessity of studying deposits in detail and with different geoanalytical methods, even if geological characteristics seem comparable at first sight.

Finally, each deposit must be studied in detail, considering the variation in mineralising styles: even world-class deposits that are considered to belong to a specific style show differences from the classic model. For example, the Ranger deposit differs from unconformity-related uranium deposits in the Athabasca Basin; at least by comparison of the chlorite composition(s) associated with metasomatism in the basement and sandstone rocks. Hence, the metallogenic model for the McArthur River SHMS deposit continues to evolve and be debated.

7.3. Fluid sources and flows at different key periods

Thanks to the results obtained in this study, possible fluid sources, pathways and their timing can be better constrained. Concerning fluid sources, the low-salinity fluids are from meteoric origin, and the brines are from the evaporation of seawater. At Ranger, it has been shown thanks to halogens and noble gas results that the brines have interacted with the basement, which was not the case in the Westmoreland area. As several layers of evaporites are present in the basin (Ahmad et al., 2013; Rawlings, 1999), fluids in equilibrium with evaporites are suitable candidates for being the brines that circulated in the basin. These fluids circulated through the basin, sometimes though major faults, to the site of metal deposition (Figure 7-2). With time, different evaporitic layers could have been mobilised, possibly the ones at the same stratigraphic level than the deposits, or in underlying units (Davidson, 1998). Moreover, the syn-sedimentary faults could have acted as pathways or seals to fluids depending on the units they affected. Deposits in the Westmoreland area don't record the 1640 Ma event, possibly because no fluid of that age had access to the area. A better knowledge of the fluid pathways and timing is key for mineral exploration, because the location and abundance of the deposits could be a function of the location of evaporite layers, the vicinity to faults, and the interaction with the crystalline basement rocks. All of these can now be quantified thanks to cutting-edge geoanalytical technologies.

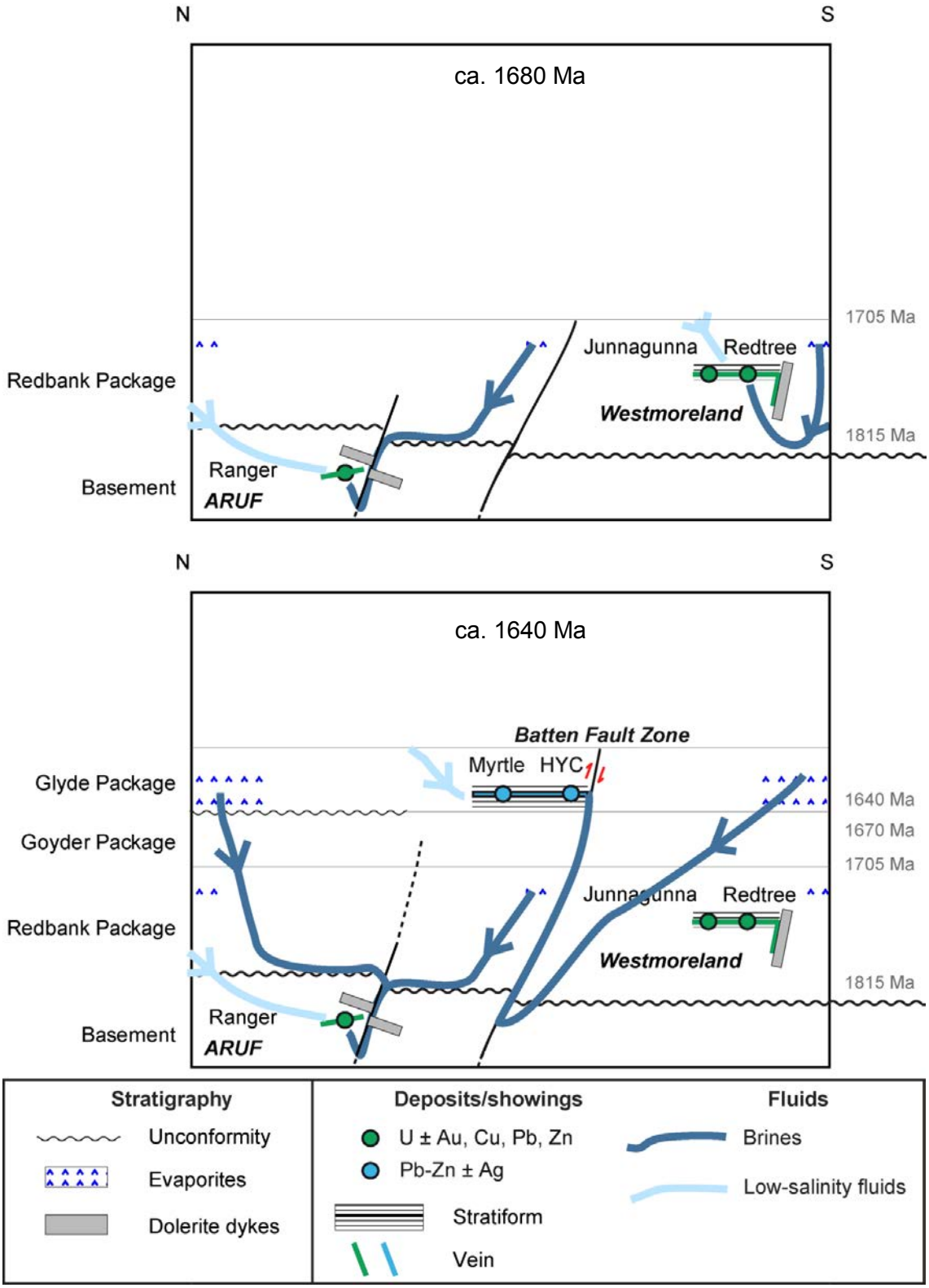

Figure 7-2: *Schematic interpretative summary of the mineralising events in the McArthur Basin at ca. 1680 Ma (top) and ca. 1640 Ma (bottom). The evaporitic layers that could have been in equilibrium with the brines and the dolerite dykes locations are reported, together with the location of the deposits in the stratigraphy, their style and the possible pathways for the low-salinity fluids from meteoric origin and the brines.*

7.4. Guidelines for mineral exploration

Different geological/mineralogical/geochemical parameters are needed (i.e useful and efficient) for making new discoveries in mineral exploration (i.e. especially at the greenfields stage). At McArthur, the Tl halo surrounding the metal-rich zones is highly visible in whole rock geochemical analyses and in pyrite compositions. This study also reveals its significant concentration in base metals. Tl has not been observed in significant concentrations in the other base metal deposits. However, it can be surmised that different markers occur in the other deposits. At the Ranger deposit, B- and Mg-rich zones are the witnesses of the metasomatism occurring shortly before uranium mineralisation. Considering the thickness of the cover (younger formations) above some areas of the basin, geochemical/mineralogical guidelines are capable of advancing future exploration programs. In particular, the highly variable undercover zones (e.g. the areas under the bogs, swamps, and lakes of Finland) are the places for the next generation of new economic mineral deposits.

7.5. A mineral system approach

A mineral system needs four major elements (parameters) to exist: sources, a driver of energy, a fluid pathway or suitable architecture and a depositional mechanism (see Figure 7-3). In this study, the implication of two lead sources for the McArthur River and Myrtle deposits, and a third one at Walford Creek and Caranbirini has been demonstrated conclusively. Additionally, models for their origin are proposed in Chapters 5 and 6. Moreover, fluids responsible for metasomatism at the Ranger U deposit show an important contribution from the basement rocks, in addition to seawater-derived fluids. For the mineralising and later fluids at Ranger and in the Westmoreland area, noble gases and halogens indicate that the fluids are derived from seawater, and as well a contribution from the crystalline basement rocks has been established in some samples.

The drivers for mineralisation tend to be large-scale geodynamic crustal events (i.e. visible in crustal-scale Pb isotope maps and in the paleomagnetic polar wander path), such as the Isan Orogeny, associated with major reactivated fault systems. The energy is visible in the temperatures observed in the Westmoreland area, with temperatures higher that 350 °C, during the metasomatism at Ranger (101 to 163 °C) and at McArthur River (150 –225 °C, compared to cooler later stages). Depending on which of these events, the temperature can be correlated with either the emplacement of mafic rocks within the crust (e.g. the Seigal Volcanics in the Westmoreland area), to the proximity with the mantle, or to higher temperature fluids heated deeper in the basin or the basement.

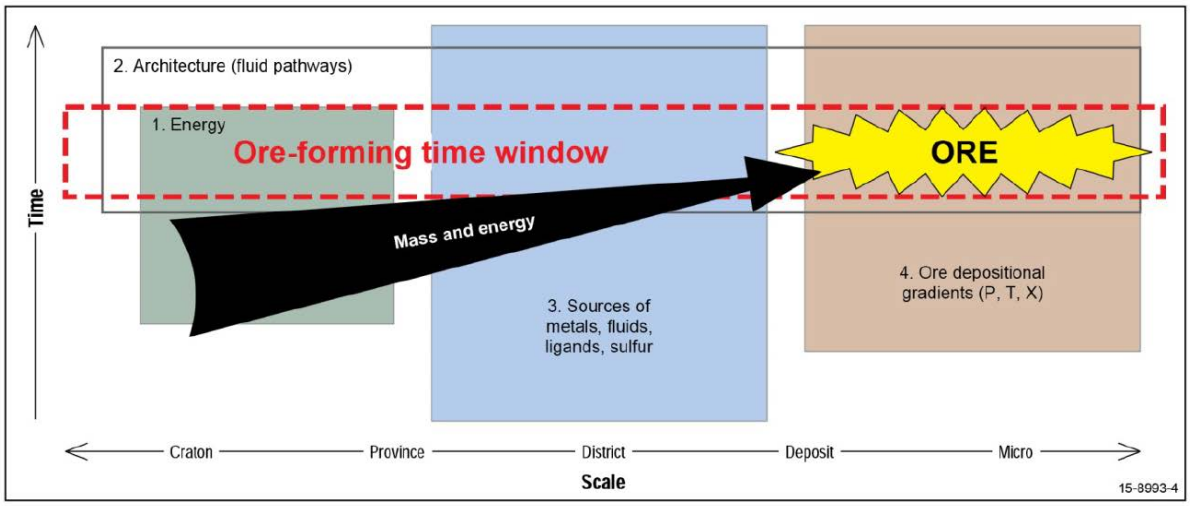

Figure 7-3: *Schematic representation of a hydrothermal or magmatic mineral system, illustrating the concept of an ore-forming time window when four essential geological components of the mineral system (numbered boxes) coincide in time and space. Each of the four mineral system components is present in the system at different scales, from cratonic (and lithospheric) to deposit (and microscopic), and each component may be active at different times. The example shown is where the architecture component (e.g. faults) is active only during the latter stages of an event when an energy source was available to drive fluid or magma flow. The diagram also illustrates that mass and energy were focussed within the system, towards the site of ore deposition, where changes in pressure and/or temperature and/or chemistry of the system (P, T, X) led to ore deposition. From Dulfer et al. (2016).*

Faults were the major pathways connecting different fluid reservoirs in the basin and the basement. The exception is that they could have acted as seals when the mudstones where not consolidated, but that represents a short time window. Mafic rocks or dikes such as the Seigal Volcanics in the Westmoreland area could also have acted as a seal, similar to fault zones; thus focussing the uranium mineralisation. In this study, it has been demonstrated that the faults were active not only at the time of primary mineralisation as demonstrated before, but also later with the mineralising fluids (e.g. at ~1300 Ma in the Caranbirini and Walford Creek areas). The episodic mineralizing fluids probably used these pathways even later in the metallogenic history.

To form world-class deposits, the above mentioned parameters must be combined with better preservation mechanisms, otherwise the metals can be leached and then the probability of having a high metal concentration is considered low. This seems to be the case for example at McArthur River, where no younger event was recorded in the lead isotopes. This is not case at Caranbirini deposit, which is located only several kilometres away.

7.6. Perspectives

This PhD study has explored some of the uranium and lead-zinc deposits of the McArthur Basin. The progress in exploration tools and in the understanding of mineral systems is presently evolving rapidly, and every step is a key parameter in the global comprehension of the events occurring hundreds of millions years ago. Debates remain for well-studied deposits such as McArthur River and Ranger in terms of structure, metal deposition mechanisms, and timing; and the less studied areas are even more so in the early greenfield stages of understanding. From this study, we can highlight four major perspectives. The first one is to characterise the different U and Pb-Zn deposits in the greater McArthur Basin to get a more detailed study of all the mineralizing events. Herein, it has been shown that the range of mineralising event is large and sometimes recorded only in one sample. The second perspective is a study of the Cu mineralisation, to link it in terms of space and time to the other metals. This has been done at the Redbank deposit (breccia type) and at Walford Creek (where Cu is associated with Pb and Zn). Then following up, the determination of the metal content in fluid inclusions could indicate if the metals are transported by the brines or the low-salinity fluids, thus refining the proposed models for the metal deposition. Finally, several schematic models were proposed during this PhD (for the mineralization and fluid circulation processes). It would be valuable to test these conceptual (soft) models as numerical (hard) models, to see if they are realistic.

In addition to these broad themes, several perspectives can be proposed to move further into the understanding of the mineral systems.

The first perspective is to apply new methods or to analyse other minerals in the same deposits or areas already studied. In Westmoreland area, fluids inclusions and alteration could be deeply investigated to better understand the different fluids events characteristics and the relation between alteration and mineralisation. For lead-zinc deposits, fluid inclusions in coarse sphalerite allow the determination of the fluid salinity and an approximation of the temperature at the time of mineralisation. This research could for example be carried out at Myrtle, Caranbirini and Walford Creek. S-isotopes within sulphides and C- and O-isotopes in carbonates and organic matter in the base metal deposits give information on the sulphur, carbon and oxygen sources. As the metal sources have been partly studied here, this would allow determination if all the sources could be linked or not. At McArthur River, considering that the metal stock has not been remobilised after its deposition, the metal tonnage observed nowadays is approximately the one deposited 1640 Ma ago (except is erosion took place). As the contribution of each lead source can be evaluated from the lead isotopes repartition in every lens at McArthur River, the metal leached and transported by the fluids can be

approximated. Then via mass-balance calculations, the volume of crust leached corresponds to several tens of square kilometres if a thickness of several hundreds of metres is postulated. Having an idea of the leached volume is a step toward better understanding the metal distribution. Other sulphides in deposits such as copper and cobalt at Walford Creek are critical economic minerals and part of the story. The Cu and Co could have been carried by the same fluids as the Zn and Pb, and/or remobilised during the same events. Copper dating by Re-Os was considered, but the precisions of the measurements are several tens of million years, which was not sufficient to constraint the timing of the copper mineralisation. The trace elements in copper- and cobalt-rich sulphides would also give information on the repartition of trace elements in all of the sulphides in addition to sphalerite and galena.

Another perspective would be to apply the methods utilised in this study to new target prospects/areas. As an example, boron and magnesium metasomatism is an exploration guideline for uranium unconformity-related deposits. Hence, the boron isotopes, in combination with tourmaline and chlorite compositions, could be applied to other deposits of this type to better characterise their source and their associated metasomatism event. The methods applied for uranium deposits (U-Pb dating, REEs on uraninite, temperature estimates from chlorite) could be applied to other prospects in the Westmoreland area, as the two studies show that six mineralising events occurred in the area, each one under specific physiochemical conditions. Increasing the data sets would allow one to determinate which events were the most important ones, corresponding to higher grades and maybe more intense events. Noble gases and halogens are precious to understand the interaction of the fluids with the basement and organic matter, and can be applied to any types of deposits where quartz and carbonates have fluid inclusions recording either the mineralising event or any fluid flow event. Lead isotopes in galena have already been acquired from different deposits or stratigraphic units in the McArthur Basin. This study highlights the importance of the number of analyses that are lying as close as possible to the end-members, and the necessity of sampling different lenses or mineralisation styles within one deposit, in order to compare them in terms of timing and sources. Moreover, the SIMS method is preferred to the TIMS method because of the isotopic variations at mineral scale that are diluted with TIMS. Analysing by SIMS galena from chosen deposits with specific mineralisation style, host rock, interpreted age, distance to major faults, and evidence or not of remobilisation could give insights about the global mineralising processes operating at district scales. The FindAge program could be applied to a considerably large lead isotopic dataset, so to get a quick-and-dirty idea of the most proliferous periods within the basin. However, caution must be exercised with the use of this program because of the possibility of data lying on mixing trends.

The possibilities for new methods, new targets or both are considered to be unlimited in an area such as the McArthur Basin. Considering the outcropping part of the McArthur Basin, and its huge undercover part below younger rocks, the playground to apply new advanced methods for discovering new mineralised targets is thought to be in the order of thousands of square kilometres; especially in remote areas of the basin. And outside of the basin, these exploration possibilities can be compared with and extended to the Greater McArthur Basin (Figure 7-4), as well as other Paleoproterozoic-Mesoproterozoic basins correlated worldwide (see Figure 7-5 below).

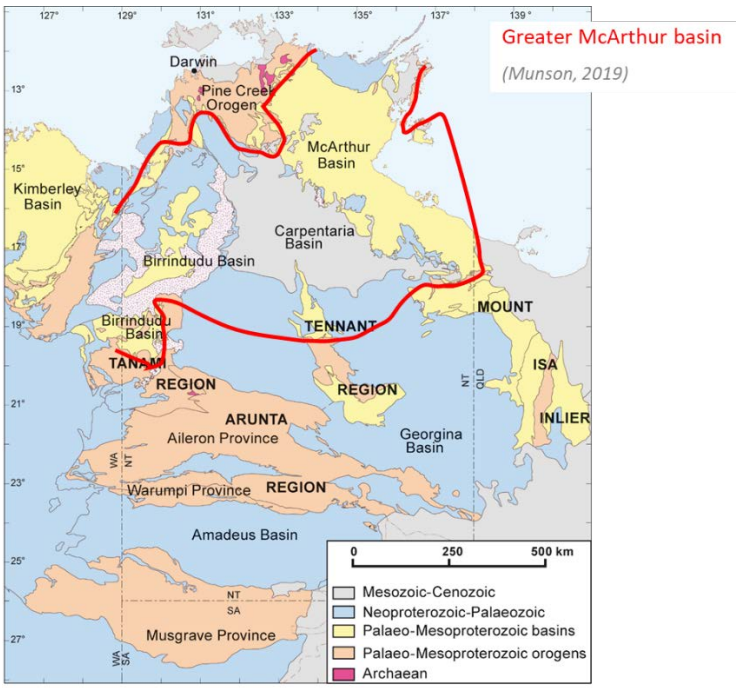

Figure 7-4: *Location of different sedimentary basins (Ahmad and Munson, 2013) and location of the Greater McArthur Basin based on stratigraphic correlations (Munson, 2019).*

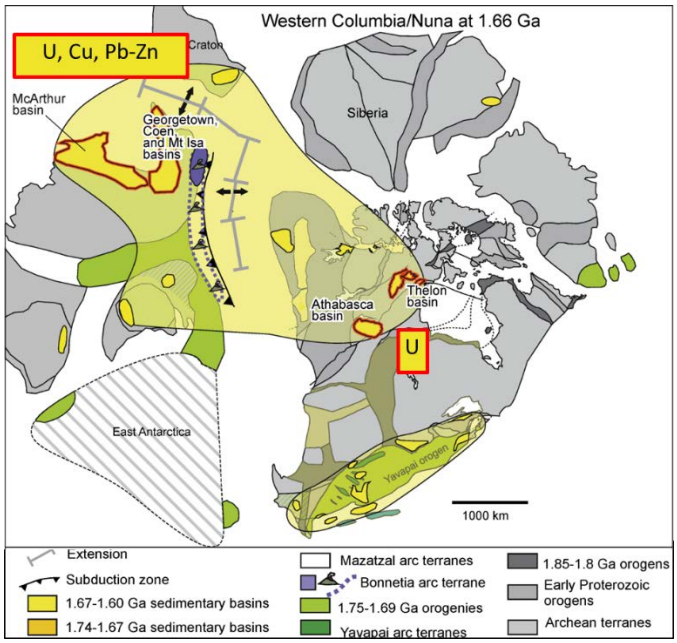

Figure 7-5: *Possible history of the Columbia at ca. 1.66 Ga. See figure 1-6 for the complete description. The metal-rich sedimentary basins are highlighted in red (after Furlanetto et al., 2016).*

References

Abbott, S.T., Sweet, I.P., Plumb, K.A., Young, D.N., Cutovinos, A., Ferenczi, P.A., Brakel, A., Pietsch, B.A., 2001. Roper Region: Urapunga and Roper River Special, Northern Territory. 1: 250 000 geological map series explanatory notes, SD 53-10, 11. Northern Territory Geological Survey and Geoscience Australia (National Geoscience Mapping Accord), Darwin.

Adlakha, E.E., Hattori, K., 2016. Paragenesis and Composition of Tourmaline Types Along the P2 Fault and Mcarthur River Uranium Deposit, Athabasca Basin, Canada. The Canadian Mineralogist 54, 661–679. https://doi.org/10.3749/canmin.1500057

Adlakha, E.E., Hattori, K., Davis, W.J., Boucher, B., 2017. Characterizing fluids associated with the McArthur River U deposit, Canada, based on tourmaline trace element and stable (B, H) isotope compositions. Chemical Geology 466, 417–435. https://doi.org/10.1016/j.chemgeo.2017.06.030

Aeon Metals, 2019. Walford Creek: Australia's premier copper cobalt development project.

Ahmad, M., Dunster, J.N., Munson, T.J., 2013a. Chapter 15: McArthur Basin: in Ahmad M and Munson TJ (compilers). 'Geology and mineral resources of the Northern Territory,' in: Northern Territory Geological Survey.

Ahmad, M., Munson, T.J. (compilers), 2013. Geology and mineral resources of the Northern Territory. Northern Territory Geological Survey.

Ahmad, M., Munson, T.J., Northern Territory Geological Survey, 2013b. Geology and mineral resources of the Northern Territory.

Ahmad, M., Wygralak, A., 1989. Calvert Hills, Northern Territory. 1: 250 000 metallogenic map series explanatory notes, SE 53-08. Northern Territory Geological Survey.

Ahmad, M., Wygralak, A.S., 1990. Murphy Inlier and environs—regional geology and mineralisation. Geology of the Mineral Deposits of Australia and Papua New Guinea (editor Hughes FE). The Australasian Institute of Mining & Metallurgy, Melbourne 819–826.

Alexandre, P., Kyser, K., Layton-Matthews, D., Beyer, S.R., Hiatt, E.E., Lafontaine, J., 2015. Formation of the enigmatic Matoush uranium deposit in the Paleoprotozoic Otish Basin, Quebec, Canada. Mineralium Deposita 50, 825–845. https://doi.org/10.1007/s00126-014-0569-5

Alexandre, P., Kyser, K., Layton-Matthews, D., Joy, B., Uvarova, Y., 2016. Chemical compositions of natural uraninite. Canadian Mineralogist 53, 1–30. https://doi.org/10.3749/canmin.1500017

Alexandre, P., Kyser, K., Thomas, D., Polito, P., Marlat, J., 2009. Geochronology of unconformity-related uranium deposits in the Athabasca Basin, Saskatchewan, Canada and their integration in the evolution of the basin. Miner Deposita 44, 41. https://doi.org/10.1007/s00126-007-0153-3

Alligator Energy, 2012. Alligator announces Caramel Resource 6.5 Mlb @ 0.31% U3O8. Alligator Energy Ltd ASX announcement 19th April 2012.

Anders, E., Grevesse, N., 1989. Abundances of the elements: Meteoritic and solar. Geochimica et Cosmochimica acta 53, 197–214. https://doi.org/10.1016/0016-7037(89)90286-X

Annesley, I.R., Madore, C., Kwok, Y.Y., Kamo, S.L., Troy, A., Hughes, L., 2002. U-Pb geochronology and petrochemistry of late Barramundi pegmatites from the Ranger U deposit, Northern Territory, Australia, in: Proceedings of the International Workshop "Uranium Deposits: From Their Genesis to Their Environmental Aspects." Nancy.

Annesley, I.R., Madore, C., McCready, A.J., Kamo, S.L., Bonli, T., 2007. U-Pb ages of zircon, monazite, and zircon tips in Hudsonian granites at the McArthur River uranium deposit: a record of U mineralizing fluids, in: Proceedings of the Ninth Biennial SGA Meeting. Dublin, pp. 1125–1128.

Bakker, R.J., 2003. Package FLUIDS 1. Computer programs for analysis of fluid inclusion data and for modelling bulk fluid properties. Chemical Geology 194, 3–23. https://doi.org/10.1016/S0009-2541(02)00268-1

Ballentine, C.J., Burnard, P.G., 2002. Production, release and transport of noble gases in the continental crust. Reviews in mineralogy and geochemistry 47, 481–538. https://doi.org/10.2138/rmg.2002.47.12

Banks, D.A., Giuliani, G., Yardley, B.W.D., Cheilletz, A., 2000. Emerald mineralisation in Colombia: fluid chemistry and the role of brine mixing. Mineralium Deposita 35, 699–713. https://doi.org/10.1007/s001260050273

Barth, S., 1993. Boron isotope variations in nature: a synthesis. Geologische Rundschau 82, 640–651. https://doi.org/10.1007/BF00191491

Beaufort, D., Patrier, P., Laverret, E., Bruneton, P., Mondy, J., 2005a. Clay alteration associated with Proterozoic unconformity-type uranium deposits in the East Alligator Rivers Uranium Field, Northern Territory, Australia. Economic Geology 100, 515–536. https://doi.org/10.2113/gsecongeo.100.3.515

Beaufort, D., Patrier, P., Laverret, E., Bruneton, P., Mondy, J., 2005b. Clay alteration associated with Proterozoic unconformity-type uranium deposits in the East Alligator Rivers uranium field, Northern Territory, Australia. Economic Geology 100, 515–536.

Belissont, R., Boiron, M.-C., Luais, B., Cathelineau, M., 2014. LA-ICP-MS analyses of minor and trace elements and bulk Ge isotopes in zoned Ge-rich sphalerites from the Noailhac–Saint-Salvy deposit (France): Insights into incorporation mechanisms and ore deposition processes. Geochimica et Cosmochimica Acta 126, 518–540. https://doi.org/10.1016/j.gca.2013.10.052

Betts, P., Giles, D., 2006. The 1800–1100Ma tectonic evolution of Australia. Precambrian Research 144, 92–125. https://doi.org/10.1016/j.precamres.2005.11.006

Betts, P.G., Giles, D., Lister, G.S., 2003. Tectonic environment of shale-hosted massive sulfide Pb-Zn-Ag deposits of Proterozoic northeastern Australia. Economic Geology 98, 557–576. https://doi.org/10.2113/gsecongeo.98.3.557

Beyer, S.R., Kyser, K., Hiatt, E.E., Polito, P.A., Alexandre, P., Hoksbergen, K., 2012. Basin Evolution and Unconformity-Related Uranium Mineralization: The Camie River U Prospect, Paleoproterozoic Otish Basin, Quebec. Economic Geology 107, 401–425. https://doi.org/10.2113/econgeo.107.3.401

Billault, V., Beaufort, D., Patrier, P., Petit, S., 2002. Crystal chemistry of Fe-sudoites from uranium deposits in the Athabasca Basin (Saskatchewan, Canada). Clays and Clay Minerals 50, 70–81. https://doi.org/10.1346/000986002761002847

Binns, R.A., Ayres, D.E., Wilmshurst, J.R., Ramsden, A.R., 1980. Petrology and geochemistry of alteration associated with uranium mineralization at Jabiluka, Northern Territory, Australia, in: Uranium in the Pine Creek Geosyncline. IAEA.

Blake, D.H., 1987. Geology of the Mount Isa Inlier and environs, Queensland and Northern Territory. Australian Govt. Pub. Service, Canberra.

Bodnar, R.J., 1993. Revised equation and table for determining the freezing point depression of H2O-Nacl solutions. Geochimica et Cosmochimica Acta 57, 683–684. https://doi.org/10.1016/0016-7037(93)90378-A

Böhlke, J.K., Irwin, J.J., 1992a. Brine history indicated by argon, krypton, chlorine, bromine, and iodine analyses of fluid inclusions from the Mississippi Valley type lead-fluorite-barite deposits at Hansonburg, New Mexico. Earth and Planetary Science Letters 110, 51–66. https://doi.org/10.1016/0012-821X(92)90038-W

Böhlke, J.K., Irwin, J.J., 1992b. Laser microprobe analyses of Cl, Br, I, and K in fluid inclusions: Implications for sources of salinity in some ancient hydrothermal fluids. Geochimica et Cosmochimica Acta 56, 203–225. https://doi.org/10.1016/0016-7037(92)90127-5

Bonnet, J., Mosser-Ruck, R., Caumon, M.-C., Rouer, O., Andre-Mayer, A.-S., Cauzid, J., Peiffert, C., 2016. Trace element distribution (Cu, Ga, Ge, Cd, and Fe) in sphalerite from the Tennessee MVT deposits, USA, by combined EMPA, LA-ICP-MS, Raman spectroscopy, and crystallography. The Canadian Mineralogist 54, 1261–1284. https://doi.org/10.3749/canmin.1500104

Bourdelle, F., Cathelineau, M., 2015. Low-temperature chlorite geothermometry: a graphical representation based on a <I>T</I>–R²⁺ –Si diagram. European Journal of Mineralogy 27, 617–626. https://doi.org/10.1127/ejm/2015/0027-2467

Bourdelle, F., Parra, T., Chopin, C., Beyssac, O., 2013. A new chlorite geothermometer for diagenetic to low-grade metamorphic conditions. Contributions to Mineralogy and Petrology 165, 723–735. https://doi.org/10.1007/s00410-012-0832-7

Britt, A., Senior, A., Summerfield, D., Hughes, A., Hitchman, A., Champion, D., Huston, D., Simpson, R., Kay, P., Sexton, M., Schofield, A., 2019. Australia's identified mineral resources 2018. Geoscience Australia. https://doi.org/10.11636/1327-1466.2018

Broadbent, G.C., Myers, R.E., Wright, J.V., 1998. Geology and origin of shale-hosted Zn-Pb-Ag mineralization at the Century deposit, northwest Queensland, Australia. Economic Geology 93, 1264–1294. https://doi.org/10.2113/gsecongeo.93.8.1264

Carr, G.R., Denton, G.J., Korsch, M.J., Gardner, B.L., Parr, A.S., Whitford, D.J., Wyborn, L.A.I., Sun, S-S., 2001a. User friendly isotope technologies in mineral exploration: Pb isotope applications, Northern Australian Proterozoic basins (No. Report 713C). CSIRO.

Carr, G.R., Denton, G.J., Korsch, M.J., Gardner, B.L., Parr, A.S., Whitford, D.J., Wyborn, L.A.I., Sun, S.-S., 2001b. User friendly isotope technologies in mineral exploration: Pb isotope applications, Northern Australian Proterozoic basins. CSIRO.

Carr, G.R., Denton, G.J., Korsch, M.J., Gardner, B.L., Parr, J.M., Andrew, A.S., Whitford, D.J., Wyborn, L.A.I., Sun, S.S., 2003. Pb isotope discrimination of geochemical anomalies using terrain-specific models—the Proterozoic of Northern Australia [abs.]: International Geochemical Exploration Symposium, 21 st, August 2003, Dublin, Ireland, in: Abstracts. pp. 47–48.

Carr, G.R., Sun, S. -s, Page, R.W., Hinman, M., 1996. Recent developments in the use of lead isotope model ages in Proterozoic terrains.

Catanzaro, E.J., 1970. Boric acid: isotopic and assay standard reference materials. National Bureau of Standards, Institute for Materials Research.

Cathelineau, M., 1988. Cation site occupancy in chlorites and illites as function of temperature. Clay minerals 23, 471–85.

Cathelineau, M., Boiron, M.C., Holliger, P., Poty, B., 1990. Metallogenesis of the French part of the Variscan orogen. Part II: Time-space relationships between U, Au and Sn-W ore deposition and geodynamic events—mineralogical and U-Pb data. Tectonophysics 177, 59–79. https://doi.org/10.1016/0040-1951(90)90274-C

Chaussidon, M., Albarède, F., 1992. Secular boron isotope variations in the continental crust: an ion microprobe study. Earth and Planetary Science Letters 108, 229–241. https://doi.org/10.1016/0012-821X(92)90025-Q

Chen, J., Walter, M.R., Logan, G.A., Hinman, M.C., Summons, R.E., 2003. The Paleoproterozoic McArthur River (HYC) Pb/Zn/Ag deposit of northern Australia: organic geochemistry and ore genesis. Earth and Planetary Science Letters 210, 467–479. https://doi.org/10.1016/S0012-821X(03)00171-7

Chew, D.M., Sylvester, P.J., Tubrett, M.N., 2011. U–Pb and Th–Pb dating of apatite by LA-ICPMS. Chemical Geology 280, 200–216. https://doi.org/10.1016/j.chemgeo.2010.11.010

Chi, G., Haid, T., Quirt, D., Fayek, M., Blamey, N., Chu, H., 2017. Petrography, fluid inclusion analysis, and geochronology of the End uranium deposit, Kiggavik, Nunavut, Canada. Mineralium Deposita 52, 211–232. https://doi.org/10.1007/s00126-016-0657-9

Clauer, N., Mercadier, J., Patrier, P., Laverret, E., Bruneton, P., 2015. Relating unconformity-type uranium mineralization of the Alligator Rivers Uranium Field (Northern Territory, Australia) to the regional Proterozoic tectono-thermal activity: An illite K–Ar dating approach. Precambrian Research 269, 107–121. https://doi.org/10.1016/j.precamres.2015.08.007

Claypool, G.E., Holser, W.T., Kaplan, I.R., Sakai, H., Zak, I., 1980. The age curves of sulfur and oxygen isotopes in marine sulfate and their mutual interpretation. Chemical Geology 28, 199–260. https://doi.org/10.1016/0009-2541(80)90047-9

Collins, W.J., Teyssier, C., 1989. Crustal scale ductile fault systems in the Arunta Inlier, central Australia. Tectonophysics 158, 49–66. https://doi.org/10.1016/0040-1951(89)90314-4

Cook, N.J., Ciobanu, C.L., Pring, A., Skinner, W., Shimizu, M., Danyushevsky, L., Saini-Eidukat, B., Melcher, F., 2009. Trace and minor elements in sphalerite: A LA-ICPMS

study. Geochimica et Cosmochimica Acta 73, 4761–4791. https://doi.org/10.1016/j.gca.2009.05.045

Cooke, D.R., Bull, S.W., Donovan, S., Rogers, J.R., 1998. K-metasomatism and base metal depletion in volcanic rocks from the McArthur basin, northern territory - Implications for base metal mineralization. Economic Geology and the Bulletin of the Society of Economic Geologists 93, 1237–1263. https://doi.org/10.2113/gsecongeo.93.8.1237

Cooke, D.R., Bull, S.W., Large, R.R., McGoldrick, P.J., 2000. The importance of oxidized brines for the formation of Australian Proterozoic stratiform sediment-hosted Pb-Zn (Sedex) deposits. Economic Geology 95, 1–18. https://doi.org/10.2113/gsecongeo.95.1.1

Cumming, G.L., Richards, J.R., 1975. Ore lead isotope ratios in a continuously changing earth. Earth and Planetary Science Letters 28, 155–171. https://doi.org/10.1016/0012-821X(75)90223-X

Cuney, M., 2010. Evolution of uranium fractionation processes through time: driving the secular variation of uranium deposit types. Economic Geology 105, 553–569. https://doi.org/10.2113/gsecongeo.105.3.553

Cuney, M., Kyser, K., 2015. Geology and geochemistry of uranium and thorium deposits. Mineralogical Association of Canada.

Cuney, M., Kyser, K., 2009. Recent and not-so-recent developments in uranium deposits and implications for exploration. Mineralogical Association of Canada Short Course Series Volume 39, 14.

Davidson, G.J., 1998. Alkali alteration styles and mechanisms, and their implications for a ‘brine factory’source of base metals in the rift-related McArthur group, Australia. Australian Journal of Earth Sciences 45, 33–49. https://doi.org/10.1080/08120099808728365

Davis, W.J., Gall, Q., Jefferson, C.W., Rainbird, R.H., 2011. Fluorapatite in the Paleoproterozoic Thelon Basin: Structural-stratigraphic context, in situ ion microprobe U-Pb ages, and fluid-flow history. Bulletin 123, 1056–1073.

De Chambost, E., Schuhmacher, M., Lovestam, G., Claesson, S., 1996. Achieving high transmission with the Cameca IMS-1270. Secondary ion mass spectrometry, SIMS X. Wiley, Chichester 1003–1006.

Deloule, E., Allegre, C.J., Doe, B.R., 1986. Lead and sulfur isotope microstratigraphy in galena crystals from Mississippi Valley-type deposits. Economic Geology 81, 1307–1321. https://doi.org/10.2113/gsecongeo.81.6.1307

Derome, D., Cathelineau, M., Fabre, C., Boiron, M.-C., Banks, D., Lhomme, T., Cuney, M., 2007. Paleo-fluid composition determined from individual fluid inclusions by Raman and LIBS: Application to mid-proterozoic evaporitic Na-Ca brines (Alligator Rivers Uranium Field, Northern Territory Australia). Chem. Geol. 237, 240–254. https://doi.org/10.1016/j.chemgeo.2006.10.015

Derome, D., Cuney, M., Cathelineau, M., Fabre, C., Dubessy, J., Bruneton, P., Hubert, A., 2003a. A detailed fluid inclusion study in silicified breccias from the Kombolgie sandstones (Northern Territory, Australia): inferences for the genesis of middle-Proterozoic unconformity-type uranium deposits. Journal of Geochemical Exploration 80, 259–275. https://doi.org/10.1016/S0375-6742(03)00194-8

Derome, D., Cuney, M., Cathelineau, M., Fabre, C., Dubessy, J., Bruneton, P., Hubert, A., 2003b. A detailed fluid inclusion study in silicified breccias from the Kombolgie sandstones (Northern Territory, Australia): inferences for the genesis of middle-Proterozoic unconformity-type uranium deposits. Journal of Geochemical Exploration 80, 259–275. https://doi.org/10.1016/S0375-6742(03)00194-8

Dubessy, J., Derome, D., Sausse, J., 2003. Numerical modelling of fluid mixings in the H2O–NaCl system application to the North Caramal U prospect (Australia). Chemical Geology 194, 25–39. https://doi.org/10.1016/S0009-2541(02)00269-3

Dulfer, H., Milligan, P.R., Coghlan, R., Czarnota, K., Highet, L.M., Champion, D.C., Skirrow, R.G., 2016. Potential for intrusion-hosted Ni-Cu-PGE sulfide deposits in Australia: a continental-scale analysis of mineral system prospectivity. Geoscience Australia.

Durak, B., Pagel, M., Poty, B., 1983. Températures et salinités des fluides au cours des silicifications diagénétiques d'une formation gréseuse surmontant un gisement d'uranium du socle: l'exemple des grès Kombolgie (Australie) (Comptes Rendus de l'Academie des Sciences, No. 296 (II)). Paris.

Dyar, M.D., Wiedenbeck, M., Robertson, D., Cross, L.R., Delaney, J.S., Ferguson, K., Francis, C.A., Grew, E.S., Guidotti, C.V., Hervig, R.L., 2001. Reference minerals for the microanalysis of light elements. Geostandards Newsletter 25, 441–463.

Earle, S.A.M., Sopuck, V.J., 1989. Regional lithogeochemistry of the eastern part of the Athabasca Basin uranium province, Saskatchewan, Canada, in: Uranium Resources and Geology of North America. International Agency of Nuclear Energy, Muller-Kahle E. (ed), Vienna, pp. 263–269.

Eldridge, C.S., Williams, N., Walshe, J.L., 1993. Sulfur isotope variability in sediment-hosted massive sulfide deposits as determined using the ion microprobe SHRIMP; II, A study of the HYC Deposit at McArthur River, Northern Territory, Australia. Economic Geology 88, 1–26. https://doi.org/10.2113/gsecongeo.88.1.1

Energy Resources of Australia Ltd, 2014. Ranger 3 Deeps Exploration Decline project - Further underground drilling results released (ASX Announcement).

ERA, 2011. Annual statement of reserves and resources. ERA Ltd, ASX Announcement.

Evans, D.A.D., 2006. Proterozoic low orbital obliquity and axial-dipolar geomagnetic field from evaporite palaeolatitudes. Nature 444, 51–55. https://doi.org/10.1038/nature05203

Evins, P.M., Smithies, R.H., Howard, H.M., Kirkland, C.L., Wingate, M.T.D., Bodorkos, S., 2010. Redefining the Giles Event within the setting of the 1120–1020 Ma Ngaanyatjarra Rift, west Musgrave Province, Central Australia. Geological Survey of Western Australia, Record 6, 36.

Fehn, U., Lu, Z., Tomaru, H., 2005. Data report: 129I/I ratios and halogen concentrations in pore water of Hydrate Ridge and their relevance for the origin of gas hydrates: a progress report. In: Tréhu, A.M., Bohrmann, G., Torres, M.E., Colwell, F.S. (Eds.), Proceedings of the Ocean Drilling Program: Scientific Results, pp. 1–5.

Fisher, L.A., Cleverley, J.S., Pownceby, M., MacRae, C., 2013. 3D representation of geochemical data, the corresponding alteration and associated REE mobility at the Ranger uranium deposit, Northern Territory, Australia. Mineralium Deposita 48, 947–966. https://doi.org/10.1007/s00126-013-0463-6

Fontes, J.C., Matray, J.M., 1993. Geochemistry and origin of formation brines from the Paris Basin, France: 1. Brines associated with Triassic salts. Chemical Geology 109, 149–175. https://doi.org/10.1016/0009-2541(93)90068-T

Foster, D.R.W., Rubenach, M.J., 2006. Isograd pattern and regional low-pressure, high-temperature metamorphism of pelitic, mafic and calc-silicate rocks along an east – west section through the Mt Isa Inlier. Australian Journal of Earth Sciences 53, 167–186. https://doi.org/10.1080/08120090500434617

Frenzel, M., Hirsch, T., Gutzmer, J., 2016. Gallium, germanium, indium, and other trace and minor elements in sphalerite as a function of deposit type — A meta-analysis. Ore Geology Reviews 76, 52–78. https://doi.org/10.1016/j.oregeorev.2015.12.017

Frimmel, H.E., Schedel, S., Brätz, H., 2014. Uraninite chemistry as forensic tool for provenance analysis. Applied Geochemistry 48, 104–121. https://doi.org/10.1016/j.apgeochem.2014.07.013

Fuchs, H.D., Schindlmayer, W.E., 1981. The Westmoreland uranium deposit, Queensland, Australia, in: Uranium Exploration Case Histories. International Atomic Energy Agency.

Furlanetto, F., Thorkelson, D.J., Rainbird, R.H., Davis, W.J., Gibson, H.D., Marshall, D.D., 2016. The Paleoproterozoic Wernecke Supergroup of Yukon, Canada: Relationships to orogeny in northwestern Laurentia and basins in North America, East Australia, and China. Gondwana Research 39, 14–40. https://doi.org/10.1016/j.gr.2016.06.007

Garven, G., Bull, S.W., Large, R.R., 2001. Hydrothermal fluid flow models of stratiform ore genesis in the McArthur Basin, Northern Territory, Australia. Geofluids 1, 289–311. https://doi.org/10.1046/j.1468-8123.2001.00021.x

George, L., Cook, N.J., Ciobanu, C.L., Wade, B.P., 2015. Trace and minor elements in galena: A reconnaissance LA-ICP-MS study. American Mineralogist 100, 548–569. https://doi.org/10.2138/am-2015-4862

Gibson, G.M., Hutton, L.J., Holzschuh, J., 2017. Basin inversion and supercontinent assembly as drivers of sediment-hosted Pb–Zn mineralization in the Mount Isa region, northern Australia. Journal of the Geological Society 174, 773–786. https://doi.org/10.1144/jgs2016-105

Gibson, G.M., Meixner, A.J., Withnall, I.W., Korsch, R.J., Hutton, L.J., Jones, L.E.A., Holzschuh, J., Costelloe, R.D., Henson, P.A., Saygin, E., 2016. Basin architecture and evolution in the Mount Isa mineral province, northern Australia: Constraints from deep seismic reflection profiling and implications for ore genesis. Ore Geology Reviews 76, 414–441. https://doi.org/10.1016/j.oregeorev.2015.07.013

Gigon, J., Deloule, E., Huston, D.L., Mercadier, J., Richard, A., Annesley, I.R., Wygralak, A.S., Skirrow, R.G., Mernagh, T.P., Masterman, K., accepted. Tracing metal sources for the giant McArthur River Zn-Pb ore deposit using Pb-isotopes. Accepted in Geology.

Gigon, J., Mercadier, J., Annesley, I.R., Richard, A., Wygralak, A.S., Skirrow, R.G., Mernagh, T.P., in prep. Conditions for uranium mobility and deposition over 1.3 Ga in the Westmoreland area (McArthur Basin, Australia). In preparation for Mineralium Deposita.

Gigon, J., Richard, A., Mercadier, J., Deloule, E., Annesley, I.R., Wygralak, A.S., Skirrow, R.G., Masterman, K., Hayward, N., Johnson, D., in prep. Proterozoic Pb-Zn mineralisations in the Batten Fault Zone and Lawn Hill Platform (Australia): insights from Pb isotopes and trace elements in sphalerite and galena. In preparation for GCA.

Gigon, J., Skirrow, R.G., Harlaux, M., Richard, A., Mercadier, J., Annesley, I.R., Villeneuve, J., 2019. Insights into B-Mg-Metasomatism at the Ranger U Deposit (NT, Australia) and Comparison with Canadian Unconformity-Related U Deposits. Minerals 9, 432. https://doi.org/10.3390/min9070432

Goldfarb, R.J., Bradley, D., Leach, D.L., 2010. Secular variation in economic geology. Economic Geology 105, 459–465. https://doi.org/10.2113/gsecongeo.105.3.459

Golding, S.D., Uysal, I.T., Glikson, M., Baublys, K.A., Southgate, P.N., 2006. Timing and chemistry of fluid-flow events in the Lawn Hill platform, northern Australia. Economic Geology 101, 1231–1250. https://doi.org/10.2113/gsecongeo.101.6.1231

Grare, A., Benedicto, A., Mercadier, J., Lacombe, O., Travé, A., Guilcher, M., Richard, A., Ledru, P., Blain, M., Robbins, J., Lach, P., n.d. Structural controls and metallogenic model of polyphase uranium mineralization in the Kiggavik area (Nunavut, Canada). In review in Mineralium Deposita.

Greene, D.C., 2010. Neoproterozoic rifting in the southern Georgina Basin, central Australia: Implications for reconstructing Australia in Rodinia. Tectonics 29, 20 p. https://doi.org/10.1029/2009TC002543

Gulson, B.L., 1985. Shale-hosted lead-zinc deposits in northern Australia; lead isotope variations. Economic Geology 80, 2001–2012. https://doi.org/10.2113/gsecongeo.80.7.2001

Haines, P.W., Hand, M., Sandiford, M., 2001. Palaeozoic synorogenic sedimentation in central and northern Australia: A review of distribution and timing with implications for the evolution of intracontinental orogens. Australian Journal of Earth Sciences 48, 911–928. https://doi.org/10.1046/j.1440-0952.2001.00909.x

Halla, J., 2018. Pb isotopes–A multi-function tool for assessing tectonothermal events and crust-mantle recycling at late Archaean convergent margins. Lithos 320–321, 207–221. https://doi.org/10.1016/j.lithos.2018.08.031

Harlaux, M., Mercadier, J., Marignac, C., Peiffert, C., Cloquet, C., Cuney, M., 2018. Tracing metal sources in peribatholitic hydrothermal W deposits based on the chemical composition of wolframite: The example of the Variscan French Massif Central. Chemical Geology 479, 58–85. https://doi.org/10.1016/j.chemgeo.2017.12.029

Hayes, S.M., McCullough, E.A., 2018. Critical minerals: A review of elemental trends in comprehensive criticality studies. Resources Policy 59, 192–199. https://doi.org/10.1016/j.resourpol.2018.06.015

Heier, K.S., 1962. Trace elements in feldspars—a review. Norsk geol. tidsskr 42, 415–454.

Hein, K.A.A., 2002. Geology of the Ranger Uranium Mine, Northern Territory, Australia: structural constraints on the timing of uranium emplacement. Ore Geology Reviews 20, 83–108. https://doi.org/10.1016/S0169-1368(02)00054-9

Henry, D.J., Novak, M., Hawthorne, F.C., Ertl, A., Dutrow, B.L., Uher, P., Pezzotta, F., 2011. Nomenclature of the tourmaline-supergroup minerals. American Mineralogist 96, 895–913. https://doi.org/10.2138/am.2011.3636

Hills, J.H., Richards, J.R., 1976. Pitchblende and galena ages in the Alligator Rivers region, Northern Territory, Australia. Mineralium Deposita 11, 133–154. https://doi.org/10.1007/BF00204477

Hofmann, A.W., 2007. Sampling Mantle Heterogeneity through Oceanic Basalts: Isotopes and Trace Elements, in: Treatise on Geochemistry. Elsevier, pp. 1–44. https://doi.org/10.1016/B0-08-043751-6/02123-X

Holliger, P., 1988. Ages U-Pb définis in situ sur oxydes d'uranium à l'analyseur ionique: méthodologie et conséquences géochimiques. Comptes rendus de l'Académie des sciences. Série 2, Mécanique, Physique, Chimie, Sciences de l'univers, Sciences de la Terre 307, 367–373.

Hollis, J.A., Carson, C.J., Glass, L.M., 2009. SHRIMP U–Pb zircon geochronological evidence for Neoarchean basement in western Arnhem Land, northern Australia. Precambrian Research 174, 364–380. https://doi.org/doi:10.1016/j.precamres.2009.08.010

Hollis, J.A., Glass, L.M., Carson, C.J., Armstrong, R., Yaxley, G.M., Kemp, A.I.S., Phillips, D., 2011. The geological evolution of the Pine Creek Orogen: New pieces in the puzzle on orogen and craton scale. Annual geoscience exploration seminar (AGES).

Hollis, J.A., Wygralak, A.S., 2012. A review of the geology and uranium, gold and iron ore deposits of the Pine Creek Orogen. Episodes 35, 264–272.

Holser, W.T., 1979. Trace elements and isotopes in evaporites, in: Marine Minerals. Mineralogical Society of America Short Course Notes Washington, DC, pp. 295–346.

Howard, H.M., Smithies, R.H., Evins, P.M., Kirkland, C.L., Werner, M., Wingate, M.T.D., Pirajno, F., 2011. Explanatory notes for the west Musgrave Province. Geological Survey of Western Australia, Record 4, 349.

Hu, R.-Z., Burnard, P.G., Bi, X.-W., Zhou, M.-F., Peng, J.-T., Su, W.-C., Zhao, J.-H., 2009. Mantle-derived gaseous components in ore-forming fluids of the Xiangshan uranium deposit, Jiangxi province, China: evidence from He, Ar and C isotopes. Chemical Geology 266, 86–95. https://doi.org/10.1016/j.chemgeo.2008.07.017

Huston, D.L., Mernagh, T.P., Hagemann, S.G., Doublier, M.P., Fiorentini, M., Champion, D.C., Lynton Jaques, A., Czarnota, K., Cayley, R., Skirrow, R., Bastrakov, E., 2016. Tectono-metallogenic systems — The place of mineral systems within tectonic evolution, with an emphasis on Australian examples. Ore Geology Reviews 76, 168–210. https://doi.org/10.1016/j.oregeorev.2015.09.005

Huston, D.L., Pehrsson, S., Eglington, B.M., Zaw, K., 2010. The geology and metallogeny of volcanic-hosted massive sulfide deposits: Variations through geologic time and with tectonic setting. Economic Geology 105, 571–591. https://doi.org/10.2113/gsecongeo.105.3.571

Huston, D.L., Stevens, B., Southgate, P.N., Muhling, P., Wyborn, L., 2006. Australian Zn-Pb-Ag ore-forming systems: a review and analysis. Economic Geology 101, 1117–1157. https://doi.org/10.2113/gsecongeo.101.6.1117

Idnurm, M., 2000. Towards a high resolution Late Palaeoproterozoic-earliest Mesoproterozoic apparent polar wander path for northern Australia. Australian Journal of Earth Sciences 47, 405–429. https://doi.org/10.1046/j.1440-0952.2000.00788.x

International Atomic Energy Agency, 2018a. Geological classification of uranium deposits and description of selected examples.

International Atomic Energy Agency, 2018b. Unconformity-related uranium deposits.

Ireland, T., Bull, S.W., Large, R.R., 2004a. Mass flow sedimentology within the HYC Zn-Pb-Ag deposit, Northern Territory, Australia: evidence for syn-sedimentary ore genesis. Mineralium Deposita 39, 143–158. https://doi.org/10.1007/s00126-003-0382-z

Ireland, T., Large, R.R., McGoldrick, P., Blake, M., 2004b. Spatial Distribution Patterns of Sulfur Isotopes, Nodular Carbonate, and Ore Textures in the McArthur River (HYC) Zn-Pb-Ag Deposit, Northern Territory, Australia. Economic Geology 99, 1687–1709. https://doi.org/10.2113/gsecongeo.99.8.1687

Jackson, M.J., Page, R.W., Bradshaw, B.E., 1999. The South Nicholson and Roper Groups: Evidence for the early Mesoproterozoic Roper Superbasin (Organisation Record No. 1999/19 (CD-ROM)), Integrated basin analysis of the Isa Superbasin using seismic, well-log and geopotential data: an evaluation of the economic potential of the northern Lawn Hill Platform. Australian Geological Survey.

Jackson, M.J., Page, R.W., Southgate, P., Scott, D., 1997. Why sequence stratigraphy and not lithostratigraphy for exploration. AGSO Research Newsletter 26, 20–22.

Jackson, M.J., Scott, D.L., Rawlings, D.J., 2000. Stratigraphic framework for the Leichhardt and Calvert Superbasins: review and correlations of the pre-1700 Ma successions between Mt Isa and McArthur River. Aust. J. Earth Sci. 47, 381–403. https://doi.org/10.1046/j.1440-0952.2000.00789.x

Jaireth, S., Meixner, T., Milligan, P., Lambert, I., Miezitis, Y., 2007. Unconformity-related uranium systems; regional-scale constraints. Publication Series—Australasian Institute of Mining and Metallurgy 76, 31–32.

Jaireth, S., Porritt, K., 2010. Australian lead and zinc resources (Sheet 1: Resources by region), March 2010 Edition.

Jaireth, S., Roach, I.C., Bastrakov, E., Liu, S., 2015. Basin-related uranium mineral systems in Australia: A review of critical features. Ore Geology Reviews 76, 360–394. https://doi.org/10.1016/j.oregeorev.2015.08.006

Jébrak, M., Marcoux, É., Laithier, M., 2008. Géologie des ressources minérales. Ressources naturelles et faune, Québec.

Jefferson, C.W., Thomas, D.J., Gandhi, S.S., Ramaekers, P., Delaney, G., Brisbin, D., Cutts, C., Portella, P., Olson, R.A., 2007. Unconformity-associated uranium deposits of the Athabasca Basin, Saskatchewan and Alberta. Bulletin / Geological Survey of Canada 588, 23.

Jenke, G.P., 1983. Caranbirini EL 1332 Annual report for the year ending 1 November 1982.

Jochum, K.P., Weis, U., Stoll, B., Kuzmin, D., Yang, Q., Raczek, I., Jacob, D.E., Stracke, A., Birbaum, K., Frick, D.A., 2011. Determination of reference values for NIST SRM 610–617 glasses following ISO guidelines. Geostandards and Geoanalytical Research 35, 397–429. https://doi.org/10.1111/j.1751-908X.2011.00120.x

Johan, Z., 1988. Indium and germanium in the structure of sphalerite: an example of coupled substitution with copper. Mineralogy and Petrology 39, 211–229. https://doi.org/10.1007/BF01163036

Johnson, L.H., Burgess, R., Turner, G., Milledge, H.J., Harris, J.W., 2000. Noble gas and halogen geochemistry of mantle fluids: comparison of African and Canadian diamonds. Geochimica et Cosmochimica Acta 64, 717–732. https://doi.org/10.1016/S0016-7037(99)00336-1

Jowett, E.C., 1991. Fitting iron and magnesium into the hydrothermal chlorite geothermometer, in: GAC/MAC/SEG Joint Annual Meeting, Toronto, May 27-29, 1991, Program with Abstracts 16.

Kendrick, M.A., 2012. High precision Cl, Br and I determinations in mineral standards using the noble gas method. Chemical Geology 292, 116–126. https://doi.org/10.1016/j.chemgeo.2011.11.021

Kendrick, M.A., Arculus, R., Burnard, P., Honda, M., 2013. Quantifying brine assimilation by submarine magmas: Examples from the Galápagos Spreading Centre and Lau Basin. Geochimica et Cosmochimica Acta 123, 150–165. https://doi.org/10.1016/j.gca.2013.09.012

Kendrick, M.A., Burgess, R., Leach, D., Pattrick, R.A.D., 2002a. Hydrothermal fluid origins in Mississippi valley-type ore districts: combined noble gas (He, Ar, Kr) and halogen (Cl, Br, I) analysis of fluid inclusions from the Illinois-Kentucky fluorspar district, Viburnum trend, and Tri-State districts, Midcontinent United States. Economic Geology 97, 453–469. https://doi.org/10.2113/gsecongeo.97.3.453

Kendrick, M.A., Burgess, R., Pattrick, R.A.D., Turner, G., 2002b. Hydrothermal fluid origins in a fluorite-rich Mississippi Valley-type district: combined noble gas (He, Ar, Kr) and halogen (Cl, Br, I) analysis of fluid inclusions from the South Pennine ore field, United Kingdom. Economic Geology 97, 435–451. https://doi.org/10.2113/gsecongeo.97.3.453

Kendrick, M.A., Burgess, R., Pattrick, R.A.D., Turner, G., 2001. Fluid inclusion noble gas and halogen evidence on the origin of Cu-porphyry mineralising fluids. Geochimica et Cosmochimica Acta 65, 2651–2668. https://doi.org/10.1016/S0016-7037(01)00618-4

Kendrick, M.A., Burnard, P., 2013. Noble gases and halogens in fluid inclusions: A journey through the Earth's crust, in: The Noble Gases as Geochemical Tracers. Springer, pp. 319–369.

Kendrick, M.A., Phillips, D., 2009. New constraints on the release of noble gases during in vacuo crushing and application to scapolite Br–Cl–I and 40Ar/39Ar age determinations. Geochimica et Cosmochimica Acta 73, 5673–5692. https://doi.org/10.1016/j.gca.2009.06.032

Kendrick, M.A., Phillips, D., Wallace, M., Miller, J.M., 2011. Halogens and noble gases in sedimentary formation waters and Zn–Pb deposits: A case study from the Lennard Shelf, Australia. Applied Geochemistry 26, 2089–2100. https://doi.org/10.1016/S0016-7037(01)00618-4

Kister, P., Laverret, E., Quirt, D., Cuney, M., Mas, P.P., Beaufort, D., Bruneton, P., 2006. Mineralogy and geochemistry of the host-rock alterations associated with the Shea Creek unconformity-type uranium deposits (Athabasca Basin, Saskatchewan, Canada). Part 2. Regional-scale spatial distribution of the Athabasca Group sandstone matrix minerals. Clays and Clay Minerals 54, 295–313. https://doi.org/10.1346/CCMN.2006.0540302

Kister, P., Vieillard, P., Cuney, M., Quirt, D., Laverret, E., 2005. Thermodynamic constraints on the mineralogical and fluid composition evolution in a clastic sedimentary basin: the Athabasca Basin (Saskatchewan, Canada). European Journal of Mineralogy 17, 325–341. https://doi.org/10.1127/0935-1221/2005/0017-0325

Kotzer, T.G., Kyser, T.K., 1995. Petrogenesis of the Proterozoic Athabasca Basin, northern Saskatchewan, Canada, and its relation to diagenesis, hydrothermal uranium mineralization and paleohydrogeology. Chemical Geology 120, 45–89. https://doi.org/10.1016/0009-2541(94)00114-N

Kowalski, P.M., Wunder, B., Jahn, S., 2013. Ab initio prediction of equilibrium boron isotope fractionation between minerals and aqueous fluids at high P and T. Geochimica et Cosmochimica Acta 101, 285–301. https://doi.org/10.1016/j.gca.2012.10.007

Kralik, M., 1982. Rb-Sb age determinations on Precambrian carbonate rocks of the Carpentarian McArthur basin, Northern Territory, Australia. Precambrian Research 18, 157–170. https://doi.org/10.1016/0301-9268(82)90044-4

Kunzmann, M., Schmid, S., Blaikie, T.N., Halverson, G.P., 2019. Facies analysis, sequence stratigraphy, and carbon isotope chemostratigraphy of a classic Zn-Pb host succession: The Proterozoic middle McArthur Group, McArthur Basin, Australia. Ore Geology Reviews 106, 150–175. https://doi.org/10.1016/j.oregeorev.2019.01.011

Kyser, K., Hiatt, E., Renac, C., Durocher, K., Holk, G., Deckart, K., 2000. Diagenetic fluids in Paleo-and Meso-Proterozoic sedimentary basins and their implications for long protracted fluid histories. Mineralogical Association of Canada Short Course 28, 225–262.

Lach, P., Mercadier, J., Dubessy, J., Boiron, M.-C., Cuney, M., 2013. *In Situ* Quantitative Measurement of Rare Earth Elements in Uranium Oxides by Laser Ablation-Inductively

Coupled Plasma-Mass Spectrometry. Geostand Geoanal Res 37, 277–296. https://doi.org/10.1111/j.1751-908X.2012.00161.x

Lally, J.H., Bajwah, Z., 2006. Uranium deposits of the Northern Territory. Northern Territory Geological Survey, Report 20.

Laramide Resources Ltd, 2019. Westmoreland Uranium Project website [WWW Document]. URL https://laramide.com/projects/westmoreland-project/ (accessed 6.26.19).

Laramide Resources Ltd, 2016. Westmoreland Uranium Project - National instrument 43-101; Technical report - scoping study.

Large, R.R., Bull, S.W., Cooke, D.R., McGoldrick, P.J., 1998. A genetic model for the HYC Deposit, Australia; based on regional sedimentology, geochemistry, and sulfide-sediment relationships. Economic Geology 93, 1345–1368. https://doi.org/10.2113/gsecongeo.93.8.1345

Large, R.R., Bull, S.W., McGoldrick, P.J., 2000. Lithogeochemical halos and geochemical vectors to stratiform sediment hosted Zn–Pb–Ag deposits. Journal of Geochemical Exploration 68, 105–126. https://doi.org/10.1016/S0375-6742(99)00084-9

Large, R.R., Bull, S.W., McGoldrick, P.J., Walters, S.G., Derrick, G. M., Carr, G.R., 2005a. Stratiform and Strata-Bound Zn-Pb-Ag Deposits in Proterozoic Sedimentary Basins, Northern Australia. Economic Geology 100th Anniversary Volume, 931–963. https://doi.org/10.5382/AV100.28

Large, R.R., Bull, S.W., McGoldrick, P.J., Walters, S.G., Derrick, G. M., Carr, G.R., 2005b. Stratiform and Strata-Bound Zn-Pb-Ag Deposits in Proterozoic Sedimentary Basins, Northern Australia. Economic Geology 100th Anniversary Volume, 931–963.

Large, R.R., Bull, S.W., Winefield, P.R., 2001. Carbon and oxygen isotope halo in carbonates related to the McArthur River (HYC) Zn-Pb-Ag deposit, north Australia: Implications for sedimentation, ore genesis, and mineral exploration. Economic Geology 96, 1567–1593. https://doi.org/10.2113/gsecongeo.96.7.1567

Laznicka, P., 2014. Giant metallic deposits—A century of progress. Ore Geology Reviews 62, 259–314. https://doi.org/10.1016/j.oregeorev.2014.03.002

Leach, D.L., Bradley, D.C., Huston, D., Pisarevsky, S.A., Taylor, R.D., Gardoll, S.J., 2010. Sediment-hosted lead-zinc deposits in Earth history. Economic Geology 105, 593–625. https://doi.org/10.2113/gsecongeo.105.3.593

Lead Zinc Silver factsheet and map [WWW Document], 2018. . The Territory's Resources Commodities in the NT. URL https://core.nt.gov.au/__data/assets/pdf_file/0006/377619/LeadZincSilver-Factsheet.pdf

Leeman, W.P., Tonarini, S., 2001. Boron isotopic analysis of proposed borosilicate mineral reference samples. Geostandards Newsletter 25, 399–403. https://doi.org/10.1111/j.1751-908X.2001.tb00614.x

Leisen, M., Boiron, M.-C., Richard, A., Dubessy, J., 2012. Determination of Cl and Br concentrations in individual fluid inclusions by combining microthermometry and LA-ICPMS analysis: Implications for the origin of salinity in crustal fluids. Chem. Geol. 330, 197–206. https://doi.org/10.1016/j.chemgeo.2012.09.003

Lesbros-Piat-Desvial, M., Beaudoin, G., Mercadier, J., Creaser, R., 2017. Age and origin of uranium mineralization in the Camie River deposit (Otish Basin, Québec, Canada). Ore Geology Reviews 91, 196–215. https://doi.org/10.1016/j.oregeorev.2017.10.006

Lindsay, J.F., 2002. Supersequences, superbasins, supercontinents evidence from the Neoproterozoic-Early Palaeozoic basins of central Australia. Basin Research 14, 207–223. https://doi.org/10.1046/j.1365-2117.2002.00170.x

Logan, G.A., Hinman, M.C., Walter, M.R., Summons, R.E., 2001. Biogeochemistry of the 1640 Ma McArthur River (HYC) lead-zinc ore and host sediments, Northern Territory, Australia. Geochimica et Cosmochimica Acta 65, 2317–2336. https://doi.org/10.1016/S0016-7037(01)00599-3

London, D., Morgan, G.B., Wolf, M.B., 1996. Boron in granitic rocks and their contact aureoles. Reviews in Mineralogy and Geochemistry 33, 299–330.

Longerich, H.P., Jackson, S.E., Günther, D., 1996. Inter-laboratory note. Laser ablation inductively coupled plasma mass spectrometric transient signal data acquisition and analyte concentration calculation. Journal of analytical atomic spectrometry 11, 899–904. https://doi.org/10.1039/JA9961100899

Ludwig, K., 2007. Isoplot/Ex version 3.41b, a geochronological toolkit for Microsoft Excel. Berkeley Geochronology Center Spec. Publ. No 4.

Ludwig, K.R., Grauch, R.I., Nutt, C.J., Nash, J.T., Frishman, D., Simmons, K.R., 1987. Age of uranium mineralization at the Jabiluka and Ranger deposits, Northern Territory, Australia; new U-Pb isotope evidence. Economic Geology 82, 857–874. https://doi.org/10.2113/gsecongeo.82.4.857

Maas, R., 1989. Nd-Sr Isotope Constraints on the Age and Origin of Unconformity-type Uranium Deposits in the Alligator Rivers Uranium Field, Northern-Territory, Australia. Economic Geology 84, 64–90. https://doi.org/10.2113/gsecongeo.84.1.64

MacGregor, J., Grew, E.S., De Hoog, J.C., Harley, S.L., Kowalski, P.M., Yates, M.G., Carson, C.J., 2013. Boron isotopic composition of tourmaline, prismatine, and grandidierite from granulite facies paragneisses in the Larsemann Hills, Prydz Bay, East Antarctica: Evidence for a non-marine evaporite source. Geochimica et Cosmochimica Acta 123, 261–283. https://doi.org/10.1016/j.gca.2013.05.030

Marschall, H.R., Jiang, S.-Y., 2011. Tourmaline Isotopes: No Element Left Behind. Elements 7, 313–319. https://doi.org/10.2113/gselements.7.5.313

Martz, P., 2017. Caractéristiques, chronologie et rôles des circulations fluides dans le bassin d'Athabasca et son socle: implications dans la formation et l'évolution du gisement d'uranium de Cigar Lake. PhD thesis; Université de Lorraine.

Martz, P., Mercadier, J., Perret, J., Villeneuve, J., Deloule, E., Cathelineau, M., Quirt, D., Doney, A., Ledru, P., 2019. Post-crystallization alteration of natural uraninites: Implications for dating, tracing, and nuclear forensics. Geochimica et Cosmochimica Acta 249, 138–159. https://doi.org/10.1016/j.gca.2019.01.025

McCuaig, T.C., Hronsky, J.M., 2014. The mineral system concept: the key to exploration targeting. Society of Economic Geologists Special Publication 18, 153–175. https://doi.org/10.1080/03717453.2017.1306274

McGoldrick, P., Winefield, P., Bull, S., Selley, D., Scott, R., 2010. Sequences, synsedimentary structures, and sub-basins: the where and when of SEDEX zinc systems in the southern McArthur Basin, Australia. Society of Economic Geologists Inc. Special Publication 15, 1–23. https://doi.org/10.5382/SP.15.2.02

McKay, A.D., Miezitis, Y., 2001. Australia's uranium resources, geology and development of deposits. AGSO-Geoscience Australia.

McKay, A.D., Miezitis, Y., Jaireth, S., 2010. Australian uranium resources (Sheet 1: Resources by region), May 2010 Edition.

Mercadier, J., Annesley, I.R., McKechnie, C.L., Bogdan, T.S., Creighton, S., 2013. Magmatic and metamorphic uraninite mineralization in the western margin of the Trans-Hudson Orogen (Saskatchewan, Canada): a uranium source for unconformity-related uranium deposits? Economic Geology 108, 1037–1065. https://doi.org/10.2113/econgeo.108.5.1037

Mercadier, J., Cuney, M., Cathelineau, M., Lacorde, M., 2011a. U redox fronts and kaolinisation in basement-hosted unconformity-related U ores of the Athabasca Basin (Canada): late U remobilisation by meteoric fluids. Mineralium Deposita 46, 105–135. https://doi.org/10.1007/s00126-010-0314-7

Mercadier, J., Cuney, M., Lach, P., Boiron, M.-C., Bonhoure, J., Richard, A., Leisen, M., Kister, P., 2011b. Origin of uranium deposits revealed by their rare earth element signature. Terra Nova 23, 264–269. https://doi.org/10.1111/j.1365-3121.2011.01008.x

Mercadier, J., Richard, A., Cathelineau, M., 2012. Boron-and magnesium-rich marine brines at the origin of giant unconformity-related uranium deposits: δ11B evidence from Mg-tourmalines. Geology 40, 231–234.

Mernagh, T.P., Wygralak, A.S., 2011. A fluid inclusion study of uranium and copper mineral systems in the Murphy Inlier, Northern Australia. Russ. Geol. Geophys. 52, 1421–1435. https://doi.org/10.1016/j.rgg.2011.10.011

Meyer, C., Wunder, B., Meixner, A., Romer, R.L., Heinrich, W., 2008. Boron-isotope fractionation between tourmaline and fluid: an experimental re-investigation. Contributions to Mineralogy and Petrology 156, 259–267.

Molnár, F., Mänttäri, I., O'Brien, H., Lahaye, Y., Pakkanen, L., Johanson, B., Käpyaho, A., Sorjonen-Ward, P., Whitehouse, M., Sakellaris, G., 2016. Boron, sulphur and copper isotope systematics in the orogenic gold deposits of the Archaean Hattu schist belt, eastern Finland. Ore Geology Reviews 77, 133–162. https://doi.org/10.1016/j.oregeorev.2016.02.012

Mudd, G.M., Jowitt, S.M., Werner, T.T., 2016. The world's lead-zinc mineral resources: scarcity, data, issues and opportunities. Ore Geology Reviews 80, 1160–1190. https://doi.org/10.1016/j.oregeorev.2016.08.010

Mukherjee, I., Large, R., 2017. Application of pyrite trace element chemistry to exploration for SEDEX style Zn-Pb deposits: McArthur Basin, Northern Territory, Australia. Ore Geology Reviews 81, 1249–1270. https://doi.org/10.1016/j.oregeorev.2016.08.004

Munson, T.J., 2019. Detrital zircon geochronology investigations of the Glyde and Favenc packages: Implications for the geological framework of the greater McArthur Basin, Northern Territory. AGES 2019 Proceedings.

Muramatsu, Y., Doi, T., Tomaru, H., Fehn, U., Takeuchi, R., Matsumoto, R., 2007. Halogen concentrations in pore waters and sediments of the Nankai Trough, Japan: implications for the origin of gas hydrates. Applied Geochemistry 22, 534–556. https://doi.org/10.1016/j.apgeochem.2006.12.015

Murphy, F.C., Hutton, L.J., Walshe, J.L., Cleverley, J.S., Kendrick, M.A., Mclellan, J., Rubenach, M.J., Oliver, N.H.S., Gessner, K., Bierlein, F.P., Jupp, B., Aillères, L., Laukamp, C., Roy, I.G., Miller, J.McL., Keys, D., Nortje, G.S., 2011. Mineral system analysis of the Mt Isa–McArthur River region, Northern Australia. Australian Journal of Earth Sciences 58, 849–873. https://doi.org/10.1080/08120099.2011.606333

Myers, J.S., Shaw, R.D., Tyler, I.M., 1996. Tectonic evolution of proterozoic Australia. Tectonics 15, 1431–1446. https://doi.org/10.1029/96TC02356

NEA - IAEA, 2016. Uranium 2016-resource, production and demand. OECD publishing, Uranium.

Needham, R.S., 1998. Geology of the Alligator Rivers Uranium Field, Northern Territory (BMR Bulletin No. 224). Department of Primary Industries and Energy, Bureau of Mineral Ressources, Geology and Geophysics, Canberra.

Nutt, C.J., 1989. Chloritization and associated alteration at the Jabiluka unconformity-type uranium deposit, Northern Territory, Australia. Canadian Mineralogist 27, 41–58.

Orth, K., 2010. Geology, volcanology and mineral potential of the Cliffdale and Seigal volcanics, Calvert Hills 1:250 000 geological mapsheet, SE53-08, Northern Territory.

Ozima, M., Podosek, F.A., 2002. Noble gas geochemistry. Cambridge University Press.

Page, R., 2018. Sample 1516743, Sample ID 95779041 [WWW Document]. Geoscience Australia OZCHRON database. URL http://www.ga.gov.au/geochron-sapub-web/geochronology/shrimp/search.htm

Page, R.W., Jackson, M.J., Krassay, A.A., 2000. Constraining sequence stratigraphy in north Australian basins: SHRIMP U–Pb zircon geochronology between Mt Isa and McArthur River. Australian Journal of Earth Sciences 47, 431–459. https://doi.org/10.1046/j.1440-0952.2000.00797.x

Page, R.W., Sun, S., Carr, G., 1994. Proterozoic sediment-hosted lead-zinc-silver deposits in northern Australia—U-Pb zircon and Pb isotope studies, in: Geological Society of Australia Abstracts. pp. 334–335.

Page, R.W., Sweet, I.P., 1998. Geochronology of basin phases in the western Mt Isa Inlier, and correlation with the McArthur Basin. Australian Journal of Earth Sciences 45, 219–232. https://doi.org/10.1080/08120099808728383

Palmer, M.R., Swihart, G.H., 1996. Boron isotope geochemistry; an overview. Reviews in Mineralogy and Geochemistry 33, 709–744.

Paton, C., Hellstrom, J., Paul, B., Woodhead, J., Hergt, J., 2011. Iolite: Freeware for the visualisation and processing of mass spectrometric data. Journal of Analytical Atomic Spectrometry 26, 2508–2518. https://doi.org/10.1039/C1JA10172B

Pettke, T., Oberli, F., Heinrich, C.A., 2010. The magma and metal source of giant porphyry-type ore deposits, based on lead isotope microanalysis of individual fluid inclusions. Earth and Planetary Science Letters 296, 267–277. https://doi.org/10.1016/j.epsl.2010.05.007

Pevely, S., Hinman, M., McLellan, A., 2017. Ranger 3 Deeps uranium deposit, in: Australian Ore Deposits. Neil Phillips, pp. 461–464.

Pitcairn, I.K., Teagle, D.A., Craw, D., Olivo, G.R., Kerrich, R., Brewer, T.S., 2006. Sources of metals and fluids in orogenic gold deposits: insights from the Otago and Alpine Schists, New Zealand. Economic Geology 101, 1525–1546. https://doi.org/10.2113/gsecongeo.101.8.1525

Plissart, G., Féménias, O., Mãruntiu, M., Diot, H., Demaiffe, D., 2009. Mineralogy and geothermometry of gabbro-derived listvenites in the Tisovita–Iuti ophiolite, Southwestern Romania. The Canadian Mineralogist 47, 81–105. https://doi.org/10.3749/canmin.47.1.81

Polito, P.A., Kyser, T.K., Alexandre, P., Hiatt, E.E., Stanley, C.R., 2011. Advances in understanding the Kombolgie Subgroup and unconformity-related uranium deposits in the Alligator Rivers Uranium Field and how to explore for them using lithogeochemical principles. Australian Journal of Earth Sciences 58, 453–474. https://doi.org/10.1080/08120099.2011.561873

Polito, P.A., Kyser, T.K., Golding, S.D., Southgate, P.N., 2006a. Zinc deposits and related mineralization of the Burketown mineral field, including the world-class Century deposit, Northern Australia: Fluid inclusion and stable isotope evidence for basin fluid sources. Econ. Geol. 101, 1251–1273. https://doi.org/10.2113/gsecongeo.101.6.1251

Polito, P.A., Kyser, T.K., Jackson, M.J., 2006b. The role of sandstone diagenesis and aquifer evolution in the formation of uranium and zinc-lead deposits, southern McArthur basin, Northern Territory, Australia. Economic Geology 101, 1189–1209. https://doi.org/10.2113/gsecongeo.101.6.1189

Polito, P.A., Kyser, T.K., Marlatt, J., Alexandre, P., Bajwah, Z., Drever, G., 2004. Significance of alteration assemblages for the origin and evolution of the Proterozoic Nabarlek unconformity-related uranium deposit, Northern Territory, Australia. Economic Geology 99, 113–139. https://doi.org/10.2113/gsecongeo.99.1.113

Polito, P.A., Kyser, T.K., Rheinberger, G., Southgate, P.N., 2005a. A Paragenetic and Isotopic Study of the Proterozoic Westmoreland Uranium Deposits, Southern McArthur Basin, Northern Territory, Australia. Economic Geology 100, 1243–1260. https://doi.org/10.2113/100.6.1243

Polito, P.A., Kyser, T.K., Rheinberger, G., Southgate, P.N., 2005b. A Paragenetic and Isotopic Study of the Proterozoic Westmoreland Uranium Deposits, Southern McArthur Basin, Northern Territory, Australia. Economic Geology 100, 1243–1260. https://doi.org/10.2113/100.6.1243

Polito, P.A., Kyser, T.K., Southgate, P.N., Jackson, M.J., 2006c. Sandstone diagenesis in the Mount Isa basin: An isotopic and fluid inclusion perspective in relationship to district-wide Zn, Pb, and Cu mineralization. Economic Geology 101, 1159–1188. https://doi.org/10.2113/gsecongeo.101.6.1159

Polito, P.A., Kyser, T.K., Thomas, D., Marlatt, J., Drever, G., 2005c. Re-evaluation of the petrogenesis of the Proterozoic Jabiluka unconformity-related uranium deposit, Northern Territory, Australia. Mineralium Deposita 40, 257–288. https://doi.org/10.1007/s00126-005-0007-9

Potma, W., Fisher, L., Schaubs, P., Cleverley, J., Corbel, S., Lau, I., Phang, C., Hough, R., 2012. JSU–ERA Ranger Mineral System Project Final Report. CSIRO National

Research Flagships, Minerals Down Under Northern Territory Geological Survey, Record 4.
Rawlings, D.J., 2006. Robinson River, Northern Territory (Second Edition). 1:250 000 geological map series explanatory notes, SE53-04. Northern Territory Geological Survey.
Rawlings, D.J., 1999. Stratigraphic resolution of a multiphase intracratonic basin system: the McArthur Basin, northern Australia. Aust. J. Earth Sci. 46, 703–723. https://doi.org/10.1046/j.1440-0952.1999.00739.x
Rawlings, D.J., Korsch, R.J., Goleby, B.R., Gibson, G.M., Johnstone, D.W., Barlow, M., 2004. The 2002 southern McArthur Basin seismic reflection survey. Geoscience Australia, Record 17, 87 p.
Renock, D., Becker, U., 2011. A first principles study of coupled substitution in galena. Ore Geology Reviews 42, 71–83. https://doi.org/10.1016/j.oregeorev.2011.04.001
Rheinberger, G.M., Hallenstein, C., Stegman, C.L., 1998. Westmoreland uranium deposits. Geology of Australian and Papua New Guinean mineral deposits: Melbourne, Australiasian Institute of Mining and Metallurgy 807–814.
Richard, A., Banks, D.A., Mercadier, J., Boiron, M.-C., Cuney, M., Cathelineau, M., 2011. An evaporated seawater origin for the ore-forming brines in unconformity-related uranium deposits (Athabasca Basin, Canada): Cl/Br and δ37Cl analysis of fluid inclusions. Geochimica et Cosmochimica Acta 75, 2792–2810. https://doi.org/10.1016/j.gca.2011.02.026
Richard, A., Boulvais, P., Mercadier, J., Boiron, M.-C., Cathelineau, M., Cuney, M., France-Lanord, C., 2013a. From evaporated seawater to uranium-mineralizing brines: Isotopic and trace element study of quartz–dolomite veins in the Athabasca system. Geochimica et Cosmochimica Acta 113, 38–59. https://doi.org/10.1016/j.gca.2013.03.009
Richard, A., Cathelineau, M., Boiron, M.-C., Mercadier, J., Banks, D.A., Cuney, M., 2016. Metal-rich fluid inclusions provide new insights into unconformity-related U deposits (Athabasca Basin and Basement, Canada). Mineralium Deposita 51, 249–270.
Richard, A., Cauzid, J., Cathelineau, M., Boiron, M.-C., Mercadier, J., Cuney, M., 2013b. Synchrotron XRF and XANES investigation of uranium speciation and element distribution in fluid inclusions from unconformity-related uranium deposits. Geofluids 13, 101–111. https://doi.org/10.1111/gfl.12009
Richard, A., Kendrick, M.A., Cathelineau, M., 2014. Noble gases (Ar, Kr, Xe) and halogens (Cl, Br, I) in fluid inclusions from the Athabasca Basin (Canada): Implications for unconformity-related U deposits. Precambrian Research 247, 110–125. https://doi.org/10.1016/j.precamres.2014.03.020
Richard, A., Rozsypal, C., Mercadier, J., Banks, D.A., Cuney, M., Boiron, M.-C., Cathelineau, M., 2012. Giant uranium deposits formed from exceptionally uranium-rich acidic brines. Nature Geoscience 5, 142–146. https://doi.org/10.1038/NGEO1338
Richards, J.P., 2013. Giant ore deposits formed by optimal alignments and combinations of geological processes. Nature Geoscience 6, 911–916. https://doi.org/10.1038/ngeo1920
Rohrlach, B.D., Fu, M., Clarke, J.D.A., 1998a. Geological setting, paragenesis and fluid history of the Walford Creek Zn-Pb-Cu-Ag prospect, Mt Isa Basin, Australia. Aust. J. Earth Sci. 45, 63–81. https://doi.org/10.1080/08120099808728367
Rohrlach, B.D., Fu, M., Clarke, J.D.A., 1998b. Geological setting, paragenesis and fluid history of the Walford Creek Zn-Pb-Cu-Ag prospect, Mt Isa Basin, Australia. Aust. J. Earth Sci. 45, 63–81. https://doi.org/10.1080/08120099808728367
Rosenberg, P.E., Foit Jr, F.F., 2006. Magnesiofoitite from the uranium deposits of the Athabasca Basin, Saskatchewan, Canada. The Canadian Mineralogist 44, 959–965.
Rox Resources, 2010. ASX/Media release - Myrtle zinc resources continues to grow.
Rox Resources Limited, 2011. Myrtle Zinc Deposit, NT. AIG Base Metals Symposium.
Rye, D.M., Williams, N., 1981. Studies of the base metal sulfide deposits at McArthur River, Northern Territory, Australia; III, The stable isotope geochemistry of the HYC, Ridge,

and Cooley deposits. Economic Geology 76, 1–26. https://doi.org/10.2113/gsecongeo.76.1.1

Sawkins, F.J., 1989. Anorogenic felsic magmatism, rift sedimentation, and giant Proterozoic Pb-Zn deposits. Geology 17, 657–660. https://doi.org/10.1130/0091-7613(1989)017<0657:AFMRSA>2.3.CO;2

Schindlmayr, W.E., Beerbaum, B., 1986. Structure related uranium mineralization in the Westmoreland district, Northern Australia.

Scott, D.L., Rawlings, D.J., Page, R.W., Tarlowski, C.Z., Idnurm, M., Jackson, M.J., Southgate, P.N., 2000. Basement framework and geodynamic evolution of the Palaeoproterozoic superbasins of north-central Australia: an integrated review of geochemical, geochronological and geophysical data. Australian Journal of Earth Sciences 47, 341–380. https://doi.org/10.1046/j.1440-0952.2000.00793.x

Scrimgeour, I., Kinny, P., Close, D., Edgoose, C., 2005. High-T granulites and polymetamorphism in the southern Arunta Region, central Australia: Evidence for a 1.64Ga accretional event. Precambrian Research 142, 1–27. https://doi.org/10.1016/j.precamres.2005.08.005

Shabaga, B.M., Fayek, M., Quirt, D., Jefferson, C.W., Camacho, A., 2017. Mineralogy, geochronology, and genesis of the Andrew Lake uranium deposit, Thelon Basin, Nunavut, Canada. Can. J. Earth Sci. 54, 850–868. https://doi.org/10.1139/cjes-2017-0024

Sharpe, R., Fayek, M., Quirt, D., Jefferson, C.W., 2015. Geochronology and Genesis of the Bong Uranium Deposit, Thelon Basin, Nunavut, Canada. Economic Geology 110, 1759–1777. https://doi.org/10.2113/econgeo.110.7.1759

Skirrow, R.G., Mercadier, J., Armstrong, R., Kuske, T., Deloule, E., 2016. The Ranger uranium deposit, northern Australia: Timing constraints, regional and ore-related alteration, and genetic implications for unconformity-related mineralisation. Ore Geology Reviews 76, 463–503. https://doi.org/10.1016/j.oregeorev.2015.09.001

Smith, S.P., Kennedy, B.M., 1983. The solubility of noble gases in water and in NaCl brine. Geochimica et Cosmochimica Acta 47, 503–515. https://doi.org/10.1016/0016-7037(83)90273-9

Smithies, R.H., Howard, H.M., Evins, P.M., Kirkland, C.L., Kelsey, D.E., Hand, M., Wingate, M.T.D., Collins, A.S., Belousova, E., 2011. High-temperature granite magmatism, crust–mantle interaction and the Mesoproterozoic intracontinental evolution of the Musgrave Province, Central Australia. Journal of Petrology 52, 931–958. https://doi.org/10.1093/petrology/egr010

Southgate, P.N., Kyser, T.K., Scott, D.L., Large, R.R., Golding, S.D., Polito, P.A., 2006. A basin system and fluid-flow analysis of the Zn-Pb-Ag Mount Isa-type deposits of northern Australia: Identifying metal source, Basinal Brine reservoirs, times of fluid expulsion, and organic matter reactions. Econ. Geol. 101, 1103–1115. https://doi.org/10.2113/gsecongeo.101.6.1103

Spinks, S., Blaikie, T., Schaubs, P., Sørensen, C., Munday, T., Schmid, S., Ley-Cooper, Y., Kunzmann, M., 2017. Multiproxy 3D Geophysical and Geochemical Characterisation of the McArthur Group Stratigraphy; Caranbirini Project, McArthur Basin, Northern Territory.

Spinks, S., Pearce, M., Ryan, C., Moorhead, G., Kirkham, R., Sheldon, H., Kunzmann, M., Liu, W., Blaikie, T.N., Schaubs, P., 2019. Ultra-high resolution trace element mapping provides new clues on the origin of the McArthur River (HYC) sediment-hosted Zn-Pb-Ag deposit. Annual Geoscience Exploration Seminar (AGES) Proceedings. Northern Territory Geological Survey 49.

Spinks, S.C., Schmid, S., Pagés, A., Bluett, J., 2016. Evidence for SEDEX-style mineralization in the 1.7 Ga Tawallah Group, McArthur Basin, Australia. Ore Geology Reviews 76, 122–139. https://doi.org/10.1016/j.oregeorev.2016.01.007

Spivack, A.J., 1986. Boron isotope geochemistry. Massachusetts Institute of Technology.

Stacey, J., Kramers, J., 1975. Approximation of terrestrial lead isotope evolution by a two-stage model. Earth and planetary science letters 26, 207–221. https://doi.org/10.1016/0012-821X(75)90088-6

Steele-MacInnis, M., Bodnar, R.J., Naden, J., 2011. Numerical model to determine the composition of H2O-NaCl-CaCl2 fluid inclusions based on microthermometric and microanalytical data. Geochimica et Cosmochimica Acta 75, 21–40. https://doi.org/10.1016/j.gca.2010.10.002

Sun, S.S., Carr, G.R., Page, R.W., 1996. A continued effort to improve lead-isotope model ages. AGSO Research Newsletter 24, 19–20.

Sun, S.-S., McDonough, W.F., 1989. Chemical and isotopic systematics of oceanic basalts: implications for mantle composition and processes. Geological Society, London, Special Publications 42, 313–345.

Sweet, I.P., Slater, P.J., 1975. Precambrian geology of the Westmoreland region, northern Australia. Part I: Regional setting and cover rocks. Bur. Miner. Resour., Aust., Rec 88.

Symons, D.T.A., 2007. Paleomagnetism of the HYC Zn-Pb SEDEX Deposit, Australia: evidence of an epigenetic origin. Economic Geology 102, 1295–1310. https://doi.org/10.2113/gsecongeo.102.7.1295

Tatsumoto, M., Knight, R.J., Allegre, C.J., 1973. Time differences in the formation of meteorites as determined from the ratio of lead-207 to lead-206. Science 180, 1279–1283. https://doi.org/10.1126/science.180.4092.1279

Taylor Jr, H.P., 1979. Oxygen and hydrogen isotope relationships in hydrothermal mineral deposits. Geochemistry of hydrothermal ore deposits 236–277.

Tera, F., Wasserburg, G.J., 1972. U-Th-Pb systematics in three Apollo 14 basalts and the problem of initial Pb in lunar rocks. Earth and Planetary Science Letters 14, 281–304. https://doi.org/10.1016/0012-821X(72)90128-8

Torgersen, T., Kennedy, B.M., van Soest, M.C., 2004. Diffusive separation of noble gases and noble gas abundance patterns in sedimentary rocks. Earth and Planetary Science Letters 226, 477–489. https://doi.org/10.1016/j.epsl.2004.07.030

U.S. Geological Survey, 2019. Mineral commodity summaries 2019: U.S. Geological Survey.

Vengosh, A., Starinsky, A., Kolodny, Y., Chivas, A.R., Raab, M., 1992. Boron isotope variations during fractional evaporation of sea water: New constraints on the marine vs. nonmarine debate. Geology 20, 799. https://doi.org/10.1130/0091-7613(1992)020<0799:BIVDFE>2.3.CO;2

Vigar, A.J., Jones, D.G., 2009. Laramide Resources Limited. Westmoreland Uranium project. Redtree Resource update (No. MA823).

Walker, R.N., Logan, R.G., Binnekamp, J.G., 1977. Recent geological advances concerning the H.Y.C. and associated deposits, McArthur river, N.Y. Journal of the Geological Society of Australia 24, 365–380. https://doi.org/10.1080/00167617708728996

Wall, V.J., 2006. Unconformity-related uranium systems: Downunder and over the top. ASEG Extended Abstracts 2006, 1–12. https://doi.org/10.1071/ASEG2006ab189

Wiewióra, A., Weiss, Z., 1990. Crystallochemical classifications of phyllosilicates based on the unified system of projection of chemical composition: II. The chlorite group. Clay Minerals 25, 83–92. https://doi.org/10.1180/claymin.1990.025.1.09

Wilde, A.R., Mernagh, T.P., Bloom, M.S., Hoffmann, C.F., 1989. Fluid inclusion evidence on the origin of some Australian unconformity-related uranium deposits. Economic Geology 84, 1627–1642. https://doi.org/10.2113/gsecongeo.84.6.1627

Wilde, A.R., Wall, V.J., 1987. Geology of the Nabarlek uranium deposit, Northern Territory, Australia. Economic Geology 82, 1152–1168. https://doi.org/10.2113/gsecongeo.82.5.1152

Wilkinson, J.J., 2014. Sediment-Hosted Zinc–Lead Mineralization, in: Treatise on Geochemistry. Elsevier, pp. 219–249. https://doi.org/10.1016/B978-0-08-095975-7.01109-8

Williams, L.B., Hervig, R.L., Holloway, J.R., Hutcheon, I., 2001. Boron isotope geochemistry during diagenesis. Part I. Experimental determination of fractionation during illitization

of smectite. Geochimica et Cosmochimica Acta 65, 1769–1782. https://doi.org/10.1016/S0016-7037(01)00557-9

Wilson, S.A., Ridley, W.I., Koenig, A.E., 2002. Development of sulfide calibration standards for the laser ablation inductively-coupled plasma mass spectrometry technique. Journal of Analytical Atomic Spectrometry 17, 406–409. https://doi.org/10.1039/B108787H

Wingate, M.T., Pirajno, F., Morris, P.A., 2004. Warakurna large igneous province: A new Mesoproterozoic large igneous province in west-central Australia. Geology 32, 105–108. https://doi.org/10.1130/G20171.1

Worden, K., Carson, C., Scrimgeour, I., Lally, J., Doyle, N., 2008. A revised Palaeoproterozoic chronostratigraphy for the Pine Creek Orogen, northern Australia: Evidence from SHRIMP U–Pb zircon geochronology. Precambrian Research 166, 122–144. https://doi.org/10.1016/j.precamres.2007.05.009

Yang, J., Large, R.R., Bull, S., Scott, D.L., 2006. Basin-scale numerical modeling to test the role of buoyancy-driven fluid flow and heat transfer in the formation of stratiform Zn-Pb-Ag deposits in the northern Mount Isa basin. Economic Geology 101, 1275–1292. https://doi.org/10.2113/gsecongeo.101.6.1275

Yavuz, F., Karakaya, N., Yıldırım, D.K., Karakaya, M.Ç., Kumral, M., 2014. A Windows program for calculation and classification of tourmaline-supergroup (IMA-2011). Computers & Geosciences 63, 70–87. https://doi.org/10.1016/j.cageo.2013.10.012

Ye, L., Cook, N.J., Ciobanu, C.L., Yuping, L., Qian, Z., Tiegeng, L., Wei, G., Yulong, Y., Danyushevskiy, L., 2011. Trace and minor elements in sphalerite from base metal deposits in South China: a LA-ICPMS study. Ore Geology Reviews 39, 188–217. https://doi.org/10.1016/j.oregeorev.2011.03.001

Yellishetty, M., Huston, D., Graedel, T.E., Werner, T.T., Reck, B.K., Mudd, G.M., 2017. Quantifying the potential for recoverable resources of gallium, germanium and antimony as companion metals in Australia. Ore Geology Reviews 82, 148–159. https://doi.org/10.1016/j.oregeorev.2016.11.020

Ypma, P.J.M., Fuzikawa, K., 1980. Fluid inclusion isotope studies of the Nabarlek and Jabiluka uranium deposits, Northern Territory, Australia, in: Proceedings of International Uranium Symposium on the Pine Creek Geosyncline. IAEA, Vienna, pp. 375–395.

Zane, A., Weiss, Z., 1998. A procedure for classifying rock-forming chlorites based on microprobe data. Rendiconti Lincei 9, 51–56. https://doi.org/10.1007/BF02904455

Zherebtsova, I.K., Volkova, N.N., 1966. Experimental study of behavior of trace elements in the process of natural solar evaporation of Black Sea water and Sasyk-Sivash brine. Geochemistry International 3, 656–670.

List of figures

Supplementary Figures

List of tables

Supplementary Tables

Appendix 1. Cu mineralisation and Settlement Creek Dolerite dating

Preamble

Copper is another base metal that is abundant in the McArthur Basin. Its timing in not well constrained, since the main resources occur in breccias whose age(s) is (are) uncertain. I had the chance to sample the Redbank deposit, but the samples were lost during their shipping. A proposed model for the copper mineralisation (A. Wygralak, personal communication) points out that the breccias could be related to the emplacement of the Settlement Creek Dolerite, a mafic unit intruding the sedimentary pile. As the direct Re-Os dating of copper sulphides as a poor resolution (several tens of million years), dating this dolerite would therefore give precious insights into the timing of copper mineralisation. During this PhD, a first attempt on dating the Settlement Creek Dolerite has been carried out.

Préambule

Le cuivre est un autre métal abondant dans le bassin de McArthur. Sa chronologie est mal contrainte, car la ressource principale se présente sous forme de brèches dont l'âge est incertain. J'ai eu la chance d'échantillonner le gisement de Redbank, l'un des plus important du bassin, mais les échantillons ont été perdus lors en leur acheminement vers la France. Un modèle de mise en place de la minéralisation (A. Wygralak, communication personnelle) suppose que les brèches pourraient être induites par la mise en place de la Settlement Creek Dolerite, une unité mafique qui est intrusive dans la pile sédimentaire. La datation absolue des sulfures de cuivre par la méthode Re-Os a une faible résolution (plusieurs dizaines de millions d'années) et dater cette dolérite pourrait donner des indications précieuses sur l'âge de la minéralisation cuprifère. Lors de cette thèse, un premier essai pour dater la Settlement Creek Dolerite a été entrepris.

Appendix 1.1. Introduction and sampling

In the Northern Territory and Queensland, mafic and dolerite dykes span over more than 1600 Ma (Figure A1-1), confirming the low probability of correlating easily the Settlement Creek Dolerite with other mafic events, and thus validating the importance of determining their age and geodynamic relavance. The Settlement Creek Dolerite is thought to be younger than the Echo Sandstone (A. Wygralak, personal communication), a formation correlated with the Nyanantu Formation (Ahmad and Munson, 2013), which hosts detrital zircons dated at 1708 ± 4 Ma (Page et al., 2000). The dolerite is therefore younger than 1708 Ma, but not other timing constraint is noted. The Settlement Creek Dolerite was previously seen as volcanics consisting of a series of lava flows (Ahmad and Wygralak, 1989), but is now considered as composite set

of dolerite sheets 20–200m thick recognised throughout the southern McArthur Basin (Rawlings, 2006). The main rock type of the Settlement Creek Dolerite is fine to medium, grey to green/black aphyric dolerite comprising plagioclase, pyroxene and opaque oxides. Dolerite is altered in most areas and assumes a green or pink/brown colour (Rawlings, 2006).

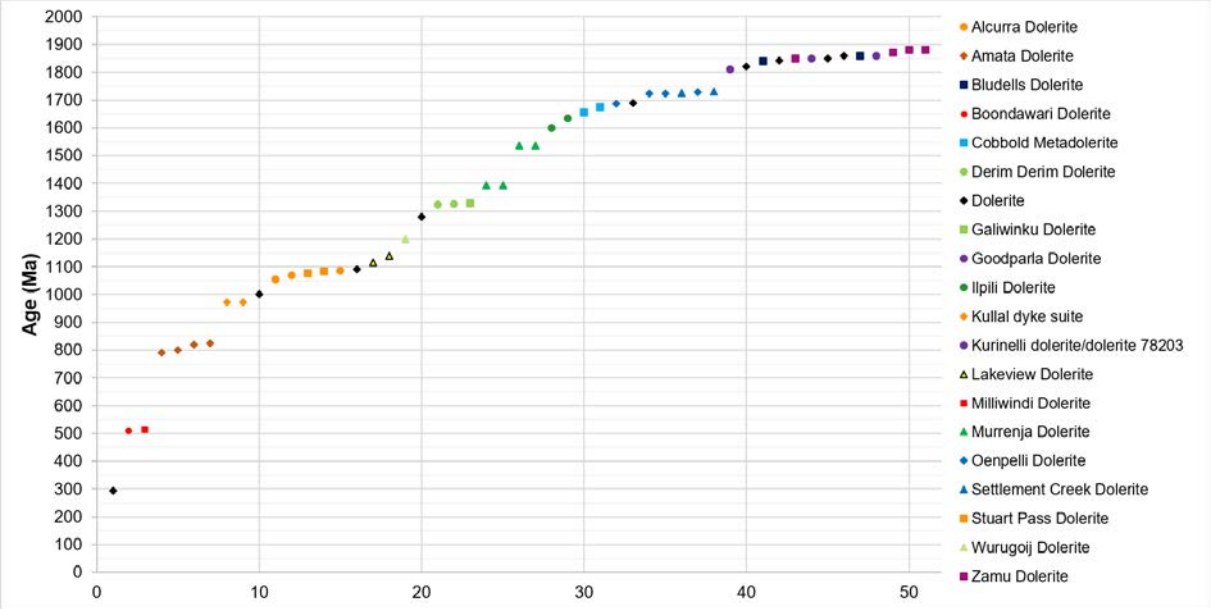

***Figure A1-1**: Synthesis of dating results on mafic and dolerite dykes in the Northern Territory and Queensland. The errors bars are not represented because they are mainly <10 Ma and could therefore not been represented at this scale. Compiled from the Australian Stratigraphic Units Database.*

Three drillcores were sampled and their location are shown on Figure A1-2, and the depth of the studied samples is presented in Table A1-1. Drillcore DD91HC1 is only 4 km from the Redbank deposit which is a breccia type deposit.

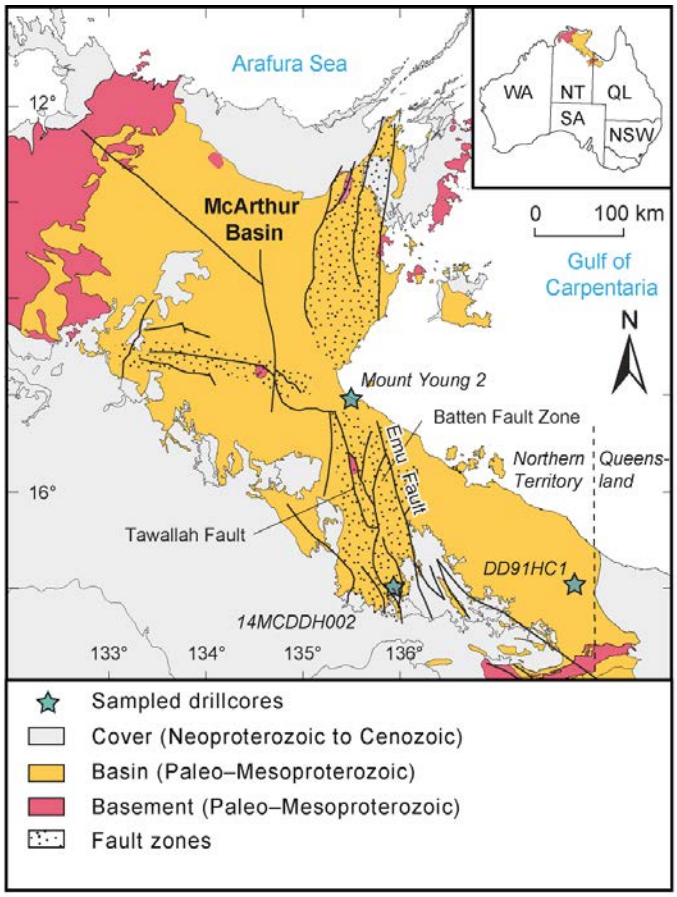

Drillhole #	Depth (m)
DD91HC1	347
DD91HC1	347.4
DD91HC1	347.5
Mount Young 2	141.6
Mount Young 2	145.8
14MCDDH002	168.7
14MCDDH002	192.8

***Table A1-1**: Drillholes sampled for U-Pb dating on zircons from the Settlement Creek Dolerite*

***Figure A1-2**: Location of the sampled drillcores from U-Pb dating on zircons of the Settlement Creek Dolerite in the McArhur Basin.*

Appendix 1.2. Results

Seven thin sections were studied to try to determine as many Zr-bearing minerals as possible for potential dating. The first criterion in choosing the samples was the grain size, so to have the chance to obtain Zr-bearing minerals as coarse as possible. Thin sections were studied by SEM (see above chapters for method). EDS give the semi-quantitative composition results of the Zr-bearing mineral: 44–50% Zr, 12–15% Si and 32–35% O, consistent with the mineral being zircon. Their grain size ranges between 20 and 60 µm (Figure A1-3). Zircons look euhedral with sharp edges, and present zoning and probably traces of detrital core (cracks). As this rock is plutonic, we can surmise that these zircons have a magmatic rim on a detrital core. Since the resetting temperature of zircons is lower than or close to the crystallisation temperature of mafic rocks, the U-Pb ages could therefore correspond to the age of the Settlement Creek Dolerite, even for the detrital parts of the zircons.

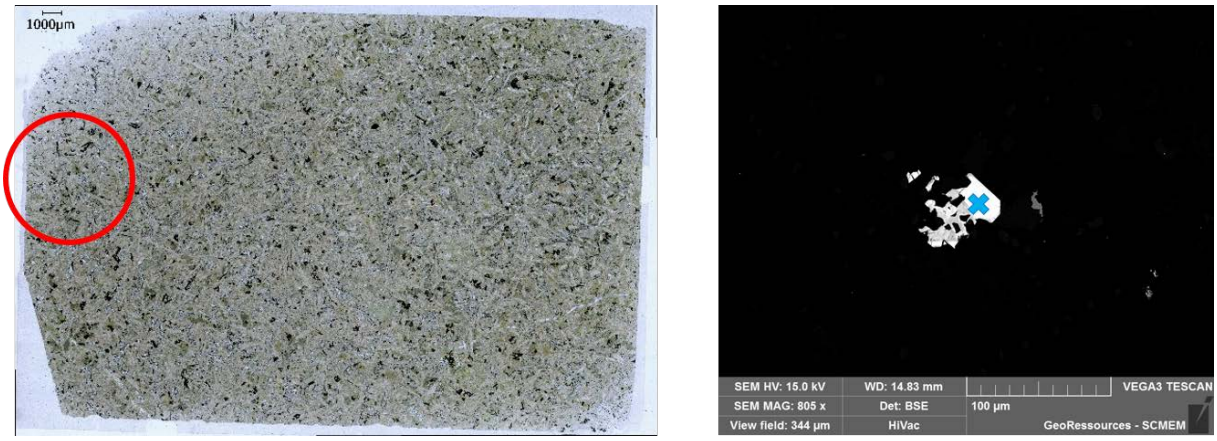

***Figure A1-3**: Example of thin section from the Settlement Creek Dolerite and SEM image of the zircon in the mafic rock with the analysed spot. Note that this analysis spot gave the highest isotopic ratio, close to the Concordia curve. Sample DD91HC1 347.0m.*

The first tested dating method was Thermal Ionisation Mass Spectrometry (TIMS) undertaken at the Department of Earth and Atmospheric Sciences (University of Alberta, Edmonton, Canada) by Larry Heaman. The precision could be several million years for the expected ages between 1.8 and 1.5 Ga. Unfortunately, no zircon grains larger than 20µm was present in the crushed sample.

The other possibility was to date thin sections by SIMS at the CRPG Lab (Vandœuvre-lès-Nancy, France) with a spot size of 10 µm that would give satisfactory results. After keeping the seven best analyses, the calculated age is 1340 ± 180 Ma (Figure A1-4). The $^{207}Pb/^{206}Pb$ ages are consistent with the calculated ages between 1539 and 1190 Ma. Even if the error and the MSWD are big, the age of the intrusion is probably younger than 1500 Ma, much younger than one that is presently expected. Since no age could be interpreted to be a detrital one, the resetting hypothesis for the detrital zircons is probably correct.

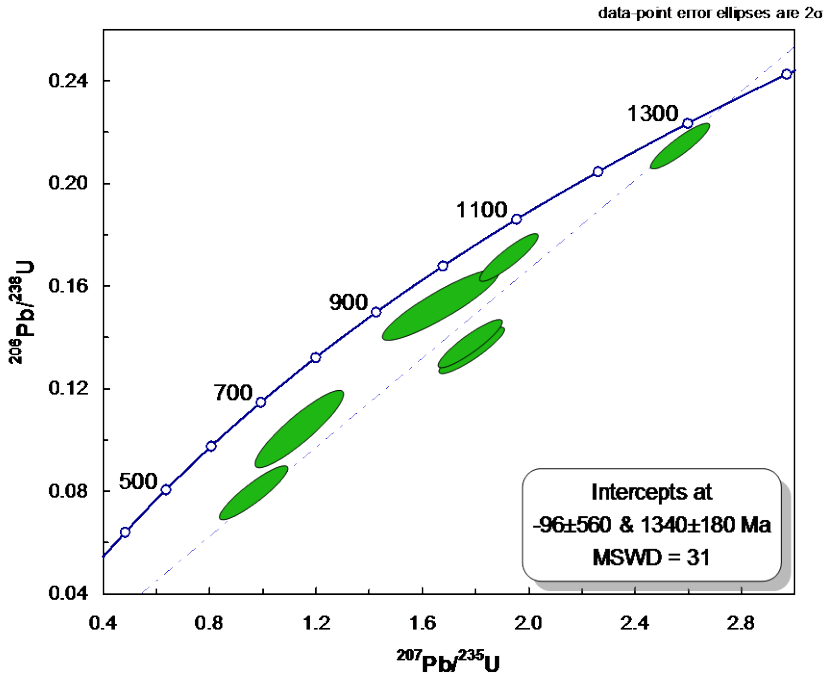

***Figure A1-4**: Concordia diagram on seven selected zircons from the Settlement Creek Dolerite, leading to 1340 ±180 Ma with a MSWD of 31.*

Appendix 1.3. Conclusion and perspectives

In conclusion, TIMS would be the favoured method for the dating of Zr-bearing minerals crystals because of its precision. However, the size of the zircons in the studied samples is too small for this method. Another method can be applied only to zircons, which is the Zr-bearing mineral in the Settlement Creek Dolerite. The size of the analyser spot with SIMS (10µm) is small enough for this kind of material. Further studies to date this formation could be tested by SIMS or SHRIMP on a large amount of zircons, and if possible with the more homogeneous and largest grains; thus leading potentially to a more precise age on the Concordia.

Appendix 2. FindAge, a Python program for model ages calculation based on Pb isotopes

Preamble

In this chapter, a Python program that can calculate rapidly different model ages is presented. This program is the result of a collaboration with Margaux Raguenel, a PhD student from the Research for Integrative Numerical Geology team in the GeoRessources lab. Based on the equations for different models, she could propose an iterative Python code that was then improved and tested with the data acquired during this PhD. The data used in this chapter are all the lead isotopes results on galena presented in the Chapters 5 and 6, respectively from the McArthur River deposit and from the Myrtle and Walford Creek deposits and Caranbirini prospect. Lead isotopes were capital to determine the number of lead source(s) for galena and their model age(s).

Préambule

Dans ce chapitre, un programme informatique permettant de calculer rapidement différents âges modèles est présenté. Ce programme est le résultat d'une collaboration avec Margaux Raguenel, une doctorante de l'équipe « Research for Integrative Numerical Geology » du laboratoire GeoRessources. En se basant sur les équations définissant différents modèles, elle a pu proposer un code Python itératif, qui a été par la suite testé et amélioré avec les données acquises durant cette thèse. Les données utilisées dans ce chapitre sont tous les résultats d'isotopes du plomb sur les galènes présentées dans les Chapitres 6 et 7, provenant respectivement du gisement de McArthur River et des gisements ou indices de Myrtle, Caranbirini et Walford Creek. Les isotopes du plomb ont été un outil indispensable pour déterminer le nombre de source(s) du plomb et leur(s) âge(s) modèle(s).

Les isotopes du plomb sont largement utilisés sur les sulfures (galène, pyrite, pyrrhotite, sphalérite, chalcopyrite, magnétite, hématite, arsénopyrite…) et sur des roches totales pour obtenir des informations sur les âges modèles des sulfures. Pour certains minéraux, cette méthode est la seule manière d'estimer leur âge. Les ratios d'isotopes du plomb sont mesurés par TIMS, SIMS ou MC-ICP-MS. L'un des modèles les plus utilisés pour estimer les âges modèles est celui de Stacey et Kramers (1975) qui se décompose en deux étapes : dans la première, le manteau évolue jusqu'à 3.7 Ga, et la formation de la croûte conduit à un deuxième épisode avec des paramètres différents. Un autre modèle a été développé par Cumming et Richards (1975), dans lequel un paramètre augmente linéairement durant toute l'histoire de la Terre. Cependant, ce modèle n'est pas approprié pour le nord de l'Australie et Sun et al. (1996) l'ont modifié pour qu'il soit en cohérence avec les données australiennes. Ce nouveau programme Python offre la possibilité de calculer rapidement les âges modèles avec les modèles de Sun et al. (1996) et de Stacey et Kramers (1975) et a été conçu pour les

échantillons Protérozoïques du Craton Nord Australien. Cependant, le modèle de Sun et al. (1996) est adapté de celui de Cumming et Richards (1975) et seule la valeur d'un paramètre change, ce qui rend cet algorithme facilement utilisable pour les trois modèles.

Appendix 2.1. Introduction

Lead isotopes are wildly used on sulphides (galena, pyrite, pyrrhotite, sphalerite, chalcopyrite, magnetite, hematite, arsenopyrite…) and whole rock to get information about the model age of the sulphides minerals. For some minerals, this method is the only way to estimate their age. Lead isotopic ratios can be measured by TIMS, SIMS or MC-ICP-MS. One of the most used method for model age estimations is the one of Stacey and Kramers (1975) which implies two stages: in the first one, the mantle evolves until 3.7 Ga, where crust formation leads to a second stage with different parameters. Another method was developed by Cumming and Richards (1975) in which a parameter increases linearly over the history of the Earth. However, this last model is not well appropriate for the Northern part of Australia and Sun et al. (1996) modified it to better fit the Australian data. This new Python program aims to quickly calculate the model ages thanks to the Sun et al. (1996) and Stacey and Kramers (1975) models as it was designed for Proterozoic samples of the North Australian Craton. However, as the Sun et al. (1996) model is adapted from the Cumming and Richards (1975) one only by changing one parameter value, this algorithm can be easily used for both models.

Appendix 2.2. Lead isotopes evolution models

Appendix 2.2.1. Cumming and Richard (1975) and Sun et al. (1996) models

The Cumming and Richards (1975) model is based on the hypothesis of a steady growth in μ (representing the $^{238}U/^{204}Pb$ ratio of a given reservoir) through time. Based on the $^{20P}Pb/^{204}Pb$ and $^{207}Pb/^{204}Pb$, ratios, it is possible to get the model age of crystallisation of the studied mineral by iteration. In this program, the model used is the one developed by Sun et al. (1996) for the North Australian Craton, which is the host of the mineralisation studied in this study. The equations in this model are the following ones:

$$\left(\frac{^{206}Pb}{^{204}Pb}\right)_t = A_0 + \mu_{206} \times \left[e^{4.509\times\lambda_{238}} \times \left(1 - \varepsilon \times \left(4.509 - \frac{1}{\lambda_{238}}\right)\right) - e^{t\times\lambda_{238}} \times \left(1 - \varepsilon \times \left(t - \frac{1}{\lambda_{238}}\right)\right)\right]$$

$$\Leftrightarrow \mu_{206} = \left(\left(\frac{^{206}Pb}{^{204}Pb}\right)_t - A_0\right)/\left[e^{4.509\times\lambda_{238}} \times \left(1 - \varepsilon \times \left(4.509 - \frac{1}{\lambda_{238}}\right)\right) - e^{t\times\lambda_{238}} \times \left(1 - \varepsilon \times \left(t - \frac{1}{\lambda_{238}}\right)\right)\right]$$

And

$$\left(\frac{^{207}Pb}{^{204}Pb}\right)_t = B_0 + \frac{\mu_{207}}{137.88} \times [e^{4.509\times\lambda_{235}} \times \left(1 - \varepsilon \times \left(4.509 - \frac{1}{\lambda_{235}}\right)\right) - e^{t\times\lambda_{235}} \times \left(1 - \varepsilon \times \left(t - \frac{1}{\lambda_{235}}\right)\right)]$$

$$\Leftrightarrow \quad \mu_{207} = 137.88 \times (\left(\frac{^{207}Pb}{^{204}Pb}\right)_t - B_0)/[e^{4.509\times\lambda_{235}} \times \left(1 - \varepsilon \times \left(4.509 - \frac{1}{\lambda_{235}}\right)\right) - e^{t\times\lambda_{235}} \times \left(1 - \varepsilon \times \left(t - \frac{1}{\lambda_{235}}\right)\right)]$$

These systems are solved when $\Delta\mu = \mu_{206} - \mu_{207}$ are close to zero, and yields t and μ_{206}~μ_{207}. Cumming and Richards (1975) have chosen the rate factor $\varepsilon = 0.050 \times 10^{-9}$ yr^{-1}. In the Sun et al. (1996) model, the ε value has been modified, with $\varepsilon = 0.0833 \times 10^{-9}$ yr^{-1} to better fit with the Australian data. This parameter can be modified in the program to calculate with one of the two models.

At the present time, the calculations are made in an Excel sheet, with an example reproduced in Table A2-1. The Excel sheet was developed by AGSO-CSIRO and was given by David Huston (Geoscience Australia). For every measured $^{206}Pb/^{204}Pb$ – $^{207}Pb/^{204}Pb$ pair, the user has to change the ages by hand. The closest to zero Δμ value gives the model age and μ value. This process takes about one minute for each analysis and when doing compilation at large scale with more than 500 data, it can take a long time.

$^{206}Pb/^{204}Pb$	$^{207}Pb/^{204}Pb$	$^{208}Pb/^{204}Pb$	T (Ga)	μ_{206}	μ_{207}	Δμ
17	15.6537	35.8796	1.3	13.0487	13.0489	-0.00022
17	15.6537	35.8796	1.2999	13.0483	13.0488	-0.00053
17	15.6537	35.8796	1.2998	13.0479	13.0487	-0.00083
17	15.6537	35.8796	1.2997	13.0475	13.0487	-0.00113
17	15.6537	35.8796	1.2996	13.0472	13.0486	-0.00143
17	15.6537	35.8796	1.2995	13.0468	13.0485	-0.00173
17	15.6537	35.8796	1.2994	13.0464	13.0485	-0.00204
17	15.6537	35.8796	1.2993	13.046	13.0484	-0.00234
17	15.6537	35.8796	1.2992	13.0457	13.0483	-0.00264
Enter data	Enter data	Enter data	Enter guess			| Δμ | < 0.0015 Target

Table A2-1 *: Example of the Excel sheet used for the age estimation according to the Sun et al. (1996) model*

Appendix 2.2.2. Stacey and Kramers (1975) model

The Stacey and Kramers (1975) model implies two stages in Earth's history: in the first one, the mantle evolves until 3.7 Ga, where crust formation leads to a second stage with different parameters. The equations in this model are the following ones:

$$\left(\frac{^{206}Pb}{^{204}Pb}\right)_t = A_0 + \mu_p \times (e^{\lambda_{238}\times 4.57} - e^{\lambda_{238}\times 3.7}) + \mu_{206} \times (e^{\lambda_{238}\times 3.7} - e^{\lambda_{238}\times t})$$

$$\Leftrightarrow \mu_{206} = [\left(\frac{^{206}Pb}{^{204}Pb}\right)_t - A_0 - \mu_p \times \left(e^{\lambda_{238}\times 4.57} - e^{\lambda_{238}\times 3.7}\right)]/(e^{\lambda_{238}\times t} - e^{\lambda_{238}\times t})$$

and

$$\left(\frac{^{207}Pb}{^{204}Pb}\right)_t = B_0 + \frac{\mu_p}{137.88} \times (e^{\lambda_{235}\times 4.57} - e^{\lambda_{235}\times 3.7}) + \frac{\mu_{207}}{137.88} \times (e^{\lambda_{235}\times 3.7} - e^{\lambda_{235}\times t})$$

$$\Leftrightarrow \mu_{207} = [\left(\frac{^{207}Pb}{^{204}Pb}\right)_t - B_0 - \frac{\mu_p}{137.88} \times \left(e^{\lambda_{235}\times 4.57} - e^{\lambda_{235}\times 3.7}\right)] \times 137.88/((e^{\lambda_{235}\times 3.7} - e^{\lambda_{235}\times t})$$

These systems are solved when $\Delta\mu = \mu_{206} - \mu_{207}$ are close to zero, and yields t and $\mu_{206} \sim \mu_{207}$.

Appendix 2.3. Program

The program takes as input an Excel sheet in .csv with four columns: Sample name, $^{206}Pb/^{204}Pb$, $^{207}Pb/^{204}Pb$ and $^{208}Pb/^{204}Pb$ ratios. The output is an Excel sheet in .csv with nine columns: Sample name, calculated age with the Sun et al. (1996) model in Ga, μ_{206} (= $^{238}U/^{204}Pb$ ratio for the ^{206}Pb decay chain in the Sun et al. (1996) model), μ_{207} (= $^{238}U/^{204}Pb$ ratio for the ^{207}Pb decay chain in the Sun et al. (1996) model), $\Delta\mu = \mu_{206} - \mu_{207}$ in the Sun et al. (1996) model, and the same parameters for the Stacey and Kramers (1975) model.

The algorithm works as follows with two loops, first for the Sun et al. (1996) model and then for the Stacey and Kramers (1975) one:

- Initialisation of the constants
- initialisation of the parameters:
  - maximum age (here fixed at 1.9 Ga because of the expected ages of the rocks/minerals)
  - incrementation: 0.0001 Ga
- reading of the input data
  - calculation of the μ values: μ_{206}, μ_{207} at the current age
- if $\Delta\mu \neq 0$
  - calculate new μ_{206}, μ_{207} and $\Delta\mu$ values with an age that is 0.0001 Ga younger than the one tested, while [abs(calculated Δμ) < [abs(previous calculated Δμ)]
- print the results in the output file

Appendix 2.4. Constants and unknowns

The program works with the following constants:

$A_0 = \left(\frac{^{206}Pb}{^{204}Pb}\right)_{t_0} = 9.307$ (Tatsumoto et al., 1973)

$B_0 = \left(\frac{^{207}Pb}{^{204}Pb}\right)_{t_0} = 10.294$ (Tatsumoto et al., 1973)

$\varepsilon = 0.0833$ (rate factor, Sun et al., 1996)

$\lambda_{238} = 0.155125 \times 10^{-9}$ yr^{-1} is the decay constant of ^{238}U

$\lambda_{235} = 0.98485 \times 10^{-9}$ yr^{-1} is the decay constant of ^{235}U

$\mu_p = 7.192$ is the $^{238}U/^{204}Pb$ ratio of the Mantle (Tatsumoto et al., 1973)

$\left(\frac{^{206}Pb}{^{204}Pb}\right)_t$ is the measured $^{206}Pb/^{204}Pb$ ratio

$\left(\frac{^{207}Pb}{^{204}Pb}\right)_t$ is the measured $^{207}Pb/^{204}Pb$ ratio

The 1/137.88 ratio corresponds to the $^{235}U/^{238}U$ ratio, known to be constant for all U of normal isotopic composition in the Earth at the present time (Halla, 2018).

The unknowns determined by the program are: t (model age of the analysed galena or sulphide) and the μ value at that time that is found when $\mu_{206} = \mu_{206}$, both parameters for the two proposed models.

Appendix 2.5. Results, discussion and perspectives

This program can be used to calculate in a short time lots of model ages and μ values based on lead isotopes ratios. As an example, it allows the calculation of approximately 500 data in a few seconds, and with different models (two in the proposed program, and the parameters are easy to change for other similar models). For the PhD, this program was used to calculate quickly the ages of the end-members presented in the previous chapters, but its bigger scope could be in synthesis at basin or regional scale where the amount of data are consequent.

The program also provides a graphical representation of the analyses (black dots) as well as the isochrones for two different models (Stacey and Kramers, 1975 and Sun et al., 1996). The isochrons defined for the moment in the program are from 1200 to 2000 Ma because they were the ones used in this PhD, but a further development with isochrons from 0 to 2000 Ma is planned. The Figure A2-1 presents the results for all the lead isotopes data acquired during the PhD.

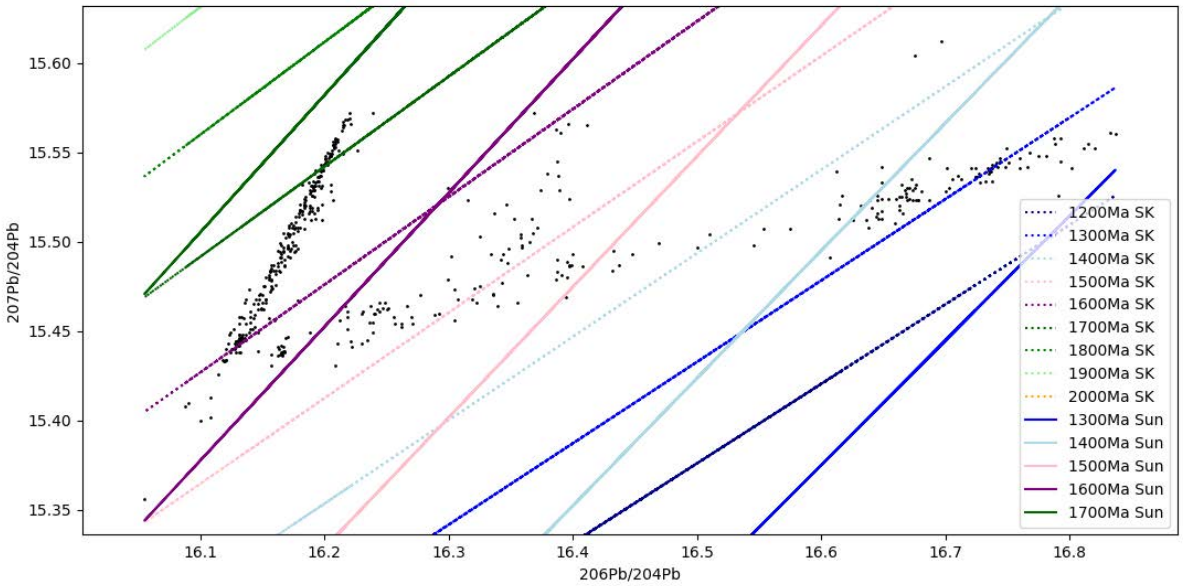

***Figure A2-1**: Example of diagram provided by the FindAge program, with several isochrons (SK = Stacey and Kramers, 1975 and Sun = Sun et al., 1996).*

The perspectives for this program are to publish it in a short paper so that the code could be used for others lead isotopes study. The objective is to design it user friendly also for people less familiar with the Python language by creating an interface in which the user could specify where the Excelsheet containing the data is, which model he wants to use if he wants the graphical representation or not. In addition, the μ curves for different chosen values could be added to the graphical representation.

Résumé

Le bassin sédimentaire de McArthur (Northern Territory et Queensland, Australie) est associé à de nombreuses minéralisations diagénétiques/hydrothermales en uranium, cuivre, plomb et zinc dont certains gisements de classe mondiale (ex : Ranger et McArthur River). Certains gisements correspondent à des types de minéralisation bien définis (ex : uranium de type discordance, plomb-zinc de type Sediment-Hosted Massive Sulphide « SHMS »), d'autres ne sont pas reliés à un type précis. Un épisode minéralisateur majeur vers 1650-1600 Ma est reconnu dans les gisements d'uranium au nord (Alligator Rivers Uranium Field – ARUF) et au sud (Westmoreland) du bassin et en plomb-zinc dans le centre (Batten Fault Zone) et a participé au stock métallifère exceptionnel du bassin. De plus, s'il n'est pas établi que les fluides responsables des minéralisations en uranium et plomb-zinc sont de même origine, leurs caractéristiques en termes de température et salinité sont similaires. Cette thèse propose de s'intéresser aux principaux facteurs contrôlant la distribution des ressources métalliques à grande échelle dans ce bassin sédimentaire intracratonique, en étudiant les minéralisations avec une approche essentiellement géochronologique et géochimique et en caractérisant les fluides associés afin de définir leur âge, leur température et certaines de leurs conditions de mise en place.

Une synthèse des données d'inclusions fluides et la détermination de leur composition en gaz rares (Ar, Kr, Xe) et en halogènes (Cl, Br, I) indiquent que des saumures chlorurées sodi-calciques d'origine évaporitique et des fluides peu salés probablement d'origine météorique ont été impliqués dans les minéralisations en uranium de l'ARUF et de la zone de Westmoreland. Cette conclusion est corroborée par l'analyse géochimique et isotopique des tourmalines magnésiennes du gisement de Ranger (ARUF) permettant de relier le métasomatisme à bore et magnésium, caractéristique des altérations proximales de la minéralisation, aux interactions entre les saumures évaporitiques et le socle cristallin. En revanche, l'étude détaillée de la minéralisation uranifère de la zone de Westmoreland (âges U-Pb, teneurs en terres rares, composition des chlorites) montre une dynamique de mise en place différente des processus typiques des gisements de type « discordance » de la zone de ARUF, une importance moindre des interactions entre les fluides minéralisateurs et le socle et une succession d'évènements minéralisateurs possiblement entre 1650 et 350 Ma.

La composition isotopique du plomb des galènes de différentes lentilles minéralisées du gisement McArthur River de type SHMS met en évidence l'implication de deux réservoirs crustaux felsiques en tant que sources de plomb. Ces deux réservoirs ont été mobilisés de manière synchrone et répétée par des fluides hydrothermaux vers 1640 Ma pour former les différentes lentilles. D'autres gisements ou indices enregistrent plusieurs épisodes plus récents (jusqu'à environ 1300 Ma) qui impliquent un mélange entre trois sources de plomb. La signature géochimique des sphalérites et galènes de ces gisements ou indices à plomb-zinc traduit notamment des températures de formation décroissantes pour les épisodes successifs (de 220 °C environ à moins de 100 °C).

En plus de l'épisode majeur vers 1650-1600 Ma, l'histoire métallogénique du bassin montre de nombreuses autres évidences de cristallisation ou de remobilisation du stock de métaux. Certains épisodes de circulation des fluides sont à relier à des grands évènements géodynamiques, comme des inversions du bassin ou des orogenèses situées à des centaines de kilomètres de la zone d'étude. Il semble que les migrations à grande échelle des fluides minéralisateurs (horizontale dans les grands aquifères gréseux, et verticale dans les zones de failles majeures) ont permis la mobilisation des métaux dans différents réservoirs du bassin et du socle et leur précipitation sélective dans des zones favorables.

Abstract

The sedimentary McArthur Basin (Northern Territory and Queensland, Australia) is associated with numerous diagenetic/hydrothermal uranium, copper, lead and zinc concentrations, including some world-class deposits (e.g., Ranger and McArthur River). Some deposits correspond to styles of mineralisation well defined such as unconformity-type for uranium and Sediment-Hosted Massive Sulphide (SHMS) for lead-zinc, but others are not linked to a specific type. A major mineralising event at around 1650-1600 Ma is recorded in the uranium deposits in the North (Alligator Rivers Uranium Field – ARUF) and South (Westmoreland) parts of the basin and in lead-zinc deposits in the centre (Batten Fault Zone), and accounted for the exceptional metalliferous stock of the basin. In addition, even if it has not been established that the fluids responsible for uranium and lead-zinc mineralisation share a common origin, their characteristics in terms of temperature and salinity are similar. This PhD focused on the major factors controlling metals resources distribution at a large scale in this intracratonic sedimentary basin by studying the mineralisation with a geochronological and geochemical approach, and by characterising the associated fluids in order to define its age, temperature and emplacement conditions.

A synthesis of fluid inclusions and the determination of their noble gas (Ar, Kr, Xe) and halogen (Cl, Br, I) composition indicate that Na-Ca-brines of evaporitic origin and low-salinity fluids probably of meteoric origin have been involved in the uranium mineralisation in the ARUF and the Westmoreland area. This is confirmed by geochemical and isotopic analyses of the Mg-rich tourmaline from the Ranger deposit (ARUF) that link the boron and magnesium metasomatism, a fingerprint of the mineralisation proximal alterations, to the interactions between evaporitic brines and crystalline basement. However, the detailed study of the uranium mineralisation in the Westmoreland area (U-Pb ages, REE content, and chlorite composition) shows emplacement dynamics that are different from the typical processes of unconformity-related deposits in the ARUF, a lower importance of the interactions between mineralising fluids and the basement, and a succession of mineralising events possibly between 1650 and 350 Ma.

The lead isotope composition in galena from different mineralised lenses of the SHMS McArthur River deposit highlights the implication of two felsic crustal reservoirs as lead sources. These two reservoirs have been synchronously and repeatedly mobilised by hydrothermal fluids around 1640 Ma to form the different lenses. Other deposits or prospects record several younger events (until around 1300 Ma) that involve a mixing between three lead sources. The geochemical signature of the sphalerite and galena from these lead-zinc deposits or prospects states specific emplacement conditions, in particular decreasing formation temperature in the successive episodes (approximately from 220 °C to less than 100 °C).

In addition to the major event at 1650-1600 Ma, the metallogenic history of the basin shows numerous other evidences for crystallisation or remobilisation of the metalliferous stock. Some of the fluid circulation stages are linked with geodynamic events such as basin inversions or orogeneses located a few hundreds of kilometres from the studied area. It seems that the large scale migrations of mineralising fluids (i.e., overall horizontal in the large sandstone aquifers, and vertical in the major faults zones) allowed the metal mobilisation in different reservoirs from the basin and the basement, and their selective precipitation within favourable zones.